

AD-A130 160

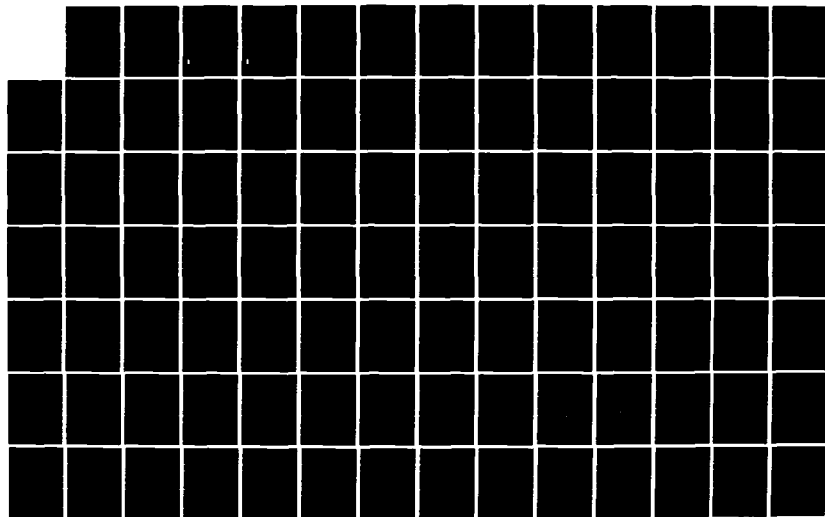
THE QUANTUM DYNAMICS OF CHEMICAL REACTIONS(U)
CALIFORNIA INST OF TECH PASADENA DIV OF CHEMISTRY AND
CHEMICAL ENGINEERING A KUPPERMANN 31 MAR 83
AFOSR-TR-83-0565 AFOSR-81-0235

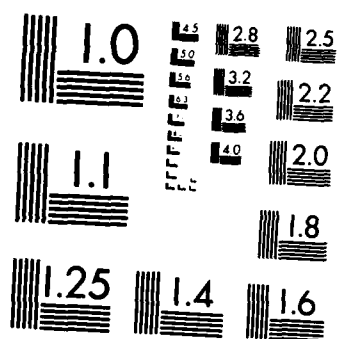
1/6

UNCLASSIFIED

F/G 20/10

NL





MICROCOPY RESOLUTION TEST CHART
NATIONAL BUREAU OF STANDARDS-1963-A

(11)

AIR FORCE OFFICE OF SCIENTIFIC RESEARCH

FINAL TECHNICAL REPORT

AD A130160

Institution: Division of Chemistry and Chemical Engineering
California Institute of Technology
Pasadena, California 91125

Title of Project: The Quantum Dynamics of Chemical Reactions

Grant/Contract No.: AFOSR-81-0235

Period: 1 July 1981 through 30 June 1982

Principal Investigator:

Aron Kuppermann
Aron Kuppermann

Date: 31 March 1983

DTIC
SELECTED
JUL 5 1983
A

DTIC FILE COPY

83 07 01 002

unclassified

SECURITY CLASSIFICATION OF THIS PAGE (When Data Entered)

REPORT DOCUMENTATION PAGE		READ INSTRUCTIONS BEFORE COMPLETING FORM
1. REPORT NUMBER AFOSR-TR- 83-0565	2. GOVT ACCESSION NO. A130160	3. RECIPIENT'S CATALOG NUMBER
4. TITLE (and Subtitle) THE QUANTUM DYNAMICS OF CHEMICAL REACTIONS		5. TYPE OF REPORT & PERIOD COVERED Final Scientific 01 July 1981 - 30 June 1982
7. AUTHOR(s) Aaron Kupperman		6. PERFORMING ORG. REPORT NUMBER
9. PERFORMING ORGANIZATION NAME AND ADDRESS Div of Chemistry & Chemical Engineering California Institute of Technology Pasadena, CA 91125		8. CONTRACT OR GRANT NUMBER(s) AFOSR-81-0235
11. CONTROLLING OFFICE NAME AND ADDRESS Air Force Office of Scientific Research/NC Building 410 Bolling AFB, DC 20332		10. PROGRAM ELEMENT, PROJECT, TASK AREA & WORK UNIT NUMBERS 61102F 2303/B1
14. MONITORING AGENCY NAME & ADDRESS (if different from Controlling Office)		12. REPORT DATE Mar 1983
		13. NUMBER OF PAGES 480
		15. SECURITY CLASS. (of this report) unclassified
		15a. DECLASSIFICATION/DOWNGRADING SCHEDULE
16. DISTRIBUTION STATEMENT (of this Report) Approved for public release; distribution unlimited.		
17. DISTRIBUTION STATEMENT (of the abstract entered in Block 20, if different from Report)		
18. SUPPLEMENTARY NOTES		
19. KEY WORDS (Continue on reverse side if necessary and identify by block number) Elementary reactions Three-atom exchange reactions Three-body recombination collisions Vibrational quenching		
20. ABSTRACT (Continue on reverse side if necessary and identify by block number) over		

DD FORM 1 JAN 73 1473

unclassified

SECURITY CLASSIFICATION OF THIS PAGE (When Data Entered)

83 07 01 002

~~UNCLASSIFIED~~

1. PROJECT ABSTRACT

In this project, we developed accurate and approximate methods for calculating cross sections of elementary reactions. These methods were applied to systems of importance for the fundamental aspects of chemical dynamics and for advanced technologies of interest to the United States Air Force. The applications included calculations of three-atom exchange reactions, break-up and three-body recombination collisions and vibrational quenching by reaction. These calculations improved our understanding of such processes and permitted an assessment of some approximate methods.

A

~~UNCLASSIFIED~~

TABLE OF CONTENTS

1. Project Abstract.....	1
2. Hyperspherical Coordinates in Collinear Atom-Diatomic Collisions.....	2
3. Collinear Quantum Mechanical Study of the Reactions H + FH, D + FH and H + FD.....	7
4. Symmetrized Hyperspherical Coordinates for Three-Dimensional Quantum Mechanical Reactive Scattering Calculations.....	9
5. Three-Dimensional Quantum Mechanical Reactive Scattering by the Matching Method.....	14
6. Methods for Quantum Mechanical Reactive Scattering.....	16
7. Professional Personnel.....	17
8. Reprints and Preprints.....	18
9. Invited Seminars, Conferences and Lectures.....	20

Appendices



Accession No.	
DTIC	
Copy	
Inspected	
2	

A

AIR FORCE OFFICE OF TECHNICAL SEARCH (AFTSO)
NOTICE
This document is a technical report and is
not to be distributed outside the Air Force.
Distribution is limited to the following:
MATTHEW J. WILSON
Chief, Technical Information Division

1. PROJECT ABSTRACT

In this project, we developed accurate and approximate methods for calculating cross sections of elementary reactions. These methods were applied to systems of importance for the fundamental aspects of chemical dynamics and for advanced technologies of interest to the United States Air Force. The applications included calculations of three-atom exchange reactions, break-up and three-body recombination collisions and vibrational quenching by reaction. These calculations improved our understanding of such processes and permitted an assessment of some approximate methods.

2. HYPERSPHERICAL COORDINATES IN COLLINEAR ATOM-DIATOMIC COLLISIONS

Prior to our development, as part of this project, of the hyperspherical coordinate method for performing accurate quantum mechanical calculations of collinear atom-diatom reactions, a variety of other methods had been invented. While those methods had been successful in studying a number of interesting systems, they could not be used for two important classes of reactions: those in which a light atom is transferred between two heavy ones, and those above the threshold for collision-induced dissociation.

The method of hyperspherical coordinates we developed was applied to a variety of systems of this and other types, and compared in several instances to the results of quasi-classical trajectory calculations. The results of these calculations and their significance is described in a series of nine papers. Four of these have been published recently and the other five are in draft stage, being readied for publication. Reprints or preprints of all nine are included in section 8, at the end of this report. We summarize here, very succinctly, these results.

2.1 Hyperspherical Coordinates in Quantum Mechanical Collinear Reactive Scattering. In this paper we describe the methods and the results of its first application. The system chosen was $H + H_2$, and the calculations are shown to be in excellent agreement with results obtained previously by other methods. They were extended to energies significantly higher than in the past, and dynamic quantum resonance effects were shown to persist to high energies and high vibrational states. In addition to being accurate, the method was shown to be more efficient than previous ones.

2.2 Collinear Quantum Mechanical Probabilities for the $I + HI \rightarrow IH + I$ Reaction Using Hyperspherical Coordinates. In this paper, the exchange of a H atom between two I atoms is considered. This is an extreme case of a

heavy-light-heavy mass combination, for which no other method has produced satisfactory results. We show that in spite of the small skew angle ($\sim 7^\circ$) in this system, the hyperspherical coordinate approach is very efficient and leads to accurate results. The resulting reaction probabilities show an oscillatory dependence on the energy, which is qualitatively reproduced by corresponding quasi-classical trajectory calculations. In addition, they display resonance behavior, which depends very strongly on the details of the potential energy surface in the strong interaction region, and which can be modeled by a vibrationally adiabatic description.

2.3 Quantum Mechanical Coupled-Channel Collision- Induced Dissociation Calculations with Hyperspherical Coordinates. In this paper we indicate how accurate collision-induced probabilities can be calculated in competition with exchange reactions, using hyperspherical coordinates. The method is applied to a simple system, and shows rapid convergence properties. These probabilities are strongly enhanced by vibrationally exciting the reagent, and their dependence on collision energy is mimicked rather well by quasi-classical trajectory calculations.

2.4 Mass Effect in Quantum Mechanical Collision-Induced Dissociation in Collinear Reactive Atom-Diatomic Molecule Collisions. I. Symmetric Systems. The calculations of the previous paper are extended to a variety of mass combinations, including heavy-light-heavy, light-heavy-light and light-light-light systems. Collision-induced dissociation is shown to be greatest in the light-heavy-light system and least in the heavy-light-heavy one. Rate constants for collision-induced-dissociation and for the competing exchange reaction channel are given and their temperature dependence is examined.

2.5 Collinear Quasi-Classical Trajectory Study of Collision-Induced Dissociation on a Model Potential Energy Surface. These quasi-classical

studies include the calculation of the partitioning of the energy of the system among the three atomic fragments, for subsequent comparison (see paper 2.6) with the corresponding quantum results. We report the formation of well defined reactivity bands for collision-induced dissociation and show that the absence of such a process at low collision energy for ground state reagent is correlated with the absence of the simplest kind of dissociative trajectory, which occurs when the reagent is vibrationally excited. The observed reactivity bands explain some interesting features of the final kinetic energy distribution functions.

2.6 Partitioning of Kinetic Energy Among Reaction Products in Collision-Induced Dissociation in Collinear Atom-Diatomic Molecule Collisions from Quantum and Classical Mechanical Calculations. The method for calculating the distribution of the kinetic energy among the dissociation fragments using quantum mechanics is presented and applied to the same system considered above (paper 2.5). By microscopic reversibility these formulas are easily applied to three-body recombination processes. These distributions have a much less irregular structure than the quasi-classical ones.

2.7 Quasi-Classical Trajectory Analysis of Reactive and Non-reactive Deactivation in the Collinear Cl + HCl System. We performed quantum calculations which show that there is near equivalence of the probabilities and rates of reactive and non-reactive deactivating processes in collisions of vibrationally excited HCl. This near equivalence is interpreted using quasi-classical trajectories for this system. We find that most vibrational deactivation occurs near the boundary between regions of reactive and non-reactive trajectories in the final action versus initial vibrational phase plots. The trajectories involved in these highly non-adiabatic collisions more or

less follow the symmetric stretch line for a period of time. We believe that this equivalence between reactive and non-reactive deactivating processes will be a feature of any symmetric heavy-light-heavy system.

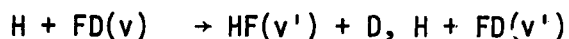
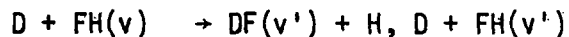
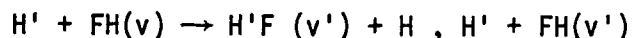
2.8 Collinear Quantum Mechanical Probabilities and Rate Constants for the $\text{Br} + \text{HCl}$ ($v=2,3,4$) Reaction Using Hyperspherical Coordinates. We find that removal of $\text{HCl}(v)$ occurs mainly by the reactive channel, leading to the nearly degenerate $\text{HBr}(v=2)$ state. The probabilities of multi-quantum transitions in non-reactive collisions and of reactive transitions to all but the near-degenerate HBr level are low, and the probabilities of reactive and non-reactive transitions to near-degenerate final states are nearly equal. These results can be understood on the basis of classical trajectories, in analogy to the discussion in paper 2.7.

2.9 Hyperspherical Coordinates in Collinear Atom-Diatomic Molecule Collisions: Convergence Properties. In this paper we present a study of the convergence properties of the hyperspherical coordinate method. In particular, state-to-state reaction probabilities and the phases of scattering matrix elements are examined as a function of the number of basis functions and the distance at which the wave function is projected from a hyperspherical coordinate basis onto a cartesian coordinate one, prior to the asymptotic analysis. The probabilities and phases are found to converge very rapidly with the size of the basis set, making this a computationally efficient method.

In addition to the results reported in these nine papers, we have initiated computational studies of the hyperspherical coordinate method using a diabatic basis function as opposed to the step-wise diabatic representation used in the calculations reported so far. We have also initiated a calculation of streamlines from the hyperspherical coordinate scattering wave functions. These studies are continuing and will be reported at a later time.

3. COLLINEAR QUANTUM MECHANICAL STUDY OF THE REACTIONS $H + FH$, $D + FH$ AND $H + FD$

In this section we present the results of quantum-mechanical coupled-channel calculations for the collinear systems



Detailed knowledge of the kinetics and dynamics of the HF/DF laser system is important if one is to successfully understand, model and improve its operation, and the studies performed, in addition to their fundamental interest, were aimed at shedding some light on this kinetics.

Enclosed at the end of this report are drafts of three papers on this topic, in near final form, being prepared for publication. A brief summary is given here.

3.1 Quantum mechanical collinear calculation of the reactions $D + FH(v = 0 - 2) \rightarrow DF(v') + H$ and $H + FD(v = 0 - 3) \rightarrow HF(v') + D$ on a realistic potential energy surface. This paper examines these exchange reactions on a potential energy surface having a realistic barrier of 40 kcal/mole. Particular attention is focused on the effectiveness of recent vibrational excitation in promoting these reactions. It is shown that the decrease in their activation energies is less than the added vibrational energy. Many aspects of their dynamics can be understood in terms of a one-dimensional vibrationally adiabatic model.

3.2 Collinear quantum mechanical calculations on the systems $\text{HF}(v) + \text{H}$ and $\text{HF}(v) + \text{D}$ on a realistic potential energy surface. In this paper we present results for reactive and non-reactive processes on the 40 kcal/mole barrier surface of the previous paper. A wide variety of dynamical properties of these systems, including state-to-state transition probabilities, activation energies and reaction product state distributions were calculated. Non-reactive processes were found to be the predominant ones, and the corresponding dynamics are understandable in terms of a simple Landau-Teller model of vibrational-to-translational energy transfer.

3.3 Barrier height dependence of dynamics in the collinear $\text{H} + \text{FH}(v)$ and $\text{D} + \text{FH}(v)$ systems. In this paper we present the results for reactive and non-reactive processes on six different potential energy surfaces which have barrier heights to exchange in the range of 1.5 to 40 kcal/mole. We analyse the effect of barrier height on the following dynamic properties: the rates and mechanisms of vibrational deactivation, the effect of reagent vibrational excitation on reaction probability and product state vibrational distribution and the importance of dynamical resonances.

4. SYMMETRIZED HYPERSPHERICAL COORDINATES FOR THREE-DIMENSIONAL QUANTUM MECHANICAL REACTIVE SCATTERING CALCULATIONS

This is an extension, to three dimensions (3D) of the method used successfully for collinear systems described in Section 2. In the collinear case, hyperspherical coordinates have permitted the study of heavy-light-heavy systems and of collision-induced dissociation, not possible by other methods, and has been a much more computationally effective method for other reactive scattering calculations which can be studied by alternative methods. It is expected that the extended 3D method will display equivalent advantages. To describe the progress achieved in this extension, let us summarize the method.

Given a system of N particles, it is possible to define in the internal configuration space of dimensions 3(N-1) a hyper-radius ρ and a set of 3N-4 hyperangles $\eta_1, \dots, \eta_{3N-4}$ in terms of which the hamiltonian of the system can be written as

$$\hat{H}(\rho, \eta) = -\frac{\hbar^2}{2\mu} \left[\frac{1}{\rho^{3N-4}} \frac{\partial}{\partial \rho} \rho^{3N-4} \frac{\partial}{\partial \rho} \right] + \frac{\hat{L}^2(\eta)}{2\mu\rho^2} + V(\rho, \eta)$$

where μ is an overall reduced mass for the system and \hat{L}^2 is a generalized angular momentum operator which depends on the set $\eta \equiv (\eta_1, \dots, \eta_{3N-4})$ of hyperangles.

The 3(N-1)-dimensional nuclear motion Schrödinger equation for an N-atom electronically adiabatic system can be written in these coordinates as

$$\hat{H}(\rho, \eta) \psi(\rho, \eta) = E\psi(\rho, \eta)$$

In order to solve it, we define a surface hamiltonian $\hat{h}(\rho; \eta)$ by the expression

$$\hat{h}(\rho; \eta) = \frac{\hat{L}^2(\eta)}{2\mu\rho^2} + V(\rho, \eta)$$

This is the portion of \hat{H} obtained by "freezing" ρ . The surface hamiltonian contains differential operators in the hyperangles η , but not in the hyper-radius ρ , which therefore appears only parametrically. We define the local surface eigenfunction $\phi_{\eta}(\eta; \rho)$ by the equation

$$\hat{h}(\eta; \rho) \phi_{\eta}(\eta; \rho) = \epsilon_{\eta}(\rho) \phi_{\eta}(\eta; \rho)$$

where $\phi_{\eta}(\eta; \rho)$ is required to be regular everywhere on the $\rho = \text{constant}$ hypersphere. The symbol η denotes a collection of quantum numbers needed to uniquely specify ϕ_{η} . The quantities $\epsilon_{\eta}(\rho)$ are the corresponding surface eigenvalues, and the curves of ϵ_{η} versus ρ are the generalization to polyatomic systems of the Bron-Oppenheimer potential energy functions for diatomic molecules. For any finite value of ρ , no matter how large, the $\phi_{\eta}(\eta; \rho)$ form an infinite discrete complete orthonormal basis set in the hyperangles η . As $\rho \rightarrow \infty$, these surface eigenfunctions correlate with the sets of atoms or molecules into which the N-atom system can be partitioned, i.e., the several possible arrangement channels for the system. We can, as a result of these considerations, expand the unknown wave function $\psi(\rho, \eta)$ in the surface function basis set ϕ_{η} everywhere in configuration space. The coefficients of this expansion will depend on the single variable ρ , and will satisfy a set of coupled ordinary differential equations in this variable.

To partially decouple these equations and decrease the numerical effort in their solution, it is convenient to adopt a partial wave expansion. Let

\hat{J}^2 and \hat{J}_z be the total system angular momentum operator (excluding spin) and its component along a laboratory-fixed z-direction. We first expand $\psi(\rho, \eta)$ in the simultaneous eigenfunctions $\psi^{JM}(\rho, \eta)$ of \hat{H} , \hat{J}^2 and \hat{J}_z , where $J(J+1)\hbar^2$ and $M\hbar$ are the eigenvalues of the last two operators, respectively. The surface functions $\phi_{\eta}^{JM}(\eta; \rho)$ are then defined as simultaneous eigenfunctions of $\hat{h}(\eta; \rho)$, \hat{J}^2 and \hat{J}_z , and the $\psi^{JM}(\rho, \eta)$ is expanded in the $\phi_{\eta}^{JM}(\rho; \eta)$. Either body- or space-fixed coordinates can be used to define the angles η .

Let us consider a triatomic system $A + BC$, in which R_{α} is the position vector of A with respect to the center of mass of BC and r_{α} is the position vector of C with respect to B. Let $\theta_{\alpha}, \phi_{\alpha}$ the polar angles of R_{α} in a laboratory-fixed frame and $\gamma_{\alpha}, \psi_{\alpha}$ the polar angles of r_{α} in a body-fixed frame whose z axis is along R_{α} . In this case, the body-fixed hyperangles are:

$$\eta \equiv \omega_{\alpha}, \theta_{\alpha}, \phi_{\alpha}, \gamma_{\alpha}, \psi_{\alpha}$$

where ω_{α} is an angle between 0 and π defined by

$$\begin{aligned} \omega_{\alpha} &= 2 \tan^{-1} \frac{r'_{\alpha}}{R'_{\alpha}} \\ R'_{\alpha} &= \left(\frac{\mu_{A,BC}}{\mu_{BC}} \right)^{1/4} R_{\alpha} \\ r'_{\alpha} &= \left(\frac{\mu_{BC}}{\mu_{A,BC}} \right)^{1/4} r_{\alpha} \end{aligned}$$

The hyper-radius is then defined by

$$\rho = (R'^2_{\alpha} + r'^2_{\alpha})^{1/2}$$

The 6 hyperspherical variables $\rho, \omega_{\alpha}, \theta_{\alpha}, \phi_{\alpha}, \gamma_{\alpha}, \psi_{\alpha}$ span the 6D configuration space of the problem. The total angular momentum operator depends only on $\theta_{\alpha}, \phi_{\alpha}, \psi_{\alpha}$ whereas the potential function only on $\rho, \omega_{\alpha}, \gamma_{\alpha}$. It is now

convenient to expand ψ^{JM} and ϕ_{Ω}^{JM} according to

$$\psi^{JM}(\rho, \Omega) = \sum_{\Omega=-J}^J D_{M\Omega}^J(\phi_{\alpha}, \theta_{\alpha}, \psi_{\alpha}) \psi_{\Omega}^J(\rho, \omega_{\alpha}, \gamma_{\alpha})$$

$$\phi_{\Omega}^{JM}(\Omega; \rho) = \sum_{\Omega=-J}^J D_{M\Omega}^J(\phi_{\alpha}, \theta_{\alpha}, \psi_{\alpha}) \phi_{\Omega}^{J\Omega}(\omega_{\alpha}, \gamma_{\alpha}; \rho)$$

where the $D_{M\Omega}^J$ are Wigner rotation functions. In order to determine the surface functions $\phi_{\Omega}^{JM}(\Omega; \rho)$ it suffices to determine the coefficients $\phi_{\Omega}^{J\Omega}(\omega_{\alpha}, \gamma_{\alpha}; \rho)$ which we shall call 2D surface functions. They satisfy coupled equations of the type

$$\begin{aligned} & \hat{\mathcal{H}}_{\Omega, \Omega-1}^J(\gamma_{\alpha}; \omega_{\alpha}, \rho) \phi_{\Omega}^{J, \Omega-1} + \hat{\mathcal{H}}_{\Omega\Omega}^J(\omega_{\alpha}, \gamma_{\alpha}; \rho) \phi_{\Omega}^{J\Omega} + \hat{\mathcal{H}}_{\Omega, \Omega+1}^J(\gamma_{\alpha}; \omega_{\alpha}, \rho) \phi_{\Omega}^{J, \Omega+1} \\ & = \epsilon_{\Omega}^J(\rho) \phi_{\Omega}^{J\Omega} \end{aligned}$$

where $\hat{\mathcal{H}}_{\Omega, \Omega+1}^J$ and $\hat{\mathcal{H}}_{\Omega\Omega}^J$ are appropriate differential operators. Once these 2D eigenfunctions $\phi_{\Omega}^{J\Omega}(\omega_{\alpha}, \gamma_{\alpha}; \rho)$ and the corresponding eigenvalues $\epsilon_{\Omega}^J(\rho)$ are obtained, we expand the 3D functions $\psi_{\Omega}^J(\rho, \omega_{\alpha}, \gamma_{\alpha})$ and obtain for each J a second order matrix differential equation for the coefficients of this expansion in the only remaining variable ρ . From their solution, we obtain the scattering matrices \underline{S}^J and the differential and integral cross sections for the collision process being considered.

So far, all of the steps of this computational scheme have been programmed for the $H + H_2$ reaction and the $J=0$ partial wave. In view of the C_{3v} permutation symmetry of this system, further decouplings are permitted by considering the solutions of class A_1 , A_2 and E separately. The results

obtained to date are as follows:

- a. Two independent methods for obtaining the surface functions were developed, checked against each other, and shown to give the same results.
- b. The coupled differential equations in ρ were solved for each of the classes A_1 , A_2 and E and the corresponding scattering matrices were calculated,
- c. From a calculation for this system, done some years ago in this laboratory by an entirely independent "matching" method, the same symmetry-specific scattering matrices were calculated.
- d. The results of the "hyperspherical" and the "matching" methods were compared. They gave equivalent absolute values for the scattering matrix elements but different phases. Since these phases affect the values of the cross sections, we are currently tracking down the source of this difference. Once it is found, the $J=0$ program will be considered operational. The only remaining step will be the generalization of the program for $J \neq 0$, which is fairly straightforward.

In spite of the large amount of effort involved in implementing this 3D reactive scattering procedure, all the indications so far are that it will lead to a significant improvement in efficiency over alternate accurate computational methods and permit applications to other reactive systems such as the important $\text{Cl} + \text{H}_2$, $\text{F} + \text{H}_2$ ones.

5. THREE-DIMENSIONAL QUANTUM MECHANICAL REACTIVE SCATTERING BY THE MATCHING METHOD

We have previously developed a method for performing accurate three-dimensional reactive scattering calculations for triatomic systems. Let the three atoms be A, B, and C. The method consists of integrating the Schrödinger equations, starting out independently from the 3 separate arrangement channel regions $A + BC$, $B + AC$ and $C + AB$ and proceeding into the strong interaction region in which A, B, and C are all close to one another. These three solutions are then linearly combined to match one another smoothly. This method was applied to the $H + H_2$ system, yielding the only accurate 3D reactive differential cross sections published so far [A. Kuppermann and G. C. Schatz, J. Chem. Phys. 62, 2502 (1975); G. C. Schatz and A. Kuppermann, *ibid*, 4642 (1976)]. The computer program, originally written for systems composed of three identical atoms, was then modified to permit calculations for systems of the type A_2B , in which only two of the three atoms are required to be identical. These include H_2D , H_2F and H_2Cl . Because of the complexity of the original program, and its extensive utilization of symmetry properties for purposes of maximum computational efficiency, these changes are rather subtle and pervasive. This modified code was extensively tested during the course of this project by using it to perform calculations of the $H + H_2$ system, for which accurate results using the original code are available. These two codes yielded the same answers. We then proceeded to perform extensive convergence calculations for the H_2D system at total angular momentum J equal to zero. The results of these studies indicated an erratic behavior with respect to the number of channels used in the coupled-channel expansions and other numerical parameters. This behavior was very difficult to rationalize. After appreciable effort, it was traced to

an accidental interchange in the program between the masses of atoms A and B. When applied to the H_3 system, this error went, of course, undetected. Once it was identified and corrected, the $J=0$ results for DH_2 showed the same degree of convergence and accuracy as the H_3 ones. Equivalent studies were then initiated for the $J>0$ case and are being continued. This program is expected to yield the first accurate 3D information on isotope effects for reaction cross sections on highly quantum systems. These results will permit a very careful test of isotope effect theories for state-to-state cross sections, which will be useful for related systems such as H_2F and H_2Cl . They should also permit a test of the accuracy of other approximate methods, such as several angular momentum decoupling schemes and distorted wave approximations, which are applicable in principle to more complex systems.

6. METHODS FOR QUANTUM MECHANICAL REACTIVE SCATTERING

A chapter for a book, describing the methodology and results of the past reactive scattering calculations performed in our group (excluding the hyperspherical coordinate method) was written [A. Kuppermann, in: Theoretical Chemistry: Advances and Perspectives, Volume 6A, D. Henderson, Ed. (Academic Press, New York, 1981), Chap. 2, pp. 79-164] and a reprint is included in section 8.

7. PROFESSIONAL PERSONNEL

During the period covered by the present report, the following personnel were associated with work of the project.

1. Aron Kuppermann, principal investigator.
2. Dr. Joseph K. C. Wong, three-dimensional reactive scattering using hyperspherical coordinates. Dr. Wong continues to work on this project part-time.
3. Dr. Nancy M. Harvey, three dimensional reactive scattering by the matching method.
4. Dr. Jack A. Kaye, collinear reactive scattering. Dr. Kaye finished his doctoral work in December 1981 and has since been a post-doctoral research fellow at the Naval Research Laboratory in Washington, D.C.
5. Diane Hood Ng, three-dimensional scattering using hyperspherical coordinates. Ms. Ng is a graduate student and should obtain her Ph.D. degree some time during 1984.
6. Paul G. Hipes, collinear reactive scattering using hyperspherical coordinates. Mr. Hipes is a graduate student who joined the group in the fall of 1981.
7. James F. Garvey, collinear reactive scattering. Mr. Garvey is mainly an experimentalist, but did some theoretical work in collaboration with Dr. Kaye.

8. REPRINTS AND PREPRINTS

Enclosed are reprints or preprints of 14 papers written during the course of this project, as follows:

1. Hyperspherical Coordinates in Quantum Mechanical Collinear Reactive Scattering, A. Kuppermann, J. A. Kaye and J. P. Dwyer, Chem. Phys. Lett. 74, 257 (1980).
2. Collinear Quantum Mechanical Probabilities for the $I + HI \rightarrow IH + I$ Reaction Using Hyperspherical Coordinates, J. A. Kaye, and A. Kuppermann, Chem. Phys. Lett., 77, 573 (1981).
3. Quantum Mechanical Coupled-Channel Collision-Induced Dissociation Calculations with Hyperspherical Coordinates, J. A. Kaye and A. Kuppermann, Chem. Phys. Lett., 78, 546 (1981).
4. Mass Effect in Quantum Mechanical Collision-Induced Dissociation in Collinear Reactive Atom-Diatomic Molecule Collisions. I. Symmetric Systems, J. A. Kaye and A. Kuppermann, draft preprint.
5. Collinear Quasi-Classical Trajectory Study of Collision-Induced Dissociation on a Model Potential Energy Surface, J. A. Kaye and A. Kuppermann, draft preprint.
6. Partitioning of Kinetic Energy Among Reaction Products in Collision-Induced Dissociation in Collinear Atom-Diatomic Molecule Collisions from Quantum and Classical Mechanical Calculations, J. A. Kaye and A. Kuppermann, draft preprint.
7. Quasi-Classical Trajectory Analysis of the Equivalence of Reactive and Non-Reactive Deactivation in the Collinear $Cl' + HCl$ System, J. A. Kaye and A. Kuppermann, draft preprint.

8. Collinear Quantum Mechanical Probabilities and Rate Constants for the $\text{Br} + \text{HCl}$ ($v=2,3,4$) Reaction Using Hyperspherical Coordinates, J. A. Kaye and A. Kuppermann, Chem. Phys. Lett., 92, 574 (1982).

9. Hyperspherical Coordinates in Collinear Atom-Diatomic Molecular Collisions: Convergence Properties, J. A. Kaye and A. Kuppermann, draft preprint.

10. Quantum Mechanical Collinear Calculation of the Reactions $\text{D} + \text{FH}$ ($v=0,1,2$) $\rightarrow \text{DF}$ (v') + H and $\text{H} + \text{FD}$ ($v=0,1,2,3$) $\rightarrow \text{HF}$ (v') + D on a Realistic Potential Energy Surface, J. A. Kaye and A. Kuppermann, draft preprint.

11. Collinear Quantum Mechanical Calculations on the Systems HF (v) + H and HF (v) + D on a Realistic Potential Energy Surface, J. A. Kaye and A. Kuppermann, draft preprint.

12. Barrier Height Dependence of Dynamics in the Collinear $\text{H} + \text{FH}$ (v) and $\text{D} + \text{FH}$ (v) Systems, J. A. Kaye, J. P. Dwyer and A. Kuppermann, draft preprint.

13. Accurate Quantum Calculation of Reactive Systmes, Aron Kuppermann, in Theoretical Chemistry-Theory of Scattering: Papers in Honor of Henry Eyring, D. Henderson, Ed. (Academic Press, New York, 1981) Vol. 6, Part A., Chap. 2, pp. 79-164.

14. Few Body Molecular Collisions: Theoretical, A. Kuppermann, Nucl. Phys. A, 353, 287c (1981).

In addition, a Ph. D. Thesis by Jack A. Kaye was submitted and approved in January 1982 entitled "Theoretical Studies of Chemical Reaction Dynamics", containing a substantial amount of work supported by this project. It consists of 817 typed pages and a copy is available on request if desired.

8. INVITED SEMINARS, CONFERENCES AND LECTURES

During the three year period covered by this report, the principal investigator gave the following invited seminars, conferences and lectures on topics related to this contract:

1. Invited lecturer, Institute of Advanced Studies on Theoretical Chemical Dynamics, The Hebrew University, Jerusalem, Israel (1-29 July 1979).

2. "An Exact Quantum Mechanical Transition State Theory. I. An Overview". Lectures on Biological and Chemical Physics, A Symposium in Honor of Schenior Lifson on his 65th Birthday, The Weizmann Institute, Rehovot, Israel (2-5 July 1979).

3. "A Simple Model of Dynamic Resonances in Collinear Reactive Scattering". XIth International Conference on the Physics of Atomic and Electronic Collisions, Kyoto, Japan (29 August - 4 September 1979).

4. "Three Dimensional Quantum Mechanical Reactive Collisions by Symmetrized Hyperspherical Coordinates". AFOSR/FJSRL Molecular Dynamics Conference, USAF Academy, Colorado Springs, CO (3-5 October 1979).

5. "Dynamical Resonances in Chemical Reactions". California State University, Los Angeles, Los Angeles, CA (18 November 1979).

6. "Dynamic Resonances in Chemical Reactions". Oak Ridge National Laboratories, Oak Ridge, TN (4 March 1980).

7. "Few-Body Molecular Collisions: Theoretical". 9th International Conference on Few-Body Problems, Institute of Theoretical Science, University of Oregon, Eugene, OR (17-23 August 1980).

8. "Hyperspherical Coordinates in Collinear and Three-Dimensional Quantum Mechanical Reactive Scattering". Symposium on Dynamic Resonances, American Chemical Society Meeting, Las Vegas, NV (24-29 August 1980).

9. "Collision Induced Dissociation Calculations by an Accurate Coupled Channel Method". AFOSR Molecular Dynamics Conference, Hanscom AFB, MA (8-12 October 1980).

10. "Hyperspherical Coordinates in Reactive Scattering". Texas Conference on Theoretical Approaches to Chemical Dynamics, Austin, TX (1-4 March 1981).

11. "Dynamic Resonances in Chemical Reactions: Prediction, Physical Interpretation, and Experimental Detection". Stanford University, Stanford, CA (21 May 1981).

12. AFOSR/AFWL Molecular Dynamics Conference, Kirtland AFB, NM (9-11 November 1981).

13. "Lifetimes of Dynamics Resonances". 15th Jerusalem Symposium in Quantum Chemistry and Biochemistry and the International Symposium on Inter-molecular Dynamics, Israel (29 March - 1 April 1982).

14. "Collision Lifetime Matrix Analysis of Reactive Scattering Resonances". 4th Annual West Coast Theoretical Chemistry Conference, University of Southern California, Los Angeles, CA (28-30 April 1982).

15. "Hyperspherical Coordinates in Reactive Scattering". Gordon Research Conference on Atomic and Molecular Interactions, Brewster Academy, New Hampshire (25-30 July 1982).

HYPERSPHERICAL COORDINATES IN QUANTUM MECHANICAL COLLINEAR REACTIVE SCATTERING *

Aron KUPPERMANN, Jack A. KAYE ** and John P. DWYER †

Arthur Amos Noyes Laboratory of Chemical Physics †, California Institute of Technology, Pasadena, California 91125, USA

Received 29 April 1980

A new hyperspherical coordinate method for performing atom-diatom quantum mechanical collinear reactive scattering calculations is described. The method is applicable at energies for which breakup channels are open. Comparison with previous results and new results at high energies for $H + H_2$ are given. The usefulness of this approach is discussed.

1. Introduction

Triatomic exchange reactions of the type $A + BC \rightarrow AB + C$, with A, B, and C representing atoms confined to move on a laboratory-fixed straight line, constitute the simplest reactive processes which present a basic characteristic of many chemical reactions: the dissolution of a chemical bond and the formation of a new one. The low mathematical dimensionality of the corresponding theory permits a straightforward analysis of this system, unencumbered by the mathematical complexities of molecular rotations. Such a collinear model is therefore useful for developing insight into the reaction process, especially for systems which are collinearly dominated, i.e., for which collinear configurations have energies considerably lower than corresponding bent ones. For these reasons, collinear reactions have been the subject of extensive theoretical studies over the last decade. Reviews of the methods developed for such studies have been published previously [1-4]. We consider in this paper

electronically adiabatic reactions of this type, although the method described is also applicable, with straightforward generalizations, to electronically non-adiabatic reactions.

The methods previously developed for studying these collinear processes are restricted to energies significantly below that for which the $A + BC \rightarrow A + B + C$ process is possible. Such breakup collisions, particularly when occurring in competition with exchange processes, have been particularly resilient to accurate quantum mechanical treatment [5]. In addition, accurate results for systems in which the central atom B is significantly lighter than the end atoms, such as the $I + HI \rightarrow IH + I$ reaction, have not been obtained so far by those methods, for reasons inherent to their nature (see section 4). The use of hyperspherical coordinates, as described in the present paper, was developed in an attempt to overcome these shortcomings. Extension of these ideas to three dimensions was also kept in mind.

2. Theory

Let r'_α, R'_α be, respectively, the BC internuclear distance and the distance of A to the center of mass G_{BC} of the BC molecule. Let r'_γ, R'_γ be the corresponding distances with the roles of A and C interchanged, as indicated in fig. 1. We define the Delves scaled co-

* This work was supported in part by a contract (No. F49620-79-C-0187) from the Air Force Office of Scientific Research.

** Work performed in partial fulfilment of the requirements for the Ph.D. degree in Chemistry at the California Institute of Technology

† Present address: School of Law, Boalt Hall, University of California, Berkeley, California 94720, USA.

* Contribution No. 6215.

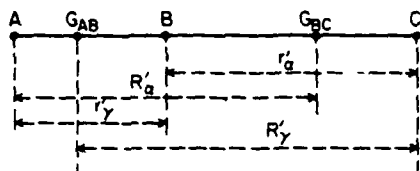


Fig. 1. Distance coordinates for collinear triatomic system.

ordinates [6,7] R_λ, r_λ ($\lambda = \alpha, \gamma$) by

$$R_\lambda = a_\lambda R'_\lambda, \quad r_\lambda = a_\lambda^{-1} r'_\lambda, \quad a_\lambda = (\mu_{\lambda, \nu\kappa} / \mu_{\nu\kappa})^{1/4}. \quad (1)$$

In these equations, $\lambda\nu\kappa$ is either $\alpha\beta\gamma$ or $\gamma\beta\alpha$, $\mu_{\nu\kappa}$ is the reduced mass of m_ν and m_κ , $\mu_{\lambda, \nu\kappa}$ is the reduced mass of m_λ and $(m_\nu + m_\kappa)$, and m_α, m_β , and m_γ are the masses of A, B, and C, respectively. In terms of R_λ, r_λ , the relative nuclear motion hamiltonian of the triatomic system is

$$H = -\frac{\hbar^2}{2\mu} \left[\frac{\partial^2}{\partial R_\lambda^2} + \frac{\partial^2}{\partial r_\lambda^2} \right] + V_\lambda(R_\lambda, r_\lambda), \quad \lambda = \alpha, \gamma, \quad (2)$$

where

$$\mu = [m_\alpha m_\beta m_\gamma / (m_\alpha + m_\beta + m_\gamma)]^{1/2} \quad (3)$$

is a reduced mass of the system and is the same whether $\lambda = \alpha$ or γ , and $V_\lambda(R_\lambda, r_\lambda)$ is the electronically adiabatic potential energy surface being considered, in λ coordinates. According to eq. (2), the internal collinear motion of the triatomic system is isomorphic with that of a single point P of mass μ in the two-mathematical-dimensional (2MD) R_λ, r_λ configuration space, subject to the potential V_λ . The corresponding Porter-Karplus (PK) ground state collinear potential energy surface for the $H + H_2$ system [8] is depicted in fig. 2.

The coupled-equations approach to solving the Schrödinger equation for the hamiltonian in eq. (2) consists in choosing an "internal" variable x and a "propagation" variable y (transverse to x) which may be different in different regions of configuration space. The wavefunction $\psi(x, y)$ is then expanded in a quasi-complete discrete pseudo-vibrational basis set $\{\phi_n(x)\}$ of variable x , and the resulting coupled equations in the coefficients $g_n(y)$ of this expansion are integrated. Enough linearly-independent solutions of this type are obtained to permit the calculation of the R matrix, and from it the S matrix and the transition

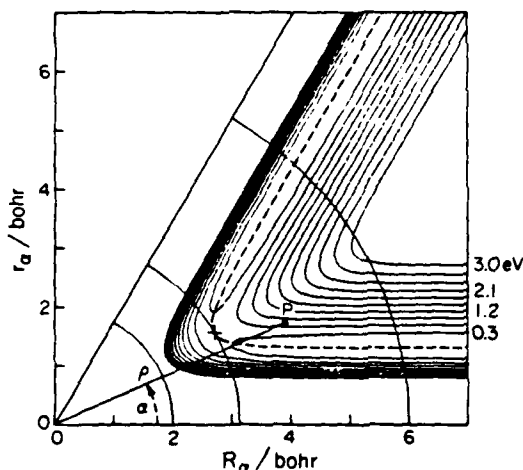


Fig. 2. Porter-Karplus potential energy surface V for the $H + H_2$ system in Delves scaled coordinates R_α, r_α . The solid curves are equipotential contours at the total energies (with respect to the bottom of the isolated H_2 well) indicated in the lower right side of the figure. The dashed line is the minimum energy path. The polar coordinates ρ, α of a general point P in this R_α, r_α configuration space are also indicated. The three arcs of circles at $\rho = 2.00, 3.13$, and 6.00 bohr are cuts along which V is displayed in fig. 3. The second of these passes through the saddle point, indicated by a cross in the figure.

probability matrix P [1,2], and care is taken to ascertain their convergence with respect to the number of terms used in this expansion. In the method developed by Light and co-workers [9], x and y have been chosen to be natural collision coordinates, whereas in that of Kuppermann [2,10], they are r_α and R_α for the reagent region of configuration space; the circular polar coordinates r and φ (centered on a point P_0 deeply imbedded in the $A + B + C$ dissociation plateau) for the strong interaction region; and r_γ and R_γ for the product region. In both these methods, the wavefunction is assumed to vanish outside a reaction gulley which excludes the dissociative regions of configuration space.

In the present method, we use for x, y the circular polar coordinates ρ, α (see fig. 2) around the origin O of the R_λ, r_λ configuration space (for which origin A, B, and C coincide). Similar coordinates have been previously used by Tang et al. to study a piece-wise flat potential energy surface system [11]. In the generalization to three-dimensional collisions [6,7,12]

ρ is a hyperdistance in a 6MD configuration space. The range of α is 0 to $\alpha_{\max} = \tan^{-1}(m_\beta M/m_\alpha m_\gamma)^{1/2}$, where $M = m_\alpha + m_\beta + m_\gamma$. At the extremes of this range (where B coincides with A or C, respectively) the potential function V becomes, for all chemical purposes, infinite and the wavefunction vanishes. The nuclear motion hamiltonian in these coordinates is

$$H(\rho, \alpha) = -\frac{\hbar^2}{2\mu} \left[\frac{\partial^2}{\partial \rho^2} + \frac{1}{\rho} \frac{\partial}{\partial \rho} + \frac{1}{\rho^2} \frac{\partial^2}{\partial \alpha^2} \right] + V(\alpha, \rho). \quad (4)$$

In fig. 3 we depict V as a function α for various constant values $\bar{\rho}$ of ρ for the PK surface. It can be seen that, because of the divergence of V at $\alpha = 0$ and $\alpha = \alpha_{\max}$, the eigenfunctions of

$$h(\alpha; \bar{\rho}) = -(\hbar^2/2\mu\bar{\rho}^2) \partial^2/\partial \alpha^2 + V(\alpha, \bar{\rho}) \quad (5)$$

form an infinite but discrete set $\{\phi_n(\alpha; \bar{\rho})\}$ which samples the entire range of α , including those values which, for large $\bar{\rho}$, correspond to dissociated A + B + C configurations. In fig. 4 we display the even (see end of this section) eigenfunctions for the PK surface, for $\bar{\rho} = 6$ bohr and $n = 0-24$ (in steps of 2), as well as

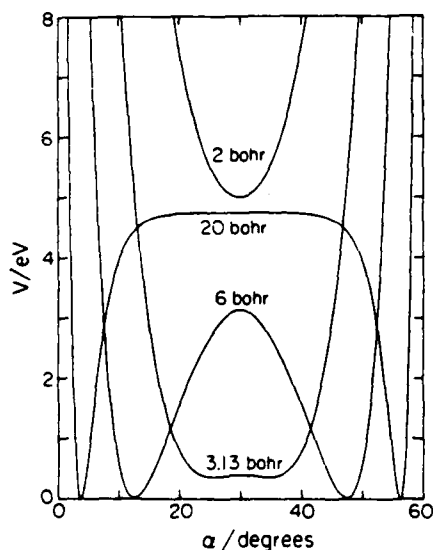


Fig. 3. Potential energy function $V(\alpha, \bar{\rho})$ of fig. 2 as a function of α for the following four constant values $\bar{\rho}$ of ρ : 2.00, 3.13, 6.00, and 20.00 bohr. The first three of these values correspond to the arcs displayed in fig. 2. The fourth one is outside of that figure.

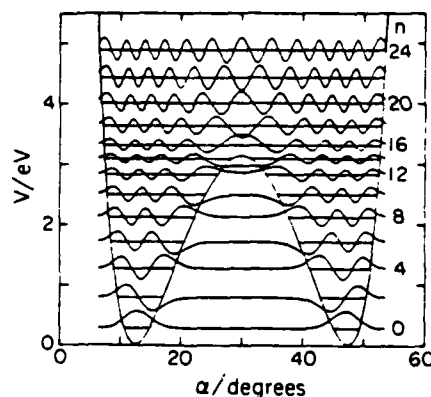


Fig. 4. Potential energy function, eigenfunctions, and eigenvalues of the one-dimensional hamiltonian of eq. (5), for $\bar{\rho} = 6$ bohr. The double-well curve is the same as that in fig. 3. The horizontal lines represent the eigenvalues for the quantum numbers given (for every other eigenvalue) at the right of the figure, for the even eigenfunctions (i.e., those which are symmetric for reflection through the $\alpha = 30^\circ$ line). The latter are the oscillatory curves around the eigenvalue lines, and have been scaled so as not to overlap each other. The corresponding relative scaling factors are 1.00, 1.12, 1.08, 1.15, 1.18, 1.28, 1.59, 1.69, 1.45, 1.18, 1.01, 0.90, and 0.87.

the corresponding eigenvalues $E_n(\bar{\rho})$. The highest of these is larger than the dissociation energy 4.75 eV of H_2 . Since the H_2 Morse curve included in the PK surface supports 17 bound states, for large $\bar{\rho}$ (larger than 11 bohr, it turns out), $E_n(\bar{\rho})$ exceeds 4.75 eV for $n \geq 32$. The corresponding eigenfunctions sample the dissociated plateau region of configuration space, which thereby, in principle, is made accessible to the system. Whether or not the system samples that region depends on energetic and dynamic considerations, rather than it being excluded by a priori considerations. Expanding an eigenfunction $\psi^n(\rho, \alpha)$ of $H(\rho, \alpha)$ according to

$$\psi^n(\rho, \alpha) = \rho^{-1/2} \sum_{n'=0}^N g_{n'}^n(\rho; \bar{\rho}) \phi_{n'}(\alpha; \bar{\rho}) \quad (6)$$

leads without much difficulty to the following differential equation in the matrix $\mathbf{g}(\rho; \bar{\rho})$, whose n' th row and n th column element is $g_{n'}^n$:

$$-\left(\hbar^2/2\mu\right) d^2 \mathbf{g}(\rho; \bar{\rho}) / d\rho^2 + \mathbf{W}(\rho; \bar{\rho}) \mathbf{g}(\rho; \bar{\rho}) = \mathbf{E}(\rho; \bar{\rho}) \mathbf{g}(\rho; \bar{\rho}). \quad (7)$$

W and E are interaction and energy matrices whose n' row and n column elements are given by

$$W_{n'}^n(\rho; \bar{\rho}) = \langle n | V(\alpha, \rho) - (\bar{\rho}^2/\rho^2) V(\alpha, \bar{\rho}) | n' \rangle, \quad (8)$$

$$E_n^{\bar{n}}(\rho; \bar{\rho}) = [E + \hbar^2/8\mu\rho^2 - E_n(\bar{\rho})] \delta_n^{\bar{n}}, \quad (9)$$

where $|n'\rangle = \phi_{n'}(\alpha; \bar{\rho})$, the integration variable implied in eq. (7) is α , E is the total energy of the system, and $\delta_n^{\bar{n}}$ the Kronecker symbol.

The reactive scattering problem is solved as follows. We choose a set of ρ_i ($i = 0, 1, \dots, i_{\max}$). In the range ρ_{i-1} to ρ_i we chose a $\bar{\rho}_i$ for which we calculate the $\phi_{n'}(\alpha; \bar{\rho}_i)$ by a numerical method (such as a finite difference one [13]). We then integrate numerically the coupled equations (7) from ρ_{i-1} to ρ_i , setting $\mathbf{g}(0; \bar{\rho}_0) = 0$ and $\mathbf{g}'(0; \bar{\rho}_0) = 1$ and requiring continuity of $\psi_n(\rho, \alpha)$ and of its derivative with respect to ρ at the boundaries $\rho = \rho_i$ between the ρ_{i-1} to ρ_i and ρ_i to ρ_{i+1} regions. The integration method used in the present calculations was that of Gordon [14], together with the reorthogonalization procedure of Riley and Kuppermann [15]. In this manner we obtain the $\psi^n(\rho; \alpha)$ for $0 \leq \alpha \leq \alpha_{\max}$ and $\rho_0 \leq \rho \leq \rho_{i_{\max}}$. We then project numerically these ψ^n onto the bound state eigenfunctions of BC and AB at a large and constant value of R_λ , from which we get by standard methods [2] the \mathbf{R} , \mathbf{S} and \mathbf{P} matrices defined above for energies below the $A + B + C$ dissociation limit. Their convergence with respect to i_{\max} , ρ_0 , $\rho_{i_{\max}}$, and the number N of terms used in eq. (6) is established empirically, as is the symmetry of the open channel part of \mathbf{R} and the unitarity of the open channel part of \mathbf{S} . For energies above that dissociation limit, the procedure described for the three-dimensional case by Delves [7] should be used.

For symmetric reactions of the type $A + BA \rightarrow AB + A$, the potential energy function $V(\alpha, \rho)$ is symmetric with respect to the $\alpha = \alpha_{\max}/2$ line in configuration space, and the solutions which are even or odd for reflection through that line may be obtained separately, thereby decreasing the amount of numerical effort.

3. Results

The results of accurate calculations for the $H + H_2 \rightarrow H_2 + H$ reaction on the PK surface, using the

hyperspherical coordinate method just described, are given in fig. 5, together with those of previous calculations. We plot in fig. 5 the vibrationally adiabatic distinguishable-atom reaction probabilities P_{nn}^R from the initial vibrational state n of the reagents to the same vibrational state of the reaction products. The points in fig. 5 are some of the present results, which are converged and accurate to about 1% or better. They have been carried out so far up to total energies of 2.88 eV (about 60% of the H_2 dissociation energy), without any signs of quality deterioration. The dashed lines are cubic spline fits to these results (which include a larger number of points than those displayed) for total energies in excess of 1.75 eV for the P_{00}^R and P_{11}^R curves, and for $E_{tr} \geq 0$ for the others. For comparison, the solid lines are cubic spline fits to the results of Schatz and Kuppermann [16], which were carried out using one of the previous methods [10], up to total energies of 1.75 eV for P_{00}^R and P_{11}^R . These latter results [16] are essentially indistinguishable from those of Diestler [17], who performed accurate calculations on the same PK surface at total energies up to 1.21 eV. For total energies for which other calculations are available (≤ 1.75 eV), the present results agree with the previous ones within the computational accuracy of about 1%. This validates the hyperspherical coordinate method.

An additional useful characteristic of this new calculational procedure is that convergence with respect to the number of basis functions used is more rapid than for other methods. For example, for E_{tr} in the range 0.22–0.43 eV, and using only two channels (one open and one closed, asymptotically), the absolute error in P_{00}^R is less than 0.02 in the new method, whereas for a previous method [2,10] that error is as high as 0.23. If four channels are used, the hyperspherical coordinate method produces reliable values of P_{00}^R (to within 0.02) up to translational energies of 1.03 eV, whereas that previous method requires seven or eight channels for equivalent convergence. This faster basis set convergence efficiency may make this method particularly well suited for three-dimensional calculations, for which high efficiency is required for calculational feasibility [18,19].

It is interesting to note that the P_{nn}^R curves for $n \geq 1$ in fig. 5 are very similar to each other and are nearly identical when plotted as functions of the initial relative translational energy. This is strongly

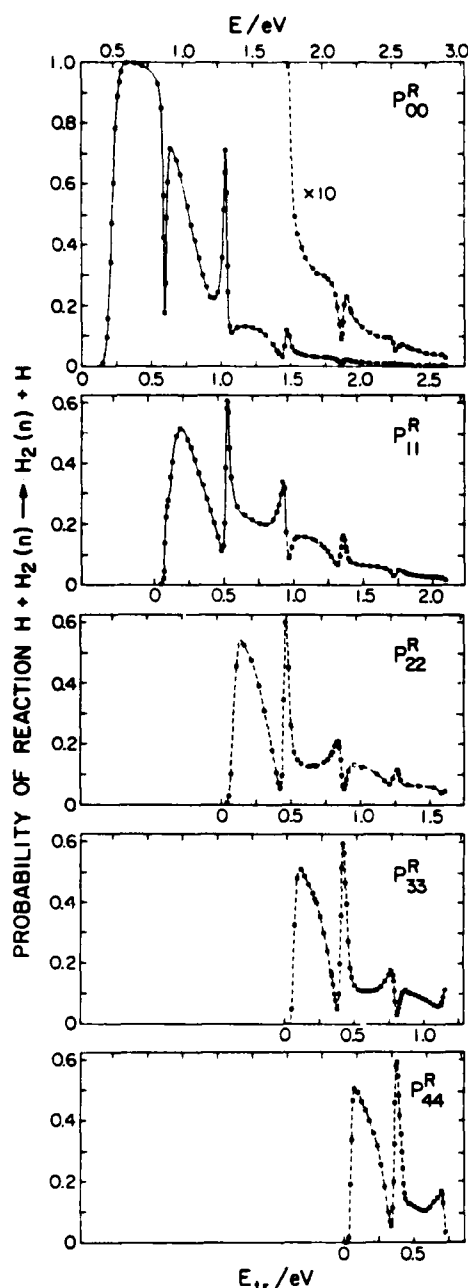


Fig. 5. Vibrationally adiabatic reaction probabilities P_{nn}^R for the $H + H_2(n) \rightarrow H_2(n) + H$ exchange reaction on the Porter-Karplus potential energy surface, as a function of initial relative translational energy E_{T_i} and total energy E (measured with respect to the bottom of the isolated H_2 well). The points are the results of the present calculations. The solid P_{00}^R and P_{11}^R curves are cubic spline fits to the previous results of Schatz and Kuppermann, which were performed up to $E = 1.75$ eV. The dashed curves are cubic spline fits to the present points, including some omitted from the plots for reasons of visibility.

suggestive that an effective IMD potential may be found which duplicates all of them. The P_{00}^R curve is also similar to the $n \geq 1$ P_{nn}^R ones if energies below that of its first resonance are neglected. This comparison suggests that the second resonance in P_{00}^R and the first one in the P_{nn}^R ($n \geq 1$) have analogous dynamical origins.

4. Discussion and conclusions

The hyperspherical coordinate method seems capable of tackling reactive scattering problems at fairly high energies. The present calculations are being extended to energies above the H_2 dissociation limit. The method can also be generalized to electronically non-adiabatic processes in a straightforward manner [20,21].

The difficulty other methods [2,9,10] have in tackling reactions with a light middle atom, such as $I + HI \rightarrow IH + I$, is related to the very sharp and rapidly changing curvature of the minimum energy path of these systems, in the strong interaction region of configuration space. This in turn is due to the smallness of the corresponding skew angle, $\alpha_{\max} = \tan^{-1}(m_p M / m_\alpha m_\gamma)^{1/2}$, which in that system is about 7° . The present method does not suffer from this difficulty, since the propagation coordinate ρ is not related to that curvature.

Finally, the hyperspherical coordinate approach seems particularly suitable to the study of 3D systems [12], since it greatly simplifies the $A + BC$ bifurcation problem associated with the existence of two kinds of reactive products, $AB + C$ and $AC + B$. The solution to this problem is contained in the nature of the $\rho = \text{constant}$ basis sets, which are the 3D generalizations of the $\phi_n(\alpha; \bar{\rho})$ eigenfunctions used in the present method. Such calculations are currently being performed in our laboratory [22].

Acknowledgement

The calculations reported in this paper were performed on the Dreyfus-NSF Theoretical Chemistry Computer (VAX 11/780) at Caltech and on the IBM 370/158 computer of Ambassador College, Pasadena, California, for which we express our appreciation. One of us (JAK) would like to thank Dr. Gregory A. Parker for helpful discussions.

References

- [1] A. Kuppermann, in: *The Physics of Electronic and Atomic Collisions, Invited Lectures, Review Papers and Progress Reports of the IXth International Conference on the Physics of Electronic and Atomic Collisions*, Seattle, Washington, 24-30 July 1975, eds. J.S. Risley and R. Geballe (University of Washington Press, Seattle, 1976) pp. 259-274.
- [2] A. Kuppermann, in: *Proceedings of the Summer School on Chemical Photophysics, Les Houches, France, 18-30 June 1979*, eds. P. Glorieux, D. Leclerc and R. Vetter (Centre de la Recherche Scientifique, Paris, 1979) pp. 293-384.
- [3] D. Micha, in: *Advances in chemical physics*, Vol. 30, ed. K.P. Lawley (Wiley, New York, 1975) pp. 7-75.
- [4] J.N.L. Connor, *Computer Phys. Commun.* 17 (1979) 117.
- [5] D.J. Diestler, in: *Atom-molecule collision theory*, ed. R.B. Bernstein (Plenum Press, New York, 1979) pp. 655-667.
- [6] L.M. Delves, *Nucl. Phys.* 9 (1959) 391.
- [7] L.M. Delves, *Nucl. Phys.* 20 (1960) 275.
- [8] R.N. Porter and M. Karplus, *J. Chem. Phys.* 40 (1964) 1105.
- [9] C.C. Rankin and J.C. Light, *J. Chem. Phys.* 51 (1969) 1701;
G. Miller and J.C. Light, *J. Chem. Phys.* 54 (1971) 1635, 1643.
- [10] A. Kuppermann, in: *Proceedings of the Conference on Potential Energy Surfaces in Chemistry*, ed. W.A. Lester, (University of California, Santa Cruz, 1970) pp. 121-124; in: *Proceedings of the 7th International Conference on the Physics of Electronic and Atomic Collisions* (North-Holland, Amsterdam, 1971) pp. 3-5.
- [11] K.T. Tang, B. Kleinman and M. Karplus, *J. Chem. Phys.* 50 (1969) 1119.
- [12] A. Kuppermann, *Chem. Phys. Letters* 32 (1975) 374.
- [13] D.G. Truhlar, *J. Comput. Phys.* 10 (1972) 123.
- [14] R. Gordon, *J. Chem. Phys.* 51 (1969) 14.
- [15] M.E. Riley and A. Kuppermann, *Chem. Phys. Letters* 1 (1968) 537.
- [16] G.C. Schatz and A. Kuppermann, *Phys. Rev. Letters* 35 (1975) 1266; unpublished results.
- [17] D.J. Diestler, *J. Chem. Phys.* 54 (1971) 4547.
- [18] G.C. Schatz and A. Kuppermann, *J. Chem. Phys.* 62 (1975) 2502; 65 (1976) 4668.
- [19] A.B. Elkowitz and R.E. Wyatt, *J. Chem. Phys.* 62 (1975) 2504; 63 (1975) 702.
- [20] J.M. Bowman, S.C. Leasure and A. Kuppermann, *Chem. Phys. Letters* 44 (1976) 499.
- [21] Z.H. Top and M. Baer, *J. Chem. Phys.* 66 (1977) 1363.
- [22] R.T. Ling and A. Kuppermann, in: *Electronic and Atomic Collisions, Abstracts of Papers of the 9th International Conference on the Physics of Electronic and Atomic Collisions*, Seattle, Washington, 24-30 July 1975, eds. J.S. Risley and R. Geballe (University of Washington Press, Seattle, 1975) pp. 353-354; J.K.C. Wong and A. Kuppermann, in: *Abstracts of Papers, Pacific Conference on Chemistry and Spectroscopy, Pasadena, California, 10-12 October 1979*, p. 39.

COLLINEAR QUANTUM MECHANICAL PROBABILITIES FOR THE $I + HI \rightarrow IH + I$ REACTION USING HYPERSPHERICAL COORDINATES *

Jack A. KAYE ** and Aron KUPPERMANN

*Arthur Amos Noyes Laboratory of Chemical Physics *, California Institute of Technology, Pasadena, California 91125, USA*

Received 24 October 1980

Calculations of quantum mechanical probabilities for the $I + HI \rightarrow IH + I$ electronically adiabatic exchange reaction were performed using hyperspherical coordinates. In spite of the small skew angle of 7° , accurate results were obtained with a small number of channels. These results are compared with those of quasi-classical trajectory calculations.

1. Introduction

Chemical reactions in which a hydrogen atom is transferred between two heavy atoms or groups of atoms of the type



have been the subject of numerous experimental and theoretical studies [1]. In many of the systems studied, X and Y are halogen atoms [2]; however, cases in which one or both of these are oxygen atoms [3] or alkyl groups [4] have also received a great deal of attention. In a number of studies [5], the halogen atom X is in its electronically excited $^2P_{1/2}$ state, and collisional quenching and electronic-to-vibrational energy (E-V) transfer have been investigated.

Theoretical studies of these reactions have consisted mainly of classical trajectory calculations on the ground electronic potential energy surface. For example, a number of calculations have been performed on the $Cl + HCl$ [6] and $Cl + HI$ [7] systems to help understand the rate of vibrational relaxation and the distribution of reaction products, respectively.

However, due to the lightness of the atom transferred, and the small skew angle associated with heavy-light-heavy (H-L-H) atom systems, quantum effects may be expected [8]. Accurate three-dimensional quantum calculations on these systems are presently impractical because of the large number of channels involved in a coupled-channel calculation [9-12]. Nevertheless, an assessment of the magnitude of such quantum effects can be made by performing accurate collinear quantum mechanical calculations and comparing their results with those of quasi-classical trajectory calculations. The small skew angle just mentioned makes even the collinear calculations difficult to perform using the methodology available until recently [13]. For example, for the reactive $Cl + HBr \rightarrow ClH + Br$ system in the only calculation of this type performed so far [14], 40 channels were required. The small skew angle permits certain dynamical approximations to be made, however, and a few approximate treatments of these H-L-H systems, both quantum mechanical and classical, have been developed [15].

In this paper we report the results of accurate coupled-channel electronically adiabatic quantum mechanical calculations for the collinear reaction,



using hyperspherical coordinates. Two slightly different potential energy surfaces were used. We also performed quasi-classical trajectory calculations on these surfaces.

* Research supported in part by the US Air Force Office of Scientific Research (Contract No. F49620-79-C-0187).

** Work performed in partial fulfillment of the requirements for the Ph.D. in Chemistry at the California Institute of Technology.

* Contribution No. 6056.

In section 2 we describe the method and the surfaces, and in section 3 we present and discuss the results.

2. Computational method and potential energy surfaces

The quantum mechanical method of hyperspherical coordinates developed previously [16][†] presents no particular difficulty when the skew angle is small, and in the calculations reported here, that method was used without change. Six even and six odd basis functions were used, and with them convergence of the transition probabilities to ± 0.005 and of flux to ± 0.0001 was usually achieved. Standard methods were used for the collinear quasi-classical trajectory calculations [19,20].

The potential energy surfaces used were of the extended LEPS form [21] and their parameters and properties are listed in table 1. The Morse oscillator [22] parameters for one of the surfaces (surface B) were those used previously [23] for trajectory calculations on the $H + I_2$ system. However, we changed the Sato parameters from 0 to 0.20 for HI and 0.125 for I_2 in order to decrease the barrier height from ≈ 14.2 kcal/mole to ≈ 1.5 kcal/mole. Although the barrier for the

[†] A related method, using the same coordinates but a different asymptotic analysis, has been developed by Hauke et al. [17] and used by Römelt [18].

Table 1
Parameters and properties of extended LEPS potential energy surfaces A and B^{a)}

	HI	I_2
β (bohr ⁻¹)	0.9260	0.9843
R_e (bohr ⁻¹)	2.0236	5.0457
D_e (eV) A	3.3303	1.5567
B	3.2002	1.5567
Δ	0.2	0.125
saddle point location (bohr)		
A	(3.336, 3.336)	
B	(3.370, 3.370)	
barrier height (kcal/mole)		
A	1.353	
B	1.526	
HI zero-point energy (eV)		
A	0.14447	
B	0.14160	

^{a)} Masses used: $m_H = 1$ amu, $m_I = 126.9$ amu.

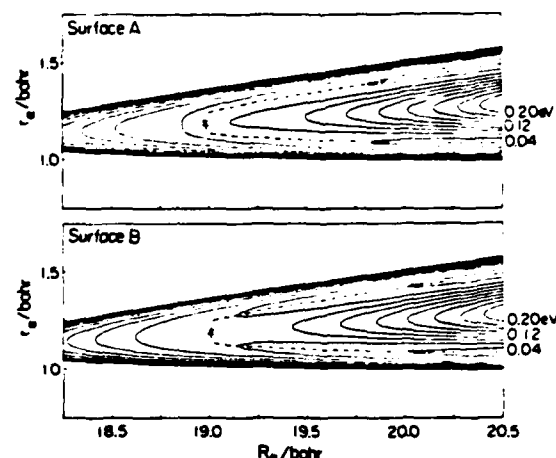


Fig. 1. Equipotential contour plots for $I + HI$, surfaces A and B, in the region near the saddle points. The solid curves are the contours and are equally spaced in increments of 0.02 eV, from 0.04 to 0.20 eV. The zero of energy is the bottom of the HI well. The surfaces are plotted in Delves' scaled coordinates [16–18]. The X mark the saddle points, the dashed lines are the steepest ascent and descent paths as calculated in Delves' scaled coordinates.

IHI system is not known, *ab initio* calculations on related systems ($F + HF$, $Cl + HCl$) suggest that a barrier of more than a few kcal/mole is unreasonably high [24]. The other surface (surface A) has the same LEPS parameters as surface B, except that the HI dissociation energy was increased by 3 kcal/mole. The main effect of this change is in the saddle point region, as can be seen by observing the 0.06 eV equipotential in the contour plots displayed in fig. 1.

3. Results and discussion

Plots of the quantum probabilities of reaction (2) from the ground vibrational state of the reagents to the same state of the products, as a function of translational energy, are given in figs. 2 and 3 for each of the two surfaces. For the low-energy (0–15 meV) range covered by fig. 3, the curve for surface A displays a sharp peak followed by a second broader peak, whereas for surface B, the sharp feature is absent and the other one is much broader and less intense. In order to assess the nature of these features, we have made an Argand plot [25] of the corresponding scattering

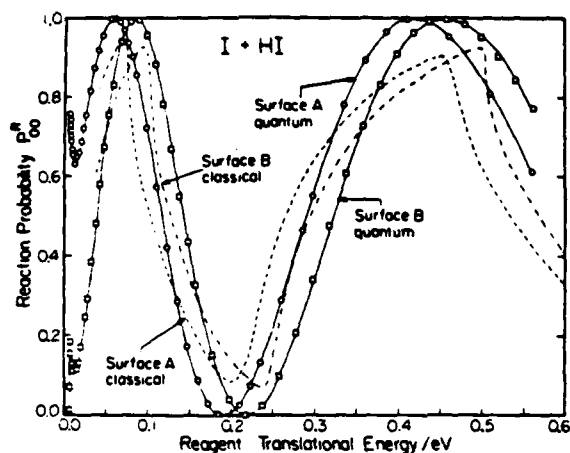


Fig. 2. Transition probability for the reaction $I + HI (v = 0) \rightarrow IH (v' = 0) + I$ as a function of reagent translational energy. Quantum mechanical results are indicated by the solid lines; the circles indicate surface A, the squares surface B. Classical trajectory results are given by the dashed line for surface A and the dashed-dotted line for surface B. The lowest energy portion of the quantum curve for surface A has been omitted for reasons of clarity.

matrix elements, S_{00}^R , for surface A in fig. 4. It can be seen that the sharp peak in fig. 3 is associated with a loop in fig. 4, along which a representative point moves counterclockwise with increasing energy, as indicated by the arrow in the upper part of fig. 4. This clearly demonstrates a scattering resonance. In the

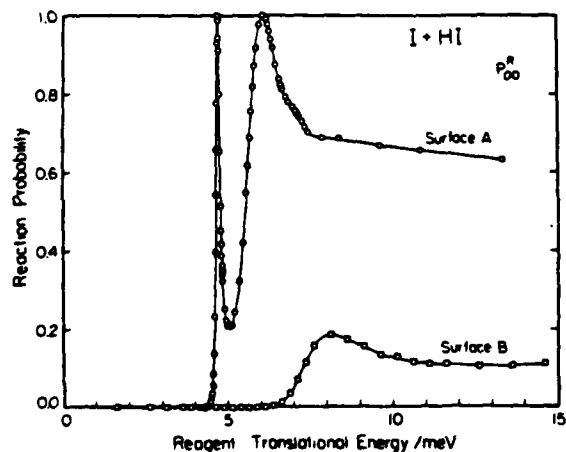


Fig. 3. Quantum mechanical transition probabilities as in fig. 2 for the low translational energy range. No classical trajectory results are shown.

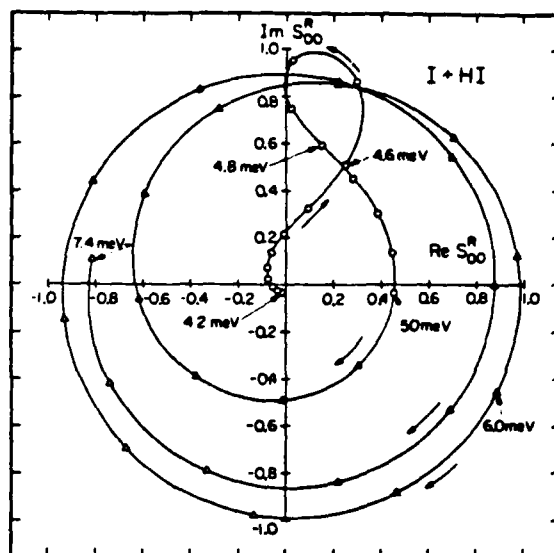


Fig. 4. Argand diagram [25] for the S matrix element S_{00}^R corresponding to the exchange reaction $I + HI (v = 0) \rightarrow (v' = 0) + I$ on surface A. Circles represent points spaced by 0.05 meV; triangles represent points spaced by 0.1 meV. The energies indicated are reagent translational energies. Arrows parallel to the curve indicate direction of increasing energy.

energy region corresponding to the second peak for surface A, the Argand diagram does not display such behavior, nor does that for surface B (not displayed), which has the appearance of a smooth clockwise spiral.

It has been shown [26] that for collinear symmetric atom-diatom systems of the form $A + BA$, at energies for which vibrationally excited channels of the BA molecule are closed, the difference, $\delta_S - \delta_A$, between the symmetric and antisymmetric eigenphase shifts increases by π across a narrow isolated resonance. In fig. 5 we display δ_S , δ_A , and their difference as a function of reagent translational energy for surface A. Over the energy range considered, only the $v = 0$ state of HI is accessible, and the open part of the R matrix has dimensions 2×2 . Its eigenvectors are independent of energy and correspond to symmetric and antisymmetric scattering states, and its eigenvalues are $\tan \delta_S$ and $\tan \delta_A$, respectively. It can be seen from fig. 5 that $\delta_S - \delta_A$ changes by ≈ 2.6 rad ($\approx 0.85 \pi$ rad) over the energy range associated with the narrow peak in fig. 3. This is slightly less than π rad because this resonance is not completely isolated, as is indicated by the fact that the reaction probability drops to 0.2

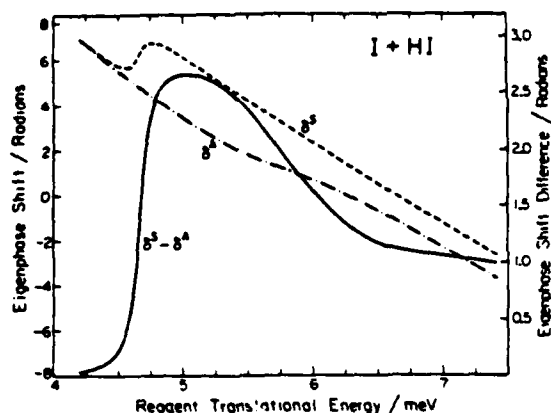


Fig. 5. Symmetric (δ_S , dashed line) and antisymmetric (δ_A , dashed-dotted line) eigenphase shifts as a function of reagent translational energy calculated for surface A. The difference $\delta_S - \delta_A$ (solid line) is also shown (the right-hand ordinate scale is the appropriate one for this quantity).

rather than 0 after that peak, before starting to increase again. The time delay associated with this resonance,

$$\tau = 2\hbar d(\delta_S - \delta_A)/dE,$$

has a maximum value of 2.04×10^{-11} s, which is much larger than the symmetric stretch vibration period of 4.60×10^{-13} s for the saddle point configuration of surface A. For comparison, across the broad peak in fig. 3 for surface B, $\delta_S - \delta_A$ increases by 0.14π rad only, the corresponding maximum value of τ is 4.74×10^{-13} s, compared with 4.64×10^{-13} s for the saddle point symmetric stretch period of that surface. We conclude that the sharp peak in fig. 3 for surface A is associated with a strong, long-lived resonance, whereas for surface B, the broad peak in fig. 3 is at most associated with a very weak resonance. This indicates once more [9,27] the great sensitivity that dynamic resonances on reactive systems can have to details of the saddle point region of potential energy surfaces. This sensitivity holds out the enticing possibility that the experimental measurement of such resonances may be useful in the determination of the characteristics of that region of potential energy surfaces.

An interpretation of this resonance can be obtained as follows. The hyperspherical coordinate method used in the present calculations [16-18] involves a radial distance ρ and a polar angle α associated with Delves' coordinates R_α, r_α of fig. 1. For fixed ρ , we can calculate the eigenvalues $E_n(\rho)$ of the α motion. A plot

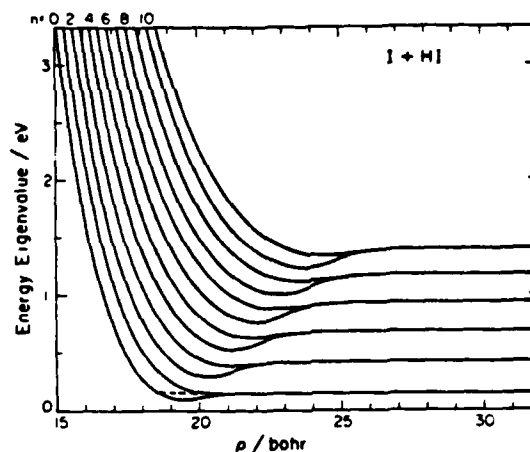


Fig. 6. Eigenvalues $E_n(\rho)$ for surface A as a function of the propagation coordinate ρ . These curves are pairwise degenerate at large ρ , the symmetric one being always lower than the corresponding antisymmetric one at small ρ . Values of n for the symmetric curves are shown at the top of the figure. The dashed line in the $E_0(\rho)$ curve shows the position of the resonance and lies slightly above $E_0(\infty)$.

of the 12 lowest such eigenvalues versus ρ is given in fig. 6, and they show minima for the ones corresponding to symmetric eigenfunctions. Since motion from reagents to products across the strong interaction region of the surface involves a relatively small change in ρ and a relatively large fractional change in α , an α -adiabatic model of resonances was proposed recently [28]. This model consists of solving the Schrödinger equation for the quasi-bound one-dimensional ρ motion on each of the individual $E_n(\rho)$ curves, in analogy to the Born-Oppenheimer separation of electronic and nuclear motions. It was shown to work well for the first resonance in $H + H_2$ and its symmetric isotope counterparts. For the $n = 0$ curve of fig. 6, this model predicted the position and width of the surface A resonance indicated by "model I" in table 2. The agreement with the exact values is satisfactory.

Babamov and Marcus [29] have recently shown that for H-L-H symmetric systems, below the opening of the first excited state, the P_{00}^R reaction probability is related to the phase shifts δ_S^{1D} and δ_A^{1D} , obtained from the one-dimensional ρ motion described above, by the expression

$$P_{00}^R = \sin^2(\delta_S^{1D} - \delta_A^{1D}).$$

Table 2
Calculated and predicted properties of peaks of reaction probability versus energy curves

	Exact	Model I ^{a)}	Model II ^{b)}
surface A			
resonance location (meV)	6.08	4.7	4.7
resonance width (meV)			
fwhm	0.16	0.12	0.13
surface B			
peak location (meV)	8.00	c)	8.2
maximum reaction probability	0.187	c)	0.19

a) Ref. [28]. b) Ref. [29]. c) Not applicable, since this feature is not a resonance.

Using this relation, we obtain the peak locations and widths given in the "model II" column of table 2. The agreement with the accurate values is about the same as for model I for the surface A resonance. However, it is better than model I in that it also predicts quite well the position and height of the broad peak for surface B, which is not a resonance, whereas model I is not applicable to features that are not resonances.

The difference in the dynamics of the reaction on the two surfaces at higher energies consists of a shift of the P_{00}^R curve by ≈ 30 or 35 meV to the right on going from surface A to surface B. This shift is significantly higher than either the difference between the corresponding barrier heights (7.5 meV) or between the reagent zero-point energies measured with respect to the corresponding barrier tops (10.3 meV). The reason for this may be that, since the reagent ground-state energies are significantly greater than the saddle point energy, the sharp skew angle of the coordinate system makes "corner cutting" quite likely. This suggests that the dominant region of the surface occurs at larger values of ρ than that of the saddle point. Additional information on this matter can be obtained from maps of quantum streamlines of probability current density or classical trajectories.

The oscillatory nature of the P_{00}^R versus energy curves at translational energies above 10 meV is not of a quantum nature, as it is also present in the classical trajectory results displayed in fig. 2

We wish to emphasize the ease with which the method of hyperspherical coordinates may be applied to collinear H-L-H systems. Applications of previous methods based on a propagation variable that scans the potential energy surface from the reagent region

through the strong interaction region to the product region [8,30,31] are made very difficult by the smallness of the skew angle. Indeed, these methods involve expansions in eigenfunctions of cuts of the surface along a direction more or less transverse to the minimum energy path, and, as a result of that small angle, such cuts are very broad and support a large number of bound states. Indeed, for the IH_1 system considered in this paper, the symmetric stretch cut through the surface A saddle point supports 50 bound states with energies below that of the $v = 2$ state of the isolated HI molecule, which is open at the highest energy considered in these calculations. In order to incorporate all such open local states and a sufficiently large number of closed states in that expansion so as to achieve reasonable convergence of the results would require an unreasonably large number of channels. By contrast, the present method requires only six even and six odd channels, as described in section 2. The essential reason for the adequacy of such a small number of channels is that the hyperspherical coordinates avoid a proliferation of open-channel basis functions. Indeed, for these coordinates the number of open channels in the strong interaction region is about the same as it is in the separated reagent or separated product regions of the potential energy surface, as shown in fig. 6. This method is therefore to be preferred for the study of collinear H-L-H systems, whether symmetric or not.

Acknowledgement

We would like to thank Dr. Vasil Babamov for many

helpful discussions. The calculations reported were performed on the Dreyfus-NSF Theoretical Chemistry Computer (VAX 11/780) which was funded through grants from the Camille and Henry Dreyfus Foundation, the National Science Foundation (Grant No. CHE78-20235), and the Sloan Fund of the California Institute of Technology, and on the IBM 370/158 computer of Ambassador College, Pasadena, California, for which we express our appreciation.

References

- [1] M.R. Levy, *Progr. Reaction Kinetics* 10 (1979) 1.
- [2] R.D.H. Brown, G.P. Glass and I.W.M. Smith, *J. Chem. Soc. Faraday Trans. II* 71 (1975) 1963;
J.R. Grover, C.R. Iden and H.V. Lilenfeld, *J. Chem. Phys.* 64 (1976) 4657;
M. Kneba and J. Wolfrum, *J. Phys. Chem.* 83 (1979) 69;
C.-C. Mei and C.B. Moore, *J. Chem. Phys.* 70 (1979) 1759;
E. Würzburg and P.L. Houston, *J. Chem. Phys.* 72 (1980) 5915.
- [3] R.D.H. Brown and I.W.M. Smith, *Intern. J. Chem. Kinetics* 10 (1978) 1;
R.G. Macdonald and C.B. Moore, *J. Chem. Phys.* 68 (1978) 513;
J.E. Butler, J.W. Hudgens, M.C. Lin and G.K. Smith, *Chem. Phys. Letters* 58 (1978) 216.
- [4] P.A. Andresen and A.C. Luntz, *J. Chem. Phys.* 72 (1978) 5842.
- [5] A.T. Pritt Jr. and R.D. Coombe, *J. Chem. Phys.* 65 (1976) 2096;
J.R. Wiesenfeld and G.L. Wolk, *J. Chem. Phys.* 67 (1977) 509;
A.J. Grimley and P.L. Houston, *J. Chem. Phys.* 68 (1978) 3366.
- [6] I.W.M. Smith and P.M. Wood, *Mol. Phys.* 25 (1973) 441;
I.W.M. Smith, *J. Chem. Soc. Faraday Trans. II* 71 (1975) 1970.
- [7] C.A. Parr, J.C. Polanyi and W.H. Wong, *J. Chem. Phys.* 58 (1973) 5;
H.E. Bass, L.S. Kenton and D.L. Thompson, *Chem. Phys. Letters* 44 (1976) 45.
- [8] A. Kuppermann, in: *Proceedings of the Summer School on Chemical Photophysics, Les Houches, France, 18-30 June 1979*, eds. P. Glorieux, D. Lecler and R. Vetter (Centre de la Recherche Scientifique, Paris, 1979) pp. 293-384; in: *Theory of scattering, Vol. 8. Theoretical chemistry: advances and perspectives*, eds. D. Henderson and H. Eyring (Academic Press, New York, 1980), to be published.
- [9] A. Kuppermann, in: *The Physics of Electronic and Atomic Collisions, Invited Lectures, Review Papers and Progress Reports of the 9th International Conference on the Physics of Electronic and Atomic Collisions, Seattle, Washington, 24-30 June 1975*, eds. J.S. Risley and R. Geballe (University of Washington Press, Seattle, 1976) pp. 259-274.
- [10] G.C. Schatz and A. Kuppermann, *J. Chem. Phys.* 65 (1976) 4652, 4668;
A. Kuppermann, *Nucl. Phys. A*, to be published.
- [11] A.B. Elkowitz and R.E. Wyatt, *J. Chem. Phys.* 62 (1975) 2504; 63 (1975) 702.
- [12] R.B. Walker, E.B. Stechel and J.C. Light, *J. Chem. Phys.* 69 (1978) 2992.
- [13] J.N.L. Connor, *Computer Phys. Commun.* 17 (1979) 117.
- [14] M. Baer, *J. Chem. Phys.* 62 (1975) 305.
- [15] E.J. Shipsey, *J. Chem. Phys.* 58 (1973) 232;
J.P. Simons and P.W. Tasker, *J. Chem. Soc. Faraday Trans. II* 70 (1974) 1496;
T. Shirai, K. Igushi and T. Watanabe, *J. Phys. Soc. Japan* 49 (1976) 1137;
M. Kimura, *Chem. Phys. Letters* 45 (1977) 489;
M.Ya. Ovchinnikova, *Chem. Phys.* 36 (1979) 85.
- [16] A. Kuppermann, J.A. Kaye and J.P. Dwyer, *Chem. Phys. Letters* 74 (1980) 257;
J.P. Dwyer, *Quantum Mechanical Studies of Molecular Scattering*, Ph.D. Thesis, California Institute of Technology (1977);
R.T. Ling and A. Kuppermann, in: *Electronic and Atomic Collisions, Abstracts of Papers of the 9th International Conference on the Physics of Electronic and Atomic Collisions, Seattle, Washington, 24-30 July 1975*, eds. J.S. Risley and R. Geballe (University of Washington Press, Seattle, 1975) pp. 353, 354.
- [17] G. Hauke, J. Manz and J. Röhmelt, *J. Chem. Phys.*, to be published.
- [18] K. Röhmelt, *Chem. Phys. Letters* 74 (1980) 263.
- [19] M. Karplus, R.N. Porter and R.D. Sharma, *J. Chem. Phys.* 43 (1965) 3259.
- [20] R.N. Porter and L.M. Raff, in: *Dynamics of molecular collisions, Part B*, ed. W.H. Miller (Plenum Press, New York, 1976) pp. 1-52;
D.G. Truhlar and J.T. Muckerman, in: *Atom-molecule collision theory*, ed. R.B. Bernstein (Plenum Press, New York, 1979) pp. 505-565.
- [21] P.J. Kuntz, E.M. Nemeth, J.C. Polanyi, S.D. Rosner and C.E. Young, *J. Chem. Phys.* 44 (1966) 1168.
- [22] H. Eyring, J. Walter and G.E. Kimball, *Quantum chemistry* (Wiley, New York, 1944) pp. 272, 273.
- [23] M.D. Pattengill and J.C. Polanyi, *Chem. Phys.* 3 (1974) 1;
M.D. Pattengill, J.C. Polanyi and J.L. Schreiber, *J. Chem. Soc. Faraday Trans. II* 72 (1976) 449.
- [24] S.V. O'Neill, H.F. Schaefer III and C.F. Bender, *Proc. Natl. Acad. Sci. US* 71 (1974) 104;
P. Botschwina and W. Meyer, *Chem. Phys. Letters* 44 (1976) 449.
- [25] G.C. Schatz and A. Kuppermann, *J. Chem. Phys.* 59 (1973) 964, and references therein.

- [26] G.C. Schatz, Ph.D. Thesis, California Institute of Technology (1975);
G.C. Schatz and A. Kuppermann, in preparation.
- [27] F.M. Chapman and E.F. Hayes, *J. Chem. Phys.* 62 (1975) 4400; 65 (1976) 1032.
- [28] J.P. Dwyer, Ph.D. Thesis, California Institute of Technology (1977);
A. Kuppermann and J.P. Dwyer, in: *Electronic and Atomic Collisions, Abstracts of Contributed Papers, 11th International Conference on the Physics of Electronic and Atomic Collisions* (Society for Atomic Collision Research, Japan, 1979) pp. 888, 889.
- [29] V.K. Babamov and R.A. Marcus, *J. Chem. Phys.* 74 (1981), to be published.
- [30] C.C. Rankin and J.C. Light, *J. Chem. Phys.* 51 (1969) 1701;
G.M. Miller and J.C. Light, *J. Chem. Phys.* 54 (1971) 1635, 1643.
- [31] A. Kuppermann, in: *Proceedings of the Conference on Potential Energy Surfaces in Chemistry*, ed. W.A. Lester (University of California, Santa Cruz, 1970) pp. 121-124; in: *Electronic and Atomic Collisions, Abstracts of Papers, 7th International Conference on the Physics of Electronic and Atomic Collisions* (North-Holland, Amsterdam, 1971) pp. 3-5;
G.C. Schatz, J.M. Bowman and A. Kuppermann, *J. Chem. Phys.* 63 (1975) 674.

QUANTUM MECHANICAL COUPLED-CHANNEL COLLISION-INDUCED DISSOCIATION CALCULATIONS WITH HYPERSPHERICAL COORDINATES ^{*}

Jack A. KAYE ^{*} and Aron KUPPERMANN

Arthur Amos Noyes Laboratory of Chemical Physics ^{}, California Institute of Technology, Pasadena, California 91125, USA*

Received 2 December 1980

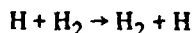
A time-independent coupled-channel method, using hyperspherical coordinates, has been developed for calculating quantum mechanical collision-induced dissociation probabilities for collinear atom-diatom systems in which the exchange reaction can also occur. The results for a model potential energy surface are compared with quasi-classical trajectory calculations and discussed.

1. Introduction

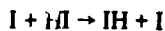
The collision-induced dissociation (CID) of diatomic molecules has been the subject of extensive experimental investigation [1-3]. In order to understand and to model this important process [4], it is necessary to obtain the bound-to-continuum transition probabilities as well as the usual bound-to-bound ones. Approximate classical [5], semi-classical [6], and quantum [7] techniques have been created for this purpose. However, the development of accurate quantum mechanical methods for systems in which CID competes with exchange processes has been hindered by the difficulty of representing the exchange product bound states in terms of the reagent bound and continuum states [7,8]. As a result, systems in which the exchange channel is absent have mainly been considered in previous calculations [7,9]. A method capable of taking such rearrangement channels into account, based on a multiple-collision expansion, has recently been applied for a potential that, however, does not support exchange products [10].

Kulander [11] has included exchange processes by solving numerically the time-dependent Schrödinger equation for cleverly chosen initial wave packets and obtained bound-to-continuum and bound-to-bound transition probabilities in collinear atom-diatom collisions. This conceptually elegant method is, however, computationally time consuming and difficult to apply at energies close to the dissociation threshold.

In this paper we report the first successful time-independent treatment of CID in a collinear atom-diatom system in which the exchange process is present. This work uses the method of hyperspherical coordinates [12-16] which has recently been applied to the collinear exchange reactions



and [17]



at energies below dissociation.

In section 2 we briefly outline the nature and the method of hyperspherical coordinates, emphasizing those aspects of it which are crucial in the treatment of CID. The potential energy surface used in these calculations is discussed in section 3, and the results obtained are presented, discussed, and compared with those from quasi-classical trajectory calculations in section 4.

^{*} Supported in part by a Contract (No. F49620-79-C-0187) from the US Air Force Office of Scientific Research.

^{*} Work performed in partial fulfillment of the requirements for the Ph.D. degree in Chemistry at the California Institute of Technology.

^{*} Contribution No. 6302.

2. Theory

Let us consider the A + BC system, with A, B, and C representing distinguishable atoms confined to move on a laboratory-fixed straight line. Let r'_α and R'_α be, respectively, the BC internuclear distance and the distance of A to the center of mass of BC. Let r'_γ and R'_γ be the corresponding distances with the roles of A and C interchanged. The Delves' scaled coordinates [12], R_λ and r_λ are defined as

$$R_\lambda = a_\lambda R'_\lambda, \quad r_\lambda = a_\lambda^{-1} r'_\lambda, \quad a_\lambda = (\mu_{\lambda,\nu\kappa}/\mu_{\nu\kappa})^{1/4}. \quad (1)$$

Here, $\lambda\nu\kappa$ is either $\alpha\beta\gamma$ or $\gamma\beta\alpha$, $\mu_{\nu\kappa}$ is the reduced mass of m_ν and m_κ , $\mu_{\lambda,\nu\kappa}$ is the reduced mass of m_λ and $m_\nu + m_\kappa$, and m_α, m_β , and m_γ are the masses of A, B, and C, respectively. The collinear hyperspherical coordinates are defined as

$$\rho = (R_\lambda^2 + r_\lambda^2)^{1/2}, \quad \alpha = \tan^{-1}(r_\alpha/R_\alpha),$$

$$0 < \alpha < \pi/2 \quad (2)$$

and are indicated in fig. 1. The Schrödinger equation for the internal motion of the ABC system is the same as that of a single particle P of mass $\mu = [m_\alpha m_\beta m_\gamma / (m_\alpha + m_\beta + m_\gamma)]^{1/2}$ moving in the two-dimensional ρ, α space and subject to the potential $V(\alpha, \rho)$ of the triatomic system. The motion of P on

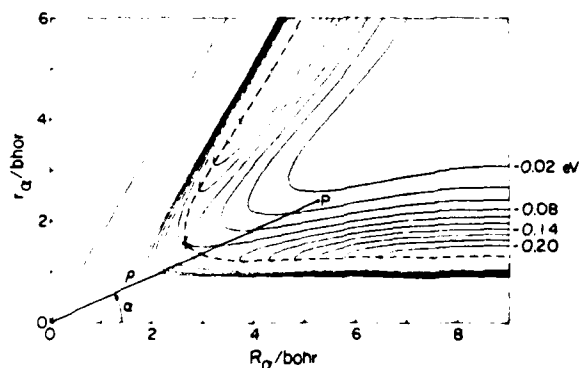


Fig. 1. Contour plot of the potential energy surface for a model collinear triatomic system in Delves' scaled coordinates R_α, r_α . The solid curves are equipotential contours at the total energies (with respect to the dissociated system) indicated in the lower side of the figure. The dashed line is the minimum energy path. The polar coordinates ρ, α of a general point P in this R_α, r_α configuration space are also indicated.

a circle of constant $\rho = \bar{\rho}$ is described by a set of energy eigenfunctions $\phi_n(\alpha; \bar{\rho})$ and eigenvalues $E_n(\bar{\rho})$. The former are called surface functions and constitute an infinite discrete set which, as $\bar{\rho} \rightarrow \infty$, spans the dissociation continuum. Expansion of the scattering wavefunction in the ϕ_n leads to a set of coupled-channel differential equations that have been derived and are integrated as described previously [13-16]# out to a sufficiently large value of ρ .

At energies at which no continuum states (those with positive eigenvalues with respect to the dissociated configuration A + B + C) need be included in the calculations, we re-expand, after that integration, the wavefunction ψ in R_α, r_α and R_γ, r_γ coordinates, using the numerically determined eigenfunctions $\phi_{\alpha n_\alpha}(r_\alpha)$ and $\phi_{\gamma n_\gamma}(r_\gamma)$ of the isolated reagent and product, respectively, as the new basis functions. In this manner, we obtain ψ and its R_λ derivative along lines of constant $R_\lambda = \bar{R}_\lambda$ ($\lambda = \alpha, \gamma$). We call this procedure a projection of ψ on the asymptotic reagent and product states. From the coefficients of this new expansion, the R, S, and P matrices are calculated by standard techniques [13,16]. For H + H₂, this procedure leads to results converged to 1% or better for values of \bar{R}_λ of ≈ 8 bohr or less [13]. Alternatively, one can omit this projection altogether, since as $\bar{\rho} \rightarrow \infty$ the $\phi_n(\alpha; \bar{\rho})$ for negative eigenvalues become the separated reagent or product eigenstates (or their even and odd linear combinations for symmetric systems). However, this leads to a large-amplitude oscillatory behavior of the reaction probabilities with ρ , as found by Römelt [19], which requires integration to appreciably larger values of ρ .

At total energies E for which dissociative channels must be included in the expansion to achieve convergence, as is the case for all collision energies above the dissociation limit, we have chosen to project the bound-state channels as described above, and not to project the continuum ones at all. In the $\bar{\rho} \rightarrow \infty$ limit these results converge to the correct ones, while maintaining the rapid rate of convergence for the bound-to-bound transition probabilities. Other projection methods are possible and are being investigated.

A method similar to that of ref. [13], using the same coordinates but a different asymptotic analysis, has been developed by Hauke et al. [18] and used by Römelt [19].

The resulting scattering matrix S is discrete, and the scattering wavefunction $\psi^{\alpha n \lambda}$, corresponding to the system being initially in bound state n_α of the diatomic target BC, has the asymptotic form (for asymmetric systems, in which atoms A and C are different)

$$\begin{aligned} \psi^{\lambda n \lambda} \sim & \sum_{\lambda' n' \lambda'} [\exp(-ik_{\lambda' n' \lambda'} R_{\lambda'}) \delta_{\lambda' n' \lambda'}^{\lambda n \lambda} \\ & + \exp(ik_{\lambda' n' \lambda'} R_{\lambda'}) (v_{\lambda n \lambda} / v_{\lambda' n' \lambda'})^{1/2} S_{\lambda' n' \lambda'}^{\lambda n \lambda}] \phi_{\lambda' n' \lambda'}(r_{\lambda'}) \\ & + \rho^{-1/2} \sum_n \exp(ik\rho) (v_{\lambda n \lambda} / v)^{1/2} S_n^{\lambda n \lambda} \phi_n(\alpha; \infty). \end{aligned} \quad (3)$$

In this expression, the sum over $\lambda' n' \lambda'$ extends over all bound states of BC and AB, whereas the sum over n extends over the continuum ($E_n > 0$) states. The several k and v represent, respectively, the appropriate channel wave numbers and velocities. In terms of the elements of the scattering matrix appearing in (3), the bound-to-bound and total bound-to-dissociated transition probabilities are given, respectively, by

$$P_{\lambda' n' \lambda'}^{\lambda n \lambda} = |S_{\lambda' n' \lambda'}^{\lambda n \lambda}|^2, \quad (4)$$

$$P_d^{\lambda n \lambda} = \sum_n |S_n^{\lambda n \lambda}|^2. \quad (5)$$

The differential probability for producing dissociated products for which atom A has a center of mass energy E_A is given by

$$\begin{aligned} \sigma_d^{\lambda n \lambda}(E_A) = & |d\alpha/dE_A| \\ & \times \text{Re} \left[\sum_{n n'} \phi_n^*(\alpha; \infty) \phi_{n'}(\alpha; \infty) (S_n^{\lambda n \lambda})^* S_{n'}^{\lambda n \lambda} \right], \end{aligned} \quad (6)$$

where α is related to E_A by

$$\begin{aligned} E_A = & E_A^{\max} \cos^2 \alpha, \\ E_A^{\max} = & [(m_\beta + m_\gamma)/(m_\alpha + m_\beta + m_\gamma)] E. \end{aligned} \quad (7)$$

The total dissociation probability is related to the differential one by

$$P_d^{\lambda n \lambda} = \int_0^{E_A^{\max}} \sigma_d^{\lambda n \lambda}(E_A) dE_A. \quad (8)$$

For symmetric systems, the $\phi_n(\alpha; \infty)$ in eqs. (3) and (6) must be replaced by appropriate linear combinations of the even and odd surface functions.

3. Potential energy surface

In order to test the method described above without excessive emphasis on bound states, we constructed a model collinear potential energy surface for which the isolated diatomic reagent or product potential energy curves supported only two such states, in analogy with weak van der Waals molecules. The mathematical form chosen for this surface was of the rotating Morse-cubic-spline type [20]. The three atoms considered were identical but distinguishable (by virtue of their relative position on the line to which they were confined), and were assigned a mass equal to that of a hydrogen atom. The corresponding isolated diatomic molecules were chosen to have Morse parameters [21] $D_e = 0.22$ eV, $\beta = 1.6$ bohr⁻¹, and $r_e = 1.40083$ bohr. The energies of the two bound states supported by each of these Morse oscillators was 0.0817 and 0.1885 eV above the bottom of the diatom well. The saddle point occurred at internuclear distances $r'_{AB} = r'_{BC} = 1.6496$ bohr, and its height was 0.14 eV. In fig. 1 we display a contour plot of this potential energy function, and in fig. 2 we indicate schematically its features along the minimum energy path.

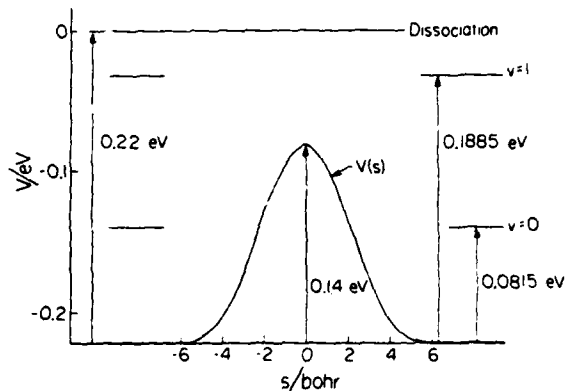


Fig. 2. Schematic diagram of the potential energy function characteristics along the minimum energy path in Delves' coordinate space. s is the distance along that path measured from the saddle point configuration, and $V(s)$ the corresponding potential energy. The horizontal lines indicate the energy levels of the bound states ($v = 0$ and 1) of the isolated diatoms and of the dissociated configuration.

4. Results and discussion

The results of these calculations as well as those of quasi-classical trajectory ones as a function of relative translational energy are given in figs. 3 and 4 for reagents in their ground and vibrationally excited states, respectively. Convergence of the transition probabilities to ± 0.02 or better was achieved with ten even and ten odd basis functions [13]. The maximum value ρ_{\max} of ρ needed to achieve this convergence was 64 bohr.

At the same translational energy, enhancement of the CID probabilities by reagent vibrational excitation is clearly observed, in agreement with a number of re-

cent studies [10,11,22]. Up to translational energies of 0.10 eV for vibrationally excited reagents and 0.15 eV for ground-state ones, the probability of the exchange reaction occurring without change of vibrational quantum number is significantly larger than the one with change in that number. Up to total energies of 0.32 eV the non-reactive inelastic process $0 \rightarrow 1$ (and $1 \rightarrow 0$) has probabilities smaller than 0.03 and is not shown in figs. 3 and 4.

The quasi-classical trajectory results display the same general features as the accurate quantum ones, giving confidence that classical mechanics furnishes an adequate qualitative description of the system's dynamics. However, errors of a factor of two or

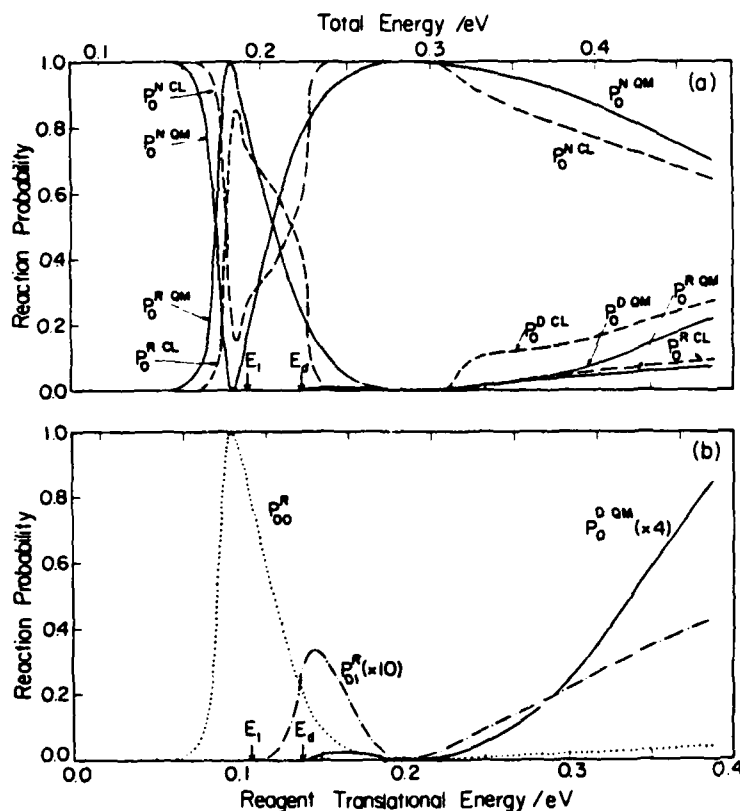


Fig. 3. Transition probabilities as a function of relative translational energy and total energy for ground-state reagents. (a) Quantum mechanical (QM, solid line) and quasi-classical (CL, dashed line) total probabilities for reactive (R), non-reactive (N), and dissociative (D) processes. The arrows on the lower abscissa labelled E_1 and E_d indicate the energies of the first vibrationally excited state of the reagent and the reagent dissociation energy, respectively. (b) State-to-state quantum mechanical probabilities for vibrationally adiabatic (P_{00}^R , dotted line) and vibrationally non-adiabatic (P_{01}^R , dashed-dotted line) reactive processes. The dissociation probability curve (P_0^D , solid line) is included again for comparison purposes. Arrows in the abscissa have the same meaning as in (a).

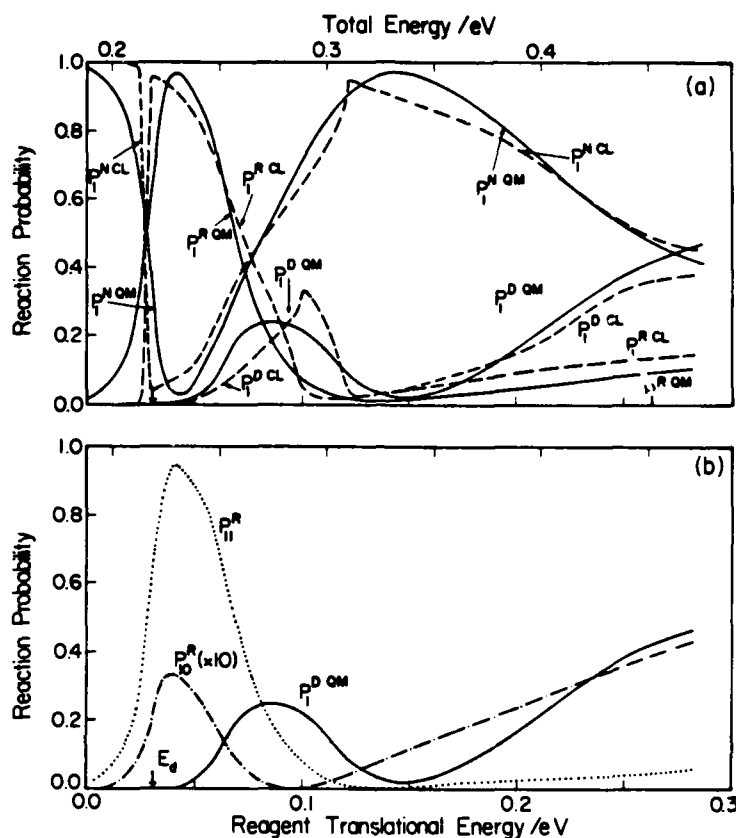


Fig. 4. Transition probabilities as a function of relative translational energy and total energy for the diatom reagent in its first (and only) vibrationally excited state. Notation is the same as for fig. 3.

greater are encountered in the quasi-classical probabilities when compared with the quantum ones.

We wish to emphasize the ease with which these calculations may be performed. The relatively large value of ρ_{\max} required for good convergence of the transition probabilities does not increase the computation time excessively since in the large ρ region the integration step is quite large (>0.1 bohr) and the calculation time increases only linearly with the number of integration steps. In addition, a more appropriate asymptotic analysis may permit a decrease in ρ_{\max} . The relatively small value of the number of $E_n > 0$ channels of each parity needed to provide an adequate discretized representation of the dissociation continuum, namely eight, for the energy range considered, is encouraging, since the computation time varies approximately as the cube of the number of coupled channels.

This hyperspherical coordinate approach has been shown recently to be very suitable for handling heavy-light-heavy collinear reactive systems [17]. The present work indicates that it is also suitable for collinear CID calculations. Extension of the method to encompass electronically non-adiabatic processes should be straightforward [23,24]. The treatment of CID in atom-diatom collisions can, in principle, be extended to the three-dimensional physical world, since the corresponding generalization of the surface functions still forms an infinite discrete set [15,16]. This extension is particularly important, since it has been observed in classical trajectory calculations [25] that a collinear model cannot adequately describe the dynamics of CID. However, the large number of channels involved in such three-dimensional systems will undoubtedly require the introduction of approximations in the calculation.

In summary, hyperspherical coordinates seem to provide a very useful language for the description and elucidation of the dynamical processes occurring in molecular collisions, including collision-induced dissociation and its reverse, three-body recombination.

Acknowledgement

The calculations reported were performed on the Dreyfus-NSF Theoretical Chemistry Computer which was funded through grants from the Camille and Henry Dreyfus Foundation, the National Science Foundation (Grant No. CHE78-20235), and the Sloan Fund of the California Institute of Technology, and on the IBM 370/158 Computer of Ambassador College, Pasadena, California, for which we express our appreciation.

References

- [1] R.L. Belford and R.A. Strehlow, *Ann. Rev. Phys. Chem.* 20 (1969) 247.
- [2] E.K. Parks, N.J. Hansen and S. Wexler, *J. Chem. Phys.* 58 (1973) 5489; V. Havemann, V. Pacák, Z. Herman, F. Schneider, Ch. Zuhrt and L. Zülicke, *Chem. Phys.* 28 (1978) 147.
- [3] R. Huber and H.G. Weber, *Chem. Phys.* 35 (1978) 461.
- [4] H. Johnston and J. Birks, *Accounts Chem. Res.* 5 (1972) 327; H.O. Pritchard, *Specialist Periodical Reports Reaction Kinetics*, Vol. 1 (Chem. Soc., London, 1975) p. 243.
- [5] P.J. Kuntz, in: *Collision-induced dissociation*, Vol. 2. Trajectories and models, in atom-molecule collision theory, ed. R.B. Bernstein (Plenum Press, New York, 1979) pp. 669-693, and references therein.
- [6] I. Rusinek, *J. Chem. Phys.* 72 (1980) 4518; I. Rusinek and R.S. Roberts, *J. Chem. Phys.* 68 (1978) 1147; 65 (1976) 872.
- [7] D.J. Diestler, in: *Collision-induced dissociation*, Vol. 1. Quantal treatment, in atom-molecule collision theory, ed. R.B. Bernstein (Plenum Press, New York, 1979) pp. 655-667, and references therein.
- [8] G. Wolken Jr., *J. Chem. Phys.* 63 (1975) 628.
- [9] L.W. Ford, D.J. Diestler and A.F. Wagner, *J. Chem. Phys.* 63 (1975) 2019; E.-W. Knapp, D.J. Diestler and Y.-W. Lin, *Chem. Phys. Letters* 49 (1977) 379; E.-W. Knapp and D.J. Diestler, *J. Chem. Phys.* 67 (1977) 4969.
- [10] L.H. Beard and D.A. Micha, *J. Chem. Phys.* 73 (1980) 1193.
- [11] K.C. Kulander, *J. Chem. Phys.* 69 (1978) 5064.
- [12] L.N. Delves, *Nucl. Phys.* 9 (1959) 391; 20 (1960) 275.
- [13] A. Kuppermann, J.A. Kaye and J.P. Dwyer, *Chem. Phys. Letters* 74 (1980) 257.
- [14] J.P. Dwyer, *Quantum Mechanical Studies of Molecular Scattering*, Ph.D. Thesis, California Institute of Technology (1977).
- [15] R.T. Ling and A. Kuppermann, in: *Electronic and Atomic Collisions*, Abstracts of Papers of the 9th International Conference on the Physics of Electronic and Atomic Collisions, Seattle, Washington, 24-30 July 1975, eds. J.S. Risley and R. Geballe (University of Washington Press, Seattle, 1975) pp. 353-354; J.K.C. Wong and A. Kuppermann, Abstracts of Papers of the Pacific Conference on Chemistry and Spectroscopy, Pasadena, California, 10-12 October 1979, p. 39.
- [16] A. Kuppermann, in: *Proceedings of the Summer School on Chemical Photophysics*, Les Houches, France, 18-30 June 1979, eds. P. Glorieux, D. Leclerc and R. Vetter (Centre National de la Recherche Scientifique, Paris, 1979) pp. 293-384.
- [17] J.A. Kaye and A. Kuppermann, *Chem. Phys. Letters* 77 (1981) 573.
- [18] G. Hauke, J. Manz and J. Römelt, *J. Chem. Phys.*, to be published.
- [19] J. Römelt, *Chem. Phys. Letters* 74 (1980) 263.
- [20] J.M. Bowman and A. Kuppermann, *Chem. Phys. Letters* 34 (1975) 523.
- [21] H. Eyring, J. Walter and G. Kimball, *Quantum chemistry* (Wiley, New York, 1944) pp. 272, 273.
- [22] J.C. Gray, G.A. Fraser and D.G. Truhlar, *Chem. Phys. Letters* 68 (1979) 359; J.C. Gray, G.A. Fraser, D.G. Truhlar and K.C. Kulander, *J. Chem. Phys.*, to be published.
- [23] J.M. Bowman, S.C. Leasure and A. Kuppermann, *Chem. Phys. Letters* 44 (1976) 499.
- [24] Z.H. Top and M. Baer, *J. Chem. Phys.* 66 (1977) 1363.
- [25] T. Lehr and J.W. Birks, *J. Chem. Phys.* 70 (1979) 4843.

Mass effect in quantum mechanical collision-induced dissociation in
collinear reactive atom-diatomic molecule collisions.

I. Symmetric systems^{a)}

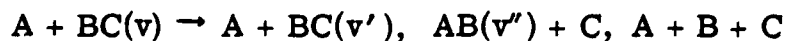
Jack A. Kaye^{b)} and Aron Kuppermann

Arthur Amos Noyes Laboratory of Chemical Physics,^{c)}

California Institute of Technology, Pasadena, California 91125

(Received)

Quantum mechanical probabilities for collision-induced dissociation (CID) and chemical reactions have been obtained for a model triatomic collinear system,



using hyperspherical coordinates. Details of the methodology used for CID are presented. Calculations were performed for three different symmetric mass combinations ($m_A = m_B = m_C$, $m_A = m_C \neq m_B$) corresponding to light-light-light, heavy-light-heavy, and light-heavy-light systems. CID was found to be enhanced by reagent vibrational energy and to be most likely in the light-heavy-light system and least likely in the heavy-light-heavy system. Vibrationally nonadiabatic processes

a) This work was supported in part by a contract (No. F49620-79-C-0187) from the Air Force Office of Scientific Research.

b) Work performed in partial fulfillment of the requirements for the Ph. D. degree in Chemistry at the California Institute of Technology.

c) Contribution No.

were found to be of only secondary importance compared with either CID or vibrationally adiabatic ones. The activation energies for CID were found to be substantially in excess of the energetic threshold. The exchange reaction was found to be vibrationally enhanced, the reagent vibrational excitation being partly effective in lowering the activation energy of the reaction. Indication of a resonance in the heavy-light-heavy system has been found in spite of the large barrier to reaction. Quasi-classical trajectory calculations on the light-light-light system suggest that classical mechanics furnishes an adequate representation of the main features of the dynamics in these systems.

I. INTRODUCTION

The collision-induced dissociation (CID) of diatomic molecules

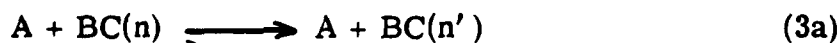


and its inverse process three-body recombination



have been of great interest over the years to both experimentalists and theoreticians. To experimentalists, much of the interest has arisen from unusual temperature dependence of the rate of these reactions: the activation energy for CID is frequently less than the dissociation energy of the diatomic molecule,¹ and the rate of three-body recombination frequently decreases with increasing temperature.²

To theoreticians, however, the challenge has been to describe the dynamics of the collision process itself from first principles. Because of the double continuum of product states inherent in CID, this is far more complicated for this process than for the usual inelastic and/or reactive atom-diatom molecule collision problem,



where n represents the set of all quantum numbers (electronic, vibrational, and rotational). Extension of the coupled-channel formulation to exact quantum mechanical calculations of CID, occurring in competition with exchange processes, has previously not been possible.³

Information about the CID process (and its inverse process three-body recombination) has been obtained from models based on kinematics,⁴ from quasi-classical trajectory calculations,⁵ from

semi-classical calculations,⁶ and from statistical models.⁷ Quantum mechanical treatments have been limited mainly to studies of systems in which only CID and inelastic nonreactive processes [such as those represented by Eq. (3a)] occur.³ Only recently have exact quantum mechanical methods for CID for systems in which chemical reactions [Eq. (3b)] may also occur been developed. These techniques consist of the time-dependent wave-packet approach developed by Kulander,¹⁰ which has been applied to the collinear $H + H_2$ system above threshold, a multiple collision formalism developed by Beard and Micha (but so far applied only to nonreactive systems),¹¹ and the time-independent hyperspherical coordinate methods, developed independently by Kuppermann et al.¹² and Manz et al.¹³

The ability to study reactive systems is important, as experiments and quasi-classical trajectory calculations suggest that CID and its inverse process, three-body recombination, is much more rapid in reactive systems than in nonreactive ones.⁸ In addition, the detailed nature of the dissociation or recombination processes may be different in reactive and nonreactive systems due to the greater diversity of types of collisions.⁹

As accurate quantum studies of CID are relatively new, it is important to perform studies that help to develop intuition about the effect on the CID process of changes in the potential energy surface and in the masses of the atoms involved. Most such studies have been limited to nonreactive systems, notably the quasi-classical trajectory calculations of Wong and Burns¹⁴ on rare-gas plus bromine collisions and the collision-induced ion-pair experiments of Tully et al. on rare gas plus alkali halide systems¹⁵ and of Parks et al. on

rare gas plus thallium halide monomer and dimer systems.¹⁶

In this work we will discuss in detail the results of exact collinear quantum mechanical CID calculations on a model reactive potential energy surface for three different mass combinations: $m_A = m_B = m_C = 1$; $m_A = m_C = 10$, $m_B = 1$; and $m_A = m_C = 1$, $m_B = 35$, in units of the H-atom mass. Results for one of these mass combinations (and comparisons with collinear quasi-classical trajectory calculations) have been summarized previously.^{12c} We will analyze and interpret the probability versus energy curves and temperature dependence of the corresponding CID and exchange reaction rate constants for the three cases studied.

In Sec. II we describe the potential energy surface and different mass combinations used in these calculations. In Sec. III we briefly review the application of the hyperspherical coordinate methods to CID. In Sec. IV we present the results obtained in these calculations, which are analyzed and discussed in Sec. V. Finally, in Sec. VI we summarize our results.

II. POTENTIAL ENERGY SURFACE

The potential energy surface V used in the calculations reported here is of the rotating Morse cubic spline type,¹⁷ and has been briefly described previously.^{12b} The three atoms are labeled A, B, and C, with B always occupying the middle position, and R_{AB} and R_{BC} representing the distance of the latter to A and C, respectively. For $R_{AB} > 7$ bohr and $R_{BC} < 7$ bohr, the potential energy function is that of a Morse oscillator

$$V(R_{AB}, R_{BC}) = D_e \{ [e^{-\beta(R_{BC}-R_{eq})} - 1]^2 - 1 \}, \quad (4)$$

where $D_e = 0.22$ eV, $\beta = 1.6$ bohr⁻¹, and $R_{eq} = 1.40083$ bohr. For $R_{BC} > 7$ bohr and $R_{AB} < 7$ bohr, an expression analogous to (4), with the roles of R_{AB} and R_{BC} interchanged, is used. For both R_{AB} and R_{BC} greater than 7 bohr, $V(R_{AB}, R_{BC}) = 0$. Finally, for R_{AB} and R_{BC} both smaller than 7 bohr, V is defined in Ref. 17. It has the form of a Morse curve,

$$V(R_{AB}, R_{BC}) = D(\theta) \{ (1 - \exp[\beta(\theta)(\ell_{eq}(\theta) - \ell)]^2 - 1 \} + D(\theta = 0).$$

In this expression, θ is the swing angle defined in Fig. 1 around the point S whose coordinates are $R_{AB} = R_{BC} = 7$ bohr, and ℓ is the distance of the point $P(R_{AB}, R_{BC})$ to S. θ varies from 0° to 90°, and the θ -dependent Morse parameters $D(\theta)$, $\ell_{eq}(\theta)$ and $\beta(\theta)$ are symmetric with respect to $\theta = 45^\circ$ and are defined as follows. $D(\theta)$ is given by the Gaussian function

$$D(\theta) = D_e - b \{ \exp[-c(\frac{\pi}{4} - \theta)^2] - \exp[-c(\frac{\pi}{4})^2] \}, \quad (5)$$

where $b = 0.14101$ eV and $c = 8.00876$ rad⁻¹, yielding a classical barrier

height of 0.14 eV. The functions $\ell_{eq}(\theta)$ and $\beta(\theta)$ are given in Table I for eight values of θ in the range 0° to 45° . For intermediary values of θ , they are obtained by a cubic spline interpolation. For θ in the range of 45° to 90° , they are obtained by the symmetry condition with respect to $\theta = 45^\circ$. A plot of the potential energy surface in Delves¹⁸ mass scaled coordinates for the mass combination 1 - 1 - 1 is given in Fig. 2. As described previously, for this mass combination, asymptotically the Morse oscillator supports two ground states, with energy eigenvalues of 0.0817 and 0.1885 eV above the bottom of the isolated diatomic well.

In order to help elucidate the nature of the dependence of CID on masses, we considered, in addition, the mass combinations 10 - 1 - 10 and 1 - 35 - 1. These were chosen to broadly scan the possible range (0° to 90°) of skew angles in Delves¹⁸ mass weighted coordinates, as it is known that this skew angle plays a major role in determining the dynamics of a reactive system independent of the nature of the forces between the atoms.¹⁹ These mass combinations give skew angles of 24.62° and 88.41° , respectively, whereas the skew angle for the 1 - 1 - 1 combination is 60° . Various properties of the different mass combinations are summarized in Table II. Of particular note is the fact that for the 10 - 1 - 10 and 1 - 35 - 1 mass combinations, there are three bound states of the isolated diatomic molecules, as opposed to two for the 1 - 1 - 1 combination. Also, the two lowest eigenvalues of the isolated 1 - 10 and 35 - 1 diatomic molecules are quite similar, which suggests that differences in CID for these two systems cannot be attributed to differing amounts of reagent vibrational excitation energy.

III. THE HYPERSPHERICAL COORDINATE METHOD AND ITS APPLICATION TO CID

The hyperspherical coordinate method has been outlined previously^{12a, 20} and we will not repeat the formalism in detail here. We have also indicated briefly how the method is applied to CID, and will expand upon that aspect of the treatment.

In the hyperspherical coordinate approach, the primitive wavefunctions $\psi_j(\rho, \alpha)$ are expanded in terms of a discrete set of basis functions,

$$\psi_j(\rho, \alpha) = \rho^{-\frac{1}{2}} \sum_{i=1}^N g_{ij}(\rho, \bar{\rho}) \phi_i(\alpha; \bar{\rho}) , \quad (6)$$

where ρ and α are, respectively, the distance and angle coordinates of a point in Delves' configuration space, and $\bar{\rho}$ is the value of ρ at which the diabatic basis functions ϕ_i are calculated. The use of a diabatic basis set gives rise to a parametric dependence of the expansion coefficients g_{ij} on $\bar{\rho}$. N is the number of channels included in the calculation.

As indicated previously,^{12a} when ρ is sufficiently large and the $A + BC$ and $AB + C$ configurations are sufficiently separated from one another by the dissociative plateau, we may rewrite that portion ψ_j^b of the wavefunction that correlates asymptotically with the BC or AB by reexpanding it in terms of the eigenfunctions of the corresponding isolated diatomic molecule [in Delves¹⁸ coordinates],

$$\psi_j^{b, A+BC}(\rho, \alpha) = \sum_{i=1}^{N_b^{BC}} h_{ij}^{A+BC}(R_A; \overline{R_A} = \infty) \chi_i^{A+BC}(r_A; \overline{R_A} = \infty), \quad (7)$$

a similar expression being used for ψ_j^{AB+C} . Using the orthogonality of the basis set $\chi^{A+BC}(r_A; \overline{R_A} = \infty)$, the h_{ij}^{A+BC} coefficients defined above

can be calculated from

$$h_{ij}^{A+BC}(R_A; \overline{R_A} = \infty) = \int_{r_A^{(\min)}}^{r_A^{(\max)}} \chi_i^{A+BC}(r_A; \overline{R_A} = \infty) \times \psi_j^{b, A+BC}(\rho, \alpha) dr_A, \quad (8)$$

where the integration limits are chosen so that contributions to the integral from outside their range are negligible. In this expression, ρ and α are functions of r_A and R_A through the relations $\rho = (r_A^2 + R_A^2)^{\frac{1}{2}}$ and $\alpha = \tan^{-1}(r_A/R_A)$. The derivative of the radial wavefunction matrix \underline{h}^{A+BC} with respect to R_A is obtained by differentiating Eq. (8) with respect to this variable.

In the symmetric systems studied here (where the mass combination is of the A + BC type), a projection onto the basis functions of the isolated AB diatomic need not be performed explicitly, as $\chi_i^{A+BC} = \chi_i^{AB+C}$ when A = C. In this case, we may obtain the corresponding radial wavefunction matrix elements from the relationship

$$h_{ij}^{AB+C}(R_C; \overline{R_C} = \infty) = \begin{cases} h_{ij}^{A+BC}(R_A; \overline{R_A} = \infty) & \text{if } \psi_j \text{ is symmetric} \\ -h_{ij}^{A+BC}(R_A; \overline{R_A} = \infty) & \text{if } \psi_j \text{ is antisymmetric,} \end{cases}$$

where the symmetry of ψ_j is about the line $\alpha = \alpha_{\max}/2$. The derivatives \underline{h}' are similarly related.

The matrix \underline{G} of the coefficients used in the asymptotic (\underline{R} and \underline{S} matrix) analysis is given by

$$G = \begin{pmatrix} h_{\equiv}^{A+BC} \\ h_{\equiv}^{AB+C} \\ \rho_0^{-\frac{1}{2}} g_{\equiv}^{un} \end{pmatrix} \quad (10)$$

where h^{A+BC} is evaluated at a large value of R_A , chosen arbitrarily, and h^{AB+C} is evaluated at $R_C = R_A$. The value of ρ at which the unprojected g_{\equiv}^{un} is evaluated can be chosen according to different criteria.

One is to make it equal to R_A . Another is to make it equal to $[R_A^2 + r_A(\max)^2]^{\frac{1}{2}}$. Still another is to pick $[R_A^2 + r_A^{eq^2}(R_A)]^{\frac{1}{2}}$, where $r_A^{eq}(R_A)$ is the value of r_A for which $V(R_A, r_A)$ has a minimum for a given R_A .

Alternate choices are obtained by interchanging the roles of A and C.

In the limit as $R_A \sim \infty$, all of these should lead to the same result. In the calculations reported here, we selected the second criterion. The derivative G' is defined by the expression

$$G' = \begin{pmatrix} h_{\equiv}'^{A+BC} \\ h_{\equiv}'^{AB+C} \\ \rho_0^{-\frac{1}{2}} g_{\equiv}'^{un} - \frac{1}{2} \rho_0^{-\frac{3}{2}} g_{\equiv}^{un} \end{pmatrix} \quad (11)$$

where $g_{\equiv}'^{un}$ is also calculated at the same value of ρ as g_{\equiv}^{un} .

In the asymptotic analysis,^{21, 22} the eigenvalues of the bound states are precisely their asymptotic values due to the invariance of the potential beyond the R_{AB}, R_{BC} cutoff defined in the previous section. The eigenvalues of the continuum states decrease continuously with increasing $\bar{\rho}$, however, and the local wavenumber associated with each channel is nonzero and unique. At an infinite value of $\bar{\rho}$ and ρ , all continuum eigenvalues would be zero, however. Thus, stopping integration short of $\rho = \infty$ leads to approximations in the method, notably the

assumption that the basis set $\{\chi^{A+BC}, \chi^{AB+C}, \phi(E > 0)\}$ is orthonormal, which is not true at finite $\bar{\rho}$.

As a result of this approximation, the convergence of state-to-state reaction probabilities with the stopping point of the integration ρ_{as} (where the asymptotic analysis is performed) is not nearly as rapid as in the bound-bound problem we have studied. For the 1-1-1 mass combination, plots of dissociation probability versus integration stopping point displayed what could best be described as damped oscillations. By carrying integration in that system to $\rho = 76$ bohr, all probabilities seem to be converged to ± 0.01 ; most probabilities, especially those involving the $v = 0$ state, should be even better converged. For the 10-1-10 and 1-35-1 mass combinations, integration was carried out to $\rho = 90$ and $\rho = 45$ bohr, which correspond to about the same value $R_{AB} = R_{BC} = 30$ bohr at which the 1-1-1 integration was stopped. The difference in these three values of ρ is due to the mass scaling inherent in the Delves coordinate systems. Ten even and ten odd channels were used in the integration of the coupled equations in the 1-1-1 system; 12 of each were used for the two others. Flux was conserved to better than 3% in the 1-1-1 calculations, 4.5% in the 10-1-10 calculations, and 12.5% in the 1-35-1 calculations. These limits were obtained at the highest energies; at lower energies, the flux conservation was far better. Since our interests here are mainly qualitative (i. e., to consider general dependence at CID on the initial reagent vibrational state and on the mass combination), we considered these calculations to be sufficiently accurate for analysis.

Rate constants were obtained from the calculated reaction probabilities by straightforward numerical integration, assuming an equilibrium (Boltzmann) distribution of relative kinetic energies. For the 1-1-1 system, rate constants were calculated using results obtained from scattering calculations in which the integration was stopped at $\rho = 32$ bohr, as calculations were performed for far more energies in these calculations than in those in which the integration was carried out to $\rho = 76$ bohr.

Arrhenius parameters (pre-exponential factors and activation energies) were obtained by a least-squares fit to the rate constant data over a region of temperature in which the Arrhenius plots (logarithm of rate constant versus inverse temperature) were linear.

IV. RESULTS

We have studied the dynamics of the model system described above for the mass combinations 1-1-1, 10-1-10, and 1-35-1 up to an energy 0.25 eV above the dissociation energy of the isolated diatomic molecules. Our attention has been focused on the probabilities of reaction and dissociation as a function of translational energy and of reagent vibrational excitation. We have looked at the amount of vibrational nonadiabaticity in the exchange reactions, and have calculated state-to-all and, in some cases, state-to-state rate constants (and their associated Arrhenius parameters).

Plots of state-to-state reaction probability versus reagent translational energy for the 1-1-1, 10-1-10, and 1-35-1 mass combinations are shown in Figs. 2, 3, and 4, respectively. The figures are constructed such that in any one figure, a vertical line always corresponds to the same total energy. Hence, the translational origins in each panel within a figure are shifted to account for the different internal energy in each reagent vibrational level. In Figs. 5, 6, and 7, similar plots are constructed for the total reactive, nonreactive, and dissociative probabilities. Reactive and dissociative rate constants in the temperature range $200^{\circ}\text{K} < T < 650^{\circ}\text{K}$ for the three mass combinations are given in the form of Arrhenius plots (in $^{\circ}\text{K}$ versus $1/T$) in Figs. 8, 9, and 10. Finally, in Fig. 11, we present Arrhenius plots of state-to-state reactive (and dissociative) rate constants for the 1-35-1 mass combination, as that is the one with the greatest amount of vibrational nonadiabaticity and dissociation.

V. DISCUSSION

Two main features are evident in the results obtained from these calculations. First, there is substantial vibrational enhancement of CID as the reagent vibrational energy is increased, in all of the systems studied. Second, there is a major difference in the CID probability versus energy curves for the three different mass combinations. In addition, important information is contained in these results about the relative importance of CID, reaction, and nonreactive processes, the magnitude of vibrational nonadiabatic processes, and the possible importance of resonances in chemical reactions occurring in this model system. We now proceed to examine these points in greater detail.

The probabilities for reaction and for CID displayed in Figs. 3 to 7 clearly demonstrate the importance of vibrational enhancement of CID. While this is clearest in the 10-1-10 mass combination, it is still quite clear in the 1-1-1 mass combination, particularly in the region of the first peak in the CID versus energy probability curves, in which the probability for CID from the $v = 1$ state is some 40 times that from the $v = 0$ state. At higher energies, the enhancement is less pronounced. The vibrational enhancement is smallest for the 1-35-1 mass combination. In fact, up through about 0.08 eV above dissociation, the probability of CID from the $v = 0$ state is higher than that from the $v = 1$ state, although this is reversed at higher energies. The probability of CID from the $v = 2$ state is nearly always higher than that from the $v = 0$ and $v = 1$ states for this mass combination, except at the energy of the minimum in the $v = 2$ CID probability versus energy curve.

The vibrational enhancement of CID can also be seen by considering the rate constants for dissociation (k_i^D) shown in Figs. 8 to 10. There is a large increase in the rate constant with reagent vibrational excitation, much of which can be attributed simply to the decrease in the energetic threshold for CID with reagent vibrational excitation. An estimate of the magnitude of this effect can be obtained by consideration of the Arrhenius pre-exponential factors and activation energies associated with the Arrhenius plots in Figs. 8 to 10. Such an analysis for the dissociation curves is complicated by their nonlinearity, but the curvature is sufficiently small that we may obtain reasonably good fits to the calculated rate constants by assuming a linear Arrhenius plot in the temperature range from 350-650°K. Pre-exponential factors b and activation energies E_a for the exchange reaction and CID are given in Table III. Considering the CID Arrhenius parameters for the 1-1-1 and 10-1-10 mass combinations, the pre-exponential factors increase and the activation energies decrease with increasing reagent vibrational excitation, both effects contributing to an increase of the rates. For the 1-35-1 mass combination, the CID pre-exponential factors are all approximately equal, and the entire vibrational state dependence of the CID rate constant stems from decreases in the activation energy with increasing v .

In all cases the activation energy for CID is far greater than the corresponding classical energetic threshold for this process, the difference between these quantities lying in the range from 40-70 meV. This indicates that not all of the reagent vibrational energy is available to overcome the barrier to dissociation, resulting in an extra amount of translational energy to do so.

Vibrational enhancement of CID has been obtained in most previous calculations of the CID process; the present calculations further support that result.^{10, 11, 22} In one previous study, CID had been found to be inhibited by reagent vibrational excitation, but this is now considered to be an artifact of the model used (impulsive force between the incident atom and the target atom of the diatomic molecule in a collinear collision).²³

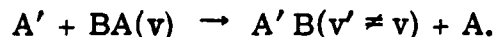
The state-to-all exchange reaction probabilities show less variation with reagent vibrational excitation than do the CID probabilities. This may be easily seen on examination of Figs. 5 to 7. The overall similarity of the P_i^R curves on each figure is striking. This particularly true for the 10-1-10 mass combination in which there are three peaks in each of the curves, with the energy spacing between the second and third peaks far greater than that between the first and second peaks. The vibrational enhancement of the rate of reaction is reflected in the rate constants for reaction plotted (using solid lines) in Figs. 8-10. The Arrhenius plots of these rate constants are linear over the entire 200-650°K temperature range, and this range was used in the calculation of the Arrhenius parameters, which are included in Table III. An examination of Table III shows that the pre-exponential factor is essentially independent of the reagent vibrational state. Thus, as in the case of CID for the 1-35-1 mass combination, reagent vibrational excitation only changes the activation energy for the exchange reaction. The decrease in activation energy with reagent vibrational excitation is substantially smaller than the added vibrational energy, however.

One especially noticeable feature of the exchange reaction probability curves is their different structure for the three different mass combinations. For the 1-1-1 case, these reaction probabilities reach their peaks and decrease to zero shortly above the opening of the dissociation channel and increase slowly at higher energies. For the 1-35-1 case, their decrease after the peak is much slower, and there is no further increase beyond the first maximum, up to the highest energies used in these calculations. For the 10-1-10 case, however, reaction probabilities vary substantially with reagent translational energy, even at the highest energies considered. It should be noted that oscillatory behavior in the reaction probability versus energy curves for heavy-light-heavy systems has been observed in the I-H-I^{12b} and Cl-H-Cl²⁴ systems. Thus, this oscillatory behavior appears to be a feature common to systems with small skew angles.

It is interesting to consider the importance of vibrationally non-adiabatic processes, both reactive and nonreactive, as they are important in the collisional vibrational excitation or relaxation relevant to experimental studies of CID, especially shock-tube experiments. We will restrict our attention here to vibrationally nonadiabatic exchange reactive processes. In general, the probabilities of inelastic nonreactive processes of the type



have been found to be fairly similar—to those of the corresponding reactive processes²⁴



An examination of the relative importance of vibrationally nonadiabatic

and CID probabilities is of interest since CID can be considered as an extreme case of vibrational excitation to a nonbound state.¹

In general, nonadiabatic processes are seen from Figs. 2-4 to be of only secondary importance (as opposed to CID and vibrationally adiabatic processes). There is a correlation between the magnitude of CID and vibrationally nonadiabatic processes in that for the case where CID is the most likely (the 1-35-1 mass combination), the latter processes are also the most likely. On the other hand, vibrationally nonadiabatic processes are more likely for the 10-1-10 mass combination than they are in the 1-1-1 case, however, even though CID is more prevalent in the latter case than in the former.

To help elucidate the relative importance of the exchange reaction, both vibrationally adiabatic and nonadiabatic, and of CID, we have obtained Arrhenius plots of the state-to-state reaction and CID rate constants for the 1-35-1 case, and these are displayed in Fig. 11. It is clear that of all the above mentioned processes, vibrationally adiabatic reaction is the most likely. Further, it is not always true that CID rates are smaller than all the other bound-to-bound rate constants, as has been assumed in some models.¹

Finally, we wish to consider the possible role of resonance processes in this model system. The large barrier to reaction in this system (relative to the dissociation energy) decreases the likelihood of resonances in the 1-35-1 and 1-1-1 mass combinations. The reason is that there will be no wells in the vibrationally adiabatic correlation diagrams, which are important mechanisms for the appearance of such resonances.^{25, 26} This picture is known to be less appropriate for

heavy-light-heavy systems like the 10-1-10 mass combination being considered here,^{12c, 26} which still leaves the possibility that there may be resonances in the 10-1-10 case, in spite of the large barrier.

In fact, the first peak in the P_{00}^R versus energy curve for this system can be shown to be associated with a resonance by construction of an Argand diagram,^{26, 27} which is displayed in Fig. 12. The switch-over from a clockwise to counterclockwise sense near 0.15 eV total energy (as the diagram is traversed in the direction of increasing energies) makes the resonant nature of this process evident.^{26, 27} The corresponding peak in the P_{11}^R versus energy curve does not appear to be associated with a resonant process on consideration of the appropriate Argand diagram (Fig. 13). The curve there has a clockwise sense over the entire range from 0.18 to 0.21 eV total energy, signifying that there is either no resonance at all or that if there is one, it is masked by a direct process and thus unobservable from an Argand diagram. An analysis via the collision lifetime matrix eigenvalue technique²⁸ would help elucidate this point.

We have performed quasi-classical trajectory calculations for the 1-1-1 mass combination and have found their results to be qualitatively similar to the quantum mechanical ones (the corresponding curves are plotted in Figs. 3 and 4 of Ref. 12b). The results are quantitatively sufficiently different, however, that rate constants for CID calculated using the quasi-classical probabilities were substantially different at times from those obtained from the quantum mechanical probabilities.

As mentioned in the Introduction, very little work has been done on the behavior of CID in reactive systems. Most of this work has been

limited to quasi-classical trajectory calculations on the $H + H_2$ system and its isotopic counterparts, frequently including systems in which there is an incident tritium atom.^{9, 29} This case corresponds closely to that studied in nuclear recoil experiments in which hot tritium atoms are used. Simple calculations using kinematic (i. e., hard sphere) models have also been performed, and have in general yielded satisfactory agreement with both experiment and quasi-classical trajectory calculations.⁴

That the masses of the colliding partners could have a major effect on the CID has been seen for some time in nonreactive systems. Fan³⁰ has performed collinear quasi-classical trajectory calculations on the $Xe + CsBr \rightarrow Xe + Cs^+ + Br^-$ system, and found that dissociation is much more likely in collisions of Xe with Br than of Xe with Cs. A similar behavior was found both experimentally and in quasi-classical trajectory calculations by Tully et al.¹⁵ Their results suggest that collisions leading to dissociative ion pair formation are near-collinear; that is, they occur with their relative velocity roughly parallel to the alkali halide axis, but with a small but non-zero impact parameter. Of particular interest is the fact that the scattering in the Xe-RbI and Xe-CsBr systems was very similar, which suggests that it is the masses of the atoms ($m_{Rb} \sim m_{Br}$, $m_{Cs} \sim m_I$) and not the details of the intermolecular forces that govern CID behavior. Further, in their experiments, Tully et al. found that CID rates were found to vary more with changes in the alkali halide molecule in Kr-MX collisions than in Xe-MX collisions.

Additional evidence of strong mass effects in CID was obtained by Shui et al.,³¹ who found that a modified phase space theory, which

normally predicts CID and three-body recombination rates fairly well for most systems, does not work in the case of HF and HCl dissociation in Ar. Their method involved the use of trajectories calculated for systems in which all the atoms and molecules had similar masses, and they attribute the inaccuracy for these systems to different dynamics than in most other cases.

In the results obtained here, we have also seen grossly different dynamics with changes in the atom masses. In particular, the dynamics of the heavy-light-heavy system are substantially different from those of the two others, lending support to the hypothesis of Shui et al.³¹ described above. Because of our restriction to symmetric systems in the present calculations, we have been unable to consider the dependence of CID on orientation (i. e. , A + BC versus A + CB), as was considered by Fan,³⁰ but we do hope to do so in the future.

VI. SUMMARY AND CONCLUSIONS

We have calculated probabilities for CID and exchange reaction for the collinear triatomic system $A + BA$ on a model potential energy surface for three different mass combinations, using the hyperspherical coordinates coupled-channel technique. The mass combinations studied are of the light-light-light, light-heavy-light, and heavy-light-heavy types. Substantial vibrational enhancement of CID was seen, and in all three systems CID was found to be most important for the 1-35-1 mass combination and least so for the 10-1-10 mass combination. Arrhenius plots of rate constants for CID are reasonably but not precisely linear, and over the temperature range 350-600° K give rise to activation energies for CID which are substantially (normally 40-70 meV) greater than the energetic thresholds.

Probabilities for the exchange reaction, both vibrationally adiabatic and nonadiabatic, have also been obtained. In general, the shapes of the reaction probability versus energy curves vary only slightly with reagent vibrational excitation. There are substantial differences between the curves for the different mass combinations, however. Arrhenius plots of the rate constants for reaction are linear over the entire 200-650° K range. For each mass combination, the Arrhenius pre-exponential factors are approximately independent of reagent vibrational state; the activation energies do decrease with reagent vibrational excitation, but the magnitude of this decrease is substantially smaller than the added reagent vibrational energy. Vibrationally nonadiabatic processes are found to be less important than vibrationally adiabatic processes and CID. Rate constants for CID are usually smaller than those for the

exchange reaction, but this is not always true, especially at the upper end of the range of temperatures considered.

We have shown that resonant processes can be important at energies not far from dissociation in this system for the heavy-light-heavy mass combination, although they do not necessarily occur for all reagent levels.

On the basis of quasi-classical trajectory calculations performed on the 1-1-1 mass combination, quantum effects, even for the weakly bound system studied here with the light masses used, are fairly small. Thus, classical mechanics should be able to give a reasonably good qualitative picture of the dynamics in these systems, although not necessarily a quantitative one.

We have recently modified the hyperspherical coordinate scattering program to allow for the study of asymmetric systems (i.e., three non-equivalent atoms), and hope to extend our studies of the CID process to them in the near future.

ACKNOWLEDGEMENTS

The calculations reported here were performed on the IBM 370/158 computer at Ambassador College in Pasadena, California, for which we express our appreciation. Additional calculations were performed on the Dreyfus-NSF Theoretical Chemistry Computer at Caltech which was funded through grants from the Camille and Henry Dreyfus Foundation, the National Science Foundation (Grant No. CHE78-20235), and the Sloan Fund of the California Institute of Technology.

REFERENCES

1. H. S. Johnston and J. Birks, *Acc. Chem. Res.* 5, 327 (1972);
H. O. Pritchard, *Specialist Periodical Reports, Reaction Kinetics*, Vol. 1 (Chemical Society, London, 1975), p. 243.
2. H. O. Pritchard, *Acc. Chem. Res.* 9, 99 (1976).
3. D. J. Diestler, in *Collision-Induced Dissociation. I. Quantal Treatment*, in *Atom-Molecule Collision Theory*, R. B. Bernstein, Ed. (Plenum Press, New York, 1979), pp. 655-667, and references therein.
4. R. J. Suplinskas, *J. Chem. Phys.* 49, 5046 (1968); D. J. Malcolme-Lawes, *ibid.* 57, 5572 (1972).
5. P. J. Kuntz, in *Collision-Induced Dissociation. II. Trajectories and Models*, in *Atom-Molecule Collision Theory*, R. B. Bernstein, Ed. (Plenum Press, New York, 1979), pp. 669-692, and references therein; T. Lehr and J. W. Birks, *J. Chem. Phys.* 70, 4843 (1979).
6. C. S. Lin, *Chem. Phys.* 3, 125 (1974); I. Rusinek and R. E. Roberts, *J. Chem. Phys.* 65, 872 (1979); 68, 1147 (1978); I. Rusinek, *ibid.* 72, 4518 (1980).
7. W. B. Maier, *J. Chem. Phys.* 41, 2174 (1964); J. C. Keck, *Adv. Chem. Phys.* 13, 85 (1967); C. Rebick and R. D. Levine, *J. Chem. Phys.* 58, 3942 (1973); A. F. Wagner and E. K. Parks, *ibid.* 65, 4343 (1976).
8. R. T. V. Kung and J. B. Anderson, *J. Chem. Phys.* 60, 3732 (1974).
9. A. Jones and J. L. J. Rosenfeld, *Proc. R. Soc. Lond. A* 333,

- 419 (1973).
10. K. C. Kulander, J. Chem. Phys. 69, 5064 (1978); Nucl. Phys. A 353, 341c (1981).
 11. L. H. Beard and D. A. Micha, J. Chem. Phys. 73, 1193 (1980).
 12. (a) A. Kuppermann, J. A. Kaye, and J. P. Dwyer, Chem. Phys. Lett. 74, 257 (1980); (b) J. A. Kaye and A. Kuppermann, *ibid.* 77, 573 (1981); (c) 78, 546 (1981).
 13. (a) G. Hauke, J. Manz, and J. Römelt, J. Chem. Phys. 73, 5040 (1980); (b) J. Römelt, Chem. Phys. Lett. 74, 263 (1980); (c) J. Manz and J. Römelt, *ibid.* 76, 337 (1980); (d) 77, 172 (1981).
 14. W. H. Wong and G. Burns, J. Chem. Phys. 62, 1712 (1975).
 15. (a) F. P. Tully, Y. T. Lee, and R. S. Berry, Chem. Phys. Lett. 9, 80 (1971); (b) F. P. Tully, N. H. Cheung, H. Haberland, and Y. T. Lee, J. Chem. Phys. 73, 4460 (1980).
 16. E. K. Parks, N. J. Hansen, and S. Wexler, J. Chem. Phys. 58, 5489 (1973).
 17. J. M. Bowman and A. Kuppermann, Chem. Phys. Lett. 34, 523 (1975).
 18. L. N. Delves, Nucl. Phys. 9, 391 (1959); 20, 275 (1960).
 19. J. C. Polanyi and J. L. Schreiber, in The Dynamics of Bimolecular Reactions, in Physical Chemistry, Advanced Treatise, Vol. 6A, Kinetics of Gas Reactions (Academic Press, New York, 1974), pp. 383-487.
 20. J. P. Dwyer, Ph.D. Thesis, California Institute of Technology (1977).
 21. A. M. Lane and R. G. Thomas, Rev. Mod. Phys. 30, 257 (1958);

- A. Kuppermann, in *Theoretical Chemistry: Advances and Perspectives*, D. Henderson, Ed. (Academic Press, New York, 1981), Vol. 6A, pp. 79-164.
22. J. C. Gray, G. A. Fraser, and D. G. Truhlar, *Chem. Phys. Lett.* 68, 359 (1979); J. C. Gray, G. A. Fraser, D. G. Truhlar, and K. C. Kulander, *J. Chem. Phys.* 73, 5726 (1980); E. W. Knapp and D. J. Diestler, *ibid.* 67, 4969 (1977).
23. L. W. Ford, D. J. Diestler, and A. F. Wagner, *J. Chem. Phys.* 63, 2019 (1975).
24. J. A. Kaye and A. Kuppermann, manuscript in preparation.
25. S. L. Latham, J. F. McNutt, R. E. Wyatt, and M. J. Redmon, *J. Chem. Phys.* 69, 3746 (1978).
26. A. Kuppermann, in *Potential Energy Surfaces and Dynamics Calculations*, D. G. Truhlar, Ed. (Plenum Press, New York, 1981), pp. 375-420.
27. G. C. Schatz and A. Kuppermann, *J. Chem. Phys.* 59, 964 (1973), and references therein.
28. F. T. Smith, *Phys. Rev.* 118, 349 (1960); G. C. Schatz, Ph.D. Thesis, California Institute of Technology (1975); A. Kuppermann and J. A. Kaye, *J. Phys. Chem.* 85, 1969 (1981); G. C. Schatz and A. Kuppermann, manuscript in preparation.
29. M. Karplus, R. N. Porter, and R. D. Sharma, *J. Chem. Phys.* 45, 3871 (1976); D. J. Malcolm-Lawes, *J. Chem. Soc. Faraday Trans. II* 71, 1183 (1975).
30. H. Fan, *J. Chem. Phys.* 55, 4628 (1971).
31. V. H. Shui, J. P. Appleton, and J. C. Keck, in the *Proceedings*

of the 13th Symposium (International) on Combustion (The
Combustion Institute, 1970), p. 21.

Table I. Parameters for rotating Morse cubic spline potential used
(notation is as in Ref. 17).

θ (deg.)	$l_{eq}(\theta)$ (bohr)	$\beta(\theta)$ (bohr ⁻¹)
0	5.5993	1.600
15	5.7968	1.544
25	6.1774	1.458
30	6.4636	1.392
35	6.8284	1.321
40	7.2669	1.218
43	7.5047	1.142
45	7.5666	1.127

Table II. Properties of potential energy surfaces for different mass combinations.

Case	I	II	III
Masses ^a	1-1-1	10-1-10	1-35-1
Skew Angle	60°	24.62°	88.41°
Reduced Mass ^{a, b}	0.5774	2.1822	0.9726
Eigenvalues of Isolated Diatomic (eV)			
v = 0	0.0817	0.0625	0.0606
v = 1	0.1885	0.1561	0.1524
v = 2	c	0.2082	0.2055

^a In units of the hydrogen atom mass.

^b Defined as $\mu = [m_A m_B m_C / (m_A + m_B + m_C)]^{\frac{1}{2}}$.

^c This system only supports two bound states.

Table III. Arrhenius parameters for rates of reaction and dissociation.^a

Mass Combination ^b	v ^c	Exchange Reaction		Dissociation	
		$\ln b^d$	E_a^e	$\ln b^d$	E_a^e
1-1-1	0	11.1	0.086	8.5	0.213
	1	11.2	0.025	10.3	0.072
10-1-10	0	10.0	0.098	3.9	0.208
	1	10.1	0.046	5.7	0.104
	2	10.1	0.015	7.4	0.082
1-35-1	0	11.7	0.014	11.0	0.215
	1	11.6	0.063	10.9	0.133
	2	11.4	0.024	11.2	0.061

^a From 200 to 650°K for the exchange reaction and 350 to 600°K for dissociation.

^b In units of hydrogen atom masses.

^c Reagent vibrational quantum number.

^d In units of $\text{cm} \cdot \text{molec}^{-1} \text{sec}^{-1}$.

^e In eV.

FIGURE CAPTIONS

Figure 1. Schematic plot of the coordinate system (ℓ, θ) for the rotating Morse cubic spline surface. S is the swing point from which the Morse oscillator is rotated.

Figure 2. Contour plot of the potential energy surface for the model collinear triatomic system studied here (1-1-1 mass combination) in Delves scaled coordinates R_α, r_α . The solid curves are equipotential contours at the total energies (with respect to the dissociated system) indicated at the high side of the figure. The dashed line is the path of steepest descent from the saddle point. The polar coordinates ρ, α of a general point P in this R_α, r_α configuration space are also indicated.

Figure 3. State-to-state reaction and CID probabilities for the 1-1-1 mass combination as a function of relative translational energy and total energy for the reagent vibrational states $v = 0$ (top panel) and $v = 1$ (bottom panel). Total energy is indicated by the common horizontal scale (tic marks are on the top of each panel), while translational energy is indicated at the bottom of each panel. Curves are for vibrationally adiabatic reaction (solid line), vibrationally nonadiabatic reaction (dashed), and CID (dashed-dotted). Arrows are drawn at energies at which higher vibrational states and dissociation become energetically allowed, and are labeled on the top figure, e. g., E_1 for $v = 1$, E_2 for $v = 2$, and E_d for dissociation.

Figure 4. State-to-state reaction and CID probabilities for the 10-1-10 mass combination as a function of relative translational energy and total energy for the reagent vibrational states $v = 0$ (top panel), $v = 1$ (center

panel), and $v = 2$ (bottom panel). Energies and arrows are as indicated in Fig. 3. The solid curves always represent the vibrationally adiabatic reaction probability, the dashed-dotted curves always represent CID, and the dashed and dotted curves represent vibrationally nonadiabatic reaction probabilities as indicated in the figure.

Figure 5. State-to-state reaction and CID probabilities for the 1-35-1 mass combination as a function of relative translational energy and total energy for reagent vibrational states $v = 0$ (top), $v = 1$ (center), and $v = 2$ (bottom) panels. All markings are as in Fig. 4.

Figure 6. Probabilities for reactive (solid curve), dissociative (dotted curve), and nonreactive (dashed curve) processes as a function of relative translational energy and total energy for the 1-1-1 mass combination for vibrational states $v = 0$ (top) and $v = 1$ (bottom). Arrows and energies are as in Fig. 3.

Figure 7. Probabilities for reactive, dissociative, and nonreactive processes as a function of relative translational energy and total energy for the 10-1-10 mass combination for reagent vibrational states $v = 0$ (top), $v = 1$ (center), and $v = 2$ (bottom). Curves are as in Fig. 6; energies and arrows are as in Fig. 4.

Figure 8. Probabilities for reactive, dissociative, and nonreactive processes as a function of relative translational energy and total energy for the 1-35-1 mass combination for reagent vibrational states $v = 0$ (top), $v = 1$ (center), and $v = 2$ (bottom). Curves are as in Fig. 6; energies and arrows are as in Fig. 5.

Figure 9. Arrhenius plot of rate constant (in units of $\text{cm} \cdot \text{molec}^{-1} \text{sec}^{-1}$)

versus inverse temperature for reactive and dissociative processes for the 1-1-1 mass combination. Solid lines are drawn for rate constants for reaction; dashed lines are used to indicate those for dissociation.

Absolute temperature is indicated at the top of the graph.

Figure 10. Arrhenius plot of rates for reactive and dissociative processes for the 10-1-10 mass combination. Lines have the same meaning as in Fig. 9.

Figure 11. Arrhenius plot of rates for reactive and dissociative processes for the 1-35-1 mass combination. Lines have the same meaning as in Fig. 9.

Figure 12. Arrhenius plot of rates of state-to-state reactive and dissociative processes for the 1-35-1 mass combination, with the reagent in its $v = 0$ (top panel), $v = 1$ (center panel), and $v = 2$ (bottom panel).

Lines have the same meaning as in Fig. 9.

Figure 13. Argand diagram for the transition $A + BC (v = 0) \rightarrow A^2B (v = 0) + C$ for the 10-1-10 mass combination. Energies are labeled every 10 meV and correspond to total energies. Points are marked with an X every 5 meV. Arrows are drawn to indicate the sense of the curve.

Figure 14. Argand diagram for the transition $A' + BA (v = 1) \rightarrow A'B (v = 1) + A$ for the 10-1-10 mass combination. All labeling is as in Fig. 13.

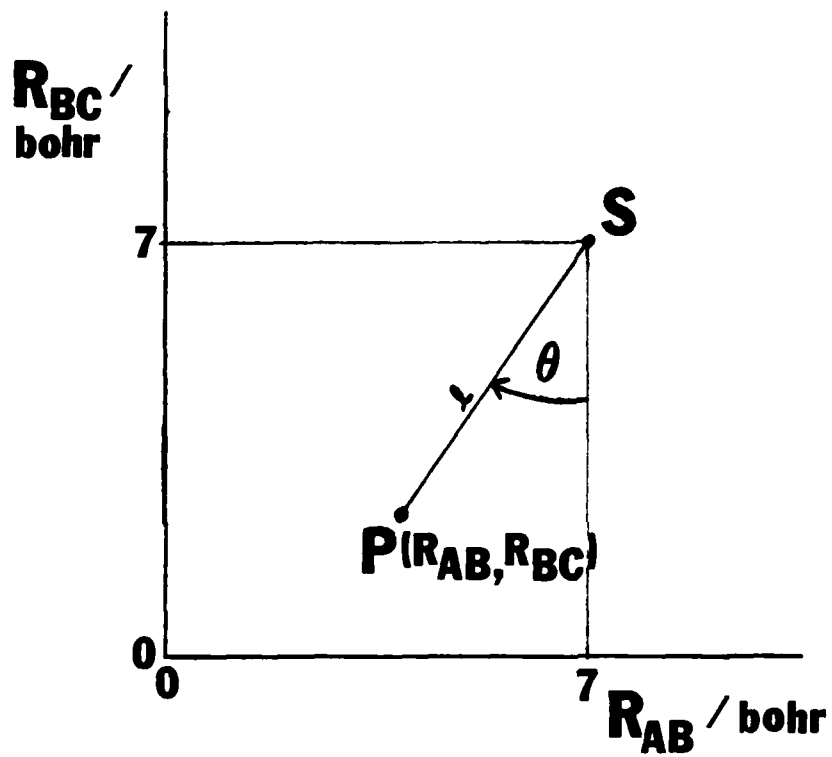


Figure 1

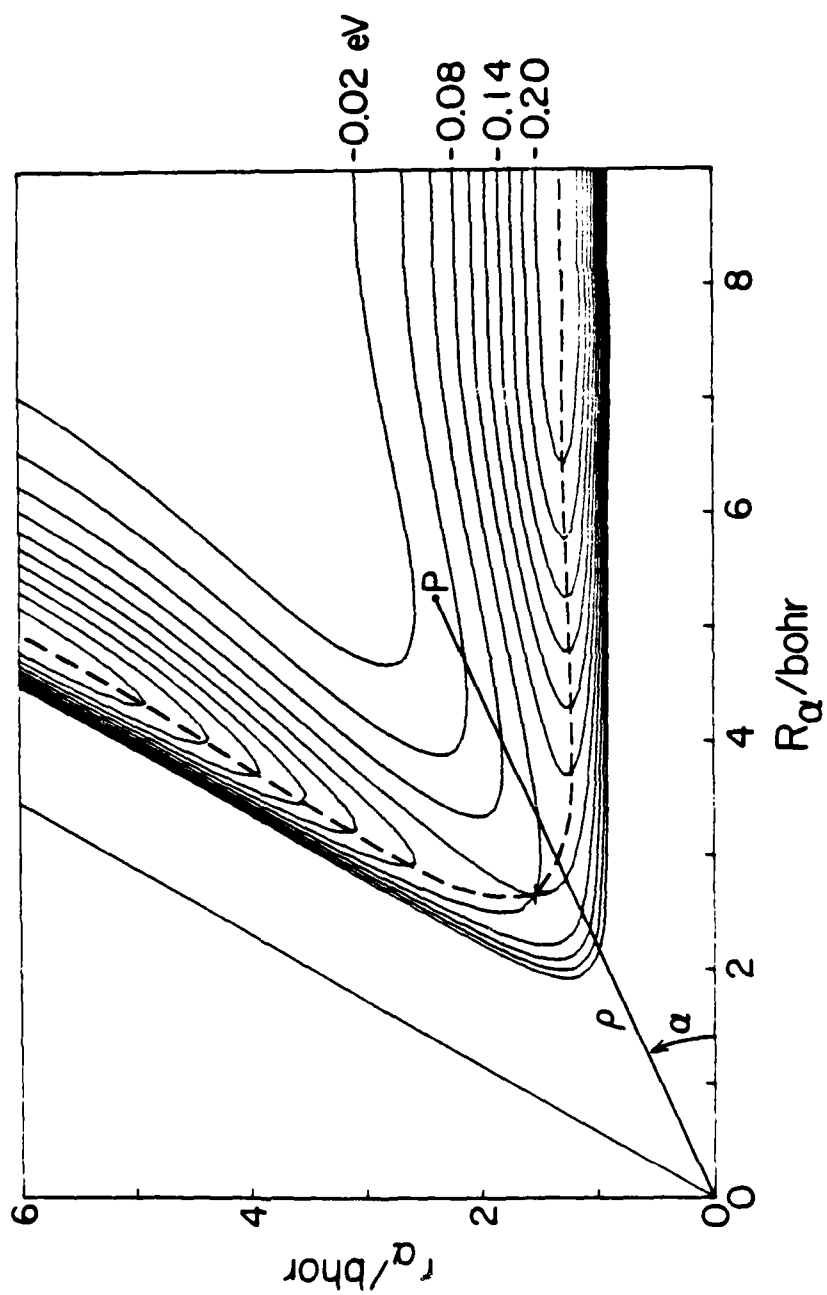


Figure 2

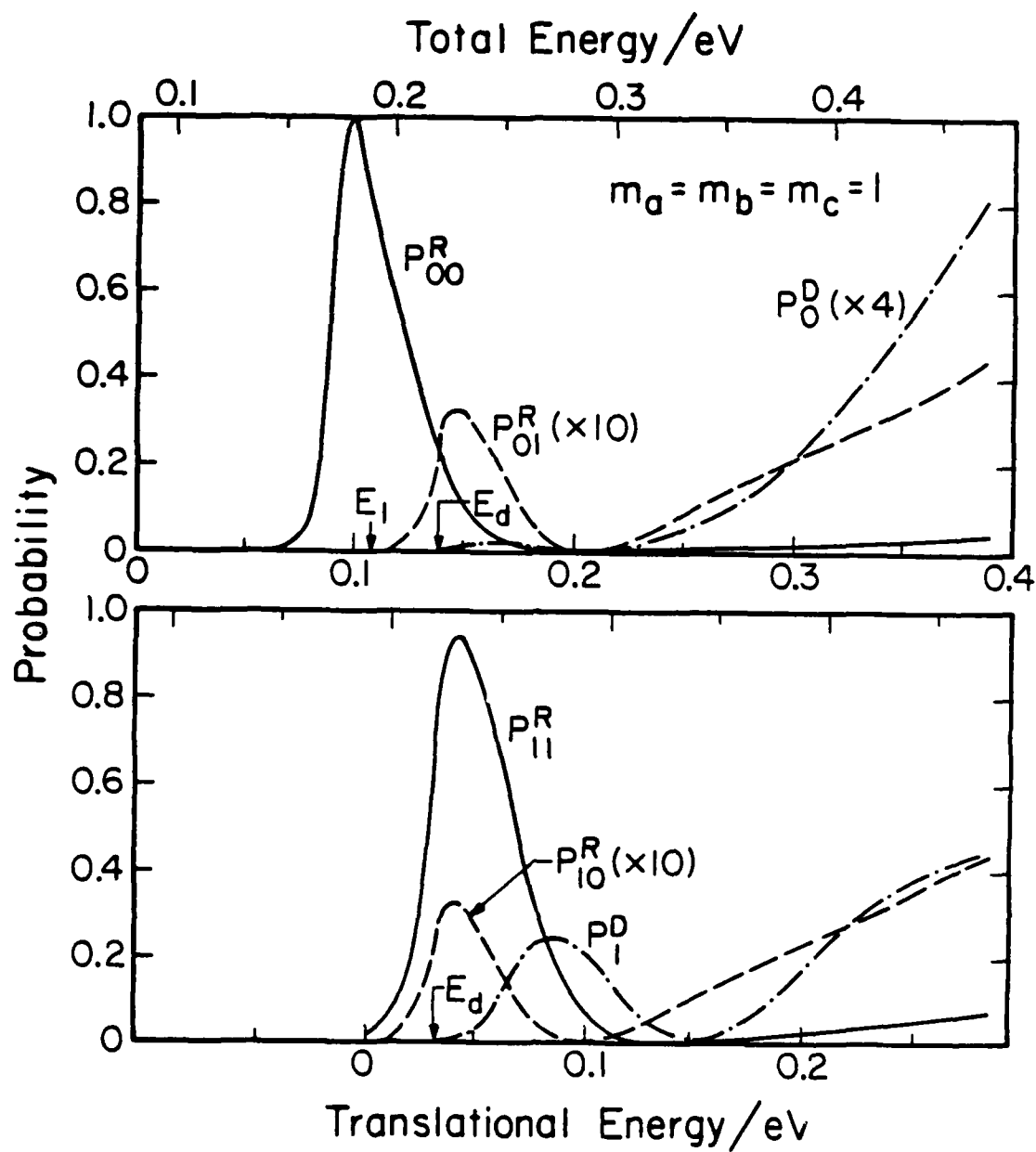
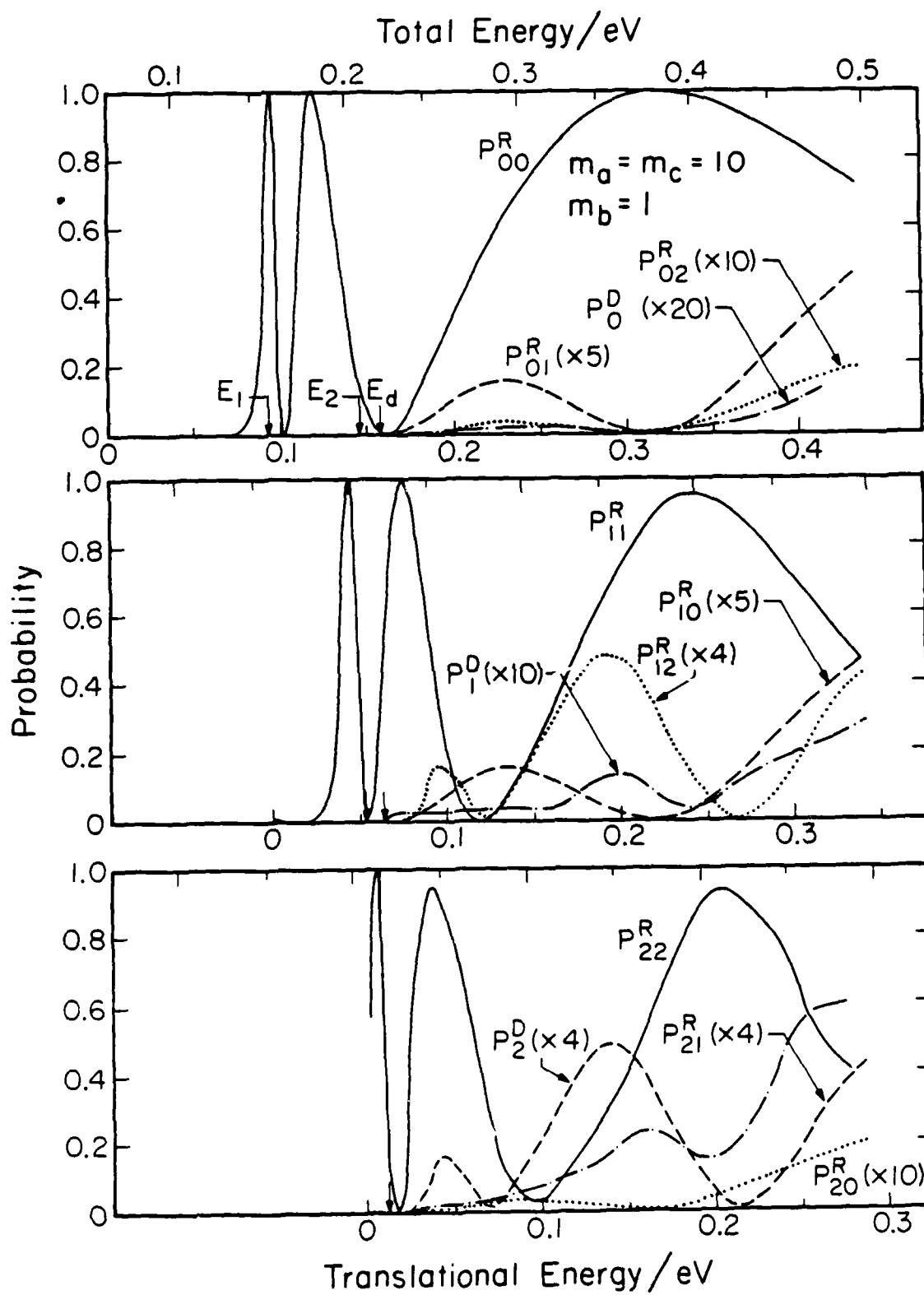


Figure 3



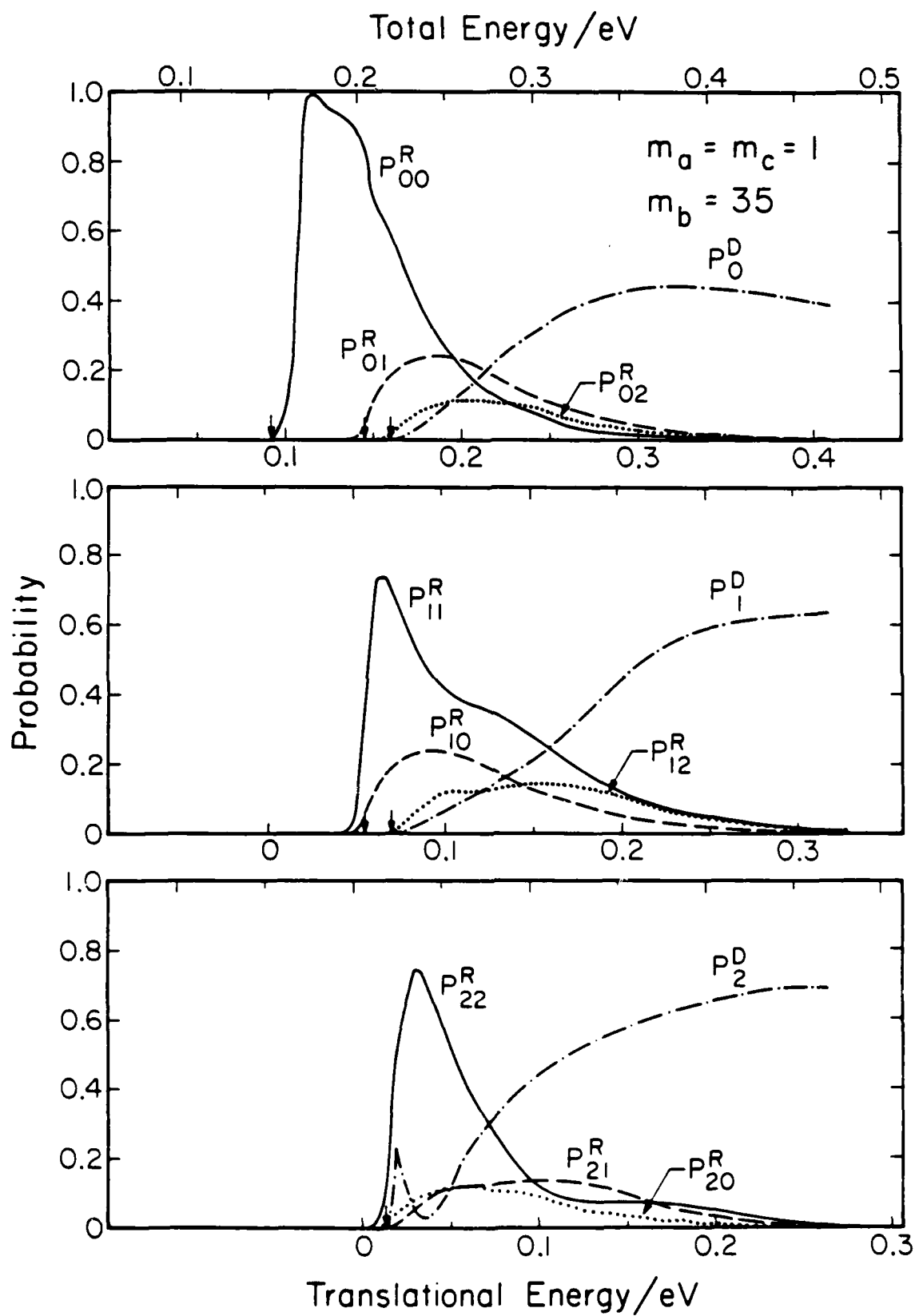


Figure 5

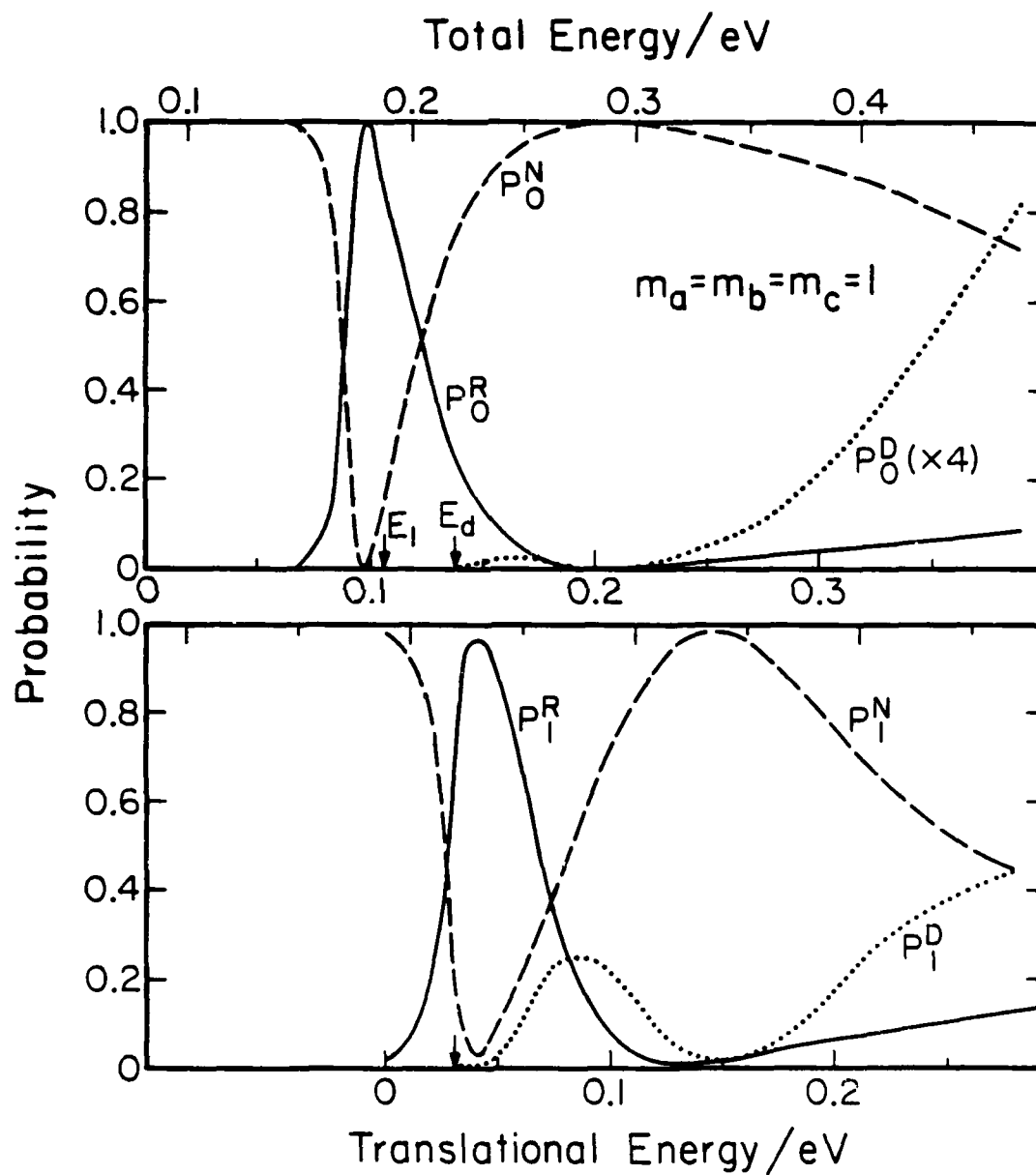


Figure 6

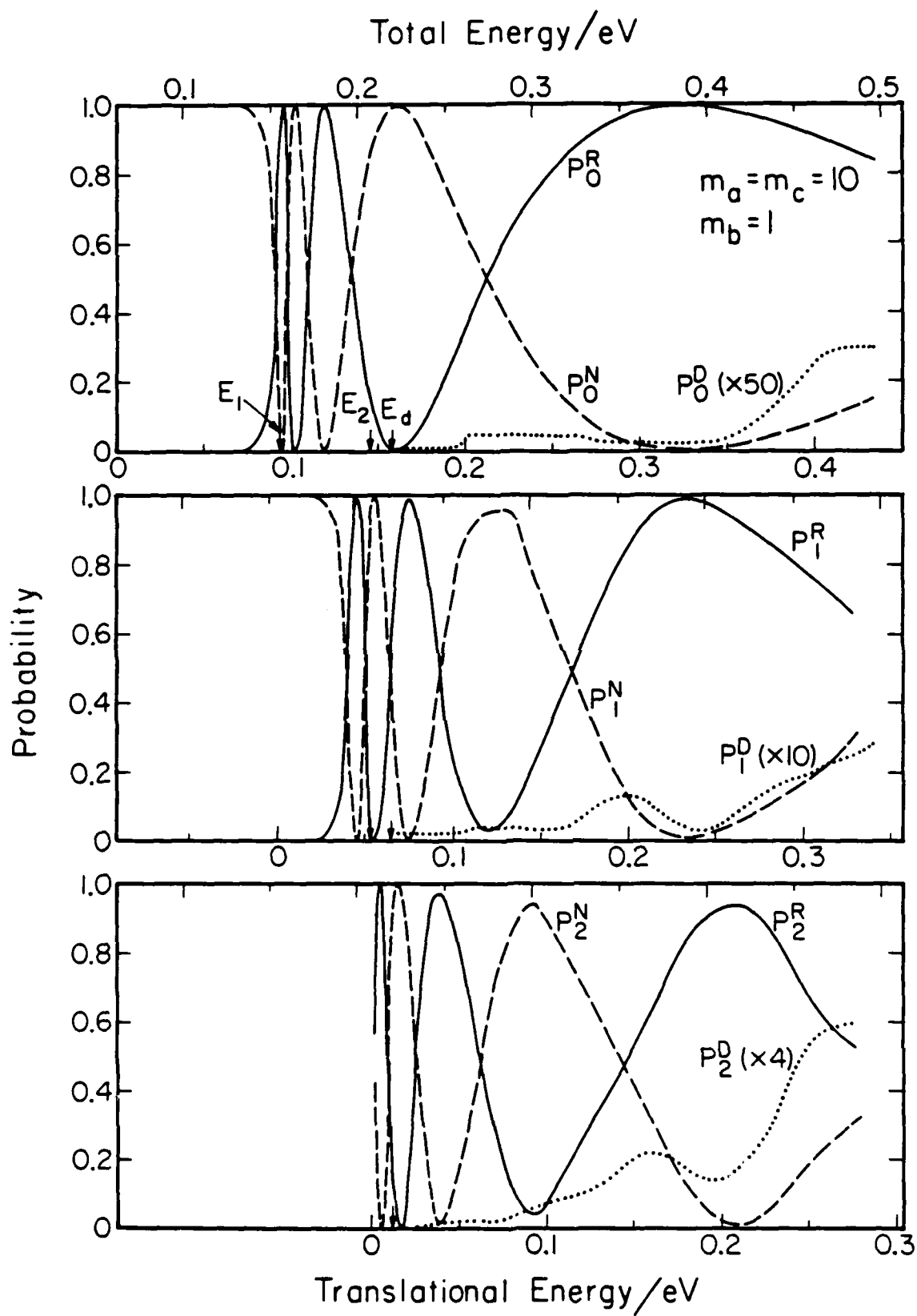


Figure 7

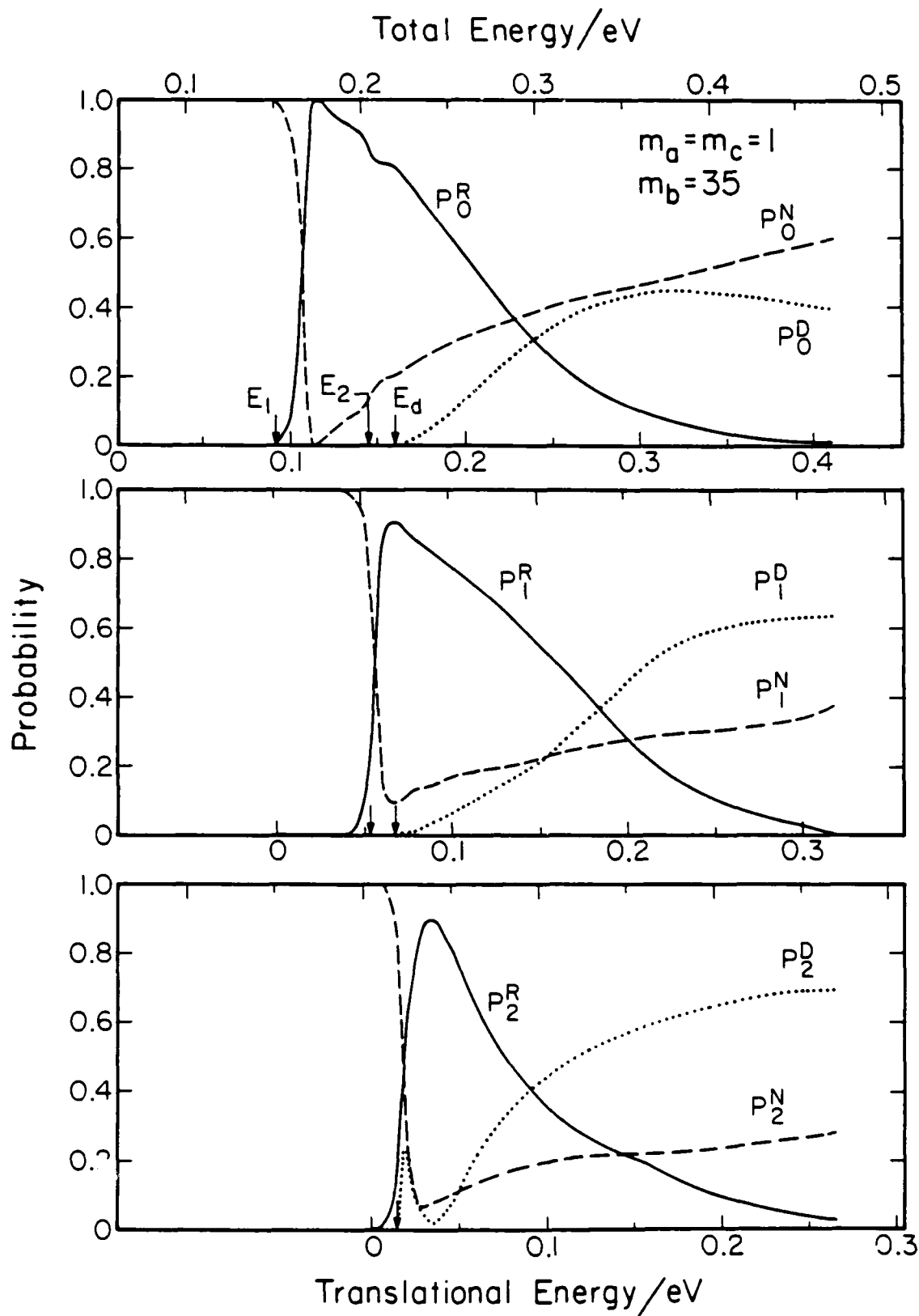


Figure 8

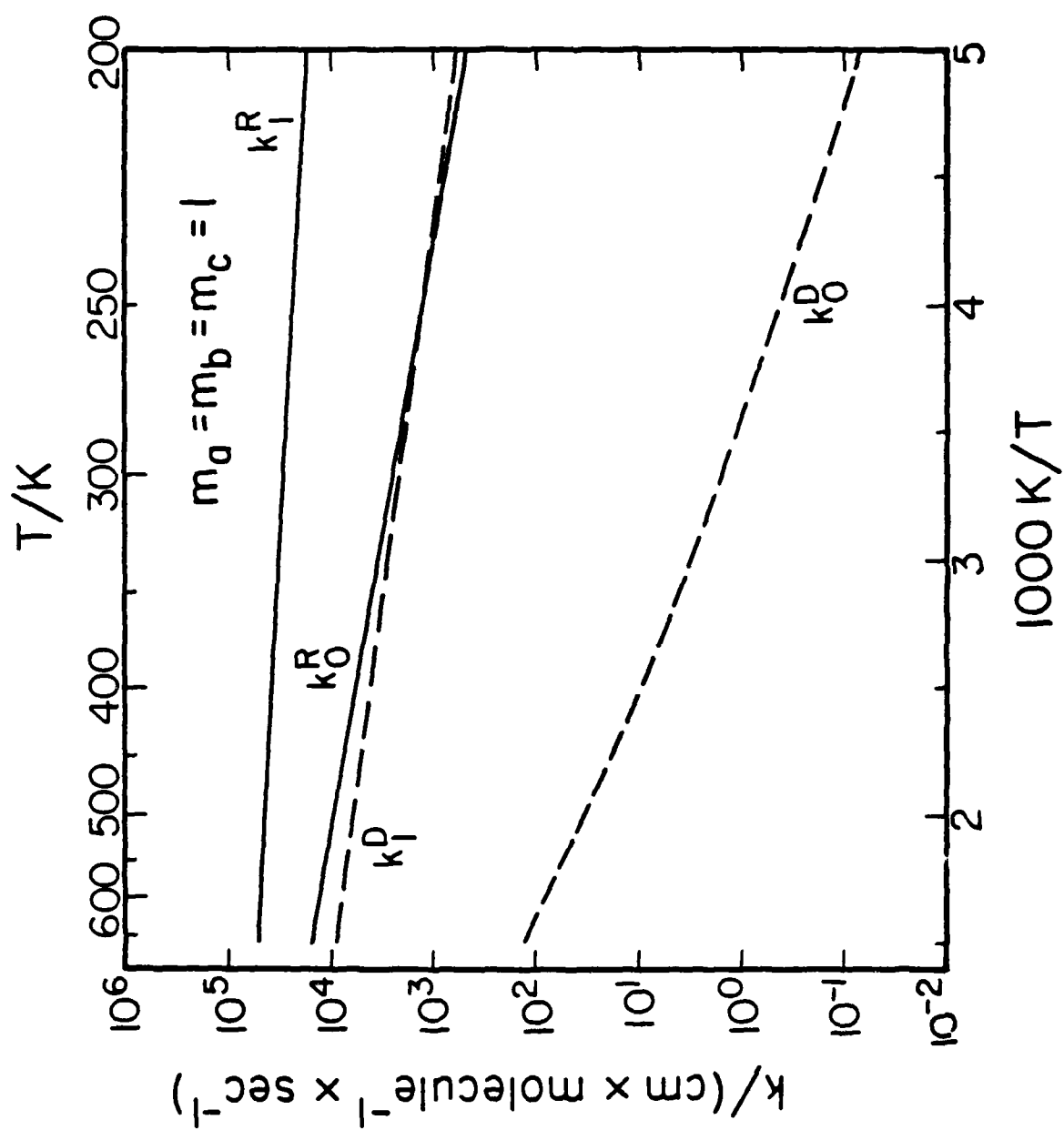


Figure 9

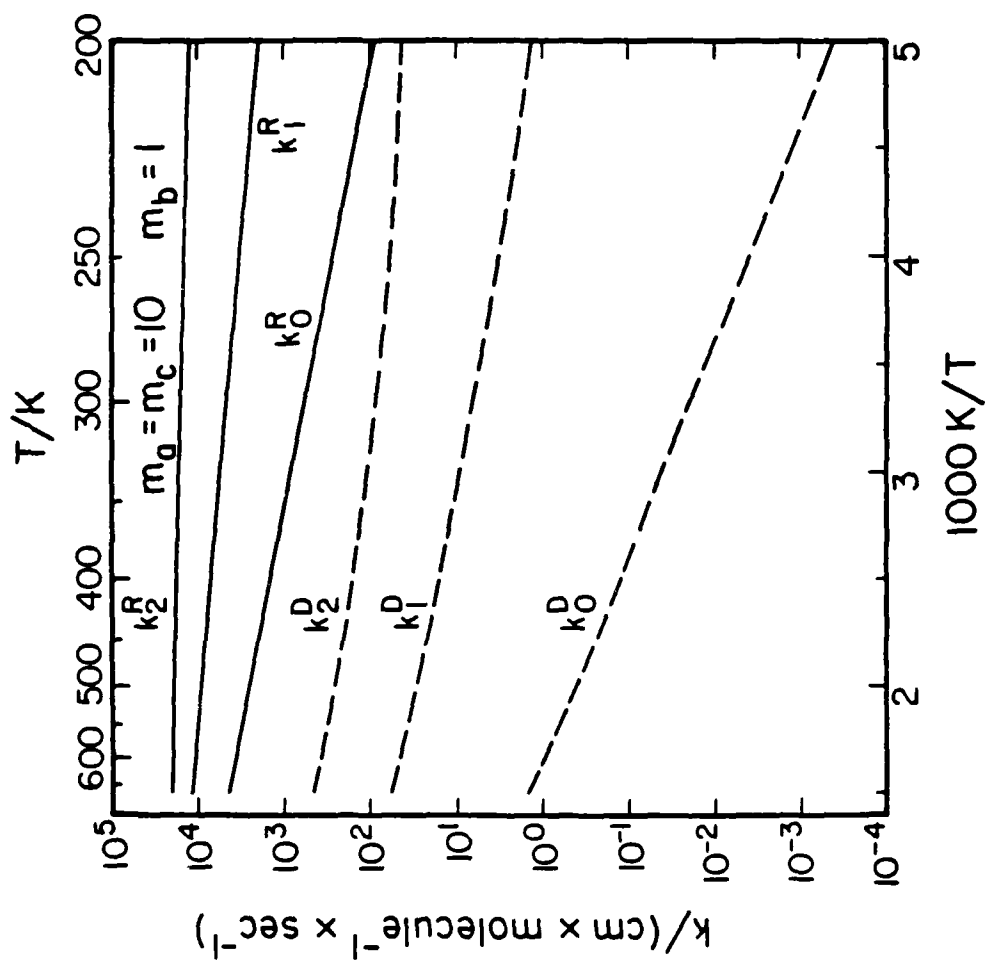


Figure 10

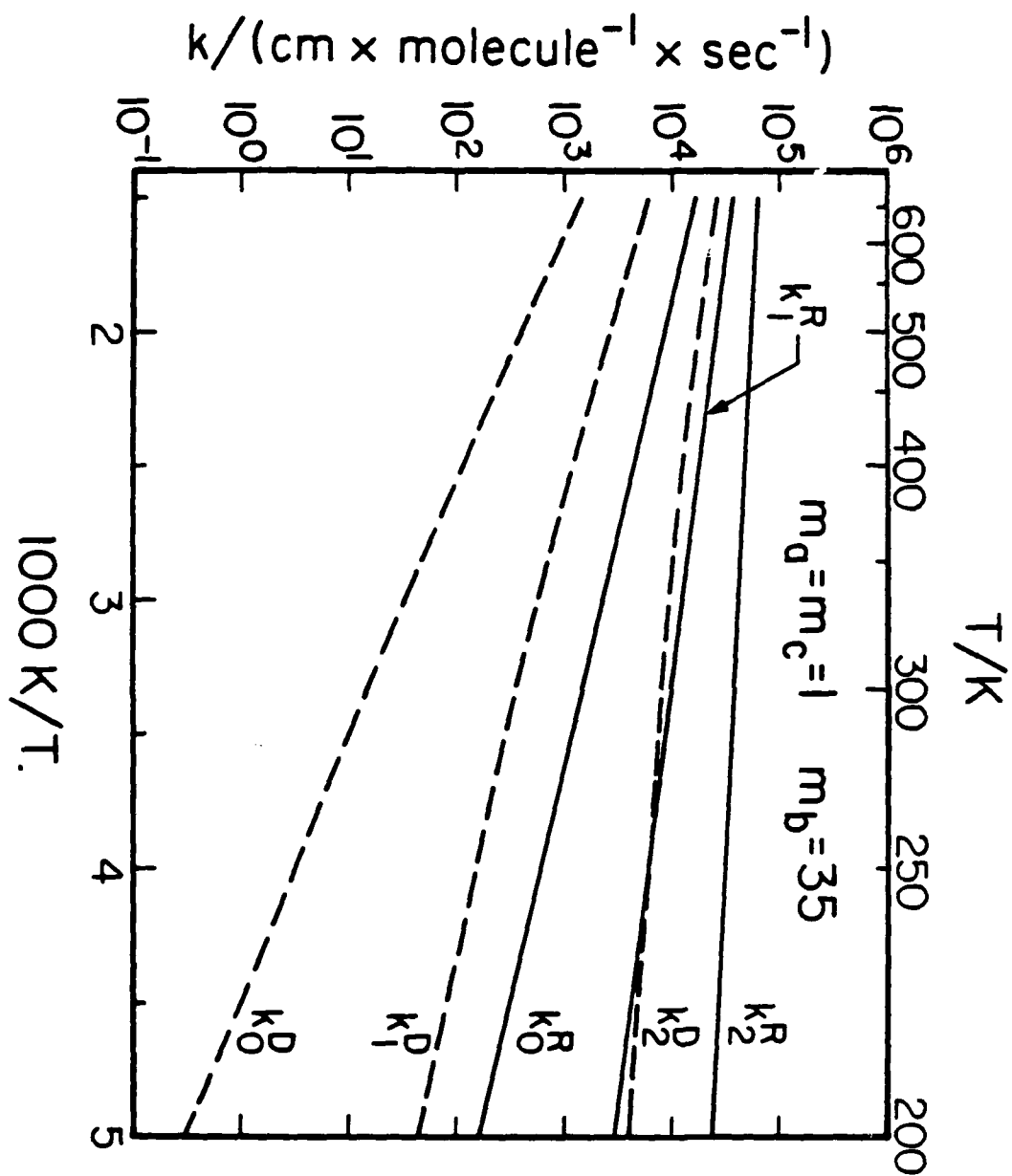


Figure 11

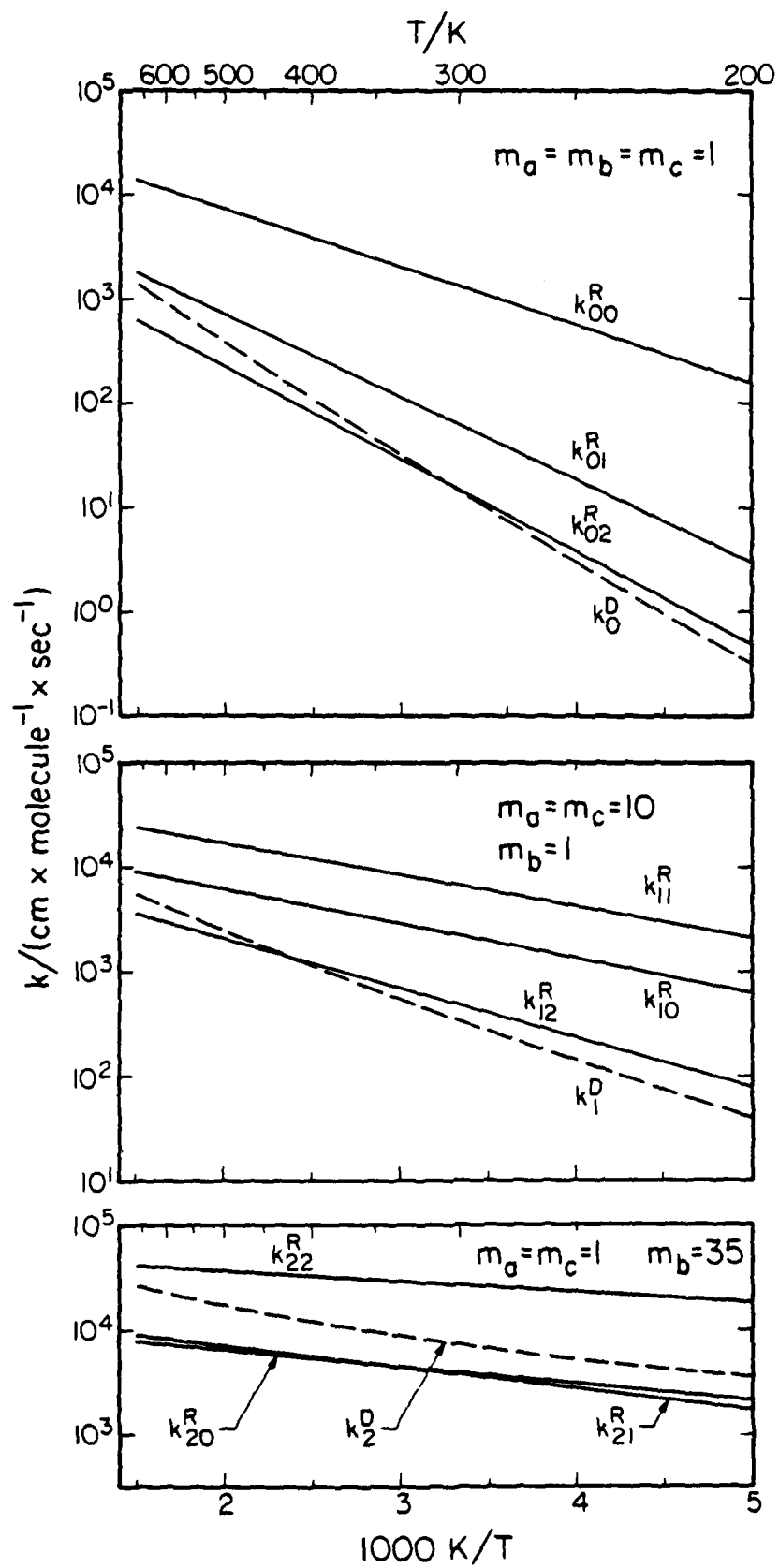


Figure 12

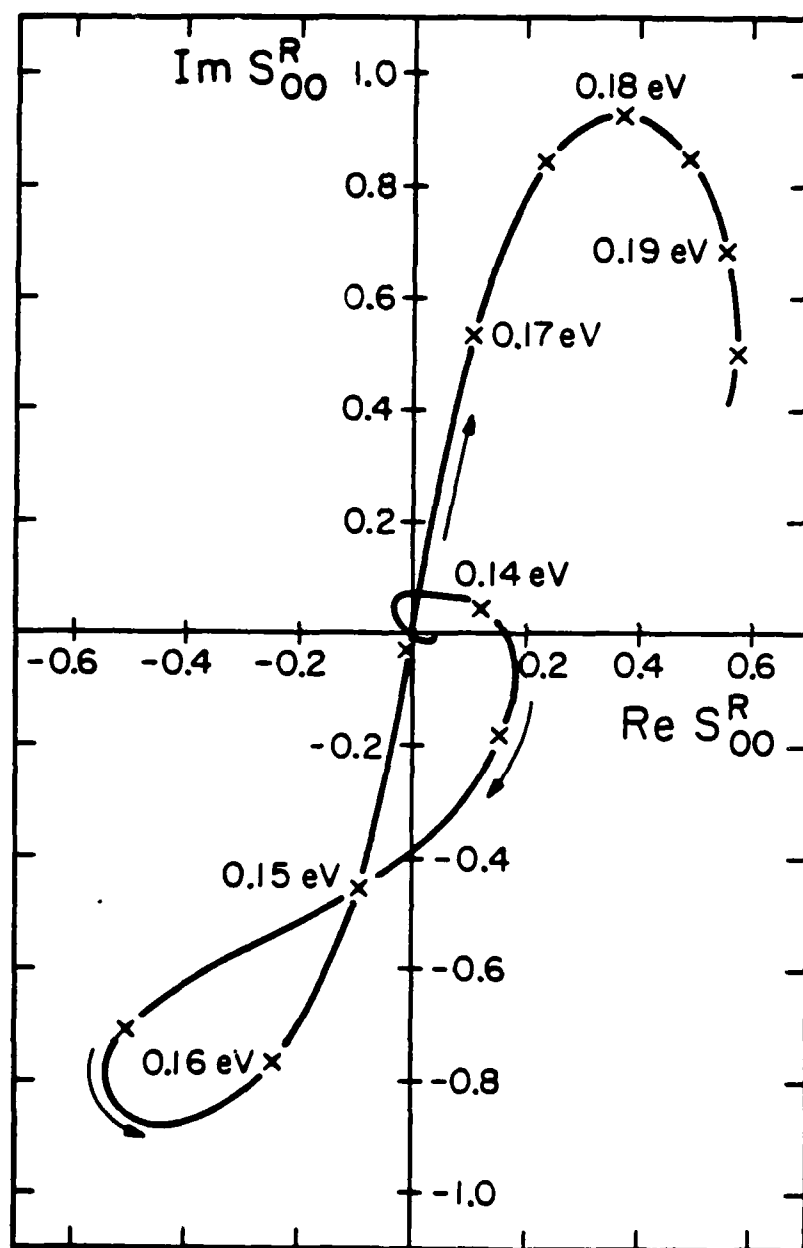


Figure 13

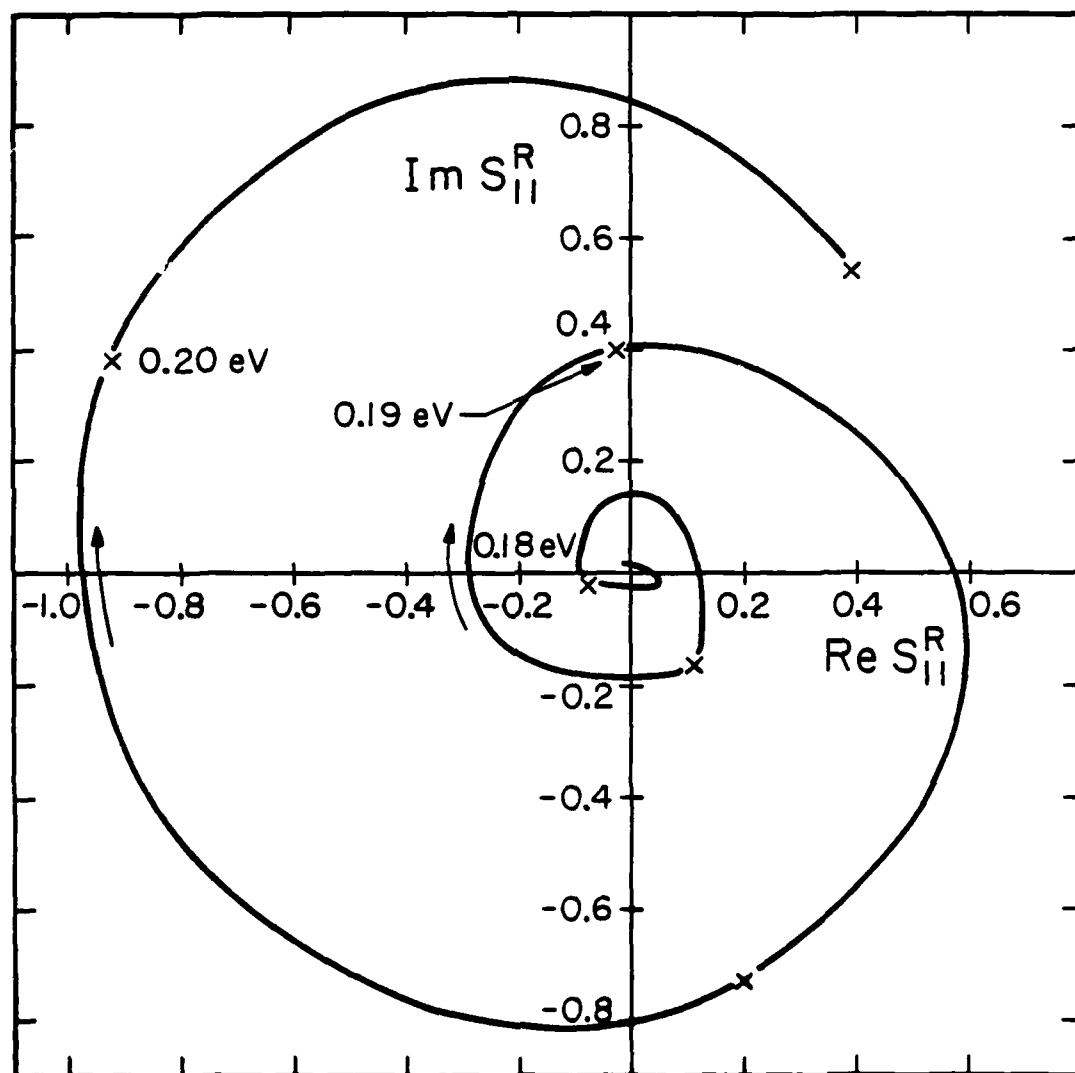


Figure 14

Collinear Quasi-Classical Trajectory Study of Collision-Induced
Dissociation on a Model Potential Energy Surface.^{a)}

Jack A. Kaye^{b)} and Aron Kuppermann

Arthur Amos Noyes Laboratory of Chemical Physics,^{c)}

California Institute of Technology, Pasadena, California 91125

(Received)

Quasi-classical trajectory calculations have been carried out at energies above the threshold for collision-induced dissociation for a model collinear atom-diatomic molecule system. Exact quantum mechanical calculations have shown that quasi-classical trajectories give a qualitatively correct picture of the dynamics in this system. Trajectories leading to dissociation are found to lie almost entirely in well defined reactivity bands, with the exception of a few occurring in a small chattering region in which the outcome of the trajectory is extremely sensitive to its initial conditions. The probability of dissociation leading to all possible distributions of the kinetic energy of the resulting atoms is obtained and is shown to vary substantially with initial conditions (reagent vibrational and translational energy). The form of these probability distributions is, to a major extent, determined by the position and width of the reactivity bands. The different dissociation reactivity bands are shown to be composed of different types of trajectories. Part of the vibrational enhancement of dissociation arises from the fact that the simplest possible trajectory leading to dissociation (one which crosses the symmetric stretch line once prior to the onset of dissociation) is not obtained with ground state reagents.

^{a)} This work was supported in part by a contract (No. F49620-79-C-0187) from the Air Force Office of Scientific Research.

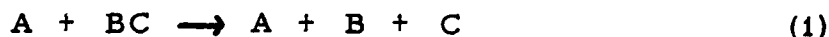
-2-

b) Work performed in partial fulfillment of the requirements for the
Ph. D. degree in Chemistry at the California Institute of Technology.

c) Contribution No.

I. INTRODUCTION

The collision-induced dissociation (CID) of diatomic molecules



is a process of great fundamental interest in chemistry, particularly in the high temperature chemistry associated with shock waves, both in the laboratory (1) and in interstellar space (2). The ab initio calculation of CID rates has proven to be extremely difficult, as one must have accurate methods for calculating the potential energy surface for the collision, solving for the dynamics, and then integrating the coupled rate equations to obtain expressions for the rate of disappearance of the diatomic molecule.

The development of accurate methods for solving for the dynamics has been especially difficult. Kinematic and quasi-classical trajectory (QCT) calculations have been extensively used to study CID (3). The number of studies incorporating quantum mechanical effects, either by a semi-classical or a purely quantum mechanical approach, is much smaller (4). Most of these studies have been restricted to collinear collisions in which reactive collisions of the type



are not permitted. Non-collinear collisions in non-reactive systems have been studied by the semi-classical method by Rusinek (5). Exceptions to this are three purely quantum methods in which reaction and dissociation may compete (these are all restricted to collinear collisions at this time): the wave packet approach of Kulander (6), the hyperspherical coordinate coupled-channel method developed independently by Kaye and Kuppermann (7) and by Manz and Römelt (8), and the multiple collision approach of Beard and Micha (9) (which has been applied only to a non-reactive system).

The availability of accurate quantum mechanical (QM) results for CID has increased interest in QCT studies. In particular, Kaye and Kuppermann (7) have shown that for the model system they studied,

the QCT results were qualitatively similar to the QM ones. Since the model system involves light masses (three hydrogen atoms) and weakly bound (0.22 eV) molecules, quantum effects might be expected to be important. This suggests that QCT calculations might be useful predictors of the gross features of CID in reactive systems. One must approach this with some caution, however, as in a non-reactive system, Gray, et al. (10) have obtained major differences in the dissociation probability between their QCT results and the QM results of Knapp and Diestler (11).

In order to help gain a better understanding of the dynamics of this model system, we have carried out a reactivity band analysis of the QCT results for this system. Such analyses have been extensively applied to reactive systems below dissociation (12, 13) and have also been applied to a non-reactive system above dissociation (10a). We examine bandedness in the plots of trajectory outcome (reaction, non-reaction, dissociation) as a function of initial vibrational phase of the diatomic molecule and the relative kinetic energy. We also consider the variation of the vibrational action of the diatomic product of non-reactive and reactive collisions with initial vibrational phase. In dissociative collisions we examine how the partitioning of the energy among the three product atoms varies with initial vibrational phase and reagent translational energy. We also examine individual trajectories in order to understand the nature of the trajectories comprising each of the reactivity bands.

II. METHOD OF CALCULATION

The QCT calculations have been performed using standard methods (14). The model potential energy surface used has been described previously (7); we repeat here its basic features. It is of the rotating Morse-cubic spline type (15), and has asymptotic Morse oscillator parameters (16) of $D_e = 0.22$ eV, $R_{eq} = 1.4083$ bohr, and $\beta = 1.6$ bohr⁻¹. There is a barrier to exchange of 0.14 eV. The surface is plotted in figure one of reference seven, and is replotted later in figures 23-31, in which we show selected trajectories. The trajectories are integrated with a time step of 5.41×10^{-17} sec. Energy is conserved to four digits in these calculations. Integration of trajectories began with the distance from the incident atom to the center of mass of the diatomic molecule at 12 bohr.

To determine dissociation probabilities and rough boundaries for reactivity bands, we have calculated 100 trajectories per energy at regularly spaced ($\pi/50$ radians) values of the initial vibrational phase. At selected energies, we have narrowed the phase grid substantially near the boundaries of the reactivity bands. Below dissociation we have calculated 50 trajectories per energy at regularly spaced ($\pi/25$ radians) values of the initial vibrational phase and successively narrowed the grid near the band boundaries.

We have also determined the partitioning of kinetic energy among the atoms after the collision. The quantity of greatest interest is the fraction f_X^D ($X = A, B, C$) of the available kinetic energy E' (the difference between the total energy E of the collision and the dissociation energy D_e of the diatomic molecule) in dissociative collisions in each of the atoms at the end of the collision. In dissociative collisions, the collision was defined to be over when both internuclear distances R_{AB} and R_{BC} were greater than 6.0 bohr and were increasing with time. The sum of the kinetic and potential energies of the AB and BC pairs was each required to be greater than D_e . We have extended

AD-A138 168

THE QUANTUM DYNAMICS OF CHEMICAL REACTIONS(U)
CALIFORNIA INST OF TECH PASADENA DIV OF CHEMISTRY AND
CHEMICAL ENGINEERING A KUPPERMANN 31 MAR 83

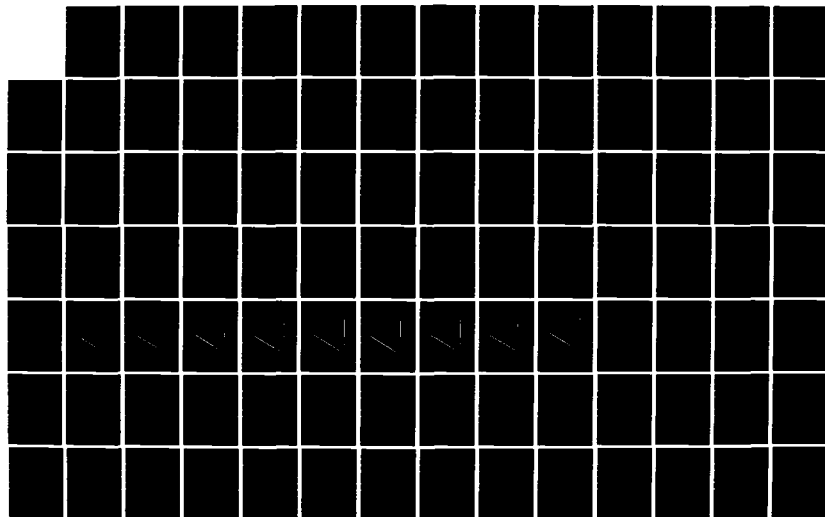
2/6

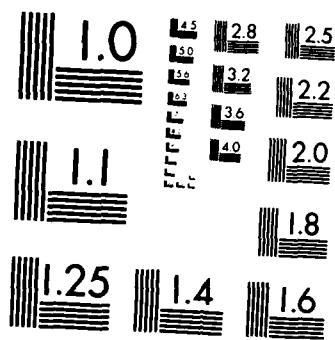
UNCLASSIFIED

AFOSR-TR-83-0565 AFOSR-81-0235

F/G 20/10

NL





MICROCOPY RESOLUTION TEST CHART
NATIONAL BUREAU OF STANDARDS-1963-A

this calculation to include this ratio for atom A in non-reactive collisions (f_A^N) and atom C in reactive collisions (f_C^R). Plots of these quantities vs. initial vibrational phase will connect smoothly to the f_A^D and f_C^D curves across the boundary of the reactivity bands. From the fractional energy vs. initial vibrational phase data, one may calculate the probability ${}^c\sigma_v^d$ of the kinetic energy of atom A after dissociation E_A being between E_A and $E_A + dE_A$ for a collision in which the diatomic molecule is in state v. This may be done by recognizing that this is related to the width of the region of phase d in which E_A will lie between E_A and $E_A + dE_A$

$${}^c\sigma_v^d(E_A) = (1/2\pi) |d\phi/dE_A| \quad (3)$$

The superscript c emphasizes the classical nature of this quantity.

The $(1/2\pi)$ factor is included so that ${}^c\sigma_v^d(E_A)$ will be appropriately normalized:

$$\int_{E_A^{\min}}^{E_A^{\max}} {}^c\sigma_v^d(E_A) dE_A = 1 \quad (4)$$

The limits of integration in eq. 4, E_A^{\min} and E_A^{\max} , have been shown previously (17) to be $E'/6$ and $2E'/3$, respectively, when the masses of all atoms are equal. To simplify comparison of these partitioning probabilities from one energy to the next, we will plot the dimensionless partitioning probabilities $E' \cdot {}^c\sigma_v^d(E_A)$, which will be indicated by a bar over the quantity, vs. f_A for all values of the energy E' , in which case the abscissa will always run from $1/6$ to $2/3$.

The evaluation of the derivative in eq. 3 is complicated by the possibility of minima or maxima in the E_A vs. ϕ curves; hence $\phi(E_A)$ may be a multiply valued function of ϕ . We separate those regions in which $d\phi/dE_A$ is positive and negative and then separately obtain the derivatives by a three-point finite difference procedure. The resulting

derivatives are then used as an input for a cubic spline procedure which allows us to obtain approximate expressions for the derivatives as a function of E_A . We next sum the absolute values of the derivatives over all separated parts of each dissociative reactivity band and over all such dissociative reactivity bands, and divide by 2π for normalization. The resulting curve (called a partitioning probability curve) may contain some numerical noise associated with the numerical differentiation procedures; we have visually smoothed out the spline-induced oscillations.

III. RESULTS

Reaction and dissociation both occur in the energy range studied here (up to 0.25 eV above the dissociation energy of the diatomic molecule). Plots of the reaction and dissociation probability obtained from the trajectory calculations are shown for reagent states $v = 0$ and $v = 1$ (the only ones possible) in figures 1 and 2, respectively. For both reagent states, the reaction probability is zero below a threshold energy, increases rapidly with energy to a large value (0.86 for $v = 0$, 0.96 for $v = 1$) and then decreases to zero (for $v = 0$) or a value just above zero (for $v = 1$). It then increases monotonically with energy. The dissociation probabilities for the $v = 0$ and $v = 1$ reagents behave quite differently from each other, however. In the $v = 0$ case, no dissociation is observed until one is substantially (0.08 eV) above its energetic threshold; as the energy increases beyond that, the probability increases slowly, reaching a value of 0.27 eV at the highest energy studied. For the $v = 1$ case, dissociation sets in at 0.02 eV above its energetic threshold, increases rapidly with energy to a maximum of 0.33 and then decreases rapidly to 0.02 before again increasing with energy up to a value of 0.39 at the highest energy studied. It should be emphasized that all of these results are qualitatively similar to the exact quantum mechanical results for this system presented in reference 7.

We next examined bandedness in plots of trajectory outcome vs. initial vibrational phase and relative translational energy. Plots of the reactivity bands for this system are shown in figures 3 and 4 for reagent states $v = 0$ and 1, respectively, for energies above the threshold for CID. Unlike reactivity band plots normally used in studies of reactive atom-diatom molecule collisions at energies below dissociation, in which there are only two possible outcomes of a trajectory (reaction or non-reaction), there are three possible outcomes

here: reaction (R), indicated by the shaded regions of the figures; dissociation (D), indicated by the speckled regions, and non-reaction (N), indicated by the clear regions. The dissociative band centered near 2.0 radians and 0.17 eV translational energy in figure 4 is enlarged in figure 5.

Fairly well defined bands are seen to exist above dissociation. When one narrows down the phase grid substantially (to on the order of 0.002 radians), one may find blurring of the boundaries and formation of a "chattering" region (18), in which the outcome of the trajectory varies strongly with small changes in the initial phase. This is most severe below 0.10 eV translational energy in the $v = 1$ case, where the high energy reaction and dissociation bands come to a "point" (see figure 4). For example, at 0.085 eV reagent translational energy, between 2.50 and 2.70 radians initial phase, there are four separate dissociation zones, two reaction zones, and one non-reaction zone obtained when the grid spacing of 0.002 radians is used. The total width of all the dissociative zones in this region is 0.52 radians. The dissociation probability produced by this region is only 0.8%, which is far smaller than the contribution at this energy from the large band centered at 5.5 radians. Chattering is also seen near the boundary between reactive and non-reactive bands at energies below dissociation.

We next consider the variation of the vibrational energy of the diatomic molecule resulting from reactive or non-reactive collisions. Normally, to examine this quantity one prepares plots of the action of the diatomic molecule at the end of the trajectory as a function of initial phase at a sequence of energies (10a, 12, 19, 20). At energies above dissociation, one cannot calculate the action in the usual way, and one is left with gaps in the action vs. phase plots. Examples of these plots are shown in figures 6 and 7 for the highest energies studied (reagent translational energies of 0.388 eV for $v = 0$ and 0.2815 eV for $v = 1$). Solid lines are used to indicate non-reactive zones and dashed lines

are used to indicate reactive zones. The shaded regions mark those regions of initial phase in which the trajectories are dissociative and hence no action can be defined. In both of these figures, the dissociation is seen to occur in between regions of high final action in reactive and non-reactive collisions (the maximum allowable final action in this system is 1.981). This is quite reasonable behavior, as for dissociation to occur, there must be more than the dissociation energy present in each diatomic molecule, hence, the boundary between reactive or non-reactive regions is expected to occur where the final action of the diatomic molecule equals its maximum value.

A different sort of diagram is shown in figure 8, in which we plot the final action vs. initial phase in a collision with $v = 1$ reagent and a reagent translational energy of 0.1615 eV. Here there are three dissociative regions. Two are sandwiched between the reactive and non-reactive regions, and one is in the middle of the large non-reactive region. This dissociative region is part of the small dissociative band located near 2 radians initial phase between 0.15 and 0.20 eV reagent translational energy in figure 4 (and enlarged in figure 5). As the initial phase is varied so it closely approached that in the dissociative region, the final action increases, suggesting that the consideration of dissociation as a limiting case of vibrational excitation is an appropriate concept.

There is a substantial difference between the product state distribution in collisions with $v = 1$ reagent at relative energies of 0.2815 eV (figure 7) and at 0.1615 eV (figure 8). At the higher energy, the likelihood of vibrational deexcitation, as measured by the large region of initial phase over which the final action is substantially smaller than one, is much greater than at the lower energy. At the lower energy, from -0.5 radians to the second dissociative band (at 4.15 radians), the final action never becomes smaller than 0.8. Thus, increasing

translational energy seems to lead to increasing vibrational non-adiabaticity in non-reactive collisions. The small likelihood of reaction in these energy regions makes it difficult to draw any conclusions concerning that process. A similar trend has been observed in the exact quantum mechanical calculations on this system (21).

Further evidence of the tendency towards vibrational adiabaticity at low energies can be seen by considering a collision with $v = 0$ molecules at an energy (0.178 eV relative translational energy) at which only non-reactive collisions occur - no dissociation or reaction was found. A plot of the final action as a function of initial phase for this collision is given in figure 9. The near adiabaticity may be seen by noting that the total range of final actions in the figure is from -0.12 to 0.19, corresponding to vibrational energies of 0.0639 eV and 0.1079 eV, respectively (the zero point energy is 0.0818 eV). Hence, at most 15% of the initial translational energy was converted to vibrational energy in the collision. Another interesting feature of this figure is the relatively complicated structure. In spite of the fact that all collisions are non-reactive and nearly adiabatic, there is still some systematic variation in the dependence of the final action on the initial phase.

To give some feeling for what happens when the boundary regions between the reactivity bands become blurred, we present in figure 10 a plot of final action vs. initial phase for the collision with $v = 1$ molecule at a relative translational energy of 0.085 eV for initial phases from 2.40 to 3.10 radians. In this region one sees five separate dissociative regions, four of which are found between 2.50 and 2.70 radians. These may be thought of as being distinct from the larger dissociative band between 2.90 and 3.10 radians. The latter band is part of the large dissociative band seen in the lower right hand portion of figure 4. The action vs. phase curves are fairly smooth in between the dissociative regions. Away from the lower tip of the large dissociation and

reaction band in figure 4, the boundaries are smoother. This figure seems to represent, then, an upper limit to the complication of such a diagram.

We next consider the partitioning of kinetic energy among the three atoms in dissociative collisions and also the amount of kinetic energy of motion of the free atom in reactive and non-reactive collisions. The calculation of these quantities has been described earlier. Plots of these quantities as a function of the initial phase are shown for initial phases in or near which dissociation occurs for a variety of initial conditions in figures 11 - 16. A few important features are observed in these figures, and we review these here.

First, the curves are quite smooth in the dissociation region. At the border between reactive and dissociative collisions, f_C smoothly matches onto the f_C^R curve, and at the border between non-reactive and dissociative collisions, f_A smoothly matches onto the f_A^N curve. In all cases, the matching occurs at a value of the energy fraction of $2/3$; this has been shown to be the maximum value f_A or f_C can take in the dissociative region for a system of three equal masses. The small values of f_B are also a requirement of the mass combination (for the case of three equal masses, f_B is required to be smaller than $1/6$).

Second, two types of partitioning curves are seen. For those dissociative bands sandwiched between one reactive and one non-reactive band, f_A and f_C must both have regions where they are large ($\sim 2/3$) and small ($\sim 1/6$). For those bands sandwiched between two non-reactive bands, the f_A vs. phase curve must have a minimum. The presence of such a minimum will have a major effect on the partitioning probabilities to be presented below. In theory, one might obtain dissociative bands sandwiched between two reactive ones, but such bands have not been observed.

Finally, we present results for the partitioning probability $c \frac{d}{dv}$ defined earlier. These are shown in figures 17 - 22 for the six sets of initial conditions for which energy fractions were shown as a function of initial phase. They all appear quite different from each other, and we can rationalize much of their form simply from the reaction and dissociation probabilities, the kinematics of the system, and the existence of well defined dissociation bands in the reactivity band plots (figures 3-5). We will extensively examine this issue in the discussion section.

There are a few features of figures 17 - 22 which will prove to be of most interest. First is the tendency of the partitioning probabilities to have their maxima near the maximum allowable fraction of $2/3$, although this is not uniformly true (see particularly figure 21, in which the partitioning probability diverges at a fraction of 0.25). Second, in four out of the six cases studied, the partitioning probability has divergences (figures 18 and 21) or sharp peaks (figures 19 and 20). Third, curves of the partitioning probability need not be smooth. If there is more than one dissociation band at a given energy, each of which has a very different slope or range of slopes in its corresponding fractional energy vs. phase curve, by summing the contributions from each band one may be adding one curve which is non-zero in the range $f_1 < f < f_2$ and another which is non-zero in the range $f_1' < f < f_2'$. Such a condition would result in a partitioning probability curve which is discontinuous at f_1' and f_2' . Normally, this will not be seen, as $f_1 = f_1' = 1/6$ and $f_2 = f_2' = 2/3$. If this is not true for a given band, discontinuities will be observed. This may be seen in figure 21, in which the hump in the region $0.42 < f < 0.49$ is due to the existence of a narrow dissociative band between 1.9930 and 2.0055 radians (not shown) in which the fractional energy varies from 0.497 to 0.415 . Two additional narrow dissociative bands located from 1.8710 to

1.8758 radians and 1.9232 to 1.92825 radians make essentially no contribution to the partitioning probability because their narrowness means that the magnitude of the derivative $|d\phi/dE_A|$ will be small (unless, of course, E_A is essentially constant over the band, as is true in the additional band mentioned earlier).

IV. DISCUSSION

In this section we will consider first the implication of the bandedness of dissociative trajectories as seen in the reactivity band plots. In particular, we will focus on how this bandedness, when coupled with the calculated reaction probabilities and the pure kinematics of the collision, can be seen to lead to the general structure of the partitioning probability curves, such as those shown in figures 16 - 21. We will then consider the origins of the bandedness of the dissociative trajectories, and show that a strong relationship can be established between the separate bands and different types of trajectories leading to dissociation.

A. IMPLICATIONS OF THE DISSOCIATIVE REACTIVITY BANDS

Trajectories which lead to dissociation have been found to occur, as a general rule, in well defined bands in the reactivity band plots (figures 3 - 5). Exceptions to this trend are found for collisions of a $v = 1$ molecule in which the reagent translational energy is in the range from 0.07 to 0.10 eV. In this region, the trajectory outcome may vary substantially with small changes in the initial phase of the diatomic molecule. This is somewhat reminiscent of the observation of chattering regions in the final action vs. initial phase plots seen in reactive atom-diatom collisions (at energies well below dissociation), particularly the $F + H_2$ (18, 20) and $Cl + HCl$ (22) reactions. Unlike in those cases, where the outcome of the trajectory appears to be random, by the use of a sufficiently small grid spacing (0.002 radians), seemingly smooth (but quite short) curves of final action vs. initial phase can be obtained. We have found that only a few discrete regions of initial phase lead to dissociative trajectories. In all cases, the dissociation probability associated with these regions is quite small (no more than 1 % of all collisions) and can thus be neglected to that accuracy in the calculations of dissociation probabilities.

In most cases, dissociative trajectories can be thought of as limiting cases of reactive or non-reactive collisions giving rise to vibrational excitation of products. This is seen in two interrelated ways. For values of the initial phase only slightly different from those of the trajectories which lead to dissociation, the diatomic molecules remaining at the end of the collision will be highly vibrationally excited. If one considers the fractional energy, such as that plotted in figure 10-15, one sees that the curve for atom A smoothly matches onto that for atom A in non-reactive collisions and that for atom C smoothly matches onto that for atom C in reactive collisions. This is not necessarily true for dissociative collisions in the chattering region; as mentioned earlier, such regions may give rise to discontinuities in the partitioning probability curves.

The nature of the dissociative band (defined by the type of bands between which it is sandwiched at a given energy) will play a major role in determining the appearance of the partitioning probability curves. If the band is sandwiched between one reactive and one non-reactive band, the partitioning probability curve should cover essentially all the accessible region of energy fractions ($1/6$ to $2/3$ in this case). If, on the other hand, the band is sandwiched between two non-reactive bands, the partitioning probability curves will cover only a subset of the allowable energy fractions and must have at least one place where they diverge. There will be no possibility of obtaining energy fractions lower than that at the lowest divergence. Thus, in such cases the partitioning probability curves for that dissociation band have the unusual property that they are zero below the diverging value, at which they jump discontinuously to infinity. At higher energy fractions, the curve is continuous. Such curves are observed in figures 18 and 21. These figures demonstrate that the value of the energy fraction at which the partitioning probability diverges can be quite close to its maximum or minimum permitted value. Precisely at what values of the energy

fraction the partitioning probability diverges will depend on the shape of the dissociation and reaction reactivity bands at the energy being considered. If, for instance, one is at an energy fairly near the opening of the reaction band, the minimum in the energy fraction vs. phase plot will occur at a value of the energy fraction close to $1/6$. This is the case in figure 21 (the important reaction and dissociation reactivity bands may be seen in figure 4). If the energy is such that one is not close to the opening of the reaction band, the minimum will occur at values of the energy fraction close to $2/3$.

Certain types of curves of energy fraction vs. phase in dissociative collisions which might occur have not been obtained. For instance, in no cases were curves with more than one minimum or maximum observed. Hence, the partitioning probability diverges at one and only one point if it diverges at all. As mentioned earlier, no dissociative bands sandwiched between two reactive bands were observed. Such bands would lead to partitioning probability plots opposite to those in figures 18 and 21 - there would be no possibility of energy fractions above that at which the partitioning probability diverges of being populated. There seems to be no reason why such bands should not exist, so we assume that their absence is a function of the particular potential and mass combination studied.

The fact that reactive processes are less probable than non-reactive ones at the energies studied suggests that in dissociative collisions one may be more likely to find kinetic energy distributions in which atom A has the greatest portion of the available energy. This would give rise to the partitioning probability being dominated by high energy fractions. The range of energy fractions allowable is determined simply by the masses of the colliding particles, which explains why only certain numerical regions of the energy fraction are allowed (17). Changing the masses would, therefore, change the partitioning probabilities for two reasons. First, the dynamics of the system would

change, and second, the ways in which kinetic energy could be distributed in dissociative collisions would be altered.

The structure of the reactivity band plots differs very strongly for $v = 0$ and $v = 1$ molecule collisions, and this fact, coupled with the definite manner in which the position and width of the reactivity bands have been shown to determine the partitioning probabilities, suggests that one might obtain substantially different kinetic energy distributions from dissociation from the two reagent states at the same total energy. The same statement applies to translational energy. The simplest way of obtaining such a case would be to locate an energy at which the dissociation from $v = 0$ occurs totally from a band which is sandwiched between two non-reactive bands, while that from $v = 1$ occurs from one or more bands sandwiched between one reactive and one non-reactive band. Thus, not only may the outcome of the collision (reaction, non-reaction, or dissociation) depend on the initial state, but the intimate details of dissociation may also be a function of the initial state.

B. ORIGIN OF THE DISSOCIATIVE REACTIVITY BANDS

Formation of reactivity bands in atom-diatomic molecule collisions has been observed in a variety of systems at energies below dissociation (12, 13); banding has also been observed in a non-reactive system studied at energies above dissociation (10a). The present study marks, to our knowledge, the first reactivity band study of dissociation in a reactive system. In studying the origin of reactivity bands, we are interested in getting a good physical picture as to what sort of trajectories comprise each band. In particular, we focus on two questions. First, we want to know whether each separate band corresponds to different types of trajectories. Second, we want to know what happens near the boundaries between bands, especially in the chattering regions, such as that shown in figure 10, in which the outcome of the trajectory is extremely sensitive to the initial conditions of the trajectory.

Wright and Tan (12c) have shown in their study of the collinear $T + HT$ system on the SSMK surface (23) that the two lowest energy reaction reactivity bands are comprised of different types of trajectories. In the lower energy band, reactive trajectories cross the symmetric stretch line only once, while in the higher energy band, they cross the symmetric stretch line three times. Representative trajectories are shown in figure 8 of reference 12c. A similar correspondence can be drawn between the two reaction reactivity bands in figure 4 for collisions of $v = 1$ molecule. For collisions of $v = 0$ molecule in figure 3 we show only the high energy reaction reactivity band; there is another band at lower energies responsible for the large values of P_0^R at low energy seen in figure 1. Trajectories comprising the lower reaction reactivity band in the $v = 1$ case cross the symmetric stretch line once (figure 23) while those in the higher band cross the symmetric stretch line three times (figure 24). Reactive trajectories must cross the symmetric stretch line an odd number of times; thus, these are the simplest sort of reactive trajectories possible. The importance of reactive trajectories which cross the symmetric stretch line more than once indicate that a purely classical transition state theory would seriously overestimate the rate constant for reaction at high temperatures when these high energy trajectories become important (24). The same behavior is seen in collisions of ground state molecules; we do not show them here.

We next consider the nature of trajectories leading to dissociation. We will focus our attention first on the single dissociation band for collisions of ground state molecule and the two large bands for collisions of $v = 1$ molecules. We will consider the small band for $v = 1$ isolated in the large non-reactive band and the overall chattering region later. Typical dissociative trajectories are shown in figures 25 - 27 for the large band in $v = 0$ collisions, the first band in $v = 1$ collision, and

the second band in $v = 1$ collisions, respectively. In figures 25 and 27, the trajectory crosses the symmetric stretch line three times; in figure 26 the symmetric stretch line is crossed only once. This suggests that the separate dissociation bands are each comprised of trajectories crossing the symmetric stretch line a different number of times, just as was seen for reactive transitions. Things are not quite so simple in the dissociation case, however, as the trajectory need not cross the symmetric stretch line an odd number of times. In fact, trajectories which cross it twice have been observed in both $v = 1$ reactivity bands. The last crossing of the symmetric stretch line may occur (as does that in the trajectory shown in figure 26) at large values of the internuclear coordinates. Whether or not such a crossing takes place will depend on the partitioning of energy in the three atoms. The final crossing, then, may be thought to occur while the atoms are in the process of dissociating, even if the crossing occurs at fairly small values of the internuclear coordinates. Thus, the first dissociation reactivity band in the reactivity band plot (in figure 4) may be thought of as being comprised of trajectories which cross the symmetric stretch line once prior to the process of actually dissociating (during which they may again cross that line). In the second dissociation band for $v = 1$ and the only such band for $v = 0$, two crossings take place prior to the onset of dissociation, after which a third crossing may occur.

These observations allow one to make a simply physical picture to account for the observed vibrational enhancement of CID in this system: The simplest trajectory which may lead to dissociation does not occur when the molecule is in its ground state. It occurs only when the molecule is in its excited state. Since more complicated trajectories appear to contribute only at higher energies, low energy dissociation is prevented in the ground state case. The qualitative agreement between the quasi-classical trajectory calculations and the exact quantum ones reported previously (7) indicates that this simple classical picture may

be a reasonable one to use in attempting to understand the calculated vibrational enhancement of CID in this system.

We next wish to consider the small dissociation band seen in figure 4 (and enlarged in figure 5) near 2 radians and 0.18 eV reagent translational energy. A typical trajectory in this band is shown in figure 28. This trajectory is quite different from the dissociative ones seen in figures 25 and 27. This should not be surprising, however, as this small dissociation band is imbedded in a large non-reactive band and the other dissociation bands tend to be sandwiched between reactive and non-reactive bands. Examination of non-reactive trajectories near the boundaries between the non-reaction and dissociation reactivity bands indicates that differences between the trajectories within them are quite small and become important only at large values of the internuclear coordinates. This is a case, then, in which the final outcome of the trajectory is not determined until well after the collision might be thought to be finished (R_{AB} large and increasing, R_{BC} fairly small).

We finally consider the chattering region indicated in figure 9. In the region of initial phase from 2.5 to 2.7 radians, the outcome of the trajectory varies greatly with small changes in the initial phase. Such regions have been observed in studies of reactions below dissociation, particularly the $H + H_2$ (13) and $F + H_2$ (18, 20) reactions. In these regions, the trajectories become very complicated, frequently bouncing back and forth many times in the strong interaction region of the potential energy surface. Atom B is said to "chatter" between atoms A and C, hence the name chattering region.

In this case, the trajectories in the chattering region are not overly complicated. Three such trajectories are shown in figures 29 - 31 corresponding to initial conditions shown in figure 9. The initial phase differs by 0.01 radians (0.57°) between each trajectory. The dominant feature of the trajectories is clear : trajectories in this region involve

motion more or less along the symmetric stretch line. The extreme sensitivity of the trajectory outcome to the initial phase can, therefore, be easily understood. Since, in moving along the symmetric stretch line, the trajectory has, to a first approximation, forgotten from where it was begun, it is reasonable that a small perturbation to the trajectory could seriously alter its course.

At energies below dissociation motion exactly along the symmetric stretch line would constitute that of a trapped trajectory - one which could oscillate back and forth forever, never leaving the interaction region of the potential energy surface (25). In the language of Pollak and Pechukas, such motion constitutes a trapped trajectory of the first kind (26). These trajectories are frequently found at the boundary between reactive and non-reactive bands in atom-diatomic molecule systems at energies below dissociation (12, 13, 20, 22). At energies above dissociation, trapped trajectories of the first kind (in which the trajectory oscillates back and forth forever between two different contours at the total energy) do not exist. A trajectory can change its character continuously from reactive to non-reactive or vice versa by going through an intermediate stage of dissociative trajectories. Thus, the requirement shown by Pechukas and Pollak that trapped trajectories must occur at the boundary between reactive and non-reactive bands at energies below dissociation seems not to apply at energies above dissociation (25). Nothing in these statements here, however, precludes the possibility of formation of trapped trajectories of the second or third kinds (26). No such trapped trajectories (or nearly trapped ones) were observed, although we have not carried out a systematic search for them.

V. CONCLUSIONS

We have performed a reactivity band analysis of CID in a model collinear reactive atom-diatomic molecule system. Quasi-classical trajectories are believed to provide a reasonable view of the dynamics in this system because of the qualitative similarity in the reaction and dissociation probabilities calculated by trajectories and by exact quantum mechanical calculations (7).

CID is shown to occur almost entirely in well defined bands, the exception being a small contribution from dissociative trajectories in a chattering region in which the outcome of the trajectory is extremely sensitive to the initial phase of the reagent molecule. Dissociation may be thought of as a limiting case of vibrational excitation, as non-dissociative (reactive or non-reactive) trajectories with initial conditions only slightly different from those leading to dissociation lead to a diatomic molecule product which is highly vibrationally excited. In most cases, dissociation reactivity bands are found sandwiched between one reactive and one non-reactive band; in the rest, they may be sandwiched between two non-reactive bands. In no instances were dissociative bands sandwiched between two reactive bands.

We have calculated the partitioning of kinetic energy among the three atomic products of dissociative collisions and showed that these quantities vary smoothly throughout the dissociation band. Kinematic considerations require that most of the available kinetic energy go into the end atoms (A or C). The fraction of the available kinetic energy in the end atoms, as a general rule, matches smoothly onto that of the free atom in non-dissociative collisions (atom A in non-reactive collisions, atom C in reactive ones).

From the curves of energy fraction vs. initial phase we have been able to determine the partitioning probability, that is, the likelihood of the dissociation process to distribute the available energy in a given

way. We have presented plots of the partitioning probabilities for six different sets of initial conditions (reagent vibrational state and translational energy), and found a wide range of appearance of the probability vs. energy fraction curves. We have shown that the general form of the partitioning probability curves can be inferred solely by examination of the reactivity band plots.

The different dissociation reactivity bands found for the reaction of vibrationally excited ($v = 1$) molecules have been shown to be comprised of different sorts of trajectories. The band which dominates at low energies (and shuts off at reagent translational energies above 0.12 eV) is seen to arise from trajectories which cross the symmetric stretch line only once prior to the onset of actual dissociation, while the higher energy band arises from trajectories which cross the symmetric stretch line twice prior to dissociation. During dissociation, the trajectories may or may not recross the symmetric stretch line an additional time. The single dissociation band observed in collisions of ground state molecules is seen to be made up of trajectories which cross the symmetric stretch line twice prior to dissociation. Hence, the vibrational enhancement of CID can be thought of as being due to the inability of ground state molecules to dissociate by the simplest possible trajectory; in that case dissociation is only possible by a more complex procedure, which only becomes important at higher energies.

The chattering region is seen to arise from trajectories which at some point follow the symmetric stretch line very closely. Since the available energy is greater than the dissociation energy, motion along the symmetric stretch line does not constitute a trapped trajectory. The existence of a dissociation channel allows for a smooth transition from reactive to non-reactive trajectories via an intermediate region of dissociative trajectories.

Our analysis here has been restricted to a single model potential

energy surface for a collinear collision. In reactive systems, changes in the masses of the atoms have been shown to produce major changes in the structure of the reactivity bands (12b). Exact quantum mechanical calculations on 'isotopically' substituted versions of the model system studied here (mass combinations 10-1-10 and 1-35-1) indicate that the effect of mass on dissociation is strong (22). Large changes in the reactivity band structure can be expected. Thus, one must use caution in attempting to generalize on the basis of the reactivity bands for one system.

Removal of the restriction to collinearity might be expected to lead to substantial changes in the reactivity bands (the model potential used here is defined solely for collinear configurations; we are addressing the general role of non-collinear collisions). In studies of the two and three dimensional $T + HT$ reaction, Wright (12e) has shown a disappearance of the bandedness observed in the collinear reaction, which is due to the diminished importance of multiple collisions (which involve multiple crossing of the symmetric stretch line) in non-collinear collisions. Thus, in a more realistic (three-dimensional) system, the rich banded structure obtained here might be expected to be substantially blurred.

ACKNOWLEDGMENTS

The calculations reported here were performed on the Dreyfus-NSF Theoretical Chemistry Computer which was funded through grants from the Camille and Henry Dreyfus Foundation, the National Science Foundation (Grant No. CHE78-20235) and the Sloan Fund of the California Institute of Technology.

REFERENCES

1. R. L. Belford and R. A. Strehlow, *Ann. Rev. Phys. Chem.* 20, 247 (1969).
2. A. Dalgarno and W.G. Roberge, *Astrophys J.* 233, L25 (1979); D. Hollenbach and C. F. McKee, *Astrophys J. Supp. Ser.* 41, 555 (1979).
3. P. J. Kuntz, in: *Atom-Molecule Collision Theory*, ed. R. B. Bernstein (Plenum Press, New York, 1979), pp. 669-692 and references therein.
4. D. J. Diestler, in: *Atom-Molecule Collision Theory*, ed. R. B. Bernstein (Plenum Press, New York, 1979), pp. 655-667 and references therein.
5. I. Rusinek, *J. Chem. Phys.* 72, 4518 (1980).
6. K. C. Kulander, *J. Chem. Phys.* 69, 5064 (1978); *Nucl. Phys.* A353, 341c (1981).
7. J. A. Kaye and A. Kuppermann, *Chem. Phys. Lett.* 78, 466 (1981).
8. J. Manz and J. Römelt, *Chem. Phys. Lett.* 77, 172 (1980).
9. L. H. Beard and D. A. Micha, *J. Chem. Phys.* 73, 1193 (1980).
10. (a) J. C. Gray, G. A. Fraser, and D. G. Truhlar, *Chem. Phys. Lett.* 68, 359 (1979); (b) J. C. Gray, G. A. Fraser, D. G. Truhlar, and K. C. Kulander, *J. Chem. Phys.* 73, 5726 (1980).
11. E.-W. Knapp and D. J. Diestler, *J. Chem. Phys.* 67, 4969 (1977).
12. (a) J. S. Wright, G. Tan, K. J. Laidler, and J. E. Hulse, *Chem. Phys. Lett.* 30, 200 (1975); (b) J. S. Wright, K. G. Tan, and K. J. Laidler, *J. Chem. Phys.* 64, 970 (1976); (c) J. S. Wright and K. G. Tan, *J. Chem. Phys.* 66, 104 (1977); (d) K. G. Tan, K. J. Laidler, and J. S. Wright, *J. Chem. Phys.* 67, 5883 (1977); (e) J. S. Wright, *J. Chem. Phys.* 69, 720 (1978); (f) K. J. Laidler, K. G. Tan, and J. S. Wright, *Chem. Phys. Lett.* 46, 56 (1977).

13. R. E. Howard, A. C. Yates, and W.A. Lester, Jr., J. Chem. Phys. 66, 1960 (1977).
14. R. N. Porter and L. M. Raff, in: Dynamics of Molecular Collisions, Part B, ed. W. H. Miller (Plenum Press, New York, 1976), pp. 1-52; D. G. Truhlar and J. T. Muckerman, in: Atom-Molecule Collision Theory, ed. R. B. Bernstein (Plenum Press, New York, 1979), pp. 505-565.
15. J. M. Bowman and A. Kuppermann, Chem. Phys. Lett. 34, 523 (1975).
16. H. Eyring, J. Walter, and G. Kimball, Quantum Chemistry (Wiley, New York, 1944), pp. 272-273.
17. J. P. Dwyer, Ph. D. Thesis, California Institute of Technology, 1977, p. 126.
18. J. S. Hutchinson and R. E. Wyatt, J. Chem. Phys. 70, 3509 (1979).
19. J. W. Duff and D. G. Truhlar, Chem. Phys. Lett. 4, 1 (1974); J. R. Stine and R. A. Marcus, Chem. Phys. Lett. 29, 575 (1974); N. Sathyamurthy, Chem. Phys. Lett. 59, 95 (1978); M. S. Child and K. B. Whaley, Faraday Disc. Chem. Soc. Lond. 67, 57 (1979).
20. F. Schnabel and S. Chapman, Chem. Phys. Lett. 57, 189 (1978).
21. J. A. Kaye and A. Kuppermann, unpublished results.
22. J. A. Kaye and A. Kuppermann, manuscript in preparation.
23. I. Shavitt, R. M. Stevens, F. L. Minn, and M. Karplus, J. Chem. Phys. 48, 2700 (1968).
24. D. G. Truhlar and B. C. Garrett, Acc. Chem. Res. 13, 440 (1980).
25. P. Pechukas and E. Pollak, J. Chem. Phys. 67, 5976 (1977).
26. E. Pollak and P. Pechukas, J. Chem. Phys. 69, 1218 (1978).

-29-

in figure 29, except that the initial phase is 2.67 radians. All markings are as in figure 23.

FIGURE CAPTIONS

Figure 1. Probabilities for reaction P_0^R (solid line) and dissociation P_0^D (dashed line) in collisions of ground vibrational state molecules as determined by quasi-classical trajectory calculations as a function of the collision energy. The reagent translational energy E_0 is indicated on the lower abscissa; the total energy E (sum of vibrational and translational energy) is indicated on the upper abscissa. The arrow points to the energy at which the molecule dissociates.

Figure 2. Probabilities for reaction P_1^R (solid line) and dissociation P_1^D (dashed line) in collisions of vibrationally excited molecules as a function of the collision energy. The axes and markings are otherwise as in figure 1.

Figure 3. Reactivity band plot for reaction and dissociation in collisions of ground state molecule. Reactive (R) bands are indicated by shading; dissociative (D) bands are indicated by speckling. The solid white region is non-reactive (N). Both the translational energy E_0 (left ordinate) and the total energy E (right ordinate) are indicated.

Figure 4. Reactivity band plot for reaction and dissociation in collisions of vibrationally excited molecule. Band type is indicated as in figure 3. Axis labeling is also as in figure 3. No effort is made to accurately portray the band structure in the "chattering" region.

Figure 5. Enlarged view of the small dissociative band (from figure 4) in collisions of vibrationally excited molecule. All markings and axes are as in figure 3.

Figure 6. Final action v_f as a function of the initial phase ϕ_0 for a collision involving a ground state diatomic molecule at a reagent translational energy E_0 of 0.388 eV. A solid line is used to connect results of non-reactive trajectories; a dashed line is used to connect results of reactive

trajectories. The shaded areas indicate those regions of the initial phase giving rise to dissociative trajectories, in which the action cannot be defined in the usual way. N, D, and R indicate non-reactive, dissociative, and reactive regions, respectively. The trajectory was begun with the distance from atom A to the center of mass of BC being 12 bohr.

Figure 7. Final action v_f as a function of initial phase ϕ_0 for a collision involving vibrationally excited molecules at a reagent translational energy E_1 of 0.2815 eV. All markings are as in figure 6.

Figure 8. Final action v_f as a function of initial phase ϕ_0 for a collision involving vibrationally excited molecules at a reagent translational energy E_1 of 0.1615 eV. All markings are as in figure 6.

Figure 9. Final action v_f as a function of initial phase ϕ_0 for a collision involving ground state molecules at a reagent translational energy E_0 of 0.178 eV. All markings are as in figure 6. Note the expanded scale of the ordinate.

Figure 10. Final action v_f as a function of the initial phase ϕ_0 for a collision involving vibrationally excited molecules at a reagent translational energy E_1 of 0.085 eV. The initial phases are limited to the chattering region described in the text and the regions to slightly lower and higher initial phase. All markings are as in figure 6.

Figure 11. Energy fractions f_X ($X = A, B, C$) (defined in section II) as a function of the initial phase ϕ_0 for the dissociative bands seen in collisions of ground state molecules at a reagent translational energy E_0 of 0.388 eV. A solid line is used for atom A, a dashed line for atom B, and a dotted line for atom C. A dashed-dotted line marks the approximate boundary between bands. The curve for atom A is continued into the non-reactive region and the curve for atom C is continued into the reactive region by

a procedure described in the text. (a) the small band from 0.90 to 1.03 radians initial phase; (b) the large band from 5.10 - 6.60 radians.

Figure 12. Energy fractions f_X as a function of initial phase ϕ_0 for dissociative bands in collisions of ground state molecules at a reagent translational energy E_0 of 0.233 eV. All markings are as in figure 11.

Figure 13. Energy fractions f_X as a function of initial phase ϕ_0 for dissociative bands in collisions of vibrationally excited molecules at a reagent translational energy E_1 of 0.2815 eV. (a) the small band from 0.25 to 0.31 radians; (b) the large band from 3.20 to 5.50 radians. All markings are as in figure 11.

Figure 14. Energy fractions f_X as a function of initial phase ϕ_0 for dissociative bands in collisions of vibrationally excited molecules at a reagent translational energy E_1 of 0.1815 eV. (a) band from 2.04 to 2.12 radians; (b) band from 4.25 to 4.80 radians; (c) band from 5.32 to 5.36 radians. All markings are as in figure 11.

Figure 15. Energy fractions f_X as a function of initial phase ϕ_0 for dissociative bands in collisions of vibrationally excited molecules at a reagent translational energy E_1 of 0.1015 eV.

Figure 16. Energy fractions f_X as a function of initial phase ϕ_0 for dissociative bands in collisions of vibrationally excited molecules at a reagent translational energy E_1 of 0.0715 eV. All markings are as in figure 11.

Figure 17. Partitioning probability $\frac{c}{\sigma_0}^d$ described in section II of the text for atom A for dissociation in collisions of ground state molecules at a reagent translational energy E_0 of 0.388 eV.

Figure 18. Partitioning probability $\frac{c}{\sigma_0}^d$ for atom A for dissociation in collisions of ground state molecules at a reagent translational energy E_0 of 0.233 eV. The probability is zero for values of the energy fraction

f_A below that at which it diverges (~ 0.58).

Figure 19. Partitioning probability $\frac{c}{\sigma_1^d}$ for atom A for dissociation in collisions of vibrationally excited molecules at a reagent translational energy E_1 of 0.2815 eV.

Figure 20. Partitioning probability $\frac{c}{\sigma_1^d}$ for atom A for dissociation in collisions of vibrationally excited molecules at a reagent translational energy E_1 of 0.1815 eV.

Figure 21. Partitioning probability $\frac{c}{\sigma_1^d}$ for atom A for dissociation in collisions of vibrationally excited molecules at a reagent translational energy of 0.1015 eV. The probability is zero for values of the energy fraction f_A below that at which it diverges (~ 0.25).

Figure 22. Partitioning probability $\frac{c}{\sigma_1^d}$ for atom A for dissociation in collisions of vibrationally excited molecules at a reagent translational energy of 0.0715 eV.

Figure 23. Plot of a typical reactive trajectory in the low energy reaction reactivity band for collisions of vibrationally excited molecule. Trajectory is for initial conditions of $E_1 = 0.0715$ eV and initial vibrational phase of 3.4558 radians. The integration of the trajectory was begun with $R = 12.8952$ bohr. The trajectory is superimposed on a plot of the potential energy surface for the system in Delves mass-scaled coordinate system. Contours are drawn every 0.06 eV starting from 0.02 eV up to 0.50 eV with respect to a zero of energy at the bottom of the well of the isolated diatomic molecule. The X marks the saddle point for the reaction. Note that there is only one crossing of the symmetric stretch line.

Figure 24. Plot of a typical reactive trajectory in the high energy reaction reactivity band for collisions of vibrationally excited molecule. Trajectory is for initial condition of $E_1 = 0.2815$ eV and initial vibrational

phase of 6.5649 radians. All markings are as in figure 23.

Figure 25. Plot of a typical dissociative trajectory in collisions of ground state molecules. Trajectory is for initial conditions of $E_0 = 0.388$ eV and initial phase of 0.3142 radians. All markings are as in figure 23.

Figure 26. Plot of a typical dissociative trajectory in the low energy dissociation reactivity band for collisions of vibrationally excited molecules. Trajectory is for initial conditions of $E_1 = 0.0715$ eV and initial phase of 5.3407 radians. All markings are as in figure 23.

Figure 27. Plot of a typical dissociative trajectory in the large, high energy dissociation reactivity band for collisions of vibrationally excited molecules. Trajectory is for initial conditions of $E_1 = 0.2815$ eV and initial phase of 5.3407 radians. All markings are as in figure 23.

Figure 28. Plot of a typical dissociative trajectory in the small dissociation reactivity band imbedded in the large non-reaction band for collisions of vibrationally excited molecules. Trajectory is for initial conditions of $E_1 = 0.1815$ eV and initial phase of 2.12 radians. All markings are as in figure 23.

Figure 29. Plot of a non-reactive trajectory in the chattering region shown in figure 10. Trajectory is for initial conditions of a vibrationally excited molecule, $E_1 = 0.085$ eV, and an initial phase of 2.65 radians. All markings are as in figure 23.

Figure 30. Plot of a dissociative trajectory in the chattering region shown in figure 10. Initial conditions are the same as for the trajectory in figure 29, except that the initial phase is 2.66 radians. All markings are as in figure 23.

Figure 31. Plot of a reactive trajectory in the chattering region shown in figure 10. Initial conditions are the same as for the trajectory

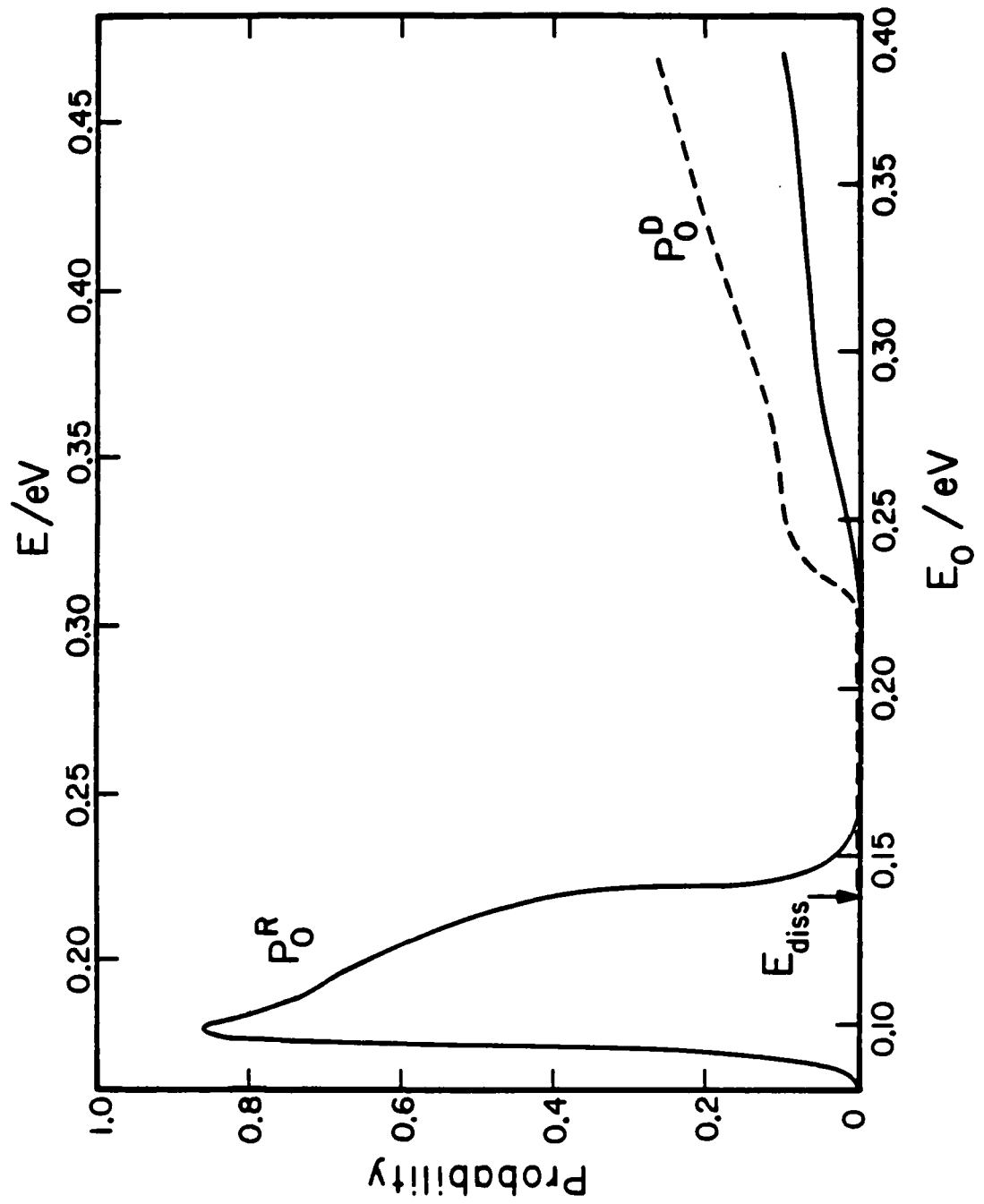


Figure 1

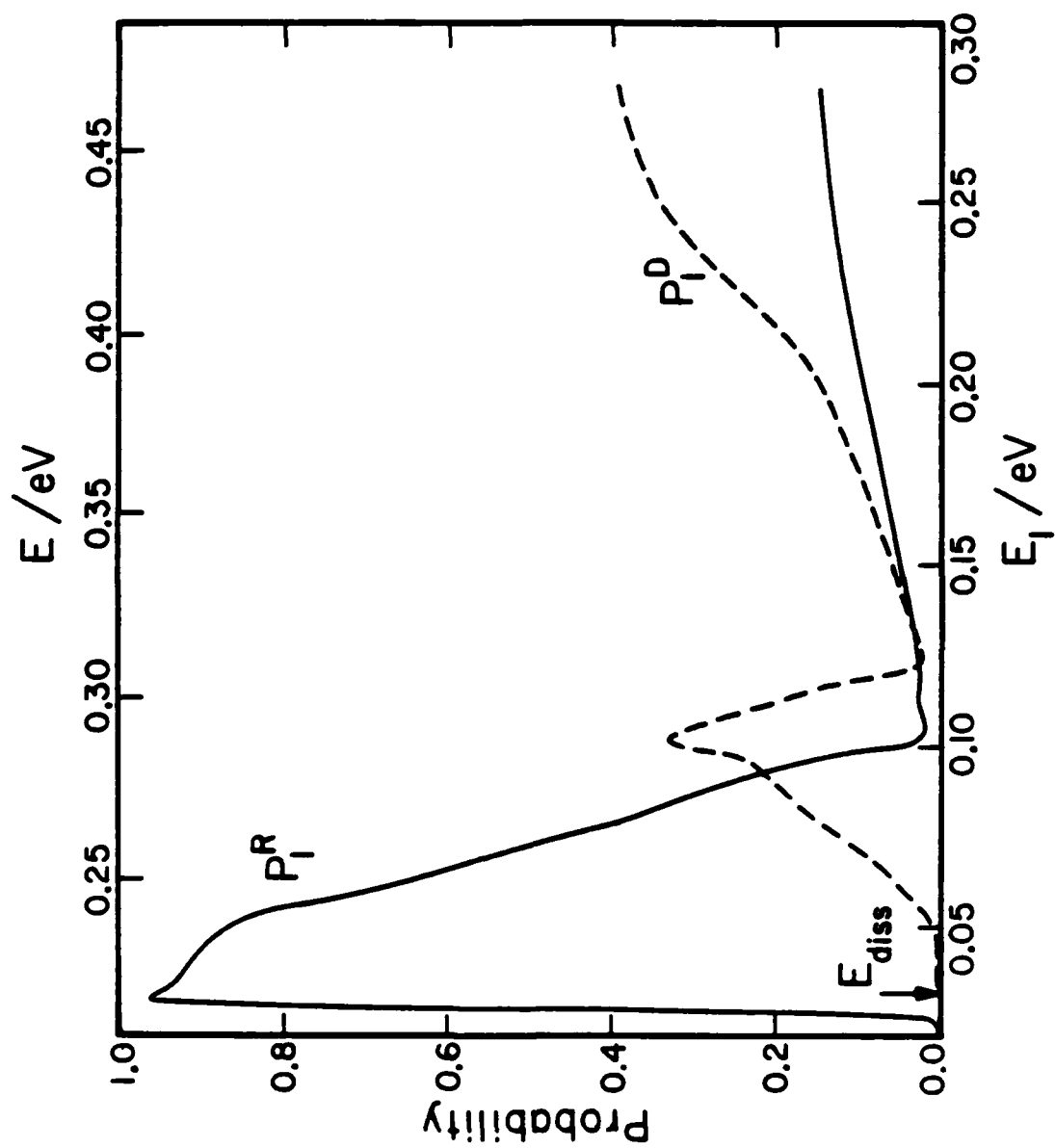


Figure 2

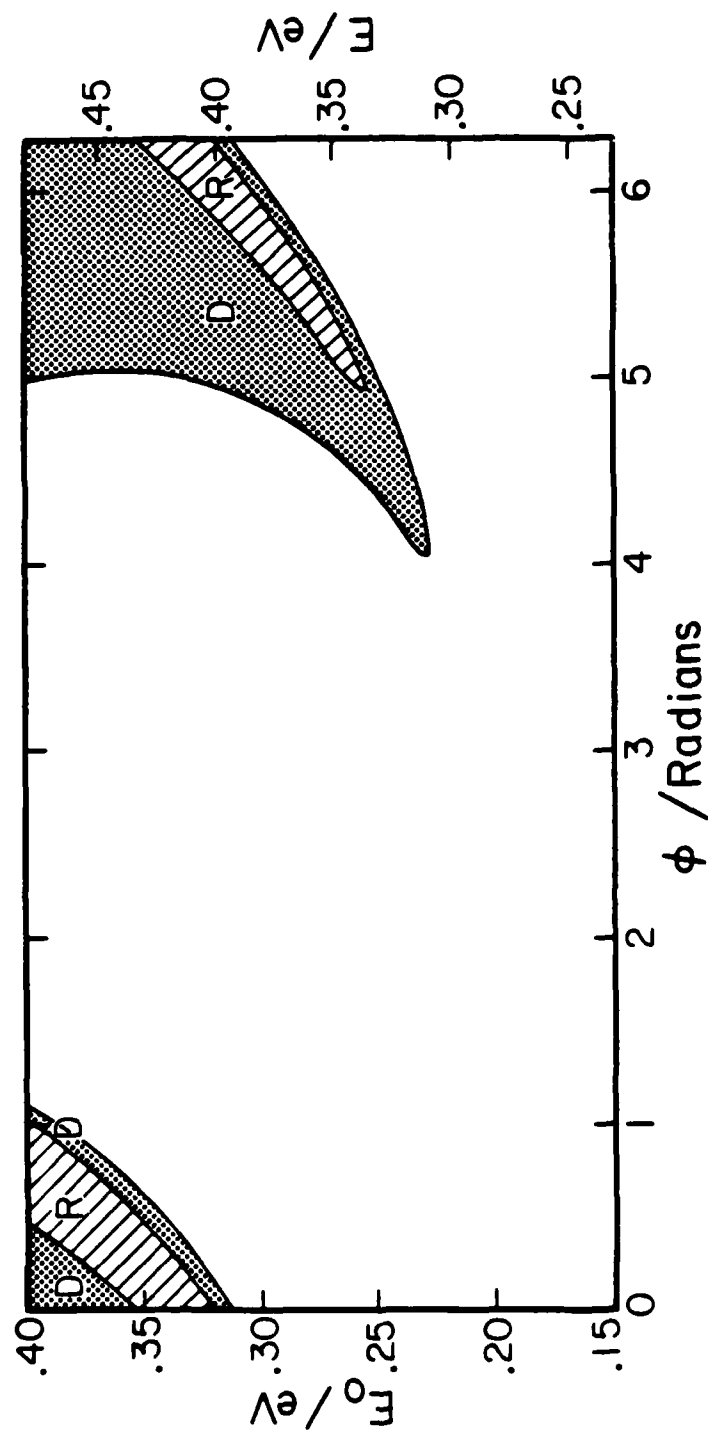


Figure 3

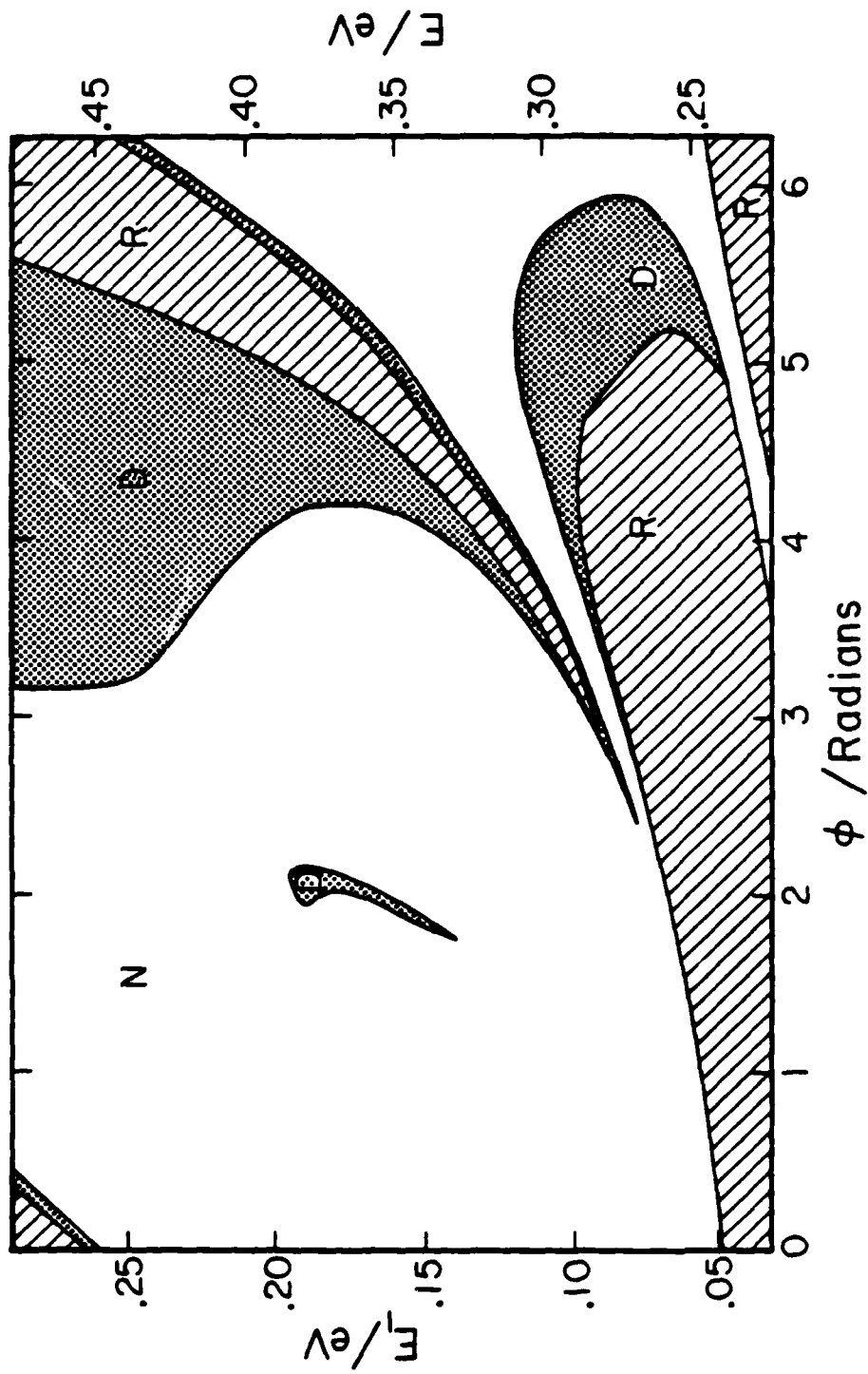


Figure 4

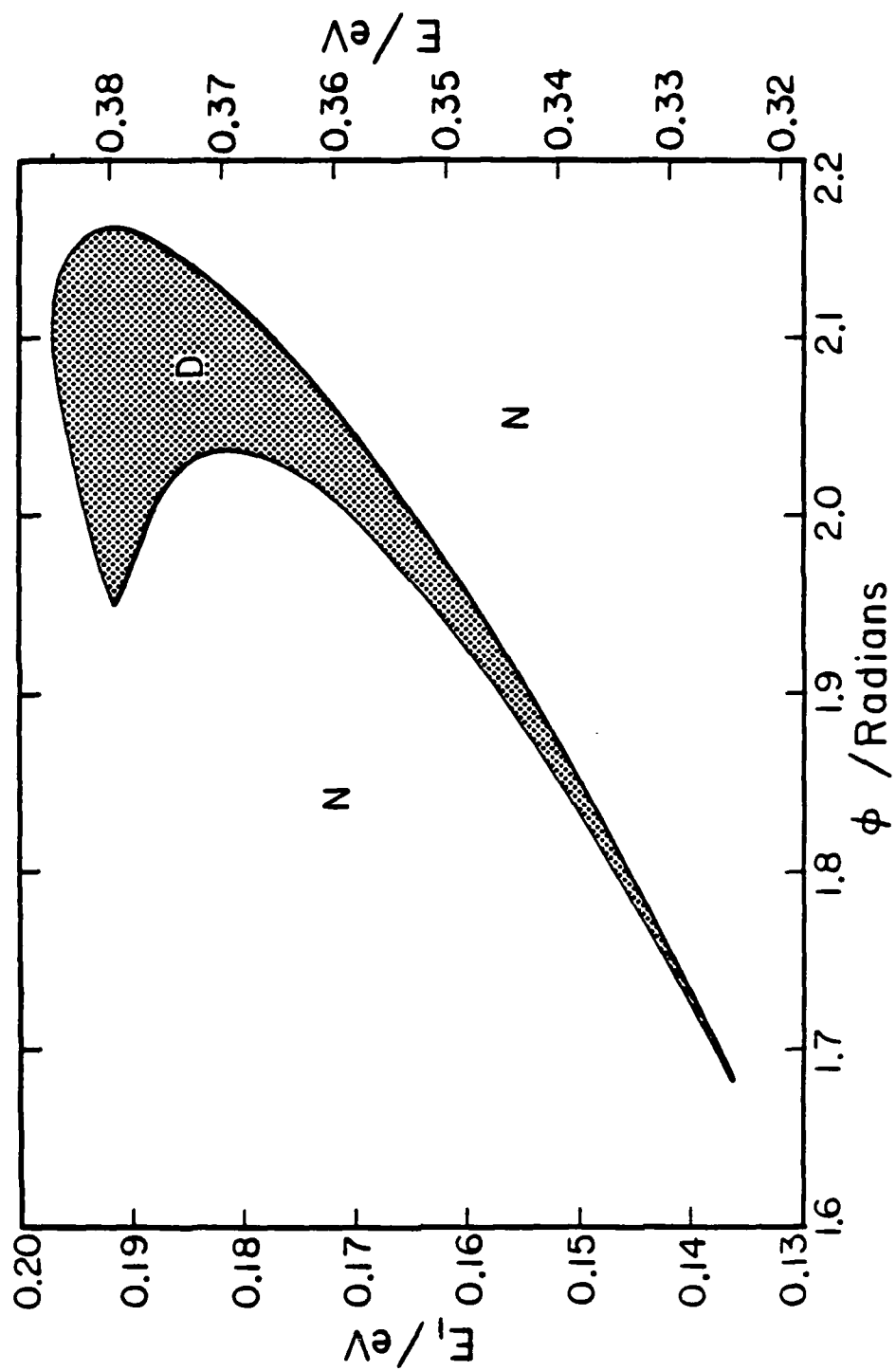


Figure 5

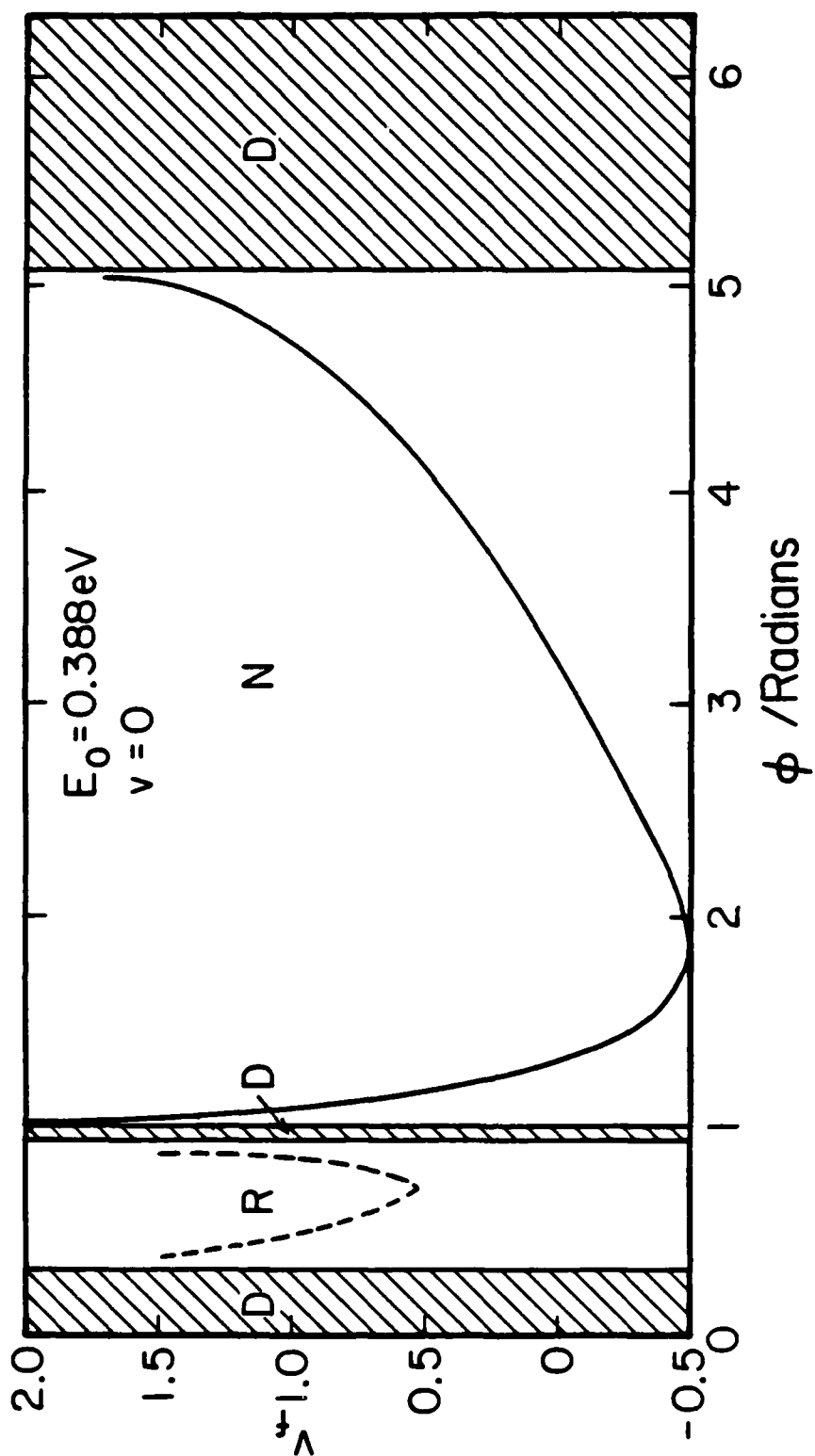


Figure 6

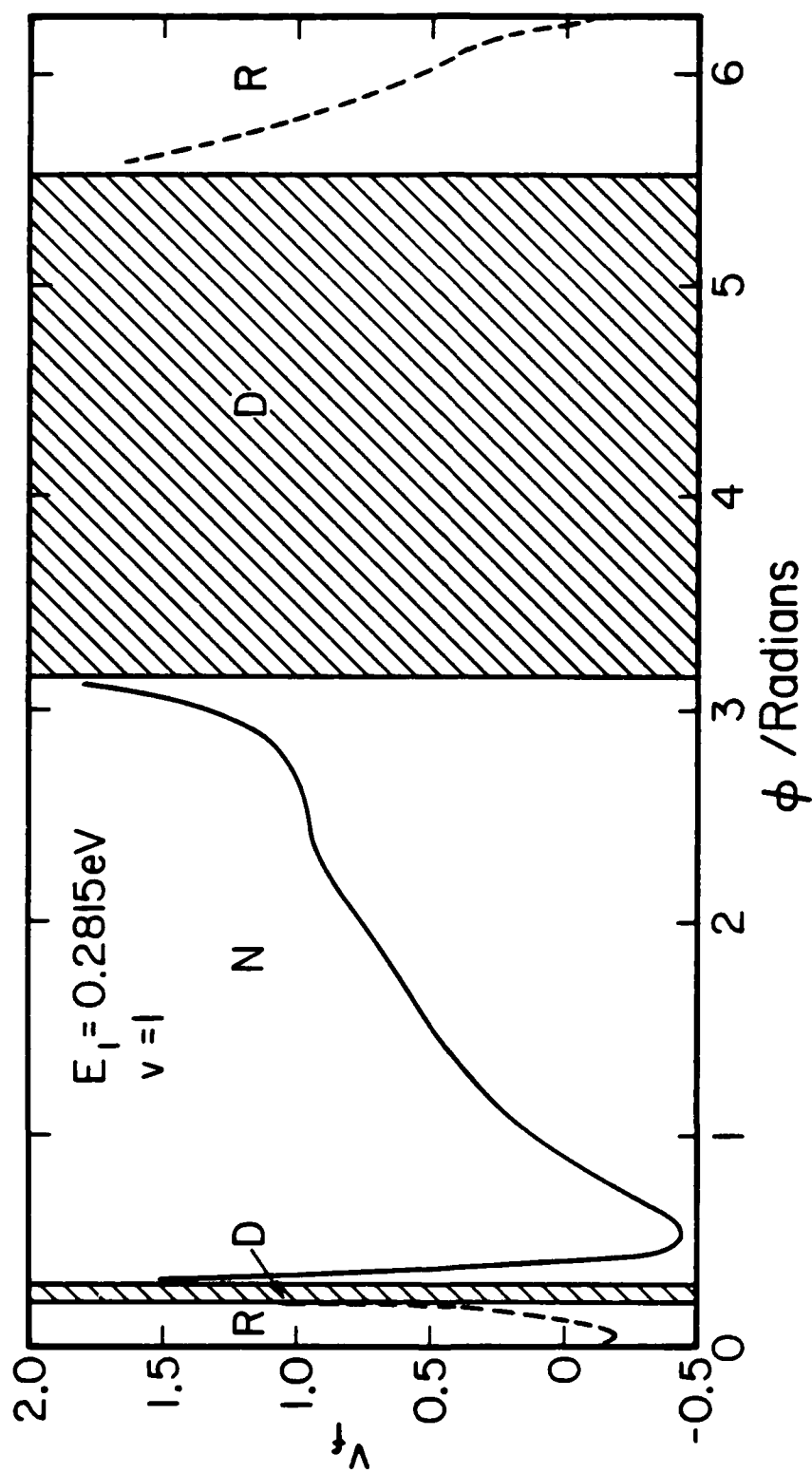


Figure 7

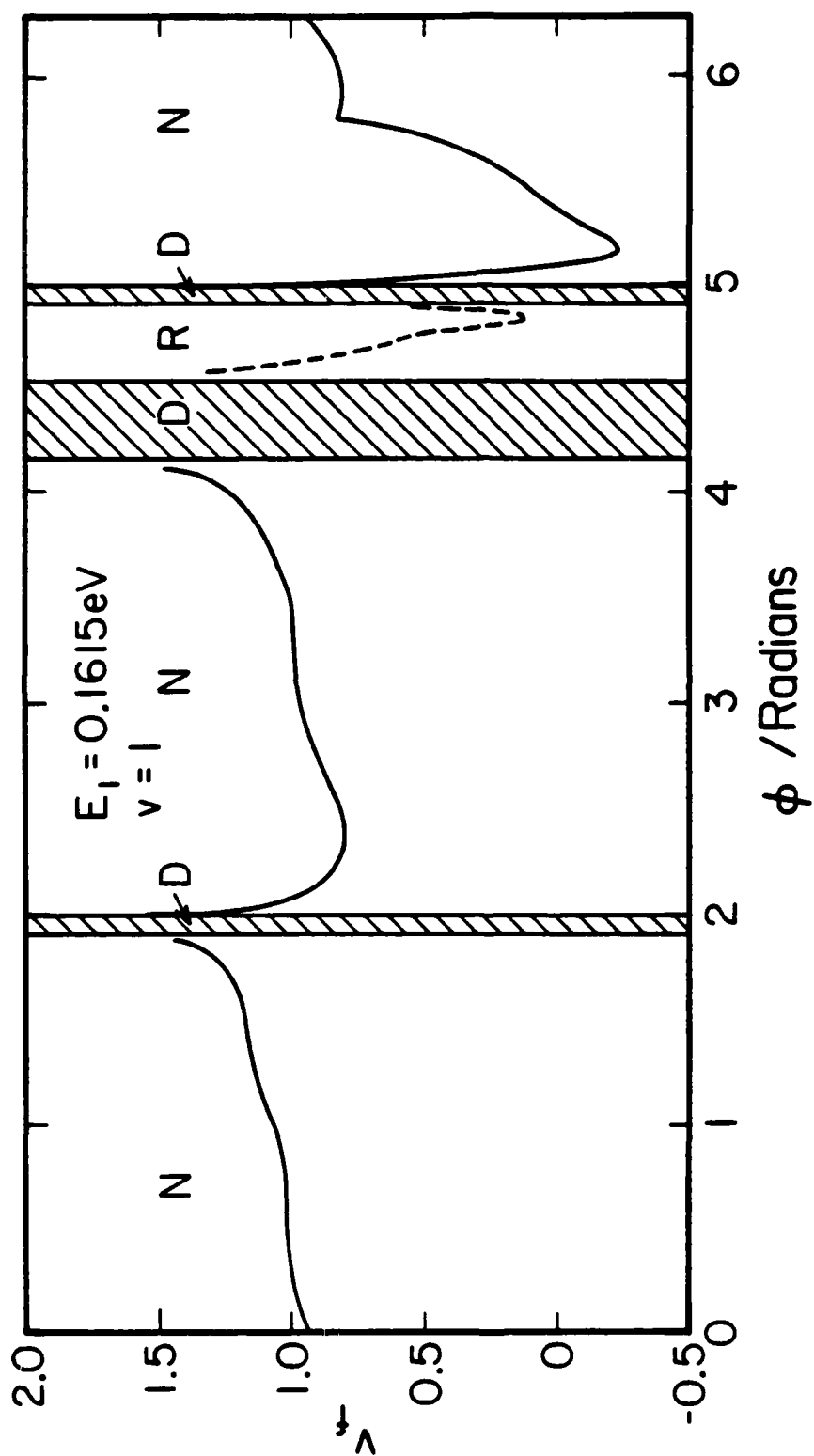


Figure 8

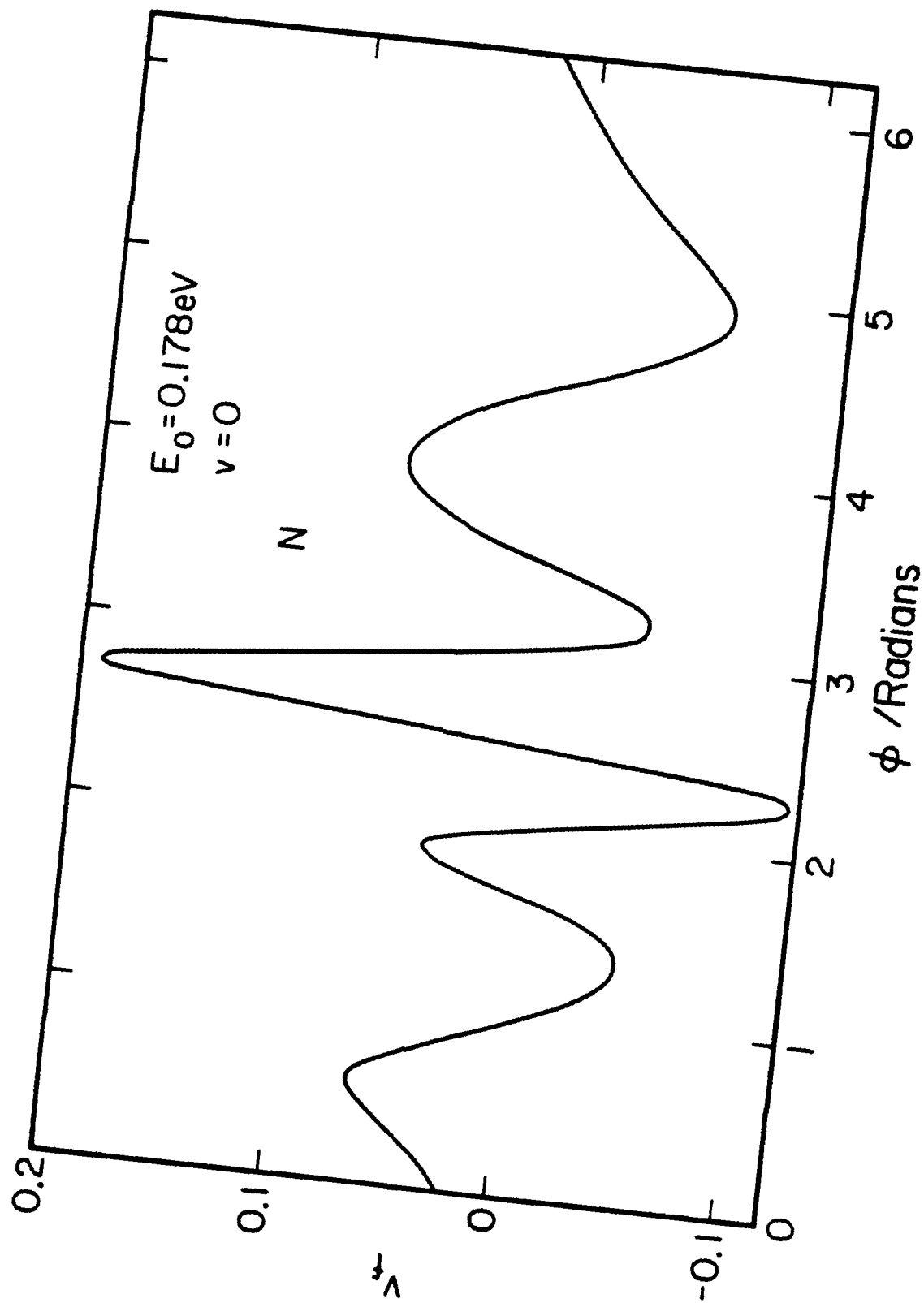


Figure 9

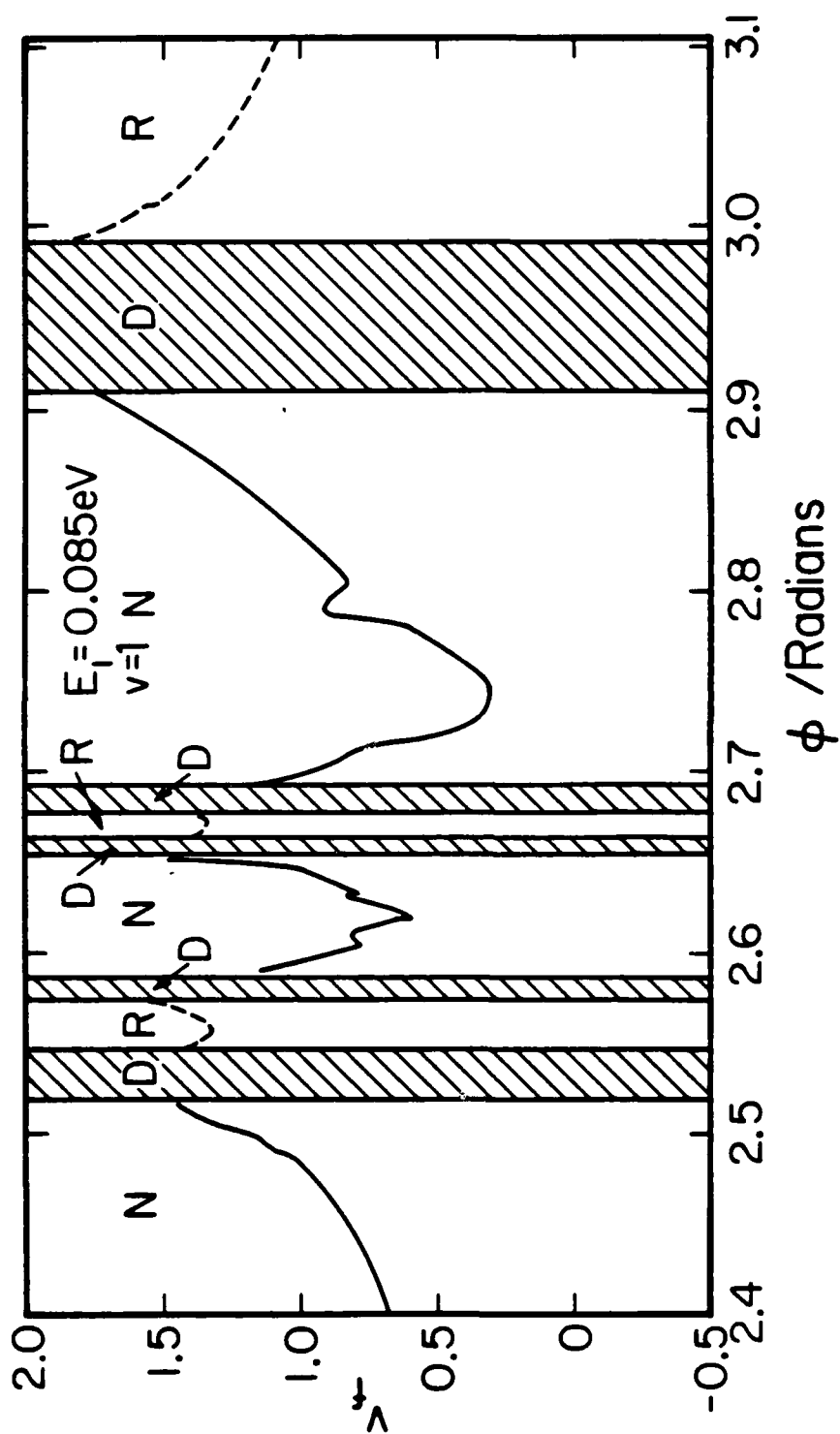


Figure 10

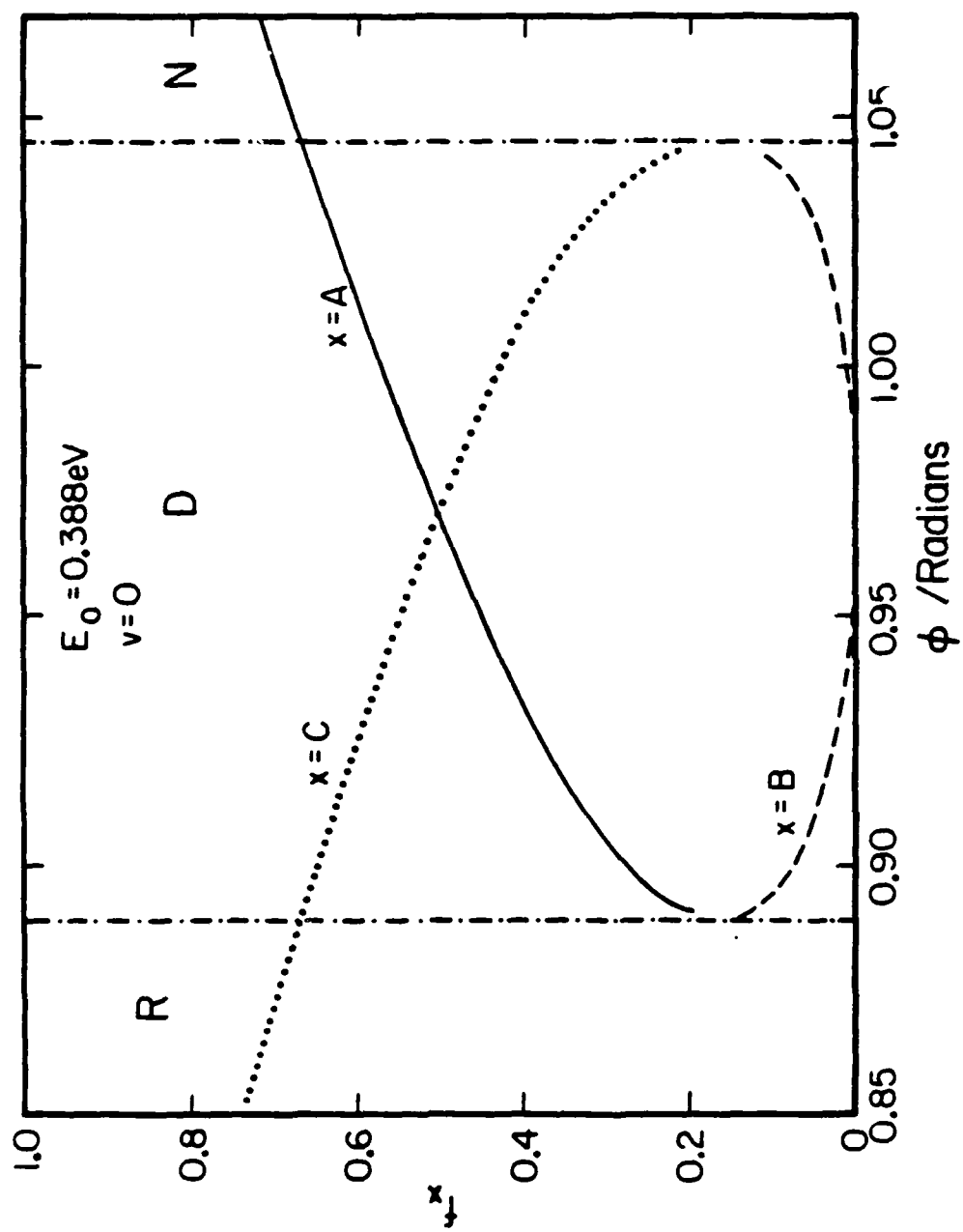


Figure 11a

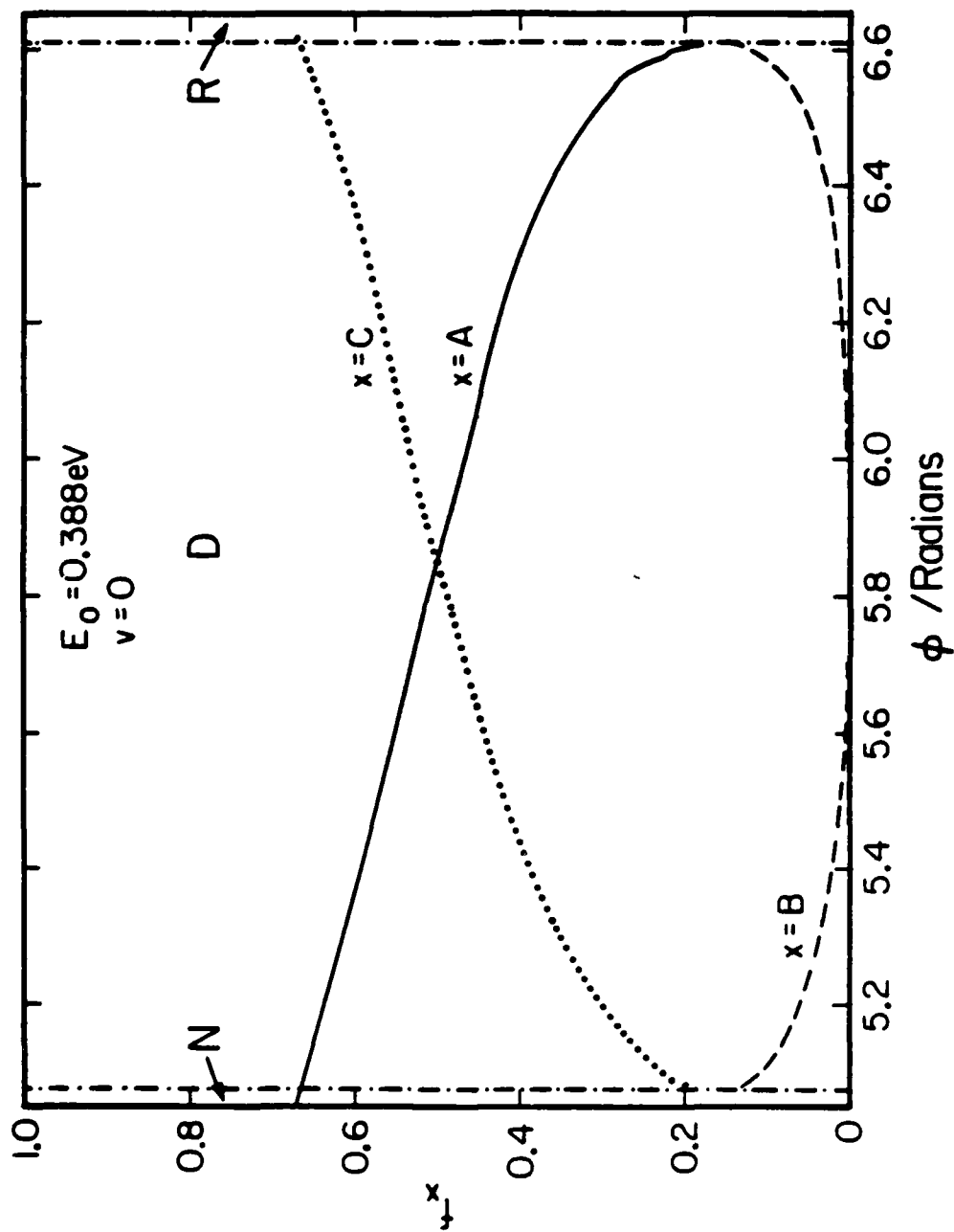


Figure 11b

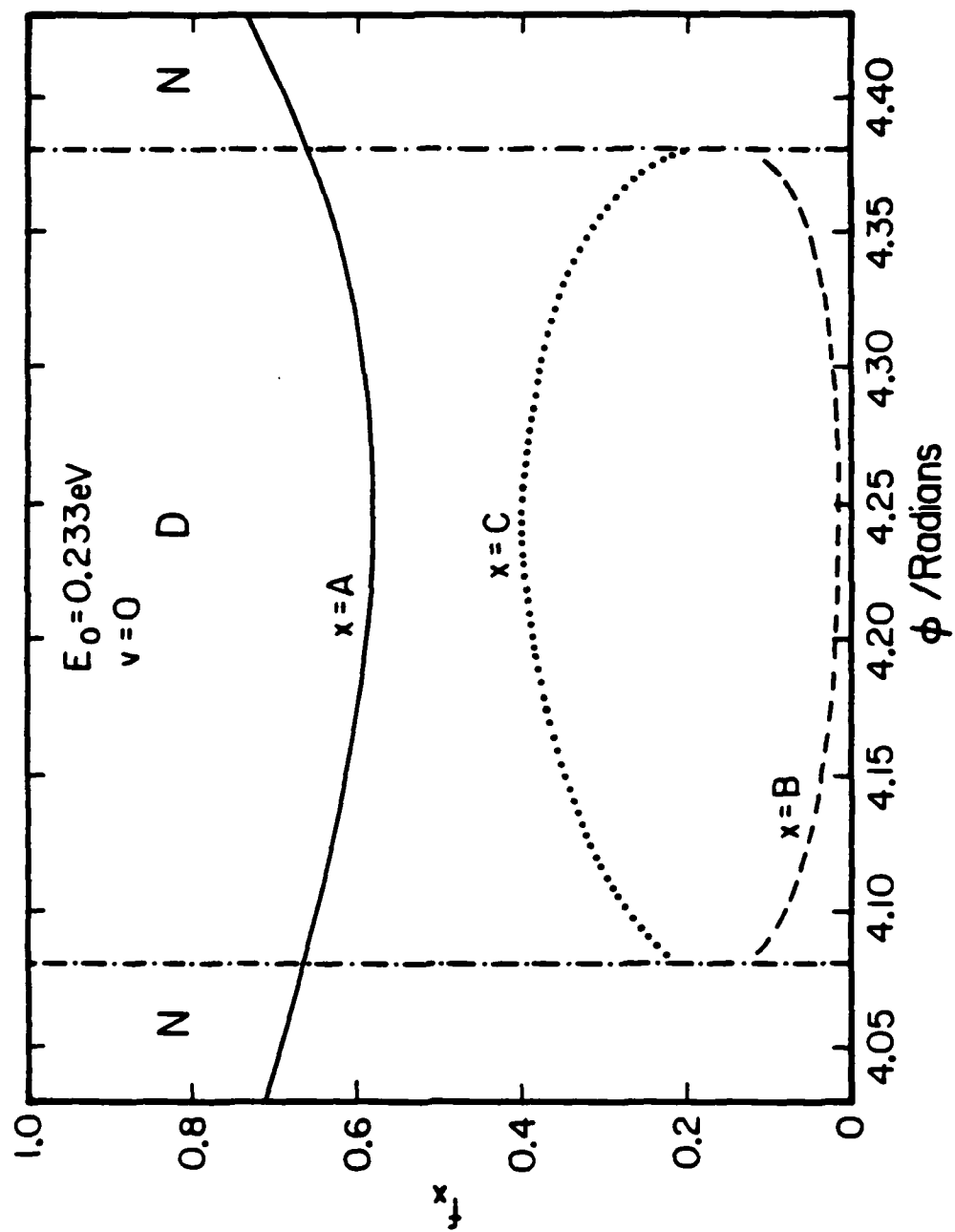


Figure 12

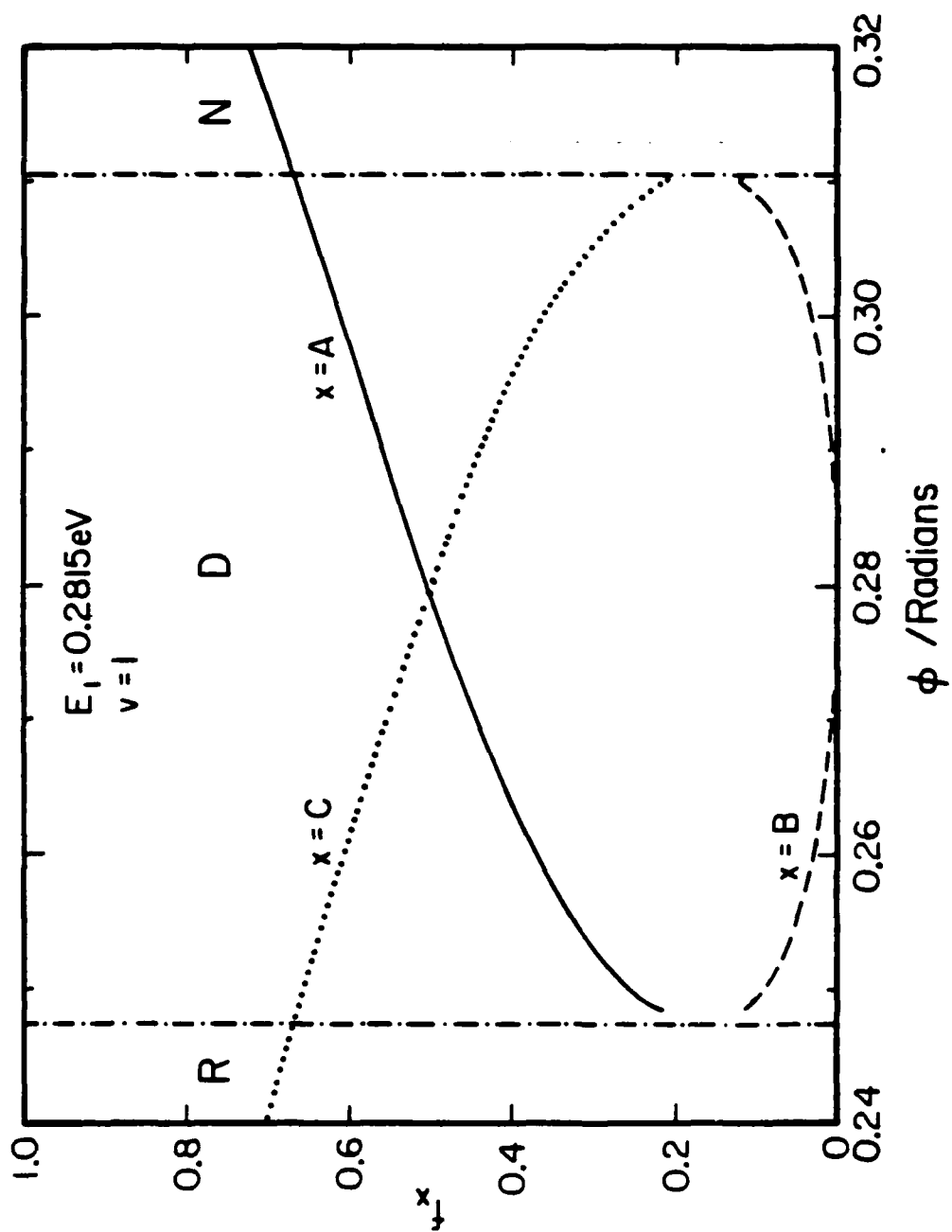


Figure 13a

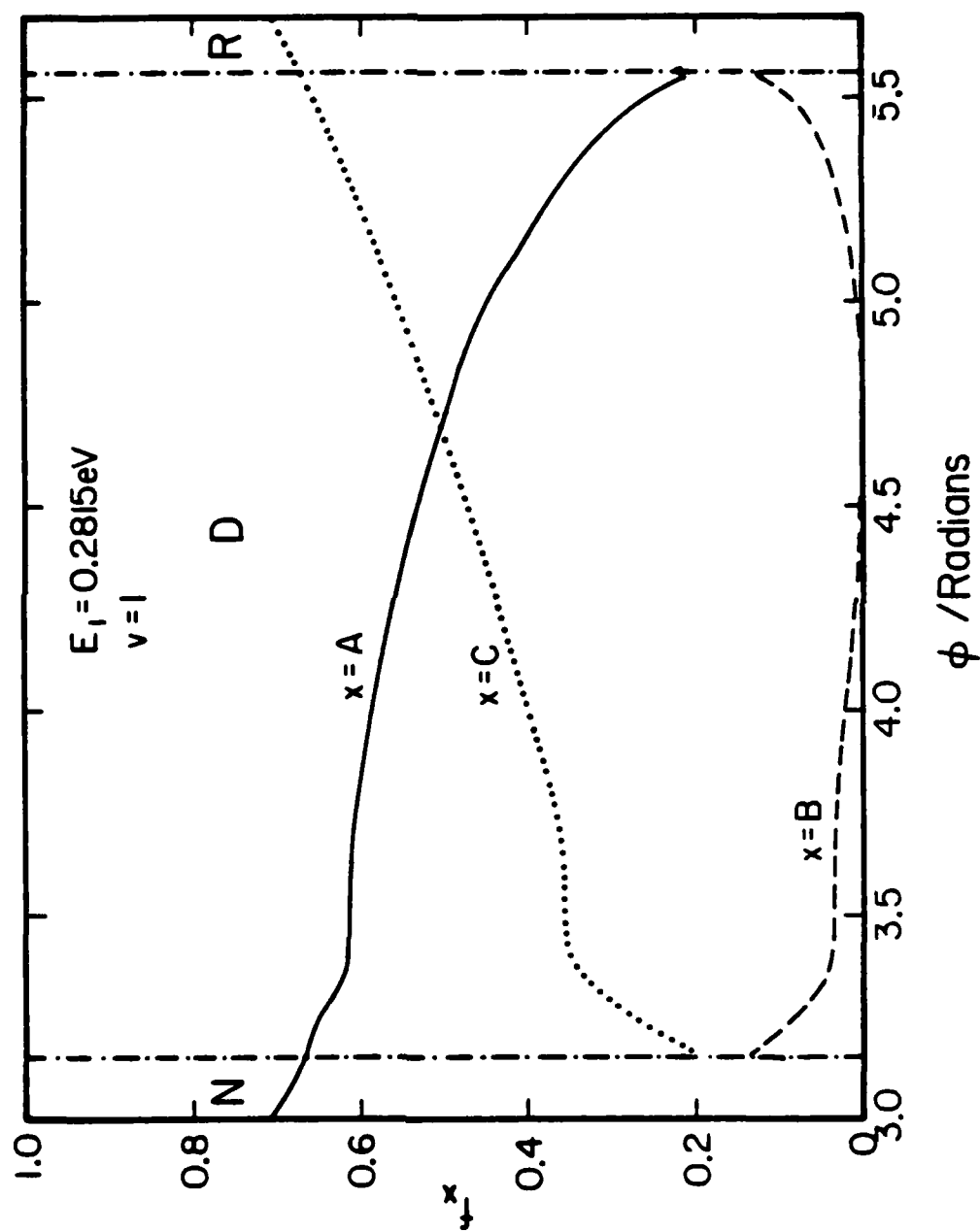


Figure 13b

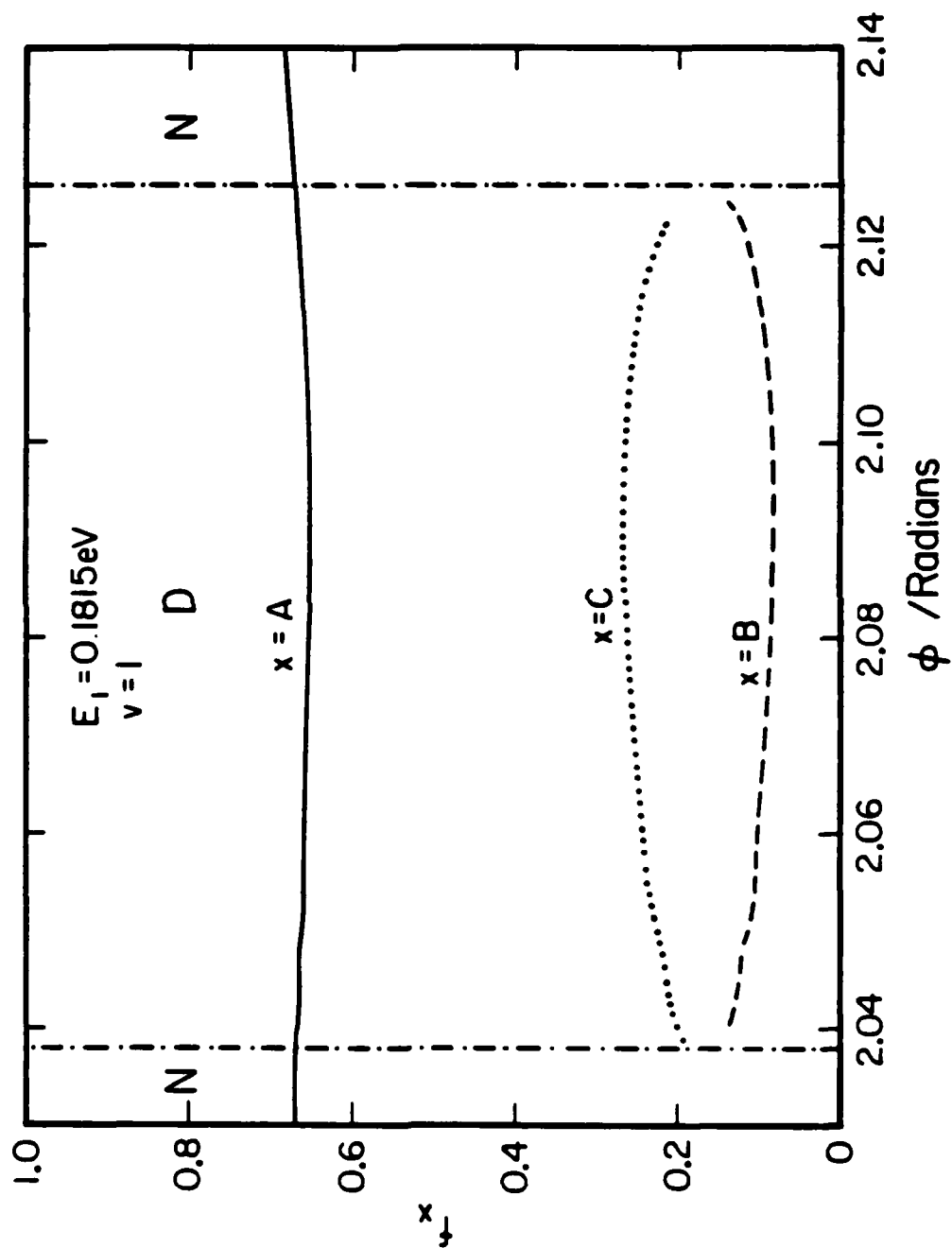


Figure 14a

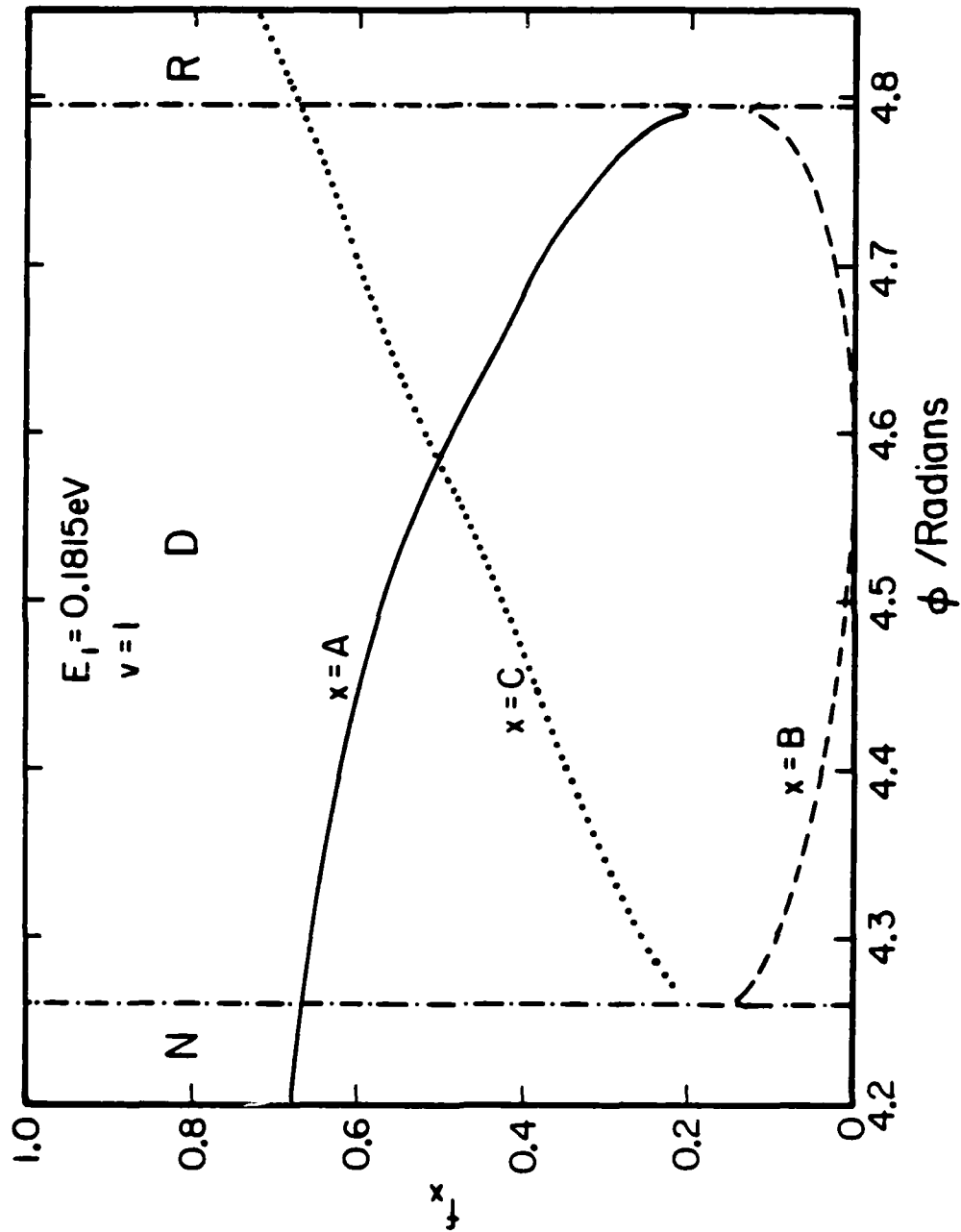


Figure 14b

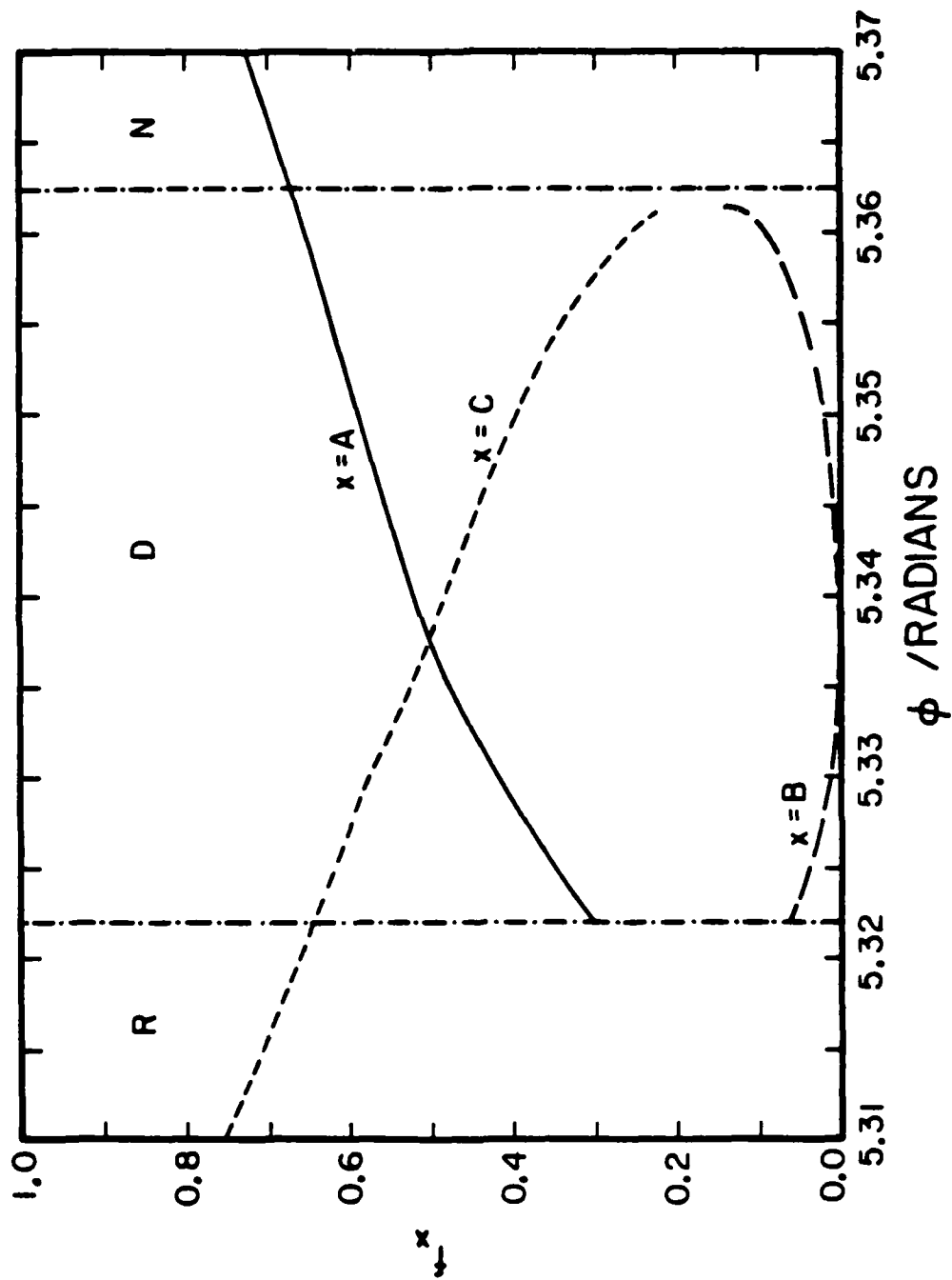


Figure 14c

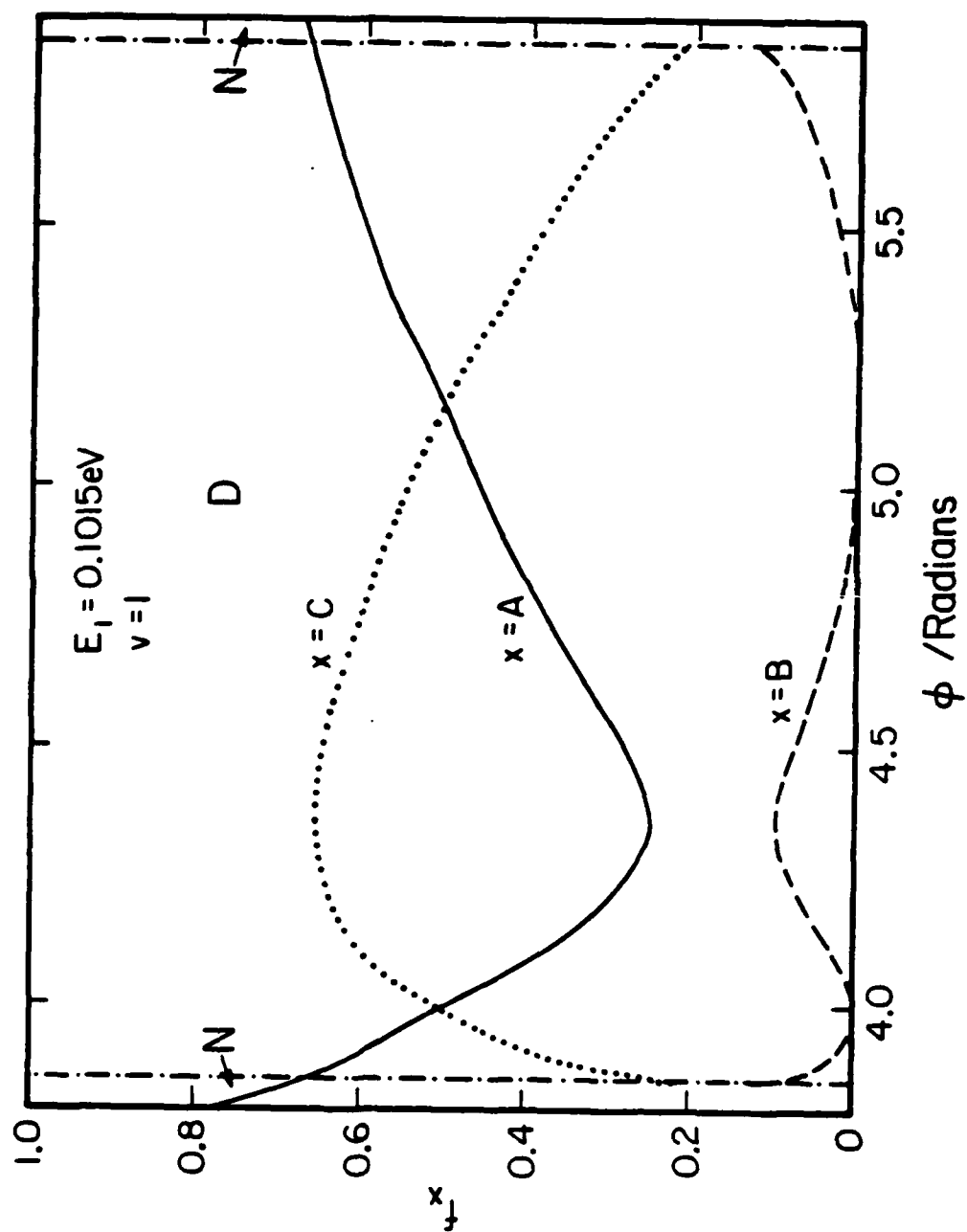


Figure 15

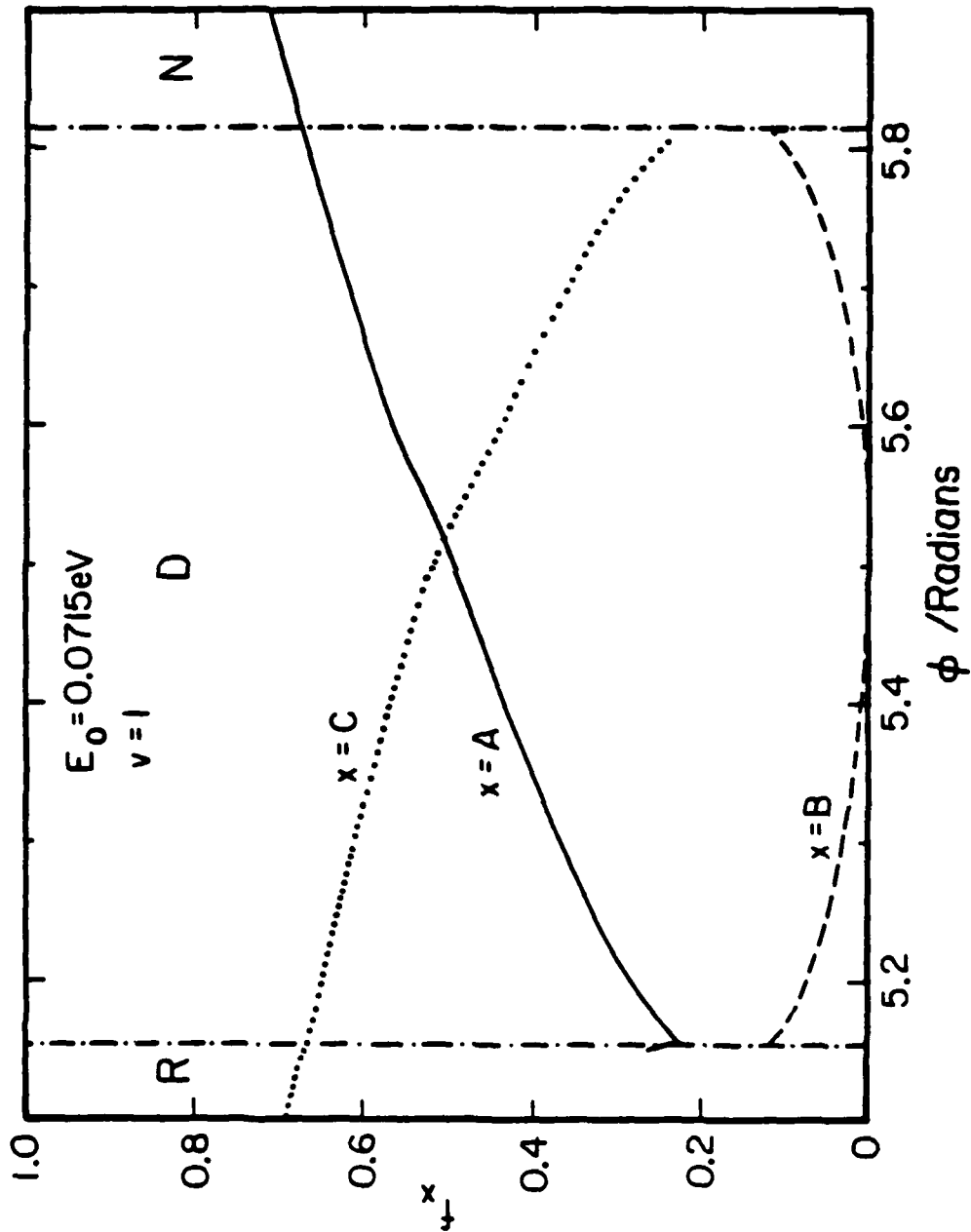


Figure 16

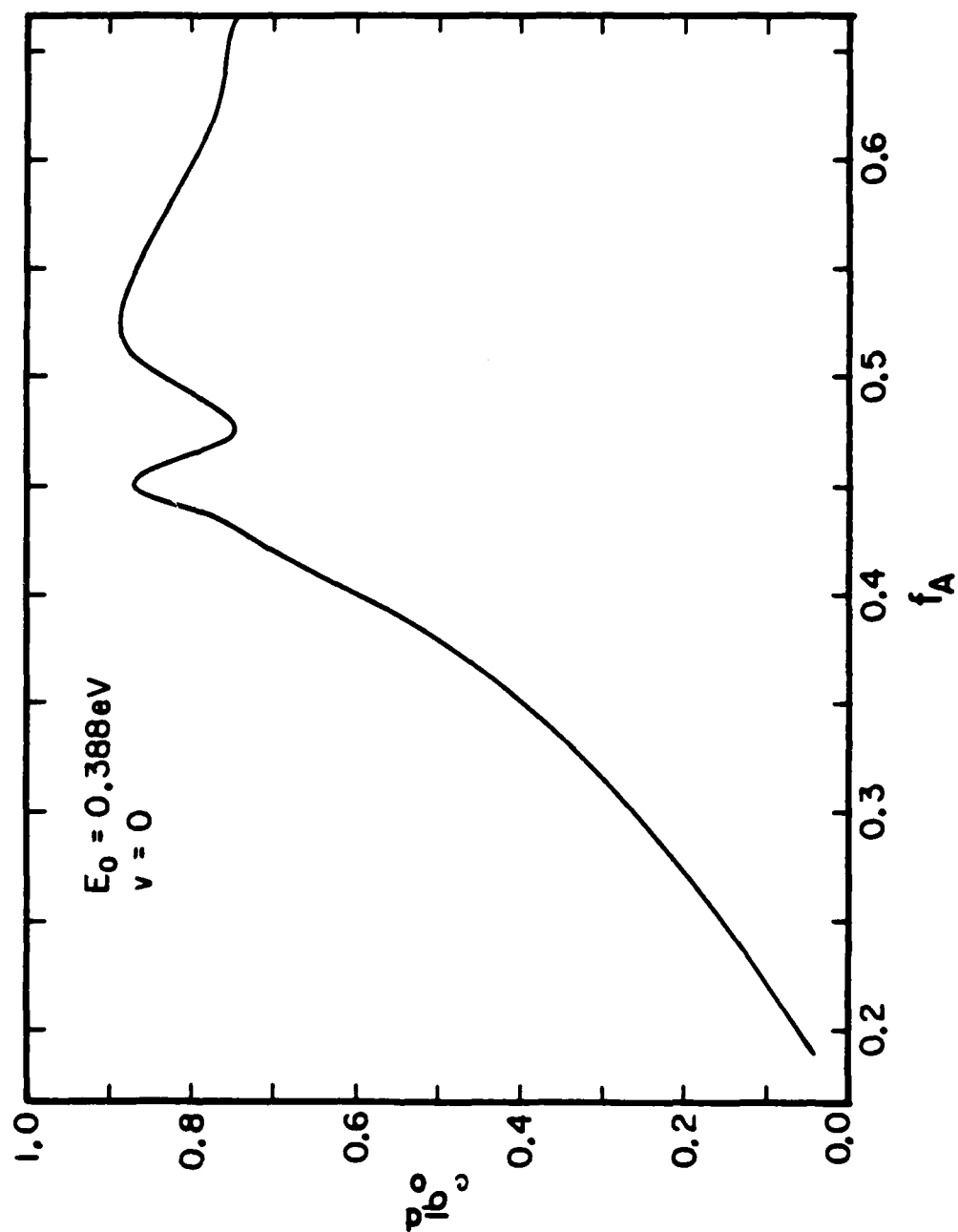


Figure 17

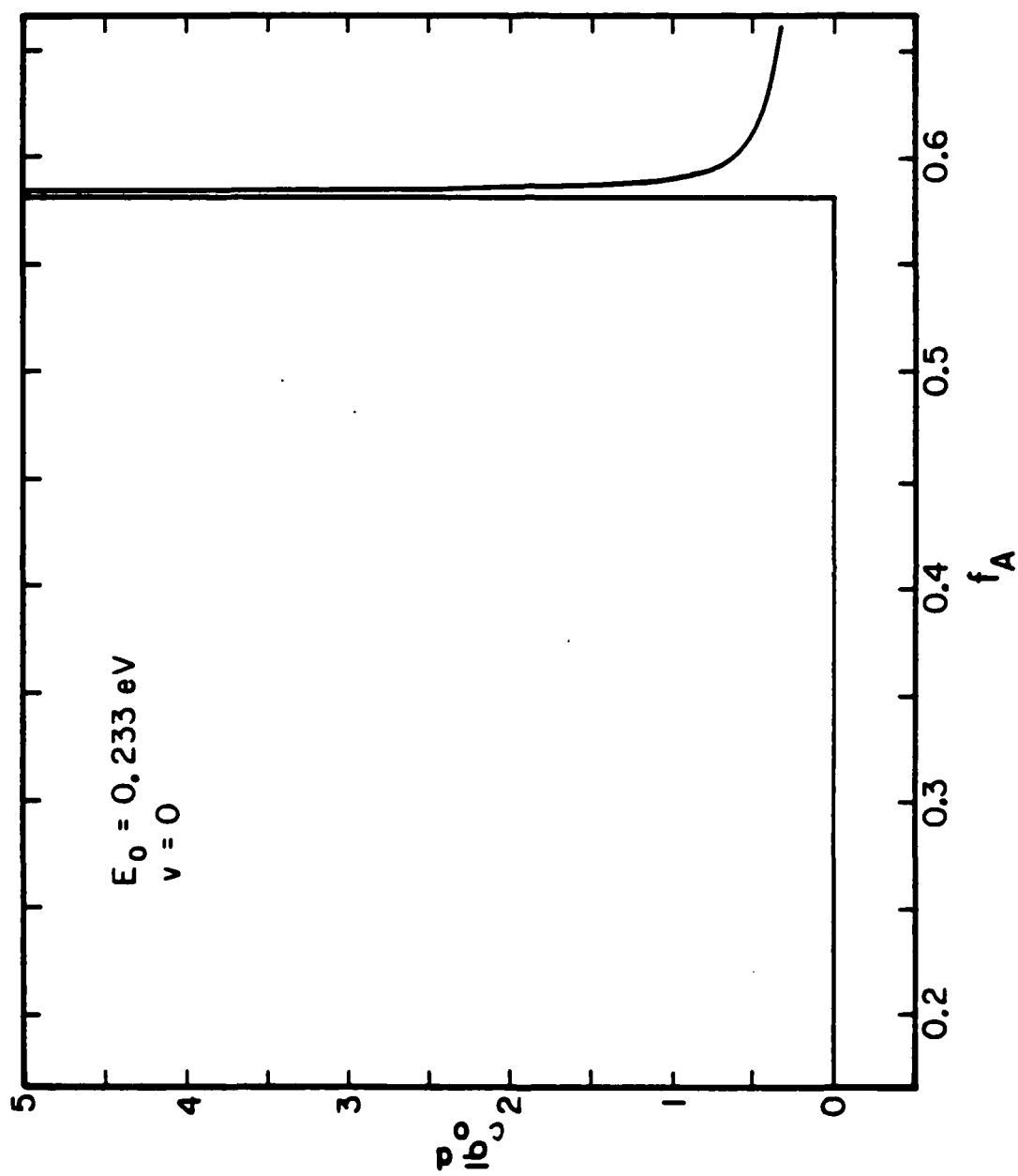


Figure 18

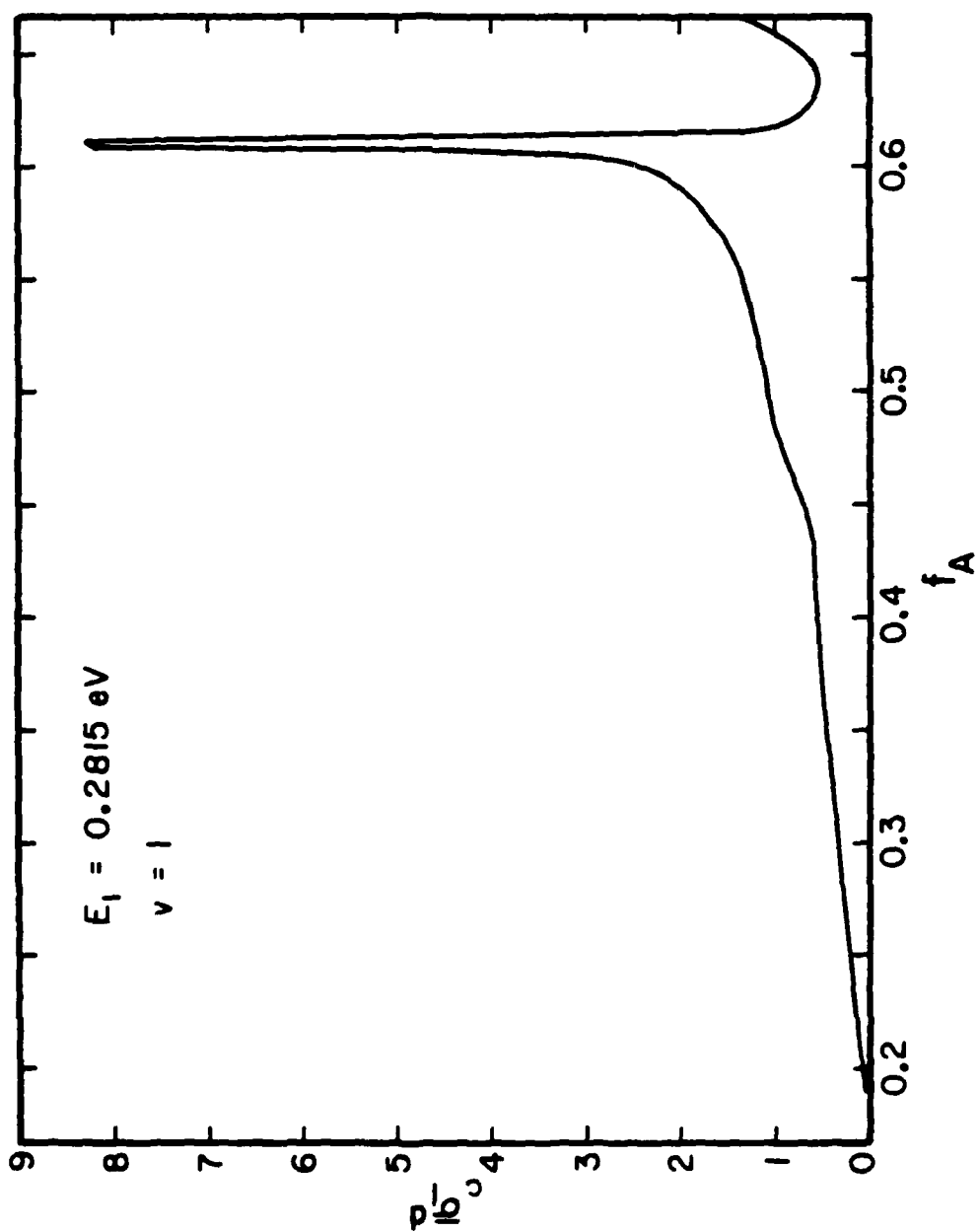


Figure 19

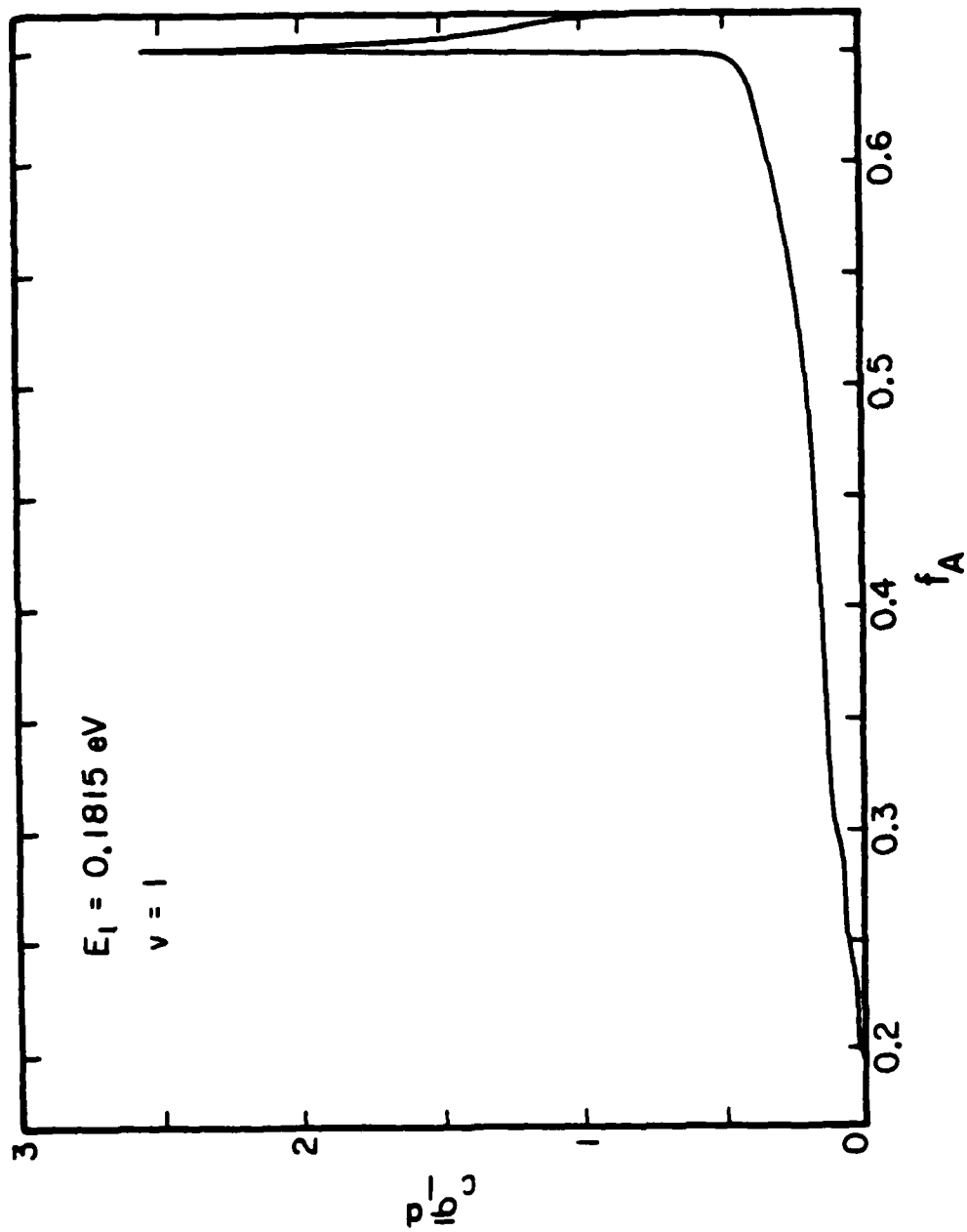


Figure 20

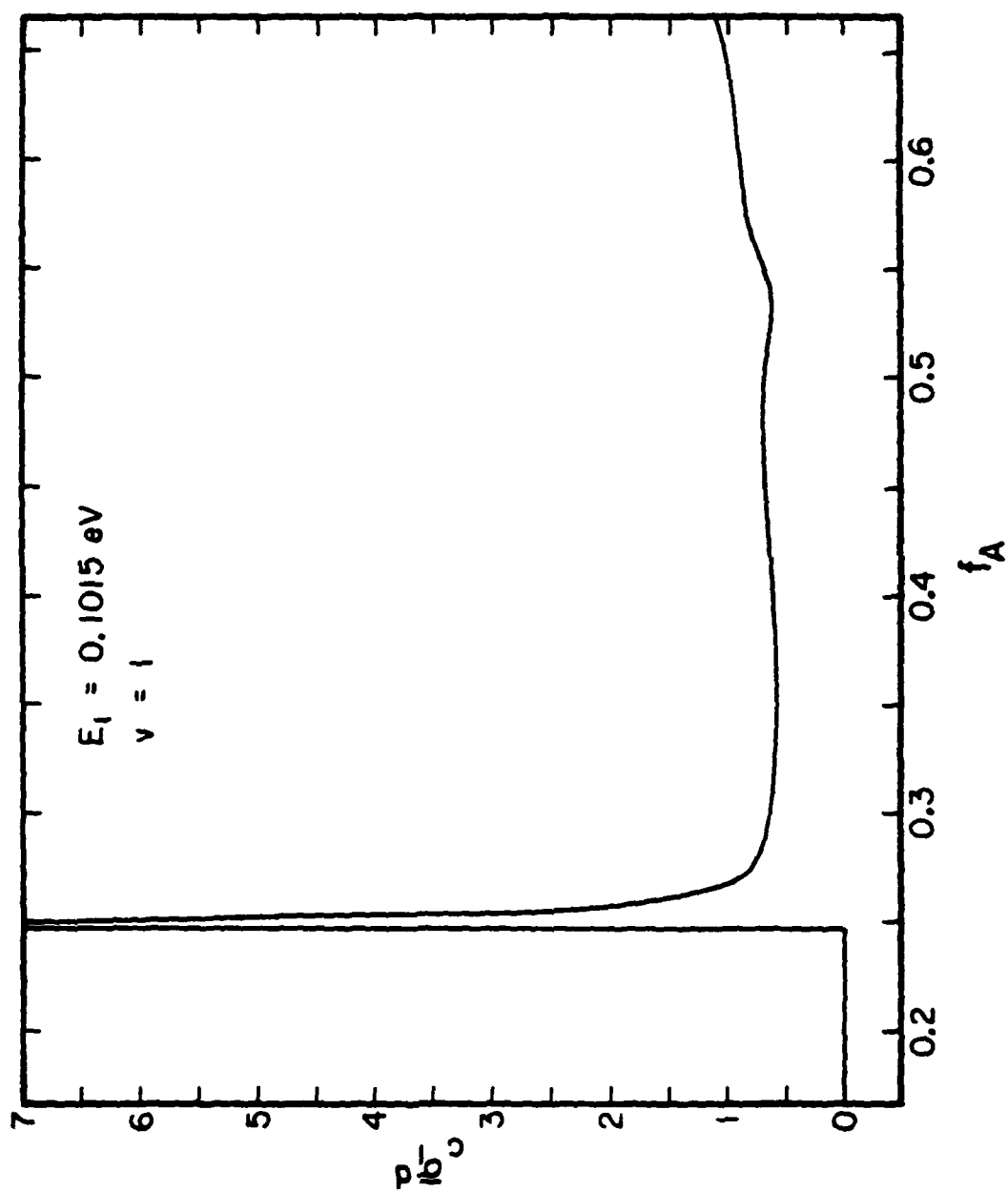


Figure 21

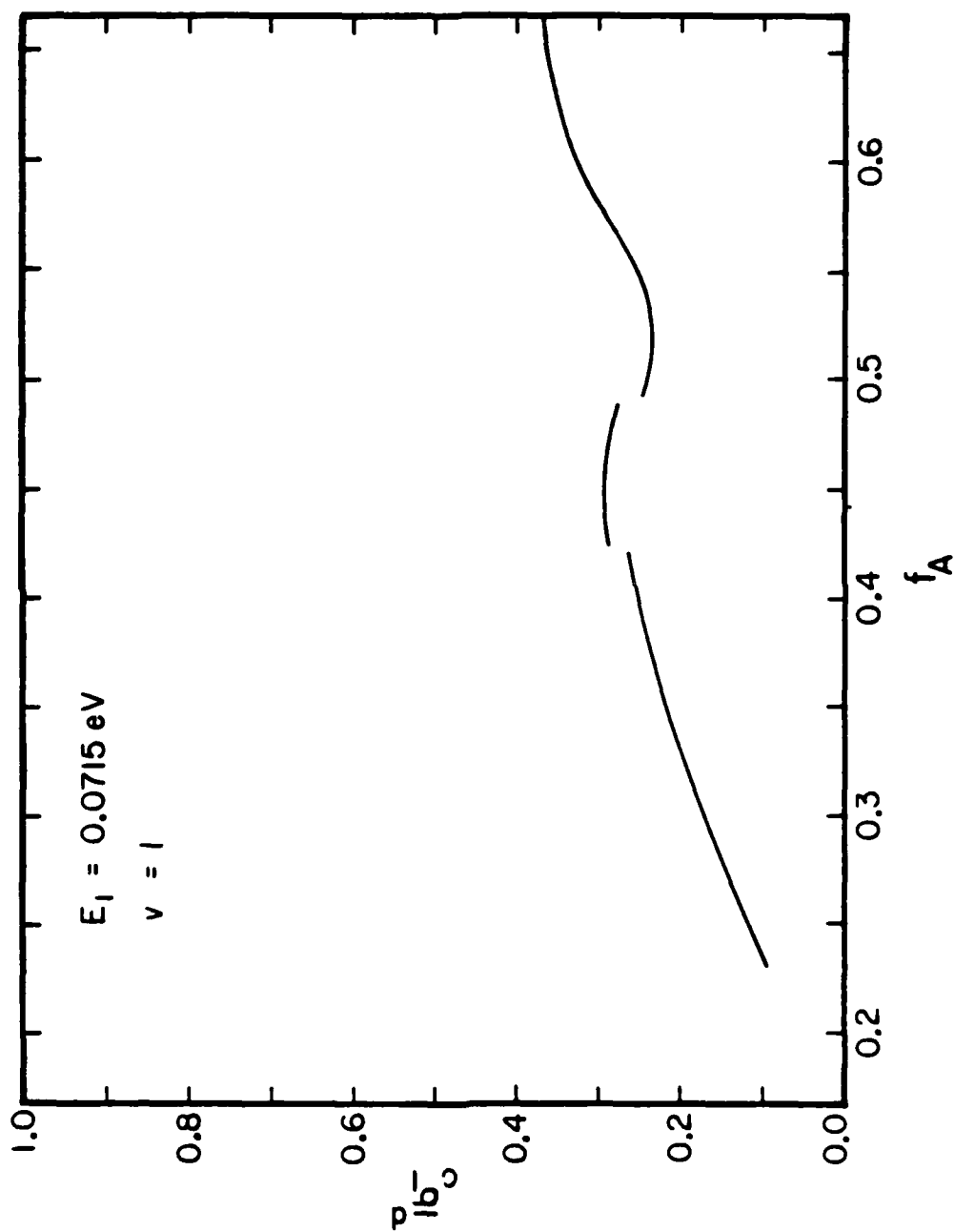


Figure 22

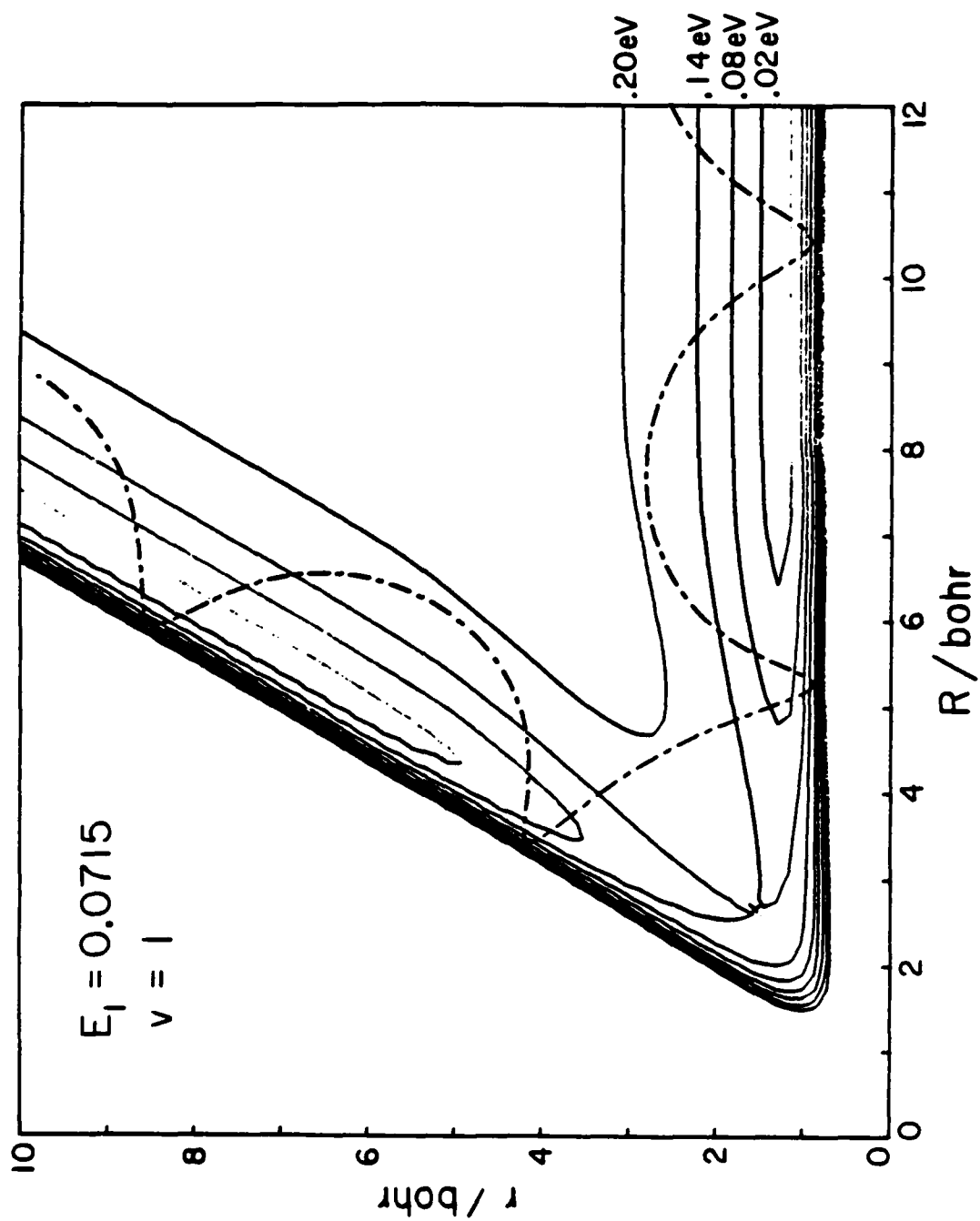


Figure 23

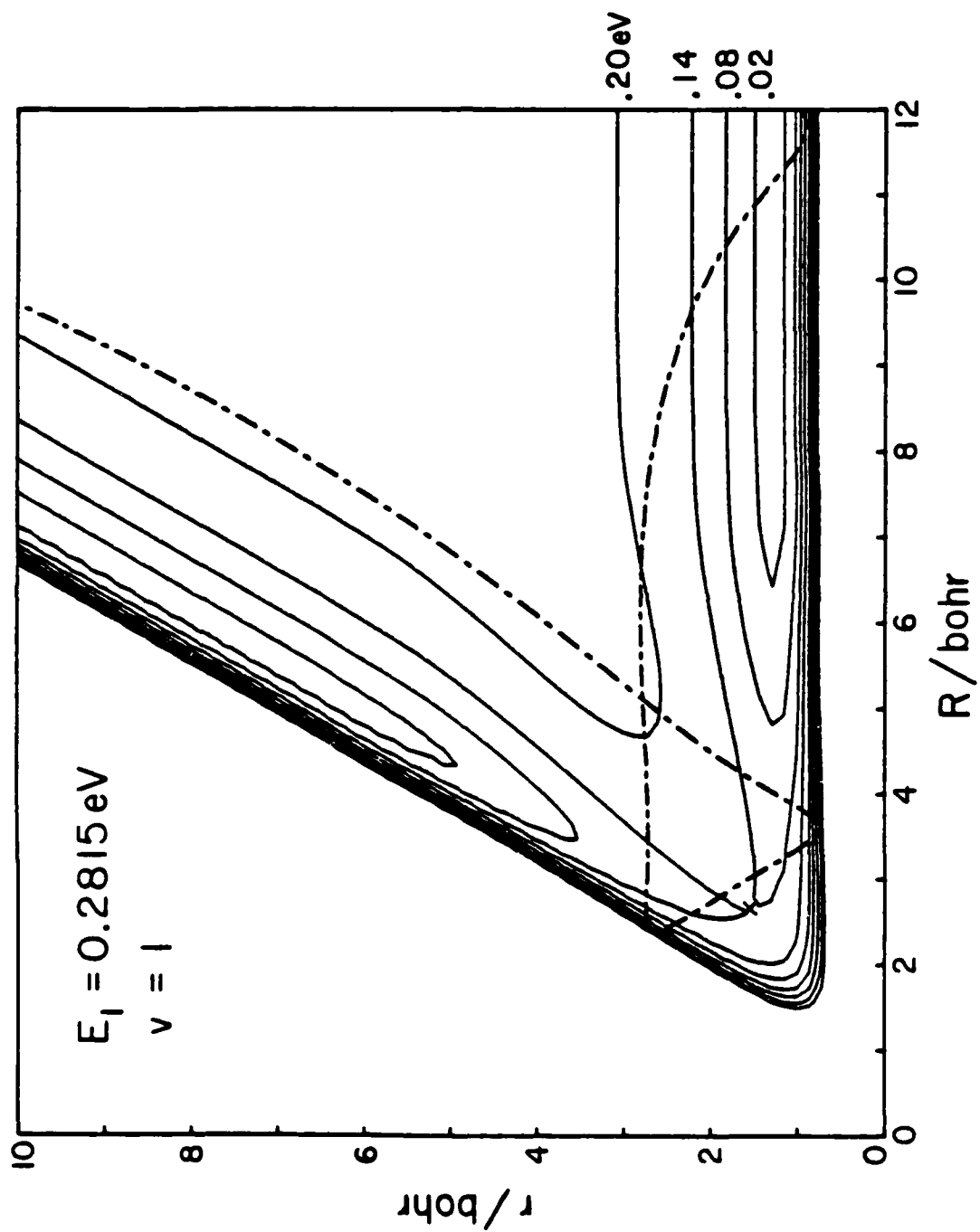


Figure 24

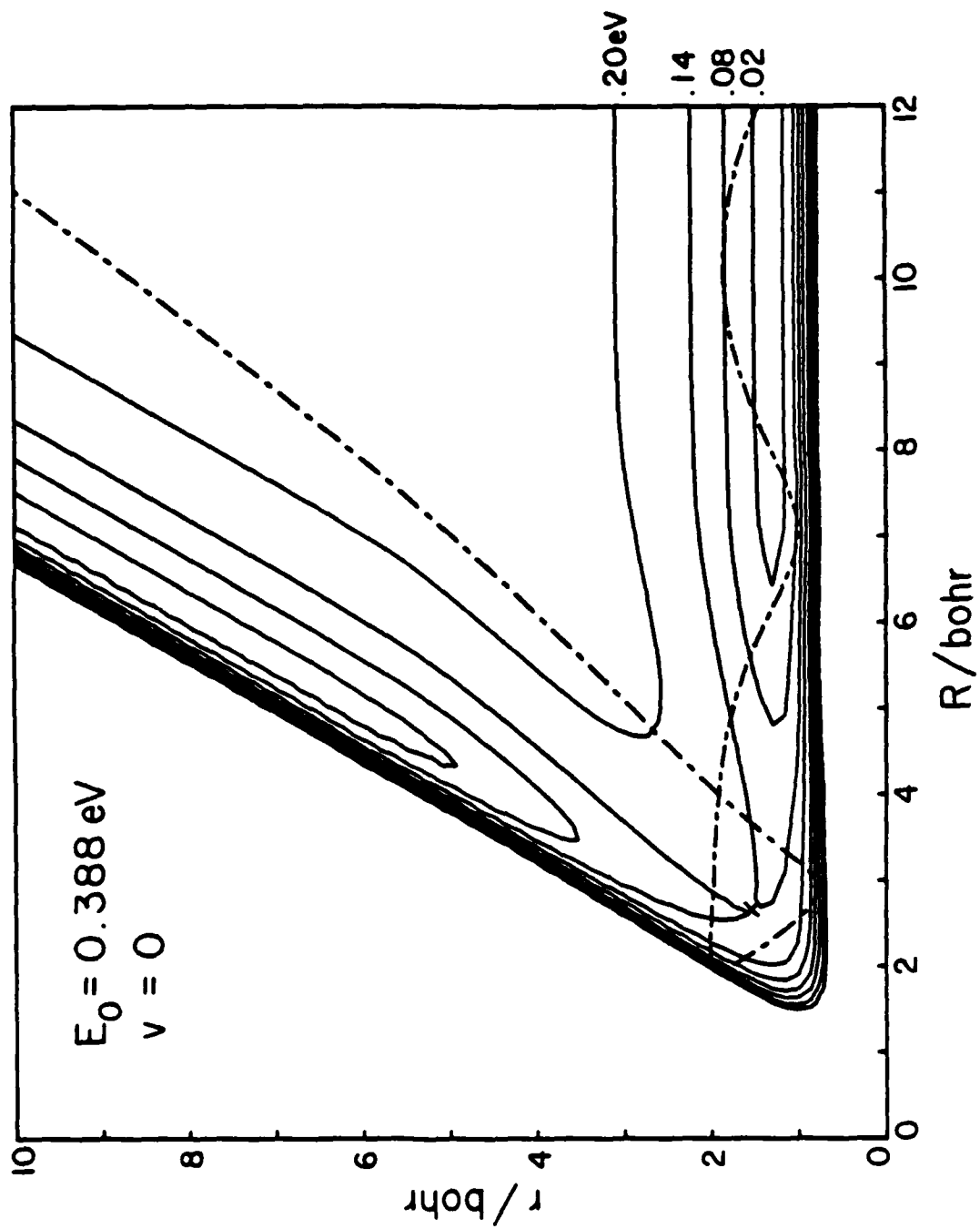


Figure 25

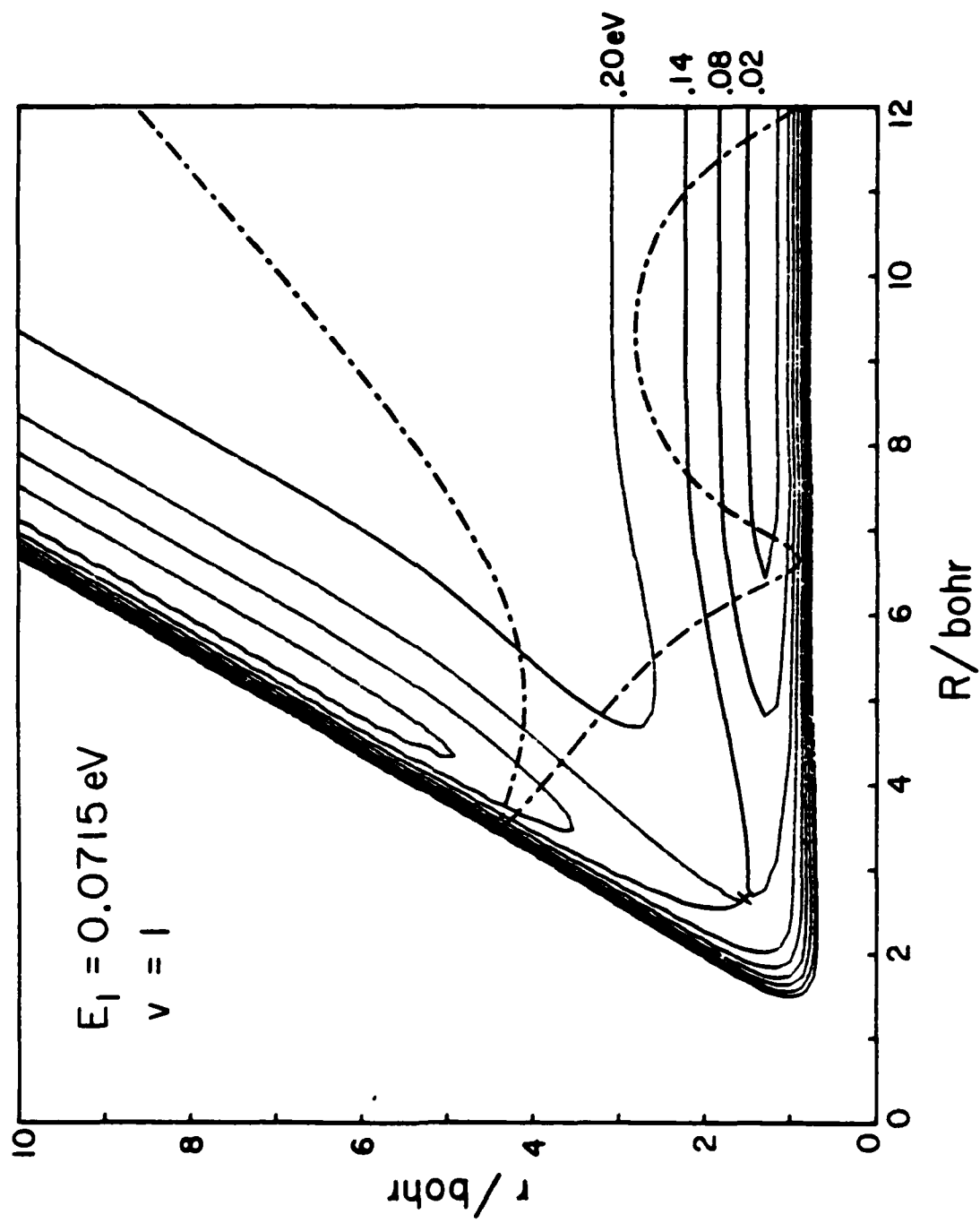


Figure 26

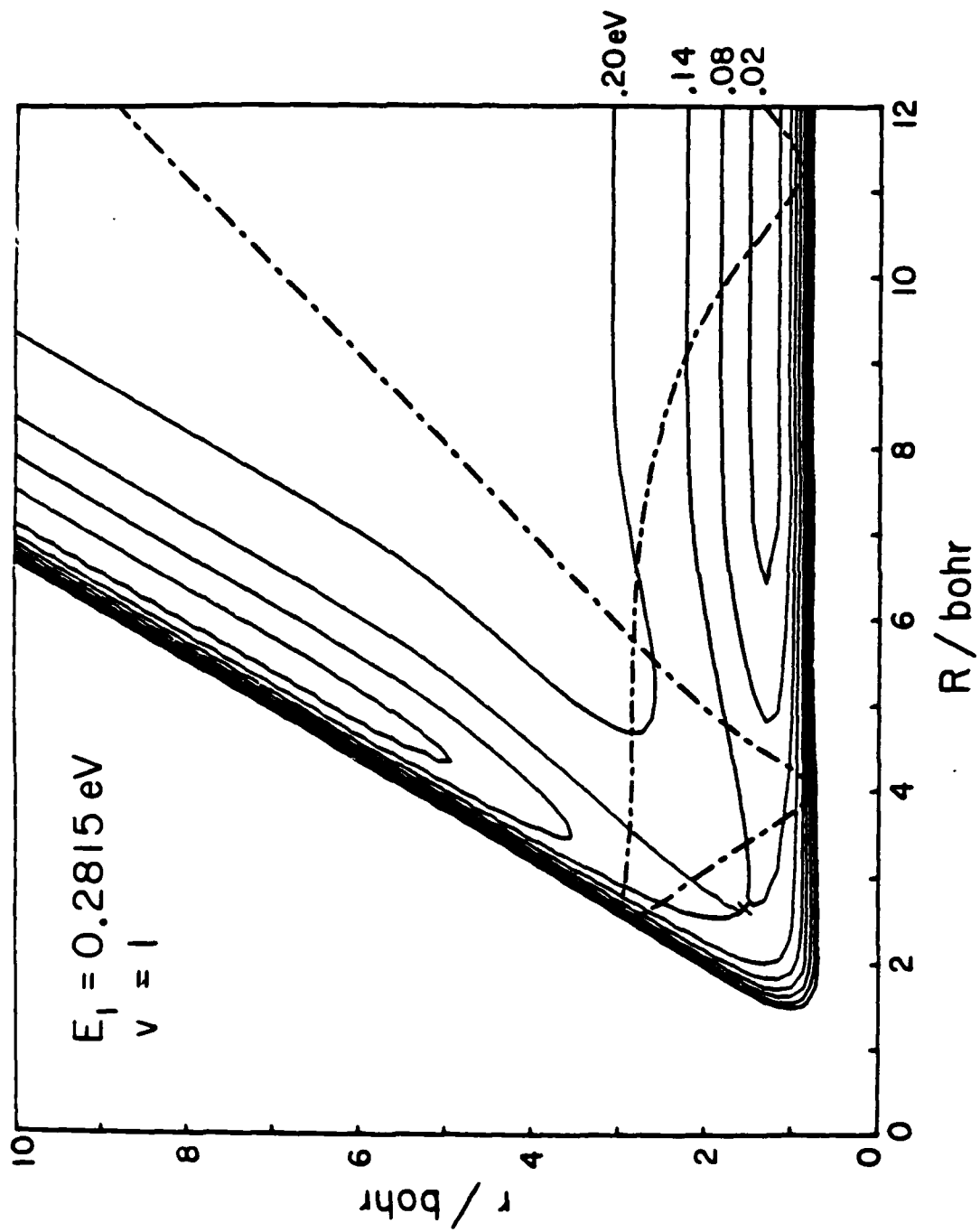


Figure 27

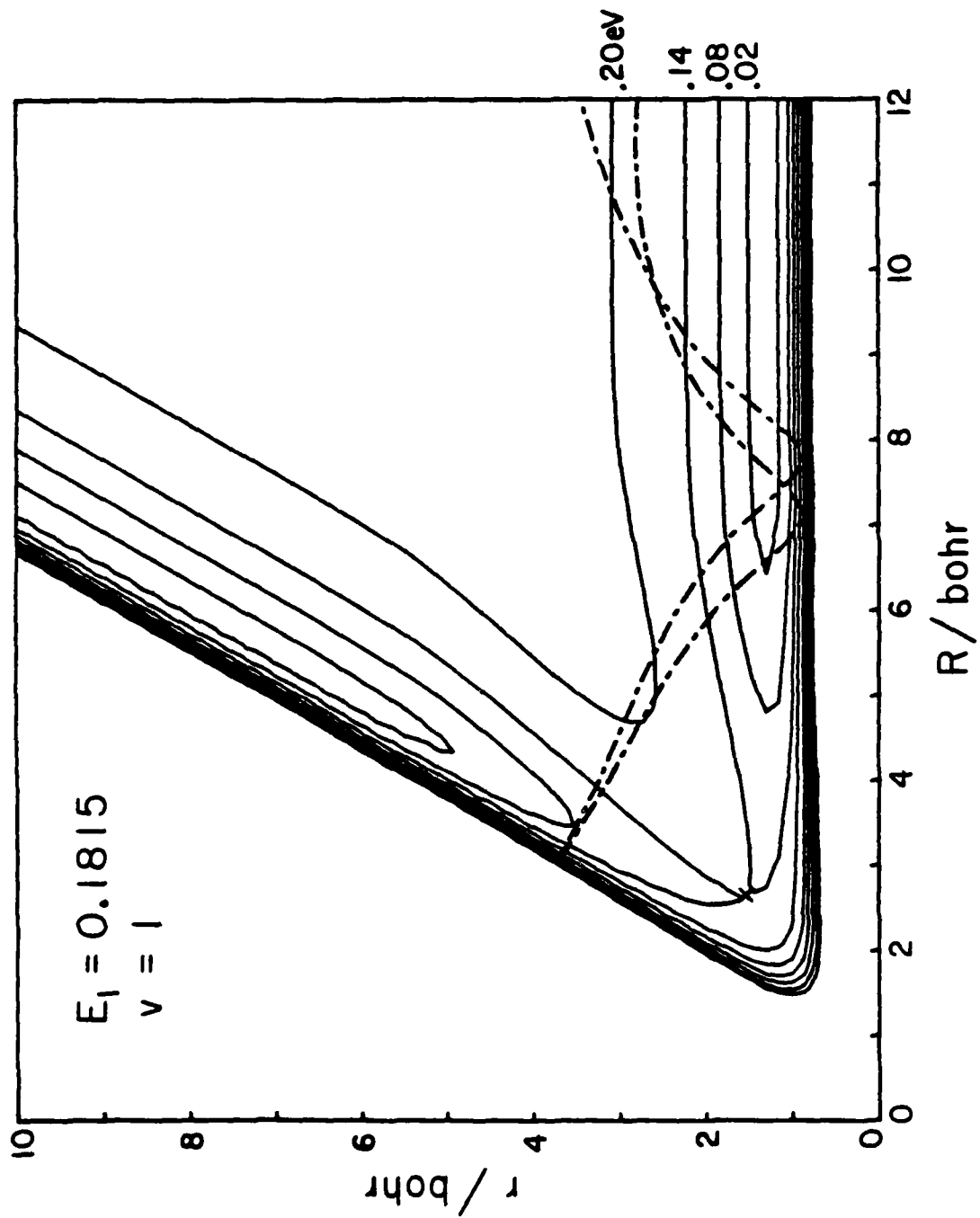


Figure 28

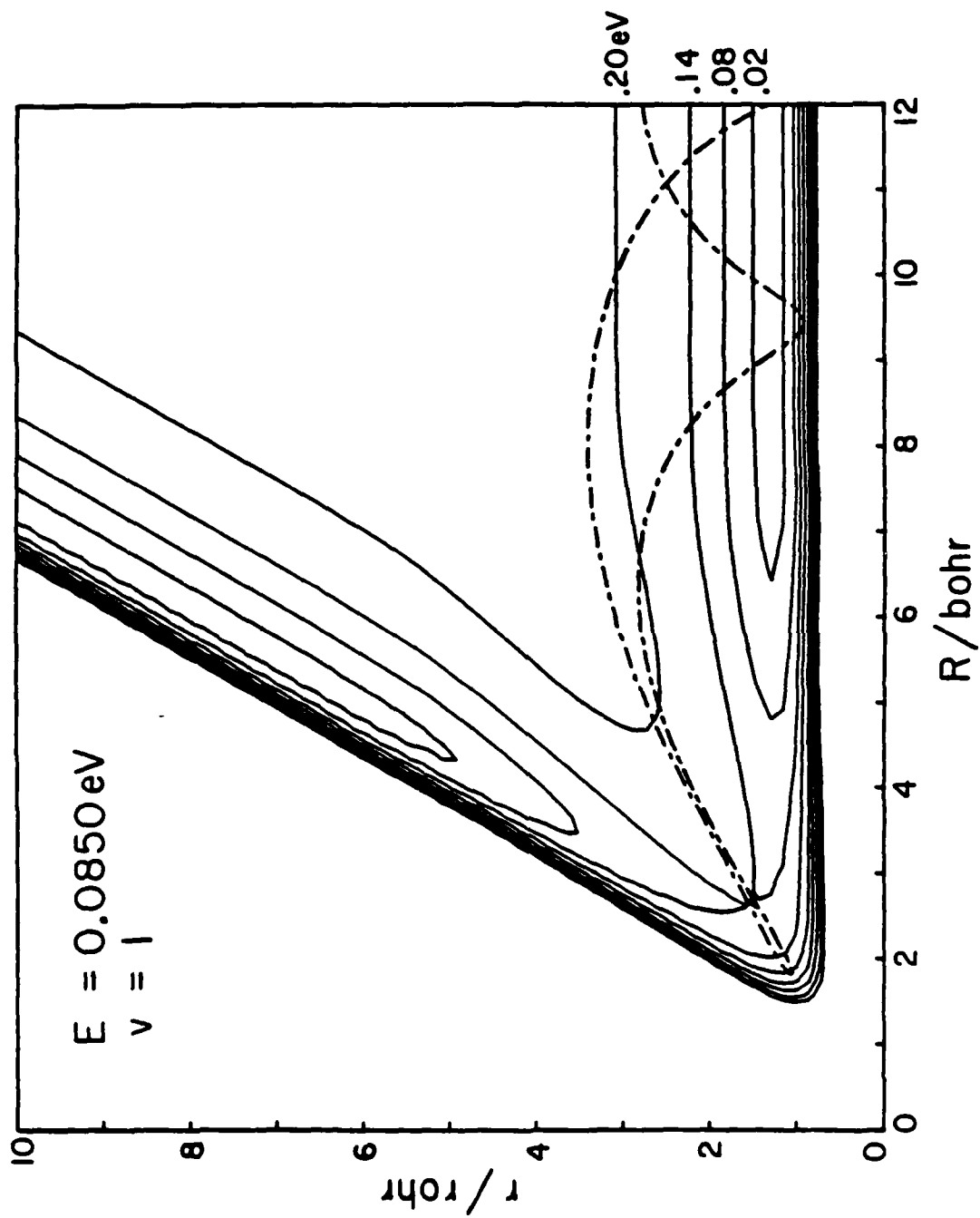


Figure 29

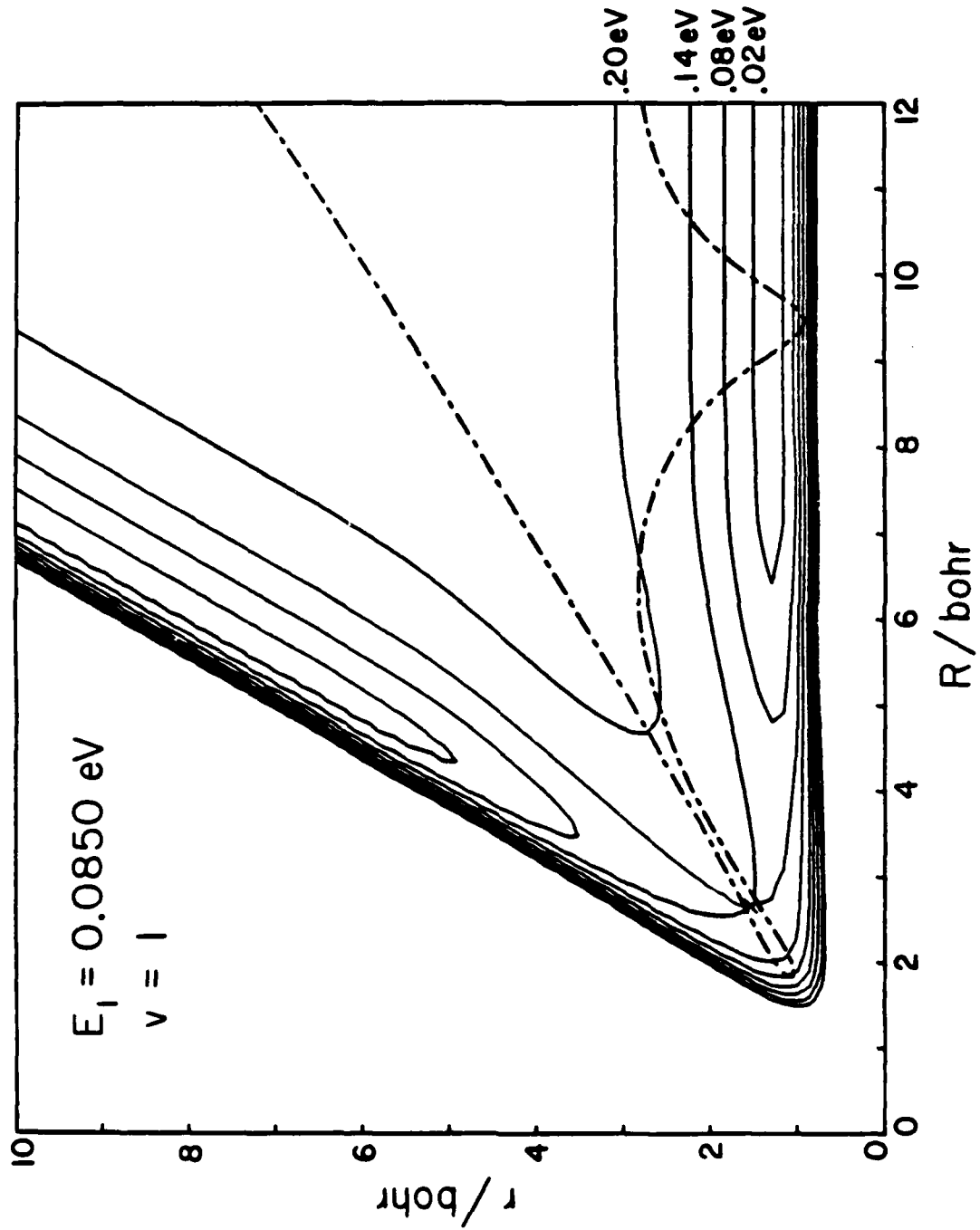


Figure 30

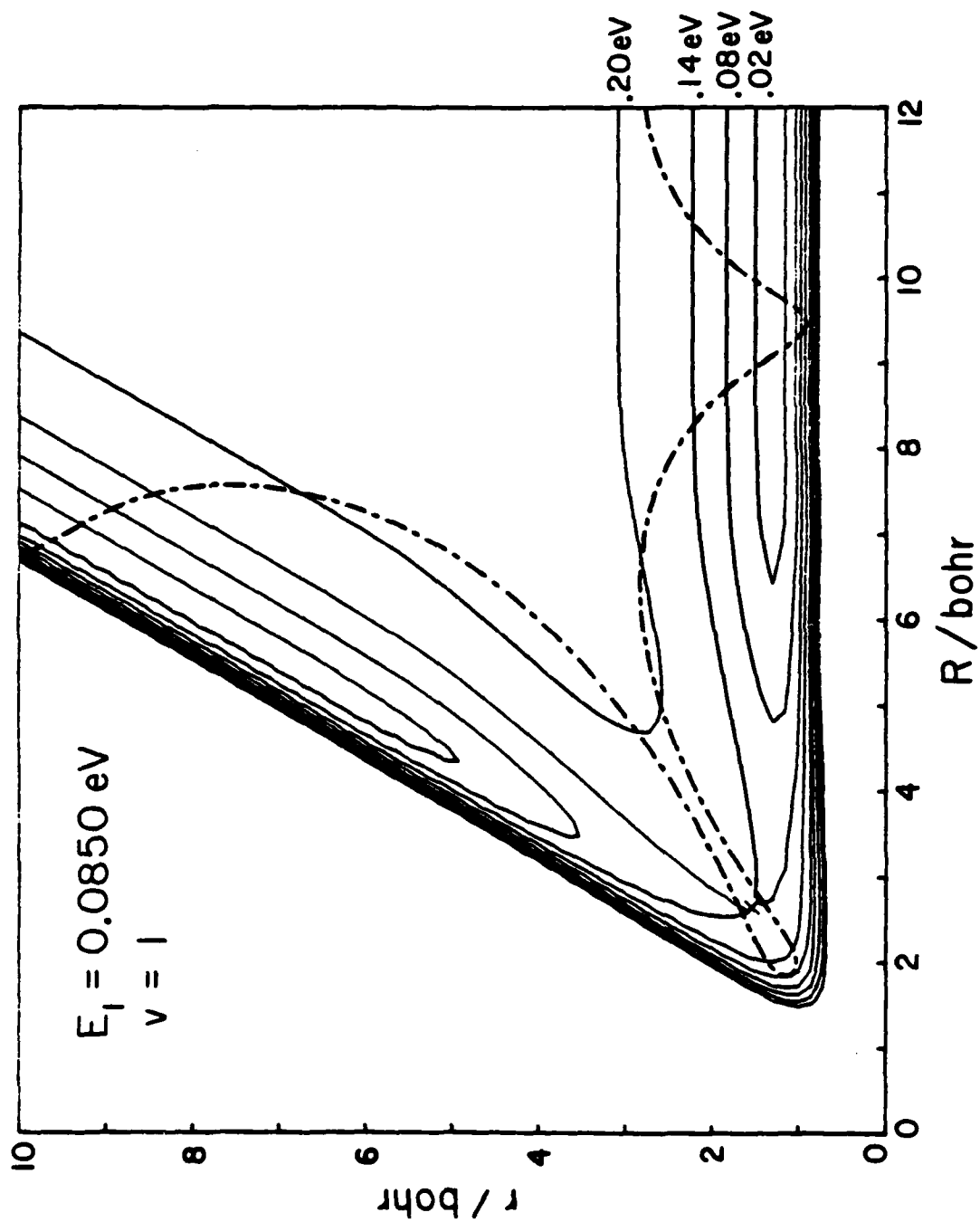
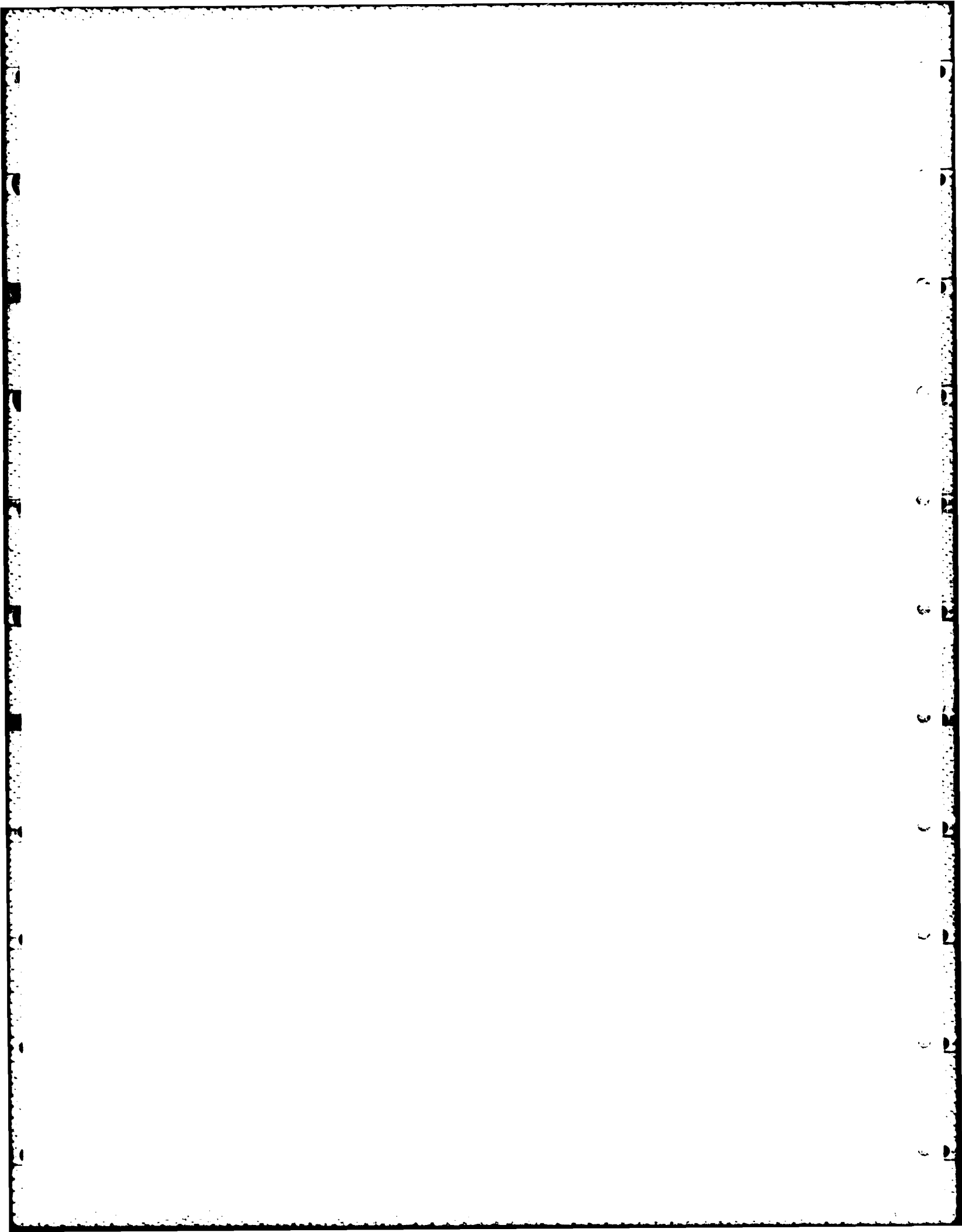


Figure 31



/

PARTITIONING OF KINETIC ENERGY AMONG REACTION PRODUCTS IN
COLLISION INDUCED DISSOCIATION IN COLLINEAR ATOM-DIATOMIC
MOLECULE COLLISIONS FROM QUANTUM AND CLASSICAL MECHANICAL
CALCULATIONS*

Jack A. KAYE** and Aron KUPPERMANN

Arthur Amos Noyes Laboratory of Chemical Physics,[†]

California Institute of Technology,

Pasadena, California 91125, USA

(Received)

Results for the kinetic energy distributions of atomic products of the collision-induced dissociation $A + BC \rightarrow A + B + C$ on a model triatomic reactive collinear system have been obtained by both quantum mechanical coupled channel and quasi-classical trajectory calculations. The results from the two methods are significantly different, indicating a strong quantum effect in this process.

*This work was supported in part by a contract (No. F49620-79-C-0187) from the Air Force Office of Scientific Research.

**Work performed in partial fulfillment of the requirements for the Ph. D. degree in Chemistry at the California Institute of Technology.

[†]Contribution No.

each trajectory resulting in dissociation, and then appropriately averages over all trajectories leading to dissociation. Their determination from quantum mechanical calculations is more complicated; they may be obtained from scattering calculations performed by the hyperspherical coordinates method.^{4,5}

In this work we present results for the partitioning probabilities, that is, the probabilities of partitioning of the available energy among the three atoms in dissociative collisions by both quantum mechanical (QM) and quasi-classical trajectory (QCT) methods in a model collinear atom-diatomic molecule collision. We first review the methods by which these quantities are obtained. We then compare the QM and QCT results and discuss the origins of the difference between the results from the two methods.

2. Theory and Numerical Methods

A. Quantum Mechanical Method

The calculation of bound-continuum total (dissociation) probabilities by the hyperspherical coordinate method has been outlined by us^{4c} and by Manz and Römelt⁵ previously. The basic formalism for the calculations of the partitioning probabilities has also been outlined previously,^{4c,b} We present it here in more detail, emphasizing details appropriate to its numerical implementation.

First we recognize that in dissociative collisions, there is only one degree of freedom in the partitioning of the available energy among the three atoms. This is best expressed as

PARTITIONING OF KINETIC ENERGY AMONG REACTION PRODUCTS IN
COLLISION INDUCED DISSOCIATION IN COLLINEAR ATOM-DIATOMIC
MOLECULE COLLISIONS FROM QUANTUM AND CLASSICAL MECHANICAL
CALCULATIONS*

Jack A. KAYE** and Aron KUPPERMANN

Arthur Amos Noyes Laboratory of Chemical Physics,[†]

California Institute of Technology,

Pasadena, California 91125, USA

(Received

)

Results for the kinetic energy distributions of atomic products of the collision-induced dissociation $A + BC \rightarrow A + B + C$ on a model triatomic reactive collinear system have been obtained by both quantum mechanical coupled channel and quasi-classical trajectory calculations. The results from the two methods are significantly different, indicating a strong quantum effect in this process.

*This work was supported in part by a contract (No. F49620-79-C-0187) from the Air Force Office of Scientific Research.

**Work performed in partial fulfillment of the requirements for the Ph. D. degree in Chemistry at the California Institute of Technology.

[†]Contribution No.

1. Introduction

The distribution of energy among the various possible degrees of freedom (electronic, vibrational, rotational, and translational) in collisions of atoms or molecules with other molecules has been a subject of intense research, both experimental¹ and theoretical,² over the past 15 years. Most of this work has been concerned with the determination of the relative populations of the possible states of the molecular product; additional work has focused on the relative rates of formation of different electronic states of atomic products.

In atom-diatom molecule collisions at energies above the threshold for dissociation, collision-induced dissociation (CID)



may occur. In CID there are no molecular products; in electronically adiabatic collisions the only degrees of freedom in the product are translational. Far less is known about the dynamics of atom-diatom molecule collisions at energies above dissociation than at those below;³ in particular, little attention has been paid to the partitioning of the available energy among the three atoms in dissociative collisions.

This information can in principle be obtained from accurate calculations on the collision process. Their determination from quasi-classical trajectory calculations of the CID process is straightforward. In these, one just calculates the kinetic energies of the three atoms when the collision is over for

each trajectory resulting in dissociation, and then appropriately averages over all trajectories leading to dissociation. Their determination from quantum mechanical calculations is more complicated; they may be obtained from scattering calculations performed by the hyperspherical coordinates method.^{4,5}

In this work we present results for the partitioning probabilities, that is, the probabilities of partitioning of the available energy among the three atoms in dissociative collisions by both quantum mechanical (QM) and quasi-classical trajectory (QCT) methods in a model collinear atom-diatomic molecule collision. We first review the methods by which these quantities are obtained. We then compare the QM and QCT results and discuss the origins of the difference between the results from the two methods.

2. Theory and Numerical Methods

A. Quantum Mechanical Method

The calculation of bound-continuum total (dissociation) probabilities by the hyperspherical coordinate method has been outlined by us^{4c} and by Manz and Römelt⁵ previously. The basic formalism for the calculations of the partitioning probabilities has also been outlined previously,^{4c,b} We present it here in more detail, emphasizing details appropriate to its numerical implementation.

First we recognize that in dissociative collisions, there is only one degree of freedom in the partitioning of the available energy among the three atoms. This is best expressed as

the angle α , which is one of the two variables in the hyper-spherical coordinate treatment of collinear atom-diatomic molecule collisions.^{4a} The kinetic energies of the three atoms are related by the expressions

$$\frac{E_A}{E'} = \frac{m_B + m_C}{M} \cos^2 \alpha \quad (2a)$$

$$\frac{E_B}{E'} = \frac{m_C}{m_B + m_C} \left[\left(\frac{m_A}{M} \right)^{\frac{1}{2}} \cos \alpha - \left(\frac{m_C}{m_B} \right)^{\frac{1}{2}} \sin \alpha \right] \quad (2b)$$

$$\frac{E_C}{E'} = \frac{m_C}{m_B + m_C} \left[\left(\frac{m_A}{M} \right)^{\frac{1}{2}} \cos \alpha + \left(\frac{m_C}{m_B} \right)^{\frac{1}{2}} \sin \alpha \right] \quad (2c)$$

where E' is the total energy of the system measured with respect to that of three infinitely separated atoms at rest and M is the sum of the atomic masses.

The differential probability $d\sigma_d^{\lambda n_\lambda}(\alpha)$ of dissociating from a bound state λn_λ , where λ represents the reagent diatomic molecule (AB or BC) and n_λ is its vibrational quantum number, into a dissociation direction specified by the angular range α to $\alpha + d\alpha$ is given by the ratio of the asymptotic radial flux into that angular range to the total incident flux $\hbar k_{\lambda n_\lambda} / \mu$, where $k_{\lambda n_\lambda}$ is the wavenumber describing the initial relative translation of the atom with respect to the diatom in Delves mass scaled coordinates,⁷ and μ is the Delves mass $(m_A m_B m_C / M)^{\frac{1}{2}}$:

$$d\sigma_d^{\lambda n \lambda}(\alpha, \rho) = \sigma_d^{\lambda n \lambda}(\alpha, \rho) d = \text{Im} [\psi^* (\frac{\partial \psi}{\partial \rho})] \rho d\alpha . \quad (3)$$

The dissociative part $\psi_d^{\lambda n \lambda}$ (the only one of interest here) of the total wavefunction $\psi^{\lambda n \lambda}$ (see eq. (3) of ref. 2) may be written (at large ρ) as

$$\psi_d^{\lambda n \lambda} = \rho^{-\frac{1}{2}} \sum_{n=1}^{N_d} \exp(ik_n \rho) (k_{\lambda n \lambda} / k_n)^{\frac{1}{2}} S_n^{\lambda n \lambda} \phi_n(\alpha, \rho) . \quad (4)$$

where index n denotes the discretized continuum channels, R_n the corresponding wave number, and $S_n^{\lambda n \lambda}$ the bond to continuum elements of the scattering matrix. If numerical integration of the coupled channel equations were carried out to $\rho = \infty$, the eigenvalues of all continuum state would be identical (and zero), all their wavenumbers k_n would be equal to a common value $k = (1/h)(2\mu E')^{\frac{1}{2}}$, and the factor $(1/k) \exp(ik\rho)$ in eq. (4) could be moved outside the summation sign. In principle, the sum in eq. (4) is infinite; in practice it is truncated at some value N_d sufficiently large for that sum to have essentially converged to its correct value. The dependence of $d\sigma_d^{\lambda n \lambda}$ and of $\phi_n(\alpha; \rho)$ on ρ disappears asymptotically as $\rho \rightarrow \infty$.

From eqs. (3) and (4) we get, assuming the k_n and ϕ_n to be independent of ρ ,

$$\begin{aligned} \sigma_d^{\lambda n \lambda}(\alpha, \rho) = \sum_{n, n'=1}^{N_d} \phi_n(\alpha; \rho) \phi_{n'}(\alpha; \rho) \frac{k^{\lambda n \lambda}}{(k_n k_{n'})^{\frac{1}{2}}} \{ A_{nn'}(\rho) [\text{Re} S_{n'}^{\lambda n \lambda} \text{Re} S_n^{\lambda n \lambda} + \\ + \text{Im} S_{n'}^{\lambda n \lambda} \text{Im} S_n^{\lambda n \lambda}] + B_{nn'}(\rho) [\text{Re} S_{n'}^{\lambda n \lambda} \text{Im} S_n^{\lambda n \lambda} - \text{Re} S_n^{\lambda n \lambda} \text{Im} S_{n'}^{\lambda n \lambda}] \} d\alpha \end{aligned} \quad (5)$$

where

$$A_{nn'}(\rho) = - \frac{1}{2\rho} \sin[(k_n - k_{n'})\rho] + k_n \cos[(k_n - k_{n'})\rho] \quad (6a)$$

$$B_{nn'}(\rho) = - \frac{1}{2\rho} \cos[(k_n - k_{n'})\rho] + k_n \sin[(k_n - k_{n'})\rho]. \quad (6b)$$

As mentioned earlier, as $\rho \rightarrow \infty$, $k_n \rightarrow k$ for all n , and therefore

$$A_{nn'} \underset{\rho \rightarrow \infty}{\sim} k \quad (7a)$$

$$B_{nn'} \underset{\rho \rightarrow \infty}{\sim} 0 \quad (7b)$$

In this limit, eq. (5) reduces to the form given previously.^{4a,6} In all numerical calculations we will use eq. (5) and not its limit as $\rho \rightarrow \infty$.

Rather than dealing with $\sigma_d^{\lambda n \lambda}(\alpha, \rho)$, in which one calculates the probability per unit α range of forming products corresponding to a given α , we prefer to consider the probability $\sigma_d^{\lambda n \lambda}(E_A, \rho)$ per unit E_A range of a dissociation in which atom A has a kinetic energy E_A with respect to the center of mass

of the triatomic system. It is given by

$$\sigma_d^{\lambda n}(E_A, \rho) = \left| \frac{d\alpha}{dE_A} \right| \sigma_d^{\lambda n}(\alpha, \rho) . \quad (8)$$

These partitioning probabilities, when integrated over all possible values* of E_A give the total dissociation probability

$$P_d^{\lambda n}(\rho) = \int_{E_A^{\min}}^{E_A^{\max}} \sigma_d^{\lambda n}(E_A, \rho) dE_A \quad (9)$$

E_A^{\min} and E_A^{\max} are determined by eq. (2a) setting $\alpha = \alpha_{\max} = \tan^{-1}(m_B m / m_A m_C)^{\frac{1}{2}}$ and $\alpha = 0$, respectively. Since $\sigma_d^{\lambda n}(E_A, \rho)$ has the dimensions of a reciprocal energy, it is convenient to define the dimensionless quantities $\bar{\sigma}_d^{\lambda n}(f_A, \rho)$ and f_A by

$$\left. \begin{aligned} \bar{\sigma}_d^{\lambda n}(f_A, \rho) &= E' \sigma_d^{\lambda n}(E_A, \rho) \\ \text{and} \\ f_A &= E_A / E' \end{aligned} \right\} \quad (10)$$

Using these dimensionless quantities, the integral in eq. (9)

*In eq. (8), ref. 4c, we mistakenly gave a value of 0 for the lower limit of integration. This is true only in the limit $\alpha_{\max} \rightarrow \pi/2$; otherwise E_A^{\min} is a finite non-zero quantity.

becomes

$$P_d^{\lambda n \lambda}(\rho) = \int_{f_A^{\min}}^{f_A^{\max}} \bar{\sigma}_d^{\lambda n \lambda}(f_A, \rho) df_A. \quad (11)$$

B. Quasi-Classical Method

The details of the calculation of $\bar{\sigma}_d^{\lambda n \lambda}(f_A)$ by the QCT method have been described elsewhere;⁸ we briefly outline them here. The equation for ${}_c\bar{\sigma}_d^{\lambda n \lambda}(E_A)$, where the subscript c indicates classical mechanics, is

$${}_c\bar{\sigma}_d^{\lambda n \lambda}(E_A) = \frac{1}{2\pi} \sum_i \frac{1}{|(df_A/d\phi_0)_i|} \quad (12)$$

where ϕ_0 is the initial phase of the vibration of the diatomic molecule (in radians) and the summation is over all of the regions of the initial range of phases which lead to dissociation, and in which E_A varies continuously with ϕ_0 . The coefficient $(1/2\pi)$ provides for correct normalization of ${}_c\bar{\sigma}_d^{\lambda n \lambda}(E_A)$.

C. Potential Energy Surface

The potential energy surface used is of the rotating-Morse-cubic spline type,⁹ and has been briefly described elsewhere.^{4c} For the mass combination considered ($m_A = m_b = m_C = 1$ in H-atom mass units), asymptotically there are two bound states, with energies of 0.0815 and 0.1885 eV with respect to the bottom of the diatomic molecule well (which is 0.22

eV deep). The Morse parameters¹⁰ of the reagent molecule are $D_e = 0.22$ eV, $\beta = 1.6$ bohr⁻¹, $R_{eq} = 1.40083$ bohr. Equipotential contour lines of this potential energy surface are displayed in Figure - of ref. 4c.

D. Numerical Methods

In the hyperspherical coordinate calculations, six even and six odd basis functions were used. Comparison with calculations done previously^{4c} using 10 even and 10 odd functions showed that the present results are essentially converged. The \underline{S} matrix was approximately unitary, the deviation from unitarity increasing as the dissociation probability increases. Average values of this deviation are given in Section 3. Integration was carried out to $\rho = 190$ bohr; asymptotic analyses were carried out at 110, 130, 150, 170, and 190 bohr. As discussed above, at finite ρ , the dissociation probabilities $P_d^{\lambda n \lambda}$ and the partitioning probabilities $\sigma_d^{\lambda n \lambda}$ vary slowly with ρ . The results we present are means of the values at the five different projection distances. We also indicate standard deviations of some of these quantities to provide a feeling for the extent of their ρ dependence. Eq. 9 permits a consistency check between the values of $P_d^{\lambda n \lambda}$ and $\sigma_d^{\lambda n \lambda}$. That equation was satisfied in general with an accuracy of $\pm 2\%$.

The quasiclassical trajectory calculations were carried out using standard methods,¹¹ The integration time step was 5.41×10^{-17} sec. Energy is conserved to four digits in these

calculations. Integration of trajectories was begun with the distance $R_{A,BC}$ from the incident atom to the center of mass of the diatomic molecule of 12.0 bohr. Initially 100 trajectories were calculated per energy (and initial state), corresponding to a grid of initial phase of $\pi/50$ radians. Near the boundary between dissociative and either non-reactive or reactive regions of the trajectory final states the phase angle grid was cut down to 0.01 radians. The derivative in eq. (12) was evaluated by fitting a parabola to every group of three points and differentiating analytically; we then interpolated these derivatives by using a cubic spline procedure.

3. Results

We have calculated dissociation probabilities P_v^D as a function of energy at a number of energies up to 0.25 eV above dissociation when the reagent molecule is initially in vibrational state v . Values of dissociation probabilities, both quantum and quasi-classical, are given for four energies in Table 1. For the quantum results, we also present the worst unitarities WU (the largest sum of the squares of the elements in a given row or column of the S matrix). All the quantum mechanical results are averages (indicated by angular brackets) over the five asymptotic analyses described above; standard deviations are given for all quantities (indicated by the letter s). The relative smallness indicates that those quantities are not a very sensitive function of the projection distance. We

now focus attention on the lowest and highest of the energies in Table 1: 0.04 and 0.25 eV, respectively,

Detailed data on the structure of the banding of the QCT calculations are given in Table 2, in which we examine the number, width, and properties of the separate regions of the initial phase giving rise to dissociative trajectories. From Table 2 it is clear that there may be more than one region of initial phase leading to dissociation, and that these regions may have minima in their plots of f_A vs. initial phase. As may be seen from eq. (12), minima in these plots give rise to divergences in $c_d^{\lambda n}$.

In considering the quantum results it is useful to understand how the individual terms of the sum in eq. (5) vary with the indices n and n' . For this purpose, we present in Fig. 1 a plot of the transition probability P_{vn}^d for going from the bound state v of the reagent diatomic molecule to the n th continuum state as a function of n . These probabilities are obtained from the corresponding \underline{S} matrix elements by the expression

$$P_{vn}^d = |S_{vn}^d|^2 . \quad (13)$$

Generally speaking, a larger P_{vn}^d indicates a larger magnitude of S_{vn}^d and correlates with a larger contribution to the summation in 5. We see that P_{vn}^d decreases appreciably (by more than two orders of magnitude) as n increases from 1 to 8, indicating that to first order, the truncation of the sum in eq. 5 at $n=n'=8$ should provide reasonable results. Note that

in two of the three cases shown, there seems to be a strong preference for dissociation to symmetric continuum states (n odd).

Plots of the quantum mechanical partitioning probabilities $\bar{\sigma}_d^v$ as a function of f_A for $E'=0.04$ eV and 0.25 eV are presented in Figs. 2 and 3. Because of the simplicity of this symmetric collinear atom-diatomic molecule system, we may replace the superscript λn_λ used previously by v , as that is the only initial quantity which may be varied. Error bars are used to indicate the standard deviations of the calculated partitioning probabilities from their mean. We deleted the portion of the curve nearest to $f_A = \frac{2}{3}$ as here the calculations are unreliable. This is due to the form of the $d\alpha/dE_A$ term in eq. (8):

$$\frac{d\alpha}{dE_A} = -\frac{1}{2}[E_A(E_A^{\max} - E_A)]^{-\frac{1}{2}} \quad (14)$$

When $E_A = E_A^{\max}$ (for this mass combination, when $f_A = \frac{2}{3}$), this factor diverges and the resulting $\bar{\sigma}_d^v$ may be large, as may their deviations.

In Figs. 4-6 we present plots of the classical partitioning probability $\bar{\sigma}_d^v$ for three sets of initial conditions: $E'=0.04$ eV and $v=0$ and $E'=0.25$ eV and $v=0$ and $v=1$, respectively. Note that the vertical scales are different in all the figures (except Figs. 4 and 5). In the ensuing section we discuss the different forms of these curves as well as their differences from the quantum mechanical ones.

4. Discussion and Conclusions

The plots of the quantum mechanical partitioning probabilities $\bar{\sigma}_v^d$ in Figs. 2 and 3 all show the same basic structure. $\bar{\sigma}_v^d$ increases fairly smoothly as f_A increases from its minimum to its maximum value. There does appear to be some structure in these curves as seen by the existence of shoulders and small maxima. The magnitude of the error bars suggests that these oscillations might be real; from the data obtained one should not discard the maximum in the $\bar{\sigma}_1^d$ curve near $f_A=0.55$ in Fig. 3. It is premature to assign too much significance to these oscillations for two reasons. First, it has been seen in preliminary calculations that termination of integration at a small value of ρ leads to spurious oscillations in the $\bar{\sigma}_v^d$ curves, which decrease in magnitude as ρ is increased. Second, the small basis set used in the present calculations may lead to errors in the resulting values of $\bar{\sigma}_v^d$. Since the higher basis functions have more oscillations than do the lower ones, their contribution to the summation in eq. (3) may be such that, while its overall magnitude is small, it could affect the fine structure of the curves. We note that in general, the $\bar{\sigma}_0^d$ and $\bar{\sigma}_1^d$ curves have the same overall behavior.

The plots of ${}_c\bar{\sigma}_v^d$ (Figs. 4-6) have a richer structure in that the various curves are all fairly different. In Fig. 4 we see that ${}_c\bar{\sigma}_1^d$ increases fairly smoothly with f_A , with the exception of a small dip near 0.52. In Fig. 5 ${}_c\bar{\sigma}_0^d$ increases rapidly with f_A , reaches a maximum, has one fairly rapid

oscillation and then decreases slowly with f_A . From Table 2 we see that there are two separate regions of initial phase contributing to dissociation; analysis of the contribution from each shows that only a small fraction (~10%) of the area under the curve in Fig. 4 comes from the first (narrow) dissociative region, and its contribution is nearly independent of f_A .

The curve for $\bar{\sigma}_1^{-d}$ in Fig. 6 at the same total energy differs appreciably from that for $\bar{\sigma}_0^{-d}$ in Fig. 5. The large spike in Fig. 6 arises because the plot of f_A vs. initial phase has a broad inflection region in which $dE_A/d\phi \sim 0$. Thus, by eq. (12), $\bar{\sigma}_1^{-d}$ must become large. This is a somewhat unusual occurrence; more normally one finds minima in the plot of E_A vs. ϕ , giving rise to discontinuous jumps in the plot of $\bar{\sigma}_v^{-d}$. These spikes or discontinuities in $\bar{\sigma}_v^{-d}$ are purely a consequence of the way in which the classical trajectories behave, in particular the origin of well defined reactivity bands. How the reactivity band structure influences the form of the partitioning probability curves is discussed in detail elsewhere.⁸

Because there is not necessarily any close relationship between the reactivity band structure for collisions involving different reactant vibrational states,⁸ the classical partitioning probabilities for different reactant states at the same total energies can have substantially different forms (i.e., have spikes or discontinuities). The quantum mechanical

partitioning probabilities appear to be fairly similar for the different reactant states, however. Thus, it may be that classical mechanics, while giving a reasonable description for the likelihood of dissociation, gives an incorrect one for the details for the dissociation process. It is quite likely that in higher dimensionality, in which reactivity band structure blurs or disappears altogether,¹² more reasonable agreement between the quantum-mechanical and quasi-classical partitioning probabilities may be obtained.

In summary, we believe we have obtained reasonably accurate (although probably not fully converged) probabilities for the partitioning of kinetic energy among the dissociation products for collinear atom-diatomic molecule collisions by a quantum mechanical method on a model system. We have compared these results to those obtained by classical mechanics, and shown that they behave quite differently.

Acknowledgments

The calculations reported here were performed on the Dreyfus-NSF Theoretical Chemistry Computer which was funded through grants from the Camille and Henry Dreyfus Foundation, the National Science Foundation (Grant No. CHE78-20235) and the Sloan Fund of the California Institute of Technology.

References

1. M. R. Levy, Prog. Reaction Kinetics 10 (1979) 1,
2. J. N. L. Connor, Computer Phys. Commun. 17 (1979) 117;
R. B. Walker and J. C. Light, Ann. Rev. Phys. Chem. 31
(1980) 401.
3. D. J. Diestler, in Atom-Molecule Collision Theory, ed.
R. B. Bernstein (Plenum Press, New York, 1979) pp. 655-
657; P. J. Kuntz, in Atom-Molecule Collision Theory, ed.
R. B. Bernstein (Plenum Press, New York, 1979) pp. 669-693.
4. (a) A. Kuppermann, J. A. Kaye, and J. P. Dwyer, Chem.
Phys. Lett. 74 (1980) 257; (b) J. A. Kaye and A. Kuppermann,
Chem. Phys. Lett. 77 (1981) 573; (c) J. A. Kaye and A.
Kuppermann, Chem. Phys. Lett. 78 (1981) 546; J. A. Kaye
and A. Kuppermann, Chem. Phys. Lett. 92 (1982) 574.
5. G. Hauke, J. Manz, and R. Romelt, J. Chem. Phys. 73 (1980)
5040; J. Romelt, Chem. Phys. Lett. 74 (1980) 263; J.
Manz and J. Romelt, Chem. Phys. Lett. 76 (1980) 337; 77
(1981) 172; 81 (1981) 179.
6. J. P. Dwyer, Quantum Mechanical Studies of Molecular
Scattering, Ph. D. Thesis, California Institute of Tech-
nology (1977).
7. L. M. Delves, Nucl. Phys. 9 (1959) 391; 20 (1960) 275.
8. J. A. Kaye and A. Kuppermann, manuscript in preparation.
9. J. M. Bowman and A. Kuppermann, Chem. Phys. Lett. 34 (1975)
523,
10. H. Eyring, J. Walter, and G. Kimball, Quantum Chemistry
(Wiley, New York, 1964), pp. 272, 273.

11. R. N. Porter and L. M. Raff, in; Dynamics of Molecular Collisions, Part B, ed. W. H. Miller (Plenum Press, New York, 1976), pp. 1-52; D. G. Truhlar and J. T. Muckerman, in Atom-Molecule Collision Theory, ed. R. B. Bernstein (Plenum Press, New York, 1979), pp. 505-565.
12. K. G. Tan, K. G. Laidler, and J. C. Wright, J. Chem. Phys. 67 (1977) 5883; J. S. Wright, J. Chem. Phys. 69 (1978) 720.

Table 1. Probabilities for Dissociation and Related Quantities

E'/eV	$\langle WU \rangle$	$s(WU)$	$\langle P_0^P \rangle_{QM}$	$s(\langle P_0^P \rangle_{QM})$	$\langle P_1^P \rangle_{QM}$	$s(\langle P_1^P \rangle_{QM})$	P_0^P	P_1^P
0.04	1.0387	0.0020	0.0088	0.0007	0.1998	0.0016	0	0.107
0.08	1.0251	0.0023	0.0024	0.0004	0.1416	0.0007	0	0.215
0.16	1.0257	0.0012	0.0501	0.0022	0.1261	0.0036	0.137	0.150
0.25	1.0719	0.0029	0.2155	0.0017	0.4284	0.0033	0.268	0.390

Table 2. Detailed Structure of Dissociative Quasi-Classical Trajectory Bands

ϵ'/eV	P_0^p	P_0^p	$n_0^{(a)}$	$\Delta\phi_{0j}^{(b)}$	$n_0^{(c)}$	P_{1QCT}^p	$n_1^{(a)}$	$\Delta\phi_{1j}^{(b)}$	$n_1^{(c)}$
0.04	0.0	-	-	-	-	0.107	1	0.67	0
0.08	0.0	-	-	-	-	0.215	2	0.09	0
0.16	0.137	2	0.77	0.09	0	0.150	3	0.20	1
0.25	0.277	2	0.15	1.53	0	0.39	2	0.05	0
								2.40	

(a) n_v^p is the number of separate regions of initial phase giving rise to dissociative trajectories in collisions of $A + BC(v)$.

(b) $\Delta\phi_{vj}$ is the approximate width in radians of the j th separate region of initial phase giving rise to dissociative trajectories in collisions of $A + BC(v)$
 $[\Delta\phi_{vj} = \phi_{vj}^{\max} - \phi_{vj}^{\min}]$, where ϕ_{vj}^{\max} and ϕ_{vj}^{\min} are the phases at the high and low phase ends of the j th dissociative region].

(c) n_{vj}^{\min} is the number of minima in the plot of E_A vs. ϕ in the j th dissociation region for collisions of $A + BC(v)$.

Figure Captions

FIG. 1. Plot of individual bound-continuum transition probabilities P_{vn}^d vs. the index n of the continuum state for three sets of initial collisions. $E' = 0.04$ eV, $v = 1$ (circles, solid line), $E' = 0.25$ eV, $v = 1$ (squares, dashed line); $E' = 0.25$ eV, $v = 0$ (triangles, dotted line). Values plotted are the means of the values obtained from five asymptotic analyses. Error bars indicate one standard deviation about the mean. Where no error bars are shown, they are sufficiently small that they would be within the plotted symbol (circle, square, or triangle).

FIG. 2. Plot of the dimensionless quantum mechanical partitioning probabilities $\bar{\sigma}_v^d$ as a function of the fraction f_A of the available kinetic energy going to atom A at an energy $E' = 0.04$ eV with respect to three infinitely separated atoms. Curves are shown for both the $v = 1$ (solid line) and $v = 0$ (dashed line) initial states. The values of $\bar{\sigma}_d^0$ have been multiplied by ten before plotting. All values plotted are the means of the values obtained from the five asymptotic analyses; the error bars indicate one standard deviation about the mean. The plot has been cut off just above $f_A = 0.65$ for reasons described in the text.

FIG. 3. Plot of the dimensionless quantum mechanical partitioning probabilities $\bar{\sigma}_v^d$ as a function f_A of the available kinetic energy going to atom A at an energy $E' = 0.25$ eV with respect to three infinitely separated atoms. All markings are as in Fig. 2.

FIG. 4. Plot of the dimensionless classical mechanical partitioning probability $\bar{\sigma}_v^{c-d}$ as a function f_A of the available kinetic energy

Figure Captions (continued)

going to atom A at an energy $E' = 0.04$ eV with respect to three infinitely separated atoms.

FIG. 5. Plot of the dimensionless classical mechanical partitioning probability $c_{\sigma_0}^{-d}$ as a function f_A of the available kinetic energy going to atom A at an energy $E' = 0.25$ eV with respect to three infinitely separated atoms.

FIG. 6. Plot of the dimensionless classical mechanical partitioning probability $c_{\sigma_1}^{-d}$ as a function f_A of the available kinetic energy going to atom A at an energy $E' = 0.25$ eV with respect to three infinitely separated atoms.

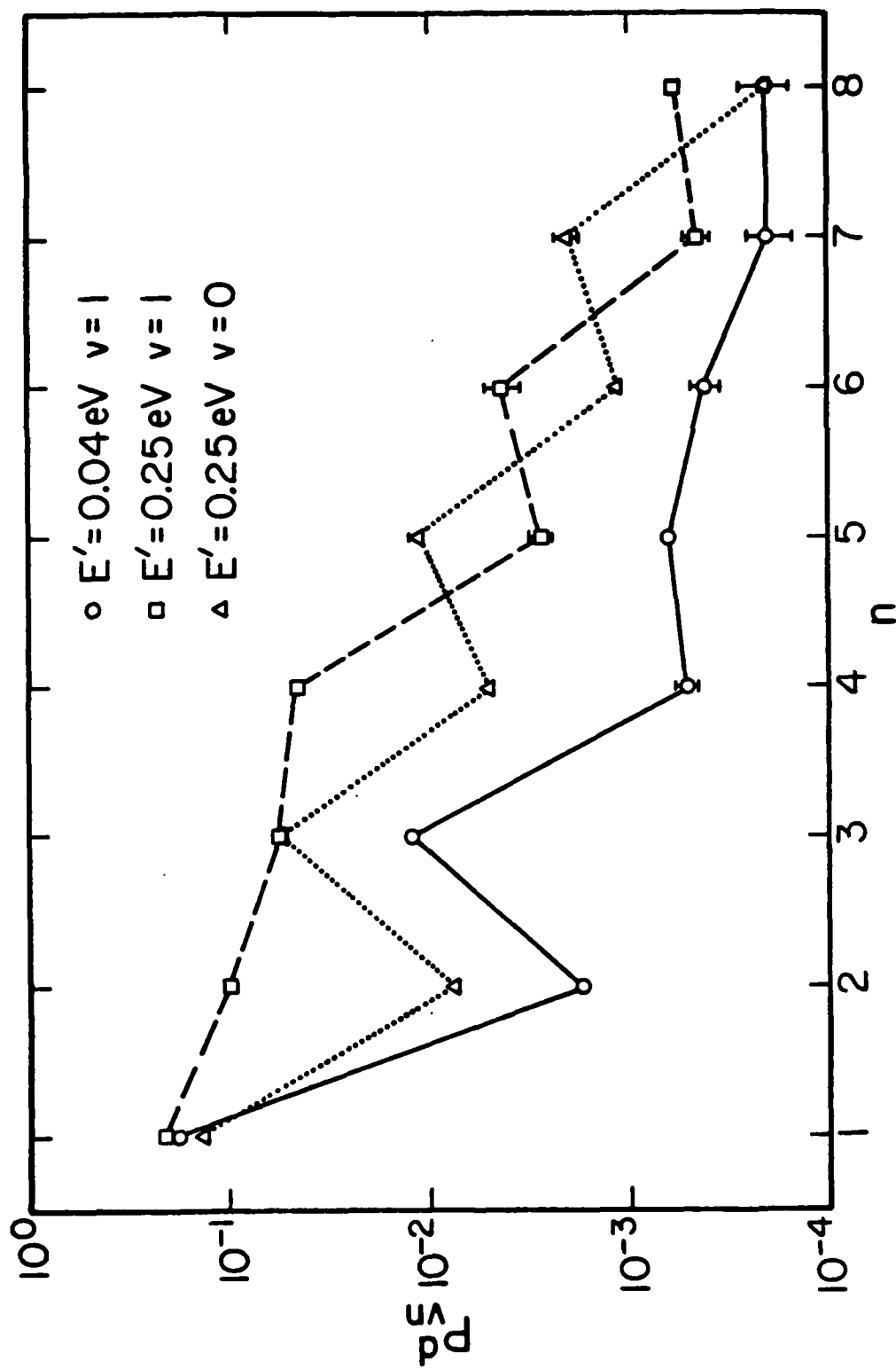


Figure 1

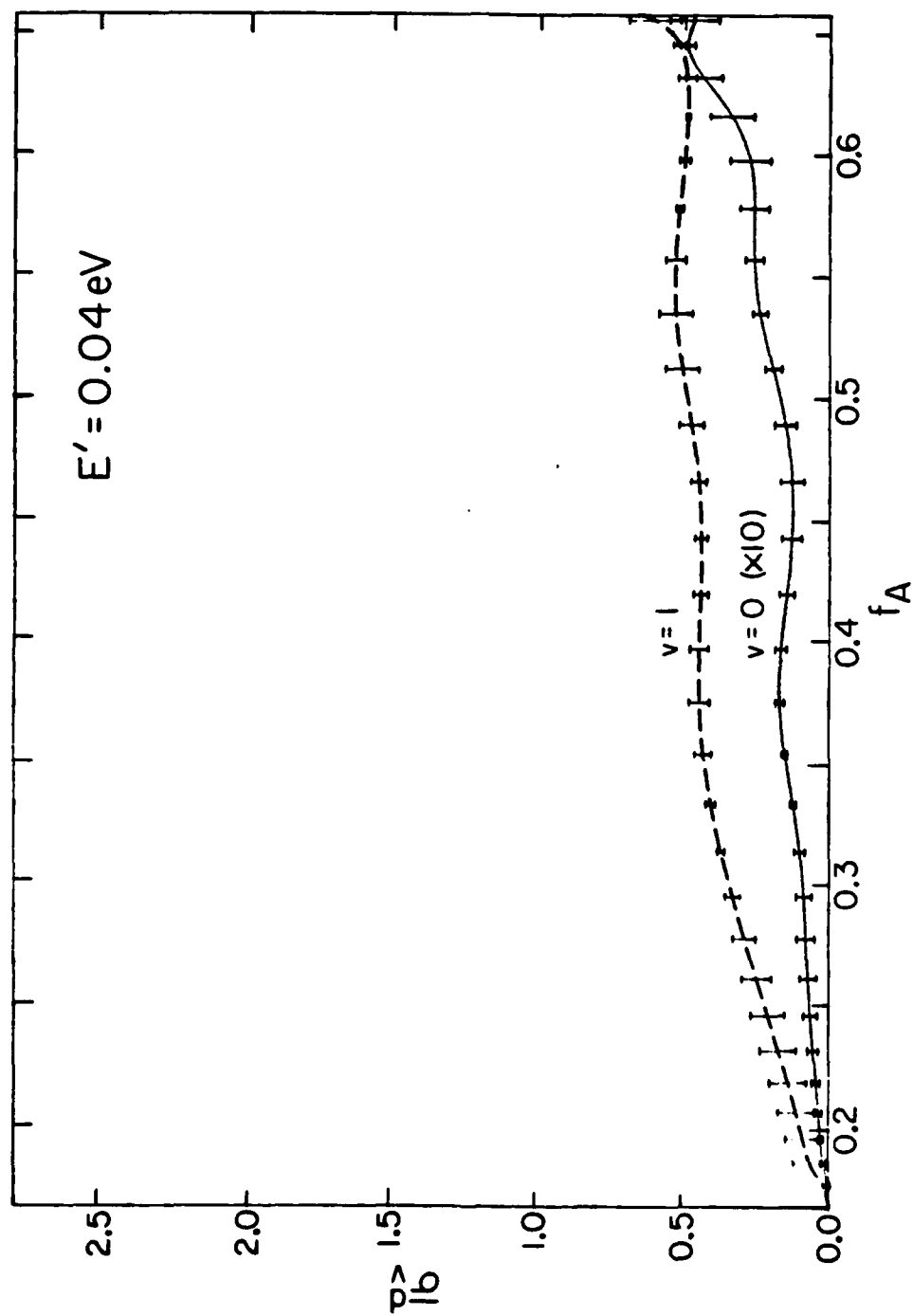


Figure 2

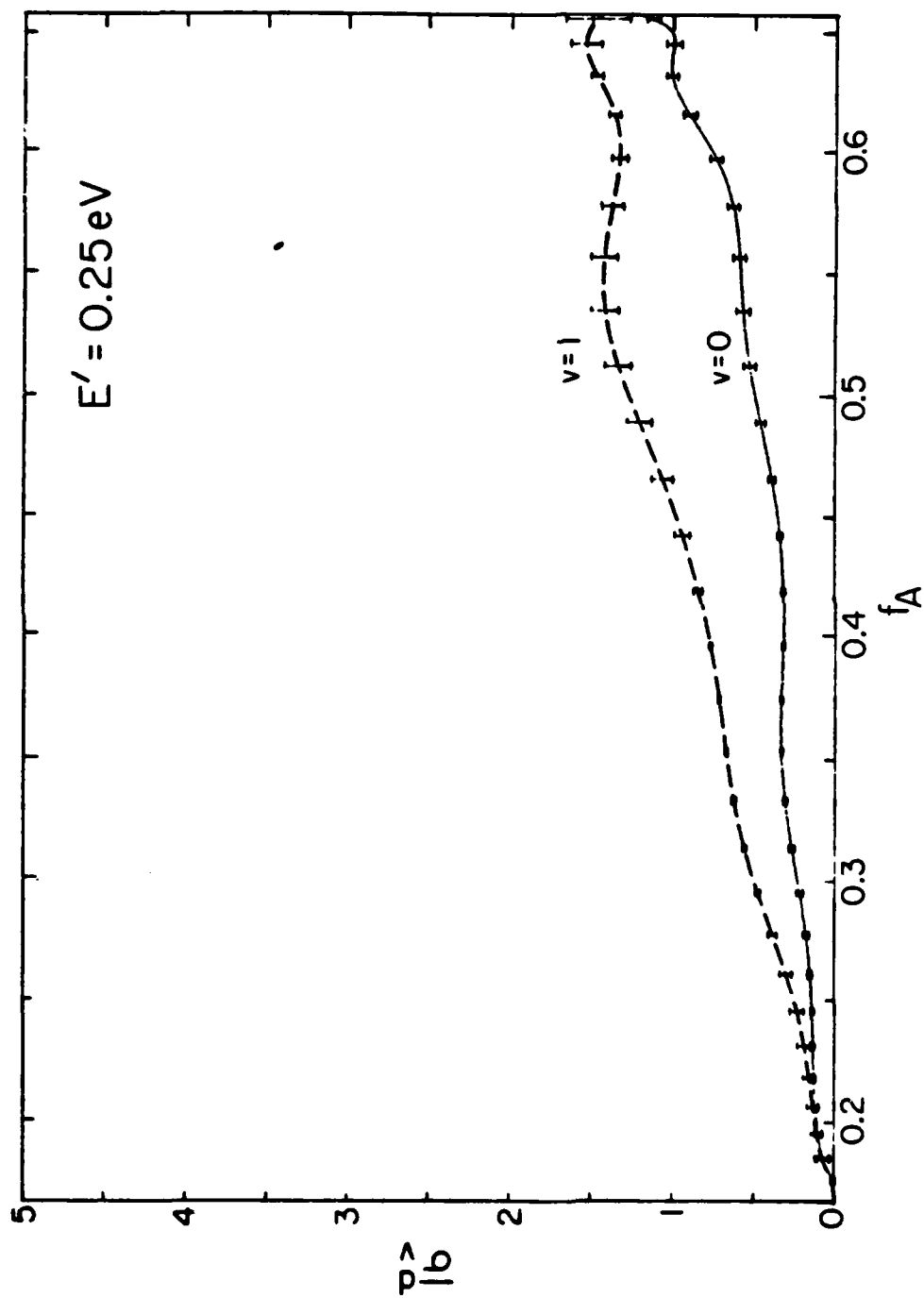


Figure 3

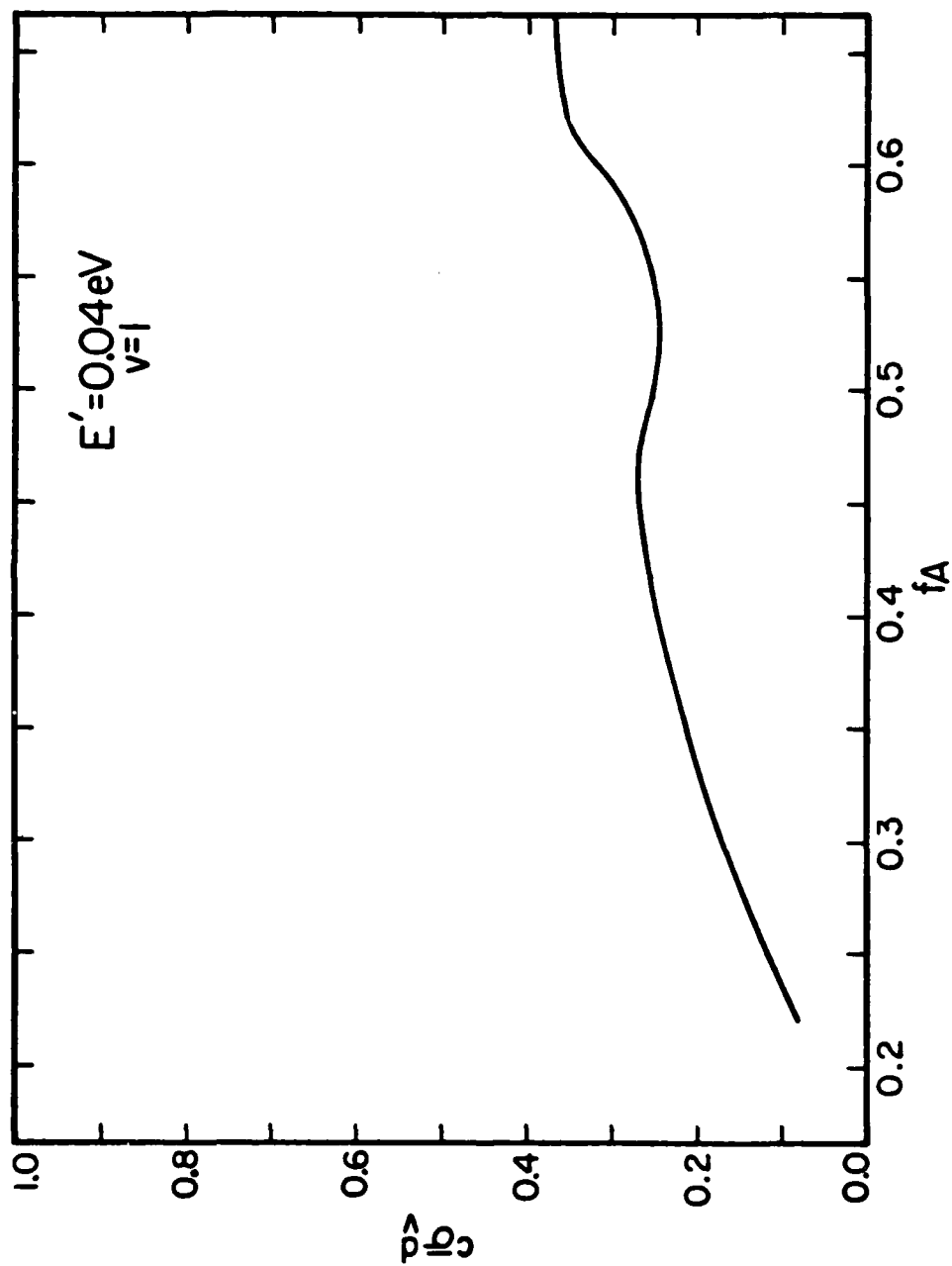


Figure 4

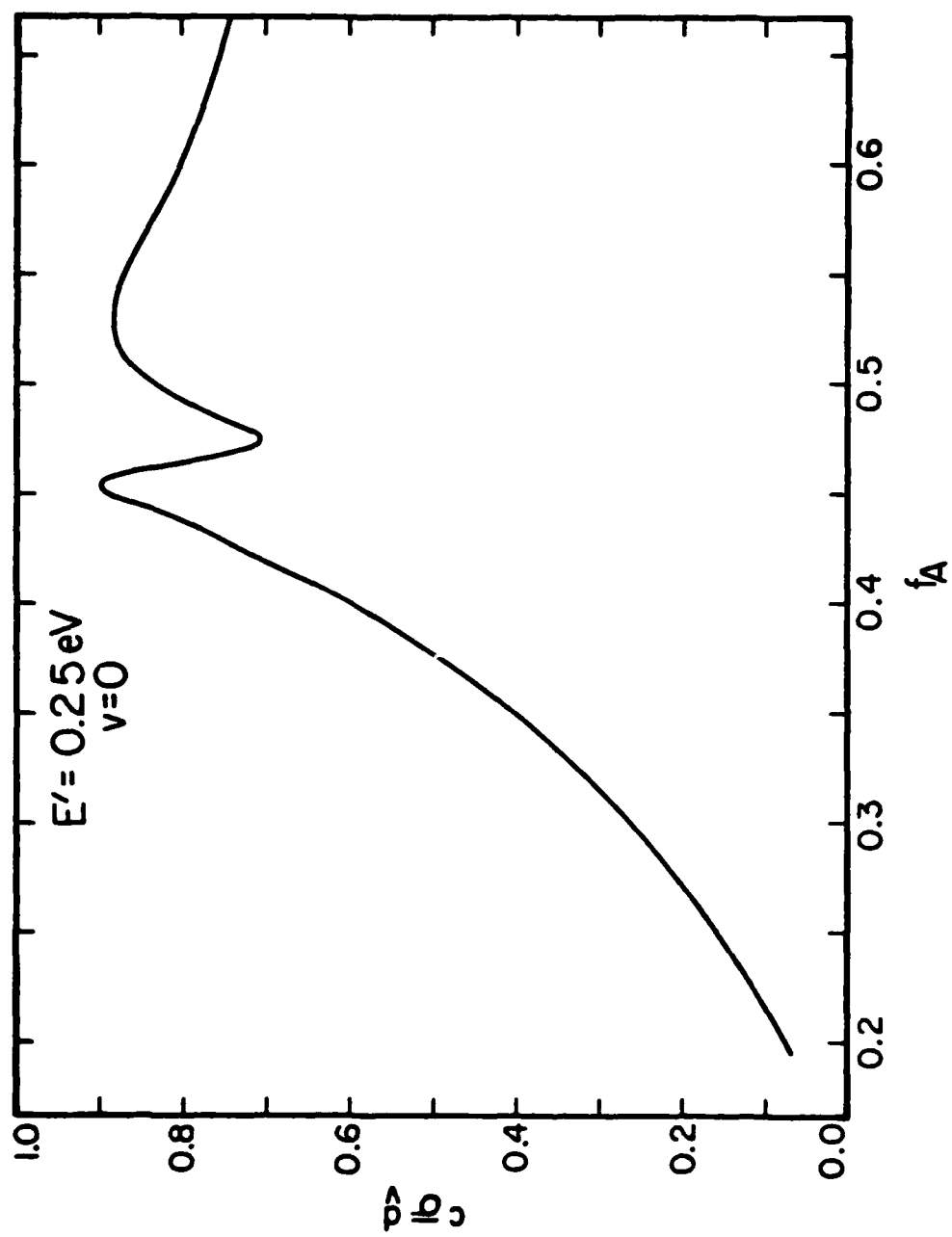


Figure 5

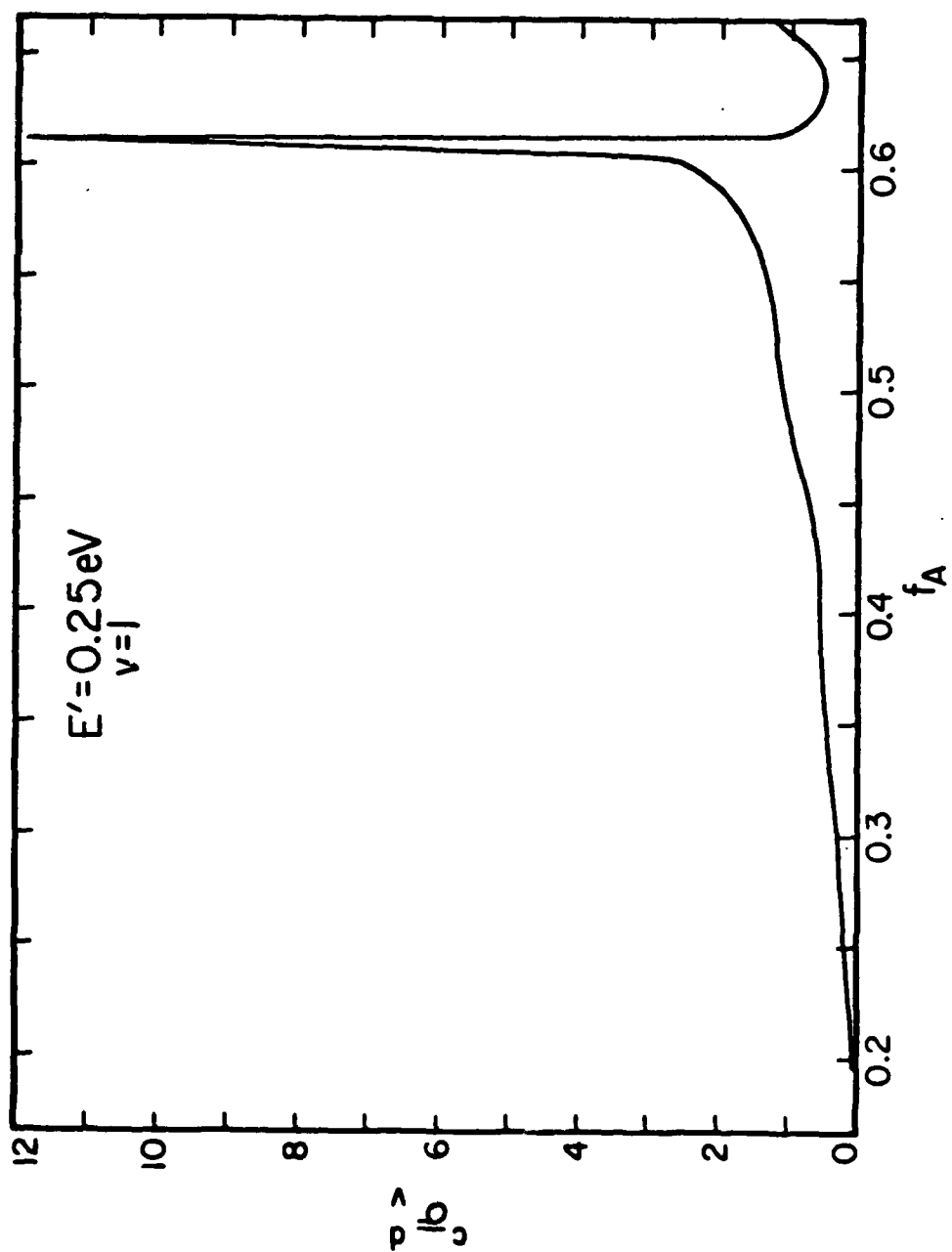
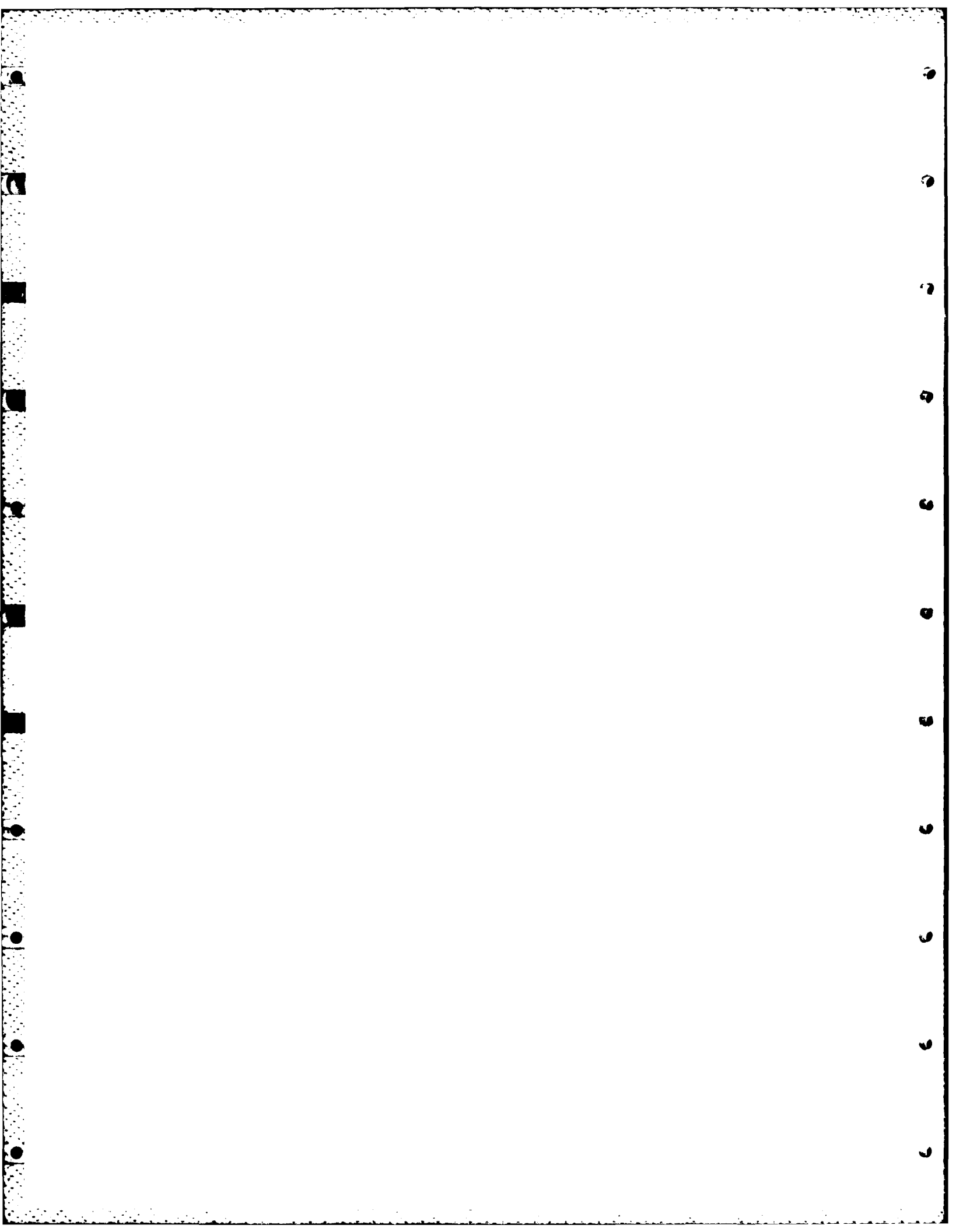


Figure 6



QUASI-CLASSICAL TRAJECTORY ANALYSIS OF THE EQUIVALENCE
OF REACTIVE AND NONREACTIVE DEACTIVATION IN THE
COLLINEAR $\text{Cl}' + \text{HCl}$ SYSTEM*

Jack A. KAYE** and Aron KUPPERMANN

Arthur Amos Noyes Laboratory of Chemical Physics,[‡]

California Institute of Technology, Pasadena, California 91125, USA

Received

Near total equivalence of the reactive and nonreactive processes in vibrationally adiabatic collisions $\text{Cl}' + \text{HCl}(\nu) \rightarrow \text{Cl}' + \text{HCl}(\nu' < \nu)$, $\text{Cl}'\text{H}(\nu'' < \nu)$ has been observed in collinear quantum mechanical scattering calculations. Analysis of reactivity bands and individual trajectories in collinear quasi-classical trajectory calculations allows one to simply understand why this should be so.

* Research supported in part by the U. S. Air Force Office of Scientific Research (Contract No. F49620-79-C-0187).

** Work performed in partial fulfillment of the requirements for the Ph.D. in Chemistry at the California Institute of Technology.

[‡] Contribution No.

AD-A130 160

THE QUANTUM DYNAMICS OF CHEMICAL REACTIONS(U)
CALIFORNIA INST OF TECH PASADENA DIV OF CHEMISTRY AND
CHEMICAL ENGINEERING A KUPPERMANN 31 MAR 83

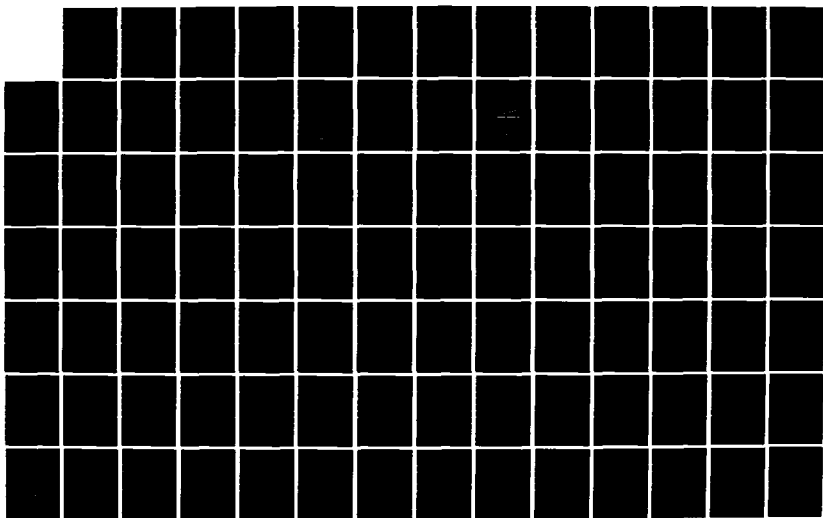
3/6

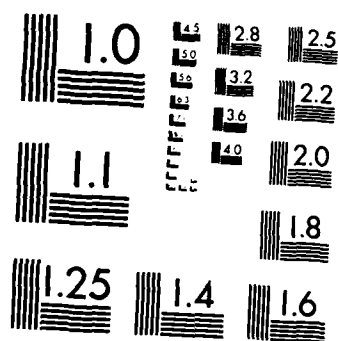
UNCLASSIFIED

AFOSR-TR-83-0565 AFOSR-81-0235

F/G 20/10

NL





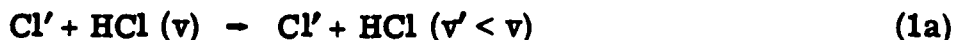
MICROCOPY RESOLUTION TEST CHART
NATIONAL BUREAU OF STANDARDS-1963-A

1. Introduction

Quasi-classical trajectory calculations have served an important role in the last 20 years in helping one gain insight into the dynamics of chemical reactions [1]. Information concerning the effect of reagent vibrational, rotational and translational excitation, and the product vibrational and rotational distributions has been obtained. In addition, by looking at trajectories, one is able to get a good physical picture of the collision process itself.

Such trajectory calculations have been particularly useful in the development of simple qualitative models for chemical reactions that allow one to understand how a change in a potential energy surface, isotopic substitution, or reagent excitation will affect the collision process [2]. These simple models and pictures are particularly useful in interpreting the results of quantum mechanical calculations [3], which, by themselves, give good values for reaction probabilities, but do not provide any insight as to how chemical reactions occur [4].

In this paper, we briefly report the results of quantum mechanical calculations on the collinear system



on two potential energy surfaces. We focus in particular on one seemingly surprising aspect of the dynamics: in vibrationally nonadiabatic collisions, the probabilities, and thus the rates, of the nonreactive (1a) and reactive (1b) processes are almost equal, although this is not true for vibrationally adiabatic collisions. We show that this result is

QUASI-CLASSICAL TRAJECTORY ANALYSIS OF THE EQUIVALENCE
OF REACTIVE AND NONREACTIVE DEACTIVATION IN THE
COLLINEAR $\text{Cl}' + \text{HCl}$ SYSTEM*

Jack A. KAYE** and Aron KUPPERMANN

Arthur Amos Noyes Laboratory of Chemical Physics,[†]

California Institute of Technology, Pasadena, California 91125, USA

Received

Near total equivalence of the reactive and nonreactive processes in vibrationally adiabatic collisions $\text{Cl}' + \text{HCl}(\nu) \rightarrow \text{Cl}' + \text{HCl}(\nu' < \nu)$, $\text{Cl}'\text{H}(\nu'' < \nu)$ has been observed in collinear quantum mechanical scattering calculations. Analysis of reactivity bands and individual trajectories in collinear quasi-classical trajectory calculations allows one to simply understand why this should be so.

* Research supported in part by the U. S. Air Force Office of Scientific Research (Contract No. F49620-79-C-0187).

** Work performed in partial fulfillment of the requirements for the Ph.D. in Chemistry at the California Institute of Technology.

[†] Contribution No.

obtained approximately in collinear quasi-classical trajectory calculations, and that by analysis of reactivity bands and individual trajectories we can understand why this should be so.

In Section 2 we briefly describe the method of calculation and the potential energy surfaces used. In Section 3 we present the results of the quantum mechanical and quasi-classical trajectory calculations. In Section 4 we discuss and interpret the results obtained.

2. Computational Methods and Potential Energy Surfaces

The quantum mechanical calculations on reactions (1) were performed using the method of hyperspherical coordinates [5, 6]. This method allows one to treat heavy-light-heavy mass combinations without difficulty, in spite of the small skew angle (13.59°) between the two arrangement channels in Delves mass-weighted coordinate system [7]. This technique has previously been used by two different groups to study the reaction [5b, 6e]

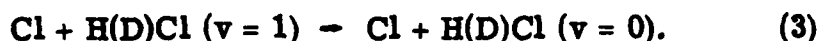


and similar results have been obtained, giving one substantial faith in its applicability to these mass combinations.

In the calculations reported here, eight even and eight odd basis functions were used at lower energies and 12 even and 12 odd at higher energies. Convergence of the transition probabilities (estimated by varying the basis set and integration stopping point) to ± 0.001 and flux to ± 0.0002 was obtained at nearly all energies. The highest energy for which calculations were performed was 1.24 eV above that of HCl ($v = 0$). Standard methods were used for the collinear quasi-classical trajectory calculations [1]. Trajectories were started with the distance from the Cl' atom to the HCl center of mass, $R_{Cl', HCl}$ at 12 bohr, and were terminated when either distance, $R_{Cl', HCl}$ or $R_{Cl, HCl'}$, was more than 12 bohr.

Two different LEPS [8] surfaces were used. The molecular parameters for HCl and Cl_2 were those of Connor et al. [9]. Two values of the Sato parameter were chosen (0.138 for surface A; 0.185 for

surface B). These correspond to surfaces (i) and (ii) of Smith [10], and have barrier heights of 6.21 and 1.89 kcal/mole, respectively. Parameters and properties of the potential energy surfaces are shown in table 1. The higher barrier height corresponds roughly to the experimental activation energy [11] and also to the upper limit to the barrier as predicted in ab initio calculations [12]; the lower barrier height is close to the predicted lower limit [12], and was found by Smith to lead to better agreement between quasi-classical trajectory calculations [10] and experiment [13] for the deactivation process



It is expected, then, that the actual barrier height is somewhere within these two limits. The potential surface is plotted in Delves [7] mass-weighted coordinates in figs. 4 and 5, where selected trajectories are plotted.

3. Results

In fig. 1, we present a plot of the probability versus energy curves for vibrationally nonadiabatic, nonreactive processes, defined as process (1a), with $v = 2$ and $v' = 0$ and 1 (P_{20}^V and P_{21}^V , respectively), and the corresponding reactive processes P_{20}^R and P_{21}^R for calculations on surface B. State-to-state rate constants are calculated from the reaction probability versus energy curves, and these are plotted in the form of Arrhenius plots for the four transitions in fig. 2. While the shape of the probability versus energy curves and rate constant curves are different on surface A, two of the most striking features are seen there also: the near equality of the corresponding reactive and non-reactive probabilities and rates, and also the dominance of single-quantum deactivating transitions. Hence, since the features of the dynamics of interest here are common to both surfaces, we will restrict further study to surface B.

The results of the quasi-classical trajectory calculations are presented in fig. 3 for a series of translational energies (energy above the $v = 2$ level). In the figure the final action of the diatomic product (HCl or HCl') is plotted versus the initial vibrational phase of the HCl reagent. The reactive or nonreactive nature of the collision is also indicated. In addition, the duration of the trajectory is plotted.

One can clearly see that the trajectories giving rise to vibrationally nonadiabatic trajectories are localized in the two regions at the boundary between the reactive and nonreactive bands. As the energy decreases, the boundary region between the bands becomes diffuse, much more so for the activating transitions than the deactivating ones.

At the lowest energies, where quantum mechanically no vibrational excitation is possible, the actions versus phase curve appears to be a collection of random points. The near symmetry of the reactive and nonreactive bands about a vertical line drawn through the center of the gap between the bands shows that one could expect nearly equal amounts of reactive and nonreactive products for vibrational deactivation, in agreement with the quantum mechanical results.

The funnel-shaped nature of the action versus phase curves near the boundary between the bands demonstrates the classical nature of the preference for single-quantum deactivations. Multiple quantum deactivations can only occur for a very small range of phases about the center of the gap. One can also see that the time for completion of the trajectory has a minimum at the deactivation gap (due no doubt to the fast nature of the exit process when all energy has been converted to translational energy) and a maximum at the activation gap. The fact that the trajectory time increases much more rapidly for activating collisions than it decreases for deactivating ones, especially at lower energies, suggests that for classically activating collisions the slowness is not a purely kinetic energy effect; the trajectories giving rise to vibrational excitation must be significantly more complex than those leading to relaxation.

4. Discussion and Conclusions

The increase in trajectory time and in the vibrational action of the diatomic product across a gap in the reactivity bands has been observed before by various workers in collisions of ground vibrational state molecules [14, 15]. Attention has seldom been directed to these phenomena in collisions of vibrationally excited molecules, however [16]. Nevertheless, the theory and intuition developed for the ground state case appears to carry over with some modification to the vibrationally excited state case considered here [14].

Pechukas and Pollak [17] have shown that the sharp increase of the final action and trajectory time versus phase plots across the band gaps is due to the existence of "trapped trajectories" that occur when the initial phase is quite close to that of the center of the gap. They have identified three different kinds of trapped trajectories [17], most importantly the first kind, in which the mass point vibrates forever between the two contours whose energy is that of the total energy present, and the second kind, in which the mass point vibrates in a way such that it touches only one of the energetically limiting trajectories. It is clear that motion along the symmetric stretch line would constitute a trapped trajectory of the first kind.

Our goal, then, is to determine what kind of trajectory, which must not be terribly different from a trapped trajectory, gives rise to vibrational deactivation. This trajectory must have the property that it causes the mass particle to "forget" from which arrangement channel it entered if there are to be equal reactive and nonreactive probabilities.

Since the trajectory time associated with vibrational deactivation

is short, this trajectory cannot have that of an especially long-lived complex (one spending a far greater time in the saddle point region of the potential energy surface than a nearby less nonadiabatic trajectory). Examination of a number of trajectories shows that the limiting trapped trajectory for vibrational deexcitation is motion along the symmetric stretch line. In vibrationally deactivating collisions at some time the mass particle, the motion of which in Delves coordinates is equivalent to that of the actual system [the single particle of mass $m_{\text{Cl}} m_{\text{H}}^{\frac{1}{2}} \cdot (2m_{\text{Cl}} + m_{\text{H}})^{-\frac{1}{2}}$], lies along the symmetric stretch line beyond the saddle point, and has its velocity directed along the line towards the saddle point, ($R_{\text{Cl}'-\text{H}} = R_{\text{H}+\text{Cl}} = R^{\ddagger}$). At that time, the trajectory obeys the equations

$$R_{\text{Cl}'-\text{H}} \approx R_{\text{H}-\text{Cl}} > R^{\ddagger} \quad (4a)$$

$$\frac{dR_{\text{Cl}'-\text{H}}}{dt} \approx \frac{dR_{\text{H}-\text{Cl}}}{dt} < 0. \quad (4b)$$

A fairly typical trajectory resulting in substantial vibrational deactivation is shown in fig. 4b. Since this trajectory involves motion essentially along the symmetric stretch line, it means that to a good approximation, the mass particle has forgotten its channel of origin. That this type of trajectory leads to conversion of vibrational energy to translational energy has been observed by Wright et al. [15] in their study of the $\text{H} + \text{H}_2$ reaction. This effect is not observed in adiabatic reactions. A typical vibrationally adiabatic trajectory is shown in fig. 4a.

Examination of trajectories shows that trajectories leading to vibrational activation are in some ways the reverse of those leading to

vibrational deactivation. Early on the trajectory first undergoes near-periodic motion near the saddle point (similar to a trapped trajectory of the second kind). At some time later the mass particle climbs the symmetric stretch line beyond the saddle point with its velocity directed towards dissociation. At lower energies, especially below the quantum mechanical energetic threshold for activation, the trajectory may then become highly complicated, undergoing near-periodic motion characteristic of motions of trapped trajectories of the first kind. For these trajectories roughly equal amounts of reactive and nonreactive products should be obtained. A typical trajectory resulting in vibrational excitation at high energy is shown in fig. 4c.

Three-dimensional trajectories have been calculated for the Cl + HCl system by a number of workers [10,19]. The calculations show competitive rates for reactive and nonreactive deactivations. The uncertainty associated with the assignment of final quantum numbers in quasi-classical trajectory calculations makes a detailed comparison of the state-to-state deactivation rates difficult. The trajectory calculations all indicate that in three dimensions, the dominant pathway for vibrational relaxation is V - R energy transfer [10,19], rather than V - T, as is necessarily the case in collinear collisions.

The fact that the same equality of reactive and nonreactive deactivation rates was obtained on the two potential energy surfaces suggests that this effect is not immensely dependent on the surface used (for a sufficiently high barrier, of course, the reactive probabilities will go to zero at low energies). As this near-equality is not obtained for the H + H₂ reaction (although as the reagent vibrational state increases,

the reactive and nonreactive deactivation rates do approach one another [20]), it seems reasonable that this equality is a mass effect, arising from the small skew angle. We hope to document this in the future.

In a future publication, we will fully discuss the results of classical and quantum calculations on these systems [21].

Acknowledgements

The calculations reported here were performed on the Dreyfus-NSF Theoretical Chemistry Computer (VAX 11/780) which was funded through grants from the Camille and Henry Dreyfus Foundation, the National Science Foundation (Grant No. CHE78-20235), and the Sloan Fund of the California Institute of Technology, and on the IBM 370/158 computer of Ambassador College, Pasadena, California, for which we express our appreciation.

References

- [1] R. N. Porter and L. M. Raff, in: Dynamics of Molecular Collisions, Part B, ed. W. H. Miller (Plenum Press, New York, 1976) pp. 1-52; D. G. Truhlar and J. T. Muckerman, in: Atom-Molecule Collision Theory, ed. R. B. Bernstein (Plenum Press, New York, 1979) pp. 505-565.
- [2] J. C. Polanyi and J. L. Schreiber, in: Physical Chemistry, An Advanced Treatise, Vol. VIA, ed. W. Jost (Academic Press, New York, 1974), Chap. 6; P. J. Kuntz, in: Dynamics of Molecular Collisions, Part B, ed. W. H. Miller (Plenum Press, New York, 1976) pp. 53-120.
- [3] A. Kuppermann, in: Theoretical Chemistry: Advances and Perspectives, Vol. 6A, ed. D. Henderson (Academic Press, New York, 1981) pp. 79-164.
- [4] Some information concerning how the reaction takes place may be obtained by looking at probability densities and streamlines of probability current density that can be calculated from the wavefunctions in quantum mechanical scattering calculations. See, for example, E. A. McCullough, Jr., and R. E. Wyatt, J. Chem. Phys. 54 (1971) 3578; A. Kuppermann, J. T. Adams, and D. G. Truhlar, in: Electronic and Atomic Collisions, Abstracts of Papers of the 8th International Conference on the Physics of Electronic and Atomic Collisions, Belgrade, Yugoslavia, eds. B. C. Čubić and M. V. Kurepa (Institute of Physics, Belgrade, 1973) p. 229; S. L. Latham, J. F. McNutt, R. E. Wyatt, and M. J. Redmon, J. Chem. Phys. 69 (1978) 3740; J. F. McNutt

- and R. E. Wyatt, in: *Potential Energy Surfaces and Dynamics Calculations*, ed. D. G. Truhlar (Plenum Press, New York, 1981) pp. 495-517.
- [5] (a) A. Kuppermann, J. A. Kaye, and J. P. Dwyer, *Chem. Phys. Letters* 75 (1980) 257;
(b) J. A. Kaye and A. Kuppermann, *ibid.* 77 (1981) 573.
(c) J. A. Kaye and A. Kuppermann, *ibid.* 78 (1981) 546.
- [6] (a) G. Hauke, J. Manz, and J. Römelt, *J. Chem. Phys.* 73 (1980) 5040.
(b) J. Römelt, *Chem. Phys. Letters* 74 (1980) 263.
(c) J. Manz and J. Römelt, *ibid.* 76 (1980) 333.
(d) J. Manz and J. Römelt, *ibid.* 77 (1981) 172.
(e) J. Manz and J. Römelt, *ibid.* 81 (1981) 179.
- [7] L. M. Delves, *Nucl. Phys.* 9 (1959) 391; 20 (1960) 275.
- [8] S. Sato, *J. Chem. Phys.* 23 (1955) 592, 2465.
- [9] J. N. L. Connor, W. Jakubetz, J. Manz, and J. C. Whitehead, *J. Chem. Phys.* 72 (1980) 6209.
- [10] I. W. M. Smith, *J. Chem. Soc. Faraday Trans. II* 71 (1975) 1970.
- [11] F. S. Klein, A. Persky, and R. E. Weston, *J. Chem. Phys.* 41 (1964) 1799; F. S. Klein and A. Persky, *ibid.* 59 (1973) 2775.
- [12] P. Botschwina and W. Meyer, *Chem. Phys. Letters* 44 (1976) 449.
- [13] R. D. H. Brown, G. P. Glass, and I. W. M. Smith, *J. Chem. Soc. Faraday Trans II* 71 (1975) 1963. See also M. Kneba and J. Wolfram, *J. Phys. Chem.* 83 (1979) 69 and R. G. MacDonald

- and C. B. Moore, J. Chem. Phys. 73 (1980) 1681, and references therein.
- [14] F. T. Wall, L. A. Hiller, Jr., and J. Mazur, J. Chem. Phys. 29 (1958) 255; J. W. Duff and D. G. Truhlar, Chem. Phys. 4 (1974) 1; Chem. Phys. Letters 40 (1976) 251; J. R. Stine and R. A. Marcus, *ibid.* 29 (1974) 575; R. E. Howard, A. C. Yates, and W. A. Lester, Jr., J. Chem. Phys. 66 (1977) 1960; J. S. Hutchinson and R. E. Wyatt, *ibid.* 70 (1979) 3509.
- [15] (a) J. S. Wright, G. Tan, K. J. Laidler, and J. E. Hulse, Chem. Phys. Letters 30 (1975) 200.
(b) J. S. Wright, K. G. Tan, and K. J. Laidler, J. Chem. Phys. 64 (1976) 970.
(c) J. S. Wright and K. G. Tan, *ibid.* 66 (1977) 104.
(d) K. G. Tan, K. J. Laidler, and J. S. Wright, *ibid.* 67 (1977) 5883.
- [16] N. Sathyamurthy, Chem. Phys. Letters 59 (1978) 95; M. S. Child and K. B. Whaley, Disc. Faraday Soc. 67 (1979) 57; J. C. Gray, G. A. Fraser, and D. G. Truhlar, Chem. Phys. Letters 68 (1979) 359.
- [17] P. Pechukas and E. Pollak, J. Chem. Phys. 67 (1977) 5976.
- [18] E. Pollak and P. Pechukas, J. Chem. Phys. 69 (1978) 1218.
- [19] D. L. Thompson, J. Chem. Phys. 56 (1972) 3570; R. L. Wilkins, *ibid.* 63 (1975) 534.
- [20] J. A. Kaye and A. Kuppermann, unpublished results.
- [21] J. A. Kaye and A. Kuppermann, manuscript in preparation.

Table 1

Parameters and properties of LEPS potential energy surfaces A and B. ^{a)}

	HCl	Cl ₂
β/bohr^{-1}	0.9892	1.0626
R_e/bohr	2.4060	3.7791
D_e/eV	4.6258	2.5169
Δ A	0.138	
B	0.185	
saddle point location/bohr		
A	(1.459, 1.459)	
B	(1.443, 1.443)	
barrier height/(kcal/mole)		
A	6.21	
B	1.89	
HCl zero point energy/eV		
A	0.1838	
B	0.1836	

^{a)} Masses used: $m_{\text{Cl}} = 34.6974 m_{\text{H}}$.

Figure Captions

Figure 1. Cubic spline fit to quantum mechanical probabilities of state-to-state transitions versus reagent translational energy for vibrational deactivation in collinear collisions of $\text{Cl} + \text{HCl}$ ($v = 2$): P_{20}^V (solid line), P_{21}^V (dashed line), P_{20}^R (dotted line), and P_{21}^R (dashed-dotted line). Note expanded vertical scale (full scale corresponds to probability of 0.04).

Figure 2. Arrhenius plots of state-to-state rate constants for vibrational activation in collinear collisions of $\text{Cl} + \text{HCl}$ ($v = 2$). The rate constants were calculated from the quantum mechanical transition probabilities. The lines represent the same transitions as in fig. 1; markers represent the points calculated. k_{20}^V (\circ), k_{21}^V (Δ), h_{20}^R ($+$), k_{21}^R (\times).

Figure 3. Plots of final vibrational action (left ordinate) versus initial phase of reagent HCl ($v = 2$) in collinear collisions of $\text{Cl} + \text{HCl}$ ($v = 2$). In the region in which the curves are smooth, a solid line represents reactive collisions and a dashed line represents nonreactive collisions. In the non-smooth regions, open circles are used to indicate reactive collisions and open squares to indicate nonreactive collisions. The time of the trajectory (the time scale is on the right ordinate) is shown by a dotted line in its smooth region and by closed circles elsewhere. Curves are for translational energies of 0.5 eV (top), 0.3 eV (middle), and 0.1 eV (bottom).

Figure 4. Plots of typical trajectories (dashed-dotted line) superimposed on a contour plot of the potential energy surface (surface B) in Delves mass-weighted coordinate system. Contours are drawn every 0.4 eV from 0.2 to 3.0 eV, measured with respect to the bottom of the

HCl well. An x is drawn at the saddle point. The trajectories were started at $R = 24.75$ bohr in the entrance channel (at the lower right) and terminated in the exit channel (upper right), well past the limits of the plot. Trajectories shown are for a translational energy of 0.3 eV. (a) Vibrationally adiabatic trajectory-initial phase = 0.50 radians, final action = 1.981; (b) vibrational deactivating trajectory-initial phase = 2.9293 radians, final action = -0.115; (c) vibrationally activating trajectory-initial phase = 4.09 radians, final action = 2.821.

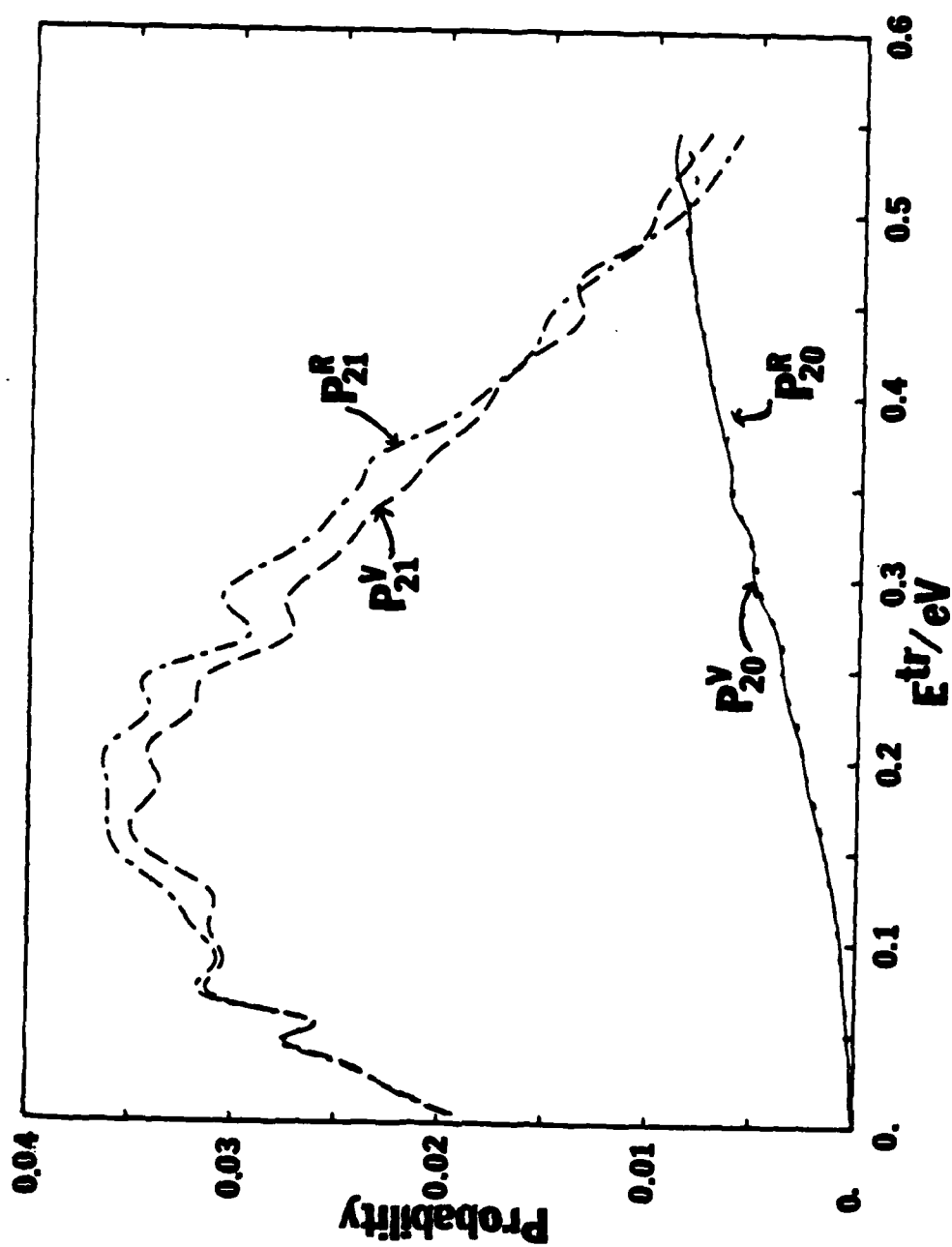


Figure 1

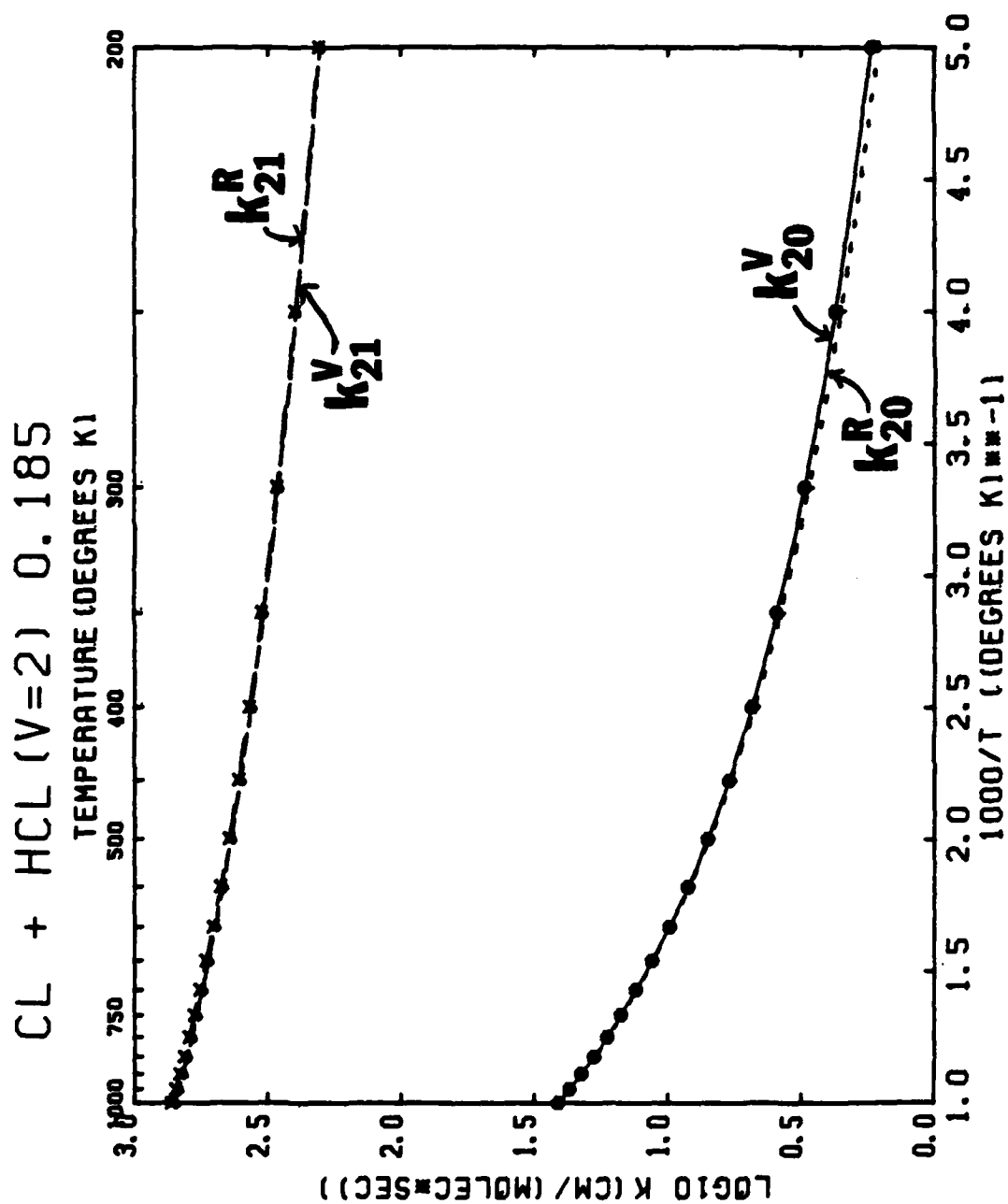


Figure 2

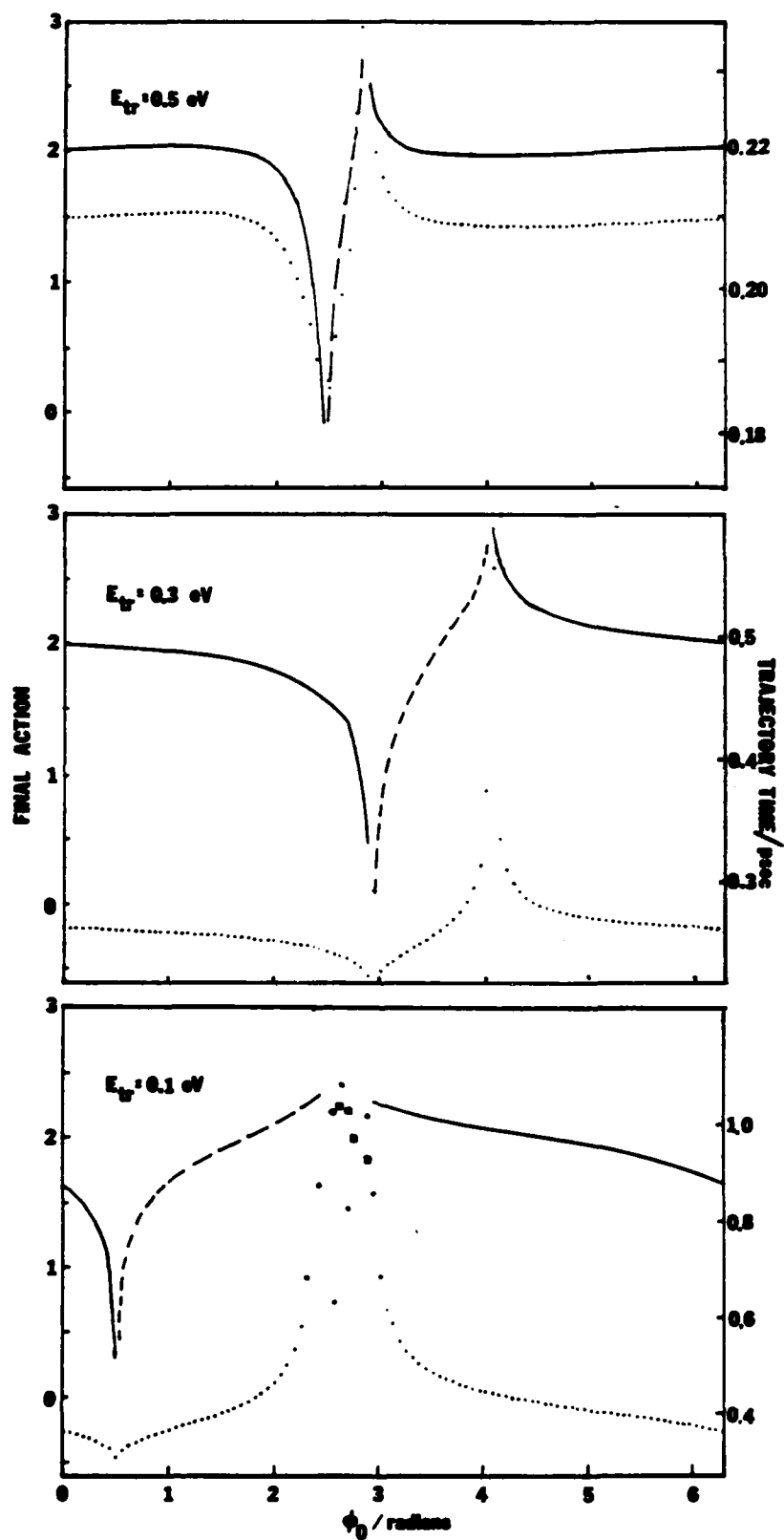


Figure 3

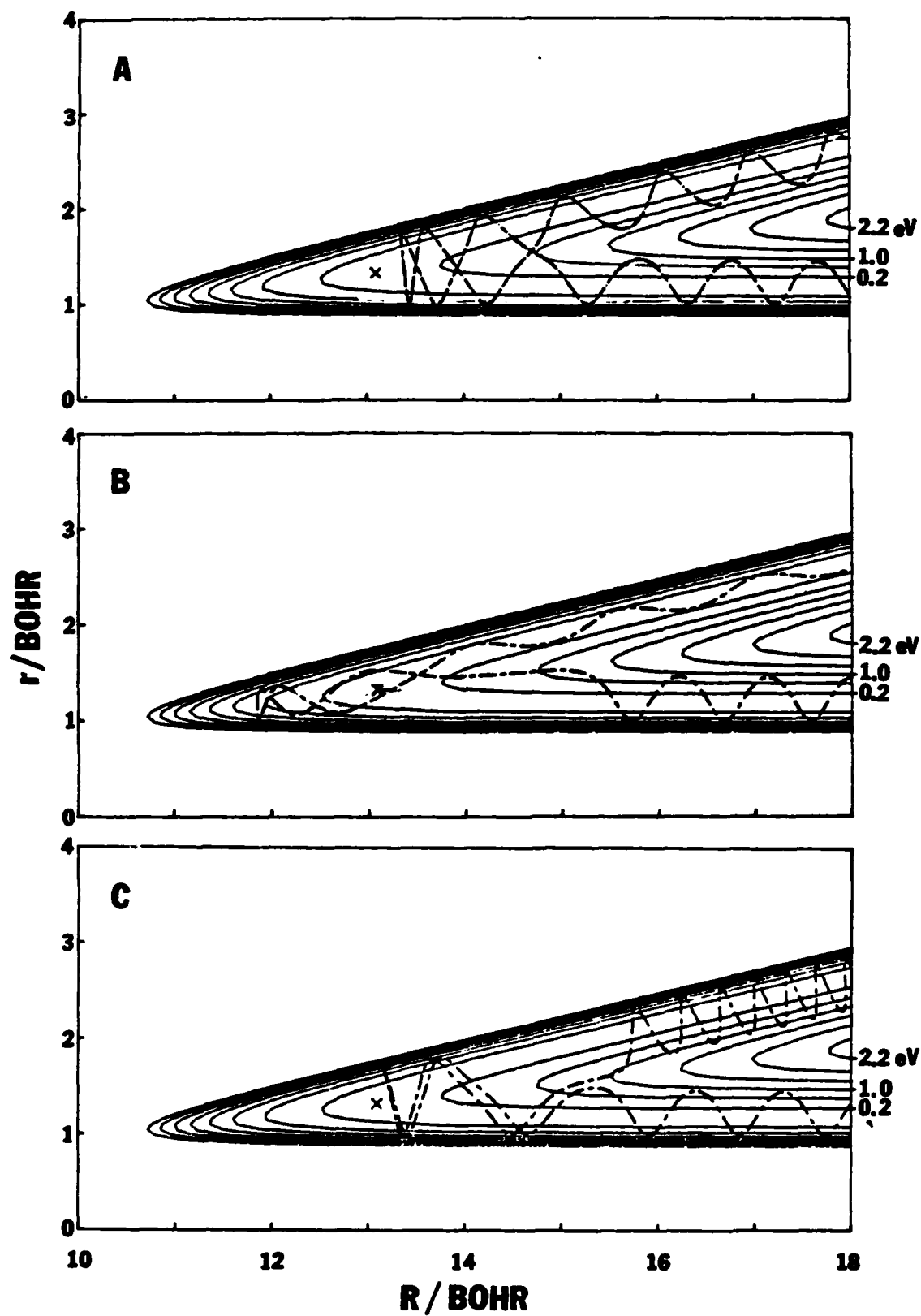
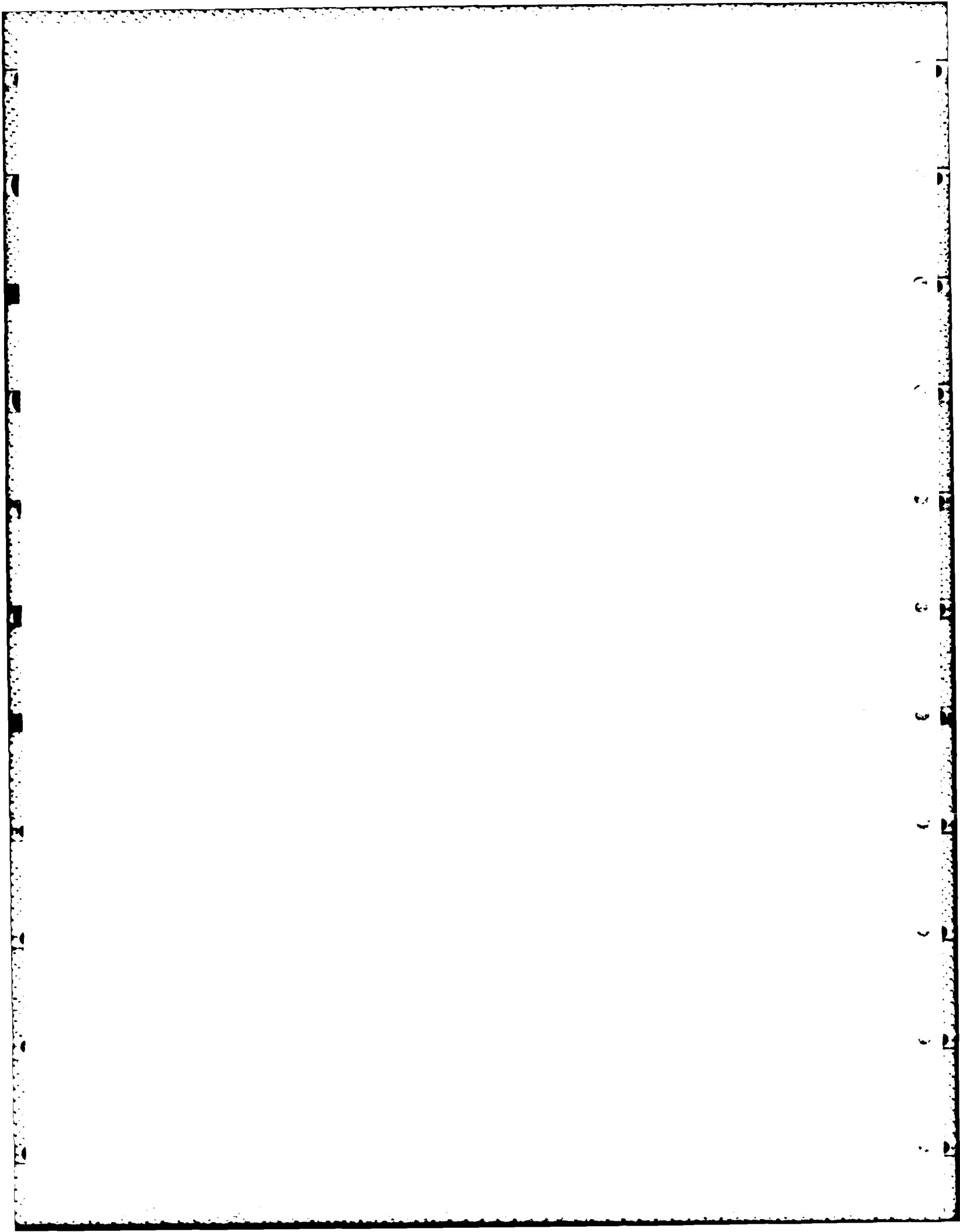


Figure 4



COLLINEAR QUANTUM MECHANICAL PROBABILITIES AND RATE CONSTANTS FOR THE $\text{Br} + \text{HCl}(v = 2, 3, 4)$ REACTION USING HYPERSPHERICAL COORDINATES ^{*†}

Jack A. KAYE [‡] and Aron KUPPERMANN

*Arthur Amos Noyes Laboratory of Chemical Physics [†], California Institute of Technology,
Pasadena, California 91125, USA*

Received 13 August 1982

Calculations of quantum mechanical probabilities and rate constants for the collinear reaction $\text{Br} + \text{HCl}(v = 2, 3, 4) \rightarrow \text{BrH} + \text{Cl}$, $\text{Br} + \text{HCl}(v' < v)$ were performed using hyperspherical coordinates. Removal of vibrationally excited HCl proceeds mainly by reaction to a nearly degenerate HBr state. Processes for which a large change in the internal energy occurs have low probabilities.

1. Introduction

Reactions of halogen atoms (X) with hydrogen halides (HY) of the type



have been the subject of a great deal of experimental and theoretical work [1]. Exothermic reactions of this type produce inverted population distributions of vibrational levels [2] and can thus be used as the pumping step in chemical lasers [3]. The fairly small energy difference between the ground ($^2P_{3/2}$) and first excited ($^2P_{1/2}$) states of the halogen atom allows one to look at the possibility of electronically non-adiabatic processes [4]. Endoergic reactions of this type are known to be greatly accelerated by vibrational excitation of the hydrogen halide reagent [5].

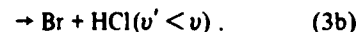
Theoretical treatments of these reactions are more difficult, however. Not only must one have an accurate potential energy surface in order to perform re-

liable scattering calculations, but one must also consider the possibility of electronically nonadiabatic processes. Single potential energy surface quasiclassical trajectory calculations on these systems have usually been able to match experimental product state distributions, but have not had much success in duplicating other experimental results such as isotope effects and the temperature dependence of rate constants [6].

Quantum mechanical treatments of these reactions have been limited because the traditional methods of performing calculations for collinear atom-diatomic molecule collisions [7–10] are not well suited for processes in which a light atom is transferred between two heavy ones. This difficulty has recently been overcome by the development of the collinear hyperspherical coordinates technique [11–19] that allows one to perform reactive scattering calculations efficiently for heavy-light-heavy (HLH) systems. Studies of systems of this type using this method have been applied primarily to exchange reactions of identical atoms (symmetric systems), such as [12,18]



In this work we report the results of calculations on the asymmetric system $\text{Br} + \text{HCl}$ for the processes



^{*} This research was supported in part by a contract (No. F49620-79-C-0187) from the US Air Force Office of Scientific Research.

[†] Presented at the 182nd National Meeting of the American Chemical Society, New York, New York, August 1981.

[‡] Work performed in partial fulfillment of the requirements for the Ph.D. in Chemistry at the California Institute of Technology. Present address: Naval Research Laboratory, Code 4780, Washington, DC 20375, USA.

[†] Contribution No. 6702.

These processes [5,20] and the reverse reaction [21]



have been studied experimentally and in three-dimensional quasi-classical trajectory calculations [5,22,23]. A preliminary account of a collinear quantum mechanical calculation on reaction (4) has been reported previously [24].

In section 2 we briefly discuss the application of the hyperspherical coordinate method to these systems and the surface used. In section 3 we present and discuss the results, and in section 4 we summarize the results and conclusions.

2. Computational method and potential energy surface

We have discussed our hyperspherical coordinate method for symmetric systems previously [11–13], and the modification of the method for asymmetric systems is straightforward. Römelt [19] has also implemented such a modification and applied it to the well-studied system $\text{F} + \text{H}_2$. The basic idea of the method is to express the problem in the polar coordinates ρ , α and to expand the wavefunction in a set of eigenfunctions of the hamiltonian at constant ρ . Two simple changes are involved in going from symmetric to asymmetric systems.

(a) Whereas in symmetric systems the integration of the coupled channel equations can be done for the symmetric and antisymmetric solutions separately, such a decoupling is no longer possible for asymmetric systems.

(b) At large values of ρ , it previously sufficed to project the wavefunction onto a basis set of the eigenfunctions of one diatomic molecule only; two such projections, for HX and HY , are now required.

We have verified the accuracy of our asymmetric hyperspherical coordinates program by performing scattering calculations on the $\text{F} + \text{H}_2$ system on the Muckerman V surface [25], and achieved agreement with previous reaction probability [26] to within 3% or better at energies near the low-energy resonance that occurs in this system. A plot showing probabilities for the reaction $\text{F} + \text{H}_2(\nu=0) \rightarrow \text{FH}(\nu=2) + \text{H}$ obtained by the present and previous methods is shown in fig. 1. The rapid convergence of the hyperspherical coordinate method with respect to the number of basis func-

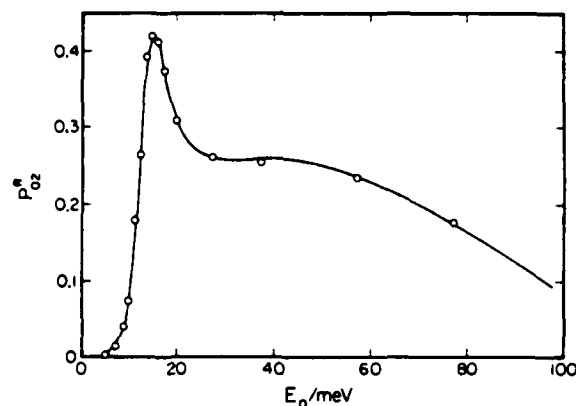


Fig. 1. Probability of the reaction $\text{F} + \text{H}_2(\nu=0) \rightarrow \text{FH}(\nu=2) + \text{H}$ on the Muckerman V surface as a function of reagent translational energy. The solid line depicts results obtained previously; the points represent results obtained with the present hyperspherical coordinate method using up to eight basis functions.

tions observed for the $\text{H} + \text{H}_2$ system [11] is also seen for the $\text{F} + \text{H}_2$ system; with sufficiently frequent changes of basis functions, results converged to $\approx \pm 0.02$ in the low-energy region (up to 0.10 eV translational energy) can be obtained with seven basis functions (five open and two closed, the latter correlating asymptotically to one closed state of each of the H_2 and HF molecules). The hyperspherical distance ρ_{as} at which projection on to the asymptotic diatom eigenfunctions was performed was 10 bohr. Beyond this ρ_{as} , no further improvement in the convergence of the probabilities was obtained.

Twelve to fourteen basis functions were used in all the calculations for the $\text{Br} + \text{HCl}$ system reported in this paper. This is far more than needed in the lowest-energy region. For example, equivalent results were obtained with only eight channels in this low-energy region. Transition probabilities should be accurate to ± 0.002 for nearly all transitions and energies; in many cases they are probably accurate to better than ± 0.001 . The value of ρ_{as} resulting in these accuracies was 26 bohr. The relative error in the reported transition probabilities of the order of 10^{-3} or less was estimated to be $\approx 10\%$. Flux was normally conserved to better than ± 0.001 . Deviation of the scattering matrix from unitarity increased gradually with energy until at the highest energies studied (1.15 eV above the HBr ground state) flux was conserved to ± 0.008 .

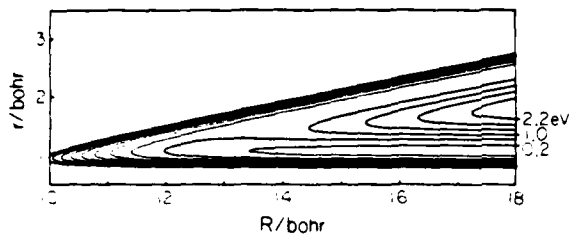


Fig. 2. Equipotential contour plot for the Br + HCl system. The solid curves are the contours and are equally spaced in increments of 0.4 eV from 0.2 to 3.8 eV. The zero of energy is the bottom of the HCl well. The surface is plotted in the Delves mass-scaled cartesian coordinate system.

The potential energy surface used is essentially the same as the one used by Baer [24]. It is a LEPS [27] surface, with all Sato parameters set to 0.154. The Morse oscillator parameters are those of Douglas et al. [5]. The surface has a barrier to exchange of 1 kcal/mole. This surface is not designed to accurately mimic the real one; inadequacies are suggested by the difference between the observed [21] and calculated [24] vibrational product state distribution for reaction (4). A plot of the surface in the Delves mass-scaled cartesian coordinate system [9,11,28] is shown in fig. 2.

3. Results and discussion

A plot of the energy eigenvalues of the basis functions as a function of the hyperspherical coordinate ρ is shown in fig. 3. The eigenvalues for the isolated HCl molecule corresponding to vibrational quantum number $v = 2, 3, 4$ lie very slightly above those for HBr with $v = 0, 1, 2$, respectively. Transition probabilities for reactions (3a) and (3b) are presented as a function of reagent translational energy in fig. 4. Corresponding Arrhenius plots of the thermal rate constants for these transitions are presented in fig. 5.

There are three major features of the dynamics, as may be readily seen by examination of figs. 4 and 5.

(a) The only transition probability that can achieve a substantial value (greater than 0.1) is that which conserves internal energy, i.e. reaction to the energetically nearest HBr state. Thus, $\text{Br} + \text{HCl}(v = 2, 3, 4)$ reacts predominantly to form $\text{HBr}(v = 0, 1, 2)$, respectively. The near-degeneracy of $\text{HCl}(v)$ and $\text{HBr}(v - 2)$ may be seen in fig. 3.

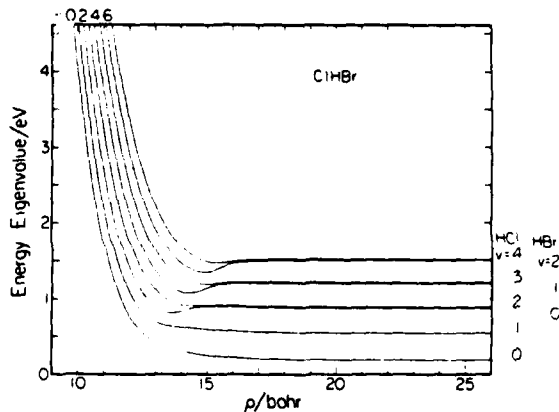
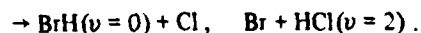
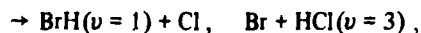


Fig. 3. Basis function eigenvalues $E_n(\rho)$ as a function of the hyperspherical coordinate ρ . Values of n for the curves are shown at the top of the figure. The asymptotic states to which each of the curves correlates is indicated at the right of the figure. The asymptotic eigenvalues for $\text{HCl}(v = 2, 3, 4)$ are almost degenerate with and lie slightly above those for $\text{HBr}(v = 0, 1, 2)$, respectively.

(b) The probabilities of transitions of a given kind (i.e. reactive or non-reactive) decrease in average as the change in vibrational quantum number increases. This may be seen especially clearly by considering the state-to-state rate constants in fig. 5, where the large separation between the curves is indicative of the large difference in rate constants and thus reaction probabilities.

(c) Probabilities and rates of transitions to near-degenerate product states are nearly equal; this may be seen for three pairs of reactions:



The fact that the only calculated transition probability reaching an appreciable value is the one to the nearly degenerate HBr state is in agreement with the results of experimental studies [5] of the removal of $\text{HCl}(v = 2, 3, 4)$ by Br atoms. In particular, those studies have indicated that the greater rapidity of removal of the $v = 3, 4$ levels of HCl than of the $v = 1$

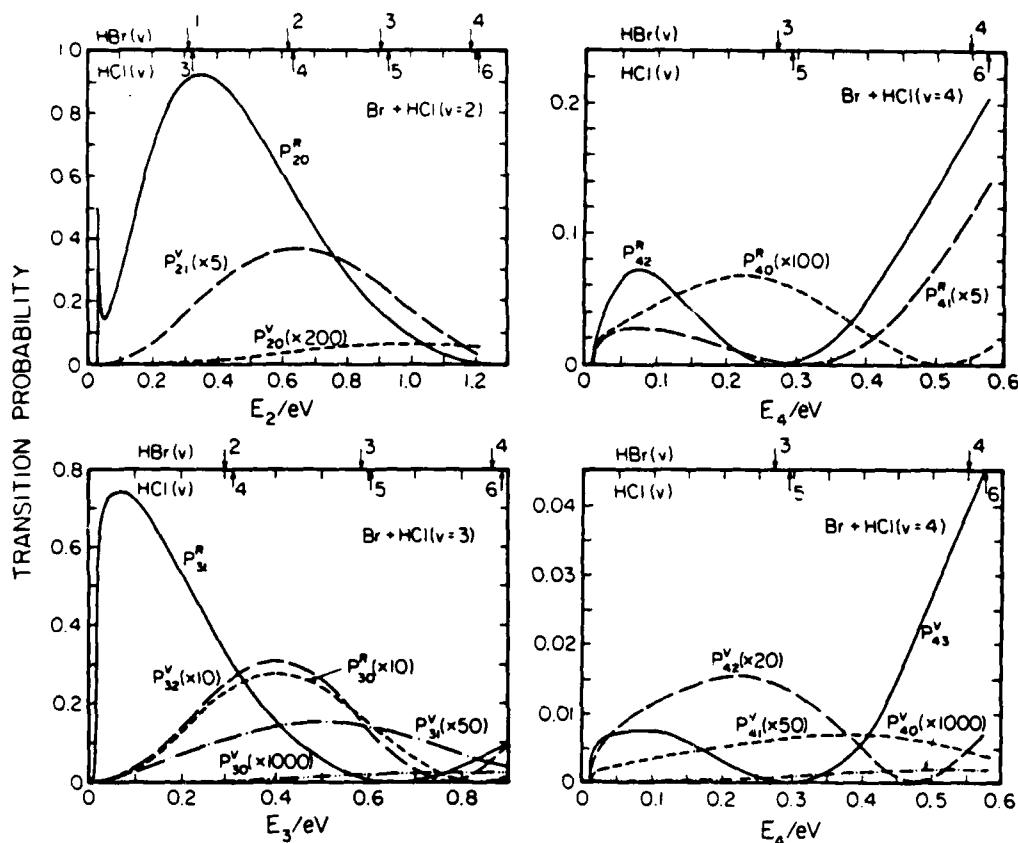


Fig. 4. Transition probabilities P_{uv}^R and P_{uv}^V for the processes $\text{Br} + \text{HCl}(v = 2, 3, 4) \rightarrow \text{HBr}(v') + \text{Cl}$ and $\text{Br} + \text{HCl}(v' < v)$, respectively, as a function of initial relative translational energy.

level must be due to chemical reaction [process (3a)] and not inelastic, non-reactive collisions [process (3b)]. While we have not extended our calculations to energies below that of the $\text{HBr}(v=0)$ level, as is necessary to calculate rates for the deactivation from $\text{HCl}(v=1)$, it seems quite reasonable to expect that that rate would be significantly slower than those shown here. The relative rates of removal of $\text{HCl}(v)$ obtained here do not agree with those determined experimentally, however. We calculate $\text{HCl}(v=3)$ to be removed more rapidly than either $\text{HCl}(v=2)$ or $\text{HCl}(v=4)$; experiments show the rate to increase as v is increased from 1 to 4 [5].

This disagreement is not surprising, however, as it has been seen in symmetric collisions that the probability versus energy curves (rate constants) for the vibrationally adiabatic exchange reaction $\text{X}' + \text{HX}(v)$

$\rightarrow \text{X}'\text{H}(v) + \text{X}$ for $\text{X} = \text{Cl}$ [29] and $\text{X} = \text{I}$ [18,29] vary substantially and irregularly with reagent excitation. In contrast, for the $\text{H} + \text{H}_2$ reaction, the differences between successive probability versus energy curves for vibrationally adiabatic reactions are much more regular [11]. The irregularity observed is most likely due to a combination of the HLH mass combination, the low activation barrier, and the restriction to collinearity. Three-dimensional quasi-classical trajectory calculations performed on a similar but not identical surface [23] show no such irregular behavior, while one-dimensional quasi-classical trajectory calculations performed on this surface show an irregularity roughly similar to that of the quantum results reported here \star .

\star We have performed collinear quasi-classical trajectory calculations for the forward and reverse reaction and will present these results later.

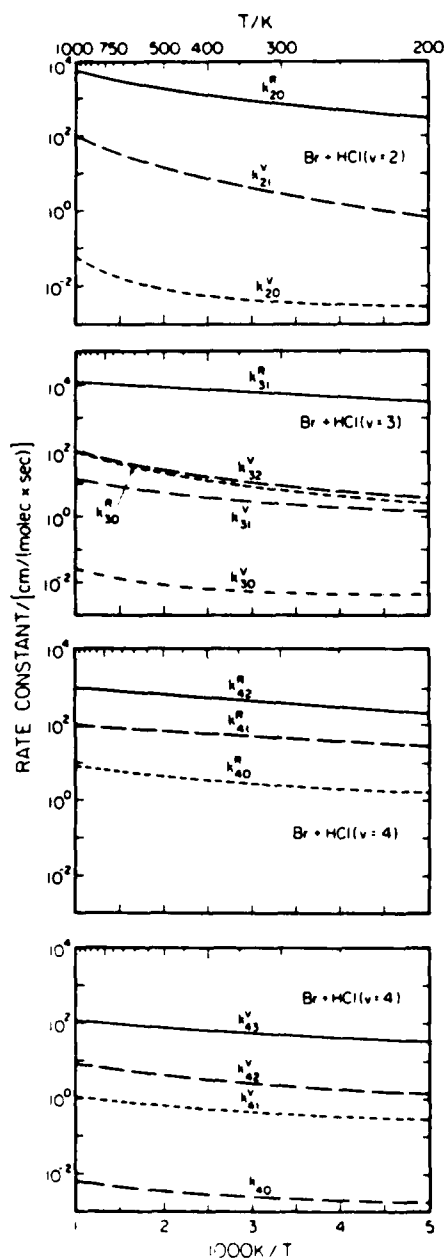


Fig. 5. Arrhenius plots of state-to-state rate constants k_{uv}^R , k_{uv}^V for the processes $\text{Br} + \text{HCl}(v) \rightarrow \text{HBr}(v') + \text{Cl}$ and $\text{Br} + \text{HCl}(v' < v)$. The line conventions correspond to those of fig. 4.

A substantial difference between collinear (theoretical) and experimental results for this system is quite reasonable in the light of experimental results on vari-

ous exoergic $\text{X} + \text{HY}$ reactions, which suggest that, at least at low energies, the reaction proceeds by attack of the X atom on the Y end of the HY molecule, with subsequent H atom migration and HX bond formation as the HY bond breaks [21,30].

The low probabilities of multi-quantum transitions in non-reactive collisions and of reactive transitions to all but the near-degenerate product level can be understood classically, as can the near equality of the probabilities of reactive and nonreactive transitions to near degenerate states. This has been demonstrated in studies of the $\text{Cl} + \text{HCl}$ reaction [31]. Transitions involving a large change in vibrational action (analogous to vibrational quantum number) occur at the boundary between reactivity bands [32] in plots of the final action versus initial vibrational phase. Near the boundary, the final action varies rapidly with initial vibrational phase, forming a cusp about some central boundary phase [31]. Transitions involving a large change in quantum number can only occur for collisions in a very limited range of initial phases and are thus unlikely. In symmetric systems such as $\text{Cl} + \text{HCl}$, these transitions involved motion essentially along the symmetric stretch line. To a first approximation, then, the system has "forgotten" in which channel it began its motion, giving rise to the near equivalence of reactive and non-reactive transitions to degenerate energy levels.

One must take great care in relating the results obtained here to experimental ones. The collinearity restriction is undoubtedly a severe one and can be expected to lead to qualitatively incorrect results. The surface used was chosen mainly for its simplicity and, although it displays the correct energetics of the system, it need not otherwise bear a close similarity to the correct one. Indeed, Smith [23] performed three-dimensional quasi-classical trajectory calculations on a related potential energy surface (LEPS with Sato parameters of 0.17) and could not get good agreement with experimental results. Finally, one must consider the possibility of collisions involving more than one electronic potential energy surface. Their possible importance has been considered previously, but the results are inconclusive.

4. Conclusions

We have shown that the hyperspherical coordinate

method is well-suited to the study of reaction (1) and have applied it to the $\text{Br} + \text{HCl}(v = 2, 3, 4)$ system. The major features of the dynamics include the dominance of the removal of vibrationally excited HCl by reaction to the near-degenerate HBr level, the small probability of transitions involving a large change in internal energy, and the near equivalence of reactive and nonreactive processes to near-degenerate HCl and HBr levels. Because of the restriction to collinear motion, uncertainty in the potential energy surface, and the possible role of collisions involving more than one electronic potential energy surface, these calculations do not have predictive quantitative value, and comparison with experiment should be done very cautiously.

Acknowledgement

The calculations reported were performed on the Dreyfus-NSF theoretical Chemistry Computer which was funded through grants from the Camille and Henry Dreyfus Foundation, the National Science Foundation (Grant No. CHE78-20235), and the Sloan Fund of the California Institute of Technology, and on the IBM 370/158 computer of Ambassador College, Pasadena, California, for which we express our appreciation.

References

- [1] M.R. Levy, *Progr. React. Kinetics* 10 (1979) 1.
- [2] K. Tamagake, D.W. Setser and J.P. Sung, *J. Chem. Phys.* 73 (1980) 2203; N.B.H. Jonathan, P.V. Sellers and A.J. Stace, *Mol. Phys.* 43 (1981) 215.
- [3] J.R. Airey, *J. Chem. Phys.* 52 (1970) 156.
- [4] J.W. Hepburn, K. Liu, R.G. Macdonald, F.J. Northrup and J.C. Polanyi, *J. Chem. Phys.* 75 (1981) 3353.
- [5] D.J. Douglas, J.C. Polanyi and J.J. Sloan, *J. Chem. Phys.* 59 (1973) 6679; *Chem. Phys.* 13 (1976) 15.
- [6] C.A. Parr, J.C. Polanyi and W.H. Wong, *J. Chem. Phys.* 58 (1973) 5.
- [7] A. Kuppermann, in: *Proceedings of the Conference on Potential Energy Surfaces in Chemistry*, ed. W.A. Lester (IBM Research Laboratory, San Jose, 1971) pp. 121-124.
- [8] A. Kuppermann, in: *Proceedings of the 7th International Conference on the Physics of Electronic and Atomic Collisions* (North-Holland, Amsterdam, 1971) pp. 3, 4.
- [9] A. Kuppermann, in: *Theoretical chemistry, theory of scattering: papers in honor of Henry Eyring*, Vol. 6, Part A, ed. D. Henderson (Academic Press, New York, 1981) pp. 79-164.
- [10] C.C. Rankin and J.C. Light, *J. Chem. Phys.* 51 (1969) 1701; G. Miller and J.C. Light, *J. Chem. Phys.* 54 (1971) 1635, 1643.
- [11] A. Kuppermann, J.A. Kaye and J.P. Dwyer, *Chem. Phys. Letters* 74 (1980) 257; J.P. Dwyer, *Quantum Mechanical Studies of Molecular Scattering*, Ph.D. Thesis, California Institute of Technology (1977).
- [12] J.A. Kaye and A. Kuppermann, *Chem. Phys. Letters* 77 (1981) 573.
- [13] J.A. Kaye and A. Kuppermann, *Chem. Phys. Letters* 78 (1981) 546.
- [14] G. Hauke, J. Manz and J. Röhmelt, *J. Chem. Phys.* 73 (1980) 5040.
- [15] J. Röhmelt, *Chem. Phys. Letters* 74 (1980) 263.
- [16] J. Manz and J. Röhmelt, *Chem. Phys. Letters* 76 (1980) 337.
- [17] J. Manz and J. Röhmelt, *Chem. Phys. Letters* 77 (1981) 172.
- [18] J. Manz and J. Röhmelt, *Chem. Phys. Letters* 81 (1981) 179.
- [19] J. Röhmelt, *Chem. Phys. Letters* 87 (1982) 259.
- [20] D. Arnoldi, K. Kaufmann and J. Wolfrum, *Phys. Rev. Letters* 34 (1975) 1597; D. Arnoldi and J. Wolfrum, *Ber. Bunsenges. Physik. Chem.* 80 (1976) 892; R.G. Macdonald and C.B. Moore, *J. Chem. Phys.* 73 (1980) 1681.
- [21] D.H. Maylotte, J.C. Polanyi and K.B. Woodall, *J. Chem. Phys.* 57 (1972) 1547; F.J. Wodarczyk and C.B. Moore, *Chem. Phys. Letters* 26 (1974) 484; C.-C. Mei and C.B. Moore, *J. Chem. Phys.* 67 (1977) 3936.
- [22] J.C. Brown, H.E. Bass and D.L. Thompson, *J. Phys. Chem.* 81 (1977) 479.
- [23] I.W.M. Smith, *Chem. Phys.* 20 (1977) 437.
- [24] M. Baer, *J. Chem. Phys.* 62 (1975) 305.
- [25] J.T. Muckerman, in: *Theoretical chemistry, theory of scattering: papers in honor of Henry Eyring*, Vol. 6, Part A, ed. D. Henderson (Academic Press, New York, 1981) pp. 1-77.
- [26] G.C. Schatz, J.M. Bowman and A. Kuppermann, *J. Chem. Phys.* 63 (1975) 674.
- [27] S. Sato, *J. Chem. Phys.* 23 (1955) 592, 2465.
- [28] A. Kuppermann, G.C. Schatz and M. Baer, *J. Chem. Phys.* 65 (1976) 4596.
- [29] J.A. Kaye and A. Kuppermann, unpublished results.
- [30] C.-C. Mei and C.B. Moore, *J. Chem. Phys.* 70 (1979) 1759; E. Wurzberg and P.L. Houston, *J. Chem. Phys.* 72 (1980) 5915.

- [31] J.A. Kaye and A. Kuppermann, manuscript in preparation;
J.A. Kaye, Ph.D. Thesis, California Institute of Technology (1982).

- [32] J.S. Wright, G. Tan, K.J. Laidler and J.E. Hulse, Chem. Phys. Letters 30 (1975) 200;
J.S. Wright, K.G. Tan and K.J. Laidler, J. Chem. Phys. 64 (1976) 970;
J.S. Wright and K.G. Tan, J. Chem. Phys. 66 (1977) 104;
K.G. Tan, K.J. Laidler and J.S. Wright, J. Chem. Phys. 67 (1977) 5883.

HYPERSPHERICAL COORDINATES IN COLLINEAR ATOM-DIATOMIC
MOLECULE COLLISIONS: CONVERGENCE PROPERTIES^{a)}

Jack A. KAYE^{b)}, Aron KUPPERMANN, and John P. DWYER^{c)}

Arthur Amos Noyes Laboratory of Chemical Physics^{d)}

California Institute of Technology, Pasadena, California 91125, USA

(Received

)

The hyperspherical coordinates method for studying the collinear reactions of atoms and diatomic molecules is presented in some detail. We apply the method to the low energy $H + H_2$ and $F + H_2$ reactions, and focus on the behavior of the reaction probabilities and scattering matrix element phases with the number of basis functions and the projection distance (essentially termination point of integration). For $H + H_2$ probabilities and phases converge quite rapidly with the number of basis functions; the convergence of $F + H_2$ is less rapid. In $H + H_2$ one must integrate to $\gtrsim 10$ bohr to get nearly converged absolute phases which agree well with those obtained from another method; relative phases are obtained accurately at much smaller ρ . The phases for $F + H_2$ appear to be converging (slowly) with projection distance, but not to the values obtained from another method.

a) This work was supported in part by a contract (No. F49629-79-C-0187) from the Air Force Office of Scientific Research.

b) Work performed in partial fulfillment of the requirements for the Ph.D. degree in Chemistry at the California Institute of Technology.

c) Present address: Supreme Court of the United States, Washington, D.C. 20543.

d) Contribution No.

1. Introduction

Quantum mechanical studies of chemical reactions have provided substantial insight into the dynamics of chemical reactions, particularly reactions of systems containing hydrogen atoms, in which quantum mechanical effects are expected to play a major role.¹⁻³ Exact three-dimensional quantum mechanical calculations are quite difficult to perform, however, and have been limited to the reaction



at low energy.⁴⁻⁶ Approximate three-dimensional quantum mechanical calculations have been performed on both this system⁷ and the reaction⁸



A far more tractable problem is that of a collinear collision of an atom and a diatomic molecule. In such a collision, the atoms are constrained to lie on a single straight line, which vastly simplifies the formalism and reduces the numerical effort in solving the appropriate Schrödinger equation compared to the three-dimensional case.¹⁻³

A number of methods have been developed to study collinear atom-diatom molecule collisions within the framework of quantum mechanics, including coupled channel methods based on natural collision coordinates⁹ and on the hybrid Cartesian coordinate/modified polar coordinate method of Kuppermann.¹⁰ In addition, the two-dimensional partial differential equation has been solved directly by finite element methods (without expansion of the wavefunction in terms of some orthonormal basis set).¹¹

While the coupled channel techniques have been used quite successfully for a number of chemical reactions, they cannot be used to study two interesting classes of reaction: Heavy-light-heavy (H-L-H) reactions in which a light atom is transferred between two heavy ones, and collision induced dissociation: (CID).



in which the reagent molecule is dissociated by the collision with the incident atom. H-L-H reactions are difficult to treat because the large amounts of skewing introduced into the potential energy surface by conversion to an appropriate set of mass-scaled coordinates causes an undesirably large number of basis functions to be needed. For example, Baer¹² reported needing 40 states in his calculations on the reaction



CID has been difficult to treat because the previous coupled channel methods have expanded the wavefunction in terms of a basis set which is zero in the dissociative ($A + B + C$) region of the potential energy surface. Quantum mechanical studies of CID have been performed in non-reactive systems, in which chemical reaction of the type



does not compete with CID¹³ (process 3). The finite element method mentioned earlier has been applied to CID in non-reactive systems.¹⁴ The first successful treatment of CID in reactive systems was the wave-packet approach of Kulander, who solved the time-dependent

Schrödinger equation for the collision.¹⁵

We have recently shown that collinear atom-diatomic molecule collisions can be studied easily and efficiently by the methods of hyperspherical coordinates,¹⁶ and that this method can be applied without difficulty to both the H-L-H¹⁷ and CID¹⁸ systems which have previously defied easy treatment. A similar approach has been developed by Manz *et al.*^{19,20} and applied to the H-L-H^{21,22} and CID²³ problem. Our work¹⁶⁻¹⁸ has shown that not only is the hyperspherical coordinates method desirable because of its ability to treat heretofore difficult problems, but that for certain problems which can be treated by the previous methods, fewer basis functions are needed when using hyperspherical coordinates.

In this paper we will review the formalism of the hyperspherical coordinates method, emphasizing those aspects of the method which differ from the treatment of Manz *et al.* We will then present results (reaction probabilities and scattering matrix element phases) for reactions 1 and 2 and, in particular, how these results depend on certain aspects of the numerical procedures. Finally, we will give an assessment of the method in light of the results obtained.

2. Theory

In the hyperspherical coordinates approach to collinear atom-diatomic molecule collisions, the two independent coordinates are the polar coordinates ρ, α , which are related to the usual Delves²⁴ coordinates R, r by the transformation

$$\rho^2 = (R_\alpha^2 + r_\alpha^2) = (R_\gamma^2 + r_\gamma^2) \quad (6a)$$

$$\alpha = \tan^{-1}(r_\alpha/R_\gamma), \quad (6b)$$

where the indices α and γ refer to the $A + BC$ and $AB + C$ arrangement channels, respectively. The Delves coordinates R_α, r_α are related to the r'_α , the distance between the two atoms in the bound molecular pair, and R'_α , the distance from the free atom to the center of mass of the diatomic molecule by the relationship

$$R_\alpha = a R'_\alpha \quad (7a)$$

$$r_\alpha = a^{-1} r'_\alpha \quad (7b)$$

where

$$a = \left(\frac{\mu_{\alpha, \beta \gamma}}{\mu_{\beta \gamma}} \right)^{\frac{1}{4}}, \quad (8)$$

where μ represents the reduced mass defined in the usual way. Similar expressions to (7) hold for R_γ and r_γ with the roles of α and γ in Eq. 8 reversed.

In Delves coordinates, the hamiltonian for nuclear motion is given by

$$H = -\frac{\hbar^2}{2\mu} \left[\frac{\partial^2}{\partial R_\lambda^2} + \frac{\partial^2}{\partial r_\lambda^2} \right] + V_\lambda(R_\lambda, r_\lambda); \quad \lambda = \alpha, \gamma \quad (9)$$

where

$$\mu = [m_\alpha m_\beta m_\gamma / M]^{\frac{1}{2}} \quad (10a)$$

where

$$M = m_{\alpha} + m_{\beta} + m_{\gamma}$$

is a reduced mass and is independent of arrangement channel.

$V_{\lambda}(R_{\lambda}, r_{\lambda})$ is the electronically adiabatic potential energy surface for the triatomic system in λ coordinates.

In hyperspherical coordinates, the hamiltonian becomes

$$H(\rho, \alpha) = -\frac{\hbar^2}{2\mu} \left[\frac{\partial^2}{\partial \rho^2} + \frac{1}{\rho} \frac{\partial}{\partial \rho} + \frac{1}{\rho^2} \frac{\partial^2}{\partial \alpha^2} \right] + V(\alpha, \rho). \quad (11)$$

We desire a set of independent solutions $\{\psi^n(\rho, \alpha)\}$ to the Schrödinger equation

$$H(\rho, \alpha) \psi^n(\rho, \alpha) = E \psi^n(\rho, \alpha). \quad (12)$$

To solve this equation we proceed to expand the wavefunction $\psi^n(\rho, \alpha)$ in terms of a set of orthonormal eigenfunctions $\{\phi_n(\alpha; \bar{\rho})\}$ of the potential along the line $\rho = \bar{\rho}$

$$\psi^n(\rho, \alpha) = \rho^{-\frac{1}{2}} \sum_{n'=0}^N g_{n'}^n(\rho; \bar{\rho}) \phi_{n'}(\alpha; \bar{\rho}), \quad (13)$$

where the $\rho^{-\frac{1}{2}}$ term is included to remove the first derivative term seen in eq. (11) from the hamiltonian, and N is the number of states included in the calculation. Because the potential $V(\rho, \alpha)$ becomes infinite at $\alpha = 0$ and $\alpha = \alpha_{\max} = \tan^{-1}(m_{\beta} M / m_{\alpha} m_{\gamma})^{\frac{1}{2}}$, (these correspond to the interatomic distances R_{BC} and R_{AB} being zero, respectively) the eigenfunctions $\phi_{n'}(\alpha; \bar{\rho})$ satisfy the boundary conditions

$$\phi_{n'}(0; \bar{\rho}) = \phi_{n'}(\alpha_{\max}; \bar{\rho}) = 0 \quad (14)$$

and the differential equation

$$-\frac{\hbar^2}{2\mu\bar{\rho}^2} \frac{\partial^2 \phi_{n'}}{\partial \alpha^2}(\alpha; \bar{\rho}) + V(\alpha, \bar{\rho}) \phi_n(\alpha, \rho) = E_n \phi_n(\alpha, \rho). \quad (15)$$

As a result of these boundary conditions, this set of eigenfunctions is infinite and discrete. It is this property of the basis set that allows one to treat CID with no artificial "discretization of the continuum", as the basis set is already discrete, even at energies above dissociation. Of course, we use only a finite number (N) of these basis functions. These are calculated numerically by a finite difference procedure.²⁵

The differential equation to be solved then is, in matrix form,

$$-\frac{\hbar^2}{2\mu} \frac{d^2 \underline{g}}{d\rho^2}(\rho; \bar{\rho}) + \underline{W}(\rho; \bar{\rho}) \underline{g}(\rho; \bar{\rho}) = \underline{E}(\rho; \bar{\rho}) \underline{g}(\rho; \bar{\rho}), \quad (16)$$

where

$$W_{nn'}^n(\rho; \bar{\rho}) = \langle n | V(\alpha; \rho) - (\bar{\rho}^2/\rho^2) V(\alpha, \bar{\rho}) | n' \rangle \quad (17a)$$

$$E_{nn'}^n(\rho; \bar{\rho}) = [E + \hbar^2/8\mu\rho^2 - E_n(\bar{\rho})] \delta_{nn'} \quad (17b)$$

where $|n'\rangle = \phi_{n'}(\alpha; \bar{\rho})$ and the angular brackets represent integration over the angle α , and $E_n(\bar{\rho})$ is the eigenvalue associated with the basis function $\phi_{n'}(\alpha; \bar{\rho})$.

Integration of the eq. (16) begins from some value of $\rho = \rho_0$ which is sufficiently small that all the eigenvalues of the eigenvectors $\phi_n(\alpha; \rho_0)$ are sufficiently greater than the total energy E of the collision. In this case we may assume the following initial conditions:

$$\underline{\underline{g}}(\rho_0; \rho_0) = \underline{\underline{0}} \quad (18a)$$

$$\underline{\underline{g}}(\rho_0; \rho_0) = \underline{\underline{1}}. \quad (18b)$$

Given these initial conditions, eq. (16) is numerically integrated by any convenient procedure (we have chosen to use the method of Gordon)²⁶. Eq. (16) is formulated in the diabatic representation. One can formulate the problem in the adiabatic representation, in which the basis functions vary continuously with ρ ; in that case an equation very different from (16) is developed; we have derived these equations in the adiabatic representation elsewhere.²⁷

Two points concerning the numerical integration should be mentioned. First, since closed channels [states whose eigenvalue $E_n(\rho)$ is greater than the total collision energy E] are normally included in the calculation (except in calculations of CID at large ρ , when all states are open), one must prevent the exponential growth associated with the closed channels. This is particularly severe in the hyper-spherical coordinates approach at small ρ , when all channels are closed. This growth is prevented by the reorthogonalization procedure of Riley and Kuppermann.²⁸ Second, since we are working in a diabatic representation, we must modify the radial wavefunction $\underline{\underline{g}}$ when changing basis functions in order to maintain continuity of $\psi^n(\rho; \alpha)$ and its derivative $\psi'^n(\rho, \alpha)$ across the boundary. This is accomplished by the transformation

$$\underline{\underline{g}}(\rho; \bar{\rho}_K) = \underline{\underline{O}} \underline{\underline{g}}(\rho; \bar{\rho}_K) \quad (19a)$$

$$g'(\rho'; \bar{\rho}_K) = O' g'(\rho; \bar{\rho}_K) \quad (19b)$$

where the overlap matrix \underline{O} is defined by the expression

$$O_{n'n}^n = \langle \phi_{n'}(\rho; \bar{\rho}_{k+1}) | \phi_n(\rho; \bar{\rho}_k) \rangle. \quad (20)$$

Ideally \underline{O} should be an orthogonal matrix; deviations from orthogonality which will produce a loss of flux, are produced by use of a finite basis set.

At large values of ρ , at which the regions of the potential energy surface corresponding to bound AB and BC diatomic molecules are localized to small and large α , respectively, we may project the bound wave function $\psi^n(\rho, \alpha)$ onto basis functions appropriate to the diatomic molecules. These basis functions $\{\chi^n(r_\lambda; \bar{R}_\lambda)\}$ are solutions of the differential equation

$$-\frac{\hbar^2}{2\mu} \frac{d^2 \chi_n^\lambda}{dr_\lambda^2}(r_\lambda; \bar{R}_\lambda) + V_\lambda(r_\lambda, \bar{R}_\lambda) \chi_n^\lambda(r_\lambda; \bar{R}_\lambda) = E_n(\bar{R}_\lambda) \chi_n^\lambda(r_\lambda; \bar{R}_\lambda). \quad (21)$$

In terms of this basis set, the wavefunction ψ^n may be written

$$\psi^n = \rho^{-\frac{1}{2}} \sum_{n'} g_{n'}^n(\rho; \bar{\rho}) \phi_{n'}(\alpha; \bar{\rho}) = \sum_{n''} h_{n''}^n(r_\lambda; \bar{R}_\lambda) \chi_{n''}^\lambda(r_\lambda; \bar{R}_\lambda) \quad (22)$$

The matrix elements $h_{n''}^n$ are evaluated from eq. (22) by taking advantage of the orthogonality of the $\{\chi_n^\lambda(r_\lambda; \bar{R}_\lambda)\}$ and assuming that the basis sets $\{\phi\}$ and $\{\chi\}$ are orthogonal. This is a very good approximation when only bound states are considered; it is less good when considering continuum states. The $h_{n''}^n$ are obtained from the expression

$$h_{n''}^n = \int_{r_\lambda^{\min}}^{r_\lambda^{\max}} \chi_{n''}^\lambda(r_\lambda; \bar{R}_\lambda) e^{-\frac{1}{2}} \sum_{n'} g_{n'}^n(\rho; \bar{\rho}) \phi_{n'}(\alpha; \bar{\rho}) dr_\lambda \quad (23)$$

where ρ , r_λ , and R_λ are related by eqs. 6.

We have discussed elsewhere²⁷ the methods by which a \underline{g} suitable for use in eq. (23) is generated (one must correct for reorthogonalizations and renormalizations by the Gordon integrator). In many cases the width of the channel $r_\lambda^{\min} < r_\lambda < r_\lambda^{\max}$ is sufficiently large that one needs to use more than one polar coordinate basis set $\phi_n(\alpha; \bar{\rho}_\kappa)$ in order to accurately represent the wavefunction $\psi^n(\rho, \alpha)$. In that case, the integral in eq. (23) must be broken up into m parts, where m is the number of basis sets used in the integration from ρ_{\min} to ρ_{\max} in polar coordinates, where

$$\rho_{\min}^2 = \bar{R}_\lambda^2 + (r_\lambda^{\min})^2 \quad (24a)$$

$$\rho_{\max}^2 = \bar{R}_\lambda^2 + (r_\lambda^{\max})^2. \quad (24b)$$

The new form of eq. (23) is

$$h_{n''}^n(R_\lambda; \bar{R}_\lambda) = \sum_\kappa \int_{(r_\lambda^{\min})_\kappa}^{(r_\lambda^{\max})_\kappa} \chi_{n''}^\lambda(r_\lambda; \bar{R}_\lambda) \rho^{-\frac{1}{2}} \sum_m g_{n'}^n(\rho; \bar{\rho}_\kappa) \phi_{n'}(\alpha; \bar{\rho}_\kappa) dr_\lambda \quad (25)$$

where r_λ^{\min} and r_λ^{\max} now depend on the index κ . Note that the overlap matrix defined in eqs. (19) and (20) above insures that the integrand in eq. (25) is continuous across the boundaries between basis sets.

An equation similar to (23) (or 25) is needed for the derivative \underline{h}' of the matrix \underline{h} . This is obtained by differentiating eq. 23 with respect to R_λ ; the result is

$$\begin{aligned}
 (h_{n''}^n)'(R_\lambda; \bar{R}_\lambda) = & \int_{r_\lambda^{\min}}^{r_\lambda^{\max}} \chi_{n''}^\lambda(r_\lambda; \bar{R}_\lambda) \left\{ -\frac{1}{2} \rho^{-\frac{3}{2}} \sum_{n'} g_{n'}^n(\rho; \bar{\rho}) \phi_{n'}(\alpha; \bar{\rho}) \right. \\
 & \left. + \sum_{n'} \rho^{-\frac{1}{2}} \frac{dg_{n'}^n}{d\rho}(\rho; \bar{\rho}) \left(\frac{\partial \rho}{\partial R_\lambda} \right) \phi_{n'}(\alpha; \bar{\rho}) + \sum_{n'} \rho^{-\frac{1}{2}} g_{n'}^n(\rho; \bar{\rho}) \frac{d\phi_{n'}(\alpha; \bar{\rho})}{d\alpha} \left(\frac{\partial \alpha}{\partial R_\lambda} \right) \right\} dr_\lambda
 \end{aligned}
 \tag{26}$$

When more than one basis set is used in the projection region, the integral in eq. (26) may be simply broken up into portions as in eq. (25). The matrices \underline{h} and \underline{h}' are used in the asymptotic analysis and calculation of the \underline{R} , \underline{S} , and $\underline{\rho}$ matrices by the usual procedure.^{3, 29}

When including "continuum" states, that is those whose asymptotic eigenvalues are greater than the dissociation energy of the diatomic molecules, the continuum states are treated differently from the bound states. This case is described in detail elsewhere.

In symmetric collisions (where atom C is identical to atom A), the potential energy function $V(\alpha, \rho)$ is symmetric about the line $\alpha = \alpha_{\max}/2$, and one can separately integrate symmetric and anti-symmetric eigenfunctions, as there is no coupling between these two sets of eigenfunctions. One could then project onto symmetric and anti-symmetric linear combinations of the diatomic molecule basis functions $\chi_n^\lambda(r_\lambda; \bar{R}_\lambda)$ and evaluate symmetric and antisymmetric scattering matrices could be evaluated and then combined to get reactive and non-reactive ones. Instead, we have projected separately onto bound states in each channel and evaluated a scattering matrix only once. We note that Manz *et al.*¹⁹⁻²³ perform no such projection, using instead their polar coordinate radial wavefunctions (the equivalent of

our g) directly in their asymptotic analysis.

3. Results

We have extensively tested the hyperspherical coordinate method on reactions 1 and 2 on the Porter-Karpplus³⁰ and Muckerman V^{31} surfaces respectively. Calculations on these systems have been performed previously in this laboratory^{32, 33-36} and we compare our results with these previous results. A number of other workers have performed calculations on reactions 1 and 2 also (referred to in refs. 1 and 2). The quantities on which we will focus our attention are certain state-to-state reaction probabilities (P_{00}^R for the $H + H_2$ reaction; P_{02}^R (for the $F + H_2$ reaction) and scattering matrix element phases (ϕ_{00}^R for the $H + H_2$ reaction; ϕ_{02}^R for the $F + H_2$ reaction). We note that scattering matrix element phases are determined only modulo 2π , and we make no effort to assign absolute values to any of the phases. We will examine these reaction probabilities and scattering matrix element phases as a function of two parameters: the number of basis functions being included in the calculation and the stopping point of the integration (essentially the value of \bar{R}_λ defined earlier).

A. The $H + H_2$ Reaction

In Table 1 we present results for the reaction probability P_{00}^R in the energy range from 0.25-1.75 eV with respect to the bottom of the H_2 well. We have results for $2 \leq N \leq 6$, where N is the number of symmetric (and of anti-symmetric) basis functions used in the calculation. Results from a previous calculation (10 basis functions) are also included. Numerical parameters used in the integration of eq. (16) are

given in Table 2.

We have also obtained P_{00}^R as a function of the projection distance ρ_{pr} , which is related to the distance \bar{R}_λ by the equation

$$\rho_{pr}^2 = \bar{R}_\lambda^2 + r_\lambda^{eq^2} \quad (27)$$

where

$$r_\lambda^{eq} = a_\lambda^{-1} r_\lambda'^{eq}. \quad (28)$$

These calculations were made with four even and four odd basis functions for $5 \leq \rho_{pr} \leq 12$ bohr. These probabilities are tabulated in Table 3, along with the previous results. Averages and standard deviations of the probabilities are given in Table 4. Both Tables 1 and 3 contain only a fraction of the energies at which we have calculated probabilities and phases. The dependence of the scattering matrix element phase ϕ_{00}^R on the number of basis functions is indicated by the data in Table 5, and on projection distance in Table 6. Additionally, we have plotted ϕ_{00}^R over a range of energies for the different projection distances in Fig. 1, and in Figs. 2 and 3 we compare the phases obtained here at energies near the first and second resonance with those from extensions of the previous calculations on this system.

B. The F + H₂ Reaction

In Table 7 we present results for the reaction probability P_{02}^R in the energy range from 0.0-0.5 eV with respect to the zero-point energy of HF, with points concentrated near the low energy resonance in this system. We have results for $7 \leq N \leq 9$, where N is now the total number of basis functions used in the calculations. Results from

previous calculations on this system (13 basis functions) are also included. Numerical parameters used in the integration of eq. (16) are given in Table 2. In Table 8 we present results for P_{02}^R as a function of the projection distance ρ_{pr} for a calculation with nine basis functions. We have examined $\rho_{pr} = 10, 12$, and 14 bohr. Note in the asymmetric case $r_{\alpha}^{eq} \neq r_{\gamma}^{eq}$, for simplicity we require $r_{\gamma}^{eq} = r_{\alpha}^{eq}$ so $R_{\alpha} = R_{\gamma}$. Tables of the phase ϕ_{02}^R of the scattering matrix element S_{02}^R as a function of basis set and projection distance are given in Table 9 and Table 10, along with their values from calculations by the previous method.

4. Discussion and Conclusions

From the results in the tables and figures, it is clear that reaction probabilities and scattering matrix element phases converge quite rapidly with basis set for the $H + H_2$ reaction, while similar convergence has not yet set in for the $F + H_2$ system. Convergence in the former system is quite remarkable (and fast) at certain energies above the threshold region, the probabilities sometimes vary by less than ± 0.0001 on addition of basis functions. The general conclusions from Tables 1 and 5 is that in the $H + H_2$ system, with two closed channels of each symmetry type one should have an adequate basis set, given the frequency of basis set calculations (every 0.10 bohr) used.

Convergence of the reaction probabilities with projection distance is less rapid. The results scatter about an average value; the scatter is fairly narrow, as we see from Table 4 that the largest standard deviation of the P_{00}^R is 0.007 (and that occurs essentially in the center

of the first resonance, where data scatter might be expected to be large). This convergence is impressive when compared to the results of Römelt²⁰ for this reaction on the Porter-Karplus surface. He obtained good reaction probabilities by interpolating between the limits of a highly oscillatory P_{00}^R vs. integration stopping point (he did no projection). For example, at an energy of 0.0404 au even at $\rho = 14$ bohr, P_{00}^R is oscillating with amplitudes of ± 0.075 about the correct probability. Since the major conceptual difference between his work and our work is our inclusion of a projection;^{16, 19, 20} it appears that it must be the projection which causes our transition probabilities to reach their accurate values so rapidly.

While the reaction probabilities for $H + H_2$ become more or less independent of the projection distance at fairly small ρ , we see that the same is not true for the scattering matrix element phases. These approach a limiting value as the projection distance increases, and approach it uniformly from above (see Fig. 1). As with the probabilities, the phases compare quite well with those of the previous method (see Figs. 2 and 3). The probabilities for $F + H_2$ behave fairly well in terms of basis set and projection distance convergence (though not as well as those for $H + H_2$). The phases (Tables 9 and 10) also converge fairly well with respect to basis set, but do not appear to converge rapidly as the projection distance increases. Further, they do not appear to be approaching the correct phases (as determined in the previous calculations). In particular, the small region of increasing phase with energy seen by the previous method is not reflected when $\rho_{pr} = 10-12$ bohr, and is only minimally reflected when $\rho_{pr} = 14$ bohr.

We have no reason why the phases for FH_2 should not be converging to the seemingly correct answer.

The rapid convergence of the reaction probabilities and phases with basis set bodes well for future development of hyperspherical coordinate methods for three-dimensional reactive scattering,³⁷ as it is hoped that in that case a smaller number of basis functions might be needed to treat $3\text{D H} + \text{H}_2$ than in the previous calculations.⁵

Acknowledgments

The calculations reported here were performed on the Dreyfus-NSF Theoretical Chemistry Computer which was funded through grants from the Camille and Henry Dreyfus Foundation, the National Science Foundation (Grant No. CH 978-20235), and the Sloan Fund of the California Institute of Technology, and on the IBM 370/158 Computer of Ambassador College, Pasadena, California, for which we express our appreciation.

References

1. J. N. L. Connor, Comp. Phys. Comm. 17, 117 (1979).
2. R. B. Walker and J. C. Light, Ann. Rev. Phys. Chem. 31, 401 (1980).
3. A. Kuppermann, in Theoretical Chemistry: Advantages and Perspectives, Vol. 6A, ed. D. Henderson (Academic Press, New York, 1981) pp. 79-164.
4. A. B. Elkowitz and R. E. Wyatt, J. Chem. Phys. 62, 2504 (1975); 63, 702 (1975).
5. A. Kuppermann and G. C. Schatz, J. Chem. Phys. 62, 2502 (1975); G. C. Schatz and A. Kuppermann, J. Chem. Phys. 65, 4642 (1976); 65, 4668 (1976).
6. R. B. Walker, E. B. Stechel, and J. C. Light, J. Chem. Phys. 69, 2922 (1978).
7. M. Baer, V. Khare, and D. J. Kouri, Chem. Phys. Lett. 68, 378 (1979); D. J. Kouri, V. Khare, and N. Baer, J. Chem. Phys. 75, 1179 (1981); J. M. Bowman and K. T. Lee, Chem. Phys. Lett. 64, 291 (1979); J. Chem. Phys. 72, 5071 (1980).
8. M. J. Redman and R. E. Wyatt, Chem. Phys. Lett. 63, 209 (1979); J. Jellinek, M. Baer, V. Khare, and D. J. Kouri, Chem. Phys. Lett. 75, 460 (1980); V. Khare, D. J. Kouri, J. Jellinek, and M. Baer, in: Potential Energy Surfaces and Dynamics Calculations, ed. D. G. Truhlar (Plenum Press, New York, 1981) pp. 475-493.
9. C. C. Rankin and J. C. Light, J. Chem. Phys. 51, 1701 (1969); G. Miller and J. C. Light, J. Chem. Phys. 54, 1635, 1643 (1971).

References (continued)

10. A. Kuppermann, in: Proceedings of the Conference on Potential Energy Surfaces in Chemistry, ed. W. A. Lester (U. Calif., Santa Cruz, 1970) pp. 121-124; in: Proceedings of the 7th International Conference on the Physics of Electronic and Atomic Collisions (North-Holland, Amsterdam, 1971) pp. 3-5.
11. H. Rabitz, A. Askar, and A. S. Cakmak, Chem. Phys. 29, 61 (1978); A. Askar, A. S. Cakmak, and H. A. Rabitz, Chem. Phys. 33, 267 (1978).
12. M. Baer, J. Chem. Phys. 62, 305 (1975).
13. D. J. Diestler, in Atomic Molecule Collision Theory, ed. R. B. Bernstein (Plenum Press, New York, 1979) pp. 655-667 and references therein.
14. G.-D. Barg and A. Askar, Chem. Phys. Lett. 76, 609 (1980).
15. K. C. Kulander, J. Chem. Phys. 69, 5064 (1978); Nucl. Phys. A353, 34c (1981).
16. A. Kuppermann, J. A. Kaye, and J. P. Dwyer, Chem. Phys. Lett. 74, 257 (1980).
17. J. A. Kaye and A. Kuppermann, Chem. Phys. Lett. 77, 573 (1981).
18. J. A. Kaye and A. Kuppermann, Chem. Phys. Lett. 78, 546 (1981).
19. G. Hauke, J. Manz, and J. Römelt, J. Chem. Phys. 73, 5040 (1980).
20. J. Römelt, Chem. Phys. Lett. 74, 263 (1980).
21. J. Manz and J. Römelt, Chem. Phys. Lett. 76, 337 (1980).

References (continued)

22. J. Manz and J. Römelt, Chem. Phys. Lett. 81, 179 (1981).
23. J. Manz and J. Römelt, Chem. Phys. Lett. 77, 172 (1981).
24. L. M. Delves, Nucl. Phys. 9, 391 (1959); 20, 275 (1960).
25. D. G. Truhlar, J. Comput. Phys. 10, 123 (1972).
26. R. G. Gordon, J. Chem. Phys. 51, 14 (1969).
27. J. A. Kaye, Ph.D. Thesis, California Institute of Technology, 1982.
28. M. E. Riley and A. Kuppermann, Chem. Phys. Lett. 1, 537 (1968).
29. A. M. Lane and R. G. Thomas, Rev. Mod. Phys. 30, 257 (1958).
30. R. N. Porter and M. Karplus, J. Chem. Phys. 40, 1105 (1964).
31. J. T. Muckerman, in: Theoretical Chemistry: Advances and Perspectives, Vol. 6A, ed. D. Henderson (Academic Press, New York, 1981) pp. 1-77.
32. G. C. Schatz and A. Kuppermann, Phys. Rev. Lett. 35, 7266 (1975); unpublished results.
33. G. C. Schatz, J. M. Bowman, and A. Kuppermann, J. Chem. Phys. 58, 4023 (1973); 63, 674 (1975).
34. A. Kuppermann, in: Potential Energy Surfaces and Dynamics Calculations, ed. D. G. Truhlar (Plenum Press, New York, 1981) pp. 375-420.
35. A. Kuppermann and J. A. Kaye, J. Phys. Chem. 85, 1969 (1981).
36. J. A. Kaye and A. Kuppermann, manuscript in preparation.
37. R. T. Ling and A. Kuppermann, in: Electronic and Atomic Collisions, Abstracts of Papers of the 9th International Conference

References (continued)

on the Physics of Electronic and Atomic Collisions, ed. J. S. Risley and R. Geballe (U. Wash., Seattle, 1975) pp. 353-354;
J. K. C. Wong and A. Kuppermann, in: Abstracts of Papers, Pacific Conference on Chemistry and Spectroscopy, Pasadena, California, 10-12 October 1979, p. 39.

Table 1. $H + H_2$ Reaction Probabilities as a Function of Basis Set.

$\epsilon/\text{au.}$	$P_{\infty}^{R^a)}$					
	N= 2	3	4	5	6	prev. method
0.0120	0.1802(-6)	0.3468(-6)	0.2467(-6)	0.2620(-6)	0.1390(-6)	0.1985(-6)
0.0140	0.3526(-3)	0.3179(-3)	0.3183(-3)	0.3070(-3)	0.3142(-3)	0.3256(-3)
0.0160	0.3135(-1)	0.3103(-1)	0.3103(-1)	0.3101(-1)	0.3107(-1)	0.3052(-1)
0.0170	0.1589	0.1569	0.1569	0.1568	0.1569	0.1554
0.0180	0.4740	0.4596	0.4596	0.4596	0.4596	0.4597
0.0190	0.8059	0.7842	0.7843	0.7843	0.7843	0.7876
0.0210	0.9902	0.9838	0.9836	0.9836	0.9836	0.9860
0.0240	0.9959	0.9968	0.9969	0.9969	0.9970	0.9976
0.0300	0.9096	0.9289	0.9301	0.9302	0.9302	0.9306
0.0320	-- ^{b)}	0.1797	0.1768	0.1765	0.1770	0.1738
0.0340	--	0.7110	0.7121	0.7115	0.7115	0.7127
0.0380	--	0.5187	0.5219	0.5222	0.5218	0.5210
0.0420	--	0.2991	0.299	0.3010	0.3011	0.2998
0.0450	--	0.2496	0.2251	0.2254	0.2253	0.2208
0.0470	--	--	0.3516	0.3557	0.3558	0.3546
0.0480	--	--	0.7050	0.7120	0.7120	0.7037
0.0490	--	--	0.1329	0.1331	0.1328	0.1288
0.0500	--	--	0.1131	0.1153	0.1155	0.1158
0.0530	--	--	0.1339	0.1330	0.1329	0.1361
0.0570	--	--	0.1157	0.1161	0.1160	0.1217
0.0610	--	--	--	0.6369(-1)	0.6333(-1)	0.6452(-1)
0.0640	--	--	--	0.1193	0.1206	0.1161

a) The number enclosed in parentheses is the power of 10 by which the non-enclosed number should be multiplied.

b) Lack of unitarity of the scattering matrix indicated that this calculation was unreliable.

Table 2. Numerical Parameters for Integration of Eq. 16.

H + H ₂		F + H ₂
ρ_{pr}	= 10 bohr	10 bohr
r_{λ}^{min}	= 0.25 bohr	0.3 bohr
r_{λ}^{max}	= 4.0 bohr	3.3 bohr
ρ_0	= 1.5 bohr	2.0 bohr
$\Delta\rho^{b)}$	= 0.1 bohr	0.1 bohr
$N^{c)}$	250	300-380
NBPT ^{d)}	150	150

a) $\rho_{pr}^2 = (\bar{R}_{\lambda}^2 + r_{\lambda}^{eq^2})$ where $r_{\lambda}^{eq} = a^{-1} r'_{\lambda}{}^{eq}$.

b) Distance between successive basis set calculations.

c) Minimum number of points in eigenfunctions $\phi_n(\alpha; \bar{\rho})$.

d) Number of points in eigenfunctions $\chi_n^{\lambda}(r_{\lambda}; \bar{R}_{\lambda})$

Table 3. H + H₂ Reaction Probabilities as a Function of Projection Distances

$\epsilon/\text{au.}$	$\rho_{\text{pr}} = 5$	6	7	8	9	10	11	12	prev. method
0.0120	0.4367(-6)	0.1941(-6)	0.3558(-6)	0.2372(-6)	0.2063 -6)	0.2487(-6)	0.2830(-6)	0.2990(-6)	0.1985(-6)
0.0140	0.3146(-3)	0.3284(-3)	0.3260(-3)	0.3110(-3)	0.3164(-3)	0.3183(-3)	0.3239(-3)	0.3247(-3)	0.3256(-3)
0.0160	0.3047(-1)	0.2975(-1)	0.3005(-1)	0.3059(-1)	0.3113(-1)	0.3103(-1)	0.3048(-1)	0.2998(-1)	0.3052(-1)
0.0170	0.1564	0.1585	0.1570	0.1523	0.1524	0.1569	0.1577	0.1540	0.1554
0.0180	0.4684	0.4612	0.4604	0.4737	0.4653	0.4596	0.4714	0.4672	0.4597
0.0190	0.7808	0.7833	0.7929	0.7770	0.7909	0.7843	0.7822	0.7911	0.7876
0.0210	0.9872	0.9844	0.9876	0.9837	0.9880	0.9836	0.9877	0.9843	0.9860
0.0240	0.9984	0.9968	0.9970	0.9983	0.9981	0.9969	0.9972	0.9982	0.9976
0.0300	0.9347	0.9357	0.9354	0.9340	0.9320	0.8301	0.9289	0.9285	0.9306
0.0320	0.1958	0.1735	0.1793	0.1774	0.1749	0.1768	0.1785	0.1775	0.1738
0.0340	0.7140	0.7132	0.7115	0.7100	0.7102	0.7121	0.7118	0.7100	0.7127
0.0380	0.5256	0.5222	0.5299	0.5190	0.5296	0.5219	0.5254	0.5254	0.5210
0.0420	0.3007	0.3021	0.3010	0.3014	0.3036	0.2999	0.3014	0.3039	0.2998
0.0450	0.2231	0.2187	0.2173	0.2213	0.2228	0.2251	0.2212	0.2209	0.2208
0.0470	0.3518	0.3538	0.3532	0.3541	0.3512	0.3516	0.3513	0.3516	0.3546
0.0480	0.7114	0.7103	0.7071	0.7078	0.7051	0.7050	0.7047	0.7052	0.7037
0.490	0.1258	0.1318	0.1320	0.1340	0.1311	0.1329	0.1322	0.1319	0.1288
0.0500	0.1126	0.1113	0.1105	0.1129	0.1126	0.1131	0.1135	0.1129	0.1158
0.0530	0.1234	0.1267	0.1265	0.1269	0.1249	0.1236	0.1252	0.1257	0.1361

Table 4. Average and Standard Deviation of H + H₂ Reaction Probabilities. (From Table 3.)

$\epsilon/\text{au.}$	$\langle P_{\infty}^R \rangle$	std. dev.	std. dev. $\langle P_{\infty} \rangle$
0.012	2.826(-7)	8.127(-8)	28.8%
0.014	3.204(-4)	6.193(-6)	1.93%
0.016	0.03044	0.00049	1.61%
0.017	0.1557	0.0024	1.55%
0.018	0.4659	0.0052	1.12%
0.019	0.7853	0.0057	0.72%
0.021	0.9858	0.0020	0.20%
0.024	0.9976	0.0007	0.07%
0.030	0.9324	0.0029	0.32%
0.032	0.1792	0.0070	3.89%
0.034	0.7116	0.0015	0.21%
0.038	0.5249	0.0038	0.72%
0.042	0.3018	0.0014	0.46%
0.045	0.2213	0.0025	1.12%
0.047	0.3523	0.0012	0.33%
0.048	0.7071	0.0026	0.37%
0.049	0.1315	0.0024	1.86%
0.050	0.1124	0.0010	0.90%
0.053	0.1254	0.0014	1.08%

Table 5. H + H₂ Phases as a Function of Basis Set

$\epsilon/\text{au.}$	$\phi_{00}^R/\text{radians}$				
	N= 2	3	4	5	6
0.021	8.149	8.083	8.082	8.082	8.082
0.024	5.787	5.787	5.784	5.784	5.785
0.026	4.338	4.323	4.319	4.319	4.319
0.028	2.949	2.950	2.946	2.946	2.946
0.030	1.717	1.705	1.701	1.700	1.700
0.0305	1.506	1.427	1.423	1.422	1.423
0.031	1.197	1.183	1.180	1.180	1.180
0.0315	0.675	1.021	1.022	1.021	1.021
0.032	0.196	0.715	0.577	0.581	0.579
0.0325	-- a)	-0.291	-0.259	-0.260	-0.259
0.033	--	-0.454	-0.442	-0.443	-0.443
0.0335	--	-0.608	-0.664	-0.664	-0.664
0.034	--	-0.916	-0.913	-0.914	-0.914
0.035	--	-1.431	-1.431	-1.431	-1.431
0.036	--	-1.958	-1.960	-1.961	-1.961
0.038	--	-2.971	-2.977	-2.989	-2.989
0.040	--	-3.999	-3.998	-4.000	-4.000

a) Lack of unitarity of the scattering matrix indicated that this calculation was unreliable.

Table 6. H + H₂ Phases as a Function of Projection Distance.

ρ_{pr} $\epsilon/\text{au.}$	$\phi_{\infty}^{\text{R}}/\text{radians}$										
	5	6	7	8	9	10	11	12			
0.021	12.713	10.364	9.196	8.576	8.247	8.082	8.003	7.966			
0.024	9.853	7.797	6.771	6.222	5.931	5.785	5.715	5.683			
0.026	8.110	6.199	5.240	4.726	4.456	4.319	4.254	4.225			
0.028	6.507	4.714	3.813	3.330	3.075	2.946	2.884	2.856			
0.030	5.068	3.374	2.522	2.065	1.823	1.701	1.641	1.614			
0.031	4.473	2.821	1.988	1.539	1.301	1.180	1.124	1.337			
0.032	3.779	2.161	1.342	0.902	0.684	0.577	0.514	0.474			
0.033	2.688	1.120	0.326	-0.102	-0.328	-0.442	-0.496	-0.517			
0.034	2.151	0.613	-0.161	-0.579	-0.802	-0.911	-0.965	-0.991			
0.036	0.979	-0.489	-1.239	-1.641	-1.853	-1.961	-2.008	-2.034			
0.038	-0.162	-1.584	-2.289	-2.684	-2.892	-2.990	-3.046	-3.002			
0.040	-1.270	-2.636	-3.325	-3.701	-3.904	-4.000	-4.051	-4.069			

Table 7. F + H₂ Reaction Probabilities as a Function of Basis Set

N = ε/au.	P ₀₂ ^{R a)}			
	7	8	9	previous method
0.010	0.1290(-2)	0.1286(-2)	0.1357(-2)	0.1245(-2)
0.0102	0.4354(-1)	0.4363(-1)	0.4363(-1)	0.4457(-1)
0.0103	0.1834	0.1843	0.1962	0.2038
0.0104	0.3856	0.3882	0.402	0.4108
0.0105	0.3752	0.3765	0.3744	0.3550
0.0108	0.2611	0.2621	0.2666	0.2630
0.011	0.2537	0.2545	0.2602	0.2562
0.012	0.2438	0.2453	0.2404	0.2338
0.013	0.1497	0.1476	0.1456	NA ^{c)}
0.014	-- ^{b)}	0.7077(-1)	0.6927(-1)	NA
0.015	0.5563(-1)	0.6106(-1)	0.6029(-1)	0.5717(-1)
0.0175	--	0.5529(-1)	0.5738(-1)	0.5477(-1)
0.020	--	0.3539(-1)	0.3623(-1)	0.3493(-1)
0.025	--	0.1162(-2)	0.1154(-2)	0.1101(-2)

a) The number enclosed in parentheses is the power of 10 by which the non-enclosed number should be multiplied.

b) Lack of unitarity of the scattering matrix (>10%) indicated that this calculation was unreliable.

c) Not available.

Table 8. F + H₂ Reaction Probabilities as a Function of
Projection Distance

$\epsilon/\text{au.}$	ρ_{pr}	$P_{\text{O}_2}^{\text{Ra)}$			previous method
		10	12	14	
0.010		0.1357(-2)	0.1205(-2)	0.1151(-2)	0.1245(-2)
0.0101		0.8221(-2)	0.7622(-2)	0.7897(-2)	0.8036(-2)
0.0102		0.4363(-1)	0.4445(-1)	0.4128(-1)	0.4457(-1)
0.01025		0.9666(-1)	0.9895(-1)	0.9666(-1)	0.9690(-1)
0.0103		0.1962	0.1969	0.2010	0.2038
0.010335		0.2870	0.2842	0.2908	0.3044
0.010365		0.3560	0.3502	0.3560	0.3711
0.0104		0.4025	0.3941	0.3963	0.4108
0.0105		0.3744	0.3719	0.3701	0.3777
0.0106		0.3176	0.3199	0.3197	0.3081
0.017		0.2839	0.2825	0.2786	0.2709
0.0108		0.2666	0.2641	0.2659	0.2630
0.011		0.2602	0.2660	0.2621	0.2562
0.0114		0.2608	0.2623	0.2618	0.2597
0.0118		0.2517	0.2475	0.2528	0.2461
0.0122		0.2231	0.2264	0.2269	0.2183
0.0125		0.1978	0.1961	0.193	0.1933

Table 9. F + H₂ Phases as a Function of Basis Set.

$\epsilon/\text{au.}$	ρ_{pr}	$\phi_{02}^{\text{R}}/\text{radians}$			previous method
		7	8	9	
0.010		7.664	7.645	7.754	5.748
0.0102		5.233	5.240	5.246	4.180
0.0103		4.764	4.746	4.769	4.003
0.0104		4.652	4.637	4.681	4.157
0.0105		4.448	4.432	4.477	4.157
0.0108		3.251	3.234	3.237	3.420
0.011		2.377	2.359	2.387	2.854
0.0115		0.550	0.529	0.533	NA ^{a)}
0.012		-1.063	-1.089	-1.086	0.400
0.0125		-2.544	-2.576	-2.553	-0.701
0.013		-3.875	-3.924	-3.928	-1.762

a) Not available.

Table 10. F + H₂ Phases as a Function of Projection Distance

$\epsilon/\text{au.}$	ρ_{pr}	$\phi_{02}^2/\text{radians}$			previous results
		10	12	14	
0.010		7.754	7.246	6.692	5.748
0.0101		6.209	5.511	5.434	4.760
0.0102		5.246	4.765	4.558	4.180
0.01025		4.942	4.411	4.297	4.034
0.0103		4.769	4.276	4.179	4.003
0.010335		4.718	4.242	4.160	4.028
0.010365		4.701	4.235	4.161	4.090
0.01004		4.681	4.226	4.158	4.157
0.0105		4.477	4.048	3.983	4.157
0.0106		4.104	3.708	3.650	3.972
0.0107		3.676	3.367	3.248	3.649
0.0108		3.237	2.878	2.816	3.420
0.011		2.387	2.065	2.028	2.854
0.0114		0.885	0.590	0.563	1.826
0.0118		-0.460	-0.720	-0.748	0.859
0.0122		-1.456	-1.921	-1.953	-0.700(-1)
0.125		-2.558	-2.783	-2.811	-0.701

Figure Captions

FIG. 1. Phase ϕ_{∞}^R of the scattering matrix element S_{∞}^R for the $H + H_2$ reaction as a function of the total energy E for different values of the projection distance ρ_{pr} . Data for $\rho_{pr} = 11, 12$ bohr are not plotted because of their similarity to the 10 bohr results. Scattering calculations were performed with four even and four odd basis functions; other numerical parameters have their values in Table 2.

FIG. 2. Phase ϕ_{∞}^R of the scattering matrix element S_{∞}^R , for the $H + H_2$ reaction as a function of the total energy E_n near the first resonance by the previous method (line) and present method (circle). Scattering calculations used $\rho_{pr} = 10$ bohr; all other parameters are as in Fig. 1.

FIG. 3. Phase ϕ_{∞}^R of the scattering matrix element S_{∞}^R for the $H + H_2$ reaction as a function of the total energy E near the second resonance. Symbols are as in Fig. 2.

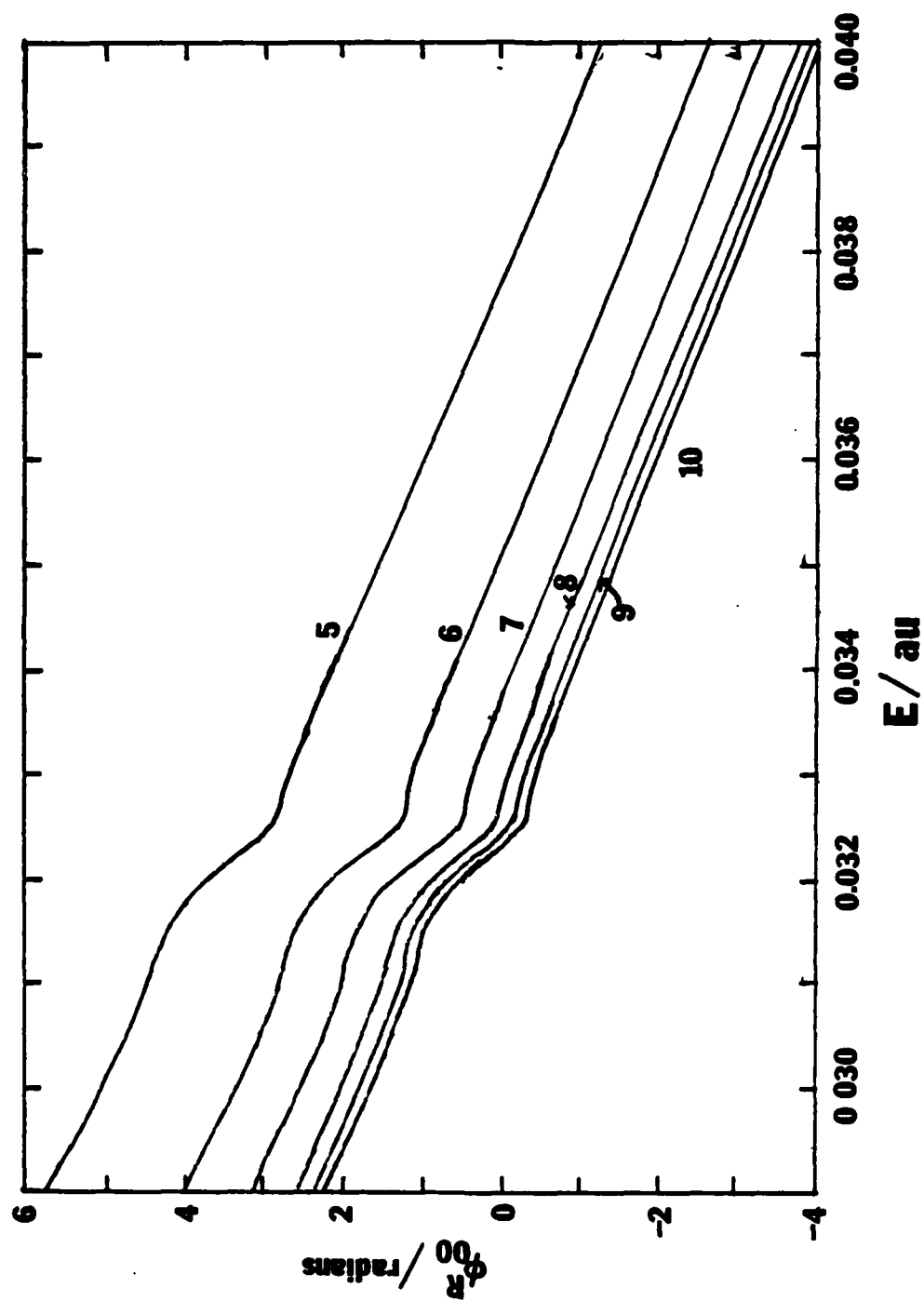


Figure 1

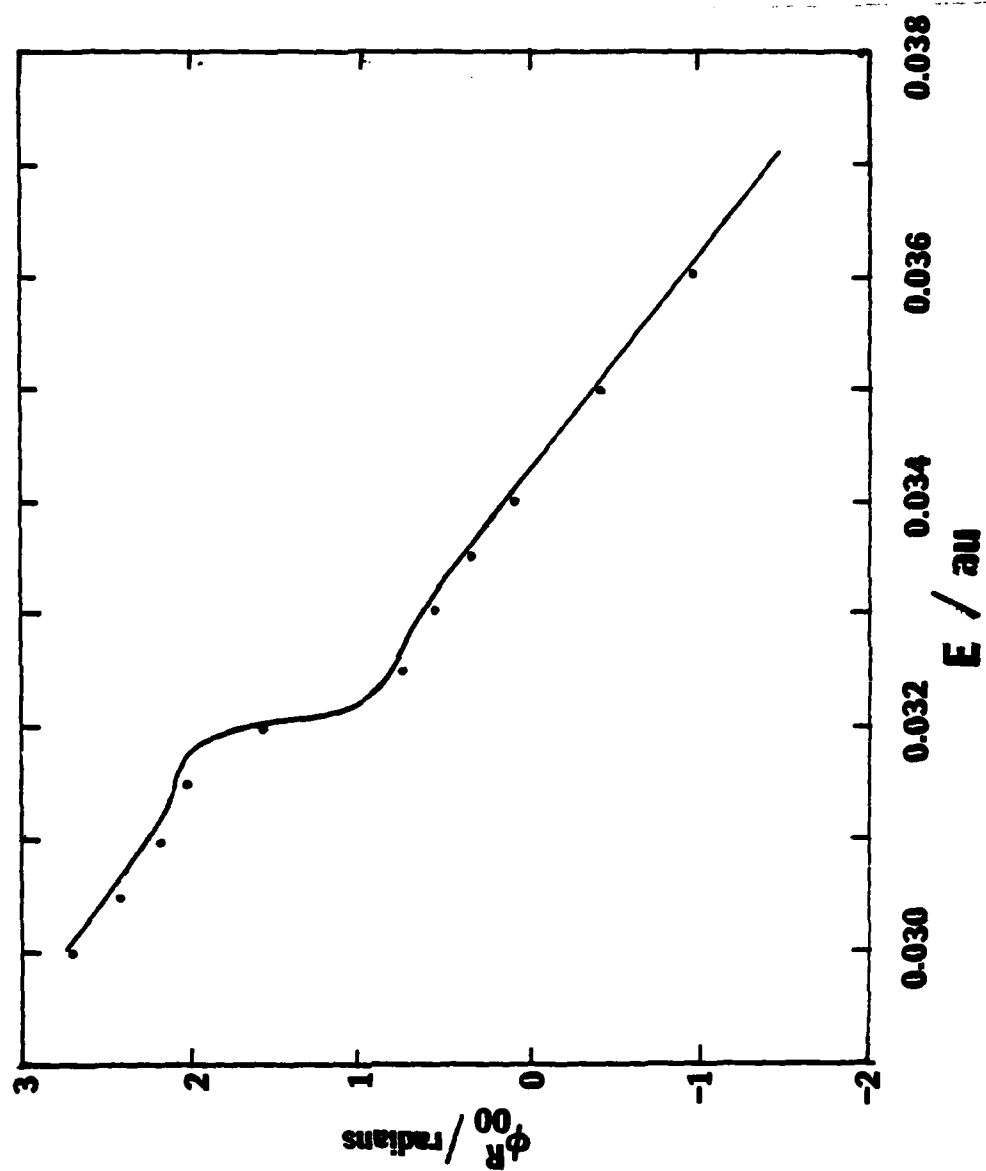


Figure 2

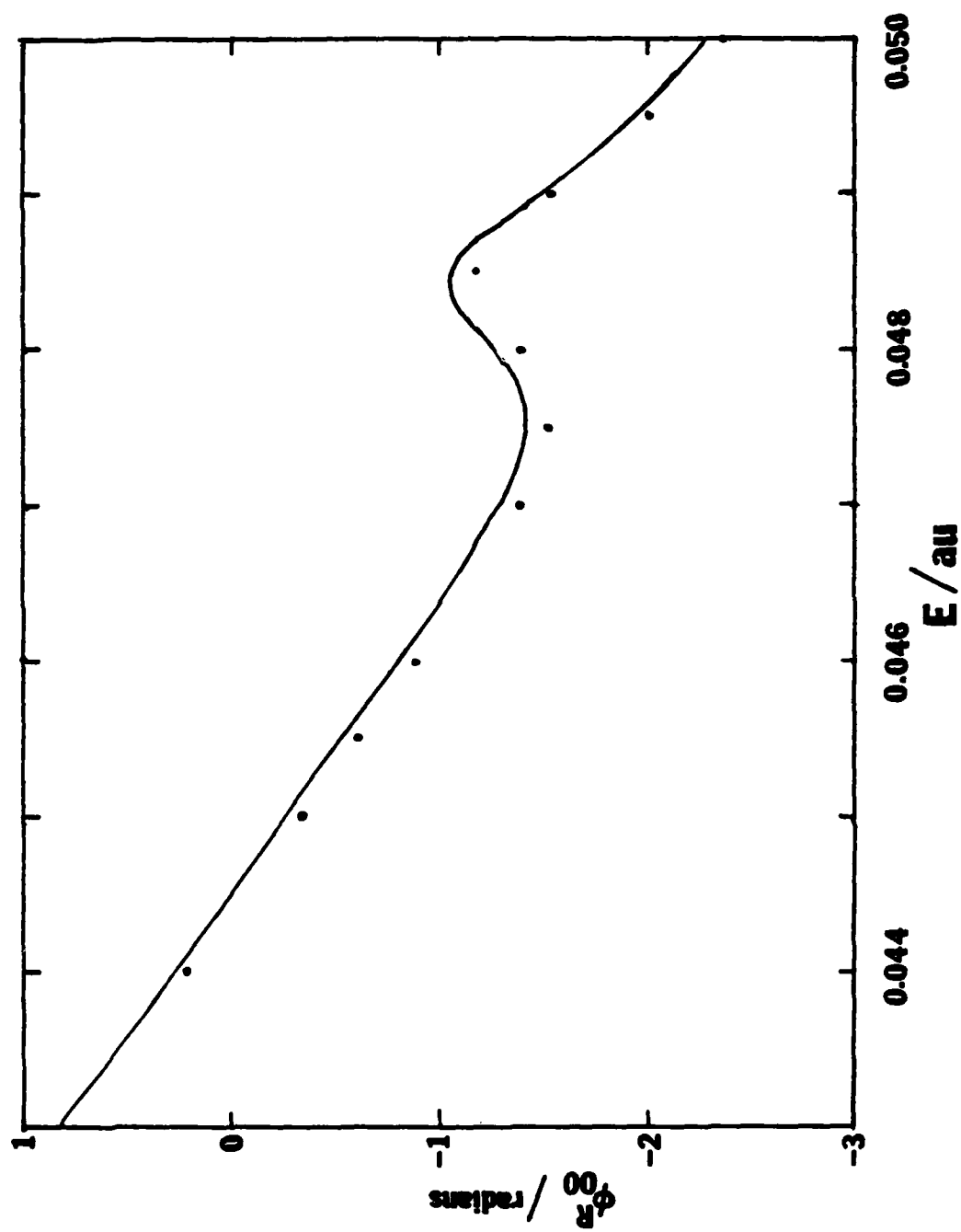


Figure 3

QUANTUM MECHANICAL COLLINEAR CALCULATIONS
OF THE REACTIONS $D + FH (v = 0, 1, 2) \rightarrow DF (v') + H$ AND
 $H + FD (v = 0, 1, 2, 3) \rightarrow HF (v') + D$ ON A REALISTIC
POTENTIAL ENERGY SURFACE*

Jack A. KAYE, ** John P. DWYER,[†] and Aron KUPPERMANN

Arthur Amos Noyes Laboratory of Chemical Physics,[‡]

California Institute of Technology, Pasadena, California 91125, USA

Received

Collinear coupled channel quantum mechanical calculations have been performed on the title reactions on a potential energy surface with a 40 kcal/mole barrier to exchange. This barrier height is close to that predicted by ab initio calculations and suggested by experiments. The relative effectiveness of reagent vibrational and translational excitation to promote reaction is considered. A one-mathematical dimensional (1MD) model for these reactions is constructed and is shown to work very well for the $D + FH$ reaction at high temperatures, and less well for that reaction at lower temperatures as well as for the $H + FD$ reaction. Possible reasons for the breakdowns of the 1MD model are discussed.

* This work was supported in part by a contract (No. F49620-79-C-0187) from the Air Force Office of Scientific Research.

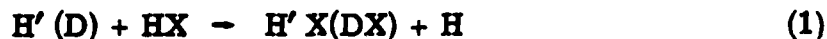
** Work performed in partial fulfillment of the requirements for the PhD degree in Chemistry at the California Institute of Technology.

[†] Present address: Supreme Court of the United States, Washington, DC 20543, USA.

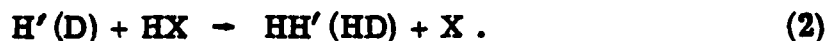
[‡]Contribution No.

1. Introduction

The exchange reactions between hydrogen or deuterium atoms and hydrogen halides

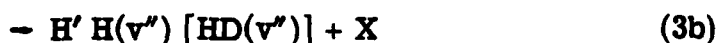
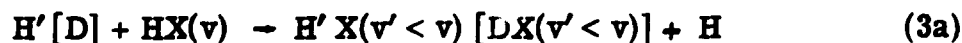


(X = F, Br, Cl, I) have been among the more studied simple chemical reactions [1]. These reactions compete with the H(D) atom abstraction process



One of the goals of studies of these systems is the understanding of the relative importance of the exchange and abstraction channels.

Interest in reactions (1) and (2) has been heightened by the recognition of their possible importance in collisional deactivation of vibrationally excited HX in HX chemical lasers, especially when X = F [2]. State-to-state rate constants for processes of the type



are necessary if one is to successfully model the kinetics of HX lasers.

The exchange reactions (1) have been extensively studied by classical trajectory calculations as well as collinear quantum mechanical calculations for X = F [3], Cl [4], and Br [5]. Interest has been greatest in the H(D) + FH and H(D) + ClH systems, which have the smallest number of electrons and are thus candidates for the calculation of accurate potential energy surfaces by ab initio techniques. Such calculations have been performed on the HFH and HClH systems, and the results suggest the existence of large barriers to exchange, in excess of

40 kcal/mole for HFH and 20 kcal/mole for HClH [6]. Recent experiments on these systems appear to confirm the existence of a high barrier to exchange [7].

Most of the early theoretical studies of these systems were carried out on potential energy surfaces with a small barrier to exchange, and therefore cannot be expected to give even qualitatively correct behavior for many important dynamical properties [8]. These surfaces were normally obtained by using global semi-empirical potential energy functions, such as the extended LEPS form [9], which were obtained by optimizing agreement between quasi-classical trajectory calculations and experiments on the reverse of reaction (2). In particular, in previous quantum mechanical studies of the HFH exchange reaction, both collinear [10] and coplanar [11], potential energy surfaces with barriers to exchange of 1.2 kcal/mole and 1.8 kcal/mole, respectively, were used.

In this work, we report the results of collinear quantum mechanical calculations of the reactions



on a potential energy surface with a barrier to exchange of 40 kcal/mole. We will be particularly concerned with the effects of reagent vibrational excitation on the rate of reactions (4a, b) as this is a quantity which is obtainable by experiment, and has been determined for reaction (4a) [7b]. The ability of a one-mathematical dimension (1MD) model to predict and explain the results will also be considered.

2. Potential Energy Surface and Computational Model

The potential energy surface used in these calculations is of the rotating Morse-cubic spline type, which has been described elsewhere [12]. In its application to this system, we have constrained the energy level at the bottom of the local Morse oscillator well as a function of the swing angle θ (defined in ref. [12]) to be a Gaussian, with a maximum at $\theta = \pi/4$ radians. The saddle point occurs at $R_{HF} = R_{FH} = 1.97$ bohr. The values of $\beta(\theta)$ were determined by fitting to the exchange channel portion of the semi-empirical (extended LEPS form) Muckerman V_{FH_2} potential energy surface [13]. Thus, the position of the minimum energy path on this surface is identical to that on the Muckerman V surface. Note that the saddle point on this surface occurs at a shorter R_{HF} distance than that predicted by ab initio calculations. A fuller description of the potential energy surface will be given in a forthcoming paper [14]. This surface is plotted for the $D + FH$ reaction in the mass-weighted Delves coordinate system [15] in fig. 1.

A vibrational correlation diagram [16] for this surface, also showing the potential along the minimum energy path, is shown in fig. 2. The potential energy $V_n(s)$ along each curve (except, of course, for that showing the minimum energy path) is the sum of the potential energy along the minimum energy path $V^{mep}(s)$ and the appropriate eigenvalue $E_v(s)$ of the potential formed by taking a cut perpendicular to the minimum energy path (in Delves coordinates)

$$V_v(s) = V^{mep}(s) + E_v(s) , \quad (5)$$

where s is the distance along the minimum energy path measured from

the saddle point, also measured in Delves coordinates. The eigenvalues $E_v(s)$ are determined numerically from the potential by a finite difference procedure [17].

The numerical calculations were performed using the coupled-channel method of Kuppermann, which has been described previously [18]. Between 20 and 24 basis functions were used in the calculations, and unitarity of the open part of the scattering matrix \underline{S} was obtained to within 3% for all energies used; for most energies it was obtained to better than 1%. Calculations were carried out to energies up to 2.45 eV above the isolated HF ($v = 0$) energy level. At the highest energies studied, there were six open HF states and eight open DF states. State-to-state rate constants were calculated from the reaction probabilities $P_{vv'}$, which are a function of the reagent translational energy E^{tr} by the expression

$$k_{vv'}(T) = (2\pi\mu_{a,bc}kT)^{-\frac{1}{2}} \int_0^{\infty} P_{vv'}(E^{tr}) e^{-E^{tr}/kT} dE^{tr}, \quad (6)$$

where $\mu_{a,bc}$ is the reduced mass of the a, bc collision pair. The exact method of evaluating this integral has been discussed by Truhlar and Kuppermann [19].

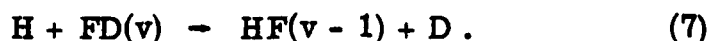
Because of the large barrier to reaction, probabilities of reaction are extremely small ($< 10^{-12}$) at small values of E^{tr} . As the collinear reactive scattering program is written in single precision (for use on an IBM 370/158 computer), we do not entirely trust the exact magnitude of these very small probabilities. Hence, we restrict the temperature range of our rate constant calculations to those temperatures where the major contribution to the integral in eq. (6) comes from energy ranges

where the reaction probabilities are larger and thus more reliable.

3. Results and Discussion

Reactions (4) only become probable in this system for fairly large values of the translational energy. In figs. 3 and 4, respectively, we plot as a function of E^{tr} the total reaction probability for reactions (4a) and (4b), respectively, for a few of the lowest reagent vibrational states. While there are some strong similarities between the two figures, such as the large threshold to reaction, the relative magnitude of the threshold lowering with vibrational excitation, and the approximately parallel nature of the probability versus energy curves in the region of greatest increase of probability with energy, there are some major differences, however.

In the immediate vicinity of and slightly above the threshold energy, there are major differences in figs. 3 and 4 for vibrationally excited reagents. For reaction (4a), for the $D + FH$ ($v = 1, 2$) reaction, the probability of reaction rises smoothly and rapidly in an s-shaped curve from 0 to 1, while for reaction (4b), for the reaction $H + FD$ ($v = 1, 2$), there exist broad shoulders in these curves. It can be seen by examining state-to-state reaction probability versus energy curves that the shoulders seen in fig. 4 are due to reactions of the type



This is shown graphically for the $v = 1$ case in fig. 5, where state-to-state reaction probabilities P_{10}^R , P_{11}^R , and P_{12}^R are shown as a function of E^{tr} . It is worth noting that at higher translational energies, P_{11}^R becomes substantially smaller than P_{10}^R and P_{12}^R .

One other difference observed between figs. 3 and 4 is that at high translational energies, the probability of reaction (4a) stays near unity, while that of reaction (4b) is smaller than unity and is highly irregular.

The vibrational correlation diagram in fig. 2 provides a useful way of looking at the DXH systems. A number of conclusions may be drawn from a quick examination of this diagram for the DFH system. First, because of the large barrier, there are no wells in the vibrationally adiabatic correlation diagram, at least for the first few levels. As wells in this diagram have been shown to be related to resonances in reaction probabilities [16], we can conclude that in the energy range considered here there should be no resonances, and, indeed, none has been observed in the dynamics. Second, because of the large difference between HF and DF vibrational frequencies, the highest point on the vibrationally adiabatic correlation diagram moves into the HF reagent channel, especially for vibrationally excited reagents. Thus, one may interpret, within a vibrationally adiabatic model, reaction (4a) as having its saddle point on the reagent side, while reaction (4b) has its on the product side. Third, the vibrational frequencies at and near the saddle point are fairly large; hence the magnitude of the vibrationally adiabatic barriers decreases with energy by an amount that is substantially smaller than the vibrational energy spacing of HF and DF. Thus, for example, the translational energy threshold for reactions (4a) should decrease by 0.21 eV on going from the ground to the first excited level of HF and 0.17 eV on going from the first to the second excited state of HF; the differences in vibrational energies between these levels are 0.49 and 0.46 eV, respectively. The lowering in threshold energies

(defined as the energy at which the probability of reaction first reaches 0.02) for reaction (4a) are 0.22 and 0.17 eV, respectively. Thus, the simple one-dimensional vibrationally adiabatic picture provides a good model for the D + FH system at low translational energies.

For the H + FD reactions one can interpret the low energy non-adiabatic reaction as occurring due to a crossing from the DF(v) curve to the HF(v - 1) curve. If this crossing occurs on the DF side of the saddle point (as seems reasonable from examination of fig. 2), the apparent barrier to reaction should be much smaller than to vibrationally adiabatic reaction. This qualitatively explains the 0.25 eV separation in fig. 5 between the center of the P_{10}^R flat maximum and that of the P_{11}^R maximum.

Rate constants for reactions (4a) and (4b) are plotted in fig. 6 as a function of temperature in the form of an Arrhenius plot (log of the rate constant versus inverse temperature). Such plots are frequently linear, over a broad temperature range, and linearity or near-linearity is seen in all of the plots shown. In the usual way, Arrhenius pre-exponential parameters (A) and activation energies (E_a) are obtained for the linear region of these curves, and the resulting data are summarized in Table 1. The vibrational energy associated with each reagent level is also included in Table 1 for comparison.

The rate constants obtained are quite small in all cases; by comparison, the gas kinetic rate constant k_{gk} (that when every collision results in reaction) is given by the formula

$$k_{gk}(T) = \left(\frac{kT}{2\pi\mu} \right)^{\frac{1}{2}} = 2.69 \times 10^3 T^{\frac{1}{2}} \text{ cm} \cdot \text{molec}^{-1} \text{ sec}^{-1} \text{ (D + FH) (6a)}$$

$$= 3.71 \times 10^3 T^{\frac{1}{2}} \text{ cm} \cdot \text{molec}^{-1} \text{ sec}^{-1} \text{ (H + FD). (6b)}$$

Even at the highest temperatures considered, the rate constants are five to seven orders of magnitude less than gas kinetic. Thus, the large barrier and the resulting large threshold for reaction produce small rate constants.

The activation energies E_a shown in Table 1 decrease as reagent vibrational excitation is increased. The lowering of the activation energy with reagent vibrational excitation is less than the amount of internal energy in the vibrationally excited reagents, however. Recall that a similar behavior was observed for the lowering of the threshold energy with reagent vibrational excitation. The decrease in activation energy with reagent vibrational excitations is, however, greater than the corresponding decrease in the vibrationally adiabatic barrier height. This difference can be explained by the dominance of vibrationally non-adiabatic reaction over vibrationally adiabatic reaction in the energy region where the reaction probabilities are small ($< 10^{-2}$). This energy region only makes a substantial contribution to the integral in eq. (5) at fairly low temperatures.

In order to further understand the applicability of the one-dimensional vibrationally adiabatic model, we have calculated transmission coefficients for the three lowest vibrationally adiabatic barriers for reaction (4a) as a function of translational energy. These calculations, involving a numerical solution of the one-dimensional Schrödinger equation, were performed with the method described by Truhlar and Kuppermann [20]. We then used these transmission coefficients (equivalent to reaction probabilities in the coupled-channel calculations) to calculate rate constants for the $D + FH$ ($v = 0, 1, 2$) reactions, and the

results (labeled 1MD for one mathematical dimension) at 500° K and 1000° K are given in Table 1, along with those obtained in the full two mathematical dimension (2MD) coupled-channel calculation. For comparison, the gas kinetic rate constants are also included.

At 1000° K, the results of the 1MD and 2MD calculations agree quite well (within 5%), while at 500° K, the agreement is less satisfactory, becoming worse as one goes from HF ($v = 0$) to HF ($v = 2$). This lack of agreement when the HF reagent is vibrationally excited is due to the above mentioned dominance of vibrationally nonadiabatic reactions at low translational energies.

The usefulness of the vibrationally adiabatic model for the DFH system makes it worthwhile to well characterize the potential energy surface in the region at the saddle point; in particular, accurate values of the local vibrational frequencies (i. e., the symmetric stretch at the saddle point) are important, as these, along with the actual barrier height itself, combine to give the vibrationally adiabatic correlation diagram shown in fig. 2 and found to be so useful.

A word of caution must be expressed concerning the applicability of a collinear model to reactions (4). Ab initio calculations by Wadt and Winter [6] suggest that the lowest barrier to exchange occurs not for a collinear H-F-H configuration, but rather for one with a 106° bond angle, and further that the barrier height is nearly independent of the bond angle. Thus, it appears that an accurate dynamical treatment of the exchange reaction would require three physical dimensions (3D). A 3D calculation on this system would have the advantage of allowing one to directly compare the importance of the abstraction and exchange

channels. Such a calculation would require a good semi-empirical potential energy surface incorporating a large barrier to exchange. A method for constructing such a surface has been developed by Baer and Last [21], and has been applied to all XH_2 systems. Their FH_2 surface has a reasonably high barrier (33.5 kcal/mole), but has much stronger dependence of the barrier height on the H-X-H bond angle than that predicted by Wadt and Winter [6].

4. Conclusions

Reaction probabilities and rate constants for reactions (4a) and (4b) have been obtained on a realistic potential energy surface by a collinear quantum mechanical calculation. Reaction has been shown to set in at large values of the translational energy (≥ 1 eV) for reagents in their first three vibrational states. Vibrational excitation has been shown to promote the reaction, although the decrease in the activation energy is less than the internal energy added to the reagents on vibrational excitation. A number of aspects of the dynamics, such as the translational energy threshold for reaction and the importance of vibrationally nonadiabatic processes near the threshold region for reaction (4b), have been shown to be explained by use of vibrationally adiabatic correlation diagrams. The overall rate of reaction (4a) has been shown to be reproduced quite well at high temperatures by a 1MD model based on these vibrationally adiabatic correlation diagrams. The results obtained help demonstrate the importance of an accurate knowledge of the potential energy surface in the immediate vicinity of the saddle point.

Acknowledgements

We thank Ambassador College for the generous use of their computational facilities for the scattering calculations. Additional calculations were carried out at the Dreyfus-NSF Theoretical Chemistry Computer at Caltech, which is funded through grants from the Camille and Henry Dreyfus Foundation, the National Science Foundation (Grant No. CHE78-20235), and the Sloan Fund of the California Institute of Technology.

Table 1

Arrhenius parameters for rate constants for reactions (4a, b)

V	T (°K)	$\ln A$ ($\text{cm} \cdot \text{molec}^{-1}$ sec^{-1})	E_a (kcal/ mole)	Internal Energy of Reagent (kcal/mole)
A. $D + FH(v) \rightarrow DF(v' = \text{all}) + H$				
0	500-950	11.8	36.8	5.8
1	450-700	9.3	28.3	17.0
2	450-600	4.8	18.0	27.7
B. $H + FD(v) \rightarrow HF(v' = \text{all}) + D$				
0	550-1000	11.9	38.6	4.2
1	450-800	9.4	30.3	12.4
2	450-700	6.8	22.8	20.4
3	450-700	4.5	16.5	28.1

Table 2

Rate constants for the reaction $D + FH(v) \rightarrow DF(v' = \text{all})$ in units
 $\text{cm} \cdot \text{molec}^{-1} \text{sec}^{-1}$

T (°K)	v = 0	v = 1	v = 2
2MD			
500	1.16 (-11)	3.91 (-9)	8.42 (-7)
1000	1.29 (-3)	1.61 (-2)	1.07 (-1)
1MD			
500	9.80 (-12)	1.43 (-9)	8.28 (-8)
1000	1.23 (-3)	1.57 (-2)	1.07 (-1)
Gas Kinetic			
500	6.02 (4)	6.02 (4)	6.02 (4)
1000	8.51 (4)	8.51 (4)	8.51 (4)

References

- [1] M. R. Levy, *Progr. Reaction Kinetics* 10 (1979) 1.
- [2] N. Cohen and J. F. Bott, in *Handbook of Chemical Lasers*, eds. F. Gross and J. F. Bott (Wiley-Interscience, New York, 1976), pp 33-94.
- [3] D. L. Thompson, *J. Chem. Phys.* 57 (1972) 4170; R. L. Wilkins, *J. Chem. Phys.* 58 (1973) 3039; R. L. Wilkins, *Mol. Phys.* 29 (1975) 555.
- [4] I. W. M. Smith and P. M. Wood, *Mol. Phys.* 25 (1973) 441; D. L. Thompson, H. H. Suzukawa, Jr., and L. M. Raff, *J. Chem. Phys.* 62 (1975) 4727; R. L. Wilkins, *J. Chem. Phys.* 63 (1975) 534.
- [5] J. M. White, *J. Chem. Phys.* 65 (1976) 3674; D. J. Malcolm-Lawes, *J. Chem. Soc. Faraday Trans. 2* 74 (1978) 182.
- [6] C. F. Bender, B. J. Garrison, and H. F. Schaeffer III, *J. Chem. Phys.* 62 (1975) 1188; P. Botschwina and W. Meyer, *Chem. Phys.* 20 (1977) 43; W. R. Wadt and N. W. Winter, *J. Chem. Phys.* 67 (1977) 3068; A. F. Voter and W. A. Goddard III, *J. Chem. Phys.* 75 (1981) 3638; T. H. Dunning, Jr., *J. Chem. Phys.* 66 (1977) 2752.
- [7] a) J. F. Bott, *J. Chem. Phys.* 65 (1976) 1976.
b) F. E. Bartoszek, D. M. Manos, and J. C. Polanyi, *J. Chem. Phys.* 69 (1978) 933.
c) W. Bauer, L. Y. Rusin, and J. P. Toennies, *J. Chem. Phys.* 68 (1978) 4490.
- [8] H. F. Schaefer III, in *Atom-Molecule Collision Theory*, ed.

- R. B. Bernstein (Plenum Press, New York, 1979), pp. 45-78.
- [9] P. J. Kuntz, E. M. Nemeth, J. C. Polanyi, S. D. Rosner, and C. E. Young, *J. Chem. Phys.* 44 (1966) 1168.
- [10] G. C. Schatz and A. Kuppermann, *J. Chem. Phys.* 72 (1980) 2737.
- [11] M. Baer, *J. Chem. Phys.* 65 (1976) 493.
- [12] J. M. Bowman and A. Kuppermann, *Chem. Phys. Lett.* 34 (1975) 523.
- [13] G. C. Schatz, J. M. Bowman and A. Kuppermann, *J. Chem. Phys.* 63 (1975) 674; J. T. Muckerman, *J. Chem. Phys.* 56 (1972) 2997.
- [14] J. A. Kaye, J. P. Dwyer, and A. Kuppermann, manuscript in preparation.
- [15] L. M. Delves, *Nucl. Phys.* 9 (1959) 391; 20 (1960) 275.
- [16] S. L. Latham, J. F. McNutt, R. E. Wyatt, and M. J. Redmon, *J. Chem. Phys.* 69 (1978) 3746; A. Kuppermann, *J. Phys. Chem.* 83 (1979) 171.
- [17] D. G. Truhlar, *J. Comp. Phys.* 10 (1972) 123.
- [18] A. Kuppermann, in *Proceedings of the Conference on Potential Energy Surfaces in Chemistry*, ed. W. A. Lester (University of California, Santa Cruz, 1979), pp. 121-124; in *Proceedings of the 7th International Conference on the Physics of Electronic and Atomic Collisions* (North-Holland, Amsterdam, 1971), pp. 3-5.
- [19] D. G. Truhlar and A. Kuppermann, *J. Chem. Phys.* 56 (1972) 2232.

- [20] D. G. Truhlar and A. Kuppermann, J. Am. Chem. Soc. 93 (1971) 1840.
- [21] M. Baer and I. Last, in Potential Energy Surfaces and Dynamics Calculations, ed. D. G. Truhlar (Plenum, New York, 1981), pp. 519-534.

Figure Captions

Figure 1. Contour plot of the potential energy surface for the reaction $D + FH \rightarrow DF + H$ in Delves scaled coordinates. The solid curves are equipotential contours at the total energies measured with respect to the bottom of the HF (DF) wells. The dashed line is the minimum energy path. The cross indicates the location of the saddle point.

Figure 2. Vibrationally adiabatic correlation diagram for the reaction $D + FH(v) \rightarrow DF(V) + H$, $v = 0, 1, 2$. The vertical scale is an energy scale. The lowest curve is the potential energy along the minimum energy path $V^{\text{mep}}(s)$ as a function of the distance s along the minimum energy path from the saddle point. Positive values of s take one towards separated $D + FH$, negative values of s towards $DF + H$. The higher curves are plots as a function of s of the potential $V_v(s)$ defined in eq. (5) of the text for $v = 0, 1, 2$.

Figure 3. Probabilities $P_{D+FH}^R(v)$ of the reactions $D + FH(v) \rightarrow DF(v' = \text{all}) + H$ for $v = 0, 1, 2$ as a function of reagent translational energy E^{tr} . The solid line is for $v = 0$, the dashed line is for $v = 1$, and the dotted line is for $v = 2$.

Figure 4. Probabilities $P_{H+FD}^R(v)$ of the reactions $H + FD(v) \rightarrow HF(v' = \text{all}) + D$ for $v = 0, 1, 2, 3$ as a function of reagent translational energy E^{tr} . The solid line is for $v = 0$, the dashed line is for $v = 1$, the dotted line is for $v = 2$, and the dashed line is for $v = 3$.

Figure 5. State-to-state reaction probabilities $P_{H+FD(1) \rightarrow HF(v') + D}^R$ of the reaction $H + FD(v = 1) \rightarrow HF(v') + D$ for $v' = 0, 1, 2$ as a function of reagent translational energy E^{tr} . The dashed line is for $v' = 0$, the

solid line is for $v' = 1$, and the dotted line is for $v' = 2$. While the $\text{HF}(v' = 3)$ product channel is energetically accessible in this energy range, the probability of reacting into it is less than 1% in this energy range, and is not shown.

Figure 6. Arrhenius plot of rate constants for the reactions $\text{D} + \text{FH}(v) \rightarrow \text{DF}(v' = \text{all}) + \text{H}$ (dashed line) and $\text{H} + \text{FD}(v) \rightarrow \text{HF}(v' = \text{all}) + \text{D}$ (solid line) over a temperature range from 450 to 1500°K. Where the curves are not continued to the highest temperatures, the scattering calculations were not carried out to sufficiently high energy for the integrand in eq. (6) to become sufficiently small. (a) $\text{H} + \text{FD}(v = 0)$, (b) $\text{D} + \text{FH}(v = 0)$, (c) $\text{H} + \text{FD}(v = 1)$, (d) $\text{D} + \text{FH}(v = 1)$, (e) $\text{H} + \text{FD}(v = 2)$, (f) $\text{D} + \text{FH}(v = 2)$, (g) $\text{H} + \text{FD}(v = 3)$.

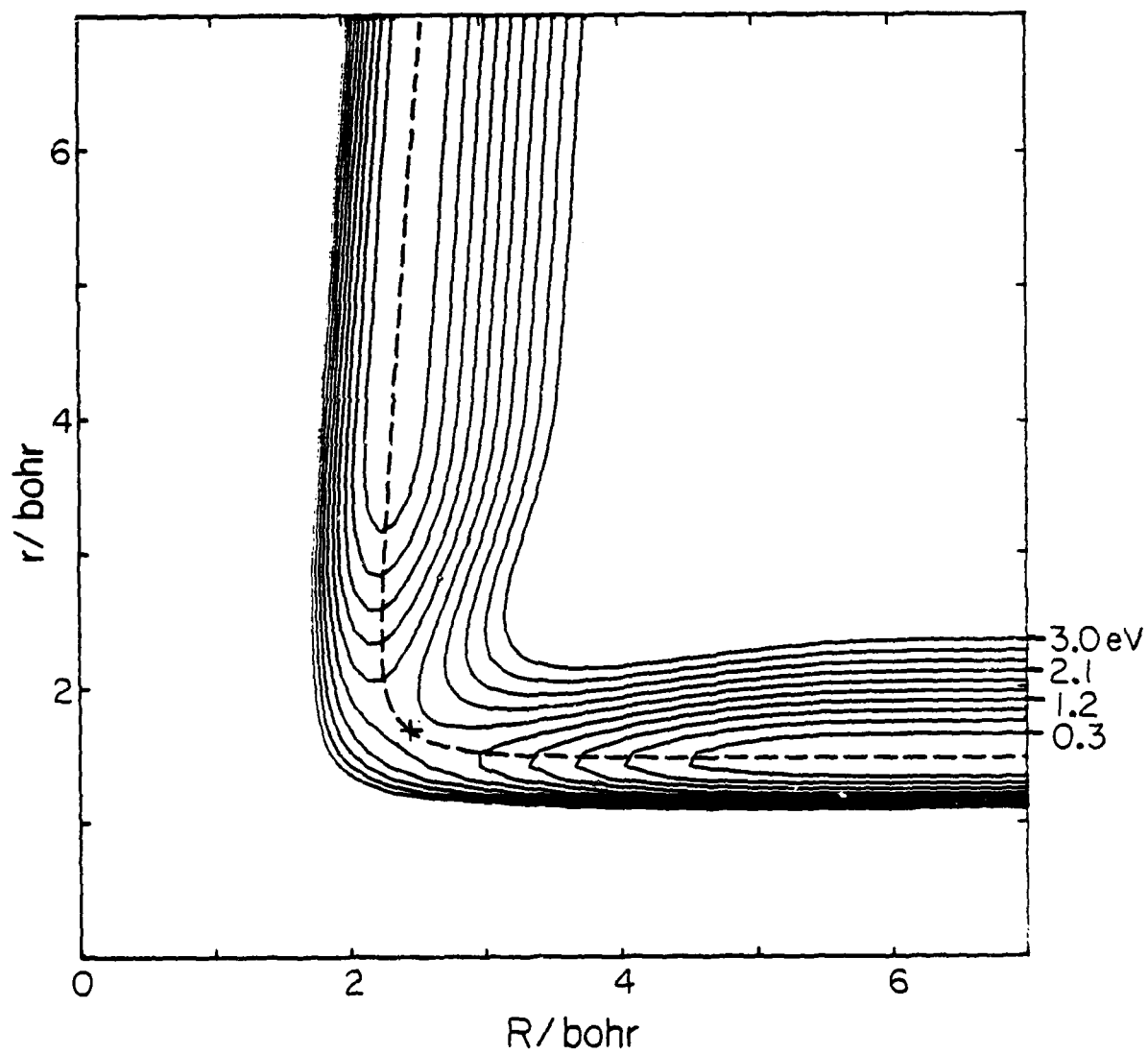


Figure 1

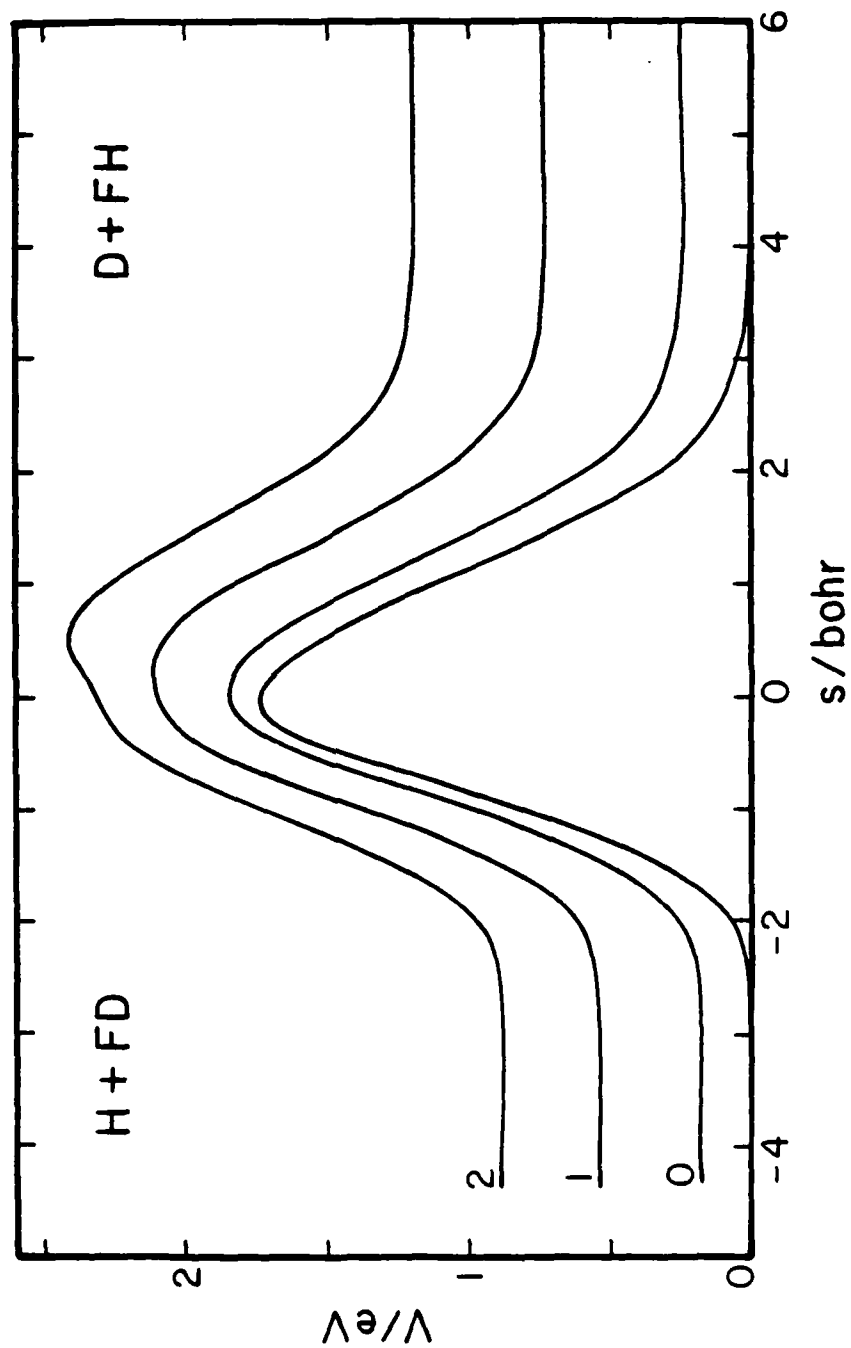


Figure 2

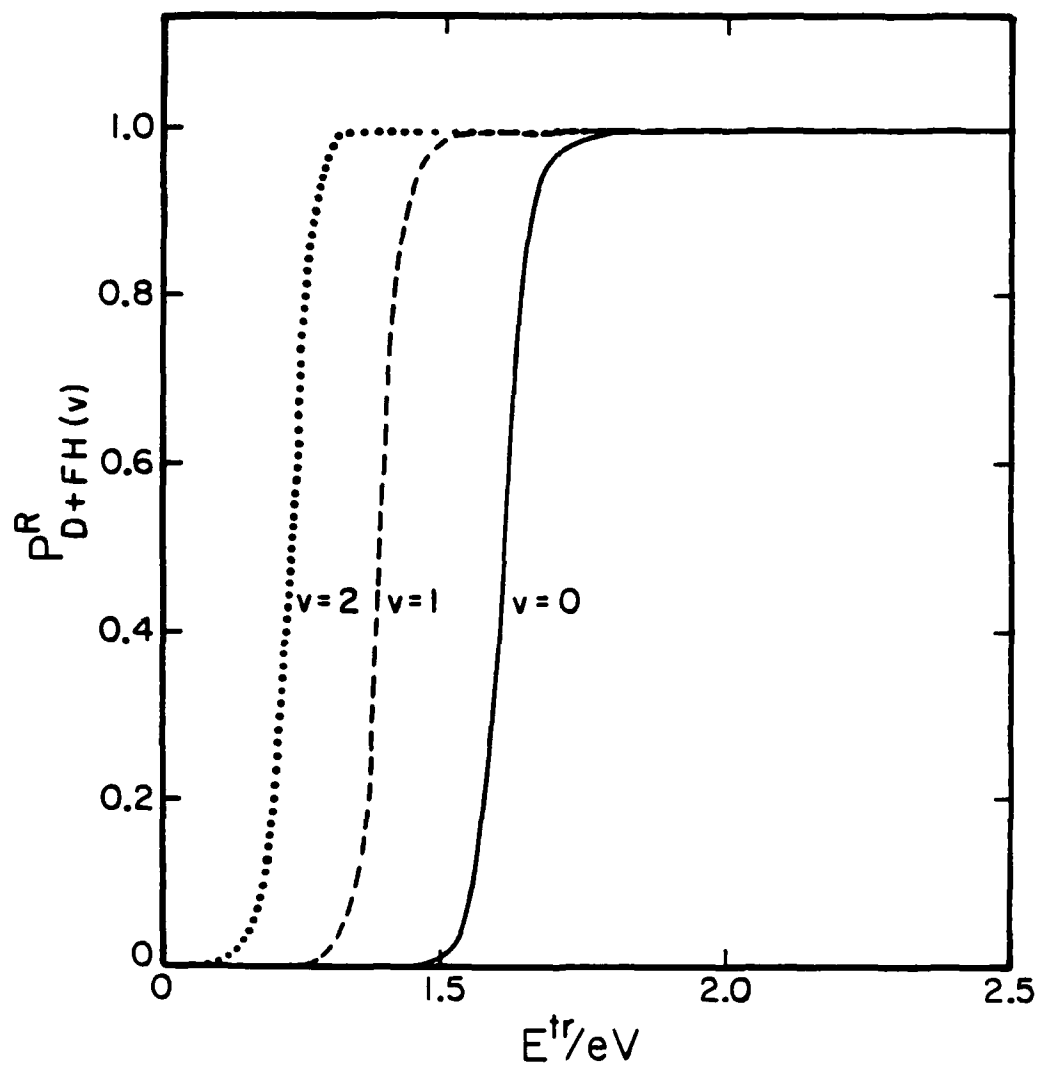


Figure 3

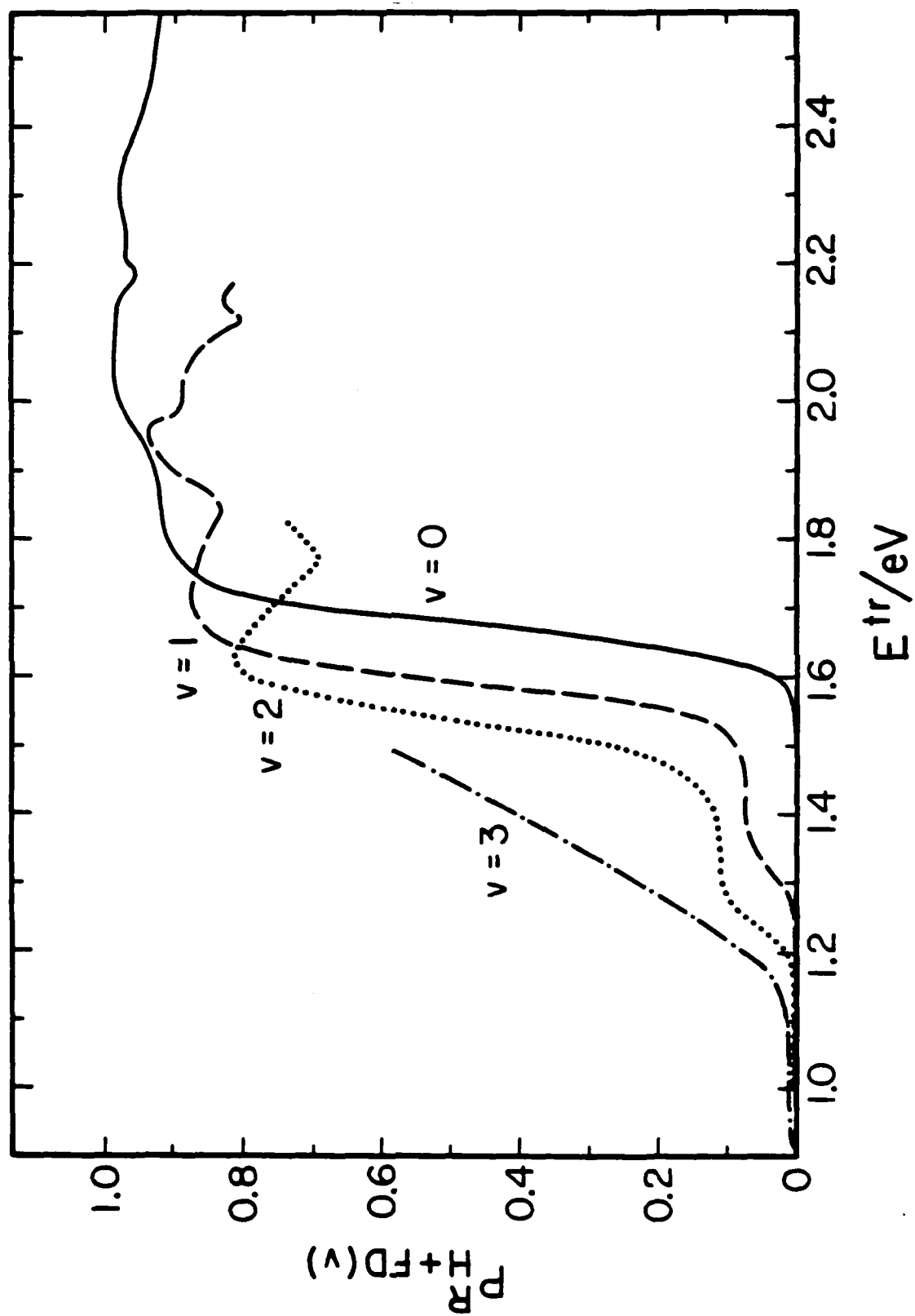


Figure 4

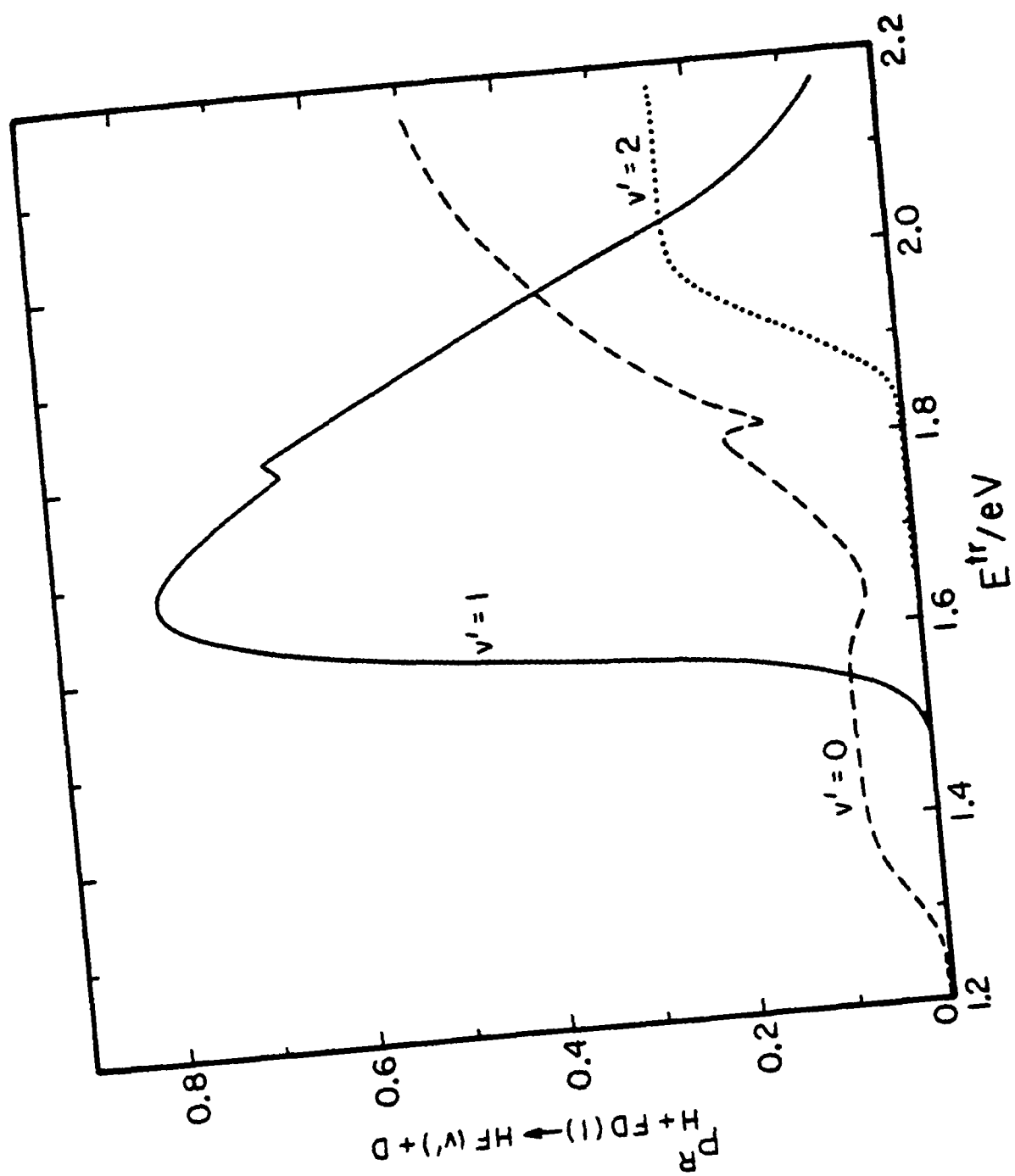


Figure 5

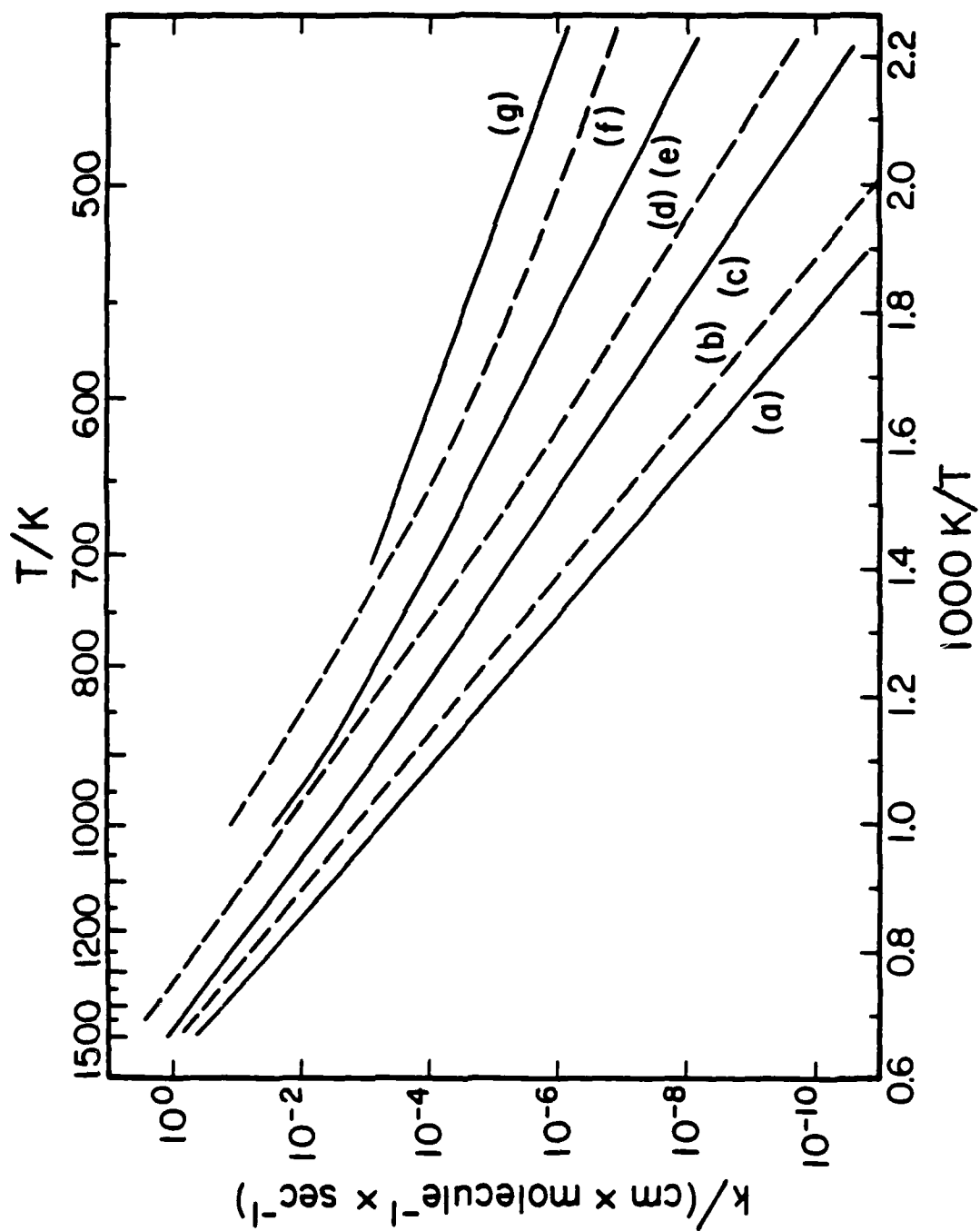


Figure 6

Collinear Quantum Mechanical Calculations on the Systems

HF(v) + H and HF(v) + D on a Realistic Potential Energy Surface.^{a)}

Jack A. Kaye^{b)}, John P. Dwyer^{c)}, and Aron Kuppermann

Arthur Amos Noyes Laboratory of Chemical Physics,^{d)}

California Institute of Technology, Pasadena, California 91125

(Received)

The rates of the reactions $\text{HF}(v) + \text{H}$ and $\text{HF}(v) + \text{D}$ as well as those of processes resulting in vibrational deactivation of HF have been studied by collinear quantum mechanical calculations on a realistic potential energy surface. The surface used has a 40 kcal/mole barrier to exchange, far greater than those used in previous calculations and in the vicinity of that suggested by ab initio calculations and recent experiments. It is found that vibrational deactivation of HF in this exchange channel occurs almost entirely by non-reactive single-quantum processes, and the rate of which varies weakly with reagent vibrational state. The rate of chemical reaction, however, is enhanced dramatically by reagent vibrational excitation, although vibrational energy lowers the threshold for reaction by far less than a vibrational quantum of energy. The relationship between vibrational and translational energy in promoting reaction will be discussed, as will the relationship of the results of these calculations to experimental data.

a) This work was supported in part by a contract (No. F49620-79-C-0187) from the Air Force Office of Scientific Research.

b) Work performed in partial fulfillment of the requirements for the Ph. D. degree in Chemistry at the California Institute of Technology.

c) Present Address: Supreme Court of the United States, Washington, D. C.
20543

d) Contribution No.

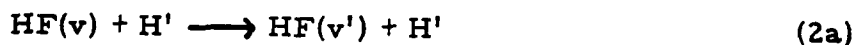
I. INTRODUCTION

A knowledge of accurate rate constants for the reactions of vibrationally excited hydrogen fluoride (HF) molecules with those atoms and molecules present in the HF laser system (1) (F_2 , H_2 , HF, H, F) is important if one is to accurately model the system's behavior. In the HF laser system, vibrationally excited HF is produced by one of the highly exoergic reactions (2)



These pumping reactions have received a great deal of attention, both experimentally (3) and theoretically (4). Of the deactivating processes present in the HF laser, the best studied are those due to inelastic collisions of vibrationally excited HF with other diatomics (ground state HF and H_2) (5). Collisions of vibrationally excited HF and H or F atoms have received less attention. Among the few studies of these processes include the experiments of Bott and Heidner (6) and Bartoszek, *et al.* (7), and the quasi-classical trajectory calculations of Wilkins (8), Thompson (9), and Thommarson and Berend (10). Recently, Schatz and Kuppermann (11) have studied the HF + H system (and its D-substituted counterparts) via a collinear quantum-mechanical calculation, although the barrier to reaction in the potential energy surface used in these calculations is now known to be unreasonably low. Baer (12) has performed a coplanar quantum mechanical calculation on the HF + H reaction, also on a surface with an unreasonably low barrier.

In this paper, we report the results of collinear quantum mechanical calculations on the systems $HF(v) + H$ and $HF(v) + D$. We consider those processes, both reactive and non-reactive, responsible for vibrational deactivation of HF, which may be represented by the reactions





The potential energy surface used in these calculations has a barrier to exchange of 40 kcal/mole. This is in line with recent ab initio calculations (13) as well as the definitive experiments of Bartoszek, et al. (7).

No attention will be given to deactivating processes in the abstraction channel



in this paper, although this channel is likely the one in which much of the deactivation of $\text{HF}(v=3)$ occurs.

We focus in this work on the relative rates of vibrational deactivation as a function of the initial state of the HF reagent, the fraction of deactivation occurring by reaction (processes 2b and 3b, respectively in the HFH and DFH systems), the relative importance of single and multi-quantum deactivating processes, and the relative effectiveness of translational energy in promoting reaction.

A brief outline of this paper is as follows. In section 2, we consider the potential energy surface used in these calculations and the reasons for which we chose to use it. In section 3, we very briefly discuss some of the important aspects of the calculation. In section 4, we present our results, which will be discussed in section 5. In section 6 we summarize by reviewing their significance.

II. POTENTIAL ENERGY SURFACE

There has been a great deal of interest over the last decade in determining the nature of the potential energy surface for reactions 2b and 3b. A large number of semi-empirical global potential energy surfaces, mainly of the extended LEPS type (14), have been developed for reaction 1a (15). The parameters for these surfaces were normally chosen to maximize agreement between the results of quasi-classical trajectory calculations and experiments on reaction 1a (quantities compared are usually rate constants and distributions of product vibrational and rotational states). Since these surfaces are global, the form of the exchange channel is determined by this optimization procedure (which has taken place in the abstraction channel). Most of these surfaces have a very small barrier to exchange, for example 1.2 kcal/mole for the well-known Muckerman V surface (4d). Such low barrier surfaces have been used in most dynamical calculations performed so far on reactions 2 and 3. A notable exception is the calculation done by Thompson (9), in which a surface with a barrier to exchange of 28.6 kcal/mole was used.

Four high quality ab initio calculations on the potential energy surface of reactions 2b and 3b yielded barrier heights of 49.0 (13a), 44.9 (13b), 47.6 (13c), and 48.3 (13d) kcal/mole, however, and the experiments of Bartoszek, et al. (7) seem to securely resolve this question in favor of a high barrier to exchange. In this calculation, therefore, we use a potential energy surface with a barrier to exchange of 40 kcal/mole, which seems to be within the range of uncertainty of the ab initio calculations.

The potential energy surface used in these calculations is of the rotating Morse- cubic spline type (16), made slightly less general by requiring that the potential energy along the minimum energy path as a function of the angle θ in reference 16 to be given by a Gaussian:

$$D(\theta) = D(\theta=0) - (A + B \exp(-C(\pi/4 - \theta)^2)) \quad (5)$$

The parameters have values $A = 0.01681$ kcal/mole, $B = 39.983$ kcal/mole, and $C = 33.879$ radians⁻¹. $\beta(\theta)$ and $l_{eq}(\theta)$ are defined in reference 16, and

are obtained by cubic spline interpolation between the values given for the supplied points listed in Table 1. The profile of the barrier height vs. reaction coordinate (distance along the minimum energy path from the saddle point as calculated in Delves mass-scaled coordinates (17)) for $H + FH$ is shown in figure 1, along with the asymptotic eigenvalues for HF and DF. A contour plot of the potential energy surface for $H + FH$ in Delves coordinates is shown in figure 2.

III. DETAILS OF THE CALCULATION

Numerical solution of the Schrödinger equation for these systems was performed using the coupled-channel method of Kuppermann (18), which has been described elsewhere. This technique has previously been applied to a number of systems, including $H + H_2$ and its isotopically substituted analogues (20), $F + H_2$ (4d), $F + D_2$ (21), $H + FH$ (on a low barrier surface) (11), and $Be + FH$ (22). 20 - 24 basis functions were used in the calculation, although no more than seven were open asymptotically at any of the energies studied.

Reactions 2a and 2b were studied in the energy range up to 2.94 eV above the zero-point energy of HF, while reactions 3a and 3b were studied up to 2.45 eV above the HF zero-point energy. The smaller range in the latter case was due to the smaller vibrational frequency of DF, which results in more open channels at a given energy than in the HF system (energy levels of isolated HF and DF are shown in figure 1). In all calculations reported here, flux was conserved to better than 3%; for most energies it was conserved to better than 1%.

From the transition probabilities obtained in these calculations, state-to-state rate constants were calculated by evaluating the usual integral

$$k_{ij}(T) = (2\pi\mu_{a,bc}kT)^{-1/2} \int_0^{\infty} P_{ij}(E^{tr}) \exp(-E^{tr}/kT) dE^{tr} \quad (6)$$

where P_{ij} is the probability for the transition from state i to state j , E^{tr} is the relative translational energy of the collision, and $\mu_{a,bc}$ is the reduced mass of the a, bc collision pair.

IV. RESULTS

We have obtained information on many aspects of the dynamics of the collinear HFH and DFH systems and will try to present some of the most important features of our results in this section. In particular, we will consider in this section and the ensuing discussion section questions such as the following:

- 1) What are the relative rates of deactivation of the vibrationally excited HF, and how do they vary with initial reagent excitation?
- 2) What is the relative importance of reactive and non-reactive processes?
- 3) What is the relative importance of single and multi-quantum transitions?
- 4) How do all of these quantities vary with temperature?
- 5) How do the roles of translational and vibrational energy in promoting reaction compare?
- 6) How do the results obtained for non-reactive processes compare with those predicted from simple models, such as the Landau-Teller model (23)?
- 7) What is the nature and magnitude of the isotope effect on going from the HFH to the DFH system?

A. H + FH

Rates for state-to-state vibrational deactivation have been calculated for temperatures in the range $200 \text{ K} \leq T \leq 1000 \text{ K}$. Values of the rate constants at three temperatures (300, 650, 1000 K) are contained in Table 2. For purposes of comparison, we also include in Table 2 the "gas kinetic" rates for the H + FH system at these three temperatures. This rate is that obtained if a transition occurred with unit probability at all energies; hence, it represents the sum of all possible state-to-state rate constants at a given temperature. It is seen that at all three temperatures, the total rates of deactivation are less than 1% of the gas kinetic rate. Thus, vibrational deactivation is a very unlikely process.

AD-A138 168

THE QUANTUM DYNAMICS OF CHEMICAL REACTIONS(U)
CALIFORNIA INST OF TECH PASADENA DIV OF CHEMISTRY AND
CHEMICAL ENGINEERING A KUPPERMANN 31 MAR 83

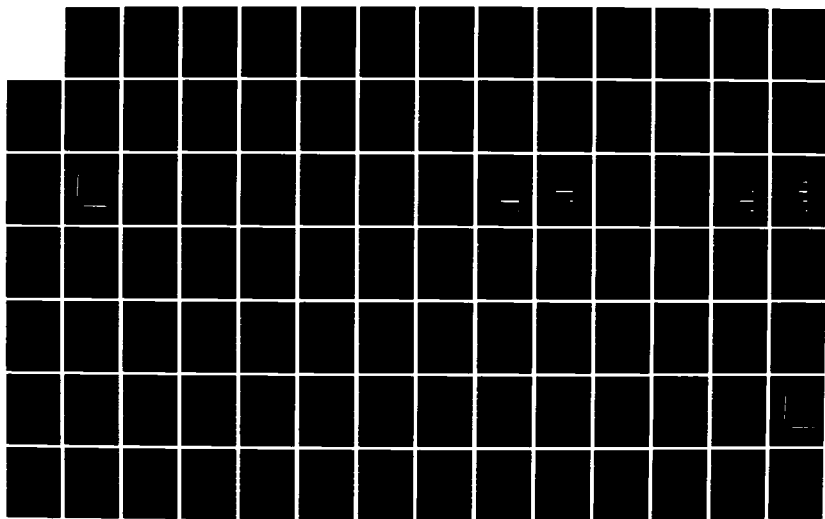
4/8

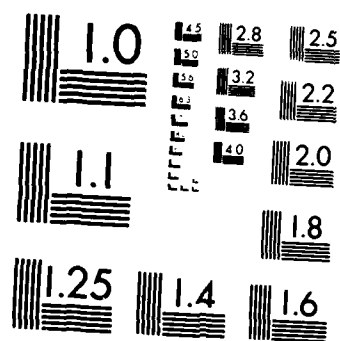
UNCLASSIFIED

AFOSR-TR-83-0565 AFOSR-81-0235

F/G 20/10

NL





MICROCOPY RESOLUTION TEST CHART
NATIONAL BUREAU OF STANDARDS 1963-A

We display total rate constants for vibrational deactivation, both reactive and non-reactive, as a function of initial HF quantum number in figure 3. Three important features of the dynamics are clearly evident on this plot:

- 1) For all initial quantum states at all temperatures, non-reactive deactivating processes are much more likely than reactive processes, and account for, to a good degree of approximation, all the deactivating processes.
- 2) The variation of the rate of deactivation occurring by non-reactive processes with initial HF quantum number is far less than that of the reactive processes.
- 3) The variation of the rate of deactivation occurring by non-reactive processes with temperature is far less than that of the reactive processes.

An additional difference between the dynamics of deactivating processes in non-reactive collisions from those occurring in reactive ones may be seen in Table 2. Specifically, in non-reactive collisions, vibrational deactivation occurs overwhelmingly by single-quantum transitions, while in reactive collisions, deactivation by multi-quantum transitions is favored. Further, while the dominance of non-reactive deactivating processes by single-quantum transitions occurs over the whole temperature range considered, in reactive deactivating processes, as temperature increases, the single-quantum processes become more important than they are at lower temperatures. This may be seen graphically in figure 4, in which four state-to-state rate constants (k_{20}^N , k_{21}^N , k_{20}^R , k_{21}^R , where the superscripts N and R refer to non-reactive and reactive processes, respectively) are plotted vs. temperature as Arrhenius plots, that is, $\ln k$ vs. $1/T$. We will consider in some detail the vibrational state distribution of the products of reactions 2b and 3b later on.

In considering the temperature dependence of the rate constants

obtained, it is frequently useful to make Arrhenius plots (defined above) of the rate constants as a function of temperature. It is known that for a wide variety of chemical reactions, such plots yield straight lines, although curved Arrhenius plots are also common (24). In the systems studied, it is frequently seen that Arrhenius plots for state-to-state rate constants are linear at high temperatures (≥ 700 K), but are non-linear at lower temperatures. Frequently, they have linear regions at high (700 - 1000 K) and low temperatures (200 - 400 K), but are curved in between.

Reactions yielding linear Arrhenius plots obey the relationship

$$k = A \exp(-E_a / k_b T) \quad (7)$$

where A is the Arrhenius pre-exponential factor, E_a is the activation energy for the reaction, and k_b is Boltzmann's constant. These quantities correspond to the y intercept and slope of the Arrhenius plots, respectively. For ground vibrational state reagents, the activation energy of a reaction is usually fairly close to the barrier height to the reaction in the potential energy surface; when the reagents are vibrationally excited, it is frequently less. We examine plots of activation energies vs. initial quantum states for n-quantum non-reactive and reactive deactivating processes in figures 5 and 6, respectively.

In figure 5, it is seen that there is no well-defined relationship between the activation energies for the non-reactive processes and reagent vibrational state. There does seem to be a clear difference in the magnitudes of the activation energies for deactivation from $v = 4$ and 5 and those from $v \leq 3$. Further, for deactivation from the higher vibrational state, the activation increases drastically for large multi-quantum transitions. Much more regular (and different) behavior is observed in figure 6, in which we consider activation energies for reactive deactivating processes. In this case, one may clearly see that the activation energies decrease substantially with reagent vibrational excitation, and in general, decrease as one goes from single-quantum to multi-quantum

transitions. This is another example of differing dynamics between non-reactive and reactive collisions. This subject will be further explored later on.

Because of the large barrier to exchange (40 kcal/mole) in the potential energy surface used in these calculations, it is reasonable that reaction should only occur at high translational energies. This may be easily seen in figure 7, in which the total probability of reaction P_v^R is plotted vs. translational energy for initial reagent vibrational states $v = 0-3$. Reaction becomes appreciable at successively smaller values of the translational energy as the vibrational level of the HF reagent is increased. The decrease in translational energy requirement for reaction threshold is in the vicinity of 0.15 - 0.20 eV per vibrational quantum, which is substantially smaller than the vibrational quantum of 0.45 - 0.49 eV. This difference will be considered more fully later. It is also evident that as the initial HF vibrational state is increased, the probability for reaction vs. translational energy curve becomes more irregular, not increasing smoothly to one as the $v = 0$ curve does.

In studying the dynamics of the reactive processes in general, it is worthwhile to consider the distribution of product vibrational states, for deactivating, vibrationally adiabatic (involving no change in quantum number) and exciting (involving an increase in the quantum number) processes. We consider some of these distributions for the HF reagent in its $v = 1$ and $v = 2$ states at differing translational energies in figures 8 and 9, respectively. In these figures, the product state distribution is given in terms of $F_{vv'}^R$, the fraction of reaction products going into the product state v'

$$F_{vv'}^R = \frac{P_{vv'}^R}{\sum_{v'=0}^{v_{\max}} P_{vv'}^R} \quad (8)$$

where v_{\max} is the maximum quantum number permitted by energy conservation. It is seen that at lower translational energies (but high enough

for a large probability for reaction), vibrationally adiabatic reaction is far more likely to occur than either deactivating or exciting reaction. This preference for vibrational adiabaticity decreases as translational energy increases. At the highest translational energies considered, the distribution of product states is fairly flat for $v = 2$ reagent and shows some evidence of bimodality for $v = 1$ reagent.

One good measure of the distribution of product states is the average fraction of available energy going into product vibration, which is defined by the formula

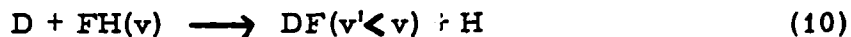
$$\langle f_v^R \rangle = \frac{\sum_{v'=0}^v P_{vv'}^R E_{v'}}{(E^{tr} + E_v) \sum_{v'=0}^v P_{vv'}^R} \quad (9)$$

where energies are measured with respect to the bottom of the product well. This quantity is displayed in figure 10 for the $H + FH(v \leq 3)$ reactions. No data are presented for the $v = 4$ and 5 initial reagent states because the calculations were not carried out to sufficiently high energy for there to be appreciable reaction. Lines are drawn to represent the value this quantity would have if all reactions proceeded adiabatically (with no change of quantum number). For $v = 0$ and $v = 1$ reagents, at low translational energies (but still high enough for appreciable reaction), this quantity is fairly close to that expected if all reaction proceeded adiabatically, but at higher translational energies, it increases. Thus, at high translational energies, vibrational excitation is more likely than deactivation in reactive collisions. For $v = 2$ and $v = 3$ reagents, the calculated points lie below the lines; hence, in the energy range considered, the net effect of the reactive collisions is a deactivating one.

B. D + FH

In considering the deactivation processes in this system, we have elected to look mainly at the processes which represent deactivation in an "absolute quantum number" sense, that is, for reactive deactivating

processes, only those of the type



Due to the smaller vibrational energy spacing in DF than in HF, it is possible, as may be seen from figure 1, for some DF(v) levels to actually have less internal energy than some HF(v-n) level, where n is an integer that is 0 for v = 0, 1, 2, 3, 1 for v = 4, and which increases irregularly with v thereafter. Further, since all vibrationally adiabatic reactions of the type 3b (where v' = v) have the DF product containing less internal energy than the reagent HF, they might be defined as deactivating processes in the "strict energetic" sense.

State-to-state rate constants for the deactivating processes 4a and 4b are given in Table 3, at 300, 650, and 1000 K along with the corresponding gas kinetic rate constants. Again, the overwhelming dominance of non-reactive processes (and single-quantum deactivating ones) is seen. A few reactive processes not satisfying the strict quantum number definition for deactivation are also included in Table 3. These processes become more important relative to the total set of reactive deactivating processes as temperature increases. As in the H + FH case, the net contribution of reactive processes to the total deactivation of vibrationally excited HF may be neglected.

On the whole, the deactivation rates for HF by collisions with D is smaller than that for deactivation by H. Some of this difference is to be expected by consideration of the gas kinetic rate constants, which are related by the expression

$$k_{D+FH}^{GK} = 0.724 k_{H+FH}^{GK} \quad (11)$$

(the superscript GK refers to gas kinetic); the magnitude of the difference observed is greater than this, however.

Because of the similarity between the dynamics of the non-reactive deactivating processes in the H + FH and D + FH systems, we will focus our attention on the reactive ones, particularly because these are most easily amenable to experimental study. We first consider the total proba-

bility for reaction as a function of translational energy for initial HF states $v = 0, 1, 2$. This is plotted in figure 11 in a manner analogous to that used in figure 7 for the $H + FH$ system. We see large thresholds, very similar in magnitude to those observed in the $H + FH$ case. The spacings between the curves are on the order of 0.15 and 0.22 eV between the $v = 1$ and 2 and the $v = 0$ and 1 curves. This is very close to the 0.15 - 0.20 eV spacings observed in the $H + FH$ system. One difference between the two systems is that the reaction probabilities seem to rise more smoothly to one (and to stay there) for reagent states $v = 1$ and 2 in $D + FH(v)$ collisions than in the corresponding $H + FH$ ones.

We have also examined the distribution of product (DF) vibrational states for initial reagent states $HF(v = 1, 2)$ at a few translational energies, some of which were the same as in the corresponding $H + FH$ cases. These are shown in figures 12 and 13 for $v = 1$ and 2, respectively. It is observed that there is slightly less tendency towards vibrational adiabaticity than in $H + FH$. As in the $H + FH$ case, the product distribution broadens as one goes to higher translational energies, and there is some evidence for bimodality in the distribution at high energies.

Finally, we have calculated the average fraction of product energy going into vibration. This is displayed in figure 14 for HF initial states $v = 0, 1, 2$ (this is analogous to figure 10 for $H + FH$). Again, lines are drawn through the points representing the value of $\langle f_v \rangle$ if the reaction proceeded adiabatically. Since the DF vibrational spacing is smaller than that of HF, $\langle f_v \rangle$ for the $D + FH$ reaction should be smaller than for the $H + FH$ one. By comparing figures 10 and 14, it can be seen that this is indeed the case.

V. DISCUSSION

The overwhelming dominance of non-reactive processes in accounting for vibrational deactivation of HF in collisions with H and D atoms in the exchange channel makes it useful to discuss the non-reactive processes separately from the reactive ones. Also, we have shown that the dynamics of the reactive and non-reactive processes are very different (for example in their preference for single or multi-quantum transitions, and in their activation energies). We will consider first the non-reactive deactivating processes, focusing on the variation of the deactivation rate with reagent vibrational state and the degree to which the calculated deactivation rates obey predictions of the approximate Landau-Teller theory. We will then consider the reactive processes, particularly the relative ability of translational and vibrational energy to promote reaction. We will also examine the results of our calculations in the light of experimental studies of the vibrational deactivation of HF by H and D atoms to show that deactivation of HF($v=1, 2, 3$) must be dominated by processes occurring in the abstraction channel 4.

A. NON-REACTIVE PROCESSES

The calculations show that, in general, the rate of vibrational deactivation increases as reagent vibrational excitation increases. This is true for HF($v=1, 2, 3$) + H and D. In the HF($v=4, 5$) + H cases one does see lower deactivation rates than for HF($v=3$) + H, although the decrease becomes smaller at higher temperatures. Because of the large barrier to exchange present in the potential energy surface, it may be reasonable to consider whether the key features in the results obtained here might have been obtained by a model based on a purely non-reactive system, i.e. one in which reactions 2b and 3b cannot occur.

Such a model is the Landau-Teller model (described in reference 23) for energy transfer in non-reactive collisions. The chief predictions of this model (that of a collision of a particle with a harmonic

oscillator governed by a repulsive exponential potential)
are as follows:

- 1) All deactivations occur by single quantum transitions.
- 2) The rate constants for deactivating processes between different vibrational levels are related to the $1 \rightarrow 0$ deactivation rates

by the expression

$$k_{v, v-1}^N = v k_{1, 0}^N \quad (12)$$

- 3) The rate constant for the deactivating process is related to the temperature T by the expression:

$$\ln k_{v, v-1}^N = A - B T^{1/3} \quad (13)$$

where

$$B = 3 \left(\frac{2\pi^4 \mu \nu^2}{\alpha^2 k_b} \right)^{1/3} \quad (14)$$

where μ is the reduced mass of the collision partners, ν is the vibrational frequency of the harmonic oscillator, and α is related to the steepness of the assumed exponential interaction potential

$$V(r) = V_0 \exp(-\alpha r) \quad (15)$$

where r is the distance from the center of mass of the harmonic oscillator to that of the second particle.

Landau-Teller plots (plots of $\ln k_{v, v-1}^N$ vs. $T^{-1/3}$) for $H + FH$ and $D + FH$ are shown in figures 15 and 16, respectively. The plots are all reasonably linear (meaning equation 13 is approximately obeyed by the data), especially at lower temperatures. Further, the slopes of the $v = 1, 2, 3$ curves for $H + FH$ are all roughly the same, as are those for the $v = 4$ and 5 curves for HF and those for $v = 1, 2, 3$ for $D + FH$. The major deviation in behavior from that predicted by Landau-Teller theory, then, is the smaller value of the rate constants for deactivation from $v = 4$ and 5 in $H + FH(v)$ collisions, and the different slope from the $v = 1, 2, 3$ curves (notice that according to eq. 13 the slope of the Landau-Teller plot should be independent of the initial vibrational state).

The effect of substituting D for H as one of the collision partners may also be examined in light of the predictions of the Landau-Teller model. From equation 13, one sees that the slope of the Landau-Teller plot should be proportional to the one-third power of the reduced mass of the collision. Since this mass for D + FH is roughly twice its value for H + FH, the slopes for D + FH deactivations should be greater than for H + FH deactivations by a factor of $2^{1/3}$ or roughly 5/4. It is difficult to calculate exact ratios of slopes due to the non-linearity in the Landau-Teller plots in figures 15 and 16 at high temperature. Using crude estimates, however, one can find that the slopes are indeed greater for the D + FH deactivations than for H + FH by a number that varies between 20% and 45%. Thus, the Landau-Teller model does predict the general behavior and magnitude of the effect of isotopic substitution on the temperature dependence of the single-quantum non-reactive deactivating processes.

The main failing of the Landau-Teller theory, then, is its inability to predict the difference in the temperature dependence and thus the magnitude of the rate constants k_{43}^N and k_{54}^N . It is tempting to attribute this failing to the fact that the total vibrational energy associated with the $v = 4$ and 5 levels is greater than the 40 kcal/mole barrier. Since there is always sufficient energy in collisions involving these states to overcome the classical barrier, one might expect different dynamics than in cases (i.e. $v \leq 3$) where a substantial amount of translational energy is needed. There is no strong evidence for this interpretation, however.

One might be able to verify such a hypothesis by reducing the barrier height of the surface somewhat such that it is between the $v = 2$ and $v = 3$ levels. In that case, one might expect different dynamics in collisions involving HF($v = 2$) and HF($v = 3$). We have carried out scattering calculations for this reaction on a variety of surfaces with reduced barriers (25) but otherwise identical to that used here (the para-

meters A, B, and C defined in eq. 5 giving the energy along the minimum energy path as a function of the angle θ differ; the functions $l_{eq}(\theta)$ and $\beta(\theta)$ as defined in ref. 16 are identical), and will conduct similar Landau-Teller analyses of the dynamics on those surfaces.

A dynamical reason for this difference might be observable in collinear quasi-classical trajectory calculations. However, the small fraction of collisions resulting in vibrational deactivation might make such a study difficult.

B. REACTIVE PROCESSES

As has been mentioned repeatedly, the net contribution of reactive processes to vibrational deactivation is essentially negligible over the temperature range studied. Thus, the interest in reactive processes centers around the effect of reagent vibrational excitation on reaction rate and the distribution of product vibrational states. For reaction 3b both of these quantities should be fairly easily accessible to experimental study (the experiments of Bartoszek, et al. (7) included a study of the former).

From table 2 and figure 3, the enhancement in the rate of reaction with vibrational excitation for reaction 2b is clear; table 3 similarly shows the effect for reaction 3b. For reaction 2b at 300 K, for example, the relative rates of reaction for $v = 1, 2, 3, 4, 5$ are approximately $1:10^4:10^{11}:10^{13}:10^{15}$. In spite of this large vibrational enhancement, we can show that the efficiency of vibrational excitation in promoting reaction is quite small. This can be seen in a variety of ways.

First, one may consider the threshold energy for reaction. We define this quantity as the translational energy at which the probability for vibrationally adiabatic reaction first reaches 0.01. This quantity is plotted as a function of vibrational energy in figure 17 for both reactions 2b (for $v = 0, 1, 2, 3, 4$) and 3b (for $v = 0, 1, 2, 3$). If vibrational energy and translational energy were equally effective in promoting reaction, the lines in figure 17 would have slopes of -1, as the total

energy threshold for reaction would be independent of reagent vibrational state. Instead, the curves are non-linear, although they can be fairly well approximated by straight lines whose slopes are approximately -0.31 for reaction 2b and -0.36 for reaction 3b. Thus, only some 1/3 of the vibrational energy goes towards promoting reaction. This fact can also be seen in the plots of total reaction probability vs. translational energy for reactions 2b and 3b (figures 7 and 11, respectively) in which it is seen that each quantum of reagent excitation lowers the region of rapid increase of probability with translational energy by only 0.15 - 0.20 eV, less than half the vibrational spacing of HF of 0.50 eV. This inefficiency of vibrational energy is also seen in figure 6, in which even in the $v = 5$ state, where the reagent has some 2.4 eV of vibrational energy above the zero-point energy, the activation energies for reaction 2b may be as high as 13 kcal/mole. Since this amount of vibrational energy is far in excess of the 40 kcal/mole classical barrier height, one can see that vibrational energy is not entirely useful in promoting reaction.

In comparing threshold energies for different reagent vibrational states, it is important not to neglect the contributions of the vibrational energies for the H--F--H configuration occurring at the saddle point (R^\ddagger, r^\ddagger) on the potential energy surface. Because the surface does not appreciably widen near the saddle point region these energies will be fairly large, and thus the vibrationally adiabatic barrier height ΔV_v^\ddagger , defined by the expression

$$\Delta V_v^\ddagger = E_v(R^\ddagger, r^\ddagger) - E_v(R=\infty) \quad (15)$$

will decrease only gradually with increasing v .

We have calculated the ΔV_v^\ddagger for reaction 2b, and plotted the reaction threshold vs. them in figure 18. The resulting plot is approximately linear with a slope of 0.8. Thus, as the reagent vibrational state is increased (decreasing ΔV_v^\ddagger), the reaction threshold does not decrease as quickly as ΔV_v^\ddagger , although the two decreases are fairly

close in magnitude. Thus, much of the inefficiency of vibrational excitation in producing reaction is due to the persistence of a large vibrationally adiabatic barrier height to large quantum numbers. Because the vibrationally adiabatic barrier heights can be expected to be slightly smaller for reaction 3b than for 2b due to the heavier D atom being substituted for one of the H atoms at the saddle point, vibrational energy should be slightly more effective at promoting reaction 3b than 2b. This is observed in figure 15, where the slope of the threshold energy vs. vibrational energy curve is some 10% higher for reaction 3b than for 2b.

This feature of the dynamics might be particularly sensitive to the exact nature of the potential energy surface near the saddle point, as a smaller vibrational frequency at the saddle point would decrease ΔV_v^\ddagger , thus increasing the efficiency of vibrational energy in promoting reaction. Similarly, increased curvature in the minimum energy path produced, for example, by moving the saddle point to large values of R_{HF} , might better couple translational and vibrational energy, thus leading to increased efficiency of reagent vibrational excitation.

C. RELATIONSHIP TO EXPERIMENT

In analyzing the vibrational deactivation of HF by H and D, one must be careful in relating the results of collinear quantum mechanical calculations to experiment. The calculations reported here do not include the abstraction channel, which may be where most of the deactivation occurs, and include only the collinear portion of the exchange channel, possibly eliminating important non-collinear reactions of the overall potential energy surface. We will attempt in what follows to deal with these two limitations.

The experiments most relevant to the study of HF vibrational deactivation by H and D atoms are those of Bartoszek, et al. (7) and of Bott and Heidner (6). Additional experiments have been performed by Quigley and Wolga (26). Bartoszek, et al. (7) showed that DF forma-

tion via the reaction 3b only becomes appreciable when the initial vibrational state of HF was five or greater. They also showed that disappearance of HF($v = 3, 4$) was due to the abstraction reaction (the D analogue of reaction 4a). In their kinetic work, Bott and Heidner (6) found relative rate constants for removal of HF($V = 1, 2, 3$) by collision with H atoms of 1:4:400, and determined that the abstraction reaction 4a can contribute only some 20% of the observed removal rate of HF($v = 3$) at 295 K. This latter result seems to contradict that of Bartoszek, et al. (7), who relate the increase in deactivation of HF($v = 3$) by D atoms to the opening up of the abstraction channel.

In our calculations in the exchange channel, we see nothing remotely resembling the 1:4:400 ratio for deactivation of HF($v = 1, 2, 3$) by H atoms observed by Bott and Heidner (6). Instead, as mentioned earlier, the deactivation rate increases nearly linearly with reagent vibrational state for $v \leq 3$. Unless these results were to change drastically on going to a full three-dimensional calculation, it seems reasonable to attribute the results of Bott and Heidner (6) to deactivating processes occurring in the abstraction channel. Our rate constants for reactions 2b and 3b do show a very dramatic increase with reagent vibrational excitation, and support the interpretation of Bartoszek, et al. (7) that the barrier to exchange for reactions 2b and 3b must be large (over 40 kcal/mole).

The usefulness of the calculations for reactions 2b and 3b depends to some extent on the accuracy of the potential energy surface, and in particular, the requirement of collinearity implicit in these calculations. While it has long been assumed that the transition states for the exchange reactions 2b and 3b are collinear, ab initio calculations (13c) suggest that the transition state should instead have an HFH angle of 106° , although the height of the barrier should be relatively insensitive to that angle, increasing from 47.1 kcal/mole at 106° to 47.6 kcal/mole at 180° . Including these non-collinear configurations could easily in-

fluence the observed dynamics of the exchange reactions.

Further, the exact form of the potential energy surface used here was chosen mainly for its flexibility. There is no reason to believe that the appearance of the minimum energy path is exactly that shown in figures 1 and 2; in fact, it is quite possible that the 40 kcal/mole barrier is a few kcal/mole less than the correct one, and that the position of the saddle point used ($R_{HF} = 1.975$ bohr) is smaller than the correct value (for example, Bender, Garrison, and Schaefer (13a) calculated it to occur at 2.15 bohr). Thus, the results obtained for the exchange reactions should not be taken to be more than qualitatively correct.

VI. CONCLUSIONS

We have studied on a realistic (high barrier) potential energy surface the dynamics of vibrational deactivation of HF in collision with H and D atoms in the exchange channel and also the dynamics of the $H + FH$ and $HF + D$ exchange reactions. The important features of the dynamics are as follows:

- 1) Vibrational deactivation in the exchange channel occurs almost entirely by single-quantum, non-reactive processes. The rate of this deactivation varies only weakly with temperature, and, in general, increases weakly with reagent vibrational excitation. The overall dynamics of the deactivation processes are in line with the predictions of Landau-Teller theory.
- 2) The rate of the exchange reactions is increased dramatically by reagent vibrational excitation, although the effective lowering of the threshold to reaction is less than half the extra energy associated with each vibrational quantum. Rates of exchange reactions are characterized by large temperature dependences, and at high translational energies, broad product state distributions. The relative inefficiency of vibrational energy in promoting reaction can be related to the large symmetric stretch vibrational frequency at the $H--F--H$ saddle point, resulting in a vibrationally adiabatic barrier height which decreases only weakly with an increase in the reagent vibrational quantum number.
- 3) The relationship of the calculated results to experimental ones on these systems is complicated because of the collinear nature of the theory; nevertheless, the results do support interpretations that the deactivation of $HF(v \leq 3)$ by H atoms must be occurring by processes in the abstraction channel and also support interpretations of experimental results that the barrier to exchange is quite high (≥ 40 kcal/mole).

A fuller understanding of the dynamics in this system awaits a study of the dynamics of the abstraction channel (preliminary work on the $H + HF$ system has been performed (27)) and the relation of the results of the two channels by some technique (i.e. information theoretic one dimensional to three dimensional transformation (28)). Finally, additional information from ab initio calculations on the potential energy surface for the exchange calculation would be useful in insuring a more accurate description of the saddle point region.

ACKNOWLEDGMENTS

We thank Ambassador College for the generous use of its computational facilities for most of the calculations reported here. Additional calculations were performed on the Dreyfus-NSF Theoretical Chemistry Computer (VAX 11/780) at Caltech, which was funded through grants from the Camille and Henry Dreyfus Foundation, the National Science Foundation (Grant No. CHE78-20235), and the Sloan Fund of the California Institute of Technology. One of us (JAK) would like to thank Dr. Nancy M. Harvey for helpful comments on an earlier version of this manuscript.

REFERENCES

1. N. Cohen and J. F. Bott, in: Handbook of Chemical Lasers, ed. R. W F. Gross and J. F. Bott (Wiley-Interscience, York, 1976), Ch. 2
2. The $F + H_2$ reaction has been reviewed in J. B. Anderson, Adv. Chem. Phys. 41, 229 (1980); an extensive review of all work on the $F + H_2$ and $H + F_2$ reactions may be found in M. R. Levy, Prog. React. Kin. 10, 1, (1979).
3. Recent references include, for $F + H_2$:
E. Würzberg and P. L. Houston, J. Chem. Phys. 72, 4811 (1980),
R. F. Heidner III, J. F. Bott, C. E. Gardner, and J. E. Melzer, J. Chem. Phys. 72, 4815 (1980); R. K. Sparks, C. C. Hayden, K. Shobatake, D. M. Neumark, and Y. T. Lee, in : Horizons of Quantum Chemistry, ed. K. Fukui and B. Pullman (D. Reidel, Boston, 1980), pp. 91 - 105.
4. For example, for $F + H_2$:
a) S. H. Suck, Chem. Phys. Lett. 77, 390 (1981);
b) M. J. Redmon and R. E. Wyatt, Chem. Phys. Lett. 63, 209 (1979); c) J. N. L. Connor, W Jakubetz, and J. Manz, Mol. Phys. 35, 1301 (1978); d) G. C. Schatz, J. M. Bowman, and A. Kuppermann, J. Chem. Phys. 63, 674 (1975).
for $H + F_2$:
e) D. C. Clary and J. N. L. Connor, Chem. Phys. Lett. 66, 493 (1979); f) W Jakubetz, Chem. Phys. 35, 129 (1978).
5. See, for example: a) G. M. Jurisch and F. F. Crim, J. Chem. Phys. 74, 4455 (1981); b) R. L. Wilkins and M. A. Kwok, J. Chem. Phys. 73, 3198 (1980); c) R. L. Wilkins, J. Chem. Phys. 70, 2700 (1979); d) M. E. Coltrin and R. A. Marcus, J. Chem. Phys. 73, 4390 (1980).
6. a) J. F. Bott and R. F. Heidner III, J. Chem. Phys. 68, 1708

- (1978); b) R. F. Heidner III and J. F. Bott, Ber. Bunsen. Gesellschaft 81, 128 (1977); c) J. F. Bott and R. F. Heidner III, J. Chem. Phys. 66, 2878 (1977); d) R. F. Heidner III and J. F. Bott, J. Chem. Phys. 63, 1810 (1975).
7. F. E. Bartoszek, D. M. Manos, and J. C. Polanyi, J. Chem. Phys. 69, 933 (1978).
 8. R. L. Wilkins, J. Chem. Phys. 58, 3038 (1975); Mol. Phys. 29, 555 (1975).
 9. D. L. Thompson, J. Chem. Phys. 57, 4~64, 4~75 (1972).
 10. R. L. Thommarson and G. C. Berend, Int. J. Chem. Kin. 6, 597 (1974).
 11. G. C. Schatz and A. Kuppermann, J. Chem. Phys. 72, 2737 (1980).
 12. M. Baer, J. Chem. Phys. 65, 493 (1976).
 13. a) C. F. Bender, B. J. Garrison, and H. F. Schaefer III, J. Chem. Phys. 62, 1188 (1975); b) P. Botschwina and W. Meyer, Chem. Phys. 20, 43 (1977); c) W. R. Wadt and N. W. Winter, J. Chem. Phys. 67, 3068 (1977); d) A. F. Voter and W. A. Goddard III, J. Chem. Phys. 75, 3638 (1981).
 14. P. J. Kuntz, E. M. Nemeth, J. C. Polanyi, S. D. Rosner, and C. E. Young, J. Chem. Phys. 44, 1168 (1966).
 15. H. F. Schaefer III, in: Atom-Molecule Collision Theory, ed. R. B. Bernstein (Plenum Press, New York, 1979), pp. 45-78.
 16. J. M. Bowman and A. Kuppermann, Chem. Phys. Lett. 34, 523 (1975).
 17. L. N. Delves, Nucl. Phys. 9, 391 (1959); 20, 275 (1960).
 18. A. Kuppermann, in: Potential Energy Surfaces in Chemistry, ed. W. A. Lester (U. Calif. Santa Cruz, 1970), pp. 121-129; in: Abstracts of Papers VII, ICPEAC, (North-Holland, Amsterdam, 1971), pp. 3-5.
 19. G. C. Schatz, J. M. Bowman, and A. Kuppermann, J. Chem. Phys. 63, 685 (1975).

20. J. P. Dwyer, Ph. D. Thesis, California Institute of Technology, 1977; A. Kuppermann and J. P. Dwyer, Abstracts of Papers XI, ICPEA C, (Society for Atomic Collision Research, Japan, 1979), pp. 888-889.
21. G. C. Schatz and A. Kuppermann, J. Chem. Phys. 59, 964 (1973).
22. J. F. Garvey, J. A. Kaye, and A. Kuppermann, in Abstracts of Papers, 1979 Pacific Conference on Chemistry and Spectroscopy, Pasadena, Ca., p. 39.
23. See, for example J. D. Lambert, Vibrational and Rotational Relaxation in Gases (Clarendon Press, Oxford, 1977).
24. W. C. Gardiner, Jr., Acc. Chem. Res. 10, 327 (1977).
25. J. A. Kaye, J. P. Dwyer, and A. Kuppermann, manuscript in preparation; a preliminary account of this work was presented at the 1979 Pacific Conference on Chemistry and Spectroscopy, Pasadena, Ca.
26. G. P. Quigley and G. J. Wolga, Chem. Phys. Lett. 27, 276 (1974).
27. J. A. Kaye and A. Kuppermann, unpublished results.
28. R. B. Bernstein and R. D. Levine, Chem. Phys. Lett. 29, 314 (1974); J. N. L. Connor, W. Jakubetz, J. Manz, and J. C. Whitehead, Chem. Phys. 39, 395 (1979).

Table 1. Parameters for Rotating Morse cubic spline surface for



$$R_{10} = R_{20} = 7.0 \text{ bohr}$$

θ (deg)	$l_{\text{eq}}(\theta)$ (bohr)	$\beta(\theta)$ (bohr ⁻¹)
0	5.267	1.163
6	5.296	1.149
15	5.453	1.122
30	6.079	1.012
39	6.742	0.9022
45	7.106	0.8194
51	6.742	0.9022
60	6.079	1.012
75	5.453	1.122
84	5.296	1.149
90	5.267	1.163

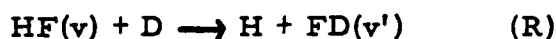
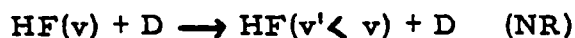
Table 2. Selected State-to-State and Summed Deactivation Rate Constants for the Processes $\text{HF}(v) + \text{H}' \rightarrow \text{HF}(v' < v) + \text{H}'$ (NR) and $\text{HF}(v) + \text{H}' \rightarrow \text{H} + \text{FH}'(v' < v)$ (R)

All rate constants* are in units of $\text{cm}^3 \text{molecule}^{-1} \text{sec}^{-1}$

v--v'	T = 300 K		T = 650 K		T = 1000 K	
	NR	R	NR	R	NR	R
1 0	1.185(2)	4.120(-16)	2.065(2)	1.821(-7)	2.782(2)	3.768(-4)
2 0	2.854(0)	5.172(-10)	4.192(0)	5.392(-5)	5.437(0)	5.097(-3)
2 1	1.189(2)	7.983(-13)	2.657(2)	2.108(-5)	3.780(2)	1.640(-2)
3 0	1.082(-1)	1.195(-4)	1.741(-1)	3.198(-3)	2.210(-1)	2.501(-2)
3 1	6.322(0)	3.548(-7)	1.098(1)	1.957(-3)	1.549(1)	9.502(-2)
3 2	3.992(2)	8.586(-9)	5.552(2)	5.454(-4)	7.412(2)	1.706(-1)
4 0	1.546(-3)	3.705(-3)	5.533(-3)	1.522(-2)	2.516(-2)	8.998(-2)
4 1	1.849(-1)	1.649(-2)	4.567(-1)	1.226(-1)	8.098(-1)	4.982(-1)
4 2	5.746(0)	8.555(-5)	1.612(1)	3.034(-2)	2.595(1)	7.082(-1)
4 3	6.039(1)	2.946(-6)	2.621(2)	4.648(-3)	5.269(2)	6.205(-1)
5 0	6.393(-4)	1.625(-2)	5.211(-3)	7.784(-2)	3.764(-2)	3.378(-1)
5 1	1.727(-2)	1.045(-1)	6.570(-2)	3.626(-1)	2.498(-1)	1.280(0)
5 2	4.121(-1)	3.043(-1)	1.345(0)	1.103(0)	3.083(0)	3.054(0)
5 3	1.151(1)	2.854(-3)	3.588(1)	4.064(-1)	5.840(1)	3.595(0)
5 4	1.098(2)	1.043(-4)	4.465(2)	1.528(-2)	7.919(2)	4.774(-1)
1 all	1.185(2)	4.120(-16)	2.065(2)	1.821(-7)	2.782(2)	3.768(-4)
2 all	1.197(2)	5.180(-10)	2.699(2)	7.500(-5)	3.834(2)	2.150(-2)
3 all	4.056(2)	1.199(-4)	5.664(2)	5.701(-3)	7.569(2)	2.906(-1)
4 all	6.605(1)	2.028(-2)	2.786(2)	1.728(-1)	5.537(2)	1.917(0)
5 all	1.217(2)	4.279(-1)	4.838(2)	1.965(0)	8.537(2)	8.744(0)
gas kin.	6.433(4)		9.469(4)		1.174(5)	

* Numbers in parentheses represent powers of 10 by which the written number should be multiplied.

Table 3. Selected State-to-State Rate Constants for the Processes



All rate constants* are in units of $\text{cm}^3 \text{molecule}^{-1} \text{sec}^{-1}$

$v \rightarrow v'$	NR	R	NR	R	NR	R
1 0	3.421(1)	1.265(-14)	6.267(1)	5.584(-7)	8.425(1)	1.266(-3)
2 0	9.141(-1)	6.015(-12)	1.812(0)	6.574(-6)	2.537(0)	4.635(-3)
2 1	6.476(1)	3.548(-13)	1.123(2)	1.454(-5)	1.556(2)	1.437(-2)
3 0	6.875(-2)	4.113(-5)	1.149(-1)	1.041(-3)	1.439(-1)	7.812(-3)
3 1	7.950(0)	3.514(-6)	1.044(1)	7.205(-4)	1.178(1)	1.997(-2)
3 2	9.057(1)	1.441(-7)	1.592(2)	1.944(-4)	2.106(2)	1.950(-2)
3 3		2.837(-9)		6.343(-5)		1.705(-2)
3 4		1.356(-10)		1.426(-5)		5.357(-3)
gas kin.	4.656(4)		6.855(4)		8.499(4)	

* Numbers in parentheses represent powers of 10 by which the written number should be multiplied.

FIGURE CAPTIONS

Figure 1. Plot of the potential energy V along the minimum energy path as a function of the reaction coordinate s for the reaction $H' + FH \rightarrow H'F + H$. $s = 0$ at the barrier (along the $H--F--H$ symmetric stretch line). The energy levels of the isolated HF reagent molecule are shown on the left side of the plot. For comparison purposes, those of the isolated DF molecule are shown at the right.

Figure 2. Contour plot of the potential energy surface for the reaction $H' + FH \rightarrow H'F + H$ in the Delves coordinate system. Equipotentials are drawn every 0.3 eV. The origin of energy is the bottom of the isolated HF well. A cross is drawn at the saddle point, and the minimum energy path is indicated by a dashed line.

Figure 3. Plot of rate constants $k_{v \rightarrow v' < v}$ for total reactive (R) and non-reactive (N) deactivation in the collision $H + FH(v) \rightarrow H + FH(v' < v)$ at $T = 300, 650$, and 1000 K as a function of the vibrational state v of the reagent molecule. All curves for reactive collisions are indicated by solid lines; those for non-reactive ones are indicated by dashed, dotted, and dashed-dotted lines, respectively, for $T = 300, 650$, and 1000 K.

Figure 4. Arrhenius plot of state-to-state rate constants $k_{vv'}$ for the reactive (superscript R) and non-reactive (superscript N) collisions $H + FH(v = 2) \rightarrow H + FH(v' = 0, 1)$. Curves for non-reactive transitions are indicated by solid lines; those for reactive ones are indicated by dashed lines.

Figure 5. Plot of high temperature (700 - 1000 K) Arrhenius activation energies $E_a^N(v \rightarrow v-n)$ for n -quantum non-reactive deactivating collisions $HF(v=1-5) + H' \rightarrow HF(v-n) + H'$ as a function of the internal energy E_{int} of the $HF(v)$ reagent. The quantum number of each reagent state is indicated on the upper abscissa. Different line types are used to connect each of the data points: $n=1$ - solid line; $n=2$ - dashed line; $n=3$ - dotted line; $n=4$ - dashed-dotted line. For $n=5$, only one data point exists; it

is marked by a plus sign.

Figure 6. Plot of high temperature (700-1000 K) Arrhenius activation energies $E_a^R(v \rightarrow v-n)$ for n -quantum reactive deactivating collisions $\text{HF}(v=1-5) + \text{H}' \rightarrow \text{H} + \text{FH}'(v-n)$ as a function of the internal energy E_{int} of the $\text{HF}(v)$ reagent. All line types and markings are as in figure 5.

Figure 7. Plot of the probability $P_{\text{HF}(v) + \text{H}}^R$ of the reaction $\text{HF}(v) + \text{H}' \rightarrow \text{H} + \text{FH}'$ as a function of the initial translational energy of the reagents E^{tr} for $v = 0, 1, 2, 3$.

Figure 8. Histogram plot of the fraction of reaction product $F_{vv'}^R$ for all possible product states v' for the reaction $\text{HF}(v=1) + \text{H}' \rightarrow \text{H} + \text{FH}'(v')$ at three values of the initial reagent translational energy E^{tr} . Bars marked a, b, and c are for $E^{\text{tr}} = 1.5361 \text{ eV}$, 1.9443 eV , and 2.4068 eV , respectively.

Figure 9. Histogram plot of the fraction of reaction product $F_{vv'}^R$ for all possible product states v' for the reaction $\text{HF}(v=2) + \text{H}' \rightarrow \text{H} + \text{FH}'(v')$ at three values of the initial reagent translational energy E^{tr} . Bars marked a, b, and c are for $E^{\text{tr}} = 1.3161 \text{ eV}$, 1.6154 eV , and 1.9964 eV , respectively.

Figure 10. Plot of the average fraction of product energy going into vibration $\langle f_v^R \rangle$ as a function of the initial reagent translational energy E^{tr} for $v = 0, 1, 2, 3$. Results for different values of v are indicated by different symbols: $v=0$ - open circles; $v=1$ - open squares; $v=2$ - open triangles; $v=3$ - filled circles. Lines correspond to the value expected if the reaction were vibrationally adiabatic. Results are shown only for energies where the probability of reaction is significantly greater than zero.

Figure 11. Plot of the probability $P_{\text{D} + \text{FH}(v)}^R$ of the reaction $\text{HF}(v) + \text{D} \rightarrow \text{DF} + \text{H}$ as a function of the initial reagent translational energy E^{tr} for $v = 0, 1, 2$. The solid line is for $v = 0$; the dashed line is for $v = 1$; and the dotted line is for $v = 2$.

Figure 12. Histogram plot of the fraction of reaction product $F_{vv'}^R$ for all possible product states v' for the reaction $\text{HF}(v=1) + \text{D} \rightarrow \text{H} + \text{FD}(v')$ at three values of the initial reagent translational energy E^{tr} . Bars marked a, b, and c are for $E^{\text{tr}} = 1.5361 \text{ eV}$, 1.7538 eV , and 1.9443 eV , respectively.

Figure 13. Histogram plot of the fraction of reaction product $F_{vv'}^R$ for all possible product states v' of the reaction $\text{HF}(v=2) + \text{D} \rightarrow \text{H} + \text{FD}(v')$ at two values of the initial reagent translational energy E^{tr} . Bars marked by a and b are for $E^{\text{tr}} = 1.3161 \text{ eV}$ and 1.5066 eV , respectively.

Figure 14. Plot of the average fraction of product energy going into vibration f_v^R as a function of the initial reagent translational energy E^{tr} for $v = 0, 1, 2$. Symbols and lines have their same meaning as in figure 10.

Figure 15. Landau-Teller plot of rate constants $k_{v, v-1}^N(\text{HF} + \text{H}')$ for single-quantum non-reactive deactivating collisions $\text{HF}(v) + \text{H}' \rightarrow \text{HF}(v-1) + \text{H}'$ for $v=1-5$. The temperature is indicated on the upper abscissa. Different line types are used for each v : $v=1$ - solid line; $v=2$ - dashed line (large dashed); $v=3$ - dotted line; $v=4$ - dashed-dotted line; $v=5$ - dashed line (small dashes).

Figure 16. Landau-Teller plot of rate constants $k_{v, v-1}^N(\text{HF} + \text{D})$ for single-quantum non-reactive deactivating collisions $\text{HF}(v) + \text{D} \rightarrow \text{HF}(v-1) + \text{D}$ for $v = 1, 2, 3$. The temperature is indicated on the upper abscissa. Different line types are used for each v : $v=1$ - solid line; $v=2$ - dashed line; $v=3$ - dotted line.

Figure 17. Plot of the threshold energy E_v^{th} for the vibrationally adiabatic reactions $\text{HF}(v) + \text{H}' \rightarrow \text{H} + \text{FH}'(v)$ (solid line) and $\text{HF}(v) + \text{D} \rightarrow \text{H} + \text{FD}(v)$ (dashed line) as a function of the internal energy E^{int} of the reagent HF molecule. Open circles and squares, respectively, are used to plot the original data points for the $\text{HF} + \text{H}'$ and $\text{HF} + \text{D}$ systems,

respectively. The quantum number of the reagent HF state is indicated on the upper abscissa.

Figure 18. Plot of the threshold energy E^{th} for the vibrationally adiabatic reaction $\text{HF}(v) + \text{H}' \longrightarrow \text{H} + \text{FH}'(v)$ as a function of the vibrationally adiabatic barrier height ΔV_v^{\ddagger} , defined in eq. 15 of the text for $v = 0-4$. The open circles mark the actual data points. The values of v are indicated on the upper abscissa.

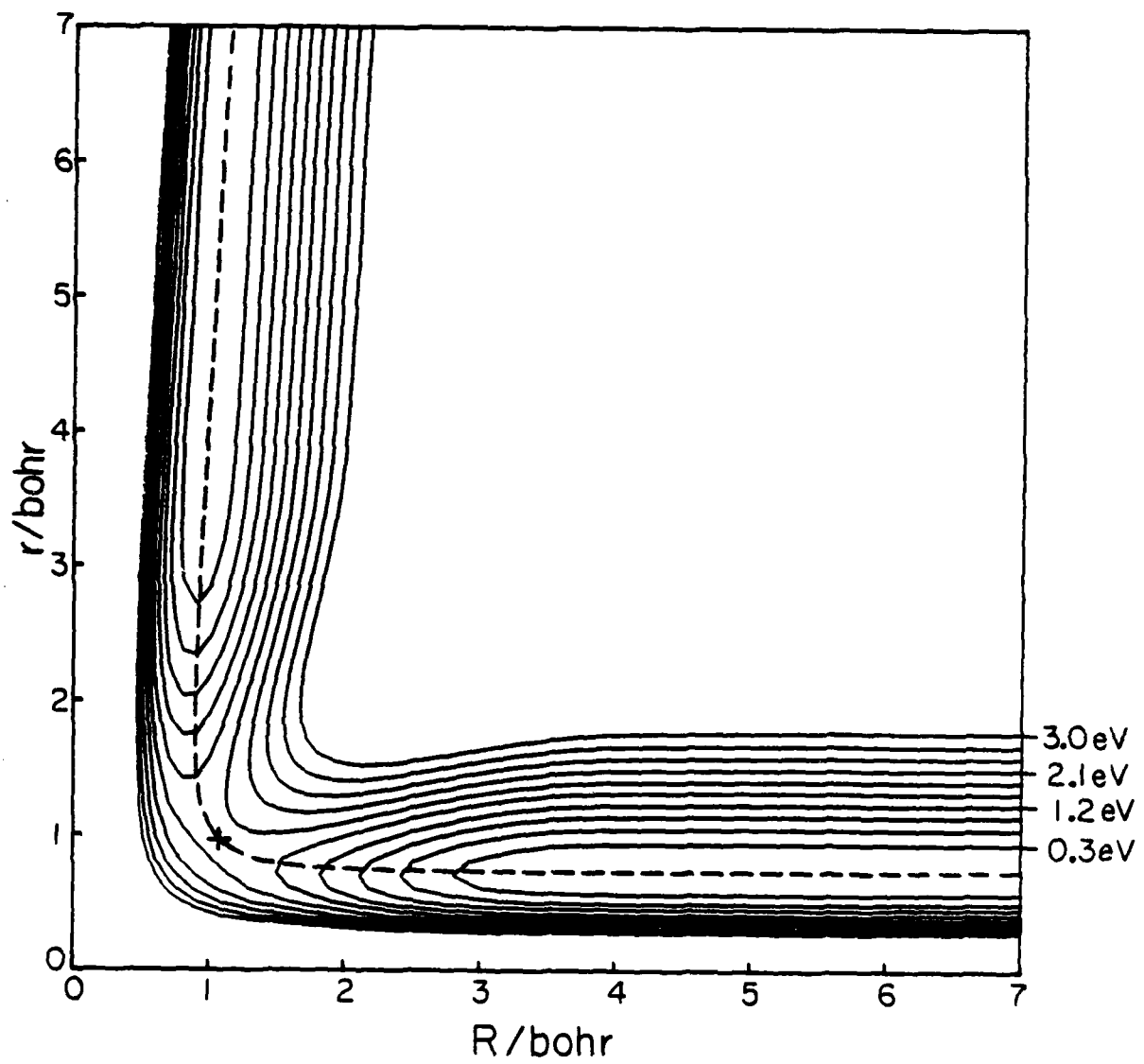


Figure 1

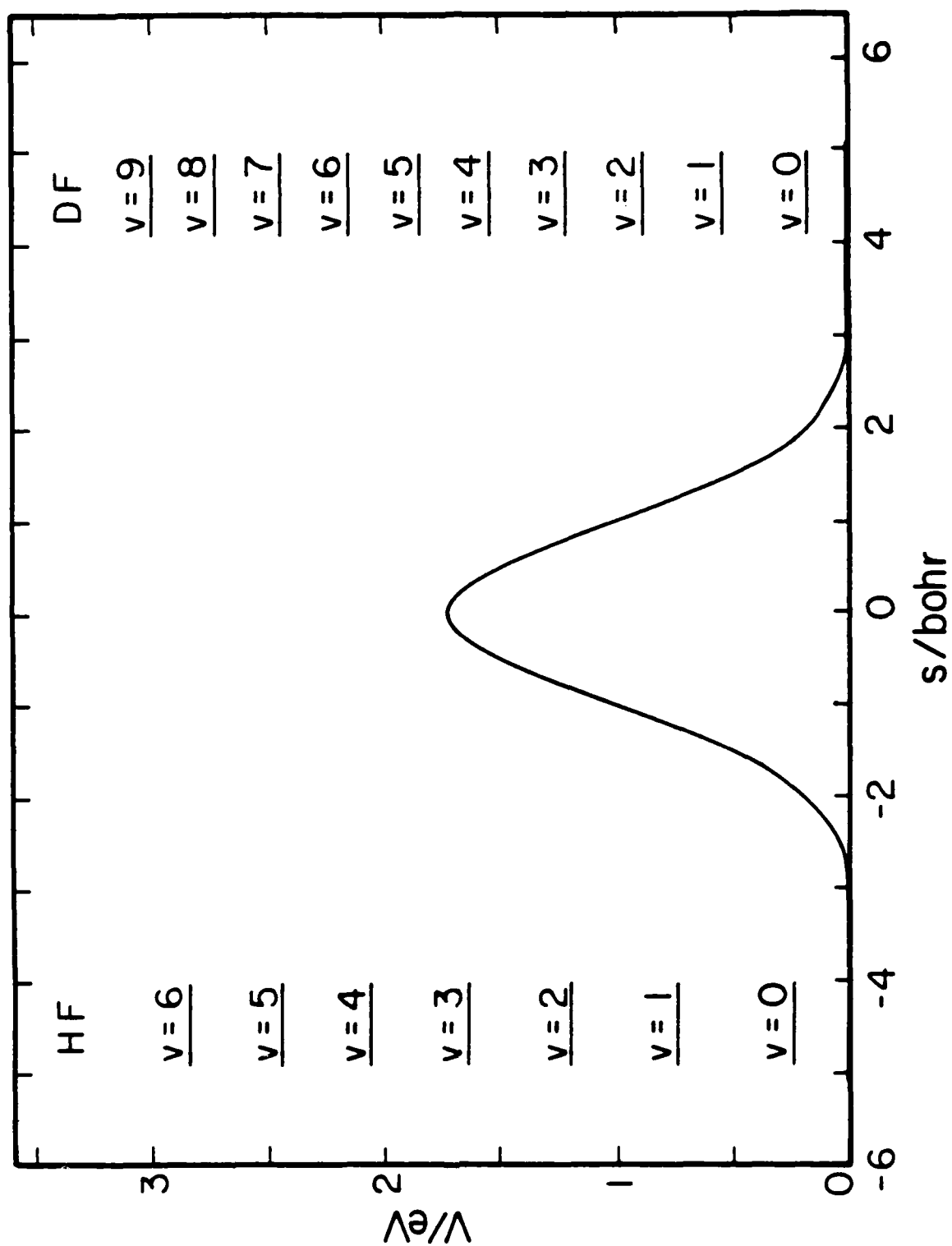


Figure 2

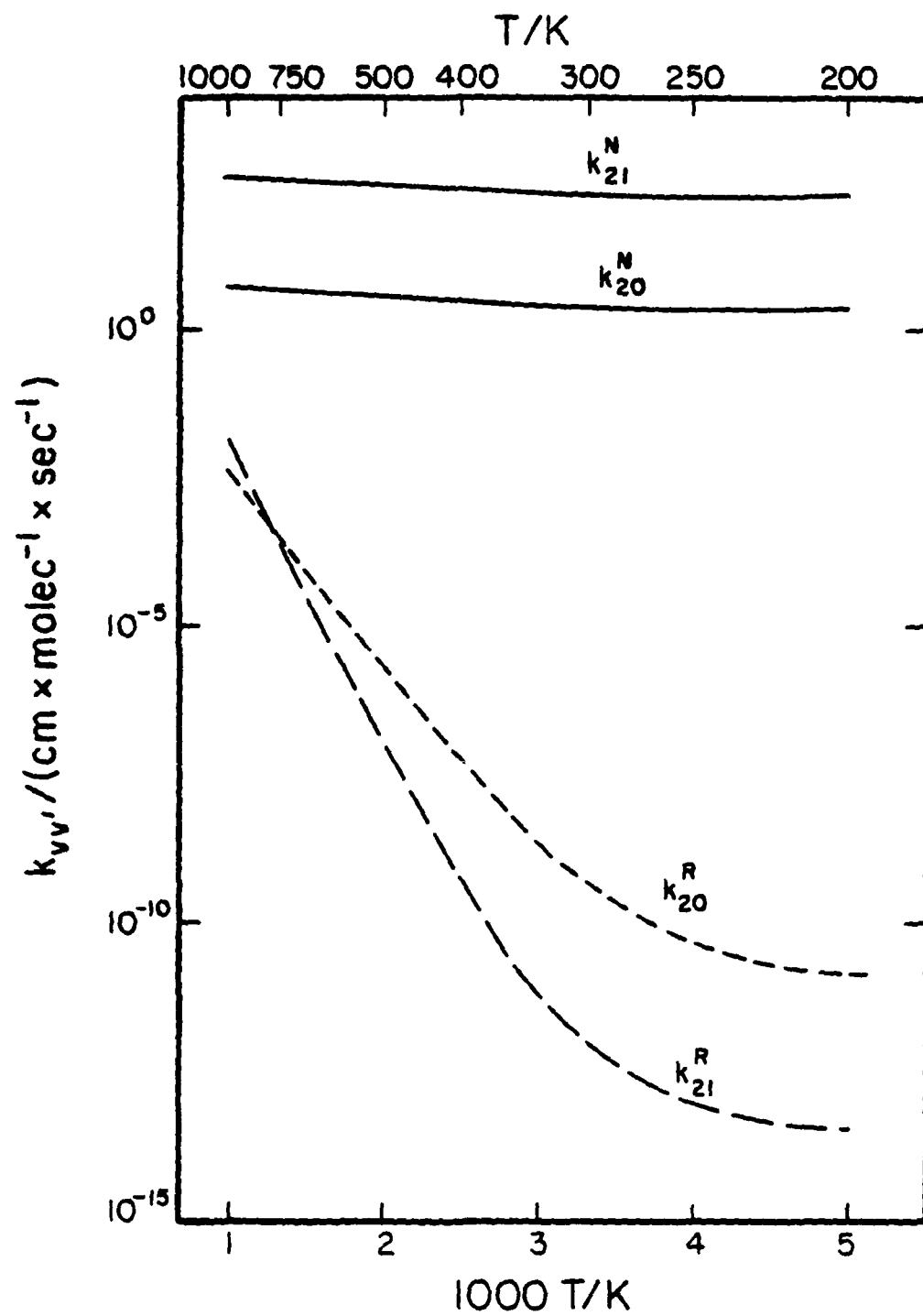


Figure 3

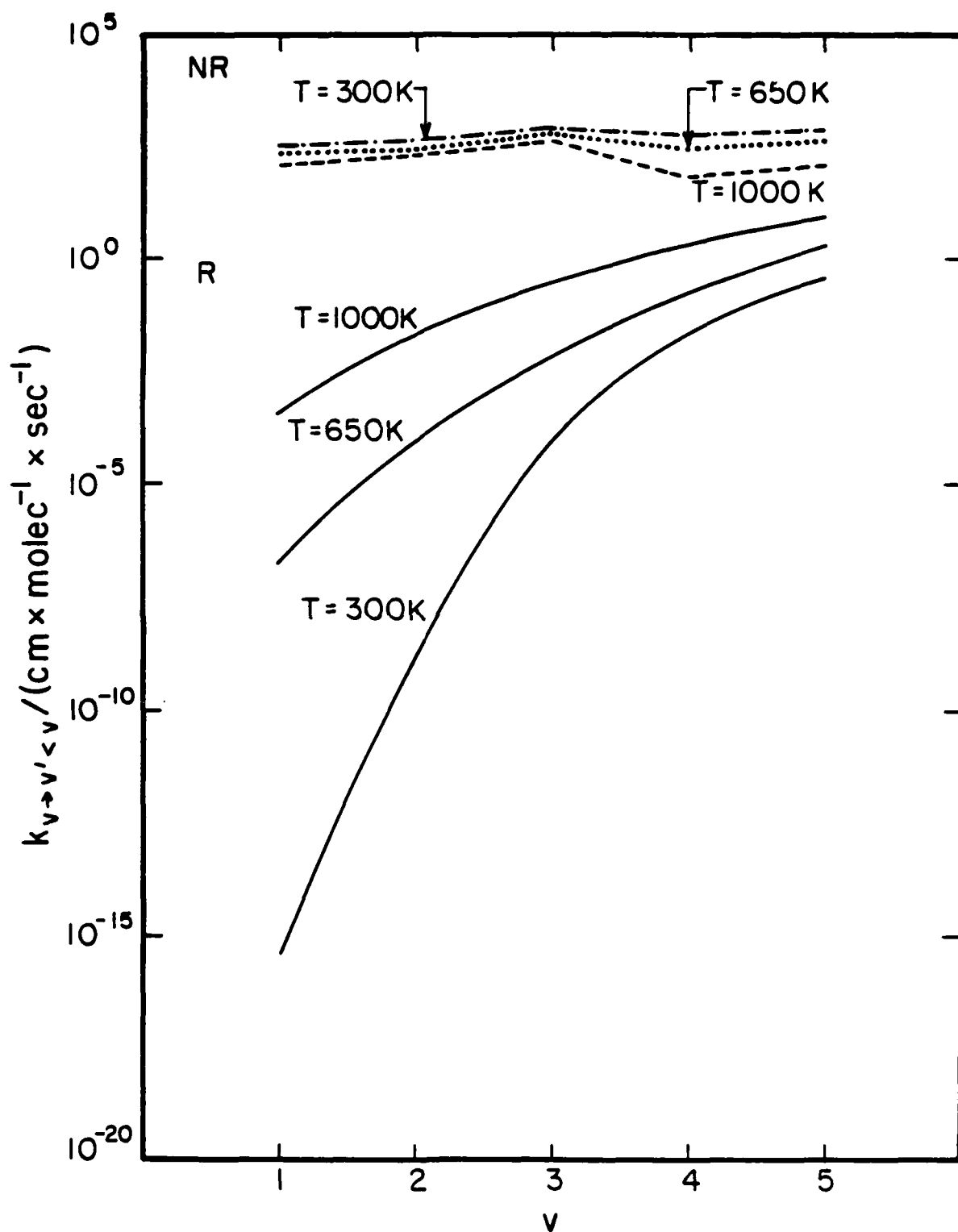


Figure 4

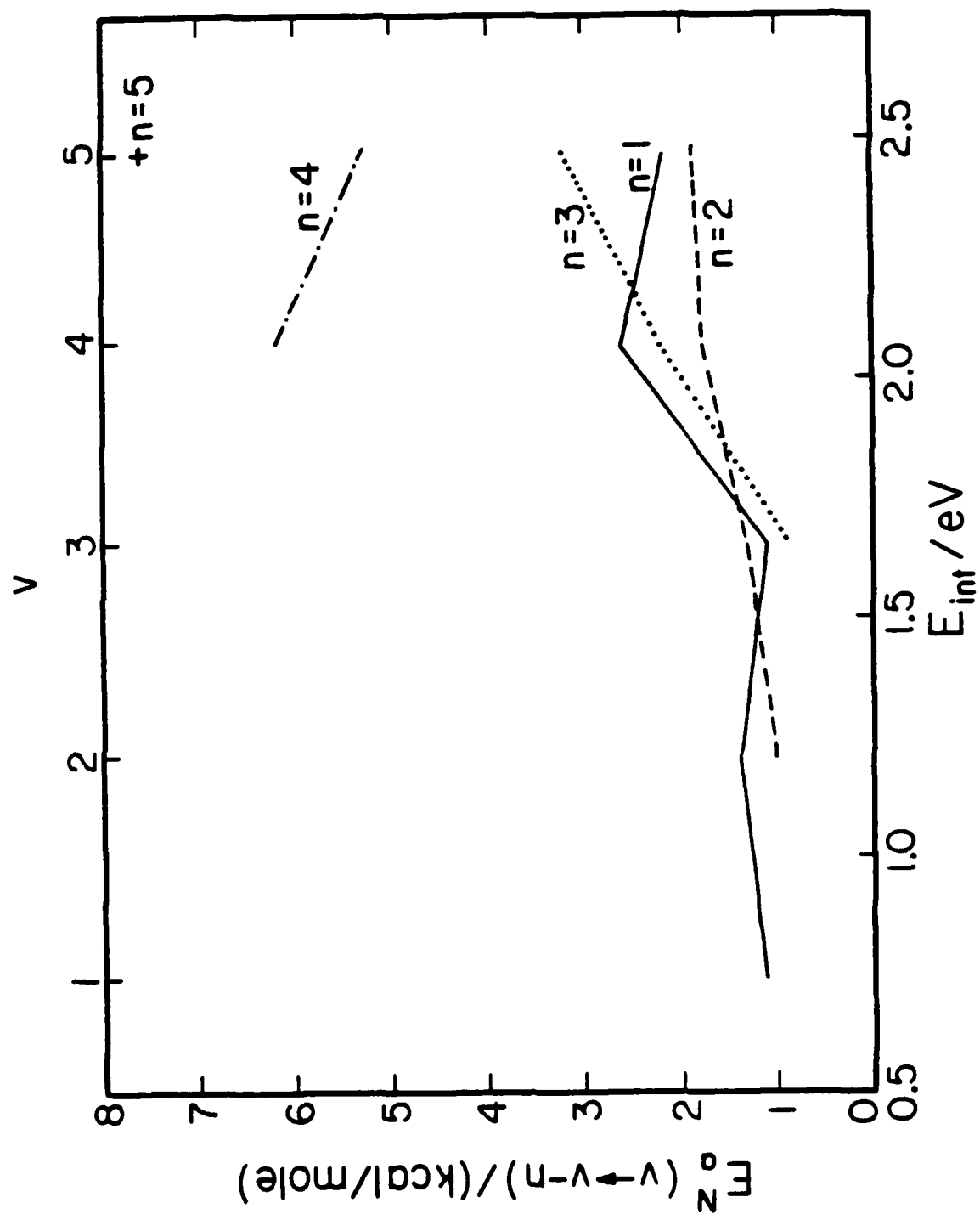


Figure 5

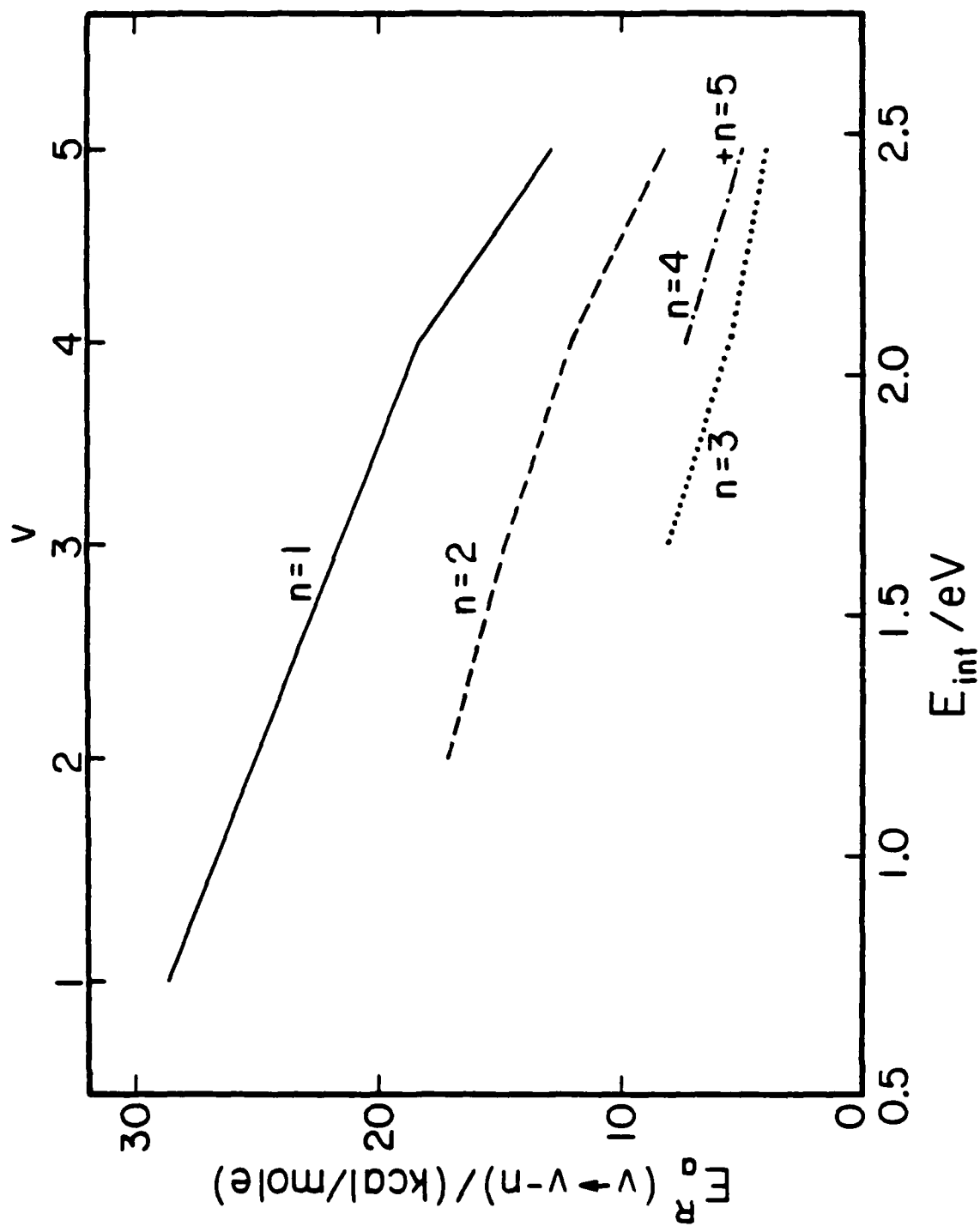


Figure 6

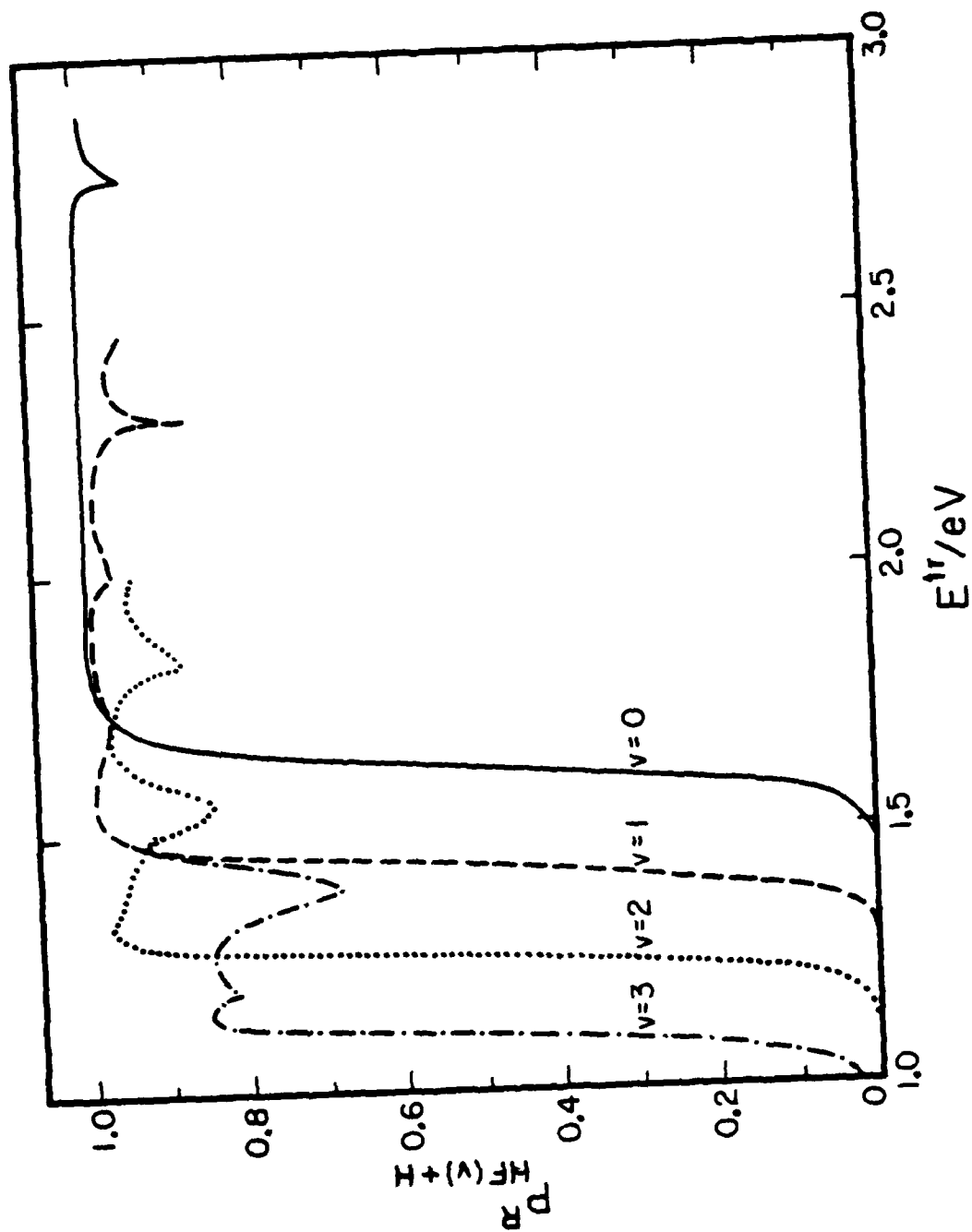


Figure 7

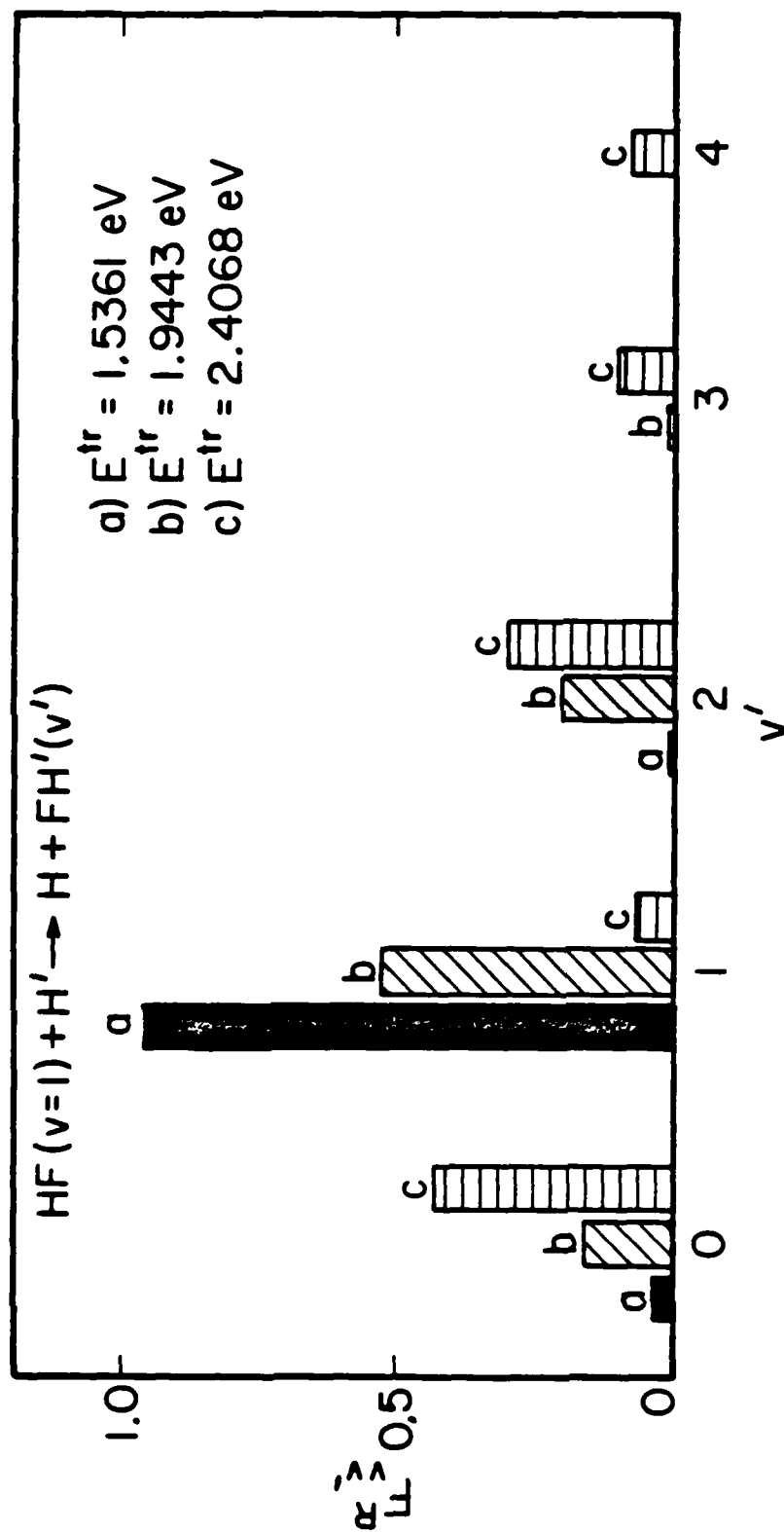


Figure 8

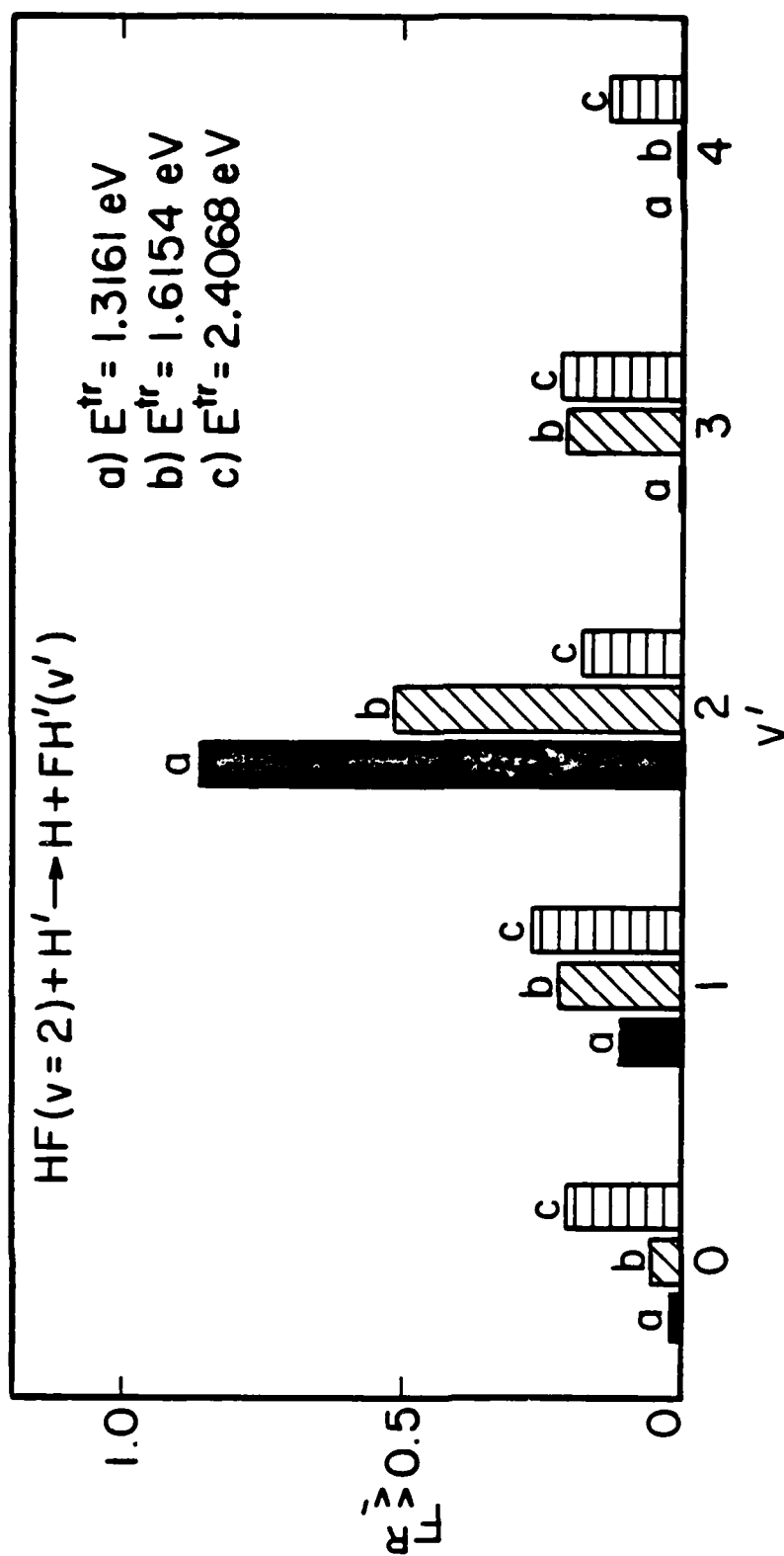


Figure 9

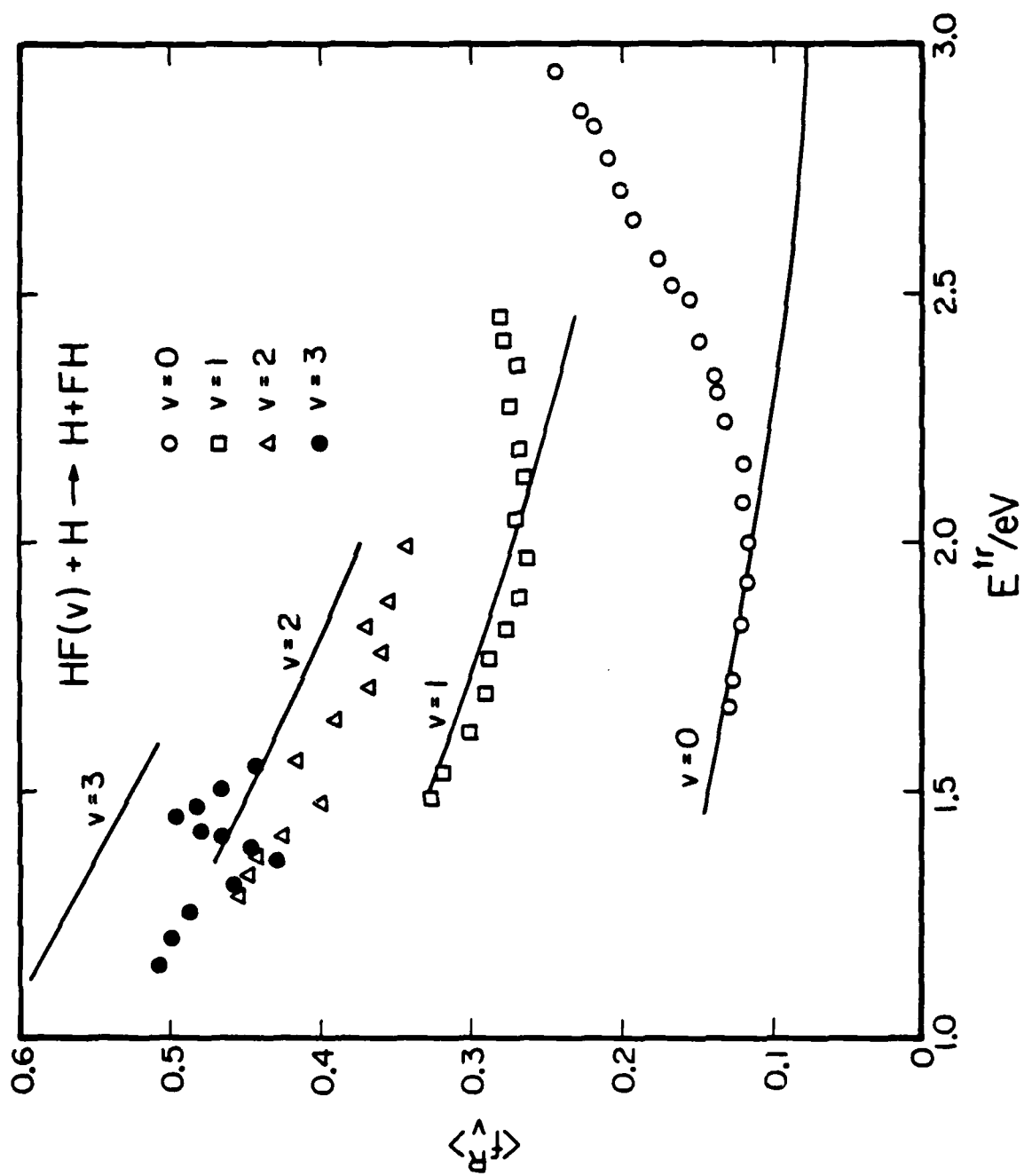


Figure 10

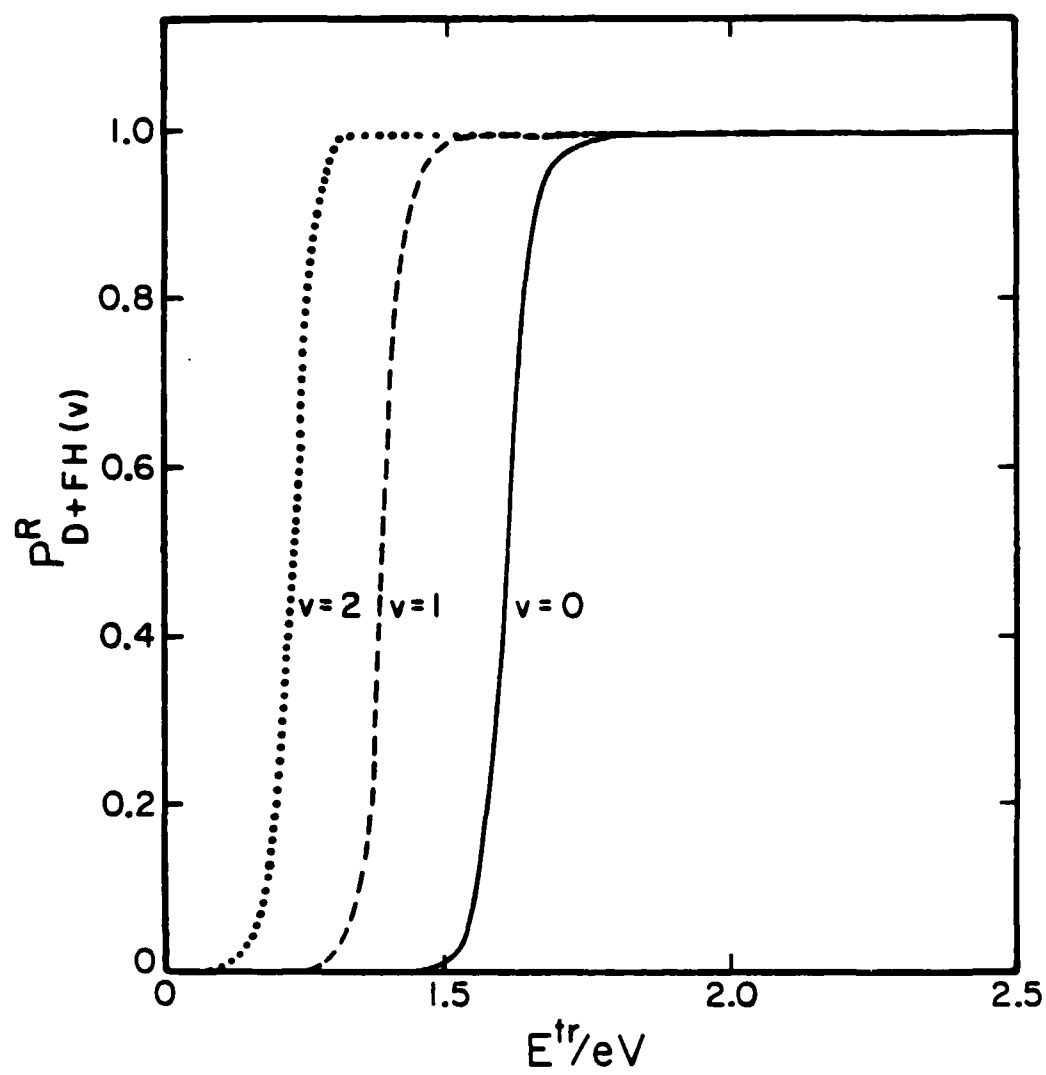


Figure 11

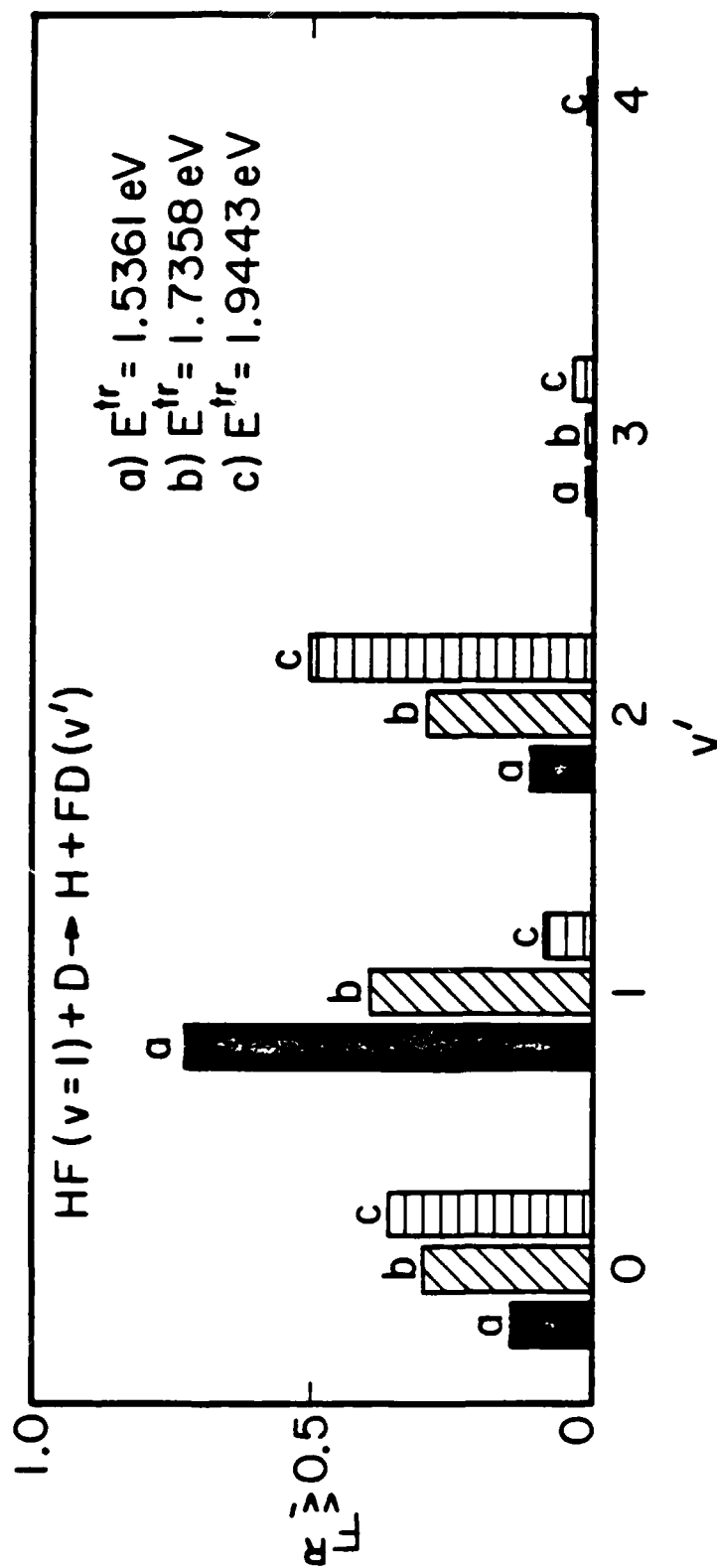


Figure 12

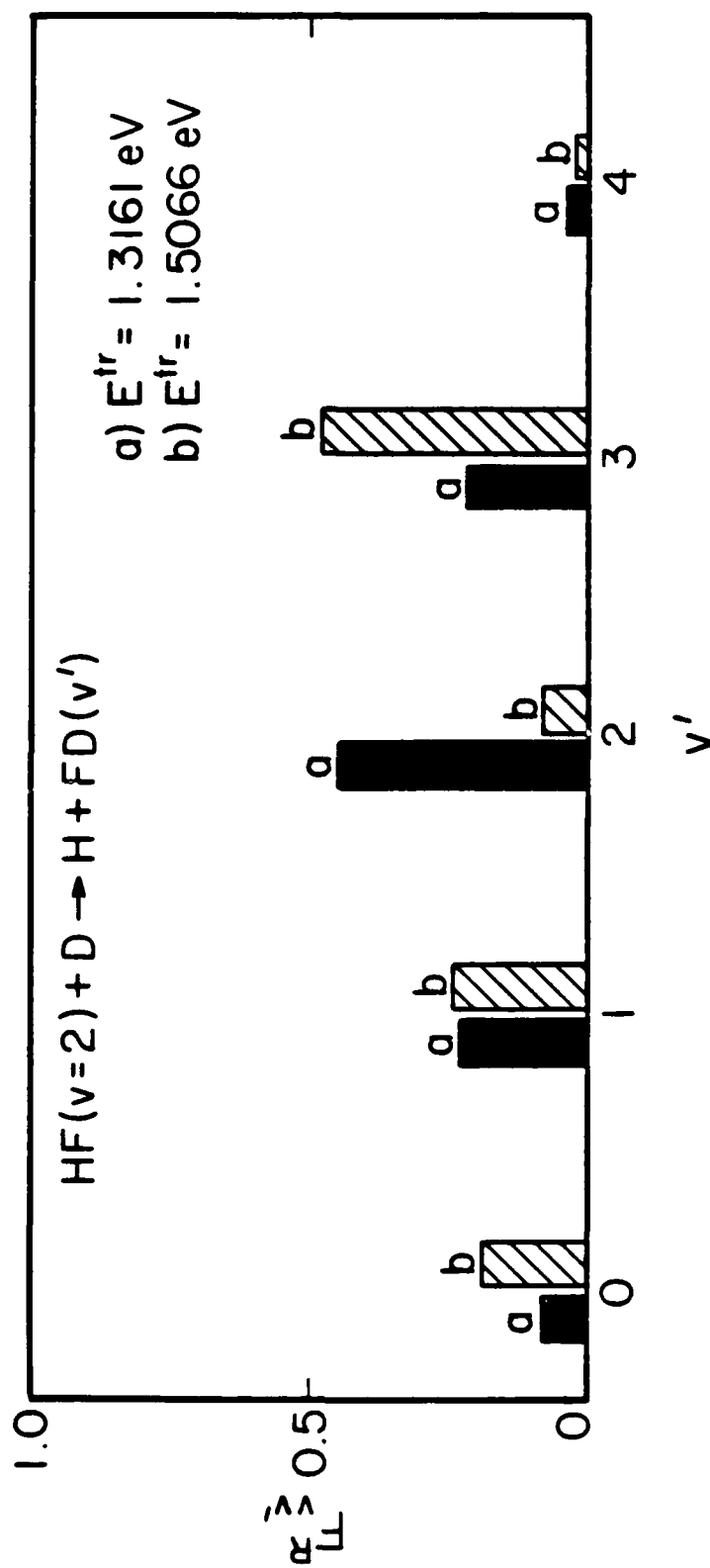


Figure 13

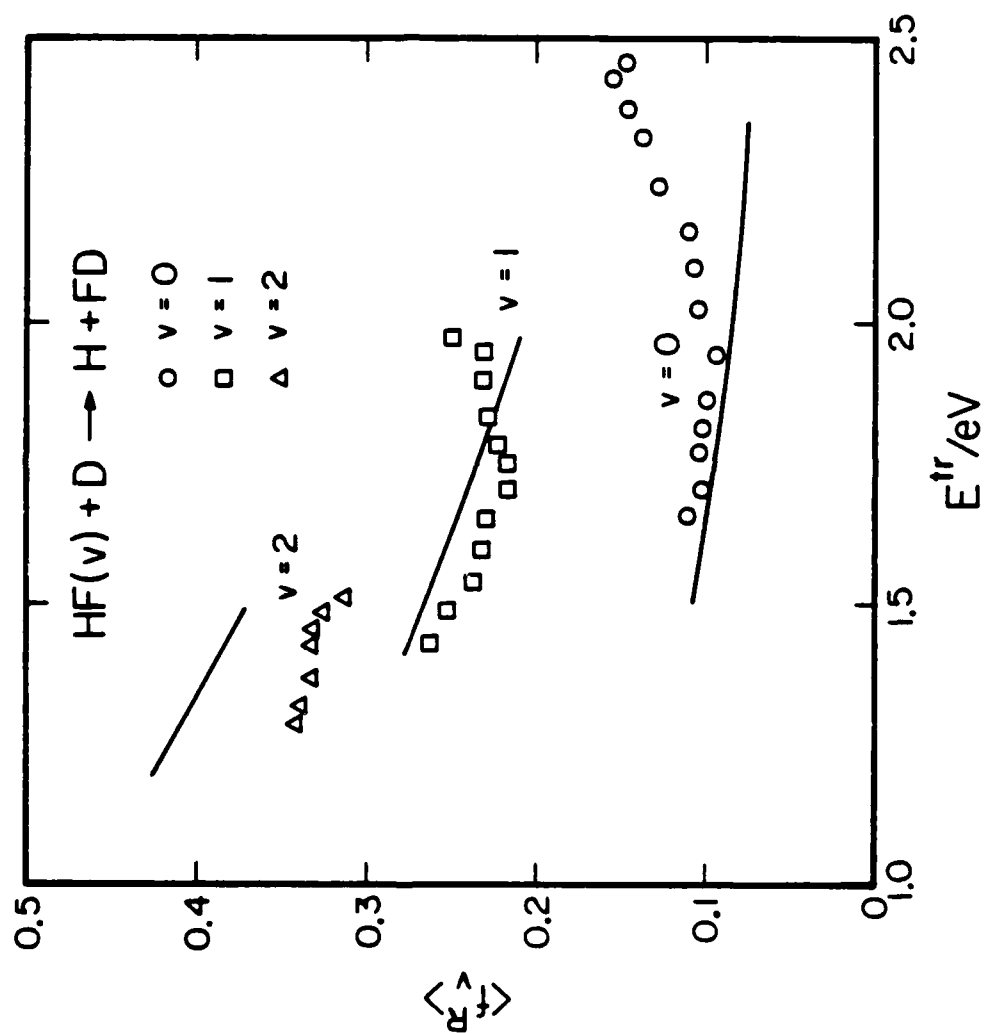


Figure 14

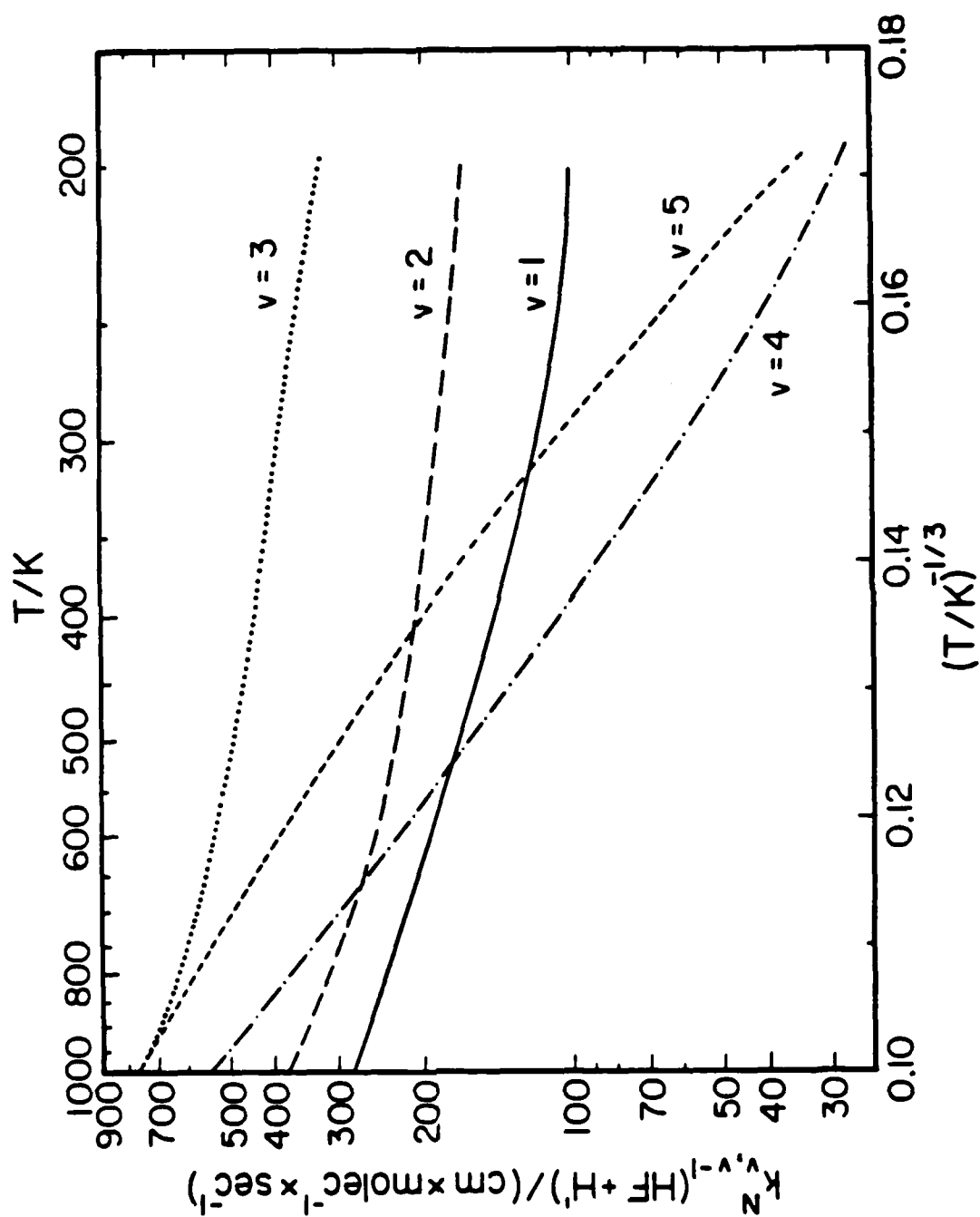


Figure 15

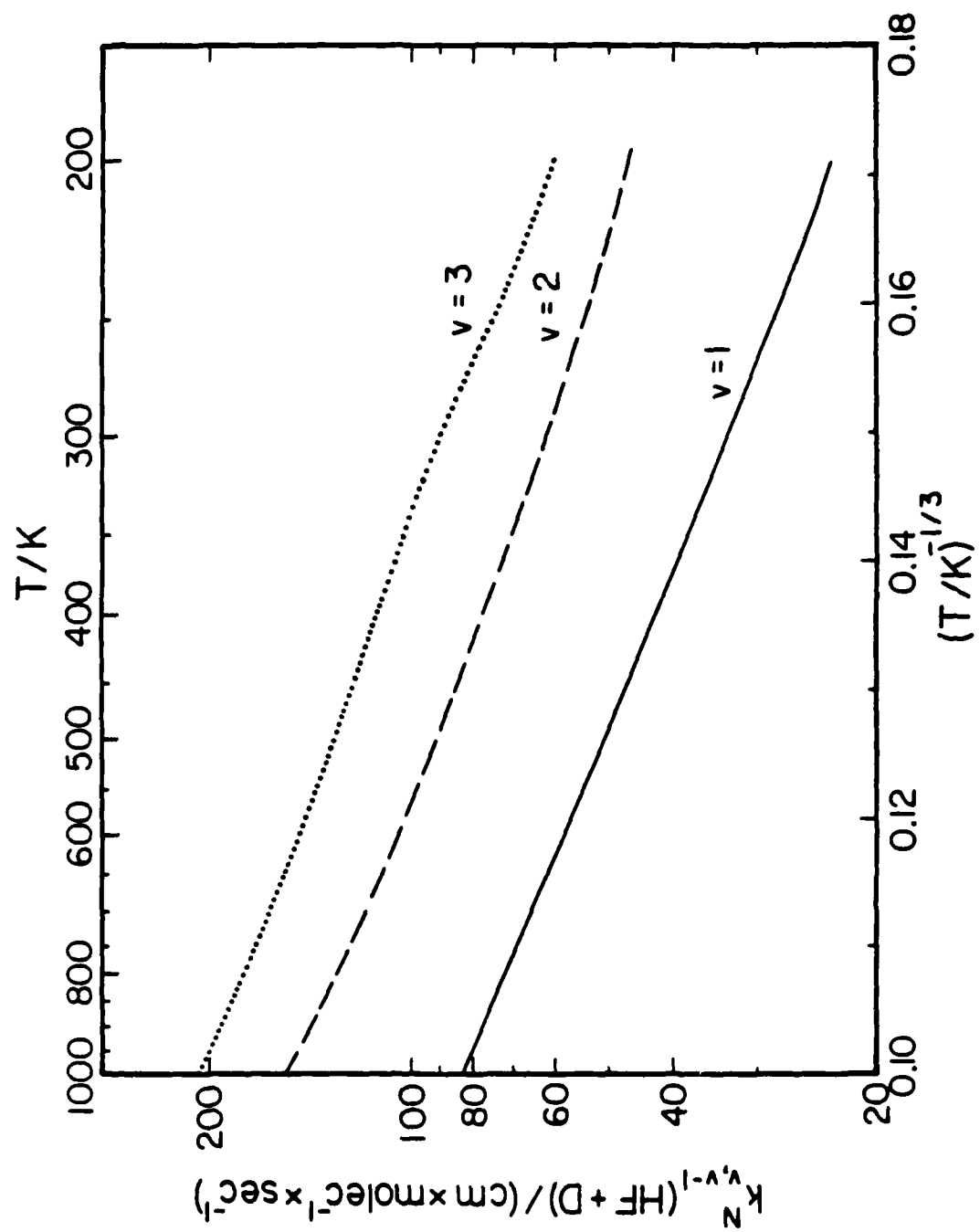


Figure 16

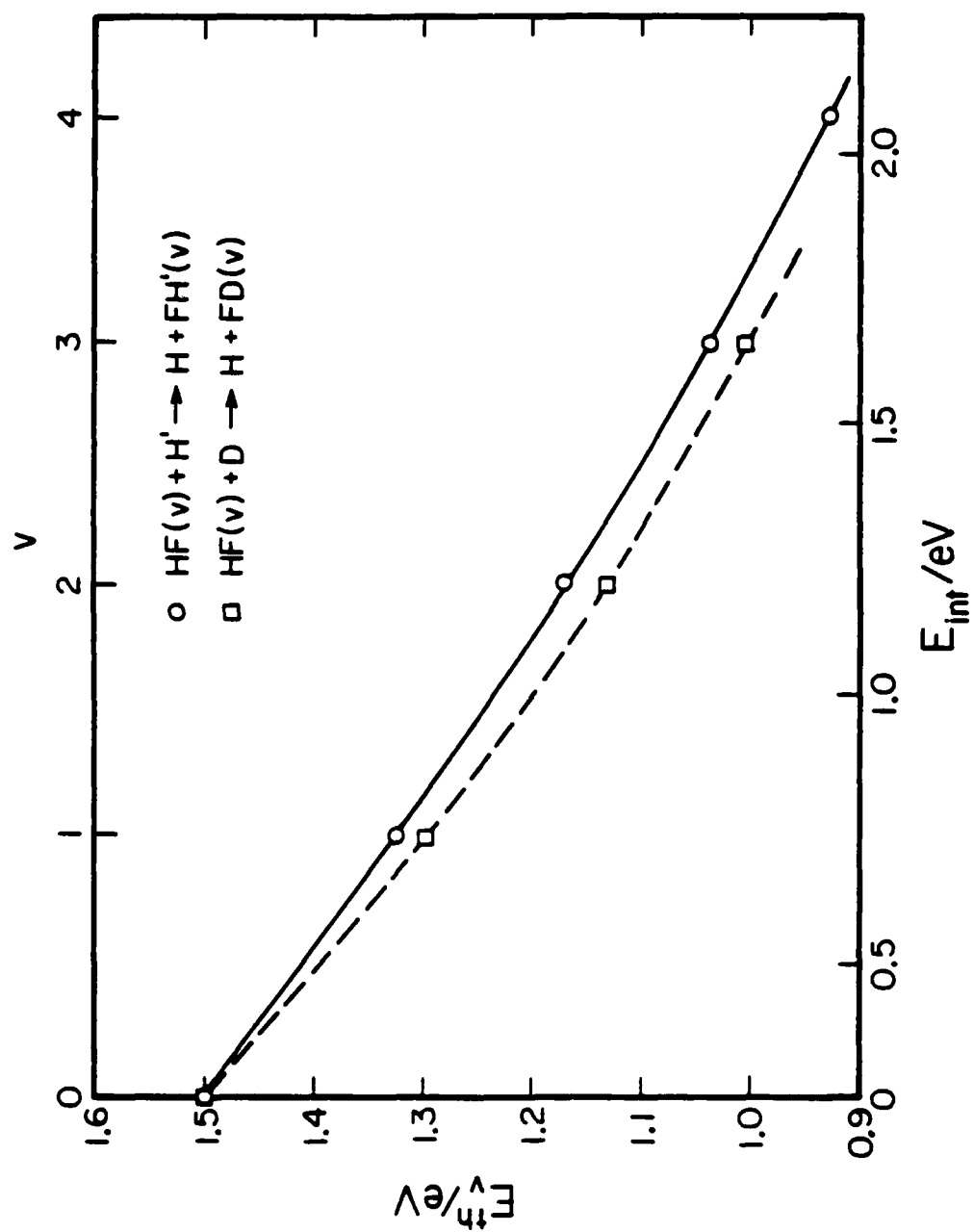


Figure 17

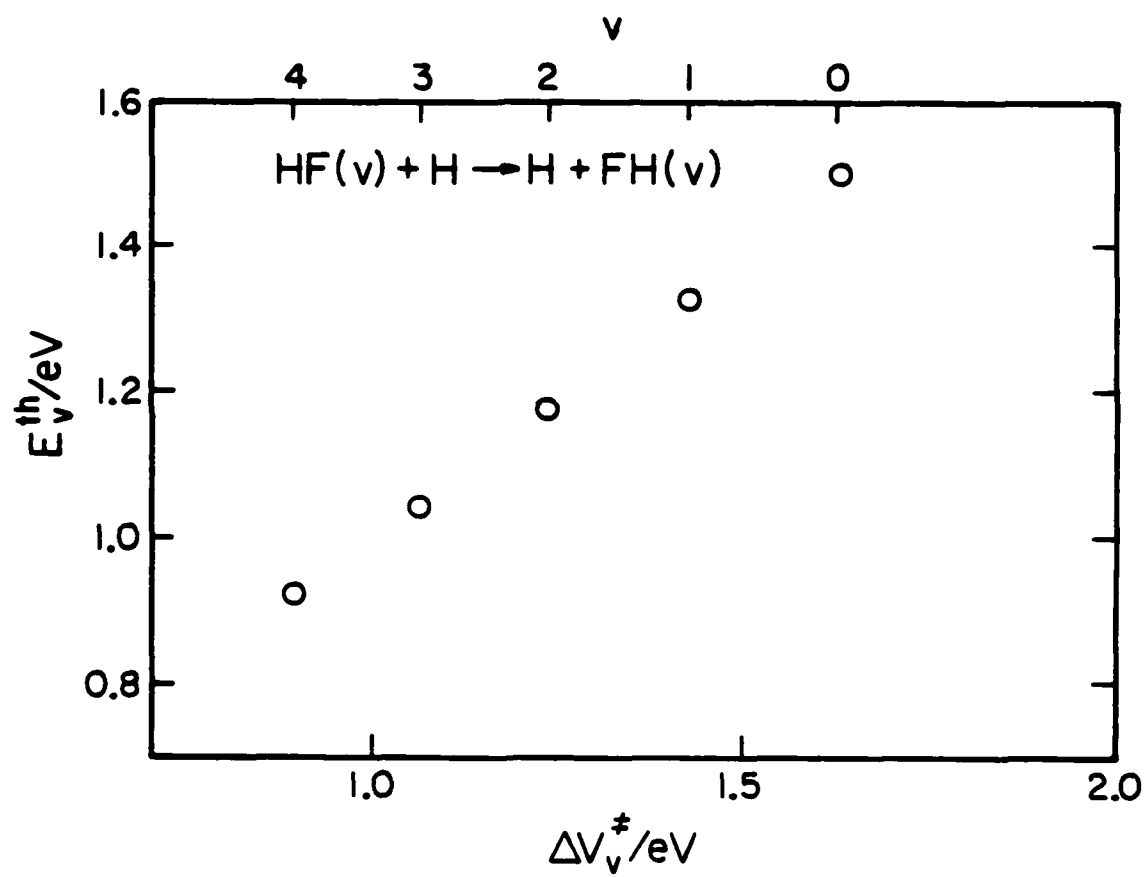


Figure 18

Barrier Height Dependence of Dynamics in the Collinear H + FH(v)
and D + FH(v) Systems.^{a)}

Jack A. Kaye^{b)}, John P. Dwyer^{c)}, and Aron Kuppermann

Arthur Amos Noyes Laboratory of Chemical Physics^{d)}

California Institute of Technology, Pasadena, California 91125

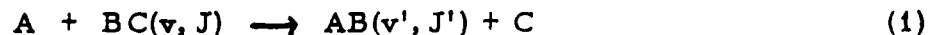
(Received)

Collinear coupled-channel quantum mechanical calculations have been performed on the title systems on potential energy surfaces with barriers to reaction of 1.5, 5, 10, 20, 30, and 40 kcal/mole. We have examined the differences in the dynamics on the different surfaces, emphasizing the rate and mechanism of vibrational deactivation of HF in H + FH(v) collisions and the influence of reagent vibrational excitation on reaction probabilities and product state distributions in the D + FH(v) reaction. The rate of vibrational deactivation decreases as the barrier height is increased for low barrier height surfaces, but becomes relatively insensitive to barrier height at higher barrier heights at the temperatures studied. On the lower barrier surfaces vibrational deactivation occurs mainly in multi-quantum reactive transitions, while for higher barrier surfaces it occurs in single-quantum non-reactive transitions. In the D + FH(v) reaction, reagent vibrational excitation reduces the translational energy threshold by an amount smaller than the vibrational quantum and can lead to different product state distributions depending on the potential energy surface. Quantum mechanical resonances observed on the low barrier surfaces can be understood by reference to vibrationally adiabatic correlation diagrams.

- a) This work was supported in part by a contract (No. F49620-79-C-0187) from the Air Force Office of Scientific Research.
- b) Work performed in partial fulfillment of the requirements for the Ph.D. degree in Chemistry at the California Institute of Technology.
- c) Present Address: Supreme Court of the United States, Washington, D. C. 20543
- d) Contribution No.

I. INTRODUCTION

The dependence of the dynamics of chemical reactions on the potential energy surface governing the motion of the nuclei has been the subject of substantial attention. In a pioneering series of papers, Polanyi and collaborators used the classical trajectory technique to study how the dynamics of the general class of reactions



varied with changes in the potential energy surface (1). Features of particular interest have been how the disposal of energy in exoergic reactions or the usefulness of various forms of internal energy in endoergic reactions depends on the position of the saddle point on the surface. Other workers have also explored the relationship between the potential energy surface and the dynamics obtained from classical mechanical calculations for both reactive and non-reactive processes (2).

For quantum mechanical calculations, such studies have been far fewer in number. As new potential energy surfaces are developed over the years, dynamical calculations are frequently performed, providing information on the sensitivity of dynamics to surface parameters. For example, for the $H + H_2$ system and its D substituted analogs, in exact and approximate quantum calculations (in one, two, and/or three dimensions) (3), surfaces studied include the scaled SSMK(4), the Porter-Karplus (5), and the SLTH (6) ones, among others. For the $F + H_2$ system, a variety of potential energy surfaces, both semi-empirical (7) and ab initio (8) have been used in collinear quantum mechanical calculations (7b, 9). Similar studies have been carried out on the $I + H_2$ (10), $O + H_2$ (11), and $I + HI$ (12) systems, among others.

In most of this work, attention has been focused on the dynamics of chemically reactive processes. If one is to understand the full dynamics of potentially reactive chemical systems, however, one

must also understand how the dynamics of non-reactive processes depend on the nature of the assumed potential energy surface. For example, in studying the dynamics of the collisional deactivation of a vibrationally excited molecule (such as that present in a chemical laser system), the quantities most of interest are the rates of vibrational deactivation and the number of quanta transferred. Rabitz and co-workers (13) have studied the sensitivity of energy transfer processes to the nature of the assumed potential energy surface in non-reactive collisions.

In this work we study the dynamics of the collinear systems



by coupled-channel quantum mechanical calculations on six related potential energy surfaces. These surfaces are identical except for their profile along the minimum energy path, and have barriers of 1.5, 5, 10, 20, 30, and 40 kcal/mole. The first is close to the barrier of the Muckerman V surface (7b) used in a previous collinear quantum mechanical study of these systems (14); the last is closest to the barrier heights indicated by the most recent experiments (15) and also by ab initio calculations (16). The results of the calculation on this surface have been presented separately (17).

In our calculations we will examine the effects of the change of barrier height on various features of the H or D atom induced collisional deactivation of HF(v), including the overall rate of deactivation, the fraction of deactivation occurring by reactive and non-reactive processes, the relative importance of single and multi-quantum transitions, and the temperature dependence of these quantities. We will also consider the general class of reactive processes (2b and 3b) and the role of quantum mechanical resonances

on the different surfaces.

The outline of this paper is as follows. In section 2 we discuss potential energy surfaces used in the calculations, and in section 3 we briefly review some important aspects of the calculations performed. The results obtained will be presented in section 4, and their significance will be discussed in section 5. Finally, in section 6 we will summarize the results and conclusions obtained.

II. POTENTIAL ENERGY SURFACES

The potential energy surfaces used in this study are all of the highly flexible rotating Morse-cubic spline form (18), in which the potential energy as a function of the internuclear coordinates R_{AB} and R_{BC} is given by the expression

$$V(R_{AB}, R_{BC}) = D(\theta) \left((1 - \exp(-\beta(\theta)(\ell_{eq}(\theta) - \ell)))^2 - 1 \right) + D(\theta=0) \quad (4)$$

where

$$\theta = \tan^{-1}((R_{AB} - R_{AB}^0)/(R_{BC} - R_{BC}^0)) \quad (5)$$

and

$$\ell = ((R_{AB} - R_{AB}^0)^2 + (R_{BC} - R_{BC}^0)^2)^{1/2} \quad (6)$$

(R_{AB}^0, R_{BC}^0) is the point from which one swings the Morse oscillator, whose parameters are thus functions of the angle θ ; when $R_{AB} > R_{AB}^0$ or when $R_{BC} > R_{BC}^0$, the potential is just that of a Morse oscillator. Normally, the point (R_{AB}^0, R_{BC}^0) is far up the dissociative plateau, that is, both R_{AB}^0 and R_{BC}^0 are large. The coordinate system and definition of terms are indicated schematically in Figure 1.

The Morse parameters $\ell_{eq}(\theta)$ and $\beta(\theta)$ are given at a small number of values of the swing angle θ , and a cubic spline interpolation is then performed. A similar interpolation could be performed for $D(\theta)$; however, in this case we assume it to be given by a Gaussian

$$D(\theta) = D(\theta=0) - (A + B \exp(-C(\pi/4 - \theta)^2)) \quad (7)$$

Values of the constants A, B, and C for each of the surfaces used are given in Table 1; values of $\ell_{eq}(\theta)$ and $\beta(\theta)$ have been presented elsewhere (17).

The values of $\ell_{eq}(\theta)$ and $\beta(\theta)$ were obtained by numerically finding their values on the Muckerman V surface (7b) in the exchange channel and then splining together; the values for A, B, and C were first obtained from the Muckerman V surface at 3 values of θ (0° , 22° , and 45°). To increase the barrier height, only parameters B and C in eq. 7 were changed.

For $R_{AB} > R_{AB}^0$ (R_{BC} small) or $R_{BC} > R_{BC}^0$ (R_{AB} small), the potential energy was taken to be independent of R_{AB} and R_{BC} , respectively. This produced a slight upward shift (~ 0.0168 kcal/mole) in the bottom of the HF diatomic well relative to its dissociation energy. For use in the calculations reported here, we have constructed surfaces with barrier heights of 1.5, 5, 10, 20, 30, and 40 kcal/mole. We have plotted the 40 kcal/mole barrier surface in the Delves mass scaled coordinate system (19) for the HFH system in figure 2. In figure 3 we display the vibrational energy levels of HF and DF along with the energies of the barriers on the six surfaces used.

III. NUMERICAL ASPECTS

Numerical solution of the Schrödinger equation has been performed by the coupled-channel method of Kuppermann (20). 20 - 24 basis functions were used in these calculations, and unitarity of the scattering matrix was obtained to better than 3% at nearly all energies studied; at most it was obtained to better than 1%. For those calculations where unitarity was not obtained to 3%, we do not include the results in our analysis.

Reactions 2a and 2b were studied in the energy range up to 2.94 eV above the zero-point energy of HF, while reactions 3a and 3b were studied up to 2.45 eV above the HF zero-point energy. The smaller range in the latter calculation was due to the smaller vibrational energy spacing of DF (see figure 3) than HF, which gives rise to more open channels at a given total energy than at the same total energy in the HF + H system.

State-to-state rate constants have been calculated from the transition probabilities obtained in the scattering calculations by the relationship

$$k_{ij}(T) = (2\pi\mu_{a,bc}k_bT)^{-1/2} \int_0^\infty P_{ij}(E^{tr}) \exp(-E^{tr}/k_bT) dE^{tr} \quad (8)$$

where P_{ij}^{tr} is the probability for the transition from state i to state j, E^{tr} is the initial reagent relative translational energy of the collision, $\mu_{a,bc}$ is the reduced mass of the a, bc collision pair, and k_b is Boltzmann's constant.

IV. RESULTS

We have studied a number of aspects of the dynamics of the col-linear HFH and DFH systems on six different, but related, potential energy surfaces, and will try to present some of the most important features of our results in this section. We will consider the following questions:

- 1) What are the relative rates of collisional deactivation of vibrationally excited HF and how do they depend on the surface used and on the reagent vibrational state?
- 2) How do deactivating processes occur (single vs. multi-quantum, reactive vs. non-reactive) on the different surfaces?
- 3) How do these quantities vary with temperature?
- 4) How do the dynamics of the reactive processes (energy thresholds, product vibrational state distribution, effect of reagent vibrational excitation) depend on the surface?
- 5) What is the nature and magnitude of the isotope effect on going from the HFH to the DFH system?
- 6) How important are quantum mechanical resonances on the different surfaces, and how do their position and strength vary as the barrier height is increased?

A. VIBRATIONAL DEACTIVATION

The rate of vibrational deactivation varies significantly as the barrier height of the potential energy surface varies. This may be seen in figures 4 and 5, in which the overall rate of vibrational deactivation in the $H + FH(v)$ system is plotted as a function of the barrier height of the surface for $v = 1-5$ at 300 and 650 K, respectively. There are three important features of these figures. First, for low barrier height surfaces, the rate of ~~deactivation~~ decreases rapidly as the barrier height of the surface increases. For example, in figure 4 one sees that as the barrier height increases from 1.5 to

10 kcal/mole, the overall deactivation rates decrease by nearly two orders of magnitude. As the barrier height is further increased beyond 10 kcal/mole, however, the deactivation rates no longer continue to decrease; instead, they remain relatively constant. Second, the variation in the deactivation rates with reagent vibrational excitation differs on the low and high barrier surfaces. In the former region, the deactivation rate in general increases as the reagent HF molecule excitation is increased, while in the latter region there appears to be no clear correlation between reagent excitation and deactivation rate. Third, the barrier height at which the transition between low barrier and high barrier behavior occurs is temperature dependent. In comparing figures 4 and 5, for example, we can see that at 300 K the division seems to occur at 10 kcal/mole; at 650 K it occurs at 20 kcal/mole.

This behavior is also seen to be independent of isotopic substitution. In figure 6 we present a plot of deactivation rates in the $\text{HF}(v) + \text{D}$ system at 300 K. In this figure we only include FD states whose quantum number v'' is smaller than that of the reagent $\text{HF}(v)$ molecule.

We next consider the details of the deactivation process (those features mentioned in item 2 above) in the $\text{HF}(v) + \text{H}$ system. Plots of the fraction $f_v^{(1)}$ of deactivation occurring by single-quantum transitions as a function of the barrier height of the surface are shown in figure 7 for $v = 2-5$ (for $v=1$ all deactivation occurs by single quantum transitions) at 300 K. Clearly this quantity varies substantially as the barrier height is increased although when the barrier is above 20 kcal/mole, the fraction for $v=2$ and 3 is close to unity and thus nearly independent of the barrier height. In general, as the barrier height increases, the importance of single-quantum deactivation increases substantially till on the 40 kcal/mole surface, it accounts

for more than 80% of the deactivation, even in collisions of $v = 4$ and 5 .

In figure 8 we plot the fraction f_v^R of deactivation occurring by reactive processes (that is, those of the type 2b rather than 2a defined above) as a function of the barrier height for $v = 1$ to 5 at $300K$. At low barrier heights, reactive deactivation is clearly the rule, as for all initial states considered, over 75% of the deactivation rate on the 1.5 kcal/mole barrier surface occurs by reaction. On high barrier surfaces, the deactivation occurs totally by non-reactive processes. From the arrows in figure 8 showing the vibrational energy of the isolated $HF(v)$ molecule, one can see that the $v = 4$ and 5 levels of HF already have sufficient energy to overcome any of the barriers studied here. Thus, the absence of reactive deactivation here indicates one of two things: either translational and vibrational energy are so weakly coupled that the latter is not useful in promoting reaction, or that reaction is possible but that it occurs overwhelmingly by a vibrationally adiabatic process. Examination of state-to-state reaction probabilities indicates that the former explanation must be the correct one, as at all but very high translational energies the vibrationally adiabatic reaction probability is smaller than the deactivating ones. For example, on the 40 kcal/mole surface, just above the opening of the $HF(v=4)$ level, the state-to-state reaction probabilities P_{40}^R and P_{41}^R are over 10^5 times greater than P_{44}^R ; at some 0.4 eV above the opening, P_{42}^R is nearly 10^4 times greater than P_{44}^R . Only at translational energies above 1.0 eV does P_{44}^R become the greatest of the reactive probabilities.

While figure 7 gives some feeling as to the importance of multi-quantum transitions, it does not provide an indication of the relative importance of the different possible multi-quantum transitions. To aid in assessing their importance, in figure 9 we plot the average

number $\langle \Delta n_v \rangle_{de}$ of vibrational quanta lost in deactivating collisions, both reactive and non-reactive, as a function of the barrier height for $v = 2 - 5$ at both 300 K (solid lines) and 1000 K (dashed lines).

This quantity is given by the formula

$$\langle \Delta n_v \rangle_{de} = \frac{\sum_{v'=0}^{v-1} (v - v') k_{vv'}^T}{\sum_{v'=0}^{v-1} k_{vv'}^T} \quad (9)$$

where $k_{vv'}^T$ is the total (sum of reactive and non-reactive) deactivation rate constant for the $v \rightarrow v'$ transition. Since the rate constants vary with temperature, so will $\langle \Delta n_v \rangle_{de}$. For a given reagent vibrational level v , the maximum value this quantity may have is also v , as would be the case when all deactivation occurred by a v -quantum process, in which only ground state molecules were formed.

From figure 9 we see four main features. First, this average number of quanta lost is always less than its maximum value, by an amount ranging from almost 4 quanta for $v = 5$ on the 40 kcal/mole barrier surface to 1/2 quanta for $v = 2$ on the 1.5 kcal/mole barrier surface. Second, this quantity decreases as the barrier height of the surface increases, till it is very close to 1 for all reagent states on the 30 kcal/mole barrier surface. Third, this quantity is strongly temperature dependent, with the temperature dependence in the 300 - 1000 K range having its greatest value for the intermediate (10 - 20 kcal/mole) barrier surfaces. Fourth, this quantity increases with v . Thus, we see that on low barrier surfaces, not only are multi-quantum transitions likely, but those multi-quantum transitions which transfer more than 2 quanta of vibrational energy are quite likely.

Finally, we wish to consider the temperature dependence of the rate constants for single-quantum deactivation as a function of the reagent vibrational state and the barrier height of the potential energy surface. To show this temperature dependence, we calculate

Arrhenius activation energies ($E_a^{v, v-1}$) for these rate constants in the high temperature (700 - 1000 K) and plot them as a function of reagent internal energy in figure 10. These are the slopes of the corresponding Arrhenius plots (logarithm of rate constant vs. inverse temperature), which have been found normally to be reasonably linear in the low (200 - 400 K) and high (700 - 1000 K) temperature regions, but curved in between. The activation energies calculated increase as the barrier height of the potential energy surface increases and, in general, decrease as the vibrational excitation of the reagent increases. This decrease is far less than the increase in internal energy, however. For example, the activation energy on the 40 kcal/mole barrier surface decreases only by some 16 kcal/mole as one adds over 40 kcal/mole of internal energy. This is another manifestation of the relative inefficiency of vibrational energy in promoting reaction.

B. REACTIVE PROCESSES

In this section we will examine a few aspects of the dynamics of reactive processes in the $\text{HF}(v) + \text{D}$ system. This system is a better one for experimental study than the $\text{HF}(v) + \text{H}$ system, as the reactive and non-reactive processes can be easily differentiated. In fact, experiments on this system taking advantage of the mass difference between the H and D atoms have already been performed (15). The aspects of the dynamics of the reactive processes which we will mainly consider are the gross features of the reaction probability and the vibrational state distribution of the DF product formed in the reaction.

We examine the threshold region of the total reaction probability for reaction of ground state HF with D atoms on the six surfaces in figure 11. In this figure, we plot the reaction probability vs. energy curves only in the threshold region, in which the probability increases

rapidly and smoothly from zero to one. We also indicate in the figure the translational energy equal to the classical barrier height of the six surfaces studied. Note that this quantity is measured with respect to the bottom of the HF well, while the translational energy is measured with respect to the HF zero-point energy. The important points to be learned from the figure are as follows. First, for all surfaces the reaction probability does rise smoothly from zero to one over a fairly narrow range of energy. Second, the threshold energy (the energy at which the probability of reaction first becomes large, say 0.02) is always smaller than the classical barrier height by an amount which increases as the barrier height increases (some 0.04 eV for the 1.5 kcal/mole barrier surface to some 0.23 eV for the 40 kcal/mole barrier surface). Third, the width of the threshold region also increases as the barrier height increases (from some 0.03 eV for the 1.5 kcal/mole barrier surface to some 0.25 eV for the 40 kcal/mole barrier surface).

In figure 12 we plot the total reaction probability for reaction of $\text{HF}(v=1)$ with D atoms vs. energy in the threshold region on the six surfaces. While this plot is fairly similar to that in figure 11, there are two major differences. First, the probability vs. energy curves have shifted to lower energy. This is reasonable, as the vibrational energy should be at least partially effective in reducing the translational energy threshold for reaction. One sees that its effectiveness is limited, however, as the translational energy threshold has been reduced by no more than 0.2 eV on vibrational excitation, even though the vibrational quantum is 0.49 eV. Second, the behavior of the probability vs. energy curves at the high energy end of the threshold region is different than it is in figure 11 for the lower barrier (1.5, 5, 10 kcal/mole) surfaces. In these cases, we see that the reaction probabilities do not stay near unity as they do in

figure 11; instead, they reach a maximum somewhat less than unity and then decrease with increasing energy. On the higher barrier surfaces, behavior is similar to that in figure 11. We will discuss later possible explanations for the more complicated nature of the dynamics on the low barrier surfaces.

The next aspect of the reactive processes which we will consider is the vibrational state distribution of the DF formed in the reaction, and how it varies with the barrier height of the potential energy surface and with reagent vibrational excitation. The quantity which we will frequently consider in order to avoid having to look at the entire product state distribution is the average fraction $\langle f_v \rangle$ of product energy going into product vibration

$$\langle f_v \rangle = \frac{\sum_{v'=0}^{v_{\max}} E_{v'} P_{vv'}^R}{\sum_{v'=0}^{v_{\max}} P_{vv'}^R} \quad (10)$$

In figure 13 we plot for energies at which the reaction probability is appreciable (more than 60%) this quantity for reactions of ground state HF on the 1.5, 20, and 40 kcal/mole barrier surfaces. From this figure we see that the barrier height of the surface has a major influence not only on the translational energy threshold for reaction, but also on the product state distribution. As the barrier height increases, there is less vibrational excitation of the DF product. We also note that $\langle f_v \rangle$ is a much smoother function of the energy for the higher barrier surfaces (20, 40 kcal/mole) than it is for the low (1.5 kcal/mole) barrier surface. Some of the lack of smoothness in the plot for that surface can be attributed to at most very small translational energy thresholds for vibrational excitation into newly opened states. The arrows on the abscissa of figure 13 indicate the energies at which DF product states become open, and we see that

the curve for the 1.5 kcal/mole barrier surface rises rapidly at almost identically those energies. This is particularly true at the energies where the DF($v=1, 2$, and 3) state become open. No such rapid increases are seen for $\langle f_v \rangle$ on the high barrier surfaces, suggesting that reaction to higher vibrational energy product states occurs with a large translational energy threshold.

To determine how reagent vibrational excitation influences the vibrational state distribution of the DF product, we examine $\langle f_v \rangle$ for $v = 0-4$ at a variety of energies on the different potential energy surfaces. The values obtained are given in Table 2. In this table we only consider those combinations of potential energy surface, energy, and reagent vibrational state for which the reaction probability has gone through its initial rise; on the high barrier surfaces we will only be able to examine the few lowest reagent vibrational states, as the translational energy thresholds for reaction are too great for reaction to occur in the energy range studied.

From the data in table 2, we can see that the influence of reagent vibrational excitation on the product state distribution depends strongly on the total energy and on the barrier height of the potential surface.

On high barrier surfaces, reagent vibrational excitation leads to a higher fraction of the product energy going into vibration, whereas on low barrier surfaces, it leads to no particular behavior. In a number of cases one actually sees less product vibrational excitation in collisions of vibrationally excited reagents (see for example the 2.410 eV results on the 1.5 kcal/mole barrier surface and the 2.002 eV results on the 5 kcal/mole barrier surface). On the intermediate barrier surfaces, one can see both types of behavior. For example, on the 10 kcal/mole barrier surface, reaction of vibrationally excited HF leads to a more highly excited DF distribution than does that of ground state HF at low energy (1.186 eV), but leads to a less highly

excited one at higher energy (2.410 eV).

We can also obtain additional information about how the product state distribution depends on the potential energy surface from the data in table 2, especially for reactions of vibrationally excited molecules (in figure 13 we considered only reaction of ground state species). It appears that this dependence is itself energy dependent. At the lowest energy considered (1.186 eV), while $\langle f_0 \rangle$ decreases as the barrier height is increased, $\langle f_1 \rangle$ increases. At most other combinations of energy and reagent vibrational state, $\langle f_v \rangle$ is essentially independent of the barrier height (or more precisely, depends on the barrier height in no easily recognizable way) on low barrier height surfaces, but decreases substantially as the barrier height further increases.

The distribution of the DF product states for reaction from HF($v=0, 1$, and 2) at a total energy of 2.410 eV is shown in figure 14 in the form of histogram plots. In these plots, the height of the bar is proportional to the reaction probability to the indicated product state. We note here the most important features of these plots. For the ground reagent state, as the barrier height increases, the product state distribution as a whole shifts to lower vibrational states, until on the 40 kcal/mole barrier surface, 75% of the reaction occurs by a vibrationally adiabatic process. On the low barrier surfaces the product state distribution is quite broad, being spread out over 3-5 product states. For the $v=1$ reagent state, the product distribution also shifts to lower vibrational states as the barrier height increases, but the shift is not as dramatic as for ground state reactions. This is true for two reasons. First, on the 40 kcal/mole barrier surface the reaction is primarily vibrationally adiabatic; hence the distribution for that surface is peaked about $v=1$ and not about $v=0$ as in the ground state reaction. Second, the product state distributions on the low

barrier surfaces are wider than for ground state reaction, so that there is appreciable population of the $DF(v'=2)$ state on all surfaces. An interesting feature is that at this energy, the probability of vibrationally adiabatic reaction on the 30 kcal/mole surface is significantly smaller than the probability for reaction with an increase or decrease of one in the vibrational quantum number. Thus, one cannot simply assume that the reaction is vibrationally adiabatic on high barrier surfaces at all energies. The product state distributions in reactions of $HF(v=2)$ are even broader than those for reactions of $HF(v=1)$, and are also somewhat irregular (they are not smoothly peaked about one quantum state). We note that some of the state-to-state reaction probabilities on the low barrier surfaces vary fairly rapidly with energy at high energy; it is this variation that gives rise to the irregular structure of the plot of $\langle f_0 \rangle$ in figure 13.

C. QUANTUM MECHANICAL RESONANCES

The existence of low energy resonances in the collinear HFH system (Muckerman V surface) has been noted previously (14), and here we consider some aspects of the resonance structure on the surfaces used. We are particularly interested in how the resonances change in position and intensity as the barrier height is raised. In figures 15-18 we present plots of state-to-state probabilities of reaction 3b on the 1.5, 5, 10, and 20 kcal/mole barrier surfaces, respectively, in the region of energy containing the threshold for reaction from $v = 0$ and continuing up some 0.4 eV above that. The plots strongly suggest the existence of a resonance in these systems. The resonance is strongest on the 1.5 kcal/mole barrier surface, and is substantially weaker on the 10 kcal/mole barrier surface. On the 20 kcal/mole barrier surface it has almost totally disappeared; it is seen only by the formation of a small shoulder in the P_{00}^R and P_{01}^R

curves. There is no minimum in P_{00}^R as there is on each of the lower barrier surfaces. It is also interesting to consider the effect of isotopic substitution on the strength of the resonance. To do this, we plot state-to-state probabilities for reaction 2b on the 10 kcal/mole barrier surface in figure 19. It is quite clear that the resonance is much stronger in this system than it is in the D substituted system. There are two other interesting features of figure 19. First, there is a small dip in the reaction probability shortly after it first reaches unity. At higher energies the probability does return to one, and stays there until the resonance. Second, the resonance occurs at a translational energy of 0.735 eV, which is some 0.1 eV greater than the energy of the weaker and broader resonance in the D + FH system. We will discuss these features of the dynamics in the ensuing discussion section.

V. DISCUSSION

The dynamics of the collinear HFH and DFH systems are shown to depend substantially on the barrier height of the potential energy surface used. As the barrier height is increased a number of important changes in the dynamics take place. In collisions of vibrationally excited HF molecules, the overall rate of vibrational deactivation of the HF decreases for a while as the barrier height increases; further increase of the barrier height makes little change in the deactivation rate. The value of the barrier height at which this takes place is a function of temperature (increasing as the temperature is increased). On low barrier surfaces, the bulk of the deactivation occurs by reactive (and multi-quantum) processes; on high barrier surfaces, it occurs by non-reactive (and single-quantum) processes. On the lowest barrier surfaces (1.5 and 5 kcal/mole), what non-reactive deactivation there is occurs from both single and multi-quantum transitions at 300 K; the higher the reagent vibrational state, the greater the contribution of multi-quantum non-reactive deactivation processes. On the highest barrier surfaces (30 - 40 kcal/mole), reactive deactivation occurs mainly by multi-quantum transitions at 300 K, for example two quantum processes in collisions of HF($v=3$) with H and 3 and 4 quantum ones in collisions of HF($v=5$) + H. We have shown elsewhere (17) that as the temperature increases, the relative importance of single quantum reactive deactivating processes increases. On the highest barrier surface studied (40 kcal/mole) the deactivation of vibrationally excited HF can be thought of, to a good approximation, as occurring entirely in single-quantum non-reactive processes.

On this class of surfaces, vibrational energy is not spectacularly effective at promoting reaction. This is seen in two ways: the fairly small decrease (0.10 to 0.22 eV) in translational thresholds for

reaction on the moderate and high barrier surfaces to the vibrational quantum (0.49 eV), and the calculation of large activation energies for reactive single-quantum deactivation processes at high temperatures (700 - 1000 K). Elsewhere, we have shown that this partial effectiveness of vibrational energy can be explained on the 40 kcal/mole surface by a vibrationally adiabatic model (17). The feature of the potential energy surface which is greatly responsible for this partial effectiveness is the relative narrowness of the reaction channel in the saddle point region (see figure 2). This narrowness produces a large vibrational frequency for symmetric stretch motion at the saddle point, meaning that the vibrationally adiabatic barriers will be fairly large, even when there are a few quanta of vibrational excitation.

For the surfaces with low or only moderate barriers, a vibrationally adiabatic model provides useful insight into the dynamics of the reaction. In figure 20 we plot a vibrationally adiabatic correlation diagram for the DFH reaction on the 1.5 kcal/mole surface. In this figure, the energy $V_n(s)$ of the vibrational state n everywhere along the reaction coordinate s is plotted. We also plot the energy $V^{\text{mep}}(s)$ along the minimum energy path. In this case, one can see that there are wells in the vibrationally adiabatic correlation diagram for all reagent states, and the wells become deeper as the vibrational state increases. Since it is known that wells in the vibrationally adiabatic correlation diagram can lead to reactive scattering resonances (21), the existence of resonances in this system is not unexpected. Indeed, in figure 15 we see a very strong resonance in the reaction probability P_{00}^R at $E_0 = 0.3$ eV. We indicate this energy on figure 20 with a dotted line. The correlation between resonances and bound states of the wells in the vibrationally adiabatic correlation diagram is obvious. For higher vibrational states the wells are quite deep and wide, suggesting that large numbers of bound states

of the curves might exist, producing numerous resonances and hence quite complicated dynamics. We also note that the curves for the different states come quite close to each other, suggesting that crossing from one to another should occur fairly easily, especially between states with n greater than 1.

If this picture is correct, it must explain both the decrease in resonance intensity as the barrier height is increased and the greater strength and higher energy of the resonance in the 10 kcal/mole barrier surface for H + FH than for D + FH. In figure 21 we present the vibrationally adiabatic correlation diagram for the DFH system on the 10 kcal/mole barrier surface. The main differences between this figure and figure 20 are the absence of the small well in the $n=0$ curve and the much smaller depth of the well in the $n=1$ curve. Because of this small well depth, the resonance is expected to be substantially broadened. The vibrationally adiabatic correlation diagram for the HFH system on the 10 kcal/mole barrier surface is shown in figure 22. As in figure 20, the energy of the resonance is indicated by a dotted line. We note two major differences between figures 21 and 22. First, in the HFH system, the well in the $v=1$ curve is fairly deep (~ 0.1 eV); the resonance energy is seen to lie about halfway between the bottom and top of the well. Second, the vibrationally adiabatic correlation diagram curves for HFH are symmetric about $s = 0$. Thus, the formation of a flat shoulder-like area on the curves, such as that seen for $n = 1$ in figure 21, cannot occur in the HFH case; any well must be symmetric about the saddle point. The greater depth of the well in the HFH case than for the DFH one is responsible for the greater strength and smaller width of the resonance in the former system. Because the vibrational frequencies near the saddle point are greater for HFH than they are for DFH, the curves in the vibrationally adiabatic correlation diagram for HFH will be at higher ener-

gy in the saddle point region than are those for DFH. Thus, the vibrationally adiabatic correlation diagrams produce the correct dependence of the resonance strength and energy on isotopic substitution.

VI. CONCLUSIONS

On the basis of the scattering calculations performed, we are able to answer the questions posed at the beginning of section 4 about the dynamics of the collinear HFH and DFH systems and how those dynamics depend on the barrier height of the potential energy surface used. We briefly summarize what we have learned in regard to each question.

1) The relative rates of collisional deactivation of vibrationally excited HF decrease substantially with increasing barrier height for small barrier height surfaces; on larger barrier surfaces they are relatively independent of the barrier height. The barrier height at which this transition occurs increases with temperature.

2) On low barrier surfaces vibrational deactivation occurs primarily by reactive multi-quantum processes, while on high barrier surfaces it occurs primarily by non-reactive single-quantum processes.

3) Vibrational deactivation rates increase with temperature. On the high barrier surfaces the rate of reactive deactivation increases with temperature much more rapidly than that of non-reactive deactivation. As the temperature increases, multi-quantum deactivations increase in importance.

4) As the barrier height of the surface increases, both the translational energy threshold for reaction increases and the average fraction of energy going into product vibration decreases. On the high barrier surfaces reagent vibrational excitation leads to a higher fraction of energy going into product vibration; on the low-barrier surfaces this is not always true.

5) The gross features of the non-reactive dynamics are not affected by isotopic substitution; the reactive dynamics differ substantially in their resonance behavior. This difference may be under-

stood in terms of the vibrationally adiabatic correlation diagram for the HFH and DFH systems.

6) Quantum mechanical resonances are strongest on the low barrier surfaces and significantly weaker or absent on the higher barrier ones. They move to higher energy as the barrier height of the surface increases. Consideration of the vibrationally adiabatic correlation diagram helps one understand this dependence.

ACKNOWLEDGMENTS

The calculations reported here were performed on the IBM 370/158 computer of Ambassador College, Pasadena, California, for which we express our appreciation. Additional calculations were performed on the Dreyfus-NSF Theoretical Chemistry Computer at Caltech, which was funded through grants from the Camille and Henry Dreyfus Foundation, the National Science Foundation (Grant No. CHE78-20235), and the Sloan Fund of the California Institute of Technology.

REFERENCES

1. J. C. Polanyi and J. L. Schreiber, in: Kinetics of Gas Reactions (Vol. VIA, Physical Chemistry, an Advanced Treatise), ed. W. Jost (Academic Press, New York, 1974) pp. 383-487 and references therein.
2. J. T. Muckerman, in: Theoretical Chemistry, Advances and Perspectives, Vol. 6A, ed. D. Henderson (Academic Press, New York, 1981), pp. 1-77.
3. D. G. Truhlar and R. E. Wyatt, Ann. Rev. Phys. Chem. 27, 1 (1976); E. B. Stechel, R. B. Walker, and J. C. Light, in: Proceedings of the CECAM Reactive Scattering Workshop, Orsay, France 1977; R. B. Walker, E. B. Stechel, and J. C. Light, J. Chem. Phys. 69, 2922 (1978); M. Baer, V. Khare, and D. J. Kouri, Chem. Phys. Lett. 68, 378 (1979); J. M. Bowman and K. T. Lee, Chem. Phys. Lett. 64, 291 (1979); J. Chem. Phys. 72, 5071 (1980); D. C. Clary and J. N. L. Connor, Chem. Phys. 48, 175 (1980); Y. Y. Yung, B. H. Choi, and K. T. Tang, J. Chem. Phys. 72, 621 (1980); J. C. Sun, B. H. Choi, R. T. Poe, and K. T. Tang, J. Chem. Phys. 73, 6095 (1980); A. Kuppermann, J. A. Kaye, and J. P. Dwyer, Chem. Phys. Lett. 74, 257 (1980); J. Römelt, Chem. Phys. Lett. 74, 263 (1980).
4. I. Shavitt, R. M. Stevens, F. L. Minn, and M. Karplus, J. Chem. Phys. 48, 2700 (1968); a simple fit to this potential energy surface has been outlined in D. G. Truhlar and A. Kuppermann, J. Chem. Phys. 56, 2232 (1972).
5. R. N. Porter and M. Karplus, J. Chem. Phys. 40, 1105 (1964).
6. P. Siegbahn and B. Liu, J. Chem. Phys. 68, 2457 (1978); D. G. Truhlar and C. J. Horowitz, J. Chem. Phys. 68, 2466 (1978).

7. a) J. T. Muckerman, J. Chem. Phys. 56, 2997 (1972);
b) G. C. Schatz, J. M. Bowman, and A. Kuppermann, J. Chem. Phys. 63, 674 (1975).
8. C. F. Bender, P. K. Pearson, S. V. O'Neil, and H. F. Schaefer III, J. Chem. Phys. 56, 4626 (1972).
9. J. N. L. Connor, W. Jakubetz, and J. Manz, Mol. Phys. 35, 1301 (1978); G. C. Schatz, J. M. Bowman, and A. Kuppermann, J. Chem. Phys. 58, 4023 (1973).
10. J. C. Gray, D. G. Truhlar, L. Clemens, J. W. Duff, F. M. Chapman, Jr., G. O. Morrell, and E. F. Hayes, J. Chem. Phys. 69, 240 (1977).
11. D. C. Clary, J. N. L. Connor, and C. J. Edge, Chem. Phys. Lett. 68, 154 (1979).
12. J. A. Kaye and A. Kuppermann, Chem. Phys. Lett. 77, 573 (1981); J. Manz and J. Römelt, Chem. Phys. Lett. 81, 179 (1981).
13. J.-T. Hwang and H. Rabitz, J. Chem. Phys. 70, 4609 (1979);
L. Eno and H. Rabitz, J. Chem. Phys. 72, 2314 (1980);
L. A. Eslava, L. Eno, and H. Rabitz, J. Chem. Phys. 73, 4998 (1980).
14. G. C. Schatz and A. Kuppermann, J. Chem. Phys. 72, 2737 (1980).
15. F. E. Bartoszek, D. M. Manos, and J. C. Polanyi, J. Chem. Phys. 69, 933 (1978).
16. C. F. Bender, B. J. Garrison, and H. F. Schaefer III, J. Chem. Phys. 62, 1188 (1975); P. Botschwina and W. Meyer, Chem. Phys. 20, 43 (1977); W. R. Wadt and N. W. Winter, J. Chem. Phys. 67, 3068 (1977); A. F. Voter and W. A. Goddard III, J. Chem. Phys. 75, 3638 (1981).

17. J. A. Kaye, J. P. Dwyer, and A. Kuppermann, manuscript in preparation.
18. J. M. Bowman and A. Kuppermann, Chem. Phys. Lett. 34, 523 (1975).
19. L. M. Delves, Nucl. Phys. 9, 391 (1959); 20, 275 (1960).
20. A. Kuppermann, in: Potential Energy Surfaces in Chemistry, ed. W. A. Lester, (U. Calif., Santa Cruz, August 1970), pp. 121-9; in: Abstracts of Papers VII International Conference on the Physics of Electronic and Atomic Collisions (North-Holland, Amsterdam, 1971), pp. 3-5; in: Theoretical Chemistry, Advances and Perspectives, Vol. 6a, ed. D. Henderson, (Academic Press, New York, 1981), pp. 79-164.
21. S. Latham, J. F. McNutt, R. E. Wyatt, and M. Redmon, J. Chem. Phys. 69, 3746 (1978).

Table 1. Parameters for Minimum Energy Path (Eq. 7)

Surface Barrier kcal/mole	A kcal/mole	B kcal/mole	C radians ⁻¹
1.5	0.01681	1.4832	1.3434
5	0.01681	4.9832	20.955
10	0.01681	9.9832	25.268
20	0.01681	19.983	29.575
30	0.01681	29.983	32.093
40	0.01681	39.983	33.879

Table 2. $\langle f_v \rangle$ for Different Energies, Reagent Vibrational States, and Potential Energy Surfaces

Surface ^a	v ^b	E/eV				
		1.186	1.594	2.002	2.410	2.655
1.5	0	0.555	0.652	0.716	0.692	0.705
	1	0.259	0.532	0.583	0.549	0.530
	2	- ^c	0.637	0.461	0.511	0.552
	3	-	-	0.501	0.460	0.554
	4	-	-	-	0.394	0.480
	5	-	-	-	-	0.585
5	0	0.494	0.543	0.627	0.647	NA ^d
	1	0.350	0.378	0.504	0.513	NA
	2	-	0.415	0.457	0.488	NA
	3	-	-	0.447	0.475	NA
	4	-	-	-	0.604	NA
10	0	0.357	0.473	0.508	0.620	0.648
	1	0.508	0.433	0.377	0.507	0.528
	2	-	0.399	0.381	0.477	0.492
	3	-	-	0.465	0.455	0.485
	4	-	-	-	-	0.521
	5	-	-	-	-	0.621
20	0	0.159	0.222	0.330	0.412	0.456
	1	-	0.348	0.344	0.422	0.448
	2	-	-	0.335	0.401	0.444
	3	-	-	-	0.434	0.427
	4	-	-	-	-	0.522
30	0	-	0.116	0.149	0.233	NA
	1	-	-	0.267	0.300	NA
	2	-	-	-	0.379	NA
40	0	-	-	0.107	0.112	0.143
	1	-	-	-	0.230	0.240
	2	-	-	-	-	0.332

a) Number indicated is the barrier height of the potential energy surface in kcal/mole

b) Reagent Vibrational State

c) There is insufficient (below ~ 60%) reaction for this combination of potential energy surface, reagent vibrational state and total energy

d) Calculations performed on this potential energy surface for this energy gave scattering matrices which were not unitary to within 3% so we did not use the results (NA = not available)

FIGURE CAPTIONS

Figure 1. Schematic diagram of coordinate system for rotating Morse-cubic spline potential energy surface.

Figure 2. Potential energy surface for the collinear H + FH system on the 40 kcal/mole barrier surface in the mass-scaled Delves coordinate system. Equipotentials are drawn every 0.3 eV from 0.3 eV with respect to the bottom of the HF well up to a maximum of 3.0 eV. The minimum energy path is indicated by a dashed line; the saddle point is marked by an 'x'.

Figure 3. Energy level diagram of the energy V of the various HF(right) and DF (left) states and the barrier heights of the surfaces (center).

Figure 4. Plot of the total rate constant (sum of reactive and non-reactive) k_v^{de} for deactivation in the collision $H + FH(v) \rightarrow H + FH(v' < v)$ at 300 K for $v = 1-5$ as a function of the barrier height E_{barr} of the potential energy surface. Arrows mark the internal energies of the four lowest HF states. Line types are as follows: $v=1$: solid line; $v=2$: dashed line; $v=3$: dashed-dotted line; $v=4$: dotted line; $v=5$: dashed-triple-dotted line.

Figure 5. Plot of the total rate constant for deactivation k_v^{de} in the collision $H + FH(v) \rightarrow H + FH(v' < v)$ at 650 K for $v = 1-5$ as a function of the barrier height E_{barr} of the potential energy surface. Arrows and line types are as in figure 4.

Figure 6. Plot of the total rate constant for deactivation k_v^{de} in the collision $D + FH(v) \rightarrow D + FH(v' < v)$, $DF(v'' < v) + H$ at 300 K for $v = 1-3$ as a function of the barrier height E_{barr} of the potential energy surface. Arrows and line types are as in figure 4.

Figure 7. Plot of the fraction $f_v^{(1)}$ of deactivation occurring by single quantum transitions in the collision $H + FH(v) \rightarrow H + FH(v-1)$ (both reactive and non-reactive) at 300 K for $v = 2-5$ as a function of the barrier height E_{barr} of the potential energy surface. Arrows and line types are as in figure 4.

Figure 8. Plot of the fraction f_v^R of deactivation occurring by reaction in the collision $H + FH(v) \rightarrow HF(v' < v) + H$ at 300 K for $v = 1-5$ as a function of the barrier height E_{barr} of the potential energy surface. Arrows and line types are as in figure 4.

Figure 9. Plot of the average number $\langle \Delta n_v \rangle_{de}$ of vibrational quanta lost in deactivating collisions in $H + FH(v) \rightarrow H + FH(v' < v)$ (both reactive and non-reactive) at 300 K (solid line) and 1000 K (dashed line) for $v = 2-5$. Arrows are used as in figure 4. Symbols used are as follows: $v = 2$: circles; $v = 3$: squares; $v = 4$: triangles; $v = 5$: diamonds. Where no line is shown, $\langle \Delta n_v \rangle_{de}$ may be taken as being one.

Figure 10. Plot of Arrhenius activation energies $E_a^{v, v-1}$ for the single-quantum deactivation reactions $H + FH(v) \rightarrow HF(v-1) + H$ for $v = 1-5$ as a function of the internal energy E_{int} of the $HF(v)$ reagent state on the six potential energy surfaces studied. The barrier height E_{barr} of these surfaces is indicated on the right side of the plot. Internal energies of the $v = 2-5$ states are indicated by arrows.

Figure 11. Plot of probability $P_{D+FH(0)}^R$ of the reaction $D + FH(0) \rightarrow DF + H$ as a function of the reagent translational energy E_0 in the threshold region on the six potential energy surfaces studied, the barrier heights of which are indicated. The arrows indicate the energies corresponding to the heights of the barriers.

Figure 12. Plot of probability $P_{D+FH(1)}^R$ of the reaction $D + FH(1) \rightarrow DF + H$ as a function of the reagent translational energy E_1 in the threshold region on the six potential energy surfaces studied.

All labeling is as in figure 11. The arrows on the abscissa indicate the energies of the surface barrier heights.

Figure 13. Plot of the average fraction of available energy $\langle f_0 \rangle$ going into product vibration in the reaction $D + FH(0) \rightarrow DF + H$ as a function of the reagent translational energy E_0 on the 1.5 (triangles), 20 (squares) and 40 (circles) kcal/mole barrier surfaces. Energies of the various DF product states are indicated on the abscissa.

Figure 14. Histogram plot showing product state distributions for the reaction $D + FH(v) \rightarrow DF(v') + H$ at a total energy of 2.410 eV for v' up to and including 6 on the 6 potential energy surfaces, the barrier height of which is indicated in the upper right corner of each strip. The height of the bar is proportional to the magnitude of the state-to-state reaction probability $P_{D+FH(v) \rightarrow DF(v')+H}$. a) $v=0$; b) $v=1$; c) $v=2$.

Figure 15. Plot of the state-to-state reaction probability $P_{D+FH(0) \rightarrow DF(v')+H}$ for the reaction $D + FH(v=0) \rightarrow DF(v') + H$ as a function of the reagent translational energy E_0 on the 1.5 kcal/mole barrier surface. The arrow marks the energy at which the DF ($v=1$) state becomes accessible. A solid line is used for the $v'=0$ transition; a dashed one is used for the $v'=1$ transition.

Figure 16. Plot of the state-to-state reaction probability $P_{D+FH(0) \rightarrow DF(v')+H}$ defined for fig. 15 as a function of the reagent translational energy E_0 on the 5 kcal/mole barrier surface. Arrows mark the energies at which the indicated states become accessible. Line types are as in figure 15.

Figure 17. Plot of the state-to-state reaction probability

$P_{D+FH(0) \rightarrow DF(v')+H}$ defined for figure 15 as a function of the reagent translational energy E_0 on the 10 kcal/mole barrier surface. Arrows and line types are as in figure 16.

Figure 18. Plot of the state-to-state reaction probability

$P_{D+FH(0) \rightarrow DF(v')+H}$ defined for figure 15 as a function of the reagent translational energy E_0 on the 20 kcal/mole barrier surface. Arrows and line types are as in figure 16.

Figure 19. Plot of the state-to-state reaction probability

$P_{H+FH(0) \rightarrow HF(v')+H}$ for the reaction $H + FH(v=0) \rightarrow HF(v') + H$ as a function of the reagent translational energy E_0 on the 10 kcal/mole barrier surface. Arrows and line types are as in figure 16.

Figure 20. Vibrationally adiabatic correlation diagram showing the energy V along the minimum energy path (MEP) and of the n^{th} local vibrational state as a function of the reaction coordinate s measured along the minimum energy path for the 1.5 kcal/mole barrier surface for the $D + FH$ reaction. The dotted line marks the energy at which the resonance seen in figure 15 is observed.

Figure 21. Vibrationally adiabatic correlation diagram for the 10 kcal/mole barrier surface for the $D + FH$ reaction.

Figure 22. Vibrationally adiabatic correlation diagram for the 10 kcal/mole barrier surface for the $H + FH$ reaction.

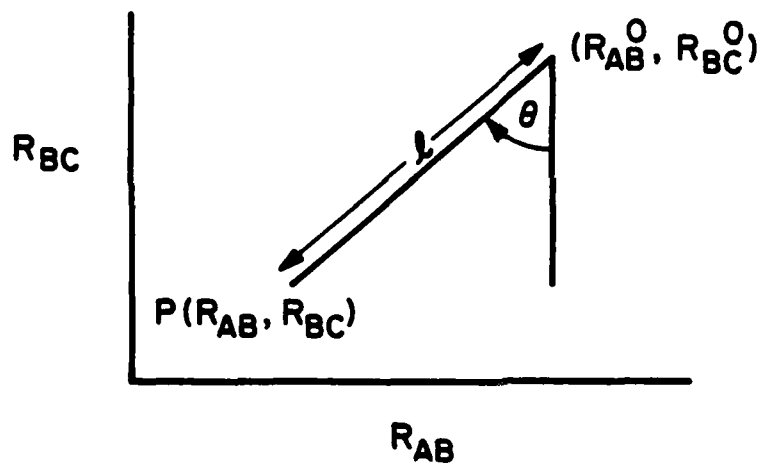


Figure 1

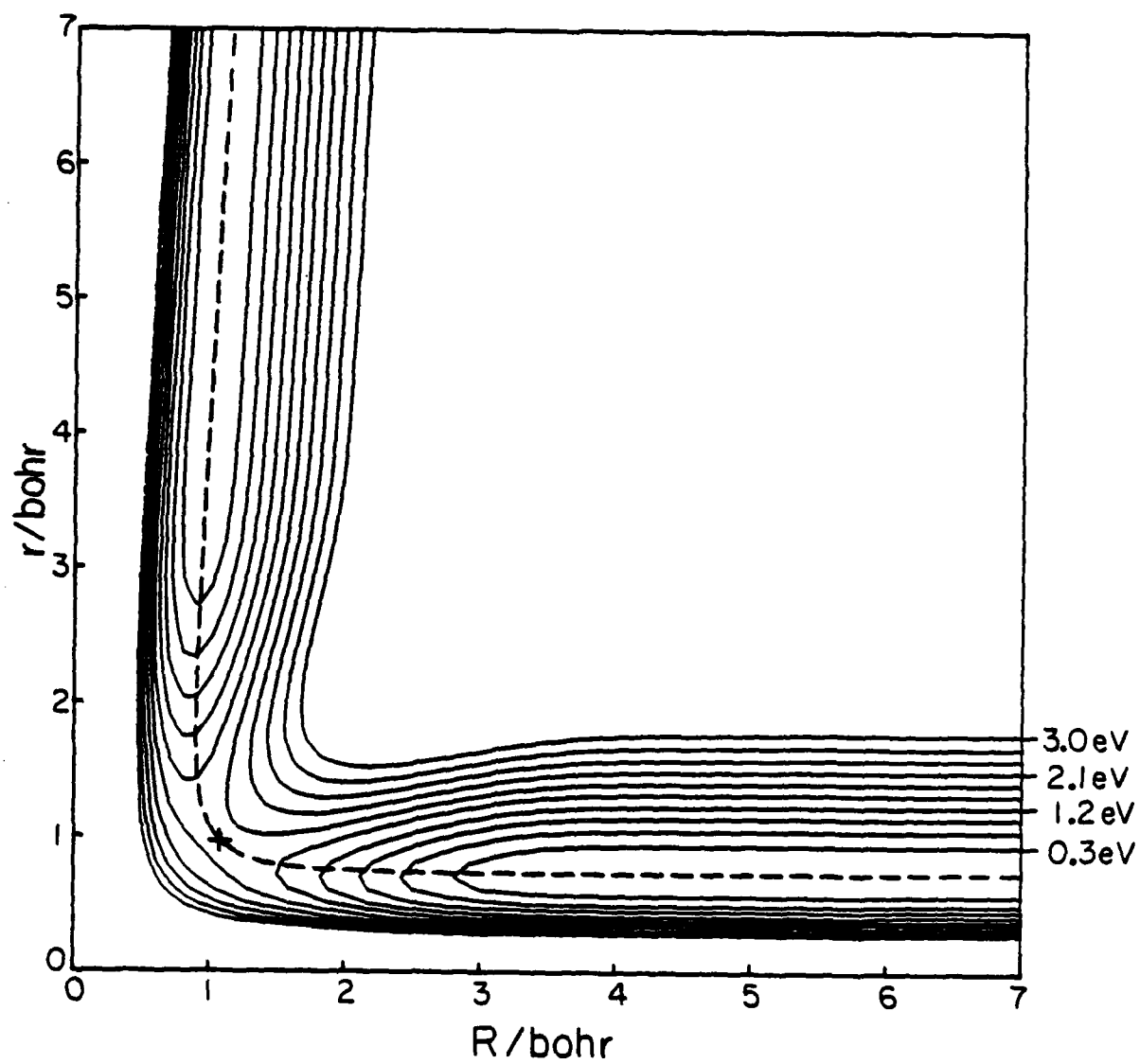


Figure 2

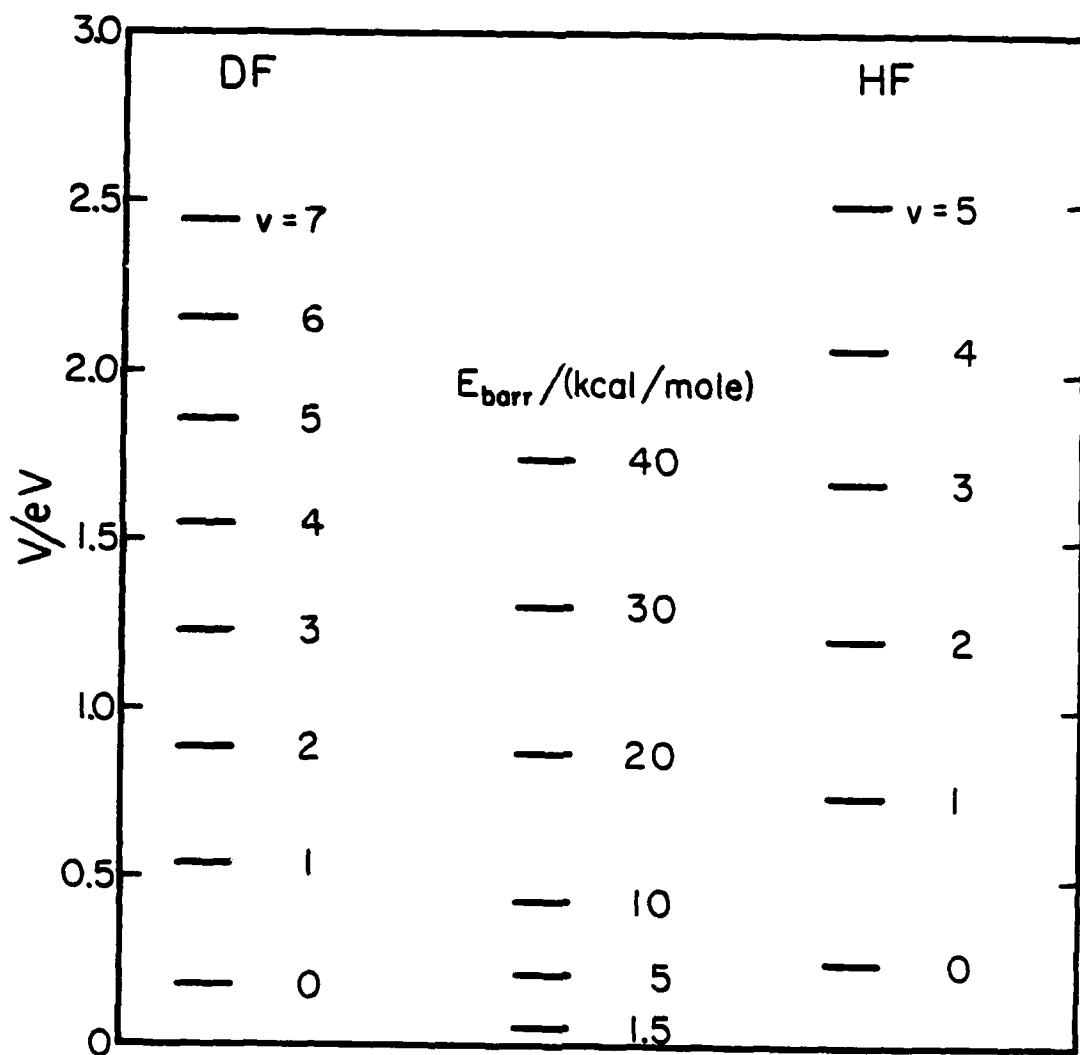


Figure 3

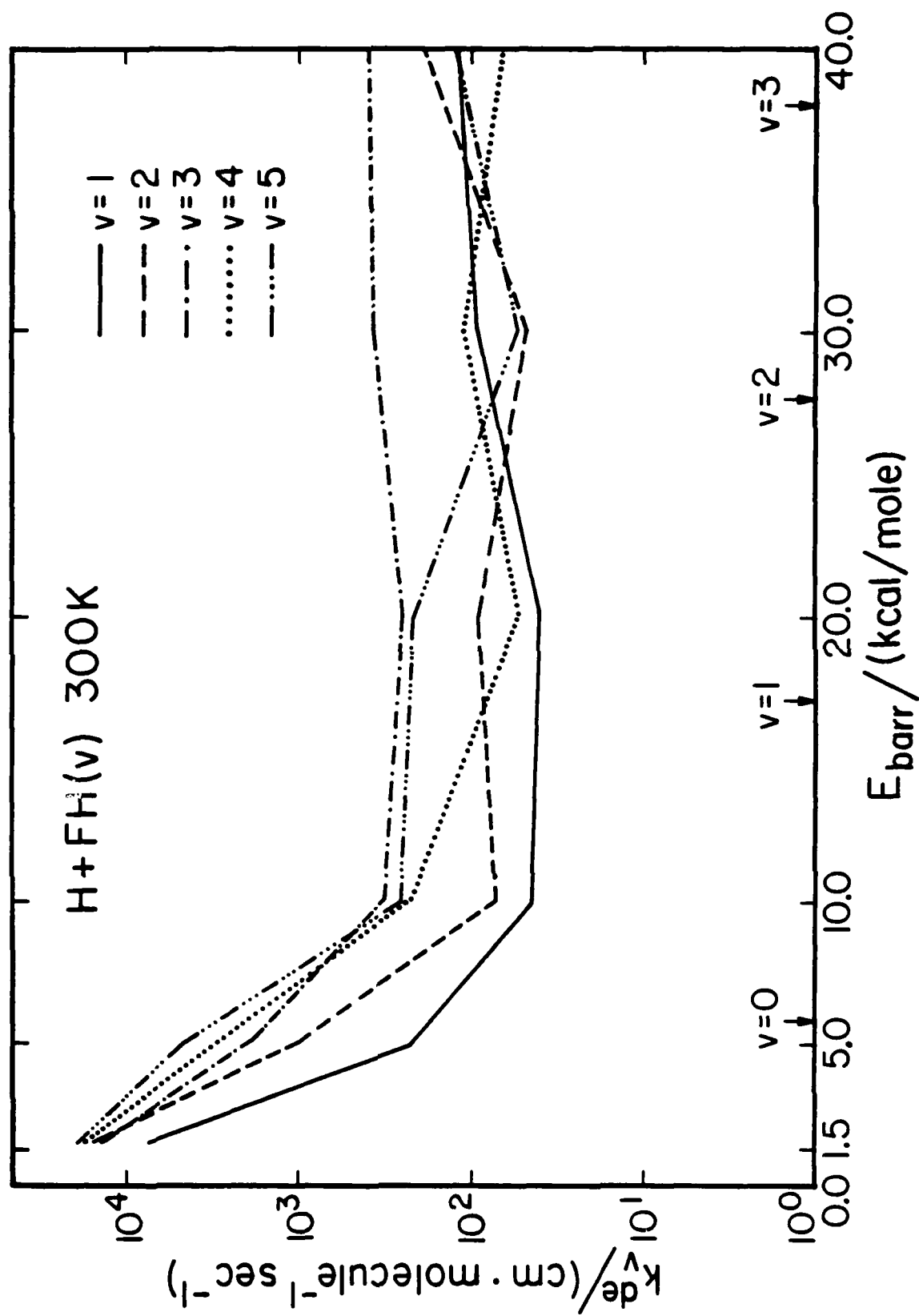


Figure 4

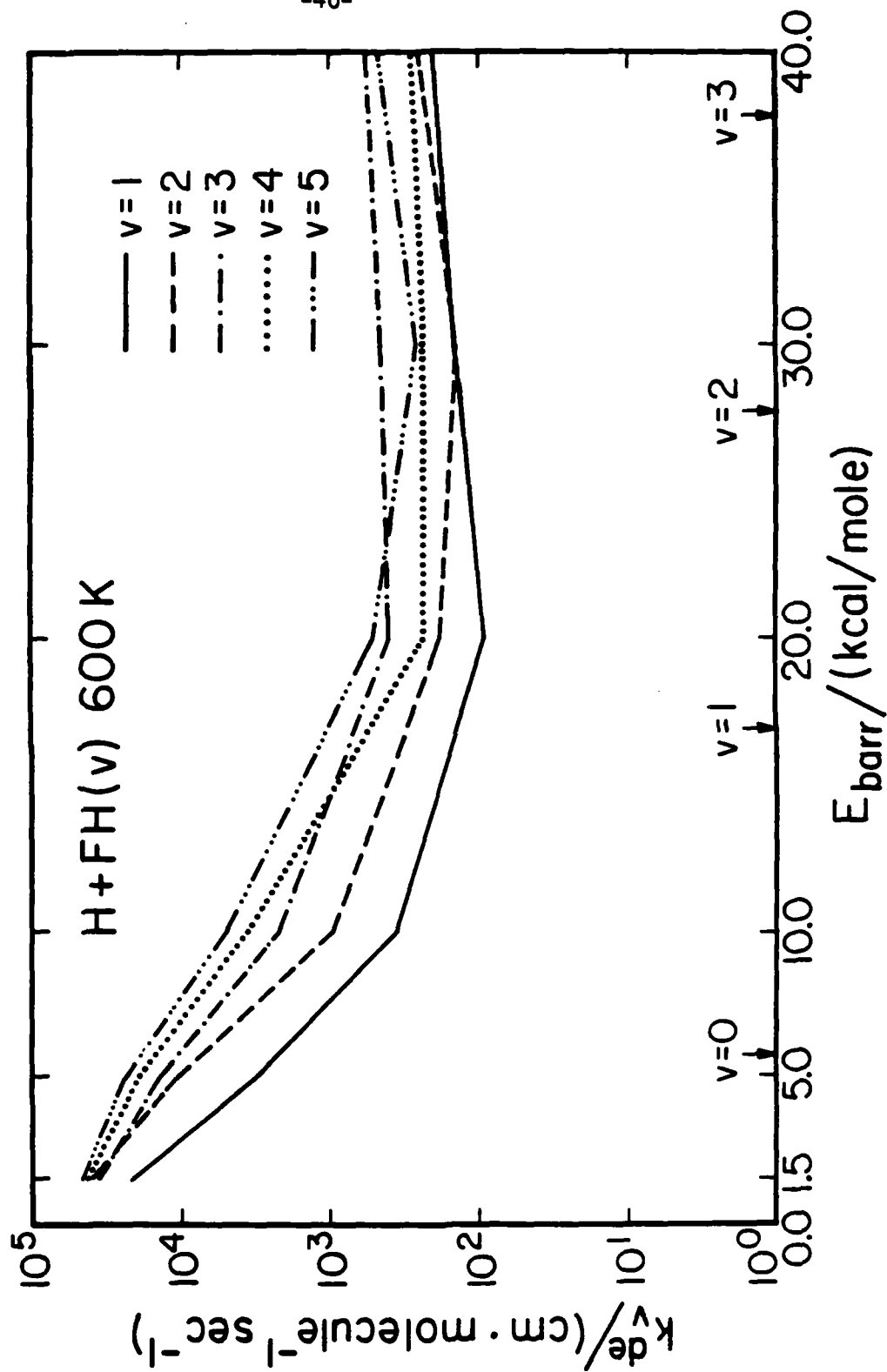


Figure 5

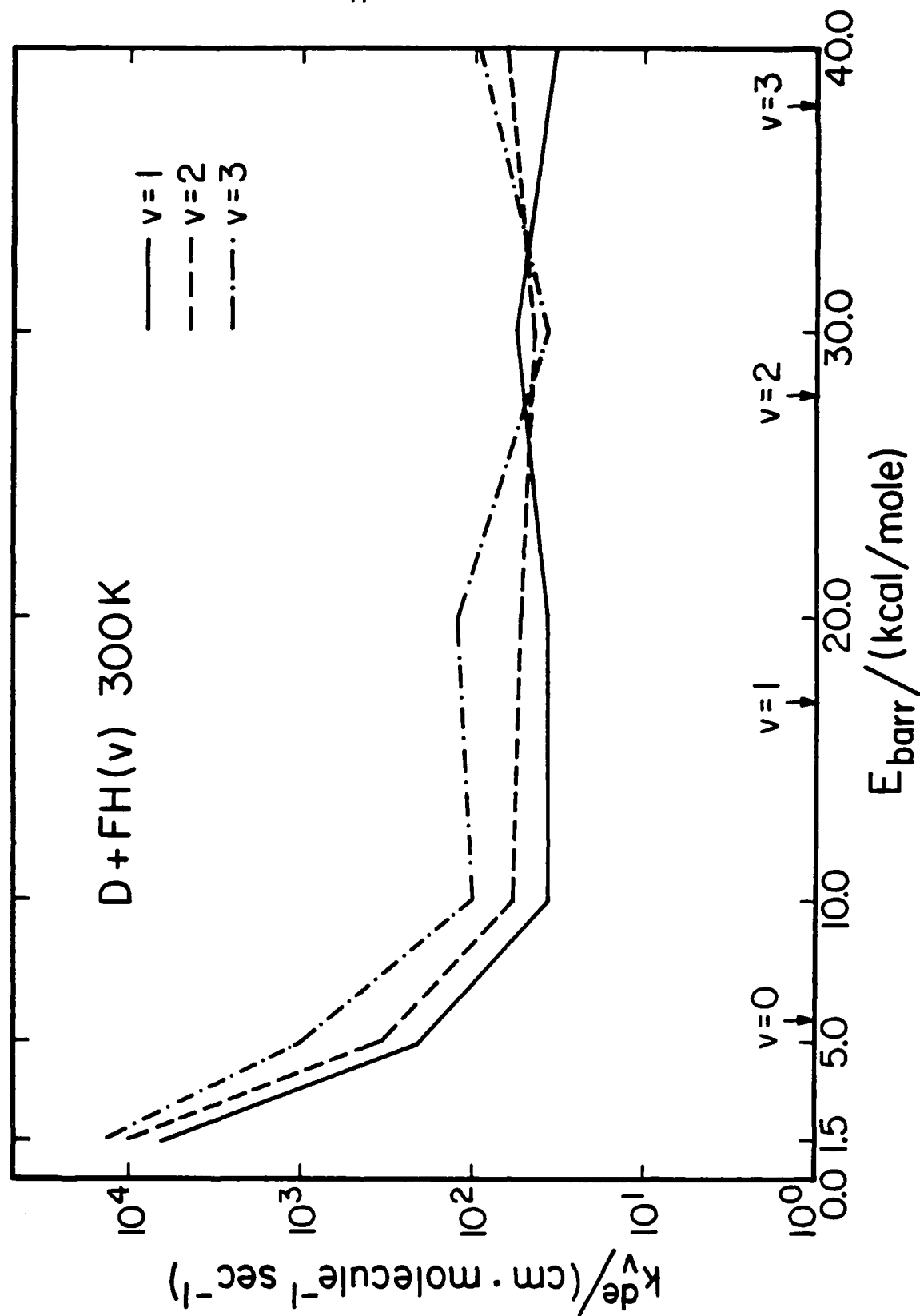


Figure 6

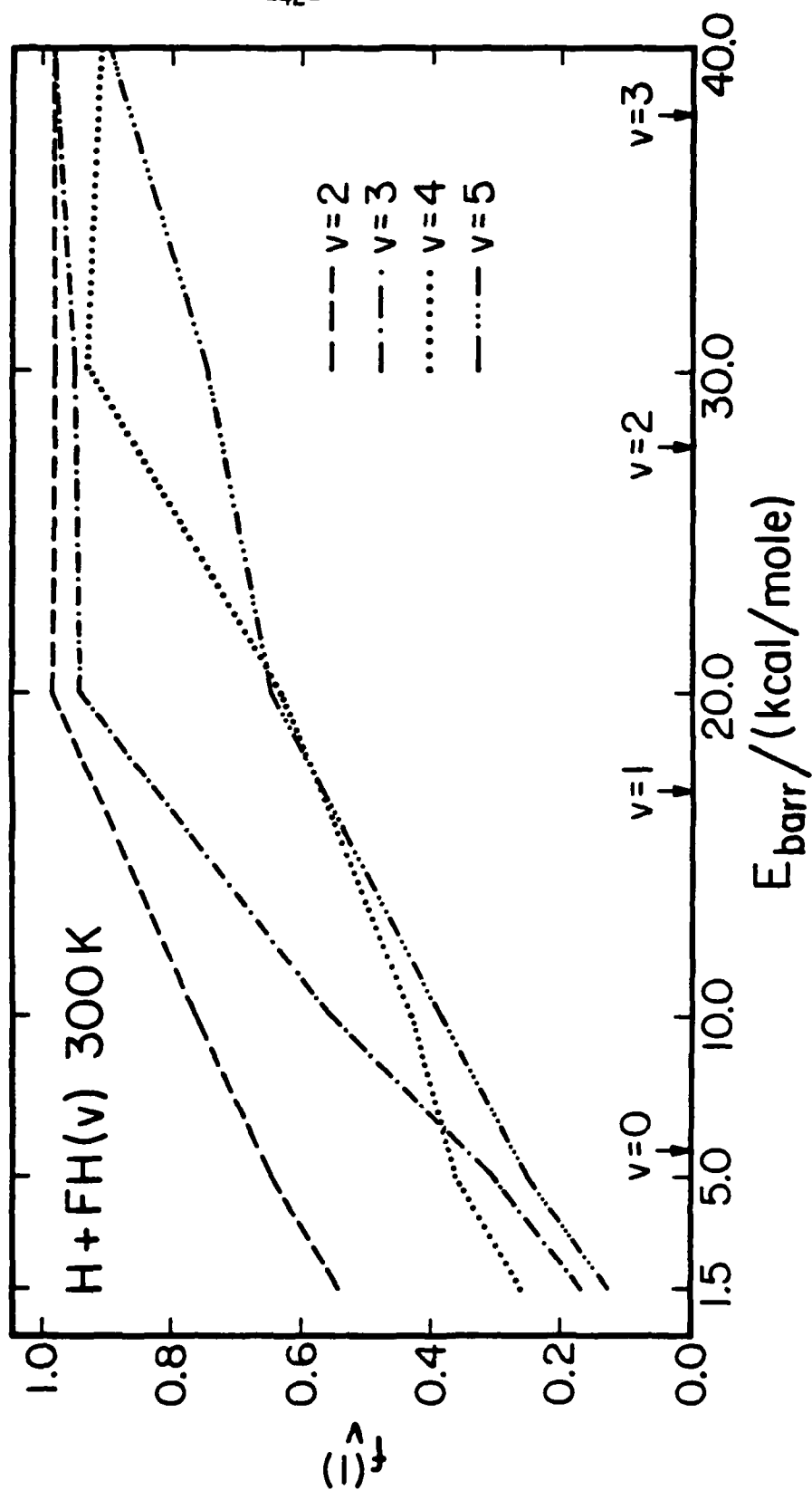


Figure 7

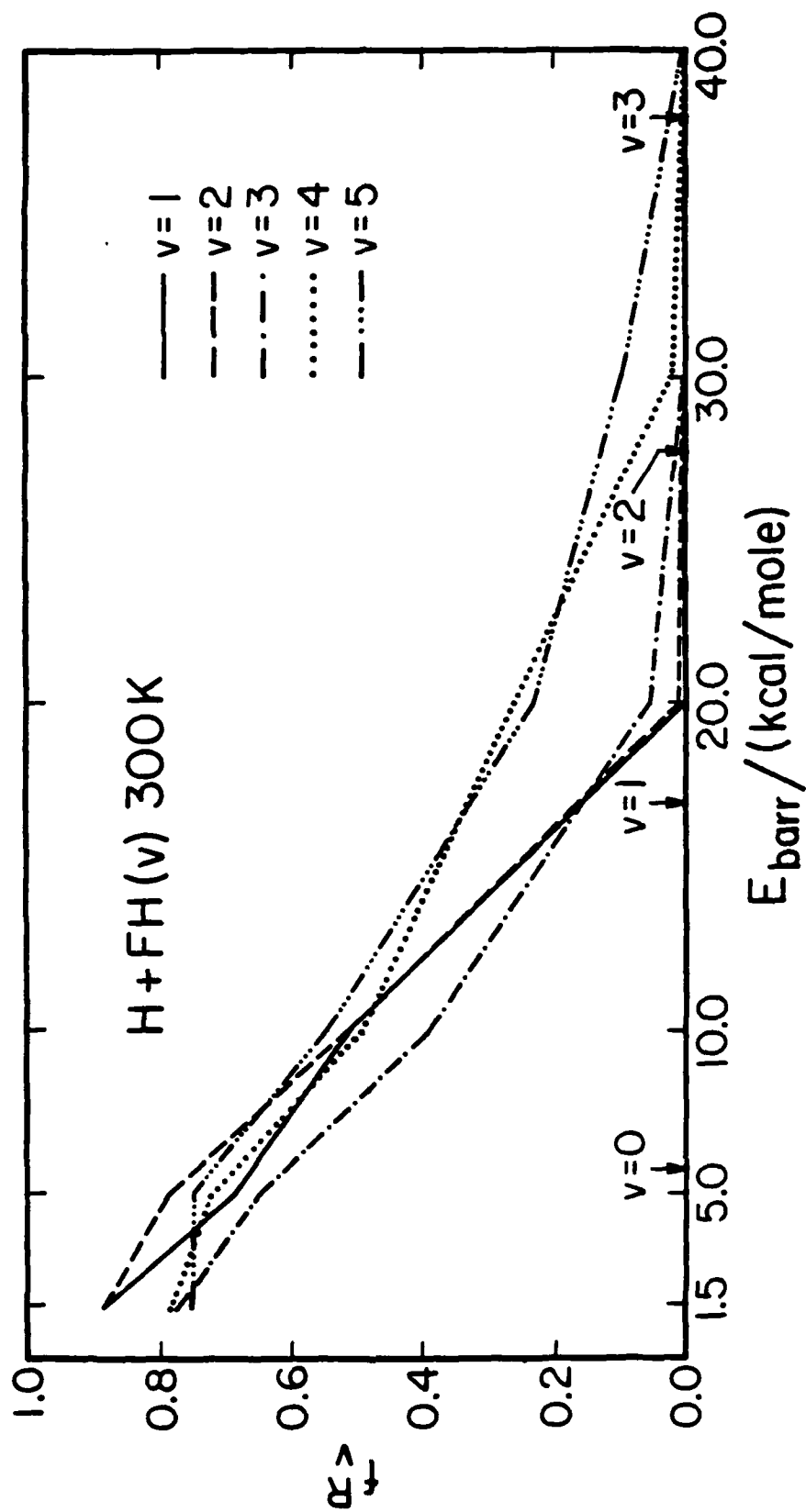


Figure 8

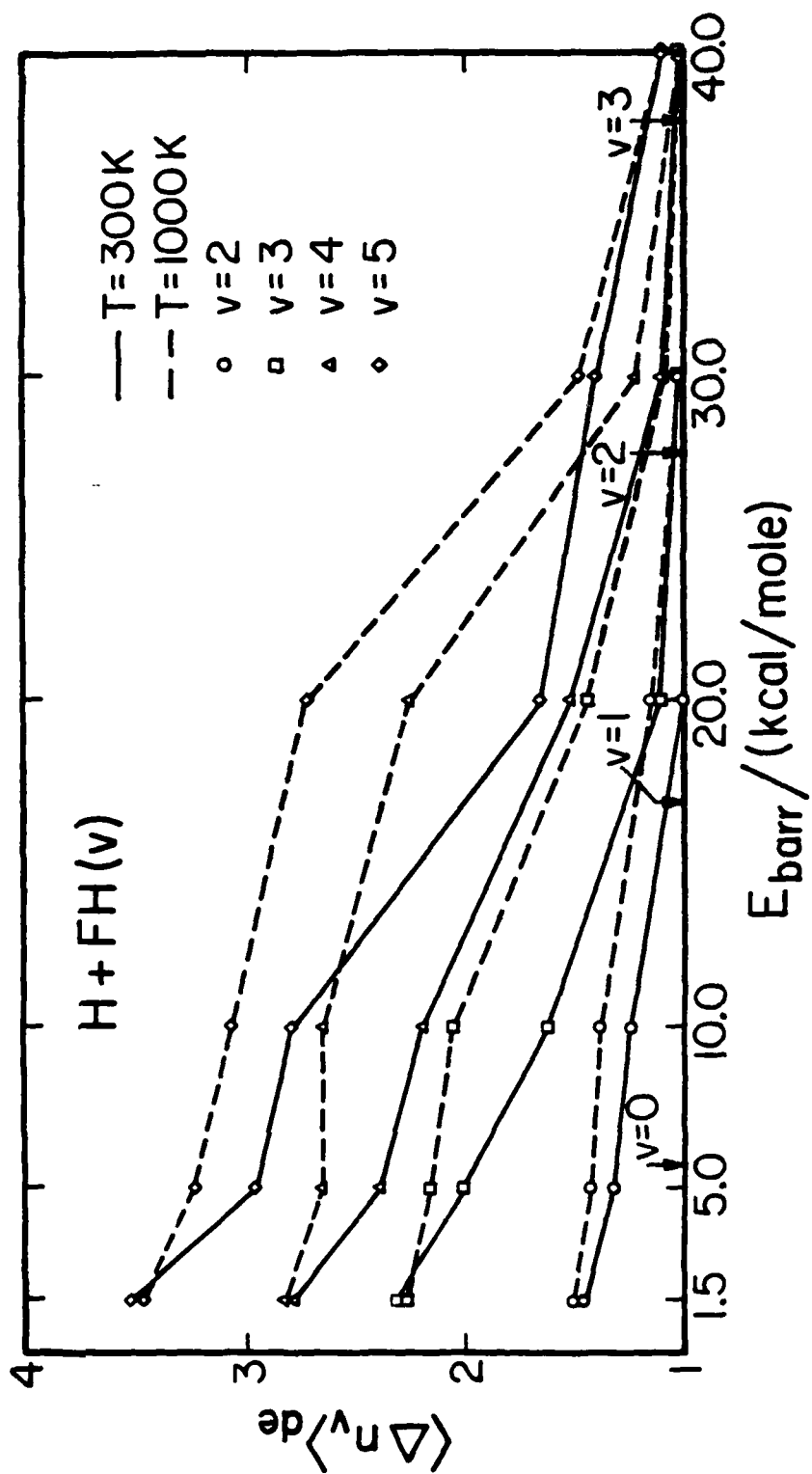


Figure 9

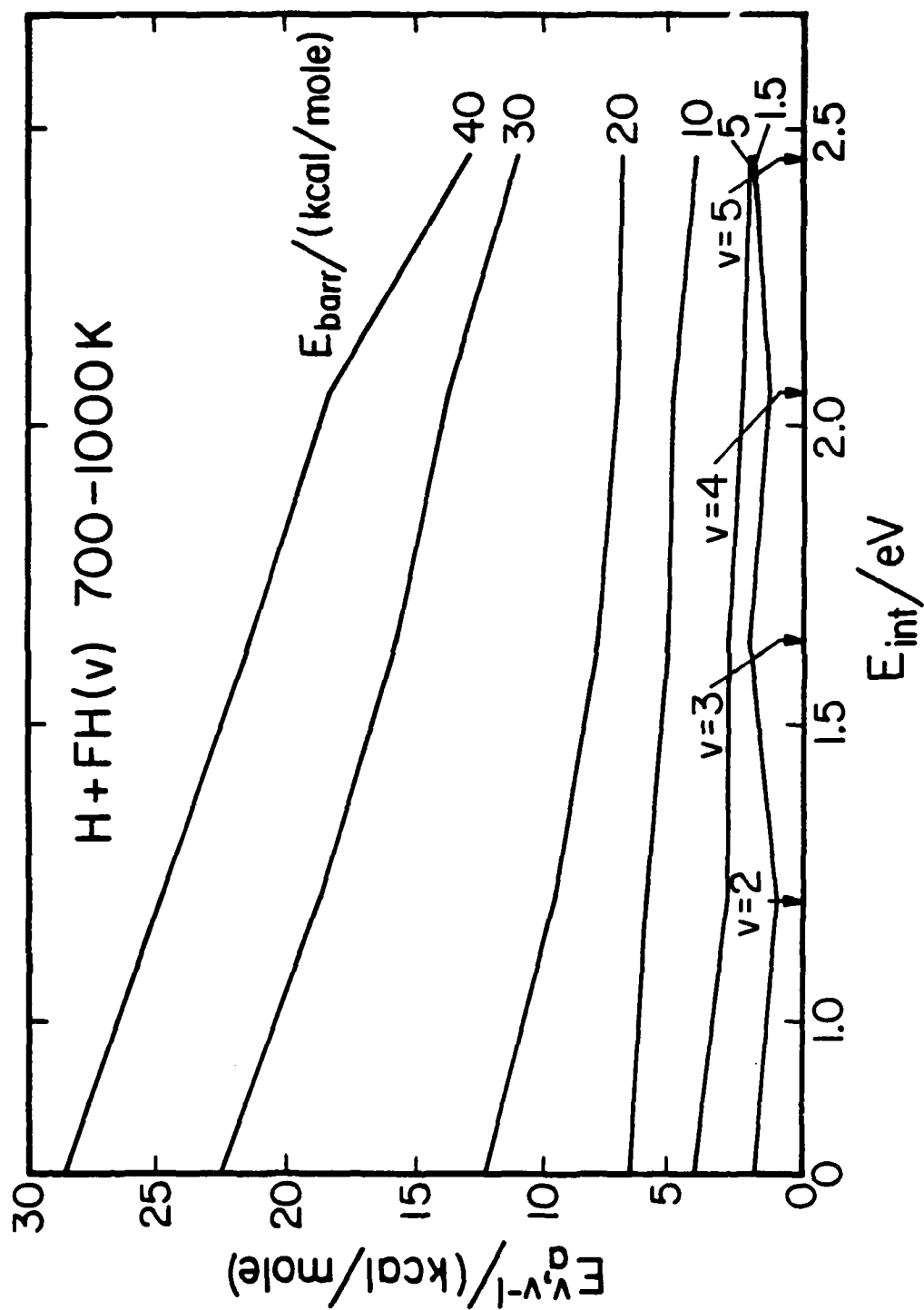


Figure 10

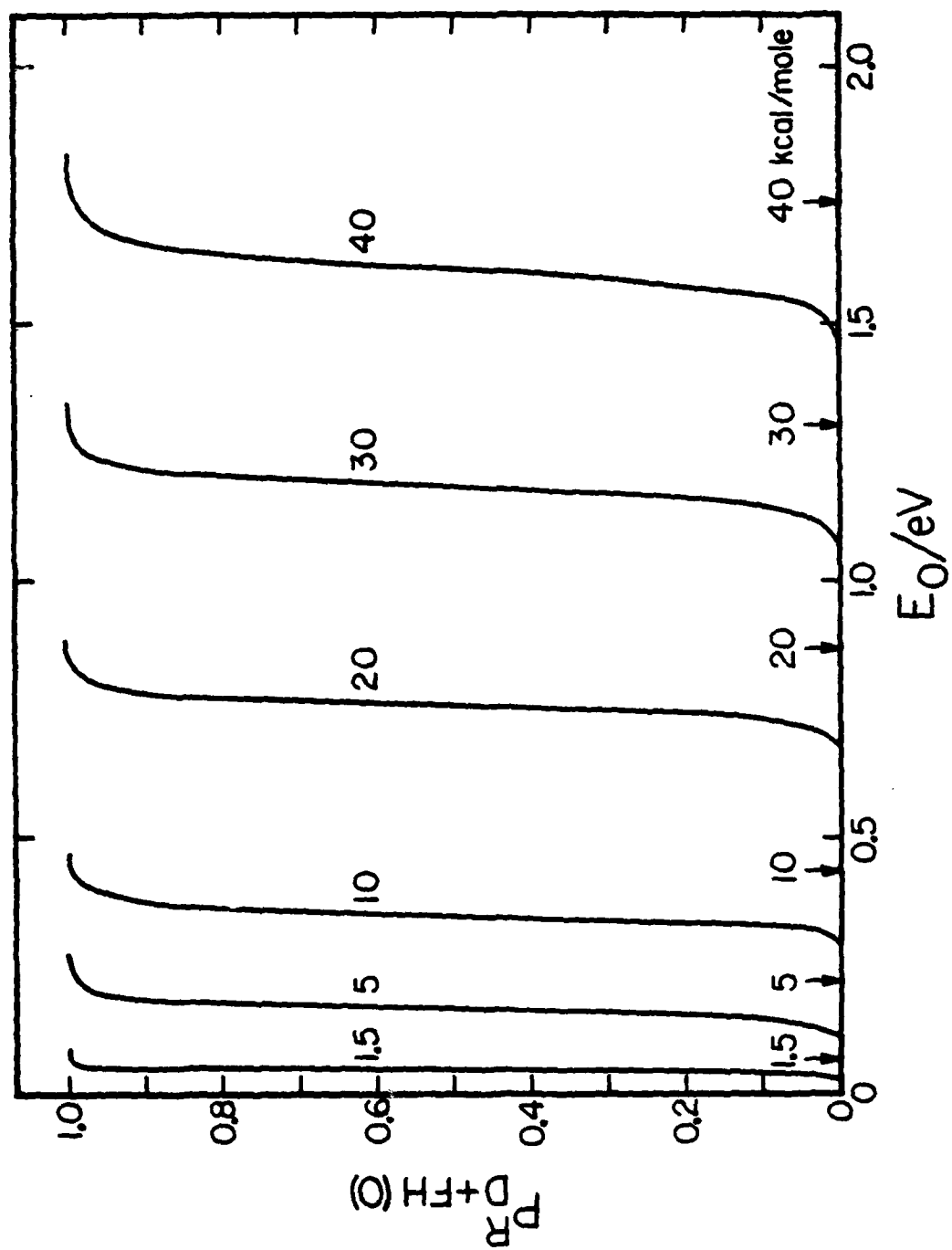


Figure 11

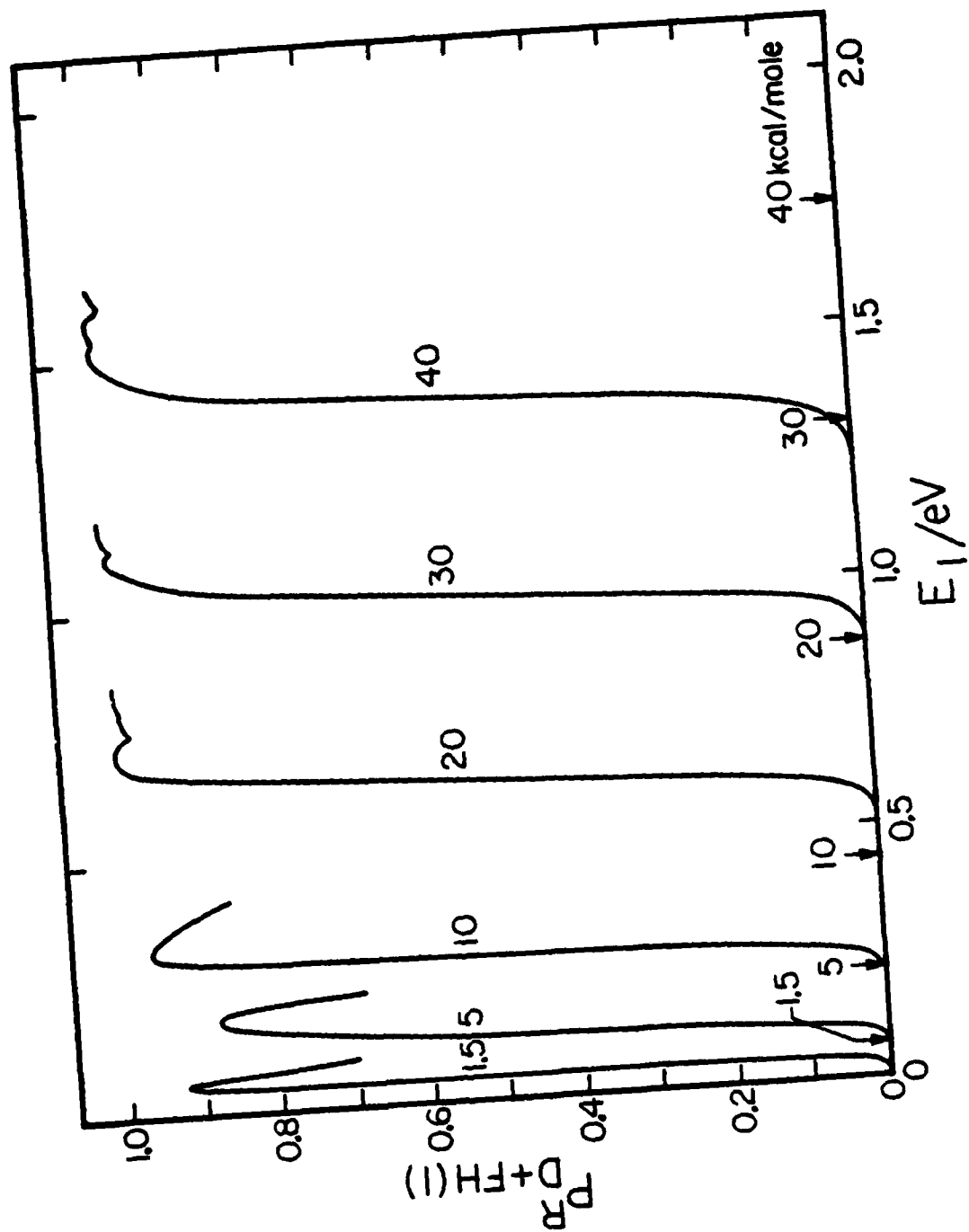


Figure 12

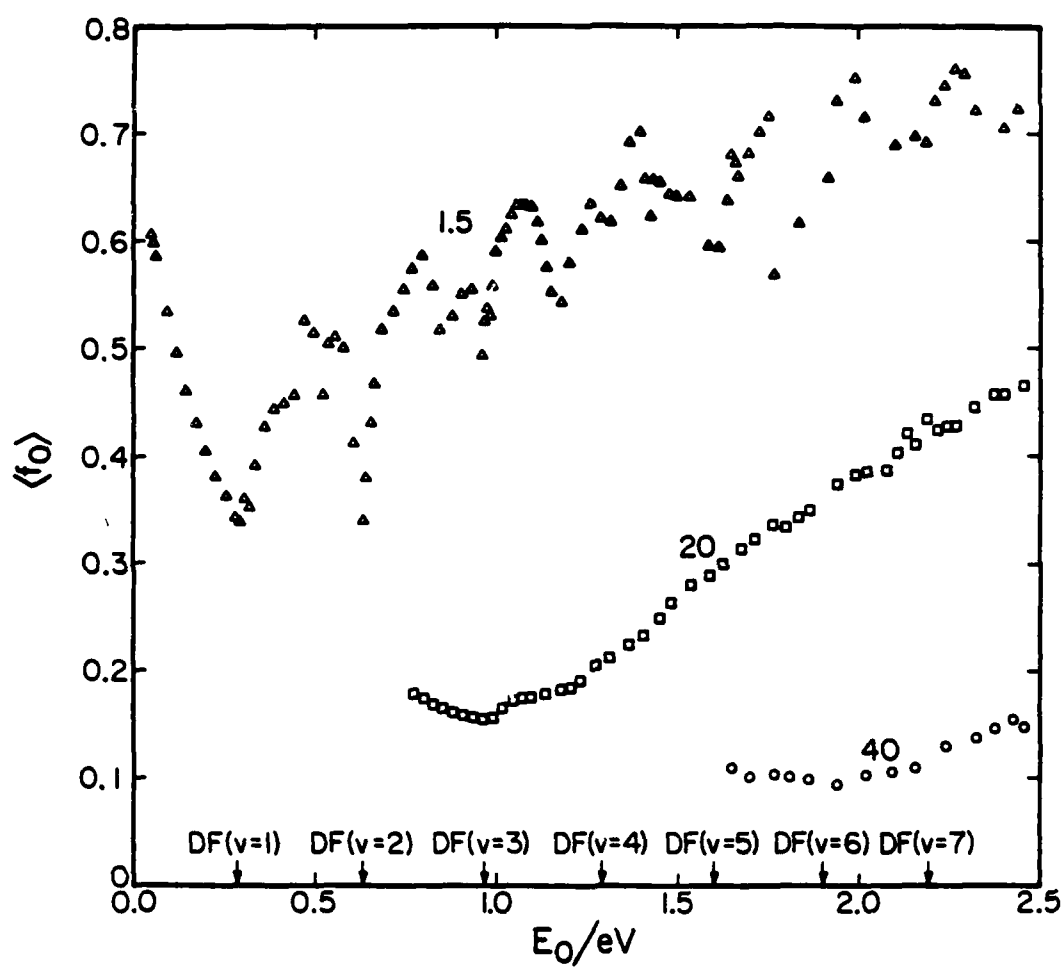


Figure 13

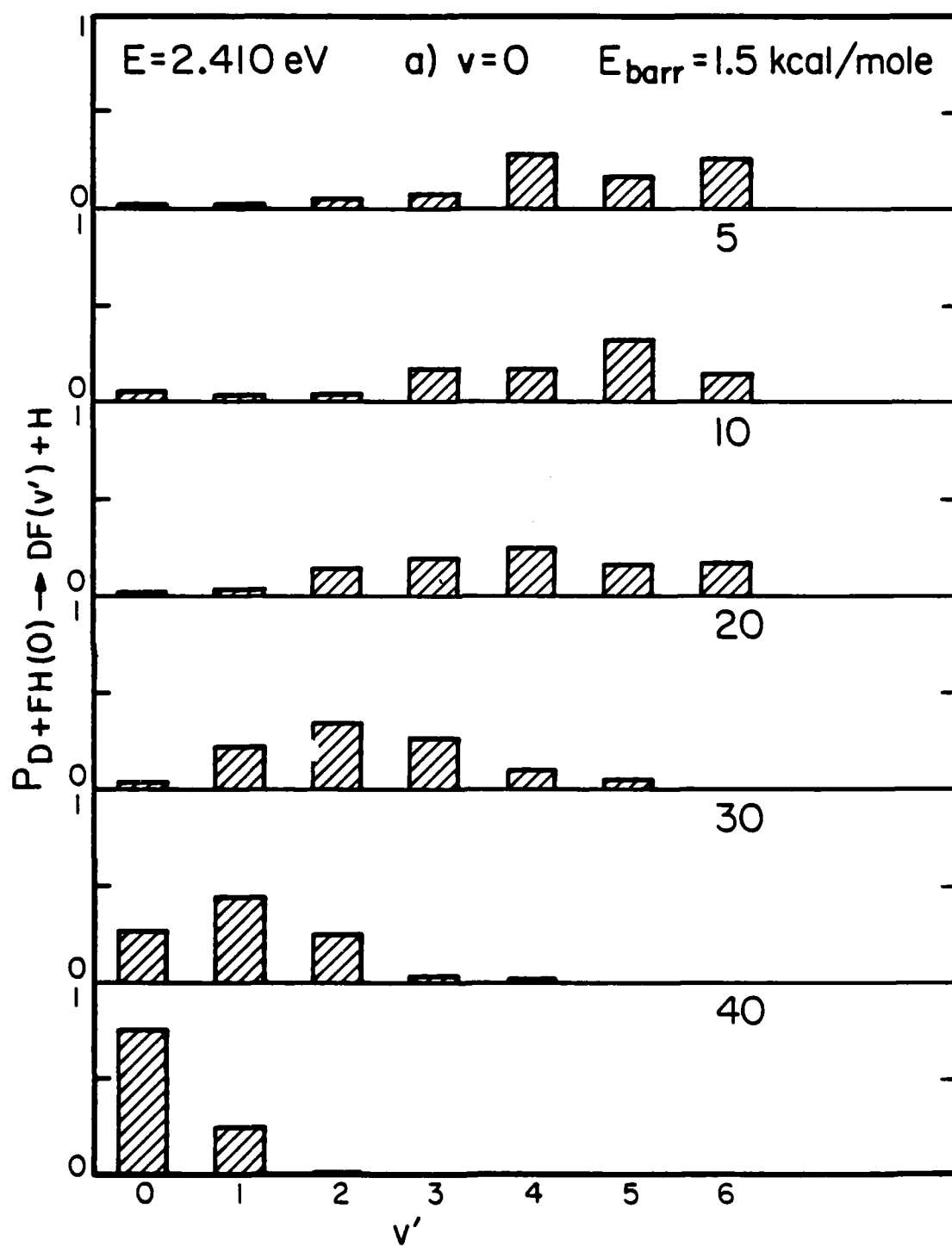


Figure 14a

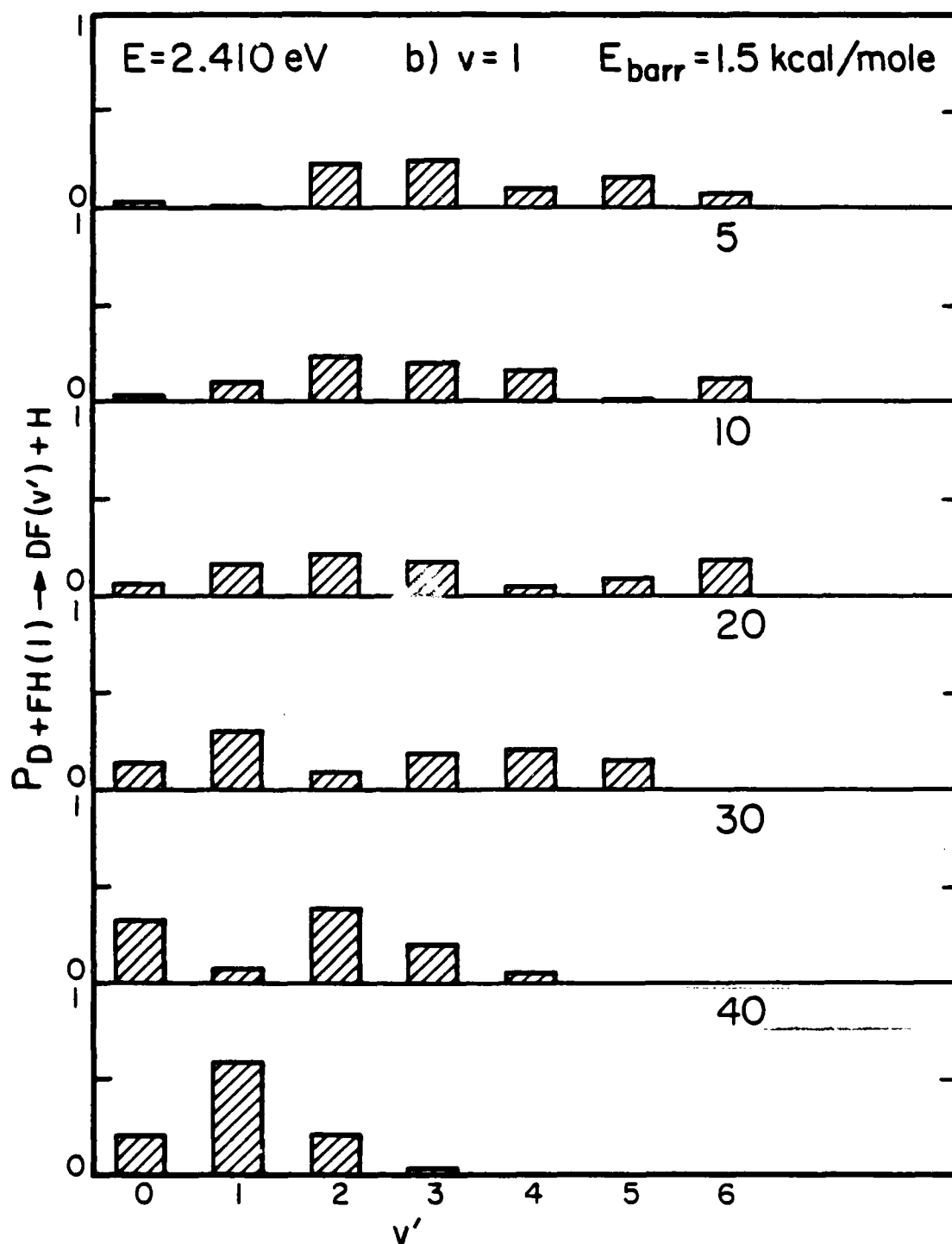


Figure 14b

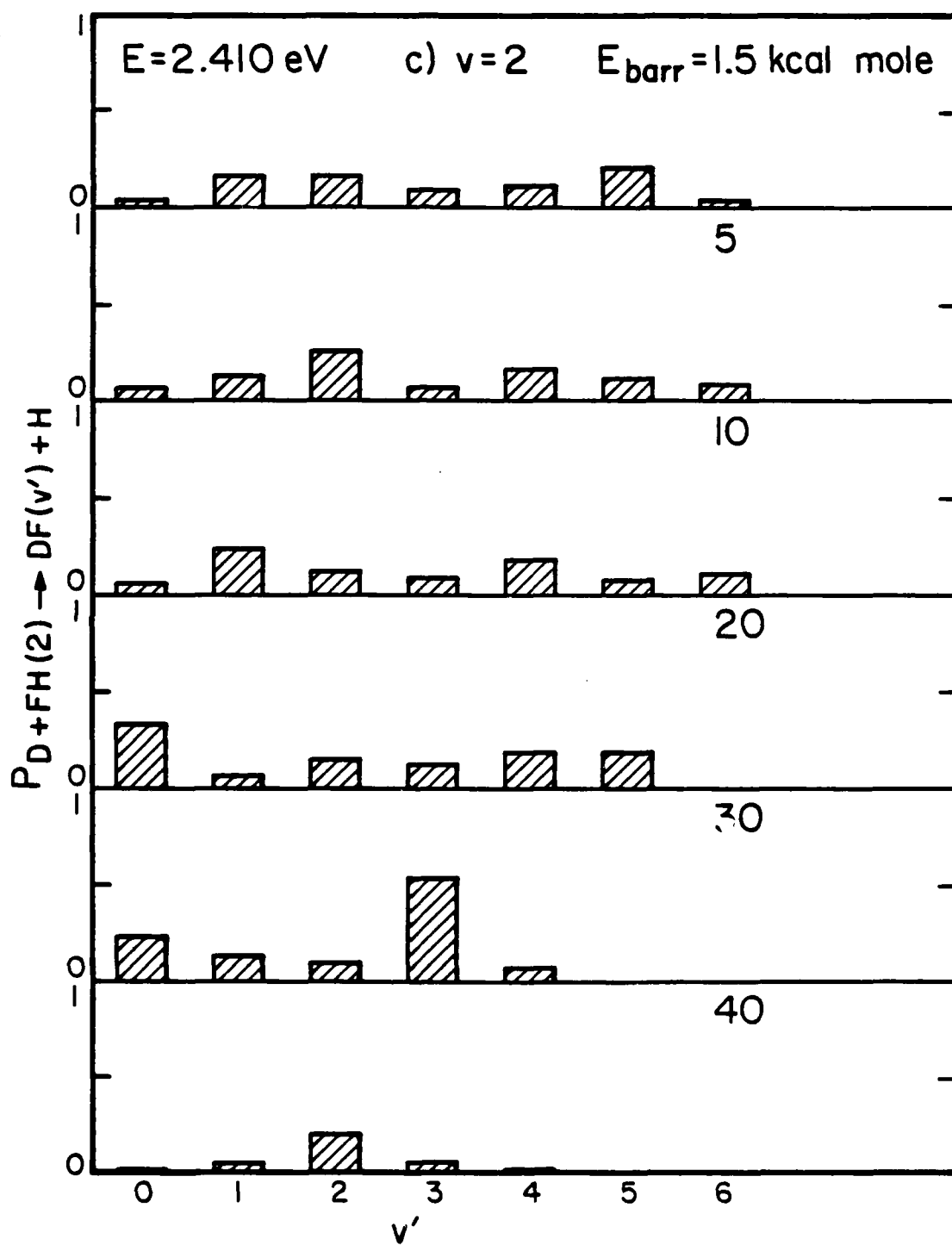


Figure 14c

AD-A130 160

THE QUANTUM DYNAMICS OF CHEMICAL REACTIONS(U)
CALIFORNIA INST OF TECH PASADENA DIV OF CHEMISTRY AND
CHEMICAL ENGINEERING A KUPPERMANN 31 MAR 83

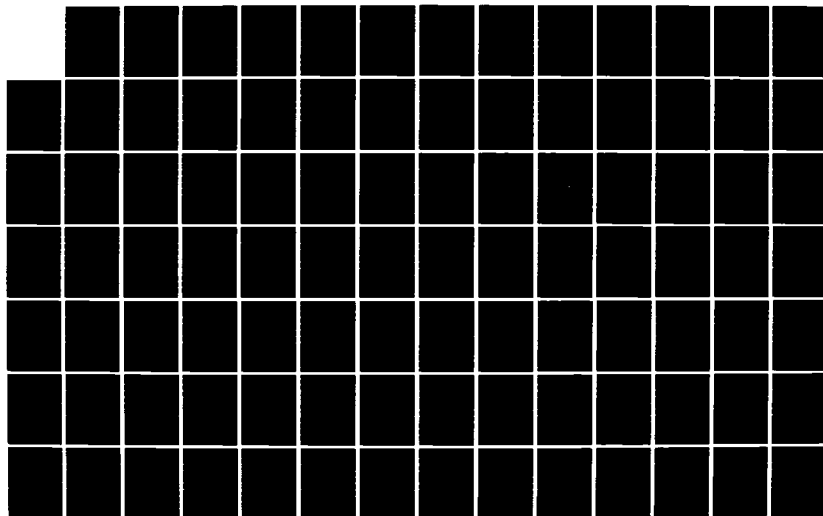
5/6

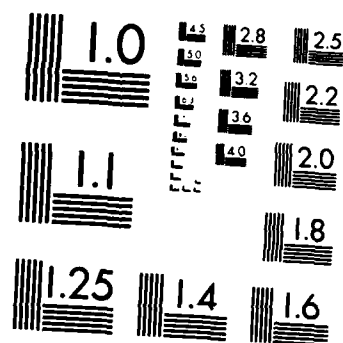
UNCLASSIFIED

AFOSR-TR-83-0565 AFOSR-81-0235

F/G 20/10

NL





MICROCOPY RESOLUTION TEST CHART
NATIONAL BUREAU OF STANDARDS-1963-A

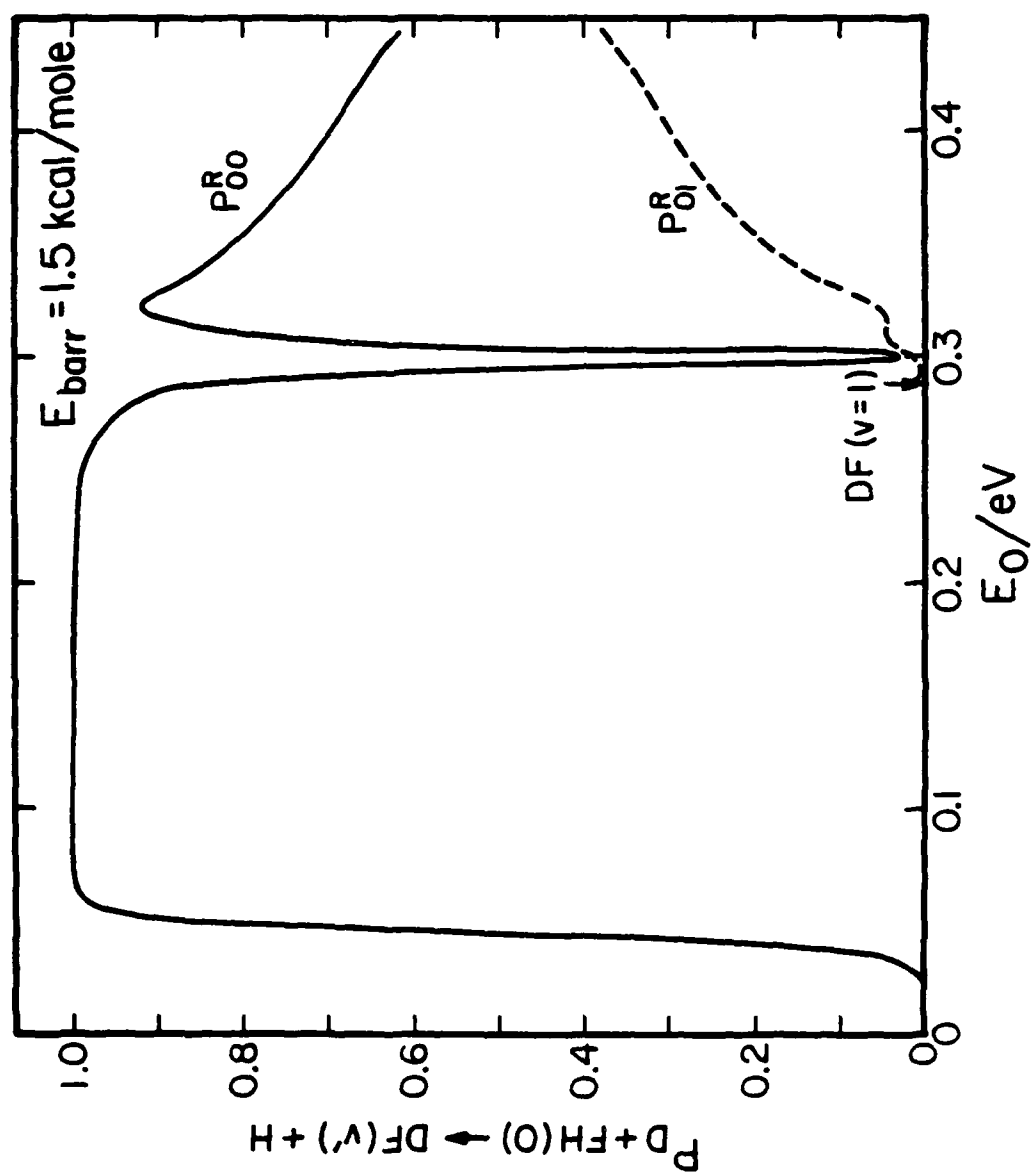


Figure 15

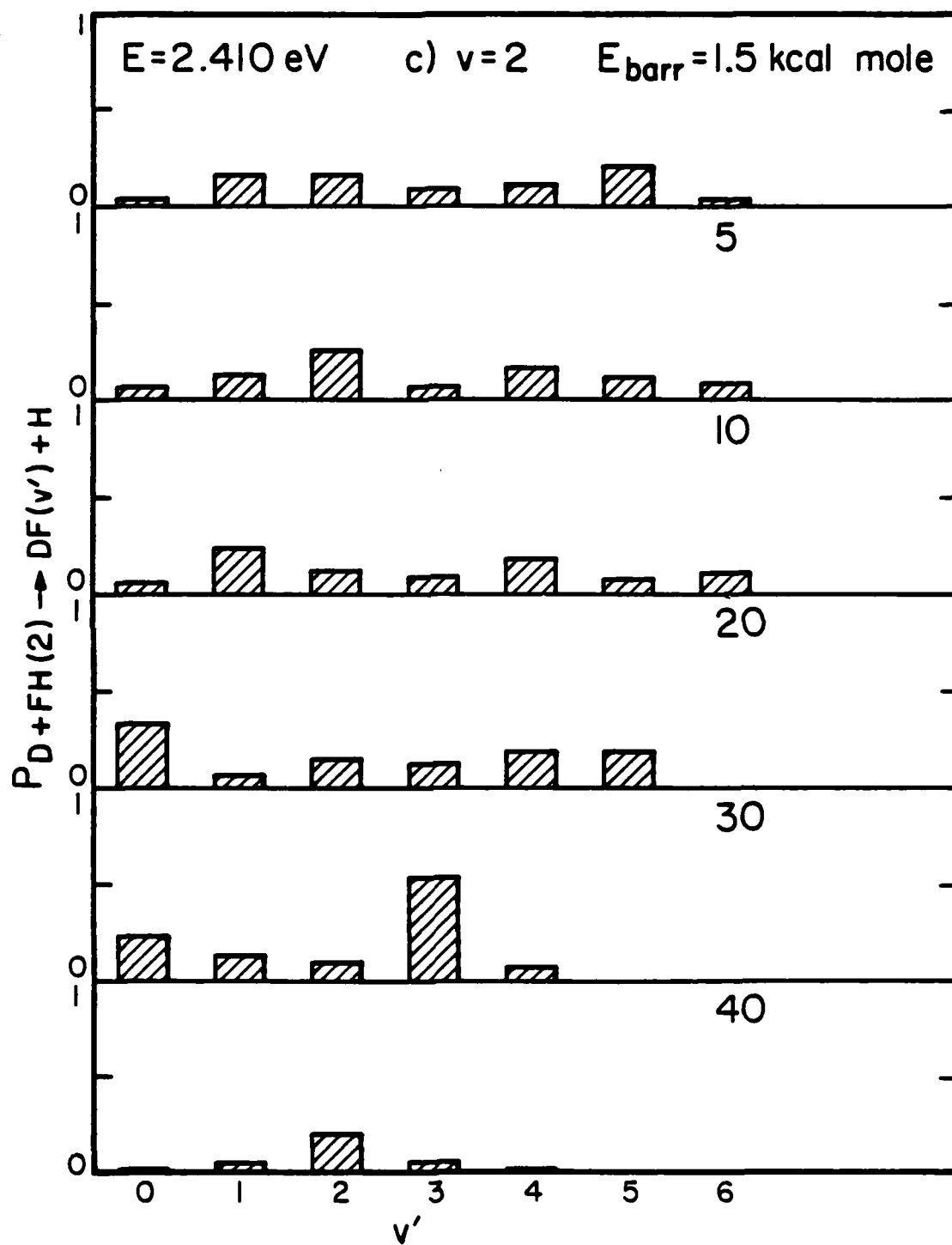


Figure 14c

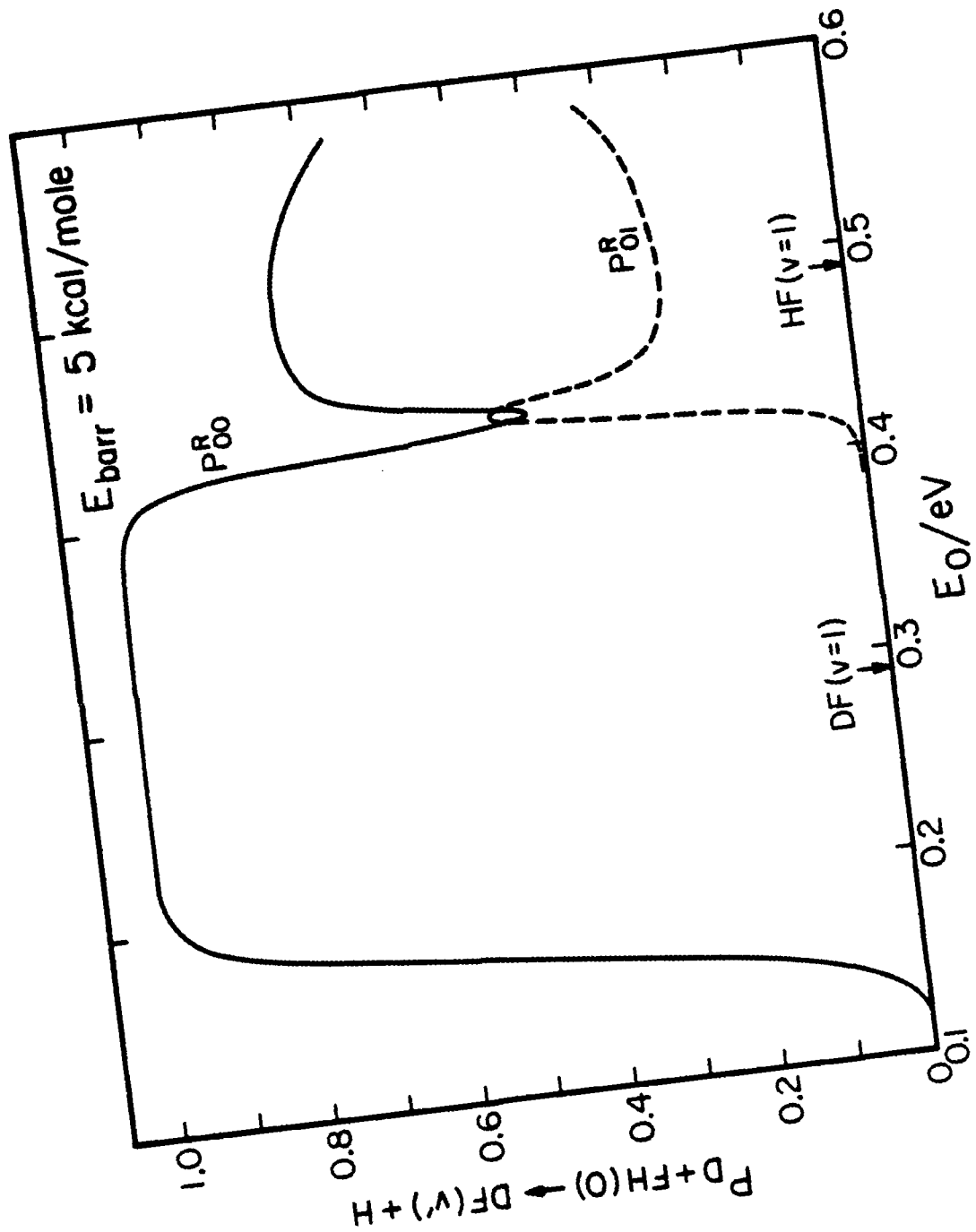


Figure 16

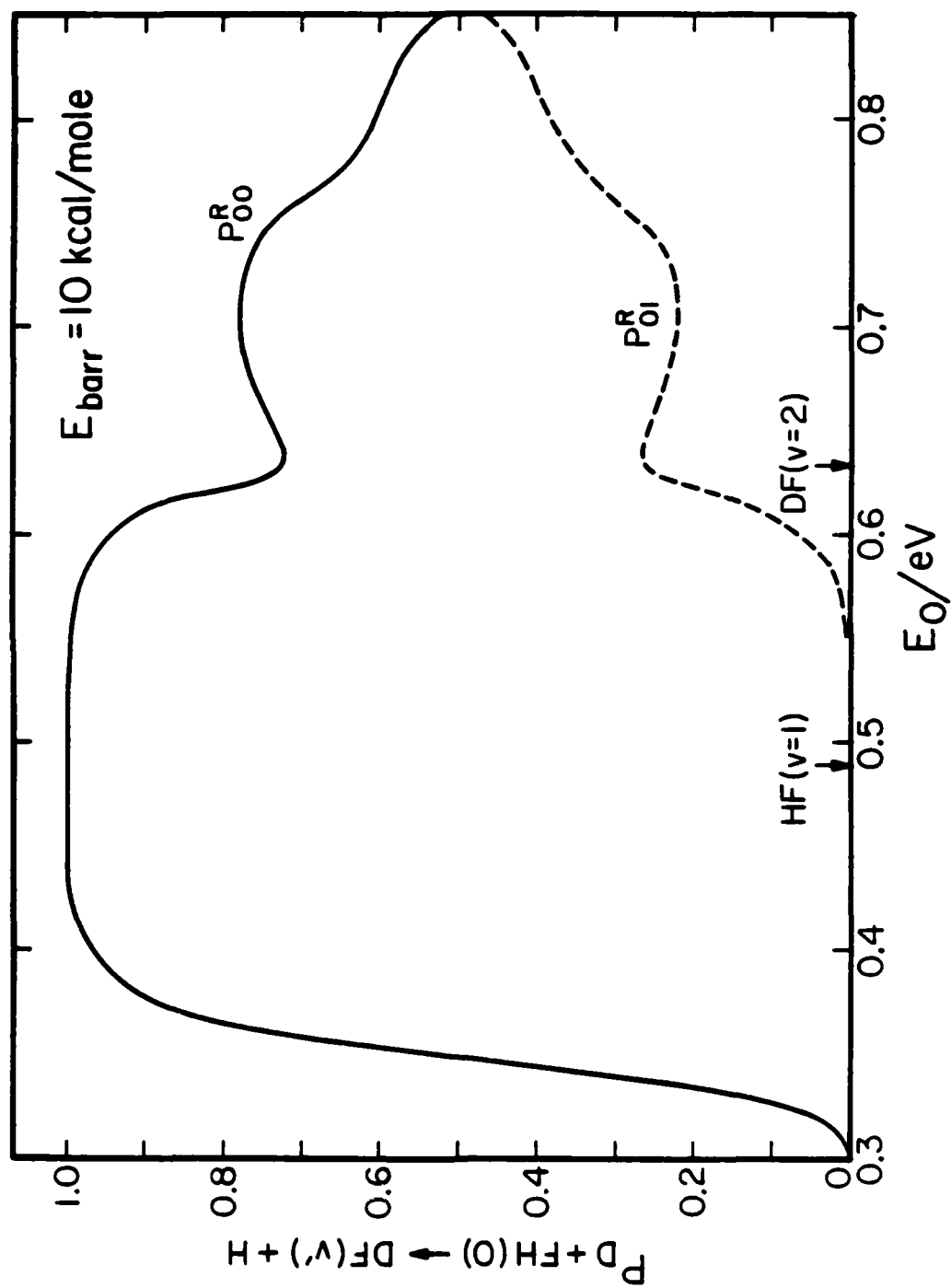


Figure 17

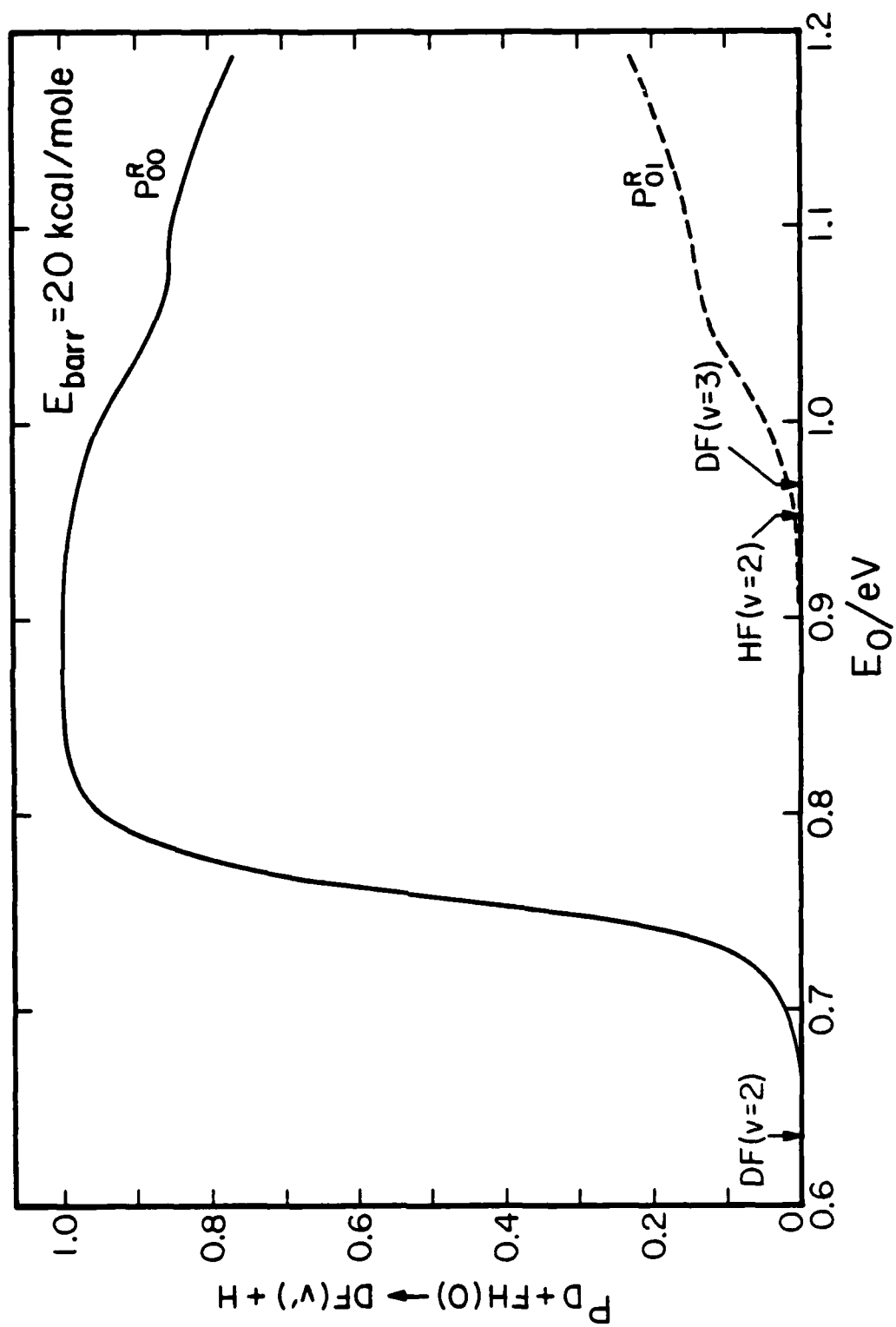


Figure 18

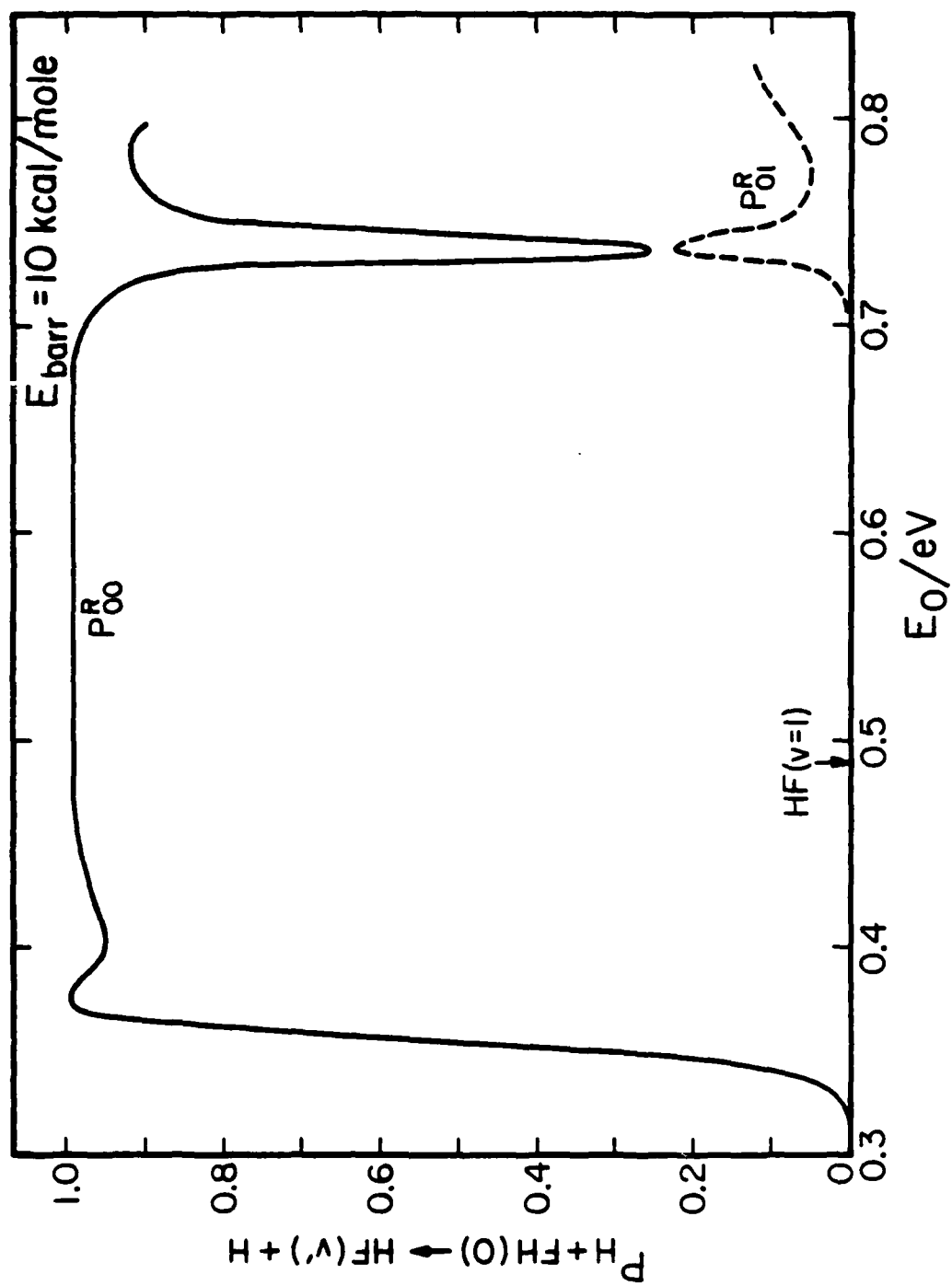


Figure 19

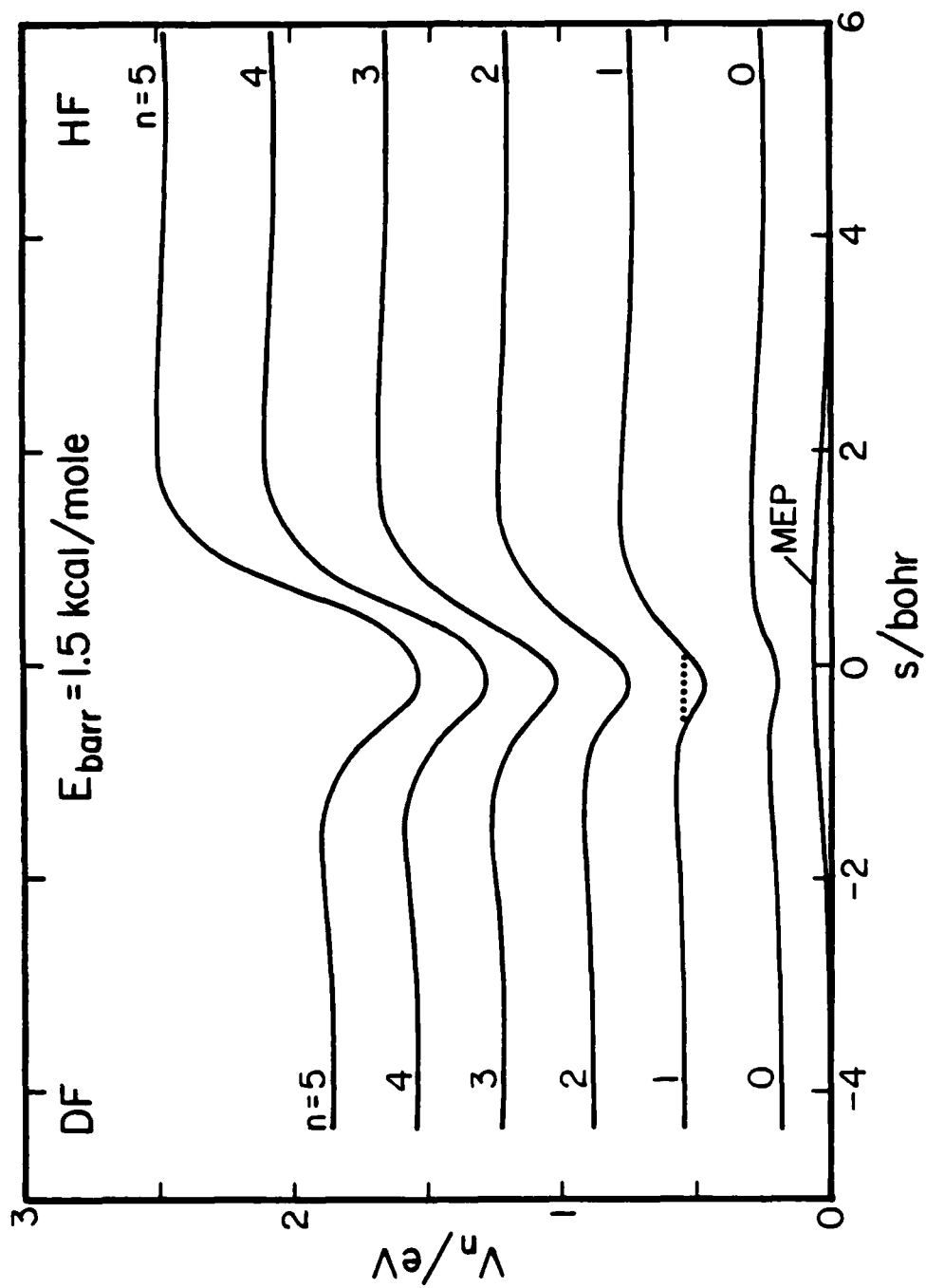


Figure 20

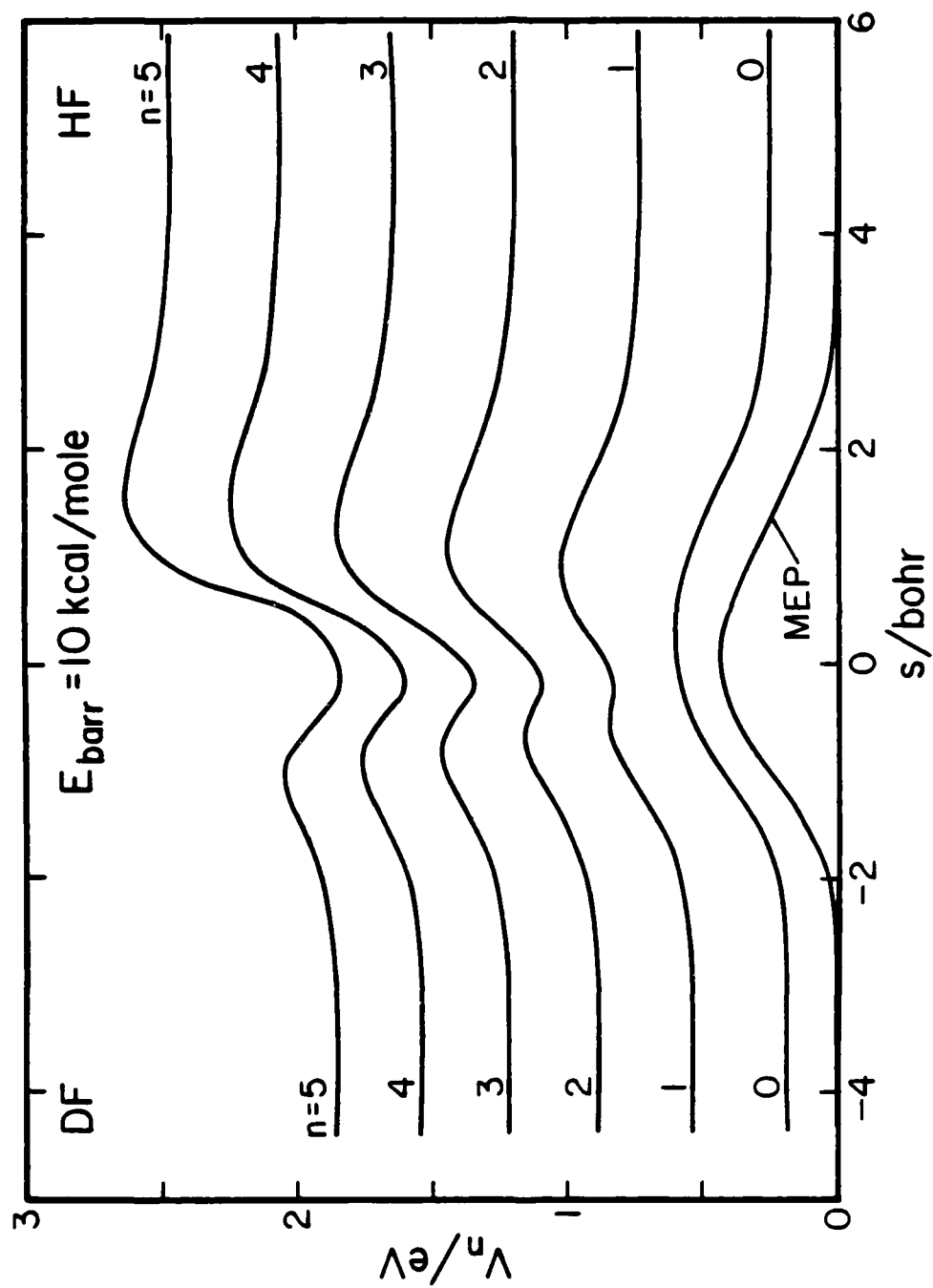


Figure 21

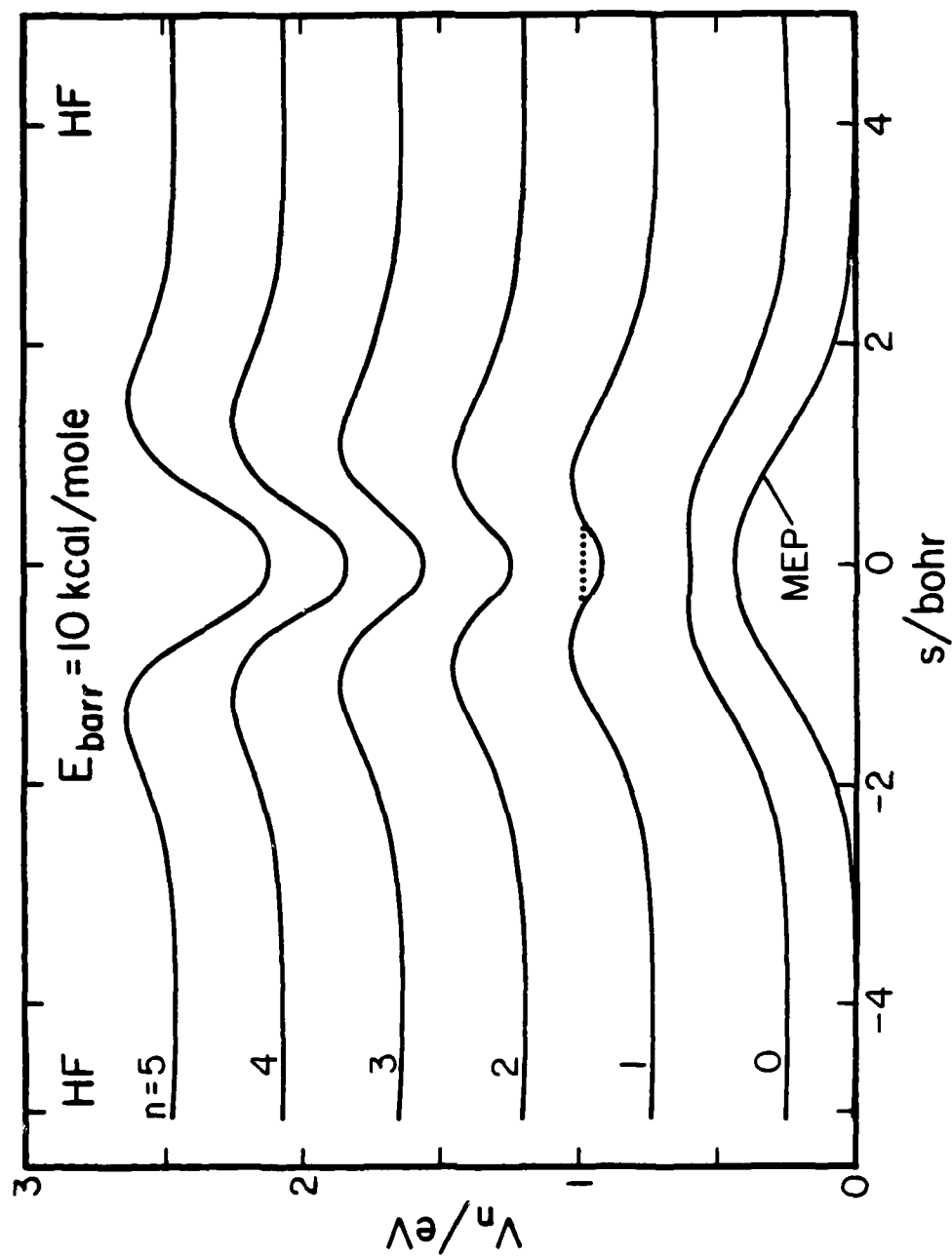


Figure 22

PART II

CHARACTERIZATION OF LOW ENERGY RESONANCES
IN THE COLLINEAR $H + H_2$ AND $F + H_2$ SYSTEMS

INTRODUCTION

Dynamical resonances have been found to be one of the most interesting results of collinear quantum mechanical calculations on the dynamics of atom-diatomic molecule reactions. Knowledge of the features of the potential energy surfaces responsible for their existence is important if one is to be able to understand their dependence on the potential energy surface, reagent vibrational excitation, and isotopic substitution. Similarly, it is important that one be able to adequately recognize and characterize dynamical resonances, especially when they are partially masked by direct processes occurring in the same energy region.

In this section we consider various characterization techniques for the recognition and characterization of dynamical resonances for two different systems: the collinear $H + H_2$ and the collinear $F + H_2$ (HD, DH, D_2) ones. Characterization techniques include studies of the variation with energy of the state-to-state reaction probabilities, scattering matrix element phases and their energy derivatives, eigenphase shifts, and diagonal elements, eigenvalues, and eigenvectors of the collision lifetime matrix of Smith.

Paper II.1 presents results of a collision lifetime matrix analysis of the low energy resonances in the collinear $F + H_2$ (HD, DH, D_2) systems. The strength of the resonances is shown to decrease in the order $FHD \gg FH_2 > FD_2 > FDH$. Because the collision lifetime matrix localizes the resonance into a single eigenchannel, it allows one to determine the resonance position, width, and lifetime with a minimum of ambiguity. The peak in the reaction probability vs. energy curve for each system is shown to occur at higher energy than the peak in the eigenvalue of the collision lifetime matrix vs. energy curve for the same system, with the energy difference increasing as the resonance weakens.

Paper II.2 consists of a detailed study of the two lowest energy

resonances in the collinear $H + H_2$ system on the Porter-Karplus potential energy surface. All of the characterization techniques mentioned above are utilized. The resonances are found to be reflected in all of these methods, most notable the eigenvalues of the collision lifetime matrix. Again, the resonances are almost entirely localized in a single eigenchannel of this matrix. The effect of the symmetry of the system in the results of the characterization procedures is discussed. There appear to be substantial differences between the two resonances as seen by the eigenvectors of the collision lifetime matrix near the resonance energies.

Paper II.3 includes a detailed study of the resonances studied in paper II.1. As in paper II.2, all of the above mentioned characterization techniques are utilized. The degree to which the resonances are reflected by the different techniques in each of the systems is discussed.

Accurate Quantum Calculations of Reactive Systems*

Aron Kuppermann

Arthur Amos Noyes Laboratory of Chemical Physics
California Institute of Technology
Pasadena, California

I. Introduction	80
II. The Quantum Dynamics of Reactive Collinear Triatomic Systems	80
A. Reactive-Scattering Formalism	81
B. Scaled Coordinates	84
C. de Broglie Wavelengths and Quantum Effects	86
D. The Scattering and Reactance Matrices	87
E. Computation Methodology	90
F. The Hydrogen Atom-Hydrogen Molecule Exchange Reaction	96
G. The $F + H_2 \rightarrow FH + H$ Reaction and Its Isotopic Counterparts	108
H. Electronically Nonadiabatic Exchange Reactions	115
I. Collision-Induced Dissociation and Three-Body Recombination Processes	120
III. The Quantum Dynamics of Three-Dimensional Reactive Triatomic Systems	122
A. Scaled Coordinates	122
B. Potential Energy Surface Mapping in Symmetrized Hyperspherical Coordinates	124
C. Reactive-Scattering Formalism	128
D. Scattering and Reactance Matrices	131
E. Distinguishable-Atom Scattering Amplitudes and Cross Sections	133
F. Cross Sections for Systems Containing Identical Atoms	136
G. Computational Methodology	138
H. Results for $H + H_2$	141
IV. General Systems and Processes	161
V. Conclusion	162
References	162

* This work was supported in part by the Air Force Office of Scientific Research, Contract No. F49620-79-C-0187.

1. Introduction

Only about five years ago the first accurate calculations of the differential and integral cross sections of a simple chemical reaction on a given potential energy surface were performed. This was the result of an evolutionary process that started shortly after the discovery of wave mechanics and accelerated about 20 years ago with the development of electronic digital computers. The purpose of this article is to outline some of the conceptual ideas and numerical methodology presently used in such calculations. In Section II we consider collinear triatomic systems; for reasons of conceptual as well as computational simplicity, most of the early work done in this field was for such systems, which served the useful purpose of testing some of the basic approaches initially used. Since the results of calculations on such model systems are approximate, in the sense that the three atoms are artificially confined to move in a straight line, they are not thoroughly reviewed, but some examples are given, mainly for illustrative purposes. These include both electronically adiabatic as well as electronically nonadiabatic processes. Some remarks on dissociation and three-body recombination processes are also made. In Section III the concepts involved for electronically adiabatic triatoms are extended to the three-dimensional world, and the results of their application to the hydrogen atom-hydrogen molecule exchange reaction on an assumed potential energy surface are given. Although this surface is approximate, the dynamical calculations performed on them are accurate. In Section IV an extension of reactive scattering concepts to more general systems is considered, and a review of conclusions is given in Section V.

II. The Quantum Dynamics of Reactive Collinear Triatomic Reactions

Triatomic exchange reactions of the type $A + BC \rightarrow AB + C$, with A, B, and C representing atoms confined to move on a laboratory-fixed straight line, constitute the simplest reactive systems that display a basic characteristic of many chemical reactions: the dissolution of a chemical bond and the formation of a new one. The low mathematical dimensionality of the theory permits a presentation unencumbered by the mathematical complexities of molecular rotations, allowing thereby a fairly direct analysis of the effects of translational and vibrational degrees of freedom. Initially we will consider the case of electronically adiabatic exchange reactions, and later these considerations will be extended to electronically nonadiabatic ones. Finally, an outline of how the theory can be extended to include collision-induced dissociation and three-body recombination processes will be presented.

We consider initially collinear reactions for which the first electronically

excited Born–Oppenheimer potential energy function is everywhere sufficiently larger than the total energy E of the reacting system for its presence and that of higher electronic states to be ignored. The reaction will therefore be assumed to occur exclusively on the ground electronic state potential energy surface. Furthermore, E will be assumed to be sufficiently lower than the bond dissociation energy of the AB and BC molecules for the dissociative processes $A + BC \rightarrow A + B + C$ and $C + BA \rightarrow C + B + A$ and the reverse recombinations to be ignored. These restrictions are convenient for simplifying the mathematical treatment. In Section II,H we consider electronically nonadiabatic reactions, and in Section IV we succinctly discuss dissociation and recombination reactions.

A. REACTIVE-SCATTERING FORMALISM

Let r'_a be the BC internuclear distance and R'_a the distance between A and the center of mass G_{BC} of BC. These coordinates are convenient for the description of the A + BC reagents. Similarly, let r'_c be the AB internuclear distance and R'_c the distance of C to the center of mass G_{AB} of AB, coordinates which are useful for the description of the final state of the products. These two sets of coordinates are depicted in Fig. 1. Equipotential curves for a representative potential energy function (surface) V are depicted in Fig. 2 in terms of the x coordinates. This function is obtained by solving the electronic motion problem, in three dimensions, for all (R'_a, r'_a) collinear ABC configurations. Its central characteristic is that it displays a line of steepest ascents and descents, the minimum energy path depicted by the dashed line in Fig. 2. Along lines orthogonal to that path, the potential function increases in both directions, portraying a behavior similar to that of a diatomic molecule. This is true everywhere along the minimum energy path, including the saddle point, denoted in that Fig. 2 by a cross. It is this basic property that suggests methods for solving the dynamic problem. Physically, the reaction consists of (quantum mechanical) motion of the system from the reagent region of the R'_a, r'_a configuration space, denoted by A + BC in Fig. 2, to the product region, denoted by AB + C. The energy of the system is assumed to be significantly below the dissociative plateau region, denoted by A + B + C, so

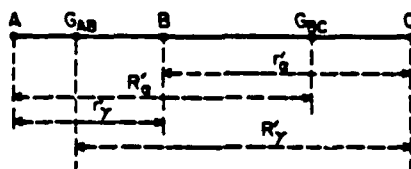


Fig. 1. Coordinates for collinear triatomic systems.

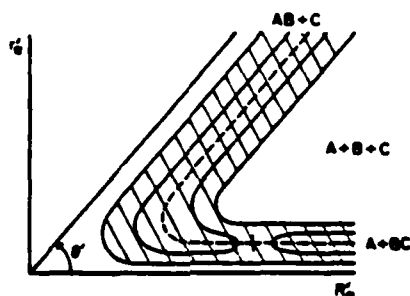


Fig. 2. Potential energy surface V for a collinear triatomic system ABC in the distance coordinates of Fig. 1. The solid curves are lines of constant V . The dashed line is the minimum energy path. The angle θ is given by Eq. (1).

that the region of configuration space sampled by the scattering wave function is limited to the relatively narrow, curved gully, identified by the hatching in Fig. 2, and located between the repulsive walls of the surface corresponding to small values of r'_e and/or r'_i (for compressed configurations) and large values of these variables (for stretched configurations). The line in Fig. 2 that passes through the origin and makes an angle θ with the R'_e axis is the one for which $r'_i = 0$, i.e., for which A coincides with B. The potential along that line, as well as along the R'_e axis, for which $r'_e = 0$ and C coincides with B, is quite large and can be taken to be infinite for the present purposes. This leads to the nonpenetrability of B by either A or C, and the relative ordering of the three atoms along the fixed straight line to which they are confined is maintained throughout their motion. The angle θ , in the range $\pi/4$ to $\pi/2$, is given by

$$\theta = \tan^{-1}[1 + m_B/m_C] \quad (1)$$

and is introduced for comparison purposes with the dynamically important angle θ to be considered in Fig. 3 and Eq. (15).

If we neglect spin interactions, which are very small compared with the other energies being considered, the nuclear motion Hamiltonian, after removal of the motion of the center of mass of the system, can be written in terms of either α or γ coordinates as

$$\begin{aligned} H &= -\frac{\hbar^2}{2\mu_{A,BC}} \frac{\partial^2}{\partial R_{\alpha}^2} - \frac{\hbar^2}{2\mu_{BC}} \frac{\partial^2}{\partial r_{\alpha}^2} + V_{\alpha}(R_{\alpha}, r_{\alpha}) \\ &= -\frac{\hbar^2}{2\mu_{C,BA}} \frac{\partial^2}{\partial R_{\gamma}^2} - \frac{\hbar^2}{2\mu_{BA}} \frac{\partial^2}{\partial r_{\gamma}^2} + V_{\gamma}(R_{\gamma}, r_{\gamma}) \end{aligned} \quad (2)$$

where

$$\mu_{A,BC} = \frac{m_A(m_B + m_C)}{m_A + m_B + m_C} \quad \text{and} \quad \mu_{BC} = \frac{m_B m_C}{m_B + m_C} \quad (3)$$

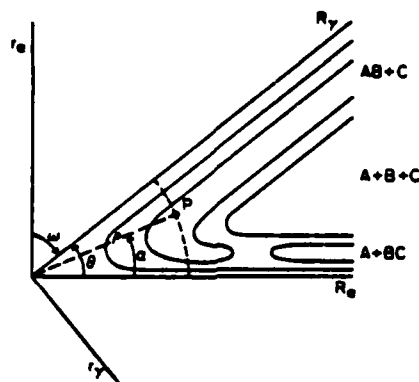


Fig. 3. Potential energy surface for a collinear triatomic system ABC in the scaled coordinates (R_a, r_a) and (R_c, r_c) of Eq. (10). The circular polar coordinates (ρ, α) are considered in Section II.1. The angles α and θ are given by Eqs. (14) and (15), respectively. Both sets of axes (R_a, r_a) and (R_c, r_c) are in the same plane.

represent, respectively, the reduced masses of the A + BC and BC systems, similar definitions being valid for $\mu_{C,BA}$ and μ_{BA} with the roles of atoms A and C interchanged. The symbols m_X represent the masses of atoms X ($= A, B, C$). The first two terms in each of the two expressions for H given by Eq. (2) represent, respectively, the kinetic energy of the relative motion of the atom with respect to the center of mass of the diatom, and of the internal diatom vibration. The problem being considered is that of obtaining solutions of the nuclear motion Schrödinger equation

$$H\psi = E\psi \quad (4)$$

subject to the asymptotic conditions appropriate for reactive scattering. These are, for A + BC collisions,

$$\psi_{\alpha}^{in} \begin{cases} \xrightarrow{R_a \rightarrow \infty} \exp(-ik'_{\alpha} R_a) \phi_{\alpha}(r_a) + \sum_{n_a} f_{\alpha}^{sc} \exp(ik'_{\alpha} R_a) \phi_{\alpha}(r_a) \\ \xrightarrow{R_c \rightarrow \infty} \sum_{n_c} f_{\alpha}^{sc} \exp(ik'_{\alpha} R_c) \phi_{\alpha}(r_c) \end{cases} \quad (5)$$

The $R_a \rightarrow \infty$ behavior is that of a BC molecule (designated α), initially in vibrational eigenstate ϕ_{α} having vibrational quantum number n_a , and approaching an atom A with relative motion wave number k'_{α} , plus a superposition of waves representing BC molecules receding from A with relative wave numbers k'_{α} and internal quantum states n_a . The $R_c \rightarrow \infty$ behavior represents reactive product AB molecules in internal states ϕ_{α} , receding from atom C with relative wave numbers k'_{α} . Conservation of energy requires that

$$\frac{\hbar^2 k_{\alpha}^2}{2\mu_{A,BC}} + E_{\alpha} = \frac{\hbar^2 k_{\alpha}^2}{2\mu_{A,BC}} + E_{\alpha} = \frac{\hbar^2 k_{\alpha}^2}{2\mu_{C,BA}} + E_{\alpha} = E \quad (6)$$

where the $E_{\lambda n_\lambda}$ ($\lambda = \alpha, \gamma$) are the vibrational energies associated with state $\phi_{\lambda n_\lambda}(r'_\lambda)$ and are all referred to a common origin of measurement of energy. It should be noted that although the $E_{\lambda n_\lambda}$ are quantized, the $k'_{\lambda n_\lambda}$ are not, and neither is E . Furthermore, in contrast with bound-state problems, the value of E is assumed known, since we can prepare reagents in known internal states moving with respect to one another with known relative kinetic energy. For values of $E_{\lambda n_\lambda} > E$, Eq. (6) furnishes $k'_{\lambda n_\lambda} < 0$. The corresponding terms in Eq. (5) are said to be associated with closed channels, and are needed for the mathematical completeness of the expansions on the right-hand side. The values of $k'_{\lambda n_\lambda}$ for such channels are pure positive imaginary, and the corresponding exponentials are real negative, decaying with increasing R'_λ or R'_γ . The complex coefficient $f'_{\lambda n_\lambda}(\lambda = \alpha, \gamma)$ is called the scattering amplitude from initial state $\lambda n'_\lambda$ to final state λn_λ . If the latter is open, the flux associated with the corresponding term is $v'_{\lambda n_\lambda} |f'_{\lambda n_\lambda}|^2$ (where $v'_{\lambda n_\lambda}$ is the relative motion velocity in that channel), whereas the flux associated with the initial collision term is v'_{inc} . The collision cross section, for this one-physical-dimensional (1-PD) world (which, however, is a two-mathematical-dimensional (2-MD) world), for the $\lambda n'_\lambda \rightarrow \lambda n_\lambda$ processes, is dimensionless and is a probability [see Eq. (36)] given by the ratio of those fluxes:

$$P_{\lambda n_\lambda}^{\lambda n'_\lambda} = (v'_{\lambda n_\lambda}/v'_{\text{inc}}) |f'_{\lambda n_\lambda}|^2 \quad (7)$$

A more convenient notation can be introduced by considering that the bound vibrational wave functions $\phi_{\lambda n_\lambda}(r'_\lambda)$ differ significantly from zero only over a relatively small range of r'_λ of atomic dimensions. Furthermore, considering also C + BA collisions, Eq. (5) can be rewritten as

$$\psi^{\lambda' n'_\lambda} \sim \sum_{\lambda n_\lambda} [\delta_{\lambda n_\lambda}^{\lambda' n'_\lambda} \exp(-ik'_{\lambda n_\lambda} R'_\lambda) + f_{\lambda n_\lambda}^{\lambda' n'_\lambda} \exp(ik'_{\lambda n_\lambda} R'_\lambda)] \phi_{\lambda n_\lambda}(r'_\lambda) \quad (8)$$

In this expression, $\lambda' n'_\lambda$ denotes the initial state of the reagents (which are A + BC for $\lambda' = \alpha$ and C + BA for $\lambda' = \gamma$, where B is always the central atom), the \sim sign indicates that we are considering asymptotically the regions of configuration space in which either $R'_\alpha \rightarrow \infty$ with r'_α finite or $R'_\gamma \rightarrow \infty$ with r'_γ finite, and $\delta_{\lambda n_\lambda}^{\lambda' n'_\lambda}$ is the Kronecker symbol, which is unity if $\lambda' = \lambda$ and $n'_\lambda = n_\lambda$ and vanishes otherwise. The probability of the $\lambda' n'_\lambda \rightarrow \lambda n_\lambda$ process (with $\lambda' n'_\lambda$ and λn_λ corresponding to open channels) is then

$$P_{\lambda n_\lambda}^{\lambda' n'_\lambda} = (v'_{\lambda n_\lambda}/v'_{\lambda' n'_\lambda}) |f_{\lambda n_\lambda}^{\lambda' n'_\lambda}|^2 \quad (9)$$

B. SCALED COORDINATES

A very convenient conceptual and computational simplification can be achieved if we introduce a coordinate scaling that results in the four reduced

masses in Eq. (2) being replaced by a single reduced mass. This can be accomplished by the scaling transformations

$$\begin{aligned} R_\alpha &= a_\alpha R'_\alpha & r_\alpha &= (a_\alpha)^{-1} r'_\alpha & a_\alpha &= (\mu_{A,BC}/\mu_{BC})^{1/4} \\ R_\gamma &= a_\gamma R'_\gamma & r_\gamma &= (a_\gamma)^{-1} r'_\gamma & a_\gamma &= (\mu_{C,BA}/\mu_{BA})^{1/4} \end{aligned} \quad (10)$$

introduced by Delves (1959, 1960). In terms of the scaled coordinates R_α , r_α , and R_γ , r_γ , the nuclear motion Hamiltonian becomes

$$\begin{aligned} H &= -\frac{\hbar^2}{2\mu} \left(\frac{\partial^2}{\partial R_\alpha^2} + \frac{\partial^2}{\partial r_\alpha^2} \right) + V_\alpha(R_\alpha, r_\alpha) \\ &= -\frac{\hbar^2}{2\mu} \left(\frac{\partial^2}{\partial R_\gamma^2} + \frac{\partial^2}{\partial r_\gamma^2} \right) + V_\gamma(R_\gamma, r_\gamma) \end{aligned} \quad (11)$$

The single reduced mass μ is independent of whether we use α or γ scaled coordinates and is given by the expression

$$\mu = [(m_A m_B m_C)/M]^{1/2}, \quad M = m_A + m_B + m_C \quad (12)$$

where the masses of the three atoms play equivalent roles. Furthermore, the $(R_\alpha, r_\alpha) \rightarrow (r_\gamma, R_\gamma)$ transformation is a 2-MD coordinate-axis rotation in the scaled configuration space:

$$\begin{pmatrix} r_\gamma \\ R_\gamma \end{pmatrix} = \begin{pmatrix} \cos \omega & -\sin \omega \\ \sin \omega & \cos \omega \end{pmatrix} \begin{pmatrix} R_\alpha \\ r_\alpha \end{pmatrix} \quad (13)$$

The clockwise rotation angle ω lies in the $0-\pi/2$ range and is given by

$$\omega = \tan^{-1}[(m_A m_C)/(m_B M)]^{1/2} \quad (14)$$

In this scaled configuration space the (R_α, r_α) and (r_γ, R_γ) systems of axes are both orthogonal and can be depicted simultaneously, as indicated in Fig. 3. Under this rotation, the r_α axis transforms into the R_γ axis, and the R_α into the r_γ . This interchange of the R and r is a peculiarity of the collinear world. The important fact is that, under the $\alpha \rightarrow \gamma$ transformation in the scaled configuration space, the equipotential surface does not change shape; this is not the case for the unscaled (R'_α, r'_α) configuration space.

As a consequence of these properties, the nuclear motion of the ABC triatomic system on a laboratory-fixed straight line is completely isomorphic with that of a single particle of mass μ moving in the 2-MD scaled configuration space and subject to the potential V . In particular, the skew angle θ between the R_α and R_γ axes now has dynamic significance and is given by

$$\theta = \tan^{-1}[(m_B M)/(m_A m_C)]^{1/2} \quad (15)$$

An analogous isomorphism property, as will be seen in Section III.A, is valid for general reacting triatomic or even polyatomic systems in the three-dimensional (3-PD) world. This is a very useful conceptual simplification, since it permits the extension of the ideas developed for single-particle quantum mechanics to multiparticle systems.

C. DE BROGLIE WAVELENGTHS AND QUANTUM EFFECTS

The WKB criterion for the absence of significant quantum effects in a single-particle system states, in simple approximate language, that such a condition prevails if over one local de Broglie wavelength the relative change in the local wave number is everywhere small compared to unity. The isomorphism just established indicates that for collinear triatomic systems the appropriate mass to be used for establishing whether this criterion is or is not satisfied is the effective mass μ . Let us consider several triatomic systems at the same local kinetic energy T but with different mass combinations. Let L stand for a light atom of mass m , and H for a heavy atom of mass M . In Table I we display approximations to the local de Broglie wavelengths λ in units of that for the LLL combination given by $3^{1/4}h/(2Tm)^{1/2}$. We see from this table that replacing one of three light atoms in the LLL combination by a heavy one only decreases the local de Broglie wavelength by about 20 percent, a rather small effect. For the LHH mass combination, if we set $m = 1$ amu (for hydrogen) and $M = 127$ amu (for iodine), the relative de Broglie wavelength decreases by a factor of about 3.7 compared to the LLL one. However, if the remaining light atom is the central one, the skew angle given by Eq. (15) decreases from 60° to about 7° , with a resulting strong compression of scaled distances in the saddle-point region and, therefore, a substantial increase in the gradient of the potential in that region. As a result, large quantum effects could still exist in such a system, in spite of the presence of two very heavy atoms. In the case of electronically nonadiabatic reactions, considered in Section II.H, the potential energy function tends to change very rapidly with configuration in the vicinity of avoided potential-energy surface crossings, a

Table I
EFFECTIVE DE BROGLIE WAVELENGTHS

Mass combination	Approximate relative de Broglie wavelength
LLL	1.0
LLH	0.8
LHH	$0.9 (m/M)^{1/4}$
HHH	$1.0 (m/M)^{1/2}$

situation which also favors quantum effects. In particular, such effects were shown to exist in a simplified triatomic collinear model for the chemiluminescent $\text{Ba} + \text{ON}_2 \rightarrow \text{BaO}(\text{a}^3\Pi) + \text{N}_2$ reaction (Bowman *et al.*, 1976). Therefore, great care should be exercised before concluding that quantum effects in collinear triatomic systems having one or more heavy atoms are negligible.

D. THE SCATTERING AND REACTANCE MATRICES

Before attempting to solve Eq. (4), subject to the boundary conditions of Eq. (8), it is convenient to define the scattering matrix S and the reactance matrix R . This permits us to decouple the problem of obtaining arbitrary solutions of the Schrödinger equation from the problem of imposing asymptotic conditions appropriate for collision processes on these solutions.

In the λ arrangement channel region of the scaled configuration space ($R_\lambda \rightarrow \infty$ as r_λ remains finite) we may expand the eigenfunction $\psi^{A'n\lambda'}$ in the basis set $\phi_{\lambda n\lambda}(r_\lambda)$, which is forced to be complete and discrete by setting the diatomic potential $v_\lambda(r_\lambda) = V(R_\lambda \rightarrow \infty, r_\lambda)$ in that channel equal to zero at and beyond a value $r_{\lambda\text{max}}$ of r_λ , a region that the scattering wave function, at the energies considered, does not sample. We write

$$\psi^{A'n\lambda'} \sim \sum_{\lambda n\lambda} g_{\lambda n\lambda}^{A'n\lambda'}(R_\lambda) \phi_{\lambda n\lambda}(r_\lambda) \quad (16)$$

where

$$-\frac{\hbar^2}{2\mu} \frac{d^2 \phi_{\lambda n\lambda}}{dr_\lambda^2} + v_\lambda(r_\lambda) \phi_{\lambda n\lambda} = E_{\lambda n\lambda} \phi_{\lambda n\lambda} \quad (17)$$

and

$$\phi_{\lambda n\lambda}(0) = \phi_{\lambda n\lambda}(r_{\lambda\text{max}}) = 0 \quad (18)$$

Replacement of Eq. (16) into Eq. (4) with H given by Eq. (11), multiplication of both sides by $\phi_{\lambda n\lambda}^*(r_\lambda)$, integration over r_λ and, in the end, replacement of λ by λ leads to the set of asymptotic uncoupled differential equations

$$-\frac{\hbar^2}{2\mu} \frac{d^2 g_{\lambda n\lambda}^{A'n\lambda'}}{dR_\lambda^2} \sim (E - E_{\lambda n\lambda}) g_{\lambda n\lambda}^{A'n\lambda'} \quad (19)$$

whose solutions can be written as

$$g_{\lambda n\lambda}^{A'n\lambda'} \sim v_{\lambda n\lambda}^{-1/2} [\mathcal{J}_{\lambda n\lambda}(R_\lambda) A_{\lambda n\lambda}^{A'n\lambda'} - \mathcal{C}_{\lambda n\lambda}(R_\lambda) B_{\lambda n\lambda}^{A'n\lambda'}] \quad (20)$$

where the $A_{\lambda n\lambda}^{A'n\lambda'}$ and $B_{\lambda n\lambda}^{A'n\lambda'}$ coefficients are integration constants, $v_{\lambda n\lambda}$ is the channel velocity $\hbar|k_{\lambda n\lambda}|/\mu$, $k_{\lambda n\lambda}$ is the channel wave number given by

$$k_{\lambda n\lambda} = \hbar^{-1} [2\mu(E - E_{\lambda n\lambda})]^{1/2} \quad (21)$$

and $\mathcal{J}_{\lambda n_A}$ and $\mathcal{O}_{\lambda n_A}$ are the incoming and outgoing waves given by

$$\mathcal{J}_{\lambda n_A}(R_1) = \begin{cases} \exp(-ik_{\lambda n_A} R_1) & \text{for open channels} \\ \exp(|k_{\lambda n_A}| R_1) & \text{for closed channels} \end{cases} \quad (22)$$

$$\mathcal{O}_{\lambda n_A}(R_1) = \begin{cases} \exp(ik_{\lambda n_A} R_1) & \text{for open channels} \\ \exp(-|k_{\lambda n_A}| R_1) & \text{for closed channels} \end{cases} \quad (23)$$

The superscripts $\lambda' n'_1$ are allowed to scan the same range of values as the subscripts λn_1 . Eq. (20) can be put in the matrix form

$$g \sim v^{-1/2} [\mathcal{J}A - \mathcal{O}B] \quad (24)$$

where g , A , and B are the matrices whose λn_1 row and $\lambda' n'_1$ column elements are given, respectively, by $g_{\lambda n_A}^{\lambda' n'_1}$, $A_{\lambda n_A}^{\lambda' n'_1}$, and $B_{\lambda n_A}^{\lambda' n'_1}$ and v , \mathcal{J} and \mathcal{O} are diagonal matrices whose diagonal elements are $v_{\lambda n_A}$, $\mathcal{J}_{\lambda n_A}$, and $\mathcal{O}_{\lambda n_A}$, respectively.

We now define the scattering matrix S by the relation

$$B = SA \quad (25)$$

In other words, S is the matrix that upon left multiplying the matrix A of incoming wave coefficients, generates the matrix B of outgoing wave coefficients. This means that if we know what the state and flux of the reagents coming into a collision is, the scattering matrix permits us to obtain the states and fluxes of the outgoing products. This matrix has a set of properties that stems directly from the mathematical structure of the Schrödinger equation. We state here the more important ones. The important review article by Lane and Thomas (1958) presents the proofs for the three-dimensional case.

(1) S is unique, i.e., is independent of the choice of A . In other words, if we arbitrarily pick two coefficient matrices A_1 and A_2 that are nonsingular, the Schrödinger equation forces the corresponding B_1 and B_2 to satisfy the relation $B_1 A_1^{-1} = B_2 A_2^{-1}$. S does, however, depend on the total energy E of the system.

(2) S is symmetric. This basic property leads to the quantum mechanical principle of microscopic reversibility or detailed balancing.

(3) The open part S^o of S , formed from its open channel rows and columns, is unitary. This results in conservation of particle flux.

Equation (24) can also be put in the equivalent form

$$g \sim v^{-1/2} [\mathcal{S}C + \mathcal{C}D] \quad (26)$$

where g and v have been previously defined, C and D are new integration constant matrices, and \mathcal{S} and \mathcal{C} are diagonal sine and cosine stationary wave

matrices whose diagonal elements are given by

$$\mathcal{S}_{\lambda n_\lambda}(R_\lambda) = \begin{cases} \sin(k_{\lambda n_\lambda} R_\lambda) & \text{for open channels} \\ \exp(|k_{\lambda n_\lambda}| R_\lambda) & \text{for closed channels} \end{cases} \quad (27)$$

$$\mathcal{C}_{\lambda n_\lambda}(R_\lambda) = \begin{cases} \cos(k_{\lambda n_\lambda} R_\lambda) & \text{for open channels} \\ \exp(-|k_{\lambda n_\lambda}| R_\lambda) & \text{for closed channels} \end{cases} \quad (28)$$

The reactance matrix R (sometimes called the K matrix) is defined by the relation

$$D = RC \quad (29)$$

It can be shown (Lane and Thomas, 1958) to have the following properties:

- (1) R is unique;
- (2) R is real;
- (3) the open part R^o of R is symmetric.

From Eqs. (24)–(29), the following relation between R^o and S^o can easily be obtained:

$$S^o = (I + iR^o)(I - iR^o)^{-1} \quad (30)$$

Here I stands for the identity matrix spanned by the open row and column indices λn_λ and $\lambda' n'_\lambda$.

The sine and cosine standing waves associated with R do not carry flux. However, this matrix has the advantage of being real, and calculable using real quantities only. From it, the complex S^o matrix can be obtained using Eq. (30), which is equivalent to

$$\begin{aligned} S^o &= \text{Re } S^o + i \text{Im } S^o \\ \text{Re } S^o &= (I - R^{o2})(I + R^{o2})^{-1}, \quad \text{Im } S^o = 2R^o(I + R^{o2})^{-1} \end{aligned} \quad (31)$$

It can also easily be shown that the scaled configuration-space scattering amplitude $f_{\lambda n_\lambda}^{\lambda' n'_\lambda}$ [defined by the unprimed version of Eq. (8)] is related to S^o by

$$f_{\lambda n_\lambda}^{\lambda' n'_\lambda} = (v_{\lambda' n'_\lambda}/v_{\lambda n_\lambda})^{1/2} S_{\lambda n_\lambda}^{\lambda' n'_\lambda} \quad (32)$$

where the $v_{\lambda n_\lambda}$ are the scaled channel velocities defined after Eq. (20). It is also true that the probabilities $P_{\lambda n_\lambda}^{\lambda' n'_\lambda}$ can also be expressed in terms of scaled channel quantities by an expression analogous to Eq. (9):

$$P_{\lambda n_\lambda}^{\lambda' n'_\lambda} = (v_{\lambda n_\lambda}/v_{\lambda'}) |f_{\lambda n_\lambda}^{\lambda' n'_\lambda}|^2 \quad (33)$$

As a result of the last two equations we have, finally:

$$P_{\lambda n_\lambda}^{\lambda' n'_\lambda} = |S_{\lambda n_\lambda}^{\lambda' n'_\lambda}|^2 \quad (34)$$

Thus, once the open part of the scattering matrix is known, so are all the reaction probabilities at the same total energy. From the symmetry of S we have

$$P_{\lambda' \lambda}^{i \rightarrow i} = P_{\lambda \lambda'}^{i \rightarrow i} \quad (35)$$

which is the principle of microscopic reversibility for this collinear system, and from the unitarity of S^o we have

$$\sum_{\lambda \lambda'} P_{\lambda \lambda'}^{i \rightarrow i} = 1 \quad (36)$$

where the sum is extended over the open channels. Equation (36) constitutes the property of flux conservation, and justifies the use of the term probability for the quantities $P_{\lambda \lambda'}^{i \rightarrow i}$.

E. COMPUTATION METHODOLOGY

From the considerations of the previous section, we conclude that to determine the transition probabilities $P_{\lambda \lambda'}^{i \rightarrow i}$, which include the reactive ($\lambda \neq \lambda'$) as well as the nonreactive ($\lambda = \lambda'$) ones, it suffices to obtain the reactance matrix R . This in turn can be determined by calculating a sufficiently large number of linearly independent solutions of the Schrödinger equation, and putting the associated g matrix in the form of Eq. (26). From this, the square coefficient matrices C and D can be obtained, and R calculated from Eq. (29) as long as care has been taken to ascertain that C is nonsingular.

Over the years, different approaches have been used to obtain such linearly independent solutions of the Schrödinger equation. Mortensen and Pitzer (1962), Mortensen (1968), Diestler and McKoy (1968), Truhlar and Kuppermann (1970, 1972), and Truhlar *et al.* (1973) used finite difference methods and Cartesian coordinates. McCollough and Wyatt (1969, 1971) also used a finite difference method, but they solved the time-dependent Schrödinger equation. In general, finite difference methods are computationally very inefficient and inappropriate for extension to problems of higher dimensionality. Another approach is to solve the integral equation equivalent to Eq. (4), as developed by Sams and Khouri (1969) and applied to several systems by Adams *et al.* (1974). A variational approach has been used by Mortensen and Gucwa (1969), and more recently, a finite element approach by Askar *et al.* (1978). However, the most widely used approach for accurately solving the collinear triatom Schrödinger equation has been the coupled-channel (i.e., close-coupling) method, in one of its several forms. The basic method consists of choosing a set of two convenient variables, x and y , to describe the configuration of the system. These variables may be different in different regions of configuration space, but satisfy the central property that for x

equal to a constant \bar{x} , the potential energy function $V(\bar{x}, y)$ assumes very large values for small and for large y . The wave function $\psi(x, y)$ is expanded in eigenfunctions of a one-mathematical-dimensional Hamiltonian in y containing $V(\bar{x}, y)$ and the resulting coupled ordinary differential equations in the x -dependent coefficients are solved. Variations of this approach have been developed by Rankin and Light (1969), Miller and Light (1971), Kuppermann (1970, 1972), Diestler (1971), Johnson (1972), and Light and Walker (1976), and applied to a variety of collinear systems (Wu and Levine, 1971; Shipsey, 1973; Schatz and Kuppermann, 1973; Schatz *et al.*, 1973, 1975a,b; Baer and Kouri, 1974; Persky and Baer, 1974; Baer *et al.*, 1974; Baer, 1974a,b; Connor *et al.*, 1978).

In the present article we will review, as an illustration, only one of these methods (Kuppermann, 1970, 1972). In this method, the scaled configuration space is divided into three regions, denoted by I, II, and III in Fig. 4, and called, respectively, the reagent, the strong interaction, and the product regions. In each of these regions different coordinates and different basis sets for expanding the wave function are used. The value of R_a for points P_1 and P_2 is sufficiently large for $V_a(R_a, r_a)$ along the line P_1P_2 to have assumed the asymptotic behavior $v_a(r_a)$. Similarly, $V_x(R_x, r_x)$ along P_6P_7 equals $v_x(r_x)$. The point P_0 is located sufficiently inside the dissociated plateau region for the wave function to vanish along the line $P_1P_0P_7$. Similarly, P_2 is chosen so as to have a sufficiently low value of r_a and P_6 of r_x for the wave function along the line $P_2P_4P_6$ to vanish. To integrate the Schrödinger equation, we use the Cartesian coordinates (R_a, r_a) and (R_x, r_x) in regions I and III, respectively, and in region II the circular polar coordinates (ρ, ϕ) with origin P_0 , as indicated in

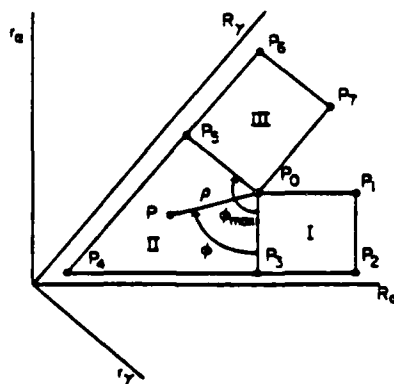


Fig. 4. Coordinates and regions of scaled configuration space for integrating the Schrödinger equation for collinear triatomic reactions.

Fig. 4. The nuclear motion Hamiltonian in terms of (R_z, r_z) and (R_z, r_z) is given by Eq. (11), whereas in the (ρ, ϕ) coordinates it is

$$H = -\frac{\hbar^2}{2\mu} \left[\frac{1}{\rho^{1/2}} \frac{\partial^2}{\partial \rho^2} \rho^{1/2} + \frac{1}{\rho^2} \frac{\partial^2}{\partial \phi^2} \right] + V(\rho, \phi) - \frac{\hbar^2}{8\mu\rho^2} \quad (37)$$

We now subdivide region I into n_i subregions separated by lines of constant R_z at $R_z = R_z^0, R_z^1, \dots, R_z^n$ where $R_z^0 = R_{z1}$ and $R_z^n = R_{zn}$ are, respectively, the R_z coordinate of points P_1 and P_n of Fig. 4. The range of the i th subregion is $R_z^{i-1} < R_z < R_z^i$. For expanding the wave function in that subregion we choose as basis functions the eigenfunctions $\phi_{m_i}(r_z; R_z^i)$ of the reference potential $V_{m_i}(r_z; R_z^i) = V(R_z^i, r_z)$ where R_z^i is a value of R_z belonging to the i th subregion, such as its midpoint. These basis functions satisfy the equations

$$\left[-\frac{\hbar^2}{2\mu} \frac{d^2}{dR_z^2} + V_{m_i}(r_z; R_z^i) \right] \phi_{m_i}(r_z; R_z^i) = E_{m_i}(R_z^i) \phi_{m_i} \quad (38)$$

$$\phi_{m_i}(r_{z1}; R_z^i) = \phi_{m_i}(r_{zn}; R_z^i) = 0$$

where r_{z1} and r_{zn} are the r_z coordinates of points P_1 and P_n , respectively. The $E_{m_i}(R_z^i)$ are the energy levels of the local transverse vibration at $R_z = R_z^i$, and the local basis set $\phi_{m_i}(r_z; R_z^i)$ furnishes a better representation of the scattering wave functions than do the diatom eigenfunctions $\phi_{m_i}(r_z; R_z \rightarrow \infty)$. We now expand those wave functions according to

$$\psi^{A'n'} = \sum_{m_i} g_{m_i}^{A'n'}(R_z; R_z^i) \phi_{m_i}(r_z; R_z^i) \quad (39)$$

Substituting this expression into Eq. (4) with H given by the first part of Eq. (11), multiplying both sides by $\phi_{m_i}^*(r_z; R_z^i)$ and integrating over r_z from r_{z1} to r_{zn} leads to the following set of coupled equations, written in matrix form:

$$-\frac{\hbar^2}{2\mu} \frac{d^2 g^I}{dR_z^2} + V^I(R_z; R_z^i) g^I = E^I(R_z^i) g^I \quad (40)$$

All matrices appearing in this equation are square, with dimensions equal to the number of terms N used in expansion (39). Although in principle this expansion should be infinite, it is truncated at a finite N , which is greater than the number of open channels at the energy being considered [i.e., expansion (39) includes closed channels], and convergence with respect to increasing N is determined numerically. The elements of g^I are the $g_{m_i}^{A'n'}$, with n_i and n'_i the row and column indices, respectively. E^I is the diagonal matrix whose diagonal elements are $E - E_{m_i}(R_z^i)$. Finally, V^I is the interaction potential matrix whose n_i, n'_i element is given by

$$V_{n_i n'_i}^I(R_z; R_z^i) = \langle \phi_{m_i}(r_z; R_z^i) | V_z(R_z, r_z) - V_z(R_z^i, r_z) | \phi_{m_i}(r_z; R_z^i) \rangle \quad (41)$$

The Schrödinger equation is integrated in region I for N independent solutions by choosing $g^i(R_{s1}; R_s^{i0}) = dg_0^i$ and $dg^i(R_{s1}; R_s^{i0})/dR_s = g_0^i$ arbitrarily, but not simultaneously zero. One such choice is to make the first equal to the identity matrix and the second equal to the null matrix. This corresponds to a choice of initial conditions at the starting value R_{s1} of R_s . We then integrate the coupled equations (40) through subregion 1, change to the basis set for subregion 2 at the boundary between these subregions, and continue in this manner until we reach the end of region I. The change in vibrational basis sets at the boundary between subregions i and $i + 1$ is accomplished by imposing the condition that the wave function $\psi^{i+1,0}$ and its derivative with respect to R_s be continuous at that boundary. This results in the relations

$$g^i(R_s^i; R_s^{i+1,0}) = S_i^i g^i(R_s^i; R_s^{i0}), \quad \frac{dg^i(R_s^i; R_s^{i+1,0})}{dR_s} = S_i^i \frac{dg^i(R_s^i; R_s^{i0})}{dR_s} \quad (42)$$

where S_i^i is the overlap matrix between the basis functions for subregions i and $i + 1$, its n_s, n_s' element being given by

$$S_{n_s n_s'}^{i+1,0} = \langle \phi_{n_s}(r_s; R_s^{i+1,0}) | \phi_{n_s'}(r_s; R_s^{i0}) \rangle \quad (43)$$

If the expansion (39) were complete S_i^i would be orthogonal. For the truncated expansions required by practical considerations, it still must be nearly orthogonal in order for the scattering matrix that results at the end to satisfy flux conservation with acceptable accuracy.

Proceeding to region II, it is also subdivided into subregions by lines of constant ϕ at $\phi = \phi^0, \phi^1, \dots, \phi^{m-1}$ where $\phi^0 = 0$ and $\phi^{m-1} = \phi_{\max}$ are, respectively, the ϕ coordinate of points P_1 and P_2 . In analogy with region I, the range of the i th subregion is $\phi^{i-1} < \phi < \phi^i$. We note that cuts of the potential energy function $V(\rho, \phi)$ along lines of constant ϕ , when plotted as a function of ρ , have the shape of diatomic molecule potential energy functions. This is a crucial property, which not only serves as a fundamental basis for reactive scattering calculations, but has also been historically used by Eyring (1935) as a basic justification for transition state theory. We make use of this characteristic behavior by choosing as basis functions for the i th subregion the eigenfunctions $\phi_{n_i}(\rho; \phi^{i0})$ of the reference potential $V_{ref}^i(\rho; \phi^{i0}) = V(\rho, \phi^{i0})$, where ϕ^{i0} is a value of ϕ in that subregion. These functions are defined by the eigenvalue equation

$$\left[-\frac{\hbar^2}{2\mu} \frac{d^2}{d\rho^2} + V_{ref}^i(\rho; \phi^{i0}) \right] \phi_{n_i}(\rho; \phi^{i0}) = E_{n_i}(\phi^{i0}) \phi_{n_i} \quad (44)$$

and the boundary conditions

$$\phi_{n_i}(\rho_{\max}^i; \phi^{i0}) = \phi_{n_i}(\rho = 0; \phi^{i0}) = 0 \quad (45)$$

where ρ_{max} is the value of ρ for the intersection point between the $\phi = \phi^{\text{in}}$ line and the line $P_3 P_4 P_5$. As in region I, ϕ_{in} and E_{in} are local transverse vibrational eigenfunctions and eigenvalues that lead to a much more rapidly converging expansion of the scattering wave function in subregion IIi than would the eigenfunctions of the isolated diatom reagent or product.

We now expand that wave function according to

$$\psi^{1'n\lambda'} = \rho^{-1/2} \sum_n g_{\text{in}}^{1'n\lambda'}(\phi; \phi^{\text{in}}) \phi_{\text{in}}(\rho; \phi^{\text{in}}) \quad (46)$$

Substituting this expression into Eq. (4) with H given by Eq. (37) and proceeding analogously to region I, we obtain the following matrix differential equation:

$$-\frac{\hbar^2}{2\mu} \frac{d^2 g^{\text{II}}}{d\phi^2} + \rho^2 (\phi^{\text{in}}) V^{\text{II}}(\phi; \phi^{\text{in}}) g^{\text{II}} = \rho^2 E^{\text{II}} (\phi^{\text{in}}) g^{\text{II}} \quad (47)$$

All the matrixes in this expression are $N \times N$ square matrices, with the same dimensions as those in Eq. (40). The elements of g^{II} are the $g_{\text{in}}^{1'n\lambda'}$, with n and n' , the row and column indices, respectively; ρ^2 , V^{II} , and E^{II} are defined by

$$\begin{aligned} \rho_n^{2n'}(\phi^{\text{in}}) &= \langle \phi_{\text{in}}(\rho; \phi^{\text{in}}) | \rho^2 | \phi_{\text{in}}(\rho; \phi^{\text{in}}) \rangle \\ V_n^{2n'}(\phi; \phi^{\text{in}}) &= \left\langle \phi_{\text{in}}(\rho; \phi^{\text{in}}) \left| V(\rho, \phi) - V(\rho, \phi^{\text{in}}) - \frac{\hbar^2}{8\mu\rho^2} \phi_{\text{in}}(\rho; \phi^{\text{in}}) \right| \right\rangle \\ E_n^{1'n'}(\phi^{\text{in}}) &= \delta_n^{n'} [E - E_{\text{in}}(\phi^{\text{in}})] \end{aligned} \quad (48)$$

The condition that at the boundary between regions I and II, $\psi^{1'n\lambda'}$ and its derivative with respect to R_s are continuous, leads to the following relations between the initial values of g^{II} or its ϕ derivative and the final values of g^{I} or its R_s derivative:

$$\begin{aligned} g^{\text{II}}(\phi = 0; \phi^{\text{in}}) &= \rho^{1/2} g^{\text{I}}(R_{20}; R_1^{\text{in}}) \\ [dg^{\text{II}}(\phi = 0; \phi^{\text{in}})]/d\phi &= -\rho^{3/2} [dg^{\text{I}}(R_{20}; R_1^{\text{in}})/dR_s] \end{aligned} \quad (49)$$

where

$$\rho_n^{1n} = \langle \phi_{\text{in}}(\rho; \phi^{\text{in}}) | \rho^b | \phi_{\text{in}}(r_{s1} - \rho; R_1^{\text{in}}) \rangle, \quad b = \frac{1}{2}, \frac{3}{2} \quad (50)$$

The change in vibrational basis set at the boundary between subregions IIi and IIi + 1 is accomplished by equations analogous to (42) and (43). Using them and Eq. (49) we can integrate Eq. (47) from the beginning through the end of region II.

For region III we use equations analogous to (38)–(43) with I and α replaced by III and γ , respectively, and other obvious notational changes. At the boundary between regions II and III, equations analogous to (49)

are applicable, with a plus rather than a minus sign in the right-hand side of the second of these equations to indicate that both ϕ and R_z increase in the direction of integration.

With the help of this procedure, we can integrate the Schrödinger equation from the beginning of region I to the end of region III. The numerical method used for integrating the coupled second-order differential equations (40), (47), and the region III equivalent of (40), is arbitrary. It should, however, be an efficient method, because otherwise the computation time may be excessive, since it grows with the cube of the number N of coupled equations. Three such methods commonly used are those of Gordon (1969), Magnus (Light, 1971, and Light and Walker (1976).

A numerical complication that should be mentioned is that due to the necessary inclusion of closed channels in the expansion of $\psi^{i \rightarrow a}$, the columns of the g matrices tend to become linearly dependent, as the integration proceeds, thereby destroying the needed linear independence of the $\psi^{i \rightarrow a}$. This can be avoided by reorthogonalization procedures, one of which involves right multiplying g and g' by g^{-1} , which means continuing the integration with $g_{\text{new}} = I$ and $g'_{\text{new}} = g'g^{-1}$. This corresponds to obtaining solutions with the modified initial conditions $g_{0\text{new}}^I = g_0^I g^{-1}$ and $g_{0\text{new}}^{II} = g_0^{II} g^{-1}$. Each time a reorthogonalization procedure is performed anywhere in regions I, II, or III, the initial conditions of region I must be modified accordingly. The efficient integration method recently developed by Light and Walker (1976) has elegantly bypassed this complication.

Let us label by g_r^{III} the final g^{III} matrix at the end of region III and by g_0^I the corresponding (modified) initial g^I matrix at the beginning of region I, and let us use an equivalent notation for the derivatives with respect to R_z and R_a , respectively. Similarly, let us perform integrations of the Schrödinger equation starting at the beginning of region III (i.e., line $P_6 P_7$ of Fig. 4) and terminating at the end of region I (line $P_1 P_2$). Let g_0^{III} and g_r^I be the corresponding initial and final matrices, with a similar notation for their derivatives. With the help of these several matrices we can determine the R matrix as follows.

We define the global g and g' matrices by

$$g = \begin{pmatrix} g_0^I & g_r^I \\ g_r^{\text{III}} & g_0^{\text{III}} \end{pmatrix}, \quad g' = \begin{pmatrix} g_0^{I'} & g_r^{I'} \\ g_r^{\text{III}'} & g_0^{\text{III}'} \end{pmatrix} \quad (51)$$

Since along lines $P_2 P_1$ and $P_6 P_7$, the potential function V has assumed its asymptotic behavior $v_a(r_a)$ and $v_r(r_r)$, respectively, g must have assumed the form given by Eq. (26):

$$g = v^{-1/2}[\mathcal{SC} + \mathcal{CD}] \quad (52)$$

Similarly, its derivative must be given by

$$g' = v^{-1/2}[\mathcal{S}'C + \mathcal{C}'D] \quad (53)$$

where \mathcal{S}' and \mathcal{C}' are the diagonal matrices whose diagonal elements are the derivatives with respect to R_i of Eq. (27) and (28), evaluated, as are \mathcal{S} and \mathcal{C} , at $R_6 = R_{61}$ and $R_7 = R_{77}$.

In Eqs. (52) and (53), all matrices except C and D are now known. From these equations we can therefore obtain these unknowns and from them R by using Eq. (29). From the open part R^o of R we obtain S^o from either Eq. (30) or Eq. (31), and finally the transition probabilities $P_{\lambda\alpha_1}^{A'\alpha_2}$ by using Eq. (34). In this manner, once V is given, these probabilities can be calculated.

F. THE HYDROGEN ATOM-HYDROGEN MOLECULE EXCHANGE REACTION

Because of the relative ease in calculating the potential energy function for the H_3 system and because of the quantum nature of this system, it has been investigated extensively in the collinear approximation. Accurate quantum calculations have been performed by Truhlar and Kuppermann (1970, 1972), Schatz and Kuppermann (1973), Diestler (1971), and Johnson (1972), and compared with classical and semiclassical calculations by Bowman and Kuppermann (1973a,b). We will summarize here some of the more important results.

In this collinear model, the three H atoms are assumed to be distinguishable, due to their fixed ordering on the straight line to which they are confined, as indicated just before Eq. (1). The scattering wave function is therefore not forced to be antisymmetric with respect to the exchange of any two of the three nuclei. In the three-dimensional calculations, to be described in Section III, it is necessary to impose the Pauli principle on the scattering wave function, since we are then dealing with the real world. However, in the fictitious collinear world, we are free to define a model in which the atoms are distinguishable. An alternate model, not considered here, would be to impose the Pauli principle on the nuclear motion in the collinear world also, in analogy to the 3-PD conditions. For facility of comparison with classical calculations and conceptual simplicity, this was not done in the present calculations.

1. Reaction Probabilities and Rate Constants

Let $P_{\alpha\alpha'}^R$ represent the probability of the reactive process $H + H_2(n) \rightarrow H_2(n') + H$. In Fig. 5 we display the results of the exact quantum mechanical (EQ) calculations of the reaction probabilities P_{00}^R for the scaled SSMK potential energy surface (Shavitt *et al.*, 1968), as a function of the total energy

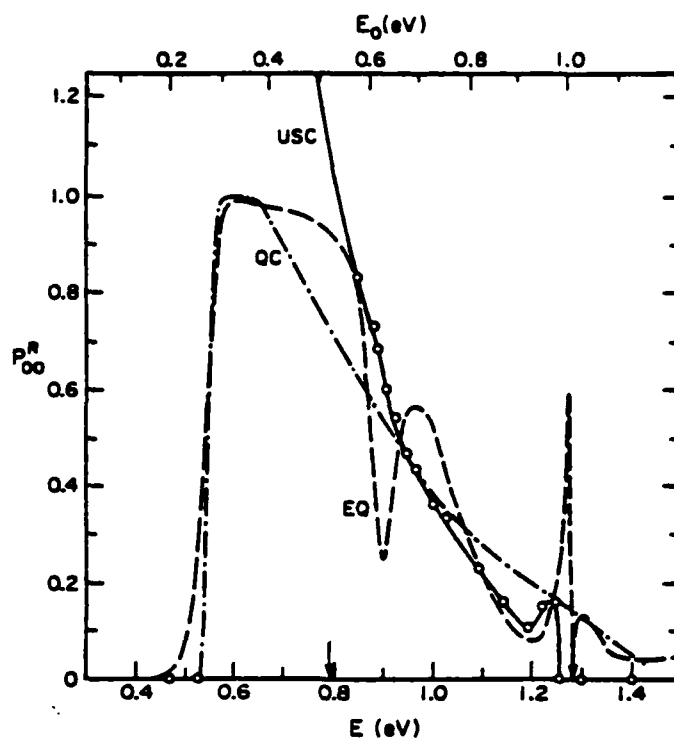


Fig. 5. Uniform semiclassical (solid curve), exact quantum (dashed curve), and quasi-classical (dashed-dotted curve) P_{00}^n transition probabilities as a function of total energy E and initial relative kinetic energy E_0 for the $\text{H} + \text{H}_2(0) \rightarrow \text{H}_2(0) + \text{H}$ collinear reaction.

E and the initial relative translational energy E_0 (Truhlar and Kuppermann, 1970, 1972; Bowman and Kuppermann, 1973a,b). Also shown are the corresponding quasi-classical trajectory (QC) and uniform semiclassical (USC) probabilities. The arrows on the lower abscissa designate the energies at which the excited vibrational states $n = 1, 2$ become energetically accessible.

The USC values are a better approximation to the EQ values than are the QC results at total energies between 1.0 and 1.2 eV, but deviate rapidly from the exact values as E decreases below 0.85 eV. The strong resonance oscillation occurring around $E = 0.9$ eV in the EQ curve is barely perceptible in the USC curve. In addition, the very sharp resonance behavior in the EQ curve at 1.27 eV is not reproduced by the USC calculations. Stine and Marcus (1974) have been able to reproduce, by a semiclassical technique, the EQ resonance at 0.9 eV. At energies at which no classical trajectories exist, the USC theory used in these calculations (Miller, 1970a,b; Bowman

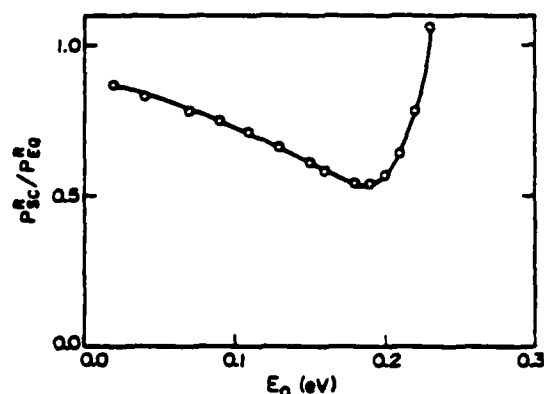


Fig. 6. Ratio of the complex-trajectory, semiclassical reaction probability P_{sc}^A to the exact quantum reaction probability P_{EQ}^A for very low initial translational energies E_0 for the $H + H_2(0) \rightarrow H_2(0) + H$ collinear reaction.

and Kuppermann, 1973a,b), furnishes a zero reaction probability. This is the case at total energies below that of the saddle point, for which the reaction proceeds entirely by tunneling.

Miller and George (1972) have used a complex trajectory semiclassical method to overcome this difficulty. In Fig. 6 we display the ratio of their probabilities, P_{sc}^A (for $n = 0$, $n' = 0$), to the corresponding EQ ones, P_{EQ}^A , as a function of translational energy E_0 , for the Porter-Karplus (1964) surface (Bowman and Kuppermann, 1973a,b). It can be seen that over the translational energy range of 0.02–0.2 eV, of importance for tunneling processes, the SC reaction probabilities range from 0.65 to 0.87 of the accurate ones. This is a major improvement over the real trajectory USC method, but it also indicates that this complex-trajectory SC method still significantly underestimates the effect of tunneling. The steep rise in the P_{sc}^A / P_{EQ}^A ratio above $E_0 = 0.2$ eV may be indicative of the same kind of divergent behavior as the one shown in Fig. 5 by the P_{00}^A USC curve.

In Fig. 7 we display the EQ total reaction probabilities P_n^A from the initial state n of the reagents to all accessible final states of the products, for the scaled SSMK surface, for $n = 0, 1, 2$ (Truhlar and Kupperman, 1972). (The dashed portions of these curves around the resonance at $E = 1.28$ eV are inaccurate; the resonance structure is sharper than indicated and is correctly given in Fig. 5.) The threshold for production of H_2 molecules in their first vibrationally excited state is $E = 0.79$ eV. From that energy to 0.89 eV, vibrationally excited reagents have a vibrational energy of 0.79 eV and 0.0–0.1 eV translational energy, whereas ground vibrational state reagents have 0.27 eV vibrational energy and 0.52–0.62 eV translational energy.

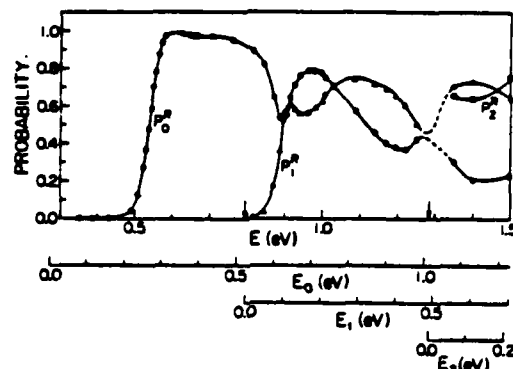


Fig. 7. Total reaction probabilities P_n^R ($n = 0, 1, 2$) as a function of total energy E and initial relative kinetic energy E_n for ground state ($n = 0$), first excited state ($n = 1$), and second excited state ($n = 2$) reagents for the collinear $\text{H} + \text{H}_2(n) \rightarrow \text{H}_2 + \text{H}$ reaction.

Figure 7 shows that for this energy region, the probability of reaction is greater for ground state reagents. This illustrates that it is not necessary merely to have enough energy to react, but that the energy must be dynamically available to overcome the barrier. Apparently the dynamics of this system require that more of the vibrational energy be tied up as motion transverse to the curved reaction path when the reagent has a greater fraction of the energy in this transverse mode. This indicates a tendency toward vibrational adiabaticity in this mode. The effective translational energy reaction threshold for ground state reagents is 0.25 eV, corresponding to a total energy of 0.52 eV. Since the barrier height is 0.42 eV, the translational energy for this effective threshold, measured with respect to the top of the barrier, is 0.1 eV. For $n = 1$ and 2 (for which E is already above the barrier height even for zero translational energy), the effective translational threshold energies are 0.08 eV and less than 0.03 eV, respectively. The difference between the translational thresholds of 0.25 and 0.08 eV for $n = 0$ and $n = 1$ results in a translationally thermal rate constant $k_n(T)$ that, at room temperature, is about 440 times greater for $n = 1$ than for $n = 0$. In Fig. 8 we display Arrhenius plots of the total rate constant $k(T)$ calculated from the EQ reaction probabilities (dashed curve, left ordinate), the $k_1(T)$ rate constant (dotted curve, right ordinate), computed from the P_1 reaction probabilities, and the Arrhenius straight-line fit to the high-temperature data (solid curve, left ordinate). Over the entire temperature range considered, $k(T) = k_0(T)$ to within 3 percent because of the very small fractional thermal population of vibrationally excited reagents at those temperatures. Comparison of the $k(T) \cong k_0(T)$ and $k_1(T)$ Arrhenius plots indicates the effectiveness of vibrational

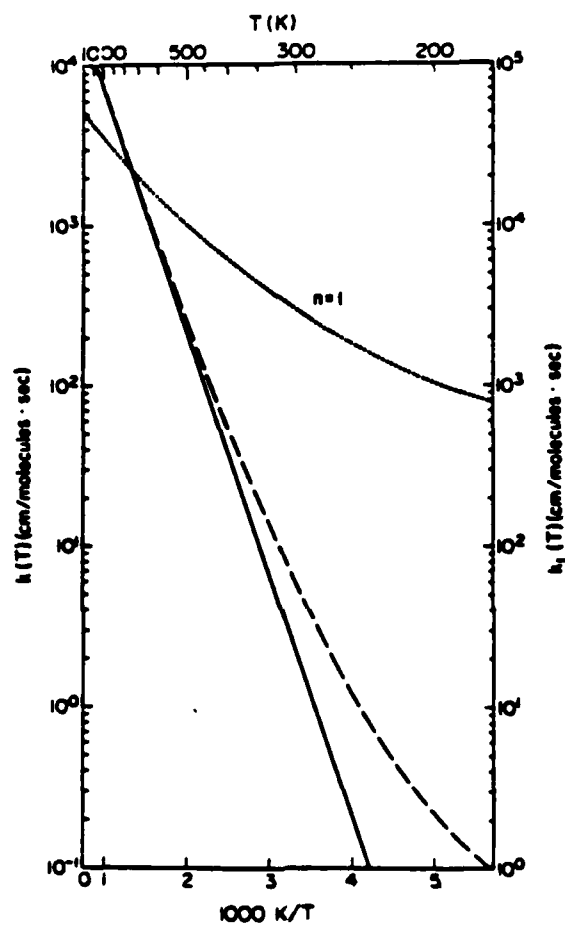


Fig. 8. Accurate rate constant $k(T)$ for a Boltzmann distribution of vibrational levels (only $n = 0$ and $n = 1$ are important in this energy range) versus reciprocal temperature (dashed curve, left ordinate) for the collinear $\text{H} + \text{H}_2 \rightarrow \text{H}_2 + \text{H}$ reaction. The dotted curve is $k_1(T)$ (right ordinate) and the solid curve (left ordinate) is the Arrhenius straight-line fit to the high-temperature $k(T)$.

energy in overcoming the barrier. The curvature of the $k(T)$ plot is related to tunneling effects and is discussed in the next section.

2. Tunneling Effects

The dynamics of the reaction from $n = 0$ occurring in the threshold energy region can be elucidated with the help of the probability current density and

its streamlines. For a Hamiltonian of the form of Eq. (11) the probability current density vector in the 2-MD configuration space is defined as

$$\mathbf{j}^{\lambda n_A}(R_1, r_1) = \text{Re}(\psi^{\lambda n_A} \nabla_{\text{op}}^{\lambda} \psi^{\lambda n_A}) \quad (54)$$

where

$$\nabla_{\text{op}}^{\lambda} = \frac{1}{\mu} \left(\hat{\mathbf{R}}_1 \frac{\hbar}{i} \frac{\partial}{\partial R_1} + \hat{\mathbf{r}}_1 \frac{\hbar}{i} \frac{\partial}{\partial r_1} \right)$$

and $\hat{\mathbf{R}}_1$ and $\hat{\mathbf{r}}_1$ are the unit vectors along the R_1 and r_1 Cartesian axes and $\psi^{\lambda n_A}$ is the solution of the Schrödinger equation satisfying the asymptotic scattering conditions of the type of Eq. (8) (with λn_A and $\lambda' n'_A$ interchanged).

The streamlines of $\mathbf{j}^{\lambda n_A}$ are curves in configuration space, which at every point $P(R_1, r_1)$ in that space are tangent to the $\mathbf{j}^{\lambda n_A}$ vector at that point. They satisfy the condition that the flux of \mathbf{j} normal to a line L_{12} connecting a point P_1 on one streamline S_1 to a point P_2 on another streamline S_2 is independent of where along those two streamlines P_1 and P_2 are chosen, and of the shape of L_{12} . For this reason, we can say that each streamline carries with it an element of flux. In particular, if P_1 is chosen to lie in the steep repulsive region of configuration space and P_2 in the plateau region [such that $\psi^{\lambda n_A}(P_1) = \psi^{\lambda n_A}(P_2) = 0$], then the flux $J^{\lambda n_A}$ through L_{12} is just the product of the total reaction probability times the incident flux $J_{\text{inc}}^{\lambda n_A}$. If we write the incident wave as $A \exp(ik_{\lambda n_A} R_1) \phi_{\lambda n_A}(r_1)$, $J_{\text{inc}}^{\lambda n_A}$ is equal to

$$J_{\text{inc}}^{\lambda n_A} = |A|^2 v_{\lambda n_A} \quad (55)$$

$$J^{\lambda n_A} = \int_{L_{12}} \mathbf{j}_{\lambda n_A} \cdot d\mathbf{L} = P^{\lambda n_A} J_{\text{inc}}^{\lambda n_A} \quad (56)$$

where $d\mathbf{L}$ is a vector element perpendicular to L_{12} . In Figs. 9 and 10 we display, respectively, streamlines of probability current density and profiles of the component of \mathbf{j}^0 normal to various straight-line cuts along the streamline field, for the $\text{H} + \text{H}_2(0) \rightarrow \text{H}_2 + \text{H}$ reaction on the SSMK surface (Kuppermann *et al.*, 1974). In Fig. 9, the \mathbf{j}^0 at every point is represented by a curved arrow starting at that point and whose length is proportional to the magnitude of \mathbf{j}^0 . The solid lines are equipotentials of V , the values of which are given in electron volts at the lower right part of the figure. The equipotentials labeled E correspond to the energy 0.470 eV of the calculation. Therefore, any classical trajectory at that energy would have to be confined to the region of configuration space between those two equipotentials. It can be seen, however, that the streamlines cut those classical margins, penetrating into regions of configuration space that are classically inaccessible and carrying with them *tunneling* flux. A quantitative definition of a tunneling coefficient γ can now be introduced as follows. Let us consider the short-dashed lines

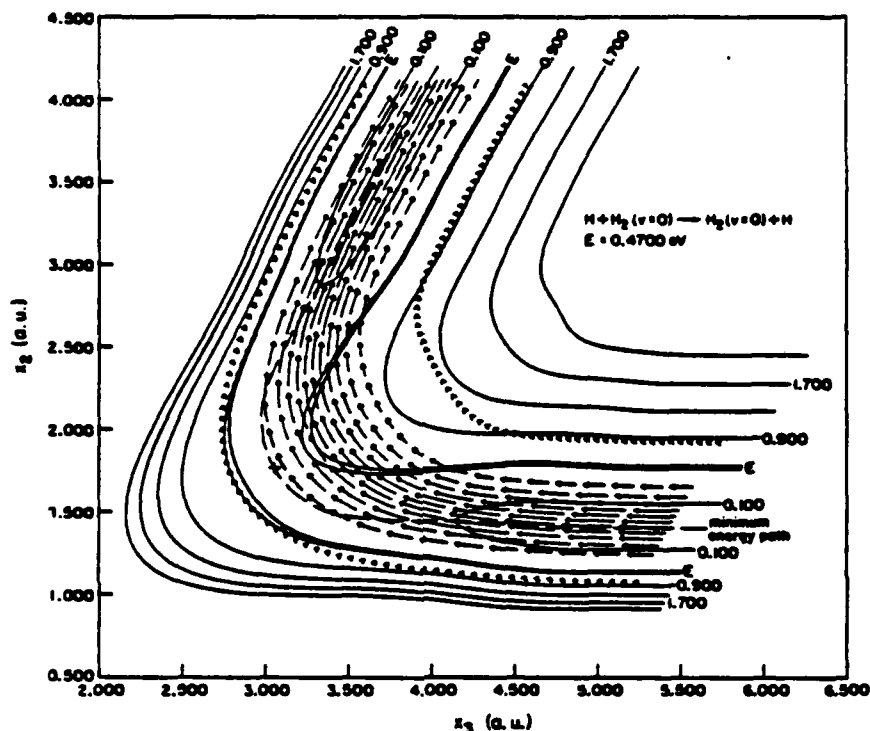


Fig. 9. Streamlines of probability current density (curves made up of arrows) for the collinear $\text{H} + \text{H}_2(0) \rightarrow \text{H}_2 + \text{H}$ reaction. The length of the arrows is proportional to the magnitude of the probability density vector. The solid lines are equipotentials at the energies, whose values, in eV, are given in the lower right part and upper middle part of the figure. The curves labeled E are equipotentials at the total collision energy of 0.470 eV. The minimum energy path is also indicated by a dashed line. The abscissa x_3 is the Delves coordinate R_1 multiplied by $(\mu_{\text{BC}}/\mu_{\text{A,BC}})^{1/2}$, whereas the ordinate x_2 is r_1 divided by that factor.

of Fig. 10. These are limiting streamlines that are each tangent to one of the two $E = 0.470$ eV equipotentials. Any other streamline in between these never penetrates into classically forbidden regions of configuration space, whereas any streamline outside this band necessarily penetrates into such forbidden regions. The total reactive flux carried by the latter streamlines will be defined as the tunneling flux $J_{\text{tun}}^{\text{A} \rightarrow \text{A}}$, and the ratio of it to the incident flux $J_{\text{inc}}^{\text{A} \rightarrow \text{A}}$ will be called the tunneling coefficient $\gamma^{\text{A} \rightarrow \text{A}}$. The product of $\gamma^{\text{A} \rightarrow \text{A}}$ by the total reaction probability is by definition the tunneling probability $P_{\text{tun}}^{\text{A} \rightarrow \text{A}}$. Therefore,

$$\gamma^{\text{A} \rightarrow \text{A}} = J_{\text{tun}}^{\text{A} \rightarrow \text{A}} / J_{\text{inc}}^{\text{A} \rightarrow \text{A}} = P_{\text{tun}}^{\text{A} \rightarrow \text{A}} / P^{\text{A} \rightarrow \text{A}} \quad (57)$$

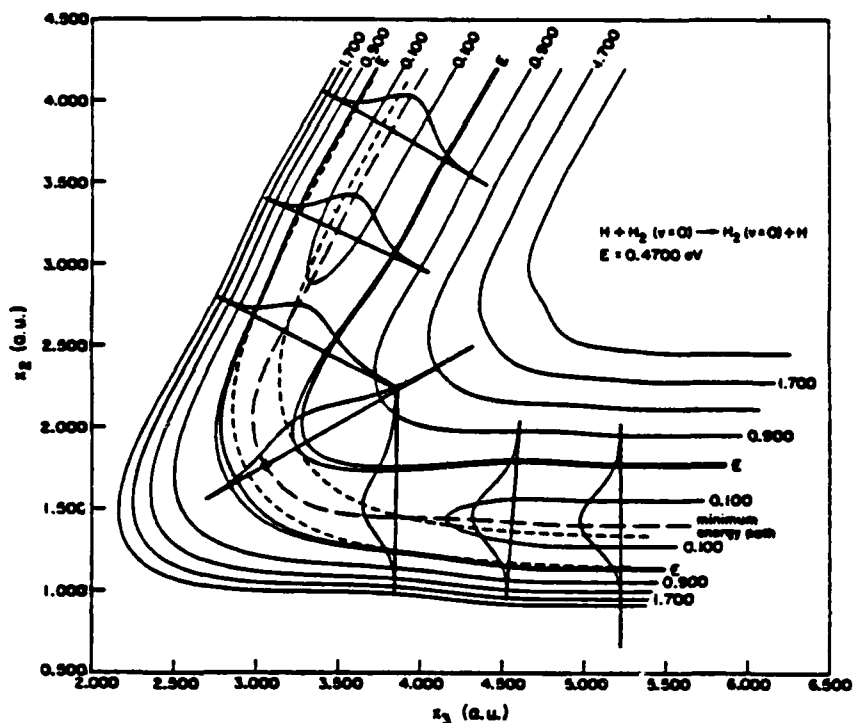


Fig. 10. Reactive flux for the collinear $\text{H} + \text{H}_2(0) \rightarrow \text{H}_2 + \text{H}$ reaction. The bell-shaped curves represent the component of probability current density normal to the segments of straight line to which they are tangent asymptotically. The remaining lines and coordinates are the same as for Fig. 9. The short, dashed lines are streamlines tangent to the 0.470-eV equipotential curves labeled E .

The bell-shaped curves of Fig. 10 represent the profiles of the component of j^0 normal to the cuts indicated by the segments of straight line. The areas between those curves and the corresponding straight lines are all equal to each other and equal to the product of the reaction probability P_0^R by the incident flux J_0^{inc} . Furthermore, the areas under the bell-shaped curves outside of the region between the limiting streamlines are also the same for all cuts and are equal to the tunneling flux. It can readily be seen that at the energy $E = 0.470$ eV considered in this figure, over 50% of the total reactive flux is due to tunneling. This is somewhat surprising, since this energy is 0.046 eV above the barrier height of 0.424 eV. This indicates that cutting across the corner of the potential energy surface is a preferred reaction pathway at these energies. In Figs. 11 and 12 we represent, respectively, the

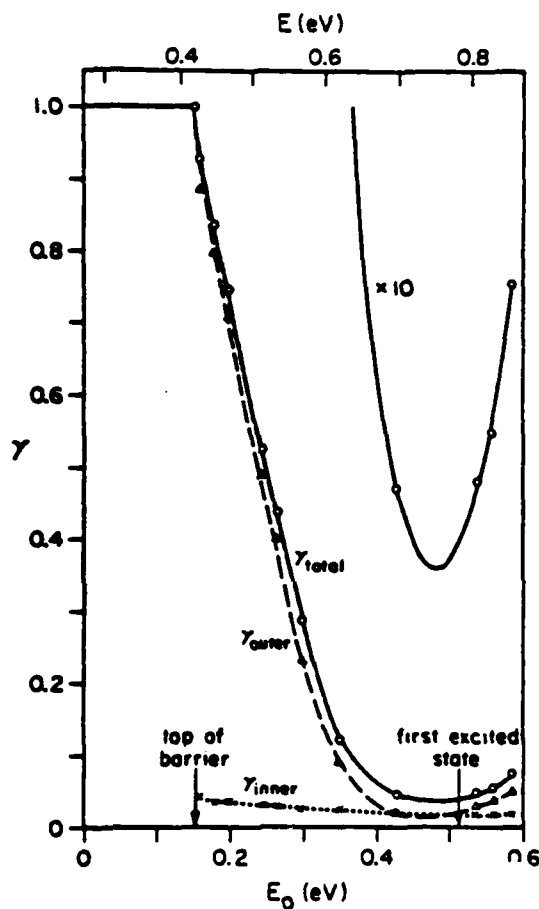


Fig. 11. Tunneling coefficient versus initial relative translational energy E_0 and total energy E for the collinear $H + H_2(0) \rightarrow H_2 + H$ reaction. The arrows on the abscissa indicate the energies of the barrier top and of the first vibrationally excited H_2 state.

tunneling coefficients γ and the tunneling and nontunneling reaction probabilities as a function of relative translational and total energy for the $H + H_2(0) \rightarrow H_2 + H$ reaction on the scaled SSMK surface (Kuppermann *et al.*, 1973; A. Kuppermann, J. T. Adams, and D. G. Truhlar, unpublished results, 1973). In Fig. 11, γ_{inner} represents the tunneling coefficient associated with the streamlines that penetrate into the classically forbidden region to the left of the left-limiting streamline (the direction of the j vectors being used to define left and right); γ_{outer} , that associated with the streamlines to the

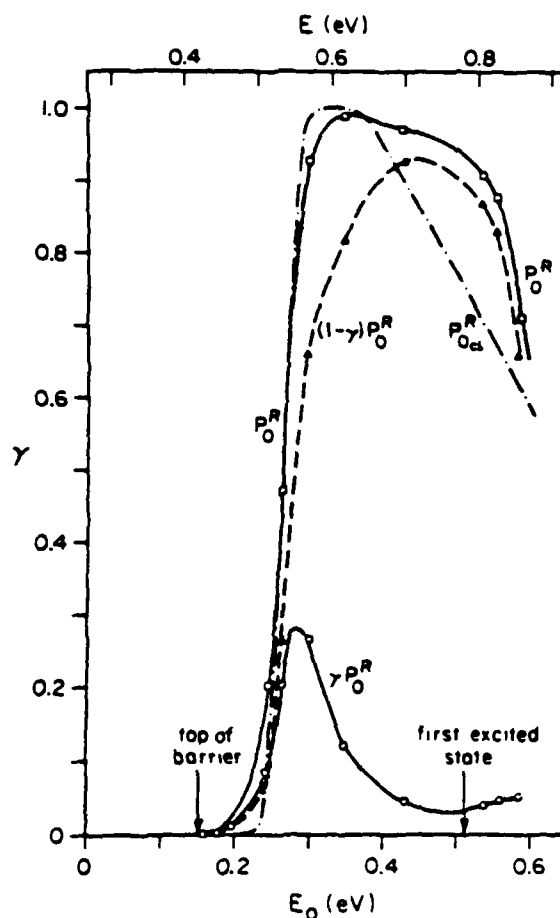


Fig. 12. Exact quantum reaction probability P_0^R , quasi-classical reaction probability $P_{0,q}^R$, tunneling reaction probability γP_0^R , and nontunneling reaction probability $(1-\gamma)P_0^R$ as a function of initial relative translational energy E_0 and total energy E for the collinear $H + H_2(0) \rightarrow H_2 + H$ reaction. The arrows on the abscissa have the same meaning as in Fig. 11.

right of the right-limiting streamline; and γ_{total} , the sum γ of γ_{inner} and γ_{outer} . In Fig. 12 we represent, as functions of energy, the EQ reaction probability P_0^R , the QC reaction probability $P_{0,q}^R$, the total tunneling reaction probability γP_0^R and the nontunneling reaction probability $(1-\gamma)P_0^R$. We see that at an initial relative translational energy of 0.30 eV (which is about 0.15 eV above the top of the barrier, and corresponds to the average translational energy of a collinear thermal distribution at about 3600 K), the tunneling coefficient

has the surprisingly high value of about 0.29. Since the total reaction probability at that energy is about 0.93, the tunneling contribution to the reaction probability is approximately 0.27. This should manifest itself in the values of the rate constants.

Since the total reaction probability has been decomposed, by the streamline analysis, into tunneling and nontunneling contributions, the corresponding collinear rate constants (Truhlar and Kuppermann, 1972) can also be expressed as the sum of a tunneling and a nontunneling contribution. In Fig. 13 we display Arrhenius plots of the total rate constant k and the tunneling rate constant k_{tun} (left ordinate scale), as well as a linear plot of the ratio k_{tun}/k (right ordinate scale) as a function of reciprocal temperature. It

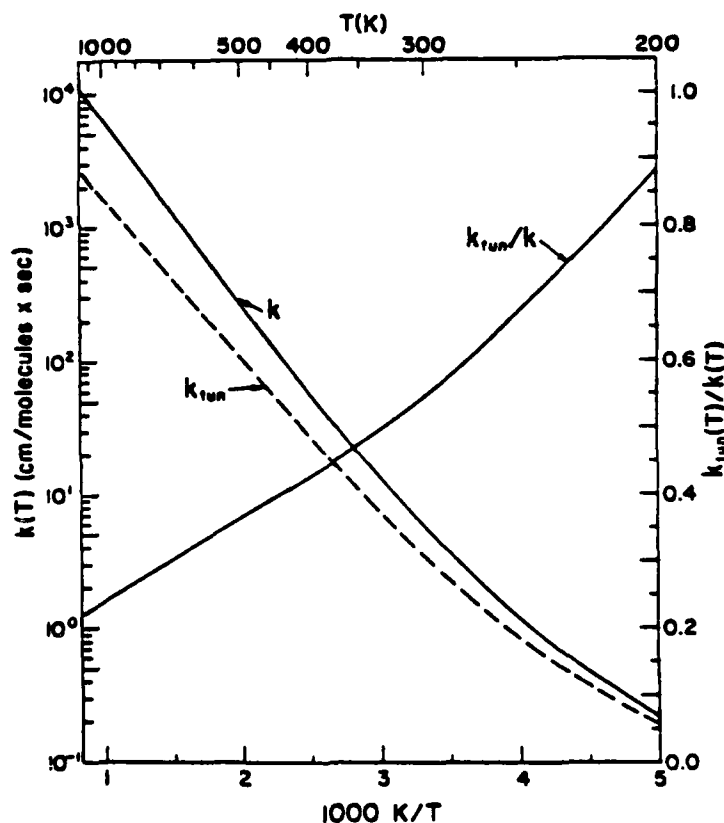


Fig. 13. Arrhenius plots of the total rate constant k and the tunneling rate constant k_{tun} (left-ordinate scale for both) for the $\text{H} + \text{H}_2 \rightarrow \text{H}_2 + \text{H}$ collinear reaction. The curve labeled k_{tun}/k represents their ratio (right-ordinate scale).

can be seen that at room temperature about 55 percent of the rate constant is due to tunneling processes, and even at 1000 K about 25 % of the rate constant comes from tunneling contributions. Furthermore, between 1000 and 400 K the Arrhenius plot of $k(T)$ is a straight line, and nevertheless, over that temperature range, the tunneling contribution to that rate constant lies between 25 and 43 %. At lower temperatures, when the effect of tunneling is even higher, the Arrhenius plot of $k(T)$ shows substantial curvature. We conclude that in this system, curvature in the Arrhenius plot of the total rate constant is not a necessary condition for substantial tunneling. The reason is that the Arrhenius plot of the tunneling rate constant is also a straight line over a substantial temperature range. Therefore, tunneling processes in both the collinear and three-dimensional worlds may be substantially greater than would be indicated by the criterion of Arrhenius plot curvature.

3. Dynamic Resonances

The EQ reaction probability versus energy curve of Fig. 5 displays two pronounced oscillations, at relative translational energies of about 0.62 and 1.06 eV. These oscillations are due to the quantum mechanical interference between direct reaction and dynamic resonance mechanisms, in which energy is trapped in internal degrees of freedom of the system (Schatz and Kuppermann, 1973). For the 1.06-eV resonance, the trapping degree of freedom is mainly due to the mode of motion transverse to the minimum energy path (Schatz and Kuppermann, 1975; Schatz, 1976; G. C. Schatz and A. Kuppermann, unpublished results, 1975). However, the one at 0.62 eV seems to be due, at least in significant part, to the trapping of energy in a longitudinal mode of motion, partly along the minimum energy path, with the repulsive walls associated with the skew axis acting as partial reflectors (Dwyer, 1978; Kuppermann and Dwyer, 1979; Kuppermann, 1981). This corresponds to an asymmetric stretch virtual mode at the saddle point, whereas the 1.06-eV resonance corresponds mainly to a symmetric stretch virtual mode, as depicted in Fig. 14 by the two orthogonal lines passing through the saddle point. This suggests that these resonances may correspond to the virtual state vibrational spectroscopy of the saddle-point region, and that the energies at which they occur may be related to the potential surface parameters in the saddle-point region just as the position of bound-state vibrational energy levels of stable molecules is related to the potential surface parameters in the region of its minimum. If this possibility, upon further investigation, turns out to be correct, an experimental determination of the energies of dynamic resonances may lead to information about geometrical and energetic details of the saddle-point region of reactive potential energy surfaces.

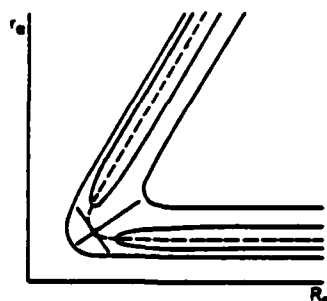


Fig. 14. Schematic representation of approximate internal motions associated with the first two Feshbach resonances in the collinear $\text{H} + \text{H}_2(0) \rightarrow \text{H}_2(0) + \text{H}$ reaction. These motions are depicted by the two segments of straight lines that cross at the saddle point of the potential energy surface, the shorter corresponding to the lowest energy resonance and the longer to the second resonance. These resonances are related to the oscillations in the EQ curve of Fig. 5 at $E_0 = 0.62$ and 1.06 eV, respectively.

G. THE $\text{F} + \text{H}_2 \rightarrow \text{FH} + \text{H}$ REACTION AND ITS ISOTOPIC COUNTERPARTS

The reactions of F atoms with H_2 , D_2 , and DH molecules have been extensively studied by infrared chemiluminescence (Polanyi and Tardy, 1969), chemical lasers (Kompa and Pimentel, 1967), and crossed-molecular-beam techniques (Schaefer *et al.*, 1970; Sparks *et al.*, 1980). These reactions are important for the fluorine-hydrogen chemical lasers, where they serve as the main pumping reaction (Kompa and Pimentel, 1967; Spencer *et al.*, 1969). They have also been studied theoretically by the collinear quantum mechanical (Schatz *et al.*, 1973, 1975a,b; Connor *et al.*, 1978; Latham *et al.*, 1978), quasi-classical (Schatz *et al.*, 1973, 1975a,b), and semiclassical methods (Schatz *et al.*, 1973, 1975a,b; Whitlock and Muckerman, 1975), and the three-dimensional quasi-classical trajectory (Muckerman, 1971, 1972; Jaffe and Anderson, 1971, 1972; Jaffe *et al.*, 1973; Wilkins, 1972, 1973; Blais and Truhlar, 1973; Ding *et al.*, 1973; Polanyi and Schreiber, 1977) and quantum-mechanical angular momentum decoupling methods (Redmon and Wyatt, 1979). The reaction is exothermic by about 32 kcal/mole, and as a result, four vibrational states of FH are normally accessible for the $\text{F} + \text{H}_2$ reagents at thermal energies, and five vibrational states of FD for the $\text{F} + \text{D}_2$ reagents at corresponding energies.

The collinear LEPS potential energy surface for $\text{F} + \text{H}_2$ proposed by Whitlock and Muckerman (1975) is depicted in Fig. 15 in scaled coordinates (Schatz *et al.*, 1975a). The position of the saddle point, which is 1.06 kcal/mole (0.046 eV) above the bottom of the entrance reagent valley, is located by the cross in that figure. The heavy solid line going through that point is the minimum energy path, and the other curves are equipotentials at the energies

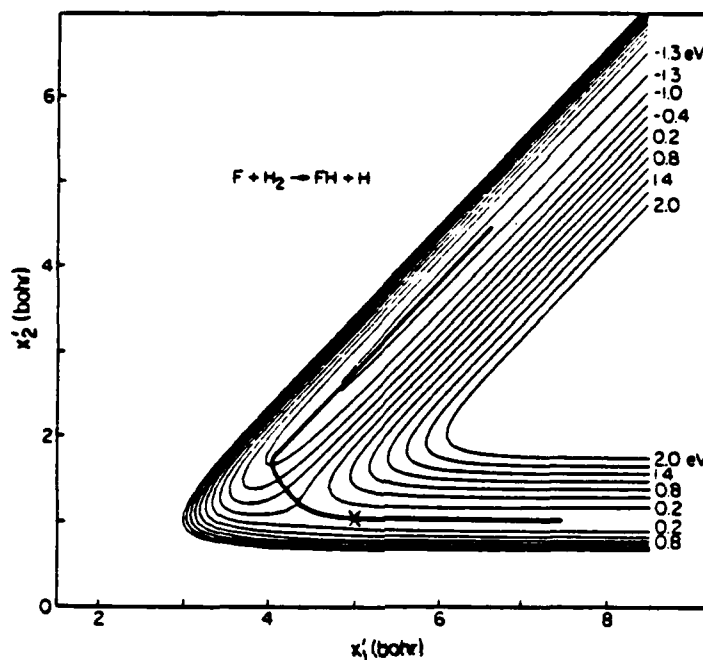


Fig. 15. Equipotential contour plot of the FH_2 collinear potential energy surface in scaled coordinates ($x_1' = R_1$; $x_2' = r_2$). The energies of the equipotentials, as indicated, are measured with respect to the minimum in the reagent H_2 diatomic potential energy curve (associated with the lower right part of the figure). The heavy line denotes the minimum energy path, with the saddle point indicated by a cross.

given in the lower right portion of the figure. The coordinates x_1' and x_2' are R_1 and r_2 , respectively, in the notation of Section II.A, where F, H, and H are A, B, and C, respectively. It can be seen that the exothermicity starts being released before the bend in the minimum energy path, and we may therefore expect the products to be vibrationally excited, due to collision of the effective mass point with the skewed repulsive wall, after that point has picked up a significant part of the energy release.

1. Reaction Probabilities and Rate Constants

In Figs. 16 and 17 we display the $F + H_2$ EQ results for P_{02}^R , P_{03}^R , and P_0^R , as well as those for the USC and quasi-classical forward (QCF) and reverse (QCR) methods (Schatz *et al.*, 1973, 1975a,b). From microscopic reversibility, as we have seen in Eq. (35), the quantum mechanical forward and reverse

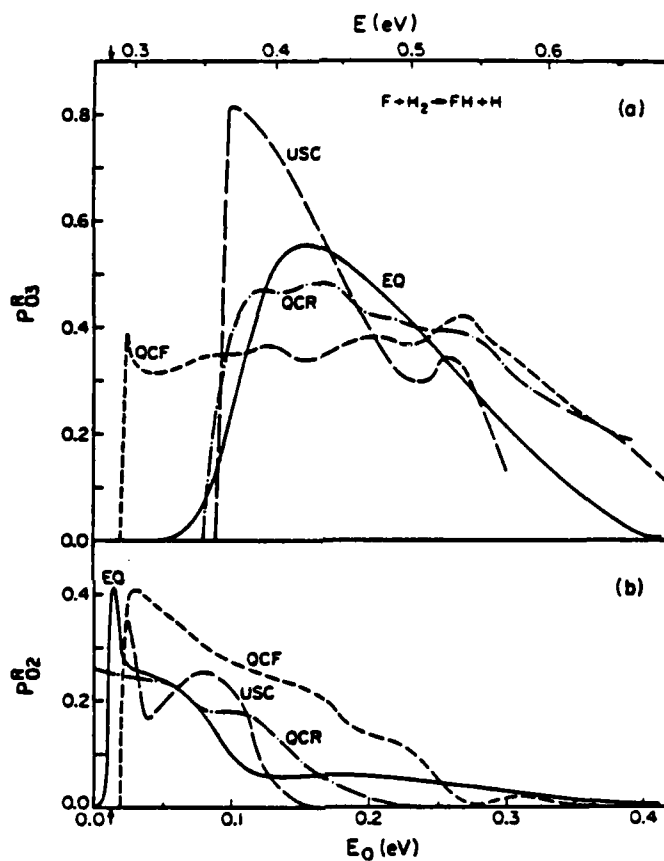


Fig. 16. Exact quantum (EQ), quasi-classical forward (QCF), quasi-classical reverse (OCR), and uniform semiclassical (USC) reaction probabilities P_{03}^a (a) and P_{02}^a (b), as a function of initial relative translational energy E_0 and total energy E , for the collinear $F + H_2 \rightarrow FH + H$ reaction. The arrow in the abscissa indicates the energy at which the $n=3$ state of the FH product opens up.

reaction probabilities are equal. This is not the case for the corresponding quasi-classical ones, because the initial and final states are treated differently. In the quasi-classical forward method, the quantum vibrational energy of the initial state n of the diatomic reagent is included in the initial conditions for the trajectory calculations, and a reaction product P is classified as having a certain vibrational quantum number n' if its final vibrational energy lies in the range $E_n^P - \frac{1}{2}(E_n^P - E_{n-1}^P)$ to $E_n^P + \frac{1}{2}(E_{n+1}^P - E_n^P)$. In the quasi-classical reverse method, the probability for the $n \rightarrow n'$ reactive process is calculated

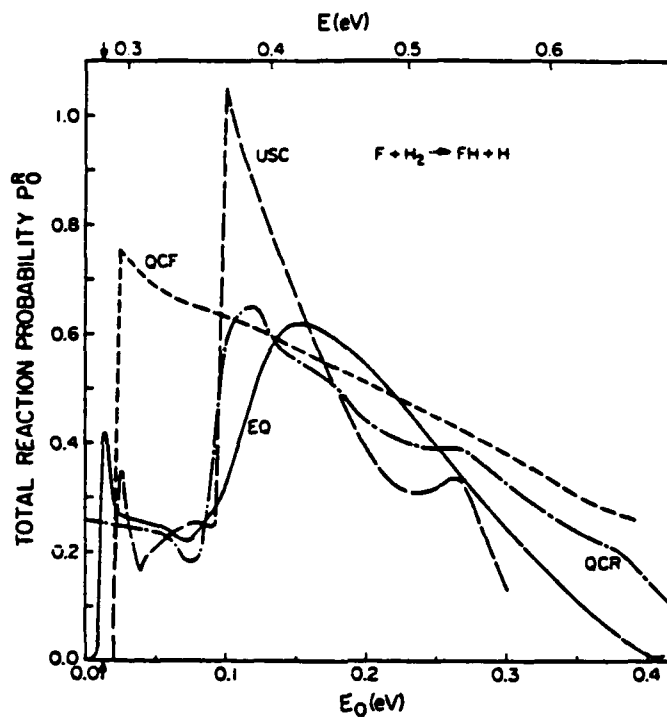


Fig. 17. EQ, QCF, QCR, and USC total reaction probabilities P_0^R for the $F + H_2 \rightarrow FH + H$ reaction. Same curve labels and abscissa as for Fig. 16.

by integration from the initial vibrational state n' of the products to the final state of the reagents R , which are defined as being in state n if their vibrational energy is in the range $E_n^R - \frac{1}{2}(E_n^R - E_{n-1}^R)$ to $E_n^R + \frac{1}{2}(E_{n+1}^R - E_n^R)$. As a result of this asymmetry in the manner in which the reagent and product states are handled, the QCF and QCR methods lead to different reaction probabilities. The usual QC method is the forward one, but Fig. 16 shows that for the collinear $F + H_2$ system, the reverse is a better approximation to the EQ results. Because of this somewhat arbitrary way of quantizing the final states of the products in the QC method, it is perhaps more appropriate to consider the total reaction probability P_n^R from state n of the reagents to all accessible states of the products. This is done in Fig. 17, which shows that P_0^R (QCF) is significantly different from P_0^R (EQ), and therefore that quantum effects are quite pronounced in this system. Although the QCR method works better in this case, there is at present no a priori way to know that this will be the case in any other system. Figures 16 and 17 show that the USC method is more successful in the collinear $F + H_2$ system than in the $H + H_2$ system.

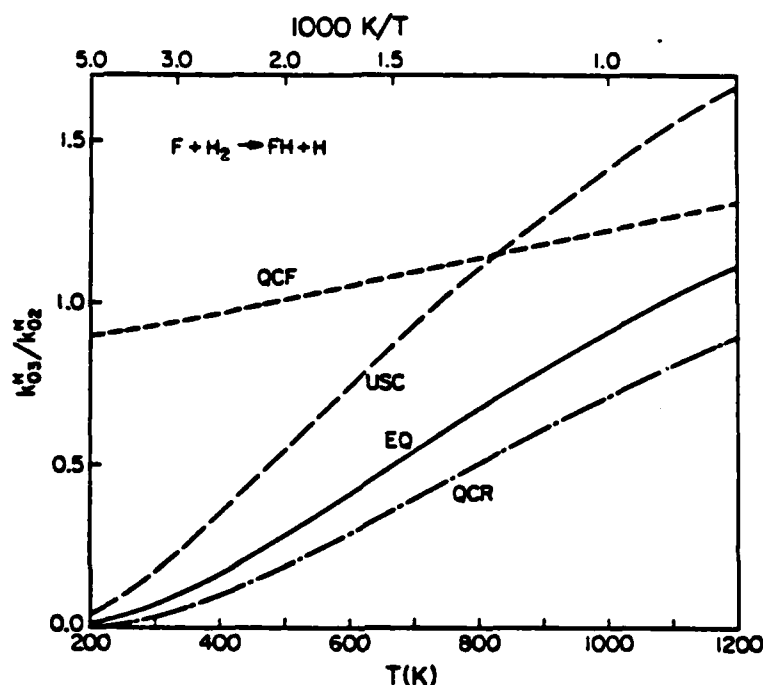


Fig. 18. Ratio of rate constants k_{03}^R/k_{02}^R for the collinear $F + H_2 \rightarrow FH + H$ reaction as a function of temperature. Same curve labels as for Fig. 16.

A question of practical interest is what the ratio k_{03}^R/k_{02}^R of the translationally averaged thermal rate constants of the $n = 0 \rightarrow n' = 3$ and $n = 0 \rightarrow n' = 2$ reactive processes is. The answer to this question is important in determining the extent to which the reactive process will generate a population inversion of the FH $n' = 3$ and $n' = 2$ product states. In Fig. 18 we have plotted this ratio as a function of temperature for the EQ, USC, QCF, and QCR results. As can be seen, the latter three are appreciably different from the former, indicating the lack of reliability of quasi-classical or semi-classical methods in predicting quantitatively the magnitude of population inversions in this chemical reaction. One should therefore be very cautious in using such approximate methods in the 3-PD world.

Another interesting question concerns itself with the extent to which quantum effects in the $F + D_2$ system are less pronounced than in the $F + H_2$ system. The FD quantum states to be considered, in comparison with the FH $n' = 2$ and 3 states, are the $n' = 3$ and 4 states, respectively, for the reasons mentioned at the beginning of this section. In Figs. 19-21 we

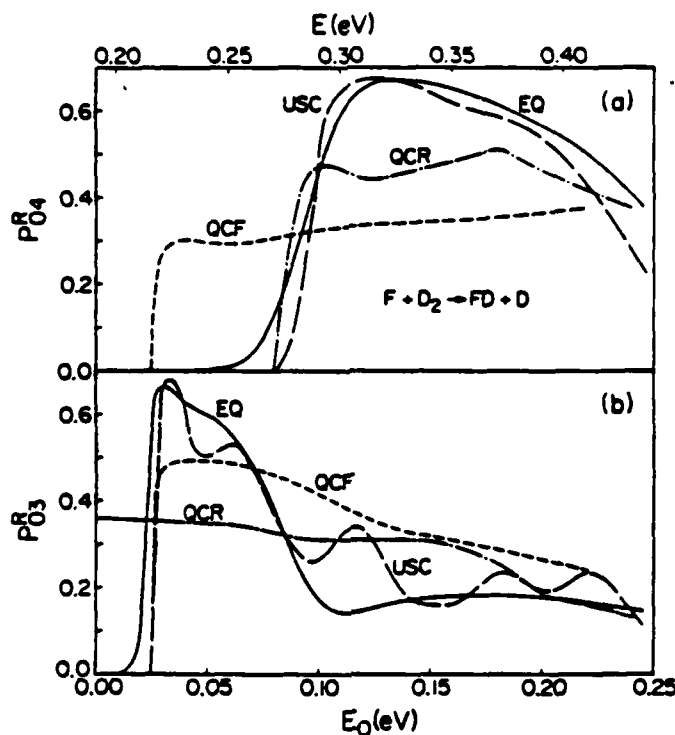


Fig. 19. EQ, QCF, QCR, and USC reaction probabilities P_{04}^R (a) and P_{03}^R (b) for the collinear $F + D_2 \rightarrow FD + D$ reaction. Same curve labels and abscissa as for Fig. 16.

have plotted, for the $F + D_2$ collinear system, the curves corresponding to the $F + H_2$ system (Figs. 16–18). As can be seen, the quantum effects are noticeably decreased. In particular, the spike appearing in the P_{03}^R (EQ) curve of Fig. 16, at low translational energies, and which is due to a Feshbach resonance, is barely noticeable in the P_{04}^R (EQ) curve of Fig. 19. Nevertheless, Fig. 21 still displays significant differences between the EQ and QC rate constant ratios, indicating that quantum effects are still quite appreciable in this system. The USC ratio, however, is very close to the EQ ratio.

We conclude that the collinear $F + H_2$ and $F + D_2$ systems display significant quantum effects that can be reproduced to a certain extent by the uniform semiclassical approach. However, quasi-classical trajectory methods are inappropriate for a quantitative determination of the disposal of energy in the reaction products for this system.

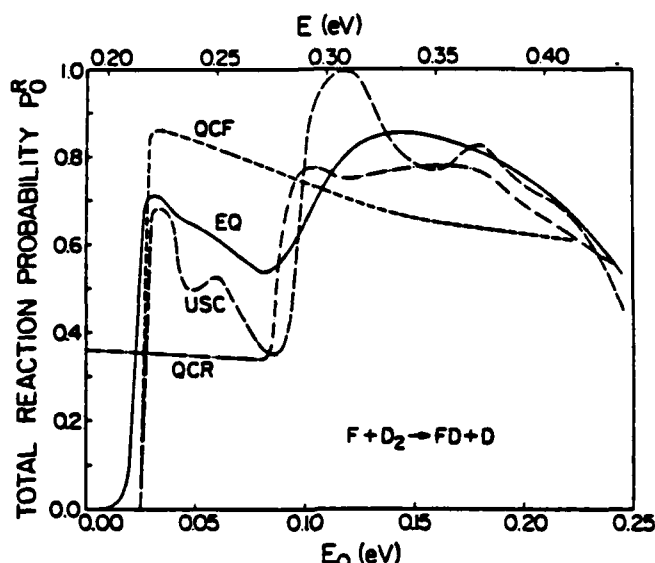


Fig. 28. EQ, QCF, QCR, and USC total reaction probabilities P_0^R for the collinear $F + D_2 \rightarrow FD + D$ reaction. Same curve labels and abscissa as for Fig. 16.

2. Dynamic Resonances

The spike in the EQ curve of Fig. 16b, at a translational energy just above threshold, is due to a dynamic resonance (Latham *et al.*, 1978; Kuppermann, 1981). Some of its characteristics in the three-dimensional world have recently been investigated by an angular momentum decoupling approximation (Redmon and Wyatt, 1979). This resonance seems to be superimposed on a large, direct reaction contribution. However, for the $F + HD \rightarrow FH + D$, $FD + H$ reaction probabilities depicted in Fig. 22 (Schatz *et al.*, 1975b), we see strong evidence of a pure resonance in the $n = 2$ $FH + D$ product channel, near threshold energy, whereas none appears in the $FD + H$ product channels. This system is ideally suited for an experimental detection of such resonances. It is expected that in the three-dimensional world the differences between these two product channels will not be as pronounced, but still very significant. At the resonance energy the angular distribution of the $v = 2$ FH product is expected to be nonbackward-peaked oscillatory, due to the likelihood that the resonance will affect only some of the partial waves that contribute to the reaction (see Section III, H, 8), whereas at other energies the direct process should produce backward-peaked nonoscillatory angular distributions. In addition, at nonresonant energies much less FH product should be observed than at resonance. Finally, the resonant energy in the

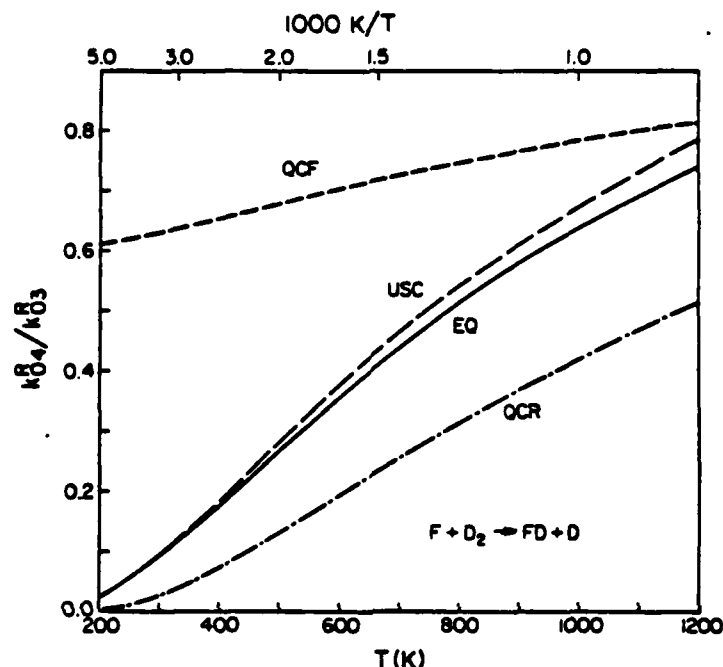


Fig. 21. Ratio of rate constants k_{04}^R/k_{03}^R for the collinear $F + D_2 \rightarrow FD + D$ reaction as a function of temperature. Same curve labels as for Fig. 16.

3-PD world should be shifted toward higher energies by twice the zero-point energy of the bending mode of the most-contributing strong interaction configuration (see Section III,H,8). These constitute theoretical predictions of the existence of a dynamic resonance in the $F + HD (v = 0) \rightarrow FH (v' = 2) + D$ reaction channel and of the fingerprint of such a resonance, as well as the absence of one in the $F + DH (v = 0) \rightarrow FD (v' = 3, 4) + H$ channels. The prospect that such predictions may be verified experimentally and lead to information about some of the details of the corresponding potential energy surface in the strong interaction region is a very exciting one.

H. ELECTRONICALLY NONADIABATIC EXCHANGE REACTIONS

When a chemical reaction occurs that involves a change in the electronic state of the triatomic system, the theoretical formulation of the exchange reaction problem given by Eqs. (4) and (8) must be extended. In one form of the general theory, we consider a family of electronically diabatic potential energy surfaces as well as a family of coupling potential energy surfaces.

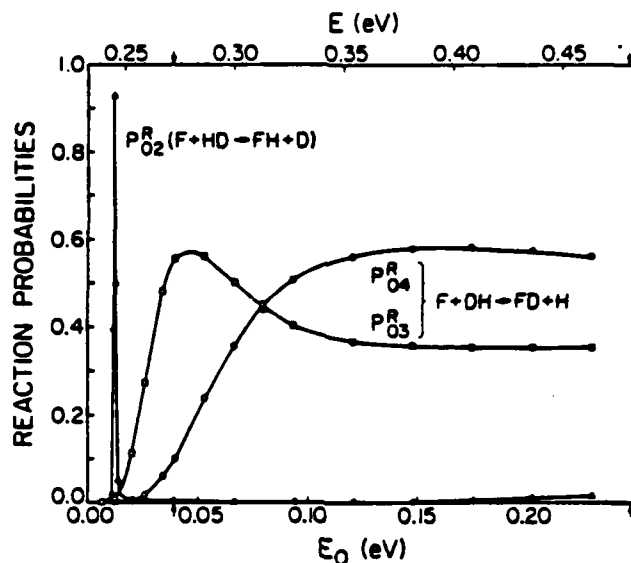


Fig. 22. Accurate quantum reaction probabilities P_{02}^R for the $F + HD \rightarrow FH + D$ collinear reaction and P_{03}^R and P_{04}^R for the $F + DH \rightarrow FD + H$ collinear reaction as a function of initial relative translational energy E_0 and total energy E (relative to the minimum in the HD diatomic potential curve). The arrow near 0.04 eV in the lower abscissa indicates the energy at which the $n = 3$ HF state opens up.

If the lowest two of these surfaces interact and the others are at energies that are high compared to the collision energy being considered, we may use the two-state approximation, in which Eq. (4), in scaled coordinates, is replaced by the system of equations

$$\left[-\frac{\hbar^2}{2\mu} \left(\frac{\partial^2}{\partial R_e^2} + \frac{\partial^2}{\partial r_e^2} \right) + V_1(R_e, r_e) - E \right] \psi_1(R_e, r_e) = -V_{12}(R_e, r_e) \psi_2(R_e, r_e) \quad (58)$$

$$\left[-\frac{\hbar^2}{2\mu} \left(\frac{\partial^2}{\partial R_e^2} + \frac{\partial^2}{\partial r_e^2} \right) + V_2(R_e, r_e) - E \right] \psi_2(R_e, r_e) = -V_{21}(R_e, r_e) \psi_1(R_e, r_e)$$

where V_1 and V_2 are the two electronically diabatic surfaces being considered and $V_{12} = V_{21}$ is the coupling-potential energy surface. The corresponding nuclear motion wave functions satisfy the asymptotic conditions

$$\begin{aligned} \psi^{iA'n_A} &\sim \sum_{\lambda n_A} [\exp(-ik_{i\lambda n_A} R_\lambda) \delta_{\lambda n_A}^{iA'n_A} + \exp(ik_{i\lambda n_A} R_\lambda) f_{i\lambda n_A}^{iA'n_A}] \phi_{i\lambda n_A}(r_\lambda), \\ &\quad i = 1, 2 \\ \psi^{jA'n_A} &\sim \sum_{\lambda n_A} f_{j\lambda n_A}^{iA'n_A} \exp(ik_{j\lambda n_A} R_\lambda) \phi_{j\lambda n_A}(R_\lambda), \quad j \neq i, \quad j = 1, 2 \end{aligned} \quad (59)$$

where the $f_{j\lambda\mu\lambda'}^{i\lambda'\mu\lambda'}$ terms represent the scattering amplitudes from state $\phi_{i\lambda'\mu\lambda'}(r_\lambda)$ of the reagents to state $\phi_{j\lambda\mu\lambda}(r_\lambda)$ of the products, with $i, j = 1, 2$. These equations can be solved by a straightforward generalization of the methods outlined in Section II.E.

The reaction of Ba atoms with N_2O molecules produces BaO molecules in its ground $X^1\Sigma$ and excited $a^3\Pi$ states. This reaction was qualitatively modeled as a collinear two-electronic-state process with N_2 treated as a single atom of atomic weight 28 and the O atom occupying the middle position (J. M. Bowman and A. Kuppermann, unpublished results, 1973; Bowman, 1975). The objective of this study was *not* to obtain agreement with experiment but, instead, to investigate the dynamic properties of this model and to test the validity of approximate methods on the same model.

A ground (singlet) state and an excited (triplet) state LEPS electronically diabatic surface, V_0 and V_1 , respectively, as well as an interaction potential surface, V_i , due to spin-orbit interactions, were assumed (J. M. Bowman and A. Kuppermann, unpublished results, 1974). These three surfaces are depicted in Figs. 23-25. In them, coordinate R_1 is the barium-oxygen (non-scaled) internuclear distance and R_2 is the oxygen-nitrogen distance. The lines in these figures along which solid squares are placed represent the intersection between V_0 and V_1 . V_0 has a barrier whose height is 0.05 eV with respect to the bottom of the N_2O ground-state potential energy curve, and its position was placed in the near-asymptotic region of the product channel. V_i was also made 0.2-eV exothermic. This is substantially lower than the experimentally determined 4-eV exothermicity, in order to keep the number of open exit channels to a manageable amount while preserving the characteristics of the surface crossing. For the total energies considered, V_i is energetically inaccessible except in the near-asymptotic and asymptotic regions of the product channel. V_i has a maximum value of 0.05 eV and is localized along the seam of the intersection of V_0 and V_1 .

The range of initial relative kinetic energies considered in these calculations was 0.0-0.12 eV. In this range the number of open vibrational states of the model $BaO(X^1\Sigma)$ is between four and six and that for the model $BaO(a^3\Pi)$ between one and three. Calculations were also performed (Bowman *et al.*, 1976) using the trajectory surface-hopping method (in the simple Landau-Zener version) of Tully and Preston (1971).

The result of some of these calculations is given in Fig. 26. $P_{i'n \rightarrow i'n'}^R$ is the reaction probability from state i, n of N_2O to state i', n' of BaO, where n and n' are vibrational quantum numbers, i or $i' = 1$ refers to the ground electronic states and $i' = 2$ to the triplet states. It can be seen that for E_0 , less than 0.05-eV $P_{10 \rightarrow 10}^R$ is the dominant reaction probability and that the quantal and quasi-classical results agree in average for this electronically adiabatic transition. The existence of quantum oscillations in this and the other $P_{i'n \rightarrow i'n'}^R$ versus

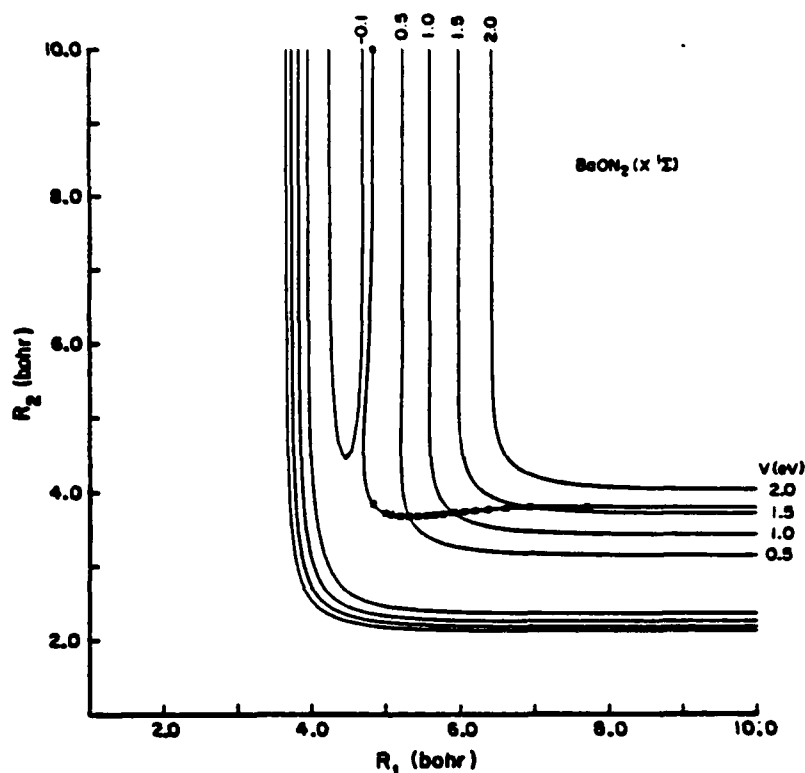


Fig. 23. Potential energy surface for the $X^1\Sigma$ state of a model collinear $BaON_2$ system. R_2 is the O- N_2 unscaled distance and R_1 , the Ba-O distance.

energy curves is compatible with the de Broglie wavelength analysis outlined in Section II.C (Bowman *et al.*, 1976).

Comparison of the quantal and quasi-classical electronically nonadiabatic reaction probabilities P_{10-20}^a of Fig. 26d shows fairly good average agreement for E_0 between 0.05 and 0.07 eV, but at somewhat higher energies, the quasi-classical result differs significantly from the accurate quantal result. This disagreement should be due at least in part to a shortcoming of the simple Landau-Zener surface-hopping model used in these calculations. The seam between the singlet and triplet surfaces used is located in the product channel and is displaced from the equilibrium internuclear position of BaO toward greater internuclear distances. This means that the ground-electronic-state BaO product must have about one quantum of vibrational energy before the seam can be reached classically. This should result in a significant decrease of the amount of quasi-classical surface hopping in comparison with

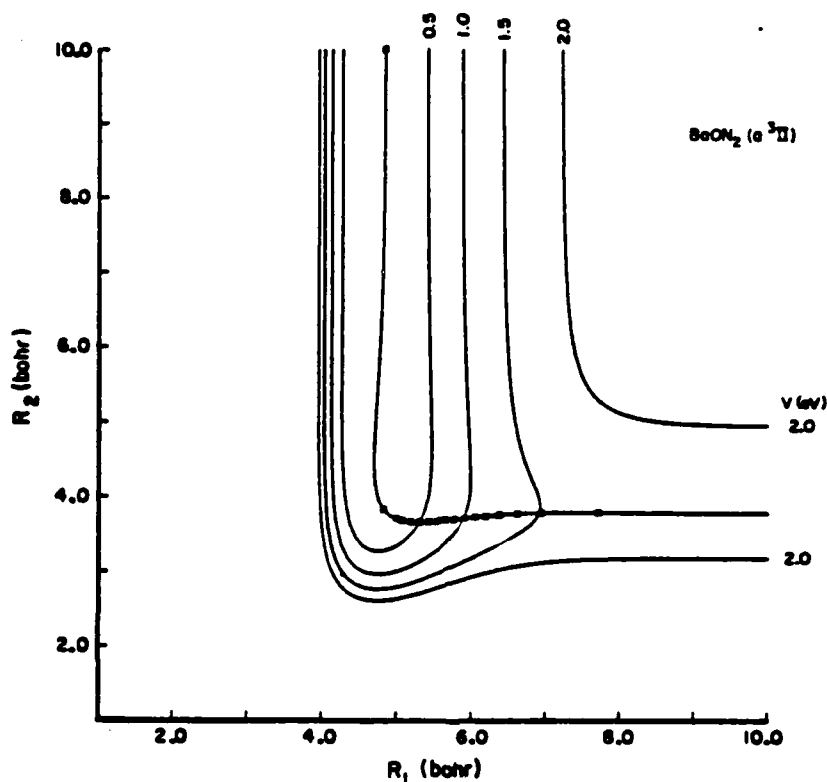


Fig. 24. Potential energy surface for the $a^3\Pi$ state of model collinear BaON_2 system. Coordinates have the same meaning as in Fig. 23.

the quantum situation, since in the latter case the seam is felt over a wider range of internuclear distances. Such analysis is consistent with the fact that the quantal and quasi-classical P_{10-20}^a effective thresholds are approximately equal to the corresponding values for the electronically adiabatic $10 \rightarrow 11$ and $10 \rightarrow 12$ reactive processes that produce vibrationally excited ground electronic state products. This suggests a correlation between vibrational excitation of $\text{BaO} (X^1\Sigma)$ and formation of $\text{BaO} (a^3\Pi)$.

One may improve the surface-hopping model by permitting hopping to occur from a band around the seam rather than at the seam only. Even then, this first-order perturbation model may not work too well for systems for which the electronically nonadiabatic transition probabilities are large. Caution in using quasi-classical methods must be exercised even for systems as heavy as the present one. The large quantum effects resulting from these

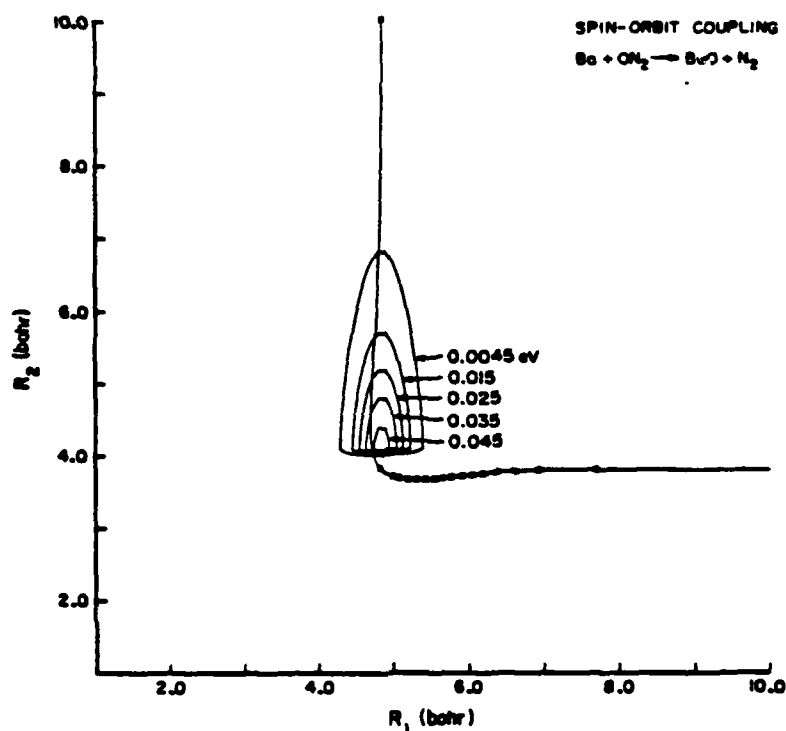


Fig. 25. Spin-orbit interaction potential energy surface for model collinear BaON_2 system. Coordinates have the same meaning as in Fig. 23.

collinear calculations will not necessarily disappear in going to the real three-dimensional world.

I. COLLISION-INDUCED DISSOCIATION AND THREE-BODY RECOMBINATION PROCESSES

The problem of calculating the quantum probabilities of the collision-induced dissociation process $A + BC \rightarrow A + B + C$ and of its reverse three-body recombination is conceptually a very difficult one. The reason is that in the three-body channel, the motion associated to both the R_e and r_e coordinates is not quantized, involving thereby a double continuum of states.

About 20 years ago, Delves (1959, 1960) suggested that the problem could be reformulated in a system of coordinates involving only one continuum.

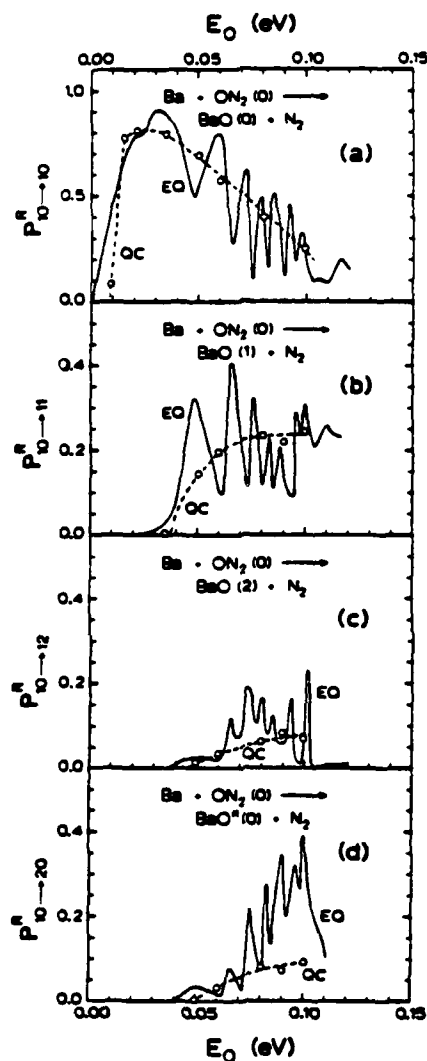


Fig. 26. Reaction probabilities for the model collinear $\text{Ba} + \text{ON}_2 \rightarrow \text{BaO}(n) + \text{N}_2$ as a function of initial relative kinetic energy E_0 . BaO and BaO^* represent the $X^1\Sigma$ and a $^3\Pi$ states of the diatomic product, respectively. (a)–(c) Reaction probabilities to form BaO in $n' = 0, 1$, and 2 , respectively, from ground vibrational state reagent ON_2 . (d) Reaction probabilities to form BaO^* in $n' = 0$ from ground vibrational state reagent. The exact quantum (EQ) and quasi-classical (QC) probabilities are represented by solid and dashed curves, respectively.

These coordinates are depicted in Fig. 3. They are the circular polar coordinates ρ, α indicated. At a fixed ρ , $V(\rho, \alpha)$ becomes practically infinite for $\alpha = 0$ and $\alpha = \alpha_{\max}$ due to the practically infinite repulsive interatomic interactions occurring when $r_s = 0$ (for which B and C coincide) or $r_r = 0$ (for which A and B coincide). This is true even for values of ρ corresponding to points in the dissociative plateau A + B + C region of Fig. 3. As a result, the eigenfunctions of the Hamiltonian

$$h(x; \rho) = -\frac{\hbar^2}{2\mu\rho^2} \frac{d^2}{d\alpha^2} + V(\rho, \alpha) \quad (60)$$

for constant ρ constitute a complete discrete (but infinite) set of orthonormal basis functions in terms of which the scattering wave function $\psi(\rho, \alpha)$ may be expanded, resulting in a discrete (but infinite) set of coupled channel equations, even at dissociative energies, which may be solved by techniques analogous in spirit to those outlined in Section II.E. Comparison of the results of such calculations with corresponding quasi-classical trajectory ones are useful in establishing the conditions under which the latter may give reliable results (Kaye and Kuppermann, 1981).

III. The Quantum Dynamics of Three-Dimensional Reactive Triatomic Systems

In this section we generalize the description of the electronically adiabatic reactive scattering of collinear triatomic systems to three physical dimensions (3-PD). The corresponding formalisms are analogous. The restrictions on the total energy will be the same as those for the 1-PD systems. One difference is that the partial first derivatives with respect to the two scalar distances are replaced by the gradients with respect to the corresponding position vectors, and appropriate spherical scattered waves replace the corresponding collinear plane waves. An additional difference is that for A + BC reagents, two reactive product arrangement channels (AB + C and AC + B) are allowed, rather than only one. This results in an interesting "bifurcation" problem, not encountered in the collinear case. The scattering and reactance matrices are introduced analogously to the 1-PD case, after an appropriate partial-wave expansion.

A. SCALED COORDINATES

It is convenient to begin by introducing the 3-PD counterpart of the 1-PD scaled coordinates. We label the three atoms A = A_s , B = A_r , and C = A_t .

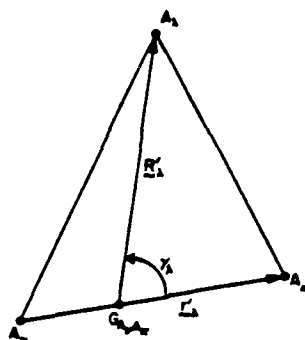


Fig. 27. Relative position vectors for triatomic system in three physical dimensions (3-PD).

Let $\lambda\nu\kappa$ be a cyclic permutation of the indices $\alpha\beta\gamma$. We define the λ coordinates ($\lambda = \alpha, \beta, \gamma$) as r'_λ , the internuclear vector from A_ν to A_κ , and R'_λ , the position vector of A_λ with respect to the center of mass $G_{A_\nu A_\kappa}$ of the $A_\nu A_\kappa$ diatom. The angle in the $0-\pi$ range between these two vectors is labelled γ_λ . These coordinates are displayed in Fig. 27. In terms of them, the nuclear motion Hamiltonian, after removal of the motion of the center of mass of the system, is

$$H = -\frac{\hbar^2}{2\mu_{\lambda,\nu\kappa}} \nabla_{R'_\lambda}^2 - \frac{\hbar^2}{2\mu_{\nu\kappa}} \nabla_{r'_\lambda}^2 + V_\lambda(R'_\lambda, r'_\lambda, \gamma_\lambda) \quad (61)$$

where the reduced masses are analogous to those given by Eq. (3) and $\nabla_{R'_\lambda}^2$ and $\nabla_{r'_\lambda}^2$ are the Laplacian operators with respect to the coordinates R'_λ and r'_λ , respectively. The potential energy function now depends on γ_λ , in addition to R'_λ and r'_λ . Its topological characteristics will be described in the next section. We now introduce the scaled position vector coordinates R_λ, r_λ as a three-dimensional generalization of Eq. (10):

$$R_\lambda = a_\lambda R'_\lambda, \quad r_\lambda = (a_\lambda)^{-1} r'_\lambda, \quad a_\lambda = (\mu_{\lambda,\nu\kappa}/\mu_{\nu\kappa})^{1/4}, \quad \lambda = \alpha, \beta, \gamma \quad (62)$$

In terms of these coordinates, Eq. (61) becomes

$$H = -(\hbar^2/2\mu)(\nabla_{R_\lambda}^2 + \nabla_{r_\lambda}^2) + V_\lambda(R_\lambda, r_\lambda, \gamma_\lambda) \quad (63)$$

The reduced mass μ , which is independent of λ , is the same as that given for the collinear case by Eq. (12).

The transformation from λ coordinates to ν coordinates is now given by

$$\begin{pmatrix} R_\nu \\ r_\nu \end{pmatrix} = \begin{pmatrix} \cos \alpha_{\nu\lambda} & -\sin \alpha_{\nu\lambda} \\ \sin \alpha_{\nu\lambda} & \cos \alpha_{\nu\lambda} \end{pmatrix} \begin{pmatrix} R_\lambda \\ r_\lambda \end{pmatrix} \quad (64)$$

where

$$\begin{aligned}\cos \alpha_{v\lambda} &= -\{m_\lambda m_v / [(m_\lambda + m_v)(m_v + m_\lambda)]\}^{1/2}, \\ \sin \alpha_{v\lambda} &= \{m_v M / [(m_\lambda + m_v)(m_v + m_\lambda)]\}^{1/2}\end{aligned}\quad (65)$$

Equations (64) and (65) represent a rigid rotation in the six-mathematical dimensional (6-MD) configuration space spanned by the Cartesian components of R_λ and r_λ . This is not the case for the corresponding transformation of the unscaled coordinates. The λ Laplacian operators have the property

$$\nabla_{R_\lambda}^2 + \nabla_{r_\lambda}^2 = \nabla_{R_\lambda}^2 + \nabla_{r_\lambda}^2 = \nabla_{R_\lambda}^2 + \nabla_{r_\lambda}^2 = \nabla^2 \quad (66)$$

where ∇^2 is the 6-MD scaled configuration space Laplacian, which, as for 3-MD, is invariant under rotations. With this notation, Eq. (63) can be rewritten as

$$H = -(\hbar^2/2\mu) \nabla^2 + V \quad (67)$$

This Hamiltonian describes the motion of a single particle P of mass μ in the 6-MD scaled configuration space subject to the potential V . Therefore, the motion of the three-particle ABC system in 3-PD space is isomorphic to the motion of P in this 6-MD space. As a result, the de Broglie wavelength analysis of Section II,C continues valid for the 3-PD case, as long as the change in local wave number is examined in the proper 6-MD space. This isomorphism permits an extension of the techniques used to treat the quantum mechanics of single particles in 3-PD space to three-particle (or actually, to many-particle) systems.

B. POTENTIAL ENERGY SURFACE MAPPING IN SYMMETRIZED HYPERSPHERICAL COORDINATES

In order to facilitate an understanding of the nature of the 3-PD reactive scattering problem, it is useful to be able to visualize the spacial characteristics of the potential energy surface $V_\lambda(R_\lambda, r_\lambda, \gamma_\lambda)$. For the collinear case, for which $\gamma_\lambda = \pi$ or 0, these characteristics were displayed in Fig. 3, in which contour lines of constant V were depicted in the 2-MD scaled configuration space R_λ, r_λ . In the present case, the configuration space is six dimensional, but V is a function of three variables only. It would be convenient therefore to display surfaces of constant V in an appropriately chosen 3-MD space in which for every configuration of the three atoms, there would correspond one and one only point Q . Since, for $\gamma_\lambda = \pi$, that space was 2-MD Cartesian, a first attempt would be to consider $R_\lambda, r_\lambda, \gamma_\lambda$ as the cylindrical coordinates of Q , such that for configurations having a constant γ_λ , $V(R_\lambda, r_\lambda, \gamma_\lambda = \text{constant})$ would be represented by contour lines on the $\gamma_\lambda = \text{constant}$ half-plane

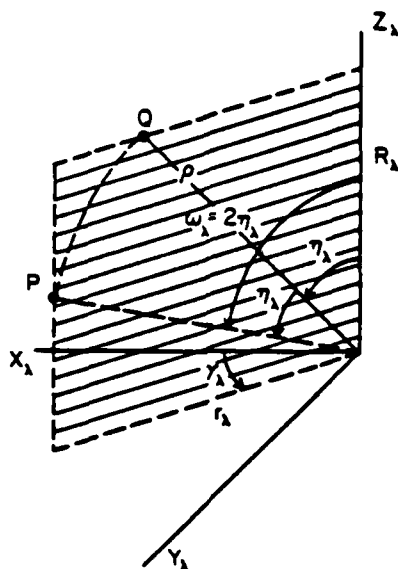


Fig. 28. Cylindrical and spherical polar coordinates for mapping potential energy function for noncollinear triatomic system.

depicted in Fig. 28. If that were done, the spherical polar coordinates of the same point Q would be ρ , η_1 , and γ_1 , where

$$\rho = (R_1^2 + r_1^2)^{1/2}, \quad \eta_1 = \tan^{-1}(r_1/R_1), \quad 0 \leq \eta_1 \leq \frac{1}{2}\pi \quad (68)$$

The quantity ρ is invariant with respect to a $\lambda \rightarrow \nu$ transformation and is called a hyperradius. These cylindrical and spherical polar coordinates are also displayed in Fig. 28. A typical equipotential surface is displayed schematically in Fig. 29, at an energy below the dissociation energy. This mapping suffers from two crucial defects. First, it does not have the basic one-to-one correspondence property between configurations and points Q . Indeed, for collinear configurations in which A_1 coincides with the center of mass of A_2A_3 , γ_1 is arbitrary. Therefore, all points on the circle C on the X_1Y_1 plane, whose radius is the scaled A_2A_3 distance, are associated with that single configuration. Second, even if the three atoms A_1 , A_2 , and A_3 are identical, as for the H_3 system, the equipotentials of V below the dissociation energy would still have the general shape indicated in Fig. 29, with the shape of the $A_1 + A_2A_3$ region (in which A_1 is not too far from A_2A_3) distinct from the shape of the $A_2 + A_3A_1$ region obtained by an interchange of atoms A_1 and A_2 . In other words, the equipotentials of V , in this map, do not have

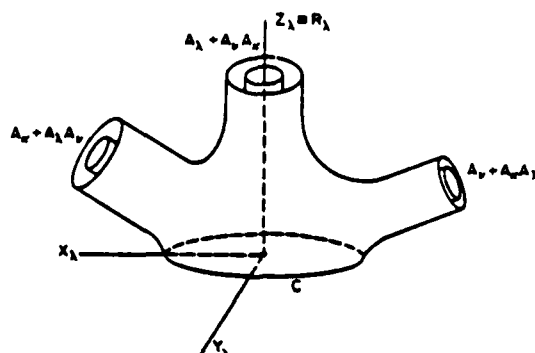


Fig. 29. Equipotential surface for noncollinear $A_1A_1A_1$ triatomic system in spherical polar coordinates $\rho = (R_1^2 + r_1^2)^{1/2}$, $\eta_1 = \tan^{-1}(r_1/R_1)$, and γ_1 .

the symmetry we would desire with respect to the interchange of identical atoms.

A way to eliminate the first of these defects is to choose for the spherical polar coordinates the quantities ρ , $\omega_1 = 2\eta_1$ and γ_1 , as indicated in Fig. 28 by point P. This "umbrella opening" transformation on ρ , η_1 , γ_1 (in which the colatitudinal angle of every point is doubled) collapses the circles C of Fig. 29 into a single point located on the negative half of the Z_1 axis (see Fig. 30). It turns out that in this same ρ , ω_1 , γ_1 system of polar coordinates, the equipotential surfaces are also symmetric with respect to the interchange of identical atoms! (Kuppermann, 1975). Therefore, for the H_3 system, they display the symmetry properties of the C_{3v} -point group. In Fig. 30 we have depicted schematically an equipotential surface at an energy below the

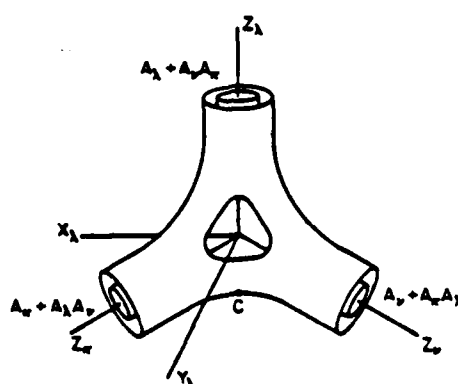


Fig. 30. Equipotential surface for noncollinear $A_1A_1A_1$ triatomic system in spherical polar coordinates $\rho = (R_1^2 + r_1^2)^{1/2}$, $\omega_1 = 2 \tan^{-1}(r_1, R_1)$, and γ_1 .

dissociation energy for a system of three identical atoms. Actually, we should have indicated only the $Y_1 \geq 0$ half-space, since γ_1 lies in the range $0-\pi$. However, we reflected this surface through the X_1Z_1 plane to facilitate visualization. As a result, every triatom configuration (except those for which $\gamma_1 = 0$ or $\gamma_1 = \pi$) is represented in Fig. 30 by a pair of points, symmetric with respect to that plane. The hole around the origin is due to the strong repulsion occurring at configurations for which all three atoms are close together.

This mapping of V has an additional property that is of great usefulness. A $\lambda \rightarrow \nu$ coordinate transformation in the 3-MD $X_1Y_1Z_1$ internal configuration subspace of Fig. 30 is a rigid rotation around the Y_1 axis (Kuppermann, 1975). This means that this transformation is equivalent to moving the Z_1 axis to the Z_ν position indicated in Fig. 30, while otherwise not changing the shape of the equipotentials. This shape invariance with respect to coordinate transformations indicates that this map represents all regions of configuration space in an equivalent way, regardless of the choice of λ . For this reason, we call the coordinates ρ, ω_1, γ_1 *symmetrized* hyperspherical coordinates. At large values of R_1 , the rotational motion of A_1A_ν is indicated by a rotation of the representative point Q around the Z_1 axis, the vibration of A_1A_ν by an oscillation of Q perpendicular to that axis, and the approach of A_1 to A_1A_ν by a motion of Q parallel to the same axis. Similar statements are valid for the $A_\nu + A_\nu A_1$ and $A_\nu + A_1 A_\nu$ configurations, with the Z_1 axis replaced by Z_ν and Z_ν , respectively. Therefore, a nonreactive collision would correspond to approaching the origin from the large Z_1 direction and then reversing its general direction, whereas a reactive one involves having Q approach the same way but move out along the Z_ν or Z_ν directions while rotating and vibrating around those axes. The dynamical details of these processes depends on the internal topology of these equipotentials, i.e., the nature of the passageways between the different arrangement channel regions of Fig. 30.

In order to visualize the nature of this topology, we display in Fig. 31 cuts of the equipotentials of V by the $X_\nu Z_\nu$ ($\gamma_\nu = 0, \pi$) and $Y_\nu Z_\nu$ ($\gamma_\nu = \pi/2, -\pi/2$) planes for the Porter and Karplus (1964) H_3 potential energy surface. The bottom part of Fig. 31b corresponds to the region halfway between configurations $A_1 + A_1 A_1$ and $A_1 + A_1 A_1$. All classically allowed pathways leading from one to the other of these configurations, at total energies not exceeding 0.6 eV, must pass through the hatched area enclosed by the corresponding equipotential. The 30° angle between the negative Z_ν axis and the line (not depicted) from the origin O tangent to the 0.6 eV equipotential is roughly indicative of the angular deviation from collinearity that classically still permits a reaction to occur at that total energy. Therefore, this mapping gives an intuitive feeling for the dynamic properties of the corresponding

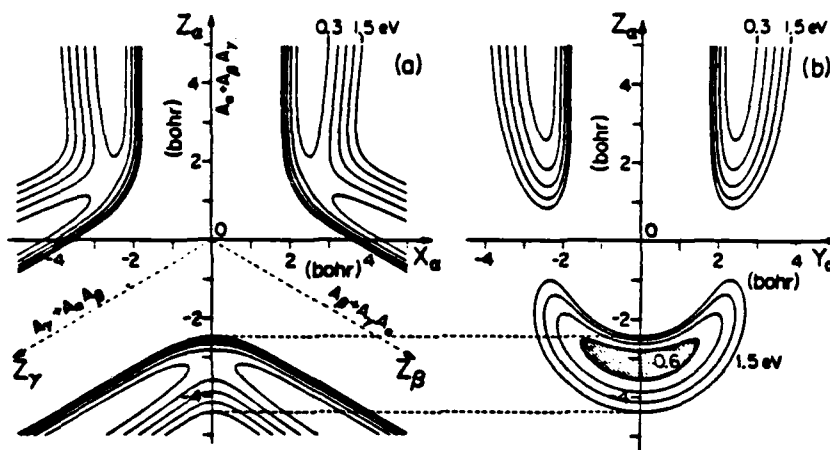


Fig. 31. Cuts of equipotential surfaces for H_3 . (a) Cut through $X_a Z_a$ plane. (b) Cut through $Y_a Z_a$ plane. The origin of measurement of the energy is the minimum of the isolated H_2 diatomic potential energy curve. The curves are intersections of the equipotentials with these planes. Their energies range from 0.3 to 1.5 eV in steps of 0.3 eV, as indicated on top of figure.

system. It is also very helpful in developing theoretical approaches to the solution of the quantum reactive scattering problem, as indicated in Section III.G.

C. REACTIVE-SCATTERING FORMALISM

We start out by choosing a system of coordinates that spans the 6-MD configuration space in which the motion of the triatomic system, after removal of the motion of the center of mass, takes place. Let $Oxyz$ be a system of coordinates whose origin O is the center of mass of the system and whose axes are parallel to a system of laboratory-fixed axes. We will call $Oxyz$ the laboratory-fixed system. The spherical polar coordinates of the scaled R_1 in this system are R_1, θ_1, ϕ_1 . Let us also define a body-fixed coordinate system $OX_1Y_1Z_1$ (not to be confused with the axes of Figs. 28–31) obtained by rotating the $Oxyz$ axis by the Euler angles $\phi_1, \theta_1, 0$. The resulting OZ_1 axis points along the R_1 direction, whereas the OY_1 axis is in the Oxy plane. The $Oxyz$ and $OX_1Y_1Z_1$ axes are displayed in Fig. 32. The spherical polar coordinates of r_1 in the space-fixed system are $r_1^s = (r_1, \theta_{r_1}, \phi_{r_1})$ and in the body-fixed system are $r_1^b = (r_1, \gamma_1, \psi_1)$ where γ_1 is, as before, the angle between R_1 and r_1 and ψ_1 is a tumbling angle around the (R_1, Oz) plane.

In this presentation we chose body-fixed coordinates because they lead to

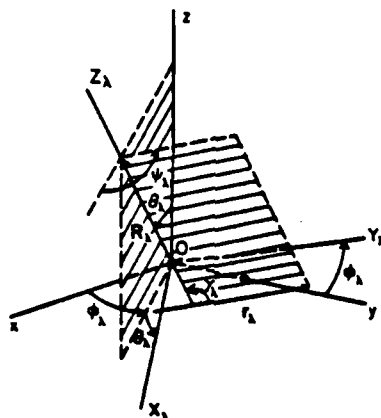


Fig. 32. Body-fixed and space-fixed coordinates for triatomic system in three physical dimensions.

simpler final expressions for the cross sections and to a simpler solution to the bifurcation problem. However, space-fixed coordinates can also be used (Pack, 1974).

In terms of these body-fixed coordinates, we wish to find the solutions of the Schrödinger equation:

$$H\psi^{\lambda'n\lambda} = E\psi^{\lambda'n\lambda} \quad (69)$$

which satisfy the asymptotic condition for large R_λ ($\lambda = \alpha, \beta, \gamma$)

$$\begin{aligned} \psi^{\lambda'n\lambda} \sim & \exp(ik_{\lambda'c\lambda,j\lambda} R_{\lambda'}) \Phi_{\lambda'n\lambda}(r_{\lambda'}^{\text{eff}}) \\ & + \sum_{\lambda n \lambda'} \int_{\lambda n \lambda'}^{\lambda' n \lambda'} (\theta_\lambda, \phi_\lambda) (R_\lambda)^{-1} \exp(ik_{\lambda c \lambda j \lambda} R_\lambda) \phi_{\lambda n \lambda}(r_{\lambda}^{\text{eff}}) \end{aligned} \quad (70)$$

In these expressions λ and λ' designate the final and initial arrangement channels, respectively, and n_λ is the set of quantum numbers $c_\lambda, j_\lambda, m_{j_\lambda}$ of the A, A_π isolated diatom where c_λ is the vibrational quantum number, j_λ its rotational angular momentum quantum number, and m_{j_λ} the quantum number associated with the projection of the diatom's rotational angular momentum along the direction of the final relative wave-number vector $k_{\lambda c \lambda j \lambda}$ (i.e., the helicity polarization quantum number) which, as $R_\lambda \sim \infty$, lies in the $\theta_\lambda, \phi_\lambda$ direction. Similarly, $n_{\lambda'}$ represents the corresponding quantum numbers $c_{\lambda'}, j_{\lambda'}, m_{j_{\lambda'}}$ of the initial diatomic reagent A, A_π , where the axis of quantization for $m_{j_{\lambda'}}$ is the direction of the initial relative wave-number vector $k_{\lambda' c \lambda' j_{\lambda'}}$ that has been chosen to lie along the laboratory-fixed Oz

axis. R_{λ_z} is the component of $R_{\lambda'}$ along that axis. As $R_{\lambda'} \sim \infty$, $R_{\lambda'}$ lies in the $-\mathbf{k}_{\lambda'c\lambda'j\lambda'}$ direction, i.e., in the negative Oz direction. In other words, in the helicity representation, the axis of quantization for the reagent and product diatoms are, respectively, the initial and final relative wave-number vectors. This particular choice of representation greatly simplifies the expression for the scattering amplitude given by Eq. (89) of Section III.E.

The $\phi_{\lambda n_A}(r_{\lambda'}^M)$ and $\phi_{\lambda' n_A}(r_{\lambda'}^M)$ in Eq. (70) represent the diatomic product and reagent rovibrational eigenfunctions, respectively, in scaled coordinates, and in the helicity representation; $(R_{\lambda'})^{-1} \exp(ik_{\lambda c\lambda j\lambda} R_{\lambda'})$ represents a spherical radial scattered wave and $\exp(ik_{\lambda'c\lambda'j\lambda'} R_{\lambda'})$ is a plane wave representing the initial relative motion of the atom $A_{\lambda'}$ with respect to the diatomic molecule $A_{\lambda}A_{\lambda'}$, in scaled coordinates; and finally $f_{\lambda n_A}^{\lambda' n_A}(\theta_{\lambda}, \phi_{\lambda})$ is the scaled coordinate scattering amplitude from initial state $\lambda' n_{\lambda'}$ of the reagent to final state λn_{λ} of the product, for initial and final relative atom-diatom wave-number vectors $\mathbf{k}_{\lambda'c\lambda'j\lambda'}$ and $\mathbf{k}_{\lambda c\lambda j\lambda}$, respectively, $\theta_{\lambda} \phi_{\lambda}$ being the polar angles of the latter with respect to the former in the $Oxyz$ system whose Oz axis lies along $\mathbf{k}_{\lambda'c\lambda'j\lambda'}$. The magnitudes of these wave numbers satisfy the energy conservation relation

$$(\hbar^2 k_{\lambda'c\lambda'j\lambda'}^2 / 2\mu) + E_{\lambda'c\lambda'j\lambda'} = (\hbar^2 k_{\lambda c\lambda j\lambda}^2 / 2\mu) + E_{\lambda c\lambda j\lambda} = E \quad (71)$$

$$\lambda = \alpha, \beta, \gamma$$

where $E_{\lambda'c\lambda'j\lambda'}$ and $E_{\lambda c\lambda j\lambda}$ are, respectively, the rovibrational energy of the initial and final diatoms and E is the total energy of the system. The unscaled coordinate scattering amplitude $f_{\lambda n_A}^{\lambda' n_A}(\theta_{\lambda}, \phi_{\lambda})$ is related to the scaled one by

$$f_{\lambda n_A}^{\lambda' n_A}(\theta_{\lambda}, \phi_{\lambda}) = (a_{\lambda})^{-1} (a_{\lambda}/a_{\lambda'})^{1/2} f_{\lambda n_A}^{\lambda' n_A}(\theta_{\lambda}, \phi_{\lambda}) \quad (72)$$

where the a_{λ} terms have been defined in Eq. (62), and the differential cross section for the $\lambda' n_{\lambda'} \rightarrow \lambda n_{\lambda}$ process can be obtained from $f_{\lambda n_A}^{\lambda' n_A}$ by the expression

$$\sigma_{\lambda n_A}^{\lambda' n_A}(\theta_{\lambda}, \phi_{\lambda}) = (v_{\lambda n_A} / v_{\lambda' n_{\lambda'}}) |f_{\lambda n_A}^{\lambda' n_A}(\theta_{\lambda}, \phi_{\lambda})|^2 \quad (73)$$

where $v_{\lambda n_A}$ and $v_{\lambda' n_{\lambda'}}$ are the final and initial unscaled coordinate velocities, respectively.

The sum in the right-hand side of Eq. (70) includes the closed-channel terms, for which $E_{\lambda c\lambda j\lambda} > E$, for the reasons given following Eq. (6) of Section II.

In the present formulation the A_a , A_b , and A_c atoms have been considered distinguishable. When they are not, the scattering wave function must be made to satisfy the Pauli principle. This can be achieved *a posteriori*, after solving the Schrödinger equation and ignoring this principle, as exemplified in Section III.F for the H_3 system.

D. SCATTERING AND REACTANCE MATRICES

As in the collinear case, it is convenient to introduce scattering and reactance matrices in order to separate the problem of finding solutions of the Schrödinger equation (69), satisfying arbitrary asymptotic conditions, from the problem of finding the scattering amplitudes of Eq. (70). We start by defining the functions $\phi_{ib}^{JM}(\hat{R}_i, r_i^M)$ where \hat{R}_i is the unit vector in the R_i direction, defined by the laboratory-fixed polar angles θ_i, ϕ_i . This function of the five scalar variables $\theta_i, \phi_i, \gamma_i, \psi_i$ is defined as a simultaneous eigenfunction of the following five operators:

- (1) the square of the triatomic system total angular momentum J_{op}^2 ;
- (2) the Oz laboratory-fixed component of that angular momentum J_{zop} ;
- (3) the energy of the isolated $A_1 A_2$ diatom h_{iop} ;
- (4) the square of the rotational angular momentum of that isolated diatom j_{iop}^2 ; and
- (5) the component of that angular momentum along the body-fixed OZ_i (i.e., R_i) axis j_{Ziop} .

The quantum numbers associated with that set of operators are J, M_J, c_i, j_i , and Ω_i , respectively, and b_i designates the c_i, j_i, Ω_i subset. The quantum number Ω_i associated with the tumbling motion of the triatom around R_i , and described by the tumbling angle ψ_i , will play a special role in the computational methodology described in Section III.G.

The functions $\phi_{ib}^{JM}(\hat{R}_i, r_i^M)$ are called surface functions. They form a complete discrete orthonormal set that spans the 5-MD $\theta_i, \phi_i, r_i, \gamma_i, \psi_i$ subspace of the 6-MD configuration space. They are given by (Schatz and Kuppermann, 1976b):

$$\phi_{ib}^{JM}(\hat{R}_i, r_i^M) = [(2J+1)/4\pi]^{1/2} D_{M_J \Omega_i}^J(\phi_i, \theta_i) \Phi_{icaj;\Omega_i}(r_i^M) \quad (74)$$

where $D_{M_J \Omega_i}^J$ is a Wigner rotation function and $\Phi_{icaj;\Omega_i}(r_i^M)$ is a simultaneous eigenfunction of the h_{iop} (Hamiltonian), j_{iop}^2 , and j_{Ziop} operators of the isolated $A_1 A_2$ diatom in the scaled-coordinated $O\hat{X}_i Y_i Z_i$ body-fixed system of axis. If the electronic state of that molecule is a Σ state, the $\Phi_{icaj;\Omega_i}$ are given by

$$\Phi_{icaj;\Omega_i}(r_i^M) = (r_i)^{-1} \phi_{icaj}(r_i) Y_{j\Omega_i}(\gamma_i, \psi_i) \quad (75)$$

where $Y_{j\Omega_i}$ is a spherical harmonic and ϕ_{icaj} satisfies the radial Schrödinger equation

$$\left[-\frac{\hbar^2}{2\mu} \frac{d^2}{dr_i^2} + v_i(r_i) + \frac{j_i(j_i+1)\hbar^2}{2\mu r_i^2} \right] \phi_{icaj}(r_i) = E_{icaj} \phi_{icaj}(r_i) \quad (76)$$

where $v_\lambda(r_\lambda)$ is the interatomic potential of the isolated A, A_κ diatomic molecule.

Let $\psi^{JM_\lambda \lambda' b'_\lambda}$ be a simultaneous eigenfunction of H , J_{op}^2 , and $J_{z_{\text{op}}}$. We can expand it asymptotically for large R_λ in terms of the surface functions according to:

$$\psi^{JM_\lambda \lambda' b'_\lambda} \sim \sum_{\lambda b_\lambda} (R_\lambda)^{-1} (g^{JM_\lambda})_{\lambda b_\lambda}^{\lambda' b'_\lambda} (R_\lambda) \phi_{\lambda b_\lambda}^{JM_\lambda}(\mathbf{R}_\lambda, \mathbf{r}_\lambda^M) \quad (77)$$

where the radial functions g behave asymptotically as

$$(g^{JM_\lambda})_{\lambda b_\lambda}^{\lambda' b'_\lambda} (R_\lambda) \sim \lim_{R_\lambda \rightarrow \infty} v_{\lambda c_\lambda j_\lambda}^{-1/2} [\mathcal{J}_{\lambda c_\lambda j_\lambda}^J(R_\lambda) (A^{JM_\lambda})_{\lambda b_\lambda}^{\lambda' b'_\lambda} - \mathcal{O}_{\lambda c_\lambda j_\lambda}^J(R_\lambda) (B^{JM_\lambda})_{\lambda b_\lambda}^{\lambda' b'_\lambda}] \quad (78)$$

This expression is the 3-PD counterpart of Eq. (20) where the symbols have similar meanings. As before, A and B are integration constants, v is the (real) velocity, k is the channel wave number given by an expression analogous to Eq. (21), and \mathcal{J}^J and \mathcal{O}^J are the incoming and outgoing waves given by

$$\mathcal{J}_{\lambda c_\lambda j_\lambda}^J(R_\lambda) = \begin{cases} \exp\{-i[k_{\lambda c_\lambda j_\lambda} R_\lambda - \frac{1}{2}(J + j_\lambda)\pi]\} & \text{for open channels} \\ \exp(|k_{\lambda c_\lambda j_\lambda}| R_\lambda) & \text{for closed channels} \end{cases} \quad (79)$$

$$\mathcal{O}_{\lambda c_\lambda j_\lambda}^J(R_\lambda) = \begin{cases} \exp[i[k_{\lambda c_\lambda j_\lambda} R_\lambda - \frac{1}{2}(J + j_\lambda)\pi]] & \text{for open channels} \\ \exp(-|k_{\lambda c_\lambda j_\lambda}| R_\lambda) & \text{for closed channels} \end{cases} \quad (80)$$

The phase $\frac{1}{2}(J + j_\lambda)\pi$ in these expressions is introduced for convenience in simplifying subsequent expressions. We can rewrite Eq. (78) in matrix form as

$$g^{JM_\lambda} \sim v^{-1/2} [\mathcal{J}^J A^{JM_\lambda} - \mathcal{O}^J B^{JM_\lambda}] \quad (81)$$

which is the 3-PD analog of Eq. (24), the corresponding matrices being defined similarly, with the rows and columns scanned by the quantum numbers λb_λ and $\lambda' b'_\lambda$, respectively.

We now define an intermediate scattering matrix \tilde{S}^J by

$$B^{JM_\lambda} = \tilde{S}^J A^{JM_\lambda} \quad (82)$$

and the body-fixed helicity scattering matrix S^J by

$$(S^J)_{\lambda c_\lambda j_\lambda m_{j_\lambda}}^{\lambda' c'_\lambda j'_\lambda m_{j'_\lambda}} = (\tilde{S}^J)_{\lambda c_\lambda j_\lambda, \Omega_\lambda = m_{j_\lambda}}^{\lambda' c'_\lambda j'_\lambda, \Omega_{\lambda'} = -m_{j'_\lambda}} \quad (83)$$

The negative sign in the column label of this expression is introduced because as $R_\lambda \sim \infty$, \mathbf{R}_λ and $\mathbf{k}_{\lambda' c'_\lambda j'_\lambda}$ become antiparallel. Again, as in the

collinear case, the scattering matrix relates the coefficients of the outgoing waves to those of the incoming ones. It has a set of properties analogous to those of the collinear case. They are (Lane and Thomas, 1958):

- (1) S^J is unique, i.e., is independent of A^{JM_J} and of M_J , but depends on E and J .
- (2) The open part S_o^J of S^J is symmetric. This property leads to the principle of microscopic reversibility.
- (3) S_o^J is unitary. This results in the conservation of particle flux. Eq. (81) can also be written as

$$g^{JM_J} \sim v^{-1/2} [\mathcal{S}^J C^{JM_J} + \mathcal{C}^J D^{JM_J}] \quad (84)$$

where g^{JM_J} and v are the same, C^{JM_J} and D^{JM_J} are new integration constant matrices and \mathcal{S}^J and \mathcal{C}^J are diagonal *sine* and *cosine* stationary wave matrices whose diagonal elements are given by

$$\mathcal{S}_{\lambda b \lambda}^J(R_\lambda) = \begin{cases} \sin[k_{\lambda b \lambda} R_\lambda - \frac{1}{2}(J + j_\lambda)\pi] & \text{for open channels} \\ \exp(|k_{\lambda b \lambda}| R_\lambda) & \text{for closed channels} \end{cases} \quad (85)$$

$$\mathcal{C}_{\lambda b \lambda}^J(R_\lambda) = \begin{cases} \cos[k_{\lambda b \lambda} R_\lambda - \frac{1}{2}(J + j_\lambda)\pi] & \text{for open channels} \\ \exp(-|k_{\lambda b \lambda}| R_\lambda) & \text{for closed channels} \end{cases} \quad (86)$$

The reactance matrices are defined, by analogy to the scattering matrices, by

$$D^{JM_J} = R^J C^{JM_J}, \quad (R^J)_{\lambda c \lambda j_\lambda m_{j_\lambda}}^{j_\lambda c \lambda j_\lambda m_{j_\lambda}} = (R^J)_{\lambda c \lambda j_\lambda m_{j_\lambda}}^{j_\lambda c \lambda j_\lambda m_{j_\lambda}} \quad (87)$$

The body-fixed helicity reactance matrix R^J has the following very important properties, analogous to those for the collinear case:

- (1) R^J is unique;
- (2) R^J is real; and
- (3) the open part R_o^J of R^J is symmetric.

The following relation, analogous to Eq. (30), is valid:

$$S_o^J = (I + iR_o^J)(I - iR_o^J)^{-1} \quad (88)$$

In addition, expressions analogous to Eqs. (31) are valid.

E. DISTINGUISHABLE-ATOM SCATTERING AMPLITUDES AND CROSS SECTIONS

From Eqs. (70) and (77)–(83) we can derive the following expression for the scaled coordinate distinguishable-atom scattering amplitude for the

$\lambda'n'_i \rightarrow \lambda n_i$ transition in the body-fixed helicity representation (Schatz and Kuppermann, 1976b):

$$f_{\lambda n_i}^{\lambda' n'_i}(\theta_i, \phi_i) = \left(\frac{v_{i'c_{i'j_{i'}}}}{v_{ic_{ij_i}}} \right)^{1/2} \frac{\exp(im_{j_i} \phi_i)}{2k_{i'c_{i'j_{i'}}}} i^{j_{i'} - j_i + 1} \sum_{J=0}^{\infty} (2J+1) d_{m_{j_i}, m_{j_i}}^J(\theta_i) (T_0^J)_{\lambda n_i}^{\lambda' n'_i} \quad (89)$$

where the transition matrix T_0^J is defined by

$$T_0^J = I - S_0^J \quad (90)$$

This expression is reminiscent of that for the scattering of a single particle by a central field. Its simplicity results from the choice of the body-fixed helicity representation. The corresponding unscaled coordinate scattering amplitudes f' can be obtained from Eqs. (89) and (72).

From Eqs. (89), (72), and (73) we can derive the following expression for the $\lambda'n'_i \rightarrow \lambda n_i$ distinguishable-atom differential cross section (Schatz and Kuppermann, 1976b):

$$\sigma_{\lambda n_i}^{\lambda' n'_i}(\theta_i) = (4k_{i'c_{i'j_{i'}}}^2)^{-1} \left| \sum_{J=0}^{\infty} (2J+1) d_{m_{j_i}, m_{j_i}}^J(\theta_i) (T_0^J)_{\lambda n_i}^{\lambda' n'_i} \right|^2 \quad (91)$$

where k' denotes the initial wave number in unscaled coordinates.

Several consequences result from this expression. One of them deals with the nature of the dependence of σ on θ_i . We note that the functions $d_{m_{j_i}, m_{j_i}}^J$ are real and that the associated Legendre functions are particular cases of these d functions, with either m_{j_i} or m'_{j_i} equal to zero (Davydov, 1965). The d^J terms display an oscillatory dependence on θ_i : the higher the value of J , the faster is the rate of oscillation. Nevertheless, for direct reactions, such as the distinguishable atom $H + H_2$ exchange reaction, the variation of σ with θ_i is monotonic (see Section III.H.4). The reason is that the phases and amplitudes of the T_0^J matrix elements bear a relationship to each other that leads, for such reactions, to the disappearance of the oscillations in σ . As a result, if differential cross sections devoid of spurious oscillations are to be obtained from ab initio quantum mechanical scattering calculations, a sufficiently accurate scattering matrix must be obtained from such calculations (Schatz and Kuppermann, 1976c). More specifically, not only must we accurately calculate the absolute values of its elements, but the corresponding phases must be determined accurately as well.

We also notice that although the scattering amplitudes depend on ϕ_λ , the differential cross sections do not. The reason is that the initial probability density is cylindrically symmetrical around the quantization axis, and therefore so must the final one be, in the absence of external fields. In addition, since $d_{m'm}^J(0) = \delta_{m'm}$ and $d_{m'm}^J(\pi) = (-1)^{J+m} \delta_{m',-m}$, we conclude from Eq. (91) that for $m'_{j_\lambda} \neq m_{j_\lambda}$, $\sigma_{\lambda n_\lambda}^{j' n_\lambda'}(0)$ vanishes, and for $m'_{j_\lambda} \neq -m_{j_\lambda}$, $\sigma_{\lambda n_\lambda}^{j' n_\lambda'}(\pi)$ vanishes. These rigorous selection rules for forward and backward scattering are related to the conservation of J_z (Schatz and Kuppermann, 1976c).

The integral cross section $Q_{\lambda n_\lambda}^{j' n_\lambda'}$, defined as the integral of the differential cross section over all scattering directions, can be obtained from Eq. (91) as

$$Q_{\lambda n_\lambda}^{j' n_\lambda'} = \frac{\pi}{k_{\lambda' c_\lambda, j_\lambda}^2} \sum_{J=0}^{\infty} (2J+1) |(T_0^J)_{\lambda n_\lambda}^{j' n_\lambda'}|^2 \quad (92)$$

In contrast to the differential cross section, we do not need accurate phases of the transition matrix to obtain accurate integral cross sections. Therefore, the latter cross sections are easier to calculate than the former.

The unitarity of S_0^J permits us to define the $\lambda' n_\lambda' \rightarrow \lambda n_\lambda J$ partial wave reaction probability as

$$P_{\lambda n_\lambda}^{j' n_\lambda'} = |(S_0^J)_{\lambda n_\lambda}^{j' n_\lambda'}|^2 \quad (93)$$

in terms of which the $\lambda' n_\lambda' \rightarrow \lambda n_\lambda$ integral cross section for transitions other than the elastic one (i.e., for $\lambda n_\lambda \neq \lambda' n_\lambda'$) can be written as

$$Q_{\lambda n_\lambda}^{j' n_\lambda'} = \frac{\pi}{k_{\lambda' c_\lambda, j_\lambda}^2} \sum_{J=0}^{\infty} (2J+1) P_{\lambda n_\lambda}^{j' n_\lambda'}, \quad \lambda n_\lambda \neq \lambda' n_\lambda' \quad (94)$$

Both $\sigma_{\lambda n_\lambda}^{j' n_\lambda'}$ and $Q_{\lambda n_\lambda}^{j' n_\lambda'}$ may be averaged over the initial m'_{j_λ} and summed over the final m_{j_λ} to give the degeneracy-averaged quantities $\sigma_{\lambda c_\lambda j_\lambda}^{j' n_\lambda'}$ and $Q_{\lambda c_\lambda j_\lambda}^{j' n_\lambda'}$, respectively. The latter can be written, for inelastic or reactive transitions, as

$$Q_{\lambda c_\lambda j_\lambda}^{j' n_\lambda'} = \frac{\pi}{k_{\lambda' c_\lambda, j_\lambda}^2} \sum_{J=0}^{\infty} (2J+1) P_{\lambda c_\lambda j_\lambda}^{j' n_\lambda'}, \quad \lambda c_\lambda j_\lambda \neq \lambda' c_\lambda' j_\lambda' \quad (95)$$

where $P_{\lambda c_\lambda j_\lambda}^{j' n_\lambda'}$ is the opacity function defined as

$$P_{\lambda c_\lambda j_\lambda}^{j' n_\lambda'} = (2j_\lambda' + 1)^{-1} \sum_{m_{j_\lambda} m_{j_\lambda'}} P_{\lambda n_\lambda}^{j' n_\lambda'} \quad (96)$$

Although the last two expressions were obtained from the body-fixed helicity representation, the same degeneracy-averaged $Q_{\lambda c_\lambda j_\lambda}^{j' n_\lambda'}$ and partial wave opacity function $P_{\lambda c_\lambda j_\lambda}^{j' n_\lambda'}$ would have been obtained if we had started from other representations.

From the properties of the open part of the scattering matrix we can derive related properties of the cross section, reaction probabilities, and opacity functions. From its unitarity we obtain:

- (1) Conservation of flux for body-fixed helicity transition probabilities,

$$\sum_{\lambda n_A} P_{\lambda n_A}^{J' n_A} = 1 \quad (97)$$

- (2) Conservation of opacity,

$$\sum_{\lambda c_A j_A} P_{\lambda c_A j_A}^{J' c_A j_A} = 1 \quad (98)$$

From the symmetry of S_o^J we obtain:

- (3) Microscopic reversibility for body-fixed helicity transition probabilities,

$$P_{\lambda n_A}^{J' n_A} = P_{\lambda' n_A}^{J n_A} \quad (99)$$

- (4) Microscopic reversibility for opacity functions,

$$(2j_{\lambda'} + 1) P_{\lambda c_A j_A}^{J' c_A j_A} = (2j_{\lambda} + 1) P_{\lambda' c_A j_A}^{J c_A j_A} \quad (100)$$

- (5) Microscopic reversibility for body-fixed integral helicity cross sections,

$$k_{\lambda' c_A j_A}^2 Q_{\lambda n_A}^{J' n_A} = k_{\lambda c_A j_A}^2 Q_{\lambda' n_A}^{J n_A} \quad (101)$$

- (6) Microscopic reversibility for degeneracy-averaged integral cross sections,

$$(2j_{\lambda'} + 1) k_{\lambda' c_A j_A}^2 Q_{\lambda c_A j_A}^{J' c_A j_A} = (2j_{\lambda} + 1) k_{\lambda c_A j_A}^2 Q_{\lambda' c_A j_A}^{J c_A j_A} \quad (102)$$

- (7) Microscopic reversibility for body-fixed helicity differential cross sections,

$$k_{\lambda' c_A j_A}^2 \sigma_{\lambda n_A}^{J' n_A}(\theta_{\lambda'}) = k_{\lambda c_A j_A}^2 \sigma_{\lambda' n_A}^{J n_A}(\theta_{\lambda'} = \theta_{\lambda}) \quad (103)$$

Equations (97)–(103) relate properties of forward ($\lambda' \rightarrow \lambda$) and backward ($\lambda \rightarrow \lambda'$) processes occurring at the same total energy E , and care must be taken not to apply them, by mistake, to such collisions occurring at equal translational energies.

F. CROSS SECTIONS FOR SYSTEMS CONTAINING IDENTICAL ATOMS

If the three atoms of the triatomic system being considered are not all distinguishable, we must include the effects of the Pauli principle on the reactive scattering problem. The interaction energies between the nuclear spin and the orbital motions are in general several orders of magnitude

smaller than the Born-Oppenheimer interaction potential in the regions of configuration space of interest to the scattering process. We will therefore neglect those spin-orbit interactions in the present considerations. Under these conditions, the Pauli principle may be introduced by the techniques of post-antisymmetrization (for identical fermions) or post-symmetrization (for identical bosons). For example, for the H_3 system, there are only two independent sets of distinguishable scattering amplitudes: reactive (or exchange) f'^n , and nonreactive (or direct), f''^n . The appropriately antisymmetrized scattering wave functions can be obtained by taking linear combinations of those of the distinguishable atom (Kuppermann *et al.*, 1976), and, as a result, the correct antisymmetrized differential cross sections can be expressed in terms of the f'^n and f''^n (Schatz and Kuppermann, 1976b) as:

(1) para \rightarrow para (j' , j even)

$$\sigma_{pn}^{pn'} = \frac{v'_{ej}}{v'_{ej'}} |f'^{nn'}_n - f'^{nn'}_n|^2 \quad (104)$$

(2) para \rightarrow ortho (j' even, j odd)

$$\sigma_{on}^{pn'} = 3 \frac{v'_{ej}}{v'_{ej'}} |f'^{nn'}_n|^2 \quad (105)$$

(3) ortho \rightarrow para (j' odd, j even)

$$\sigma_{pn}^{pn'} = \frac{v'_{ej}}{v'_{ej'}} |f'^{nn'}_n|^2 \quad (106)$$

(4) ortho \rightarrow ortho (j' , j odd)

$$\sigma_{on}^{pn'} = \frac{v'_{ej}}{v'_{ej'}} (|f'^{nn'}_n + f'^{nn'}_n|^2 + 2|f'^{nn'}_n|^2) \quad (107)$$

In these expressions, the indices λ and λ' were omitted, due to the identity of the three atoms. As before, the v' quantities are the channel velocities and n stands for the set of diatom quantum numbers c, j, m in the body-fixed helicity representation. Although the calculations that furnish the f'^n and f''^n are for distinguishable atoms, for which the Pauli principle is ignored, Eqs. (104)–(107) furnish the correct cross sections, which can be compared with experimental results. It should be noticed that in Eqs. (104) and (107), to which both f'^n and f''^n contribute, interference effects between these two scattering amplitudes are present due to the $f'^n \pm f''^n$ terms.

G. COMPUTATIONAL METHODOLOGY

So far we have indicated how once the scattering matrix of a reactive system is known, the scattering amplitudes and cross sections can be obtained. In this section we outline how that matrix can be calculated once the system's electronically adiabatic potential energy function $V_\lambda(R_\lambda, r_\lambda, \gamma_\lambda)$ is known.

As in the collinear case (Section II,E), several approaches are possible. However, only three coupled-channel methods have been used so far in cross-section calculations for 3-PD systems. One of them, developed by Elkowitz and Wyatt (1975a,b), uses natural collision coordinates (NCC) and local hindered asymmetric-top-vibrator basis sets, as reviewed recently by Wyatt (1979). Another, developed by Kuppermann and Schatz (1975), uses asymptotic free rotor and local vibrator basis sets, and different coordinates in different regions of configuration space, similar to those described in Section II,E. The advantage of Elkowitz and Wyatt's approach is that their basis functions furnish an efficient representation of the local motion and contain very useful interpretive information in the form of asymmetric top-rotational energy correlation diagrams. However, the NCC are more cumbersome to use in the representation of the potential energy function and in the calculation of the matrix elements that appear in the coupled-channel equations. The third method was developed by Walker *et al.* (1976, 1978) and has elements in common with both the Elkowitz and Wyatt and the Kuppermann and Schatz approaches. We now review the latter (Schatz and Kuppermann, 1976b). We first define the complete discrete orthonormal body-fixed basis set:

$$\mathcal{Y}_{j\lambda\Omega_\lambda}^{JM_\lambda}(\theta_\lambda, \phi_\lambda, \gamma_\lambda, \psi_\lambda) = \left(\frac{2J+1}{4\pi}\right)^{1/2} D_{M_\lambda, \Omega_\lambda}^J(\phi_\lambda, \theta_\lambda, 0) Y_{j\lambda\Omega_\lambda}(\gamma_\lambda, \psi_\lambda) \quad (108)$$

These are simultaneous eigenfunctions of the operators J_{op}^2 , $J_{z_{op}}$, $j_{\lambda_{op}}^2$, and $j_{z_{\lambda_{op}}}$ defined at the beginning of Section III,D. They span the 4-MD subspace defined by the angular coordinates $\theta_\lambda, \phi_\lambda, \gamma_\lambda, \psi_\lambda$. We now expand, in this basis set, the wave functions $\psi_1^{JM_\lambda}$, which are simultaneous eigenfunctions of H , J_{op}^2 , and $J_{z_{op}}$, expressed in λ -arrangement channel coordinates R_λ, r_λ^M :

$$\psi_1^{JM_\lambda}(R_\lambda, r_\lambda^M) = \sum_{\Omega_\lambda=-J}^J \sum_{j\lambda=\lvert\Omega_\lambda\rvert}^{\infty} (R_\lambda r_\lambda)^{-1} F_{j\lambda\Omega_\lambda}^J(R_\lambda, r_\lambda) \mathcal{Y}_{j\lambda\Omega_\lambda}^{JM_\lambda}(\theta_\lambda, \phi_\lambda, \gamma_\lambda, \psi_\lambda) \quad (109)$$

Replacement of this expansion in the Schrödinger equation furnishes the

following set of coupled-channel partial differential equations for the functions $F_{j\lambda\Omega_\lambda}^J$:

$$\begin{aligned} t_{\Omega_\lambda, \Omega_\lambda-1}^{J\lambda j_\lambda} F_{j\lambda, \Omega_\lambda-1}^J + t_{\Omega_\lambda, \Omega_\lambda}^{J\lambda j_\lambda} F_{j\lambda, \Omega_\lambda}^J + t_{\Omega_\lambda, \Omega_\lambda+1}^{J\lambda j_\lambda} F_{j\lambda, \Omega_\lambda+1}^J \\ + \sum_{j_\lambda} V_{j\lambda j_\lambda}^{i\Omega_\lambda} F_{j\lambda, \Omega_\lambda}^J = E F_{j\lambda, \Omega_\lambda}^J \end{aligned} \quad (110)$$

where the kinetic energy operators t are given by

$$\begin{aligned} t_{\Omega_\lambda, \Omega_\lambda}^{J\lambda j_\lambda}(R_\lambda, r_\lambda) &= -\frac{\hbar^2}{2\mu} \left(\frac{\partial^2}{\partial R_\lambda^2} + \frac{\partial^2}{\partial r_\lambda^2} \right) + \frac{j_\lambda(j_\lambda+1)\hbar^2}{2\mu r_\lambda^2} \\ &\quad + \frac{\hbar^2}{2\mu R_\lambda^2} [J(J+1) - 2\Omega_\lambda^2 + j_\lambda(j_\lambda+1)] \\ t_{\Omega_\lambda, \Omega_\lambda \pm 1}^{J\lambda j_\lambda}(R_\lambda) &= -\frac{\hbar^2}{2\mu R_\lambda^2} \xi_\pm(J, \Omega_\lambda) \xi_\pm(j_\lambda, \Omega_\lambda) \end{aligned} \quad (111)$$

$$\xi_\pm(j, m) = [j(j+1) - m(m \pm 1)]^{1/2}, \quad |m| \leq j$$

and the potential energy function matrix element $V_{j\lambda j_\lambda}^{i\Omega_\lambda}$ is

$$V_{j\lambda j_\lambda}^{i\Omega_\lambda}(R_\lambda, r_\lambda) = \langle j_\lambda \Omega_\lambda | V_\lambda(R_\lambda, r_\lambda, \gamma_\lambda) | j_\lambda \Omega_\lambda \rangle \quad (112)$$

In Eq. (110), the $t_{\Omega_\lambda, \Omega_\lambda \pm 1}^{J\lambda j_\lambda}$ terms are centrifugal coupling terms that are independent of V and couple $F_{j\lambda, \Omega_\lambda}^J$ with $F_{j\lambda, \Omega_\lambda \pm 1}^J$. They depend only on R_λ and the quantum numbers $J, j_\lambda, \Omega_\lambda$. For reactive systems, the range of total angular momentum quantum numbers J that contribute appreciably to the reactive cross sections is usually much smaller than that which contributes to nonreactive inelastic cross sections, and in many instances these $t_{\Omega_\lambda, \Omega_\lambda \pm 1}^{J\lambda j_\lambda}$ terms can be neglected. In this case Eq. (110) becomes diagonal in Ω_λ , i.e., the $F_{j\lambda, \Omega_\lambda}^J$ for different tumbling angular momenta in arrangement channel λ are decoupled, since the $V_{j\lambda j_\lambda}^{i\Omega_\lambda}$ do not couple such functions. This leads to the tumbling decoupling approximation, considered in Section III.H.10.

Equation (110) contains the same two distances R_λ, r_λ as did the Schrödinger equation for collinear triatomic systems considered in Section II.A. The main difference is that instead of a single equation, we now have, for each J , a system of coupled equations scanned by the rotational quantum numbers j_λ and Ω_λ . The potential energy function couples different j_λ (because of its dependence on γ_λ), whereas the angular-momentum tumbling centrifugal terms couple different Ω_λ . In addition, instead of only two arrangement channels (reagents and reactive products), we now have three such channels (one reagent and two product arrangements). The method of solution of these coupled-channel equations is described most easily by considering the internal configuration space $R_\lambda, r_\lambda, \gamma_\lambda$ in the symmetrized hyperspherical coordinate mapping of Section III.B, whose coordinate axes

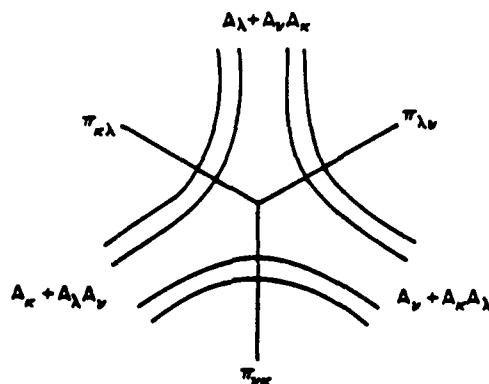


Fig. 33. Intersection of matching half-planes π_{λ} , π_{ν} , π_{κ} with the $X_1 Z_1$ plane of Fig. 30. Curves are intersections of an equipotential surface with that same coordinate plane.

are $X_1 Y_1 Z_1$ (not to be confused with the axis of Fig. 32). In Fig. 33, we indicate an outline of a equipotential on the $X_1 Z_1$ plane (which coincides with the $X_1 Z_1$ and $X_2 Z_2$ planes), and the intersection with that plane of three half-planes, labeled π_{λ} , π_{ν} , and π_{κ} , whose common edge is the Y_1 axis (which coincides with the Y_1 and Y_2 axes), perpendicular to the plane of the figure. These half-planes divide the internal configuration space into three arrangement-channel subspaces, λ , ν , and κ . When augmented by the θ_1, ϕ_1, ψ_1 space they define three subspaces of the total configuration space. The method of solution consists of integrating the coupled Eqs. (110) over the range of R_1, r_1 , which, together with γ_1 , spans the λ arrangement-channel subspace. This integration is performed by dividing the R_1, r_1 subspace into regions, as was done in the collinear case, and using appropriate variables and basis sets in each region (Schatz and Kuppermann, 1976b). We thereby get, in each region, a set of coupled ordinary differential equations that can be integrated numerically by the use of an appropriate efficient algorithm, such as that of Gordon (1969) or Light and Walker (1976). This procedure generates a set of linearly independent wave functions $\psi_{\lambda b \lambda}^{JM}(R_1, r_1^M)$ that span the λ arrangement-channel subspace, but do not cover the entire configuration space. We similarly generate wave functions $\psi_{\nu b \nu}^{JM}(R_\nu, r_\nu^M)$ and $\psi_{\kappa b \kappa}^{JM}(R_\kappa, r_\kappa^M)$ that span the ν and κ arrangement-channel subspaces. These λ , ν , and κ solutions overlap on the $\pi_{\lambda\nu}$, $\pi_{\nu\kappa}$, and $\pi_{\kappa\lambda}$ half-planes, but have in general different values on those surfaces. In order to generate solutions of the Schrödinger equation for a given J and M_J , which are everywhere continuous and smooth, we take linear combinations of the $\psi_{\lambda b \lambda}^{JM}$ in the λ arrangement-channel subspace, of the $\psi_{\nu b \nu}^{JM}$ in the ν subspace and of the $\psi_{\kappa b \kappa}^{JM}$ in the κ subspace and impose on these three different sets of linear combinations the conditions that they be continuous on the $\pi_{\lambda\nu}$, $\pi_{\nu\kappa}$, and $\pi_{\kappa\lambda}$ half-planes and that their

derivatives normal to these half-planes also be continuous. In this manner, we generate solutions of the Schrödinger equation at a given energy E that are also eigenfunctions of $J_{\phi\phi}^2$ and $J_{\phi\omega}$ corresponding to the quantum numbers J and M_J , respectively, and that are everywhere smoothly continuous. An examination of the asymptotic behavior of these solutions, as described in Section III.D, furnishes the desired reactance and scattering matrices. From these, the scattering amplitudes and cross sections are obtained, as described in Sections III.E and III.F.

H. RESULTS FOR $H + H_2$

The only system for which accurate 3-D quantum mechanical reactive scattering cross-section calculations have been performed thus far is the $H + H_2$ system. Such calculations have been done independently by three groups, using three different methods. At Caltech, we have performed such calculations (Kuppermann and Schatz, 1975; Schatz and Kuppermann, 1976c) using the methodology described in Section III.G. At the University of Texas, Elkowitz and Wyatt (1975a,b) used a natural collision coordinate method and rotationally adiabatic basis functions. Both groups used the Porter-Karplus H_3 surface (Porter and Karplus, 1964). The Caltech group expanded it in Legendre polynomials of γ_1 , using enough terms for convergence of the results to be achieved. The Texas group cast the surface in a mathematical form, in terms of natural collision coordinates, convenient for the calculations. As a result, the two surfaces as actually used are not quite the same, differing nonnegligibly from one another in the saddle-point region. The Caltech group used sufficient vibrational basis functions in the calculation to achieve convergence of the results to within about 5%. This required between four and six vibrational basis functions. The third group, at Chicago (Walker *et al.*, 1978), reported some preliminary results on the Porter-Karplus and the SLTH (Truhlar and Horowitz, 1978) potential energy surfaces. We will describe next some of the results of the Caltech calculations, and make a partial comparison with the Texas results in Section III.H.2. Unprimed quantum numbers will designate reagents and primed ones products, the opposite convention from that of Sections III.E and IV.F.

1. Partial-Wave Reaction Probabilities

In Fig. 34a we display, as a function of the total angular momentum quantum number J , and for several total energies E , the distinguishable-atom reaction probability $P_{J,00 \rightarrow 01}^R$, from the $v = 0, j = 0, m_j = 0$ state of the reagents to the $v' = 0, j' = 1$ state of the products, summed over all final m_j' , which is the same as the opacity function of Eq. (96) for the $00 \rightarrow 01$ reactive transition. This figure indicates that such opacity function has a

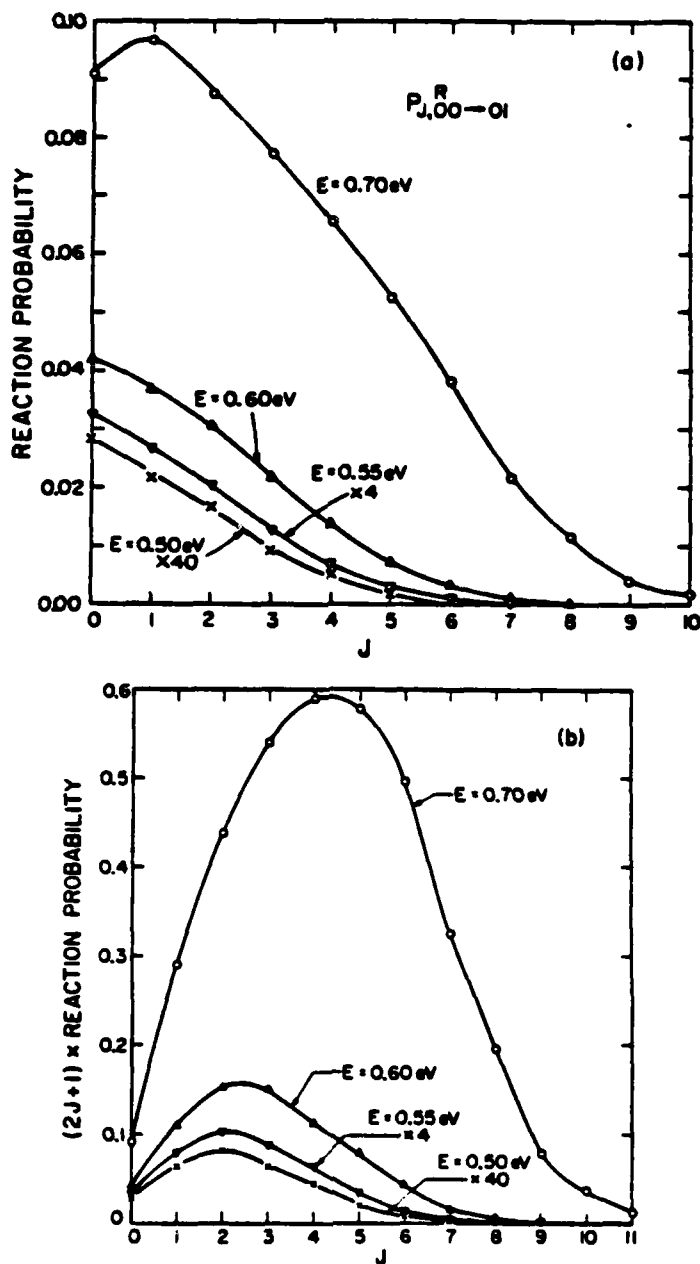


Fig. 34. Reaction probabilities for distinguishable-atom three-dimensional H + H₂ collisions. (a) Reaction probabilities $P_{J,00-01}^R$ (summed over final m_j) as a function of J for total energies $E = 0.50, 0.55, 0.60, 0.65$, and 0.70 eV. (b) $2J + 1$ times these probabilities. The scale factors for the first two energies are the numbers by which the probabilities were multiplied before being plotted.

maximum value at a low J and decreases rapidly with increasing J , beyond that maximum. If we define J_{\max} as the lowest value of J for which $P_{J_{ej}-c'j'}^R$ has decreased to less than 1% of its maximum value, then J_{\max} is 4 at 0.3 eV and increases monotonically to about 10 at 0.7 eV. The contribution of this opacity function to the degeneracy-averaged integral reaction cross section is weighted by the factor $(2J+1)$ as indicated in Eq. (95). Figure 34b displays the product $(2J+1)P_{J,00-01}^R$ as a function of J . The partial wave that gives the largest contribution to Q_{00-01}^R varies from $J=1$ at $E=0.3$ eV to $J=4$ at 0.7 eV. We see that over this energy range 12 partial waves suffice to obtain integral reaction cross sections with an accuracy of a few percent or better. It is this property that will also be responsible for the accuracy of the angular-momentum decoupling approximation described in Section III.H.10.

2. Integral Reaction Cross Sections

In Fig. 35 we display, as a function of the total energy E , several distinguishable-atom integral reaction cross sections Q_{ij}^R , which are the degeneracy-averaged cross sections of Eq. (95) summed over all final $c'j'$ states of the products. The curves labeled SK are the Schatz and Kuppermann (1976c) quantum mechanical results, those labeled KPS are the Karplus *et al.* (1965) quasi-classical trajectory calculations, and the EW curves are the quantum mechanical curves of Elkowitz and Wyatt (1975a). The best agreement is between the $Q_{00}^R(\text{SK})$ and $Q_{01}^R(\text{SK})$ curves and the corresponding quasi-classical ones. Below the classical threshold we observe characteristic tunneling behavior in the SK quantum results, which will be discussed in the following section.

Agreement between the SK curves and the corresponding EW curves is not as good as one would have expected, considering that both calculations were nominally done on the same potential energy surface and that both employed accurate methods and extended vibration-rotation basis sets. Part of this lack of complete agreement was due to a different proportionality factor in the expression for the cross sections (R. E. Wyatt, private communication). After that difference is eliminated, the difference between the SK and EW Q_{00-01}^A (antisymmetrized) values in the energy range 0.6–0.7 eV is about 20%. In addition, the EW Q_{00-03}^A/Q_{00-01}^A product rotational population ratio at $E=0.70$ eV is 0.61, whereas the SK one is 0.25. Considerable effort was devoted to identifying the causes of these differences, since these are the only two exact, detailed 3-PD reactive scattering calculations published so far. The conclusions reached are that they are mainly due to two causes. One is that the EW representation of the Porter-Karplus surface differs non-negligibly from the surface itself. To correct for this difference, J. P. Dwyer and A. Kuppermann (unpublished results, 1977) made calculations using exactly the surface that EW used, for $J=0$ and $E=0.60$ eV. The resulting reaction probabilities were closer to the corresponding EWs than previously,

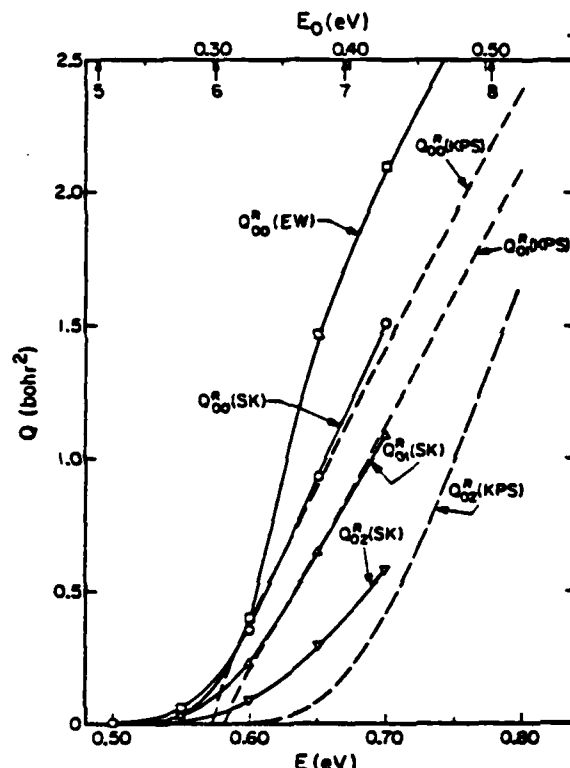


Fig. 35. Comparison of $\text{H} + \text{H}_2$ 3-PD reactive integral cross sections as a function of the total energy E and initial relative translational energy E_0 for several calculations. The Q_{0j}^R (KPS) for $j = 0, 1$, and 2 are the quasi-classical results of Karplus, Porter, and Sharma (dashed lines), while Q_{00}^R (EW) is the analogous total reaction cross section obtained by Elkowitz and Wyatt (squares). The Schatz and Kuppermann results are connected by solid lines and labeled Q_{0j}^R (SK) with $j = 0, 1, 2$. The arrows below the upper abscissa indicate the energies at which the ground vibrational state product rotational levels having the j values indicated become energetically accessible.

but about one-half of the difference still persisted. This is assumed to be due to lack of complete convergence of the EW calculation at some E and J (Wyatt, 1979).

3. Tunneling Effects

The deviation between the SK and KPS Q_{00}^R and Q_{01}^R curves of Fig. 35 around $E = 0.58$ eV is similar to the corresponding deviation for the collinear reaction where, as described in Section II.F.2, a streamline of probability current-density analysis has shown unequivocally the presence of large

tunneling contributions. These differences, although small, affect in a significant way the corresponding thermal reaction rate constants. Karplus *et al.* (1965) have computed such rate constants $k^R(T)$ from their quasi-classical trajectory cross sections. These can be converted to the para \rightarrow ortho rate constants by multiplication by the ratio $K_{eq}(T)/[1 + K_{eq}(T)]$ where $K_{eq}(T)$ is the corresponding ortho \leftrightarrow para equilibrium constant at temperature T obtained from the potential energy surface using quantum statistical mechanics (Schatz and Kuppermann, 1976c). In Fig. 36 we present Arrhenius plots of the SK and KPS para \rightarrow ortho rate constants $k_{p \rightarrow o}(T)$ over the temperature range 100–600 K permitted by the available 3-PD quantum cross sections. Also presented is the corresponding transition-state theory curve (TST) with unit transmission coefficient.

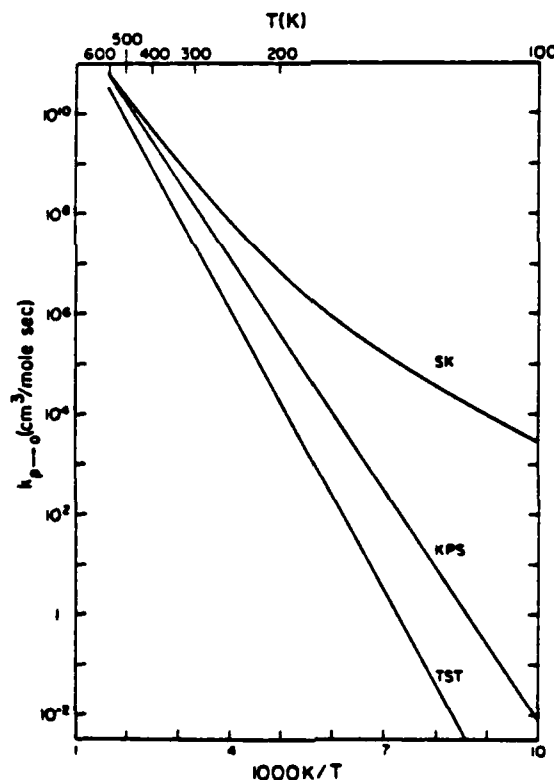


Fig. 36. Arrhenius plot of the para \rightarrow ortho 3-PD H + H₂ thermal rate constant. The quantum result of Schatz and Kuppermann is denoted by SK, while the classical result of Karplus, Porter, and Sharma is labeled KPS and the transition state theory result with unit transmission coefficient is labeled TST.

At 600 K the quasi-classical $k_{p \rightarrow 0}$ differs from the quantum one by only 7%. This close agreement is due to the agreement between the corresponding Q_{00}^R and Q_{01}^R of Fig. 35, at energies above the quasi-classical threshold. However, because of tunneling effects, the quantum $k_{p \rightarrow 0}$ is 3.3 times larger than the quasi-classical one at 300 K, and 18 times larger at 200 K. The significant nonlinearity in the quantum curve of Fig. 36 is also apparently related to tunneling, although as described in Section II.F.2, tunneling in the collinear $H + H_2$ reaction can make significant contributions to the rate constant even at 1000 K where the collinear reaction-rate constant Arrhenius plot is quite linear.

The TST rate constant deviates from the quantum rate constant even more than the quasi-classical one with $k_{p \rightarrow 0}(\text{SK})/k_{p \rightarrow 0}(\text{TST})$ being 20 at 300 K and 427 at 200 K. Part of this error is due to the neglect of tunneling corrections (Kuppermann, 1979).

4. Differential Cross Sections

In Fig. 37 we present the properly antisymmetrized differential cross sections $\sigma_{000-03m_j}^A$ as a function of the reactive scattering angle θ_R between $H-H_2$ final wave-number vector and the H_2-H initial wave-number vector, for $E = 0.6$ eV and m_j having all possible values. We see that only for the $m_j = 0$ polarization quantum number is there a peak in the backward direction. As $|m_j|$ increases, the reactive scattering shifts to a more forward direction, with the cross sections peaking at $\theta_R = 139^\circ$, 117° , and 102° for $|m_j| = 1, 2$, and 3 , respectively. The fact that for $m_j \neq 0$ these differential cross sections vanish at $\theta_R = 0^\circ$ and 180° is a consequence of Eq. (91) as explained in Section III.E. As can be seen, these differential cross sections are smooth functions of θ_R , giving no indication of spurious oscillations. This is a sensitive indication of the accuracy of the calculation, as also explained in Section III.E. In order to achieve it, special care was taken to assure convergence of the scattering matrix amplitudes and phases at each partial wave, as well as to include a sufficiently large number of partial waves in the expansion. Elkowitz and Wyatt (1975a,b) have not published differential cross sections, presumably because of the difficulty of achieving such convergence. In any event, the SK results represent the only accurate quantum mechanical reactive differential cross sections published so far.

In Fig. 38 we have plotted the distinguishable atom nonreactive differential cross sections $\sigma_{000-02m_j}^N$ as a function of the scattering angle (between the H_2-H final and initial wave-number vectors) for $E = 0.5$ eV and m_j having all possible values. We see that significant cross sections occur at all m_j and at all scattering angles not too close, for $m_j \neq 0$, to 0° or 180° . This behavior of the nonreactive cross sections contrasts with that of the antisymmetrized

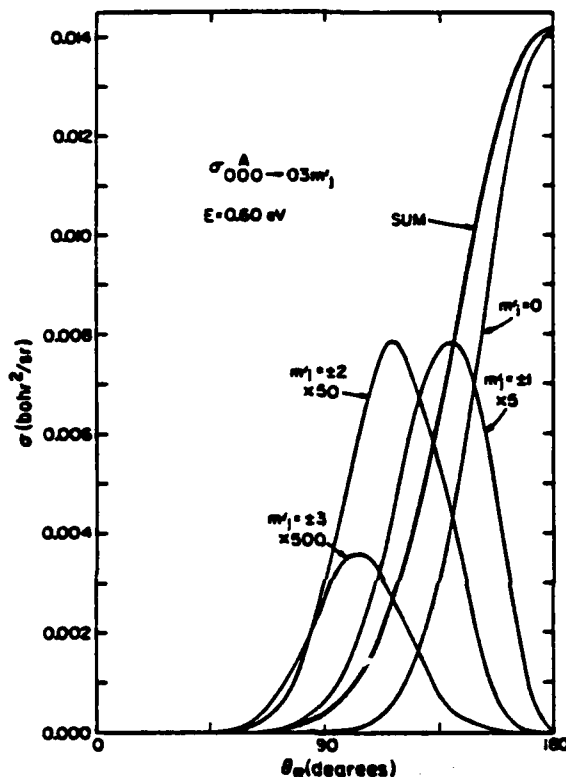


Fig. 37. Differential cross section $\sigma_{000 \rightarrow 03m_j}^A$ for the 3-PD $\text{H} + \text{H}_2 \rightarrow \text{H}_2 + \text{H}$ reaction as a function of the reactive scattering angle θ_R for $E = 0.6 \text{ eV}$ and all possible m_j . The curve labeled sum is the sum of all seven cross sections and is equal to the degeneracy-averaged $\sigma_{00 \rightarrow 03}^A$. Scale factors have meanings analogous to those of Fig. 34.

one in Fig. 37, which according to Eq. (105) is proportional to the reactive cross section. The latter has significant contributions only for $m_j' = 0$ and for θ_R close to 180° . The reason for this difference in behavior is the fact that for this system the potential energy function has a strong minimum, at the energies considered, in the collinear direction, as indicated in Fig. 31. As a result, for reactive collisions to occur, the reagents must approach almost collinearly and the products recede from each other almost collinearly. The latter effect produces the backward-peaked reactive angular distribution. In addition, a polarization propensity rule, which favors $m_j = 0 \rightarrow m_j' = 0$ reactive transitions, results, and is further discussed in the following subsection.

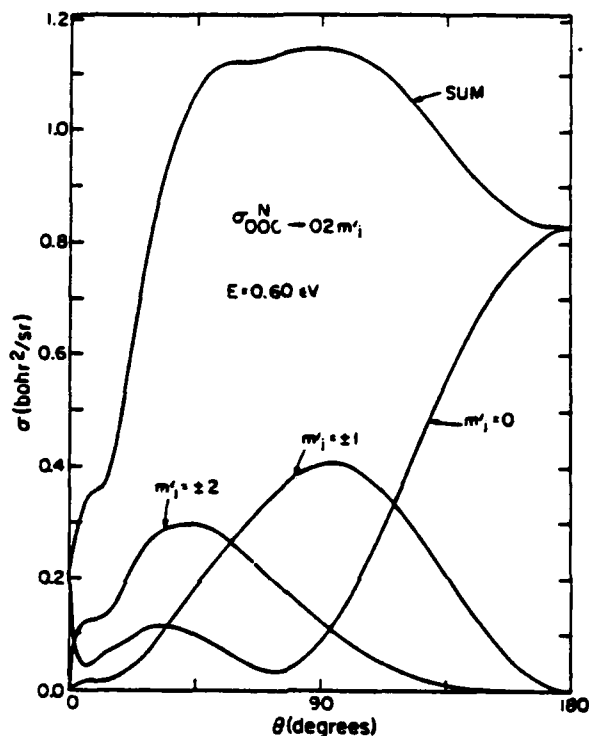


Fig. 38. Differential nonreactive cross section $\sigma_{000 \rightarrow 02m_j}^N$ as a function of scattering angle θ for $E = 0.6$ eV and all possible m_j . The curve labeled sum is the sum of all five cross sections and is equal to the degeneracy-averaged $\sigma_{00 \rightarrow 02}^N$.

5. Polarization Propensity Rules

It can be seen from Fig. 37 that the maximum differential cross section for the $m_i = 0 \rightarrow m_j = \pm 1$ reactive transitions is about one order of magnitude smaller than that for $0 \rightarrow 0$ and that it decreases by another order of magnitude in going to the $0 \rightarrow \pm 2$ ones and an additional order of magnitude in going to the $0 \rightarrow \pm 3$ reactive transitions. Such effect does not exist for the nonreactive transitions of Fig. 38. In addition, an analysis of the integral cross sections over the energy range $E = 0.30$ – 0.70 eV for the $0jm_i \rightarrow 0j'm_j$ reactive transitions indicates that the $m_j = m_i = 0$ cross section is typically 10–20 times larger than any other with the same $c'j'$ and cj . In addition, for a given cjm_j and $c'j'$, this cross section is a decreasing function of $|m_j|$. By microscopic reversibility, for given cj and $c'j'm_j'$, it is a decreasing function of $|m_j|$. This indicates a significant reagent and product rotational angular momentum polarization effect in the helicity representation.

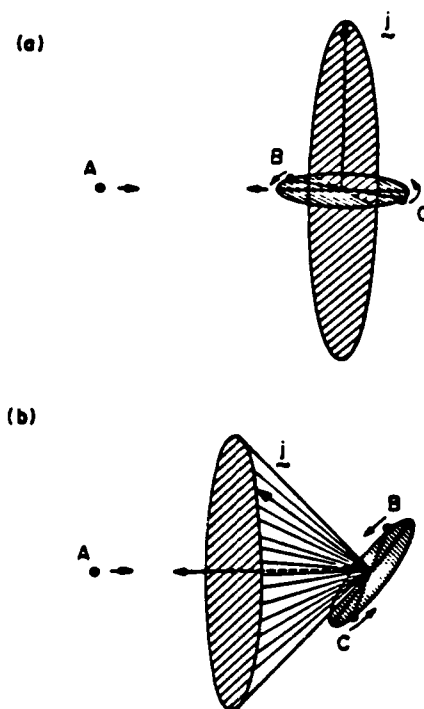


Fig. 39. Influence of reagent projection quantum number m_j (for $j > 0$) on the allowed relative orientations of atom A with respect to diatom BC for zero-impact collisions: (a) $m_j = 0$ initially so that the rotational angular momentum vector is perpendicular to the direction of relative motion; (b) $m_j > 0$ initially so that the j vector lies on a cone about the relative motion vector and makes an acute angle with it. In both (a) and (b) the rotation plane of the diatom is indicated by the smaller ellipse.

These empirical propensity rules can be rationalized on the basis of the collinear-type characteristics of the 3-D potential energy function for the $H + H_2$ system. Indeed, the rotational wave function of the diatom at large distances from the atom is $Y_{j_A m_{j_A}}(\gamma_A, \psi_A)$ before the collision and $Y_{j_A' m_{j_A'}}(\gamma_A', \psi_A')$ after the collision. These functions have nodal lines along the γ_A or γ_A' equal to 0 or π directions favored by the potential, unless the polarization quantum numbers vanish. This implies that the $m_{j_A} = m_{j_A'} = 0$ reaction cross sections should be larger than all others, in agreement with the calculation results. This can also be visualized classically by recalling that initially $\Omega = -m_j$, so that $m_j = 0$ implies (for nonzero j) that the axis of rotation is perpendicular to the direction of approach, as schematically indicated in Fig. 39. In this situation, twice during each diatom rotation the three atoms

go through a collinear configuration (for zero impact parameter). For $m_j \neq 0$ no collinear configurations are sampled. After the collision, $m'_j = \Omega'$ so that again only for $m'_j = 0$ can we have a postcollision collinear orientation.

As a consequence of this model, we would expect that integral reaction cross sections for which $m'_j = 0$ or $m_j = 0$ (but not both) should be significantly larger than those for which neither of these helicity polarization quantum numbers vanish. This is indeed the case (Schatz and Kuppermann, 1976c).

6. Reagent and Product Rotational State Distributions

The degeneracy-averaged integral reaction cross sections $Q_{c'j' \leftarrow c j}^R$ for $c = c' = 0$ depend both on the rotation states j of the reagents and j' of the products. In Figs. 40 and 41 we present surprisal-type plots of the product

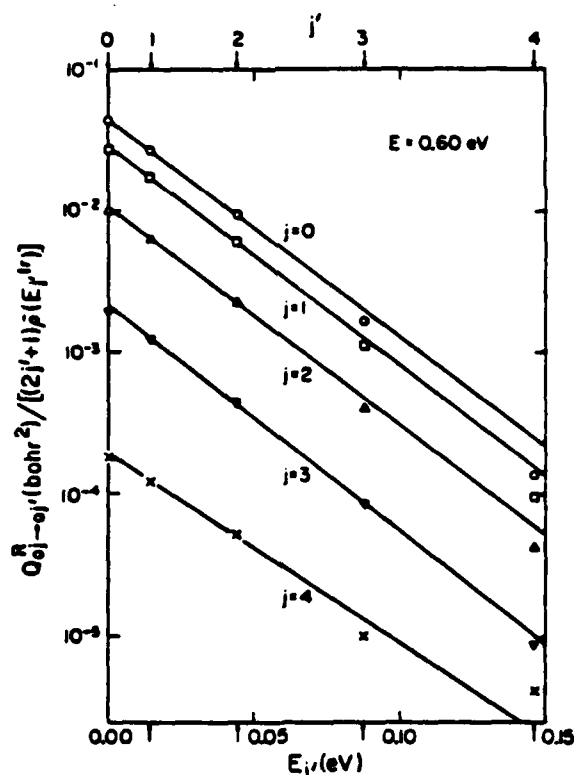


Fig. 40. Reactive degeneracy-averaged integral cross sections $Q_{0j' \leftarrow 0j}^R$ for the $H + H_2$ 3-PD exchange reaction divided by $(2j' + 1) \times \tilde{\rho}(E_f^{j'})$, as a function of the product rotational energy $E_{j'}$ and rotational quantum number j' at 0.60-eV total energy for initial rotational quantum numbers $j = 0-4$. $\tilde{\rho}(E_f^{j'})$ is a relative translational density of states which for $j' = 0$ equals 1.

rotational state distributions (Ben-Shaul *et al.*, 1972a,b; Levine and Kinsey, 1979). We see from Fig. 40 that at $E = 0.6$ eV and for low j the plots for each j are linear, and for the first four values of j they have the same slope. For $j = 0$ and E between 0.45 and 0.70 eV, Fig. 41 indicates a similar linear behavior, with the slopes of the surprisal plots depending on the total energy. Therefore, surprisal parameters are a useful compact way of describing the dependence of these reactive scattering cross sections on the rotational states of the reagents and products.

7. Interference Effects between Direct and Exchange Processes

According to Eq. (104), we expect to see interference effects between the nonreactive f^N and reactive f^R scattering amplitude contributions to the

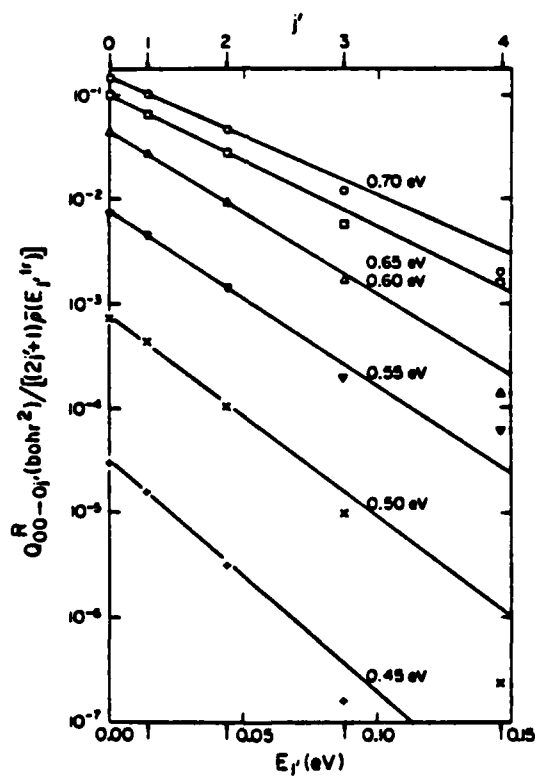


Fig. 41. Reactive degeneracy-averaged integral cross sections Q_{00-0j}^R for the $H + H_2$ 3-PD exchange reaction divided by $(2j + 1) \times \bar{\mu}(E_j^R)$ as a function of the product rotational energy E_j^R and rotational quantum number j at 0.45, 0.50, 0.55, 0.60, 0.65, and 0.70 eV total energy. $\bar{\mu}(E_j^R)$ has the same meaning as in Fig. 40.

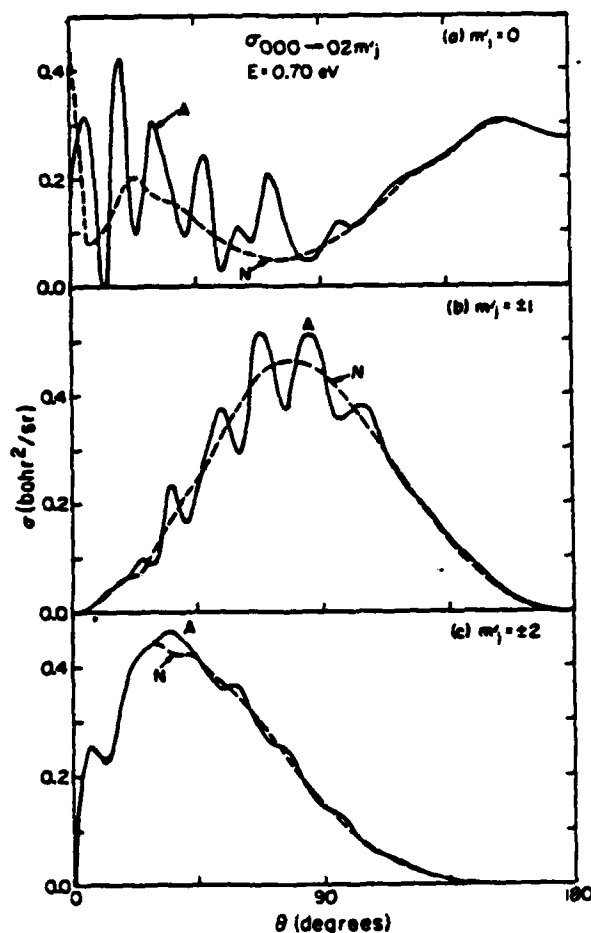


Fig. 42. Differential cross sections $\sigma_{000-02m_j}^A$ (solid lines labeled A) and $\sigma_{000-02m_j}^N$ (dashed lines labeled N) as a function of the scattering angle θ for (a) $m_j = 0$, (b) $m_j = \pm 1$, and (c) $m_j = \pm 2$ at $E = 0.70$ eV, for the $H + H_2$ 3-PD exchange reaction.

para \rightarrow para differential cross sections. This is displayed in Fig. 42 where we plot, as a function of scattering angle, the nonreactive and antisymmetrized differential cross sections $\sigma_{000-02m_j}$ at $E = 0.70$ eV, for m_j assuming all of its possible values. The oscillations in the antisymmetrized curves are due to the interference just mentioned. These oscillations are still present in the corresponding degeneracy-averaged differential cross section σ_{00-02}^A , as displayed in Fig. 43 where, for comparison purposes, the reactive cross section

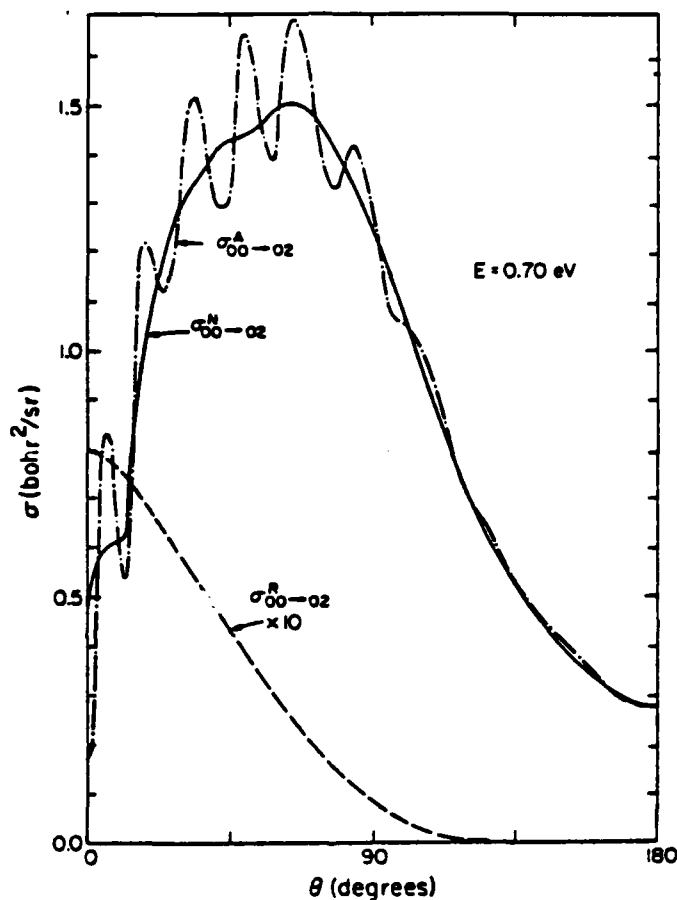


Fig. 43. Degeneracy-averaged $\sigma_{00 \rightarrow 02}^N$, $\sigma_{00 \rightarrow 02}^L$, and $\sigma_{00 \rightarrow 02}^L \times 10$ as a function of scattering angle θ at a total energy of 0.70 eV, corresponding to the state-to-state cross sections of Fig. 42.

$\sigma_{00 \rightarrow 02}^L$ is also shown. It is interesting to notice that these oscillations are quite pronounced even at scattering angles between 60° and 80° , in which range $\sigma_{00 \rightarrow 02}^L$ is about two orders of magnitude smaller than $\sigma_{00 \rightarrow 02}^N$. Although these indistinguishable-atom interference effects are known for the scattering of identical atoms, such as in He-He collisions, it is somewhat surprising that they should be so pronounced for the highly anisotropic reactive system considered, where averagings associated with partial-wave sums and reagent and product orientations might be expected to produce a significant attenuation of these oscillations.

8. Dynamic Feshbach Resonances

In Fig. 44 we display, as a function of total energy E and relative reagent translational energy E_0 , the distinguishable-atom reaction probabilities P_{00-0}^R and P_{00-1}^R for $J = 0$ (solid curves labeled 3D) (Schatz and Kuppermann, 1975). These are the sums of the 3-PD reaction probabilities $P_{000-0f_m}^R$ and $P_{000-1f_m}^R$, over all final product j' and m_j . The other curves, labeled 1D and 2D, are corresponding curves for collinear (1-PD) and coplanar (2-PD) reactions, and are given for comparison purposes. The potential energy surface used was that of Porter and Karplus (1964). The oscillation centered at a total energy of 0.97 eV in the 3D curve is due to a dynamic Feshbach resonance, and involves a quantum interference between a direct reaction mechanism and a compound state one, in which the energy is temporarily trapped in internal degrees of freedom of the system (Schatz and Kuppermann, 1973, 1975).

The nature of these degrees of freedom was discussed in Section III.F.3. We see that an energy shift of about 0.05 eV occurs in the position of the resonance in going from 1-PD to 2-PD and again in going from 2-PD to 3-PD. This shift can be rationalized as arising from the zero-point energy of about 0.06 eV of the bending mode of the saddle-point configuration of the potential energy surface. In the coplanar case the shift is approximately equal to that zero-point energy. In the 3-PD case, this bending mode is doubly degenerate, so that an additional amount of zero-point energy is required. This suggests how the position of 1-PD resonances can be used to predict where the 3-PD resonances should lie for collinearly dominated reactions.

Estimates of the energy dependence of the integral cross section for the reaction from the ground rotational-vibrational state of the reagent to the first vibrationally excited state of the product, for 3-PD collisions, is similar to that of the corresponding $J = 0$ reaction probability, depicted in the lower panel of Fig. 44, and has a peak value of 0.05 bohr². Therefore, the partial-wave and product rotational state sums involved in the calculation of this cross section do not wash out the resonances obtained for the collinear system, at least for the present collinearly dominated reaction. We therefore expect this resonance to exist in the real world.

Both coplanar and 3-PD calculations indicate that the resonance has a significant effect only on the $J = 0-7$ partial waves, whereas away from the resonance but at energies close to it nonnegligible reaction probabilities occur for the wider $J = 0-17$ range. Therefore, at the resonance energy, one should expect oscillations to develop in the angular dependence of the reactive differential cross section. The reason is that as pointed out in Section III.E, the individual partial-wave contributions to the scattering amplitudes are highly oscillatory in nature, and fairly slight calculational inaccuracies

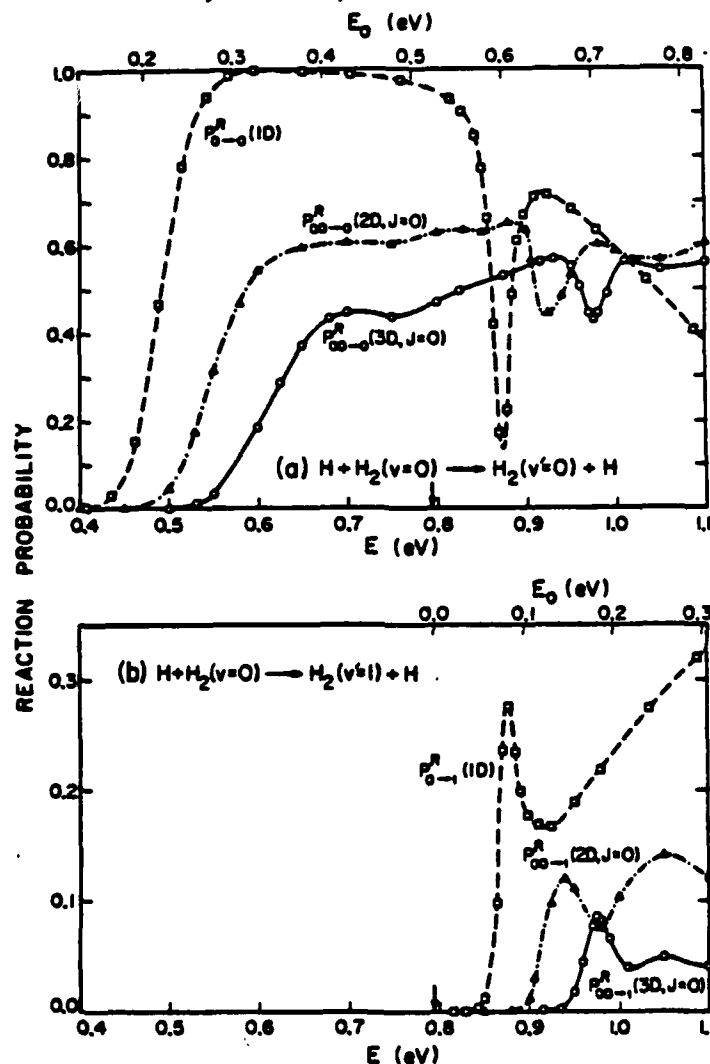


Fig. 44. Collinear (1D), coplanar (2D), and three-dimensional (3D) reaction probabilities for the $\text{H} + \text{H}_2$ exchange reaction as a function of the total energy E and relative translational energy E_0 . $P_{0 \rightarrow 0}^R$ and $P_{0 \rightarrow 1}^R$ are the collinear reaction probabilities from $n=0$ of the reagent H_2 to $n'=0$ and $n'=1$, respectively, of the product H_2 . $P_{0 \rightarrow 0}^R$ and $P_{0 \rightarrow 1}^R$ are the 2D or 3D (as specified) reaction probabilities for the total angular momentum $J=0$ partial wave from $n=0$, $j=0$ of the reagent H_2 to $n'=0$ and $n'=1$, respectively, of the product H_2 summed over all product rotational states within a given vibrational manifold. Panel (a) curves depict vibrationally elastic reaction probabilities, whereas panel (b) curves depict vibrationally inelastic ones. Arrows in abscissa indicate the energy at which the $n=1$ state of H_2 becomes accessible.

in the elements of the scattering matrix for one partial wave are usually enough to upset the delicate balance between partial waves, which leads to nonoscillatory differential cross sections, thereby resulting in strong spurious oscillations. It is reasonable to expect that the presence of resonances in some of the partial waves that contribute significantly to the cross sections should have a similar effect, as is experimentally observed for inelastic electron scattering (Erhardt, 1969). This argument, developed for distinguishable-atom cross sections, retains its validity for indistinguishable-atom para \rightarrow ortho channels.

9. Relation between Collinear, Coplanar, and Three-Dimensional Results

Since the $H + H_2$ 3-PD reaction is collinearly dominated, i.e., $V(R, r, \gamma)$ has a deep minimum with respect to γ at $\gamma = 0, \pi$, it might be expected that the results for the collinear and 3-PD systems are related. Furthermore, since both the coplanar (2-PD) and 3-PD systems feel the entire $V(R, r, \gamma)$ potential energy function, they should also be related. For these reasons, we now compare the results of these three calculations. This is done in Fig. 45, where we plot, as a function of total energy E and translational energy E_0 , the total reaction probabilities from the ground vibrational (and rotational, for the 2-PD and 3-PD cases) state of the reagents to all accessible states of the products (for $J = 0$ in the 2-PD and 3-PD cases). The figure indicates a surprisingly similar energy dependence over several orders of magnitude of these probabilities. There are, however, two important differences, both of which provide significant insight into the reactive collision dynamics. First, an energy shift approximately equal to the zero-point energy of the bending mode of the saddle-point region occurs, as it did for the resonance positions, in going from 1-PD to 2-PD to 3-PD. This indicates that the bending mode zero-point energy is not available to the reactive process. The second difference between the 1-PD, 2-PD, and 3-PD results lies in the probabilities at the first maximum, which occurs in the upper panel of Fig. 44. The collinear probability peaks near unity, whereas that of the coplanar levels off at about 0.6, and the 3-PD one roughly at 0.45. This behavior can be qualitatively understood if it is assumed that in both the 2-PD and 3-PD cases the probability of reaction, considered as a function of γ , is unity for $0 \leq \gamma \leq 54^\circ$ and $126 \leq \gamma \leq 180^\circ$ and vanishes otherwise (Schatz and Kuppermann, 1976a,c). This indicates that the 2-PD and 3-PD orientation dependence is probably quite similar with primarily dimensionality considerations responsible for the difference in reaction probabilities.

The 2-PD and 3-PD differential cross sections $\sigma_{00 \rightarrow 01}^A$ are plotted in Fig. 46, the corresponding ordinate scales being those at the right and the left, respectively. These scales were adjusted to bring the corresponding points

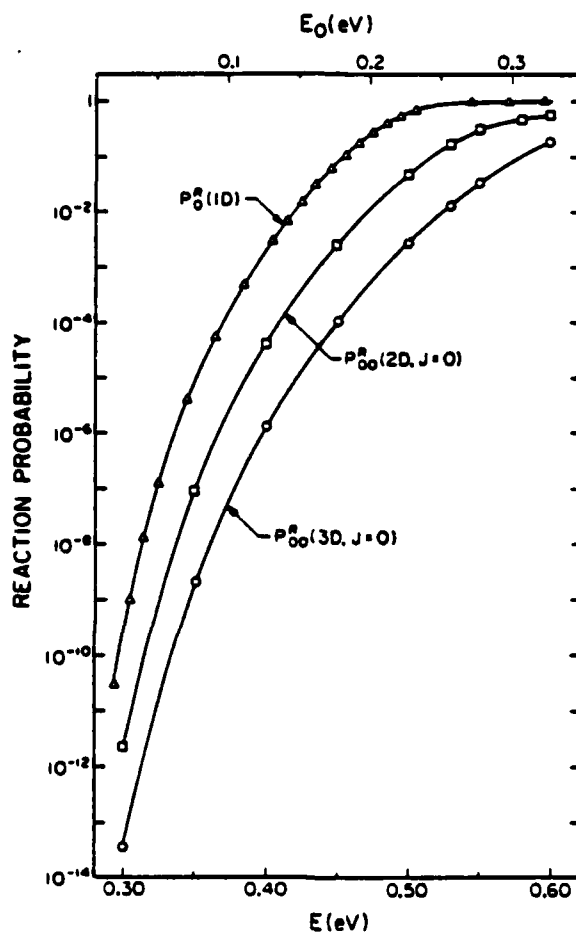


Fig. 45. One-, two-, and three-dimensional total reaction probabilities P_0^R (1D), P_{00}^R (2D, $J = 0$), and P_{00}^R (3D, $J = 0$), summed over all final states, as a function of the total energy E and initial relative translational energy E_0 , for the $H + H_2$ exchange reaction.

into approximate agreement at $\theta_R = 180^\circ$. The energy for the 2-PD curve is 0.55 eV, and that of the 3-PD curve, 0.60 eV so as to include the energy shift due to the bending energy. These two cross sections show a remarkably similar angular dependence over the entire range of scattering angles. A similar comparison at other energies in the 0.3–0.7 eV range leads to comparable agreement. This suggests that the 2-PD and 3-PD dynamics are quite similar and conversion of 2-PD to 3-PD results could prove to be an accurate approximate technique.

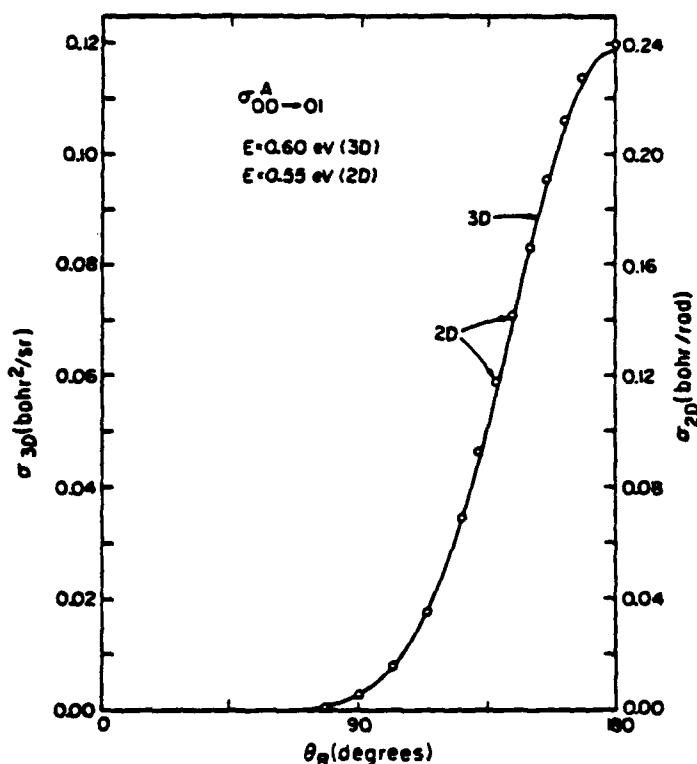


Fig. 46. Two- and three-dimensional cross sections $\sigma_{00 \rightarrow 01}^A$ (2D) and $\sigma_{00 \rightarrow 01}^A$ (3D) as a function of reactive scattering angle θ_R for the $H + H_2$ exchange reaction. The 3D cross section (solid curve), at 0.60-eV total energy, is referenced to the left-side ordinate scale, whereas the 2D result (circles) at 0.55 eV is referenced to the right-side scale.

10. Angular Momentum Decoupling Approximations

To perform 3-PD reactive-scattering quantum mechanical calculations requires a very considerable amount of computational effort. For example, for the $H + H_2$ system, which is ideally suited for such calculations, the amount of computation time on an IBM 370/158, for $J \geq 4$, was approximately 1 hr per value of J per energy, and the number of values of J to achieve convergence at $E = 0.6 \text{ eV}$ was about 15 for reactive cross sections and 35 for nonreactive inelastic cross sections. For other systems, involving more closely spaced vibrational-rotational levels, the number of coupled channels involved can be considerably larger, and the amount of computation time required increases approximately with the cube of such a number. Therefore,

except for a few carefully chosen benchmark systems, only approximate methods will be applicable using present-day computers or those likely to be developed within the next decade. As a result, it is important to test the validity of such approximate methods for the systems for which accurate calculations have been performed. So far, this includes only the $H + H_2$ system.

One approximate method that can be conceived of is the 2-PD to 3-PD conversion mentioned in the previous section. Another is based on the remarks about Eq. (110), made after Eq. (112). For reactive systems, the potential coupling terms $V_{j_A j_A}^{\Omega_A}$ in the former equation may be expected to be more important than the tumbling angular-momentum centrifugal coupling terms $r_{\Omega_A, \Omega_A \pm 1}^{j_A j_A}$. In order to test this assumption, calculations were made in which the latter terms were dropped (Kuppermann *et al.*, 1977). This approximation was implemented in two forms. In one, when linearly combining the λ -arrangement channel-wave functions $\psi_{j_A j_A}^{JM}$ generated by the solutions of the Ω_A -decoupled approximation to Eq. (110), in order to obtain solutions to the Schrödinger equation that are everywhere smoothly continuous, all Ω_A terms were included. This is called the *proper* decoupling scheme, and labeled PD. In the other, labeled SD for *simple* decoupling, only solutions of equal Ω were included in this smooth matching procedure.

In Figs. 47 and 48, we display the results of such calculations for reactive and nonreactive transitions. In both figures, the solid lines are the results of exact 3-PD calculations, the squares refer to the PD scheme, and the triangles to the SD scheme. In Fig. 47, the total energy was 0.6 eV, the open symbols represent the approximate nonreactive probabilities and the closed symbols represent the approximate reactive probabilities, all for the $000 \rightarrow 020$ distinguishable-atom process. It can be seen that the PD scheme is an excellent one for the reactive process, but rather poor for the nonreactive process. In Fig. 48, the distinguishable-atom integral reaction cross sections for the $000 \rightarrow 020$ (closed symbols) and $000 \rightarrow 010$ (open symbols) are given as a function of E_0 and E . Again it can be seen that the PD approximation is excellent, agreeing with the exact results to within 7.5% over the range of total energy of 0.45–0.65 eV. However, for reactive processes for which the condition $m_j' = m_j = 0$ is *not* fulfilled, the PD and SD probabilities can be in error by one or more orders of magnitude. For example, for the Ω -conserving $01-1 \rightarrow 011$ reactive process at $E = 0.6$ eV and $J = 5$, the ratio of the PD probability to the accurate one is 0.47×10^{-3} , and for the non- Ω -conserving $000 \rightarrow 011$ reactive process this ratio is 0.041. On the other hand, as seen in Section II.1.5, the reactive transitions $vjm_j \rightarrow v'j'm_j'$ for which $m_j' = m_j = 0$ are an order of magnitude or more intense than the reactive ones. Consequently, the corresponding summed and averaged integral reaction cross sections $Q_{0j-0j'}^R$ are still reasonably accurate for low j and j' .

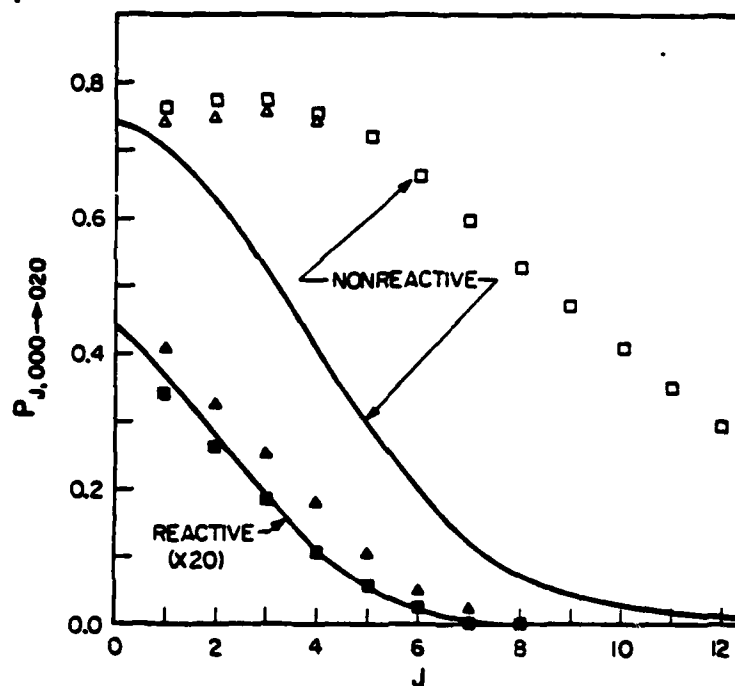


Fig. 47. Distinguishable-atom probabilities for the $000 \rightarrow 020$ transition as a function of total angular momentum quantum number J for reactive and nonreactive 3D collisions of H with H_2 at a total energy of 0.6 eV. The solid curves are accurate quantum calculations. The triangles correspond to the simple decoupling (SD) angular momentum scheme and the squares to the proper decoupling (PD) one.

Although for the nonreactive state-to-state $0jm_j \rightarrow 0j'm'_j$ transitions, these Ω -decoupling schemes, as shown in Fig. 47, give poor results, the corresponding summed and averaged integral cross sections are in very good agreement with the exact calculations, indicating that for a given j these approximations transfer nonreactive flux from $m_j \neq 0$ to $m_j = 0$.

We conclude that for the $H + H_2$ system, these Ω -angular momentum decoupling schemes are quite accurate approximate ways of calculating reactive and nonreactive summed and averaged integral reaction cross sections. In view of the large saving in computer time these approximations entail, they should permit approximate 3-PD quantum mechanical reactive scattering calculations to be performed for systems involving large numbers of channels. A first calculation of this type was recently performed by Redmon and Wyatt (1979) for the $F + H_2 \rightarrow FH + H$ reaction.

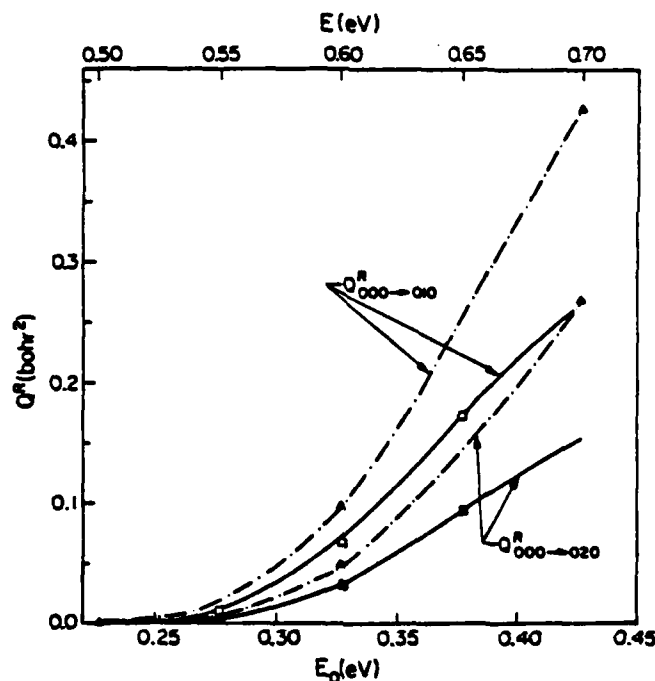


Fig. 48. Distinguishable-atom integral reaction cross sections for the $000 \rightarrow 020$ transitions as a function of initial relative translational energy E_0 and total energy E for 3D collisions of H with H_2 . The solid curves are accurate quantum calculations. The triangles (connected by dashed-dotted curves) correspond to the BS scheme and the squares to the PD scheme (see Fig. 47).

IV. General Systems and Processes

In Delves' scaled coordinates, the rotational invariance properties given by Eqs. (13) and (64) can be generalized to N -atom 3-PD systems. Therefore, the physical ideas and computational methodology developed for triatomic systems can be conceptually generalized to polyatomic systems without difficulty. This includes electronically nonadiabatic reactions, which can be described by a straightforward generalization of the formalism used in Section II.H, as well as dissociative and recombinative processes, as considered in Section II.I. In the latter case, the symmetrized hyperspherical coordinates introduced in Section III.B for triatomic systems and their generalization for polyatomic systems, are particularly useful. The difficulties in tackling such systems and processes of higher dimensionality and complexity is therefore not conceptual, but practical. The number of coupled-channel equations

needed becomes rapidly excessive not only for present-generation computers, but also for those of the imaginable future. However, once sufficiently accurate benchmark calculations are available for simple systems, they can be used to test the validity of the approximate reactive scattering methods currently in existence or being developed. The hope for the future is that reliable and highly efficient methods of this kind can be found and used with the formalism just outlined to provide a theoretical description and interpretation of such more complex systems and processes.

V. Conclusion

A detailed formulation of the quantum mechanical exchange reaction problem between an atom and a diatomic molecule has led to the development of accurate methods for obtaining ab initio cross sections for such reactions, and to their implementation for the $H + H_2$ three-dimensional system. The results of such calculations have provided a detailed understanding of the dynamics of this reaction and to the prediction of the existence of polarization propensity rules for collinearly dominated reactions as well as of the existence of a dynamic Feshbach resonance in this system. An angular momentum decoupling approximate scheme for solving the Schrödinger equation for this reaction has been tested and shown to lead to accurate results. The formalism has been extended to dissociative and many-body recombinative processes as well as to electronically non-adiabatic ones. This field is in its infancy, and substantial progress is expected in the future, leading to the development of reliable approximate methods capable of describing more complex systems and processes.

References

- Adams, J. T., Smith, R. L., and Hayes, E. F. (1974). *J. Chem. Phys.* 61, 2193-2199.
 Askar, A., Cakmak, A. S., and Rabitz, H. A. (1978). *Chem. Phys.* 33, 267-286.
 Baer, M. (1974a). *Mol. Phys.* 27, 1429-1435.
 Baer, M. (1974b). *J. Chem. Phys.* 60, 1057-1063.
 Baer, M., and Kouri, D. J. (1974). *Chem. Phys. Lett.* 24, 37-40.
 Baer, M., Halavee, V., and Persky, A. (1974). *J. Chem. Phys.* 61, 5122-5131.
 Ben-Shaul, A., Levine, R. D., and Bernstein, R. B. (1972a). *Chem. Phys. Lett.* 15, 160-164.
 Ben-Shaul, A., Levine, R. D., and Bernstein, R. B. (1972b). *J. Chem. Phys.* 57, 5427-5447. The function $\rho(E_j^*)$ used in the present Figs. 40 and 41 is equal to the translational density of states $\rho(E_j^*)$ of the products divided by that density at the translational energy $E - E^0$, where E^0 is the product zero point energy. E_j^* is the translational energy of the product in rotational state j and is equal to $E - E_j - E^0$, where E_j is the product rotational energy with respect to its own zero-point energy; for $j = 0$, $\beta \approx 1$.
 Blas, N. C., and Truhlar, D. G. (1973). *J. Chem. Phys.* 58, 1090-1108.
 Bowman, J. M. (1975). Ph.D. Thesis, California Institute of Technology, Pasadena.
 Bowman, J. M., and Kuppermann, A. (1973a). *Chem. Phys. Lett.* 19, 166-170.

AD-A130 160

THE QUANTUM DYNAMICS OF CHEMICAL REACTIONS(U)
CALIFORNIA INST OF TECH PASADENA DIV OF CHEMISTRY AND
CHEMICAL ENGINEERING A KUPPERMANN 31 MAR 83

6/8

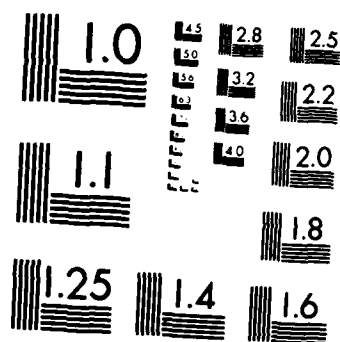
UNCLASSIFIED

AFOSR-TR-83-0565 AFOSR-81-0235

F/G 20/10

NL





MICROCOPY RESOLUTION TEST CHART
NATIONAL BUREAU OF STANDARDS 1963 A

- Bowman, J. M., and Kuppermann, A. (1973b). *J. Chem. Phys.* 59, 6524-6534.
- Bowman, J. M., Leasure, S. C., and Kuppermann, A. (1976). *Chem. Phys. Lett.* 43, 374-376.
- Connor, J. N. L., Jakubetz, W., and Manz, J. (1978). *Mol. Phys.* 35, 1301-1323.
- Davydov, A. S. (1965). "Quantum Mechanics" (D. ter Haar, transl.), Chapter VI. Addison-Wesley, Reading, Massachusetts.
- Delves, L. M. (1959). *Nucl. Phys.* 9, 391-399.
- Delves, L. M. (1960). *Nucl. Phys.* 20, 275-308.
- Diestler, D. J. (1971). *J. Chem. Phys.* 54, 4547-4553.
- Diestler, D. J., and McKoy, V. (1968). *J. Chem. Phys.* 48, 2951-2959.
- Ding, A., Kirsch, L., Perry, D., Polanyi, J. C., and Schreiber, J. (1973). *Discuss. Faraday Soc.* 55, 252-276.
- Dwyer, J. P. (1978). Ph.D. Thesis, California Institute of Technology, Pasadena.
- Elkowitz, A. B., and Wyatt, R. E. (1975a). *J. Chem. Phys.* 62, 2504-2506.
- Elkowitz, A. B., and Wyatt, R. E. (1975b). *J. Chem. Phys.* 63, 702-721.
- Erhardt, H. (1969). In "Physics of the One- and Two-Electron Atoms" (F. Bopp and H. Kleinpoppen, eds.), pp. 598-611. North-Holland Pub., Amsterdam.
- Eyring, H. (1935). *J. Chem. Phys.* 3, 107-115.
- Gordon, R. G. (1969). *J. Chem. Phys.* 51, 14-25.
- Jaffe, R. L., and Anderson, J. B. (1971). *J. Chem. Phys.* 54, 2224-2236.
- Jaffe, R. L., and Anderson, J. B. (1972). *J. Chem. Phys.* 56, 682.
- Jaffe, R. L., Henry, J. M., and Anderson, J. B. (1973). *J. Chem. Phys.* 59, 1128-1141.
- Johnson, B. R. (1972). *Chem. Phys. Lett.* 13, 172-175.
- Karplus, M., Porter, R. N., and Sharma, R. D. (1965). *J. Chem. Phys.* 43, 3259-3290.
- Kaye, J. A., and Kuppermann, A. (1981). *Chem. Phys. Lett.* (in press).
- Kompa, K. L., and Pimentel, G. C. (1967). *J. Chem. Phys.* 47, 857-858.
- Kuppermann, A. (1970). In "Proceedings of the Conference on Potential Energy Surfaces in Chemistry" (W. A. Lester, ed.), pp. 121-124. University of California, Santa Cruz.
- Kuppermann, A. (1972). *Proc. Int. Conf. Phys. Electron. At. Collisions, 7th, 1971*, pp. 3-5.
- Kuppermann, A. (1975). *Chem. Phys. Lett.* 32, 374-375.
- Kuppermann, A. (1979). *J. Phys. Chem.* 83, 171-187.
- Kuppermann, A. (1981). In "Potential Energy Surfaces and Dynamics Calculations" (D. G. Truhlar, ed.), Plenum Press, New York (in press).
- Kuppermann, A., and Schatz, G. C. (1975). *J. Chem. Phys.* 62, 2502-2504.
- Kuppermann, A., and Dwyer, J. P., (1979). *Abstr. Pap. Int. Conf. Phys. Electron., At. Collisions, 11th, 1979*, pp. 888-889.
- Kuppermann, A., Adams, J. T., and Truhlar, D. G. (1973). *Abstr. Pap. Int. Conf. Phys. Electron. At. Collisions, 8th, 1973*, pp. 149-150.
- Kuppermann, A., Schatz, G. C., and Baer, M. (1976). *J. Chem. Phys.* 65, 4596-4623.
- Kuppermann, A., Schatz, G. C., and Dwyer, J. P. (1977). *Chem. Phys. Lett.* 45, 71-73.
- Kuppermann, A., Kaye, J. A., and Dwyer, J. P. (1980). *Chem. Phys. Lett.* 74, 257-262.
- Lane, A. M., and Thomas, R. G. (1958). *Rev. Mod. Phys.* 30, 257-353. These authors use the term "collision matrix" and the symbol U to denote the scattering matrix S of the present chapter.
- Latham, S. L., McNutt, J. F., Wyatt, R. E. and Redman, M. J. (1978). *J. Chem. Phys.* 69, 3746-3755.
- Levine, R. D., and Kinsey, J. L. (1979). In "Atom-Molecule Collision Theory" (R. B. Bernstein, ed.), Chapter 22. Plenum, New York.
- Light, J. C. (1971). *Methods Comput. Phys.* 10, 111-143.
- Light, J. C., and Walker, R. B. (1976). *J. Chem. Phys.* 65, 4272-4282.
- McCullough, E. A., Jr., and Wyatt, R. E. (1969). *J. Chem. Phys.* 51, 1253-1254.
- McCullough, E. A., Jr., and Wyatt, R. E. (1971). *J. Chem. Phys.* 54, 3578-3591, 3592-3600.

- Miller, G., and Light, J. C. (1971). *J. Chem. Phys.* 54, 1635-1642, 1643-1651.
- Miller, W. H. (1970a). *J. Chem. Phys.* 53, 1949-1959; 3578-3587.
- Miller, W. H. (1970b). *Chem. Phys. Lett.* 7, 431-435.
- Miller, W. H., and George, T. F. (1972). *J. Chem. Phys.* 57, 2458-2467.
- Mortensen, E. M. (1968). *J. Chem. Phys.* 48, 4029-4039.
- Mortensen, E. M., and Gucwa, L. D. (1969). *J. Chem. Phys.* 51, 5695-5702.
- Mortensen, E. M., and Pitzer, K. S. (1962). *J. Chem. Soc., Spec. Publ.* 16, 57-75.
- Muckerman, J. T. (1971). *J. Chem. Phys.* 54, 1155-1164.
- Muckerman, J. T. (1972). *J. Chem. Phys.* 56, 2997-3006.
- Pack, R. T. (1974). *J. Chem. Phys.* 60, 633-639.
- Persky, A., and Baer, M. (1974). *J. Chem. Phys.* 60, 133-136.
- Polanyi, J. C., and Schreiber, J. L. (1977). *Faraday Discuss. Chem. Soc.* 62, 267-290.
- Polanyi, J. C., and Tardy, D. C. (1969). *J. Chem. Phys.* 51, 5717-5719.
- Porter, R. N., and Karplus, M. (1964). *J. Chem. Phys.* 40, 1105-1115.
- Rankin, C. C., and Light, J. C. (1969). *J. Chem. Phys.* 51, 1701-1719.
- Redmon, M. J., and Wyatt, R. E. (1979). *Chem. Phys. Lett.* 63, 209-216.
- Sams, W. M., and Kouri, D. J. (1969). *J. Chem. Phys.* 51, 4809-4814, 4815-4819.
- Schaefer, T. P., and Siska, P. E., Parson, J. M., Tully, F. P., Wong, Y. C., and Lee, Y. T. (1970). *J. Chem. Phys.* 53, 3385-3367.
- Schatz, G. C. (1976). Ph.D. Thesis, California Institute of Technology, Pasadena.
- Schatz, G. C., and Kuppermann, A. (1973). *J. Chem. Phys.* 59, 964-965.
- Schatz, G. C., and Kuppermann, A. (1975). *Phys. Rev. Lett.* 35, 1266-1269.
- Schatz, G. C., and Kuppermann, A. (1976a). *J. Chem. Phys.* 65, 4624-4641.
- Schatz, G. C., and Kuppermann, A. (1976b). *J. Chem. Phys.* 65, 4642-4667.
- Schatz, G. C., and Kuppermann, A. (1976c). *J. Chem. Phys.* 65, 4668-4692.
- Schatz, G. C., Bowman, J. M., and Kuppermann, A. (1973). *J. Chem. Phys.* 58, 4023-4025.
- Schatz, G. C., Bowman, J. M., and Kuppermann, A. (1975a). *J. Chem. Phys.* 63, 674-684.
- Schatz, G. C., Bowman, J. M., and Kuppermann, A. (1975b). *J. Chem. Phys.* 63, 685-696.
- Shavitt, I., Stevens, R. M., Minn, F. L. and Karplus, M. (1968). *J. Chem. Phys.* 48, 2700-2713; erratum (1968) 49, 4048-4056.
- Shipsey, E. J. (1973). *J. Chem. Phys.* 58, 232-236.
- Sparks, R. K., Hayden, C. C., Shobatake, K., Neumark, D. M. and Lee, Y. T. (1980). In "Horizons of Quantum Chemistry" (K. Fukui and B. Pullman, eds.), D. Reidel Publishing Company, Boston, pp. 91-105.
- Spencer, D. J., Jacobs, T. A., Mirels, H., and Gross, R. W. F. (1969). *Int. J. Chem. Kinet.* 1, 493-494.
- Sune, J. R., and Marcus, R. A. (1974). *Chem. Phys. Lett.* 29, 575-579.
- Truhlar, D. G. and Horowitz, C. G. (1978). *J. Chem. Phys.* 68, 2466-2476.
- Truhlar, D. G., and Kuppermann, A. (1970). *J. Chem. Phys.* 52, 3841-3843.
- Truhlar, D. G., and Kuppermann, A. (1972). *J. Chem. Phys.* 56, 2232-2252.
- Truhlar, D. G., Kuppermann, A., and Adams, J. T. (1973). *J. Chem. Phys.* 59, 395-402.
- Tully, J. C., and Preston, R. K. (1971). *J. Chem. Phys.* 55, 562-572.
- Walker, R. B., Light, J. C., and Altenberger-Siczek, A. (1976). *J. Chem. Phys.* 64, 1166-1181.
- Walker, R. B., Stechel, E. B. and Light, J. C. (1978). *J. Chem. Phys.* 69, 2922-2923.
- Whitlock, P. A., and Muckerman, J. T. (1975). *J. Chem. Phys.* 61, 4618-4629.
- Wilkins, R. L. (1972). *J. Chem. Phys.* 57, 912-917.
- Wilkins, R. L. (1973). *J. Phys. Chem.* 77, 3081-3084.
- Wu, S. F., and Levine, R. D. (1971). *Mol. Phys.* 22, 881-897.
- Wyatt, R. E. (1979). In "Atom-Molecule Collision Theory" (R. B. Bernstein, ed.), Chapter 17. Plenum, New York.

FEW BODY MOLECULAR COLLISIONS: THEORETICAL

Aron KUPPERMANN

Arthur Amos Noyes Laboratory of Chemical Physics, *
California Institute of Technology, Pasadena, California 91125

Abstract: This paper discusses the theory of atom-diatom exchange collisions without breakup. Methods involving a direct solution of the Schrödinger equation by accurate and approximate techniques are described. The main focus is on reactions on single electronically adiabatic potential energy surfaces, with some consideration given to two electronic state calculations.

1. Introduction

The only accurate three-dimensional (3D) quantum mechanical calculations of the cross sections of bimolecular chemical reactions performed so far have utilized coupled-channel techniques for solving the Schrödinger equation in configuration space. We will describe the nature of such methods as well as approximations derived from them. The paper by D. Micha, in this volume, will include the use of transition operator methods for dealing with these problems, including breakup processes. More comprehensive reviews have appeared recently¹⁻³⁾ or will appear soon.⁴⁾ Because of possible transferability to few-body nuclear problems, methodology rather than results will be emphasized.

2. Electronically adiabatic expansion

In view of the interdisciplinary nature of this Conference, and the diversity of nomenclature used by the different disciplines involved, we will first consider a general formulation of the molecular scattering problem in order to introduce the language and solution methodologies involved. Let us consider a general molecular system and denote by \underline{r} and \underline{R} the complete sets of spatial electronic and nuclear coordinates, respectively, needed to position these particles. We write the hamiltonian of the system as

$$H(\underline{r}, \underline{R}) = T^e(\underline{r}) + T^n(\underline{R}) + V(\underline{r}, \underline{R}), \quad (1)$$

where $T^e(\underline{r})$ and $T^n(\underline{R})$ are the electronic and nuclear kinetic energy operators, and $V(\underline{r}, \underline{R})$ denotes the coulombic interaction energy among all the molecular electrons and nuclei. Spin-spin and spin-orbit interactions are assumed to be small for the low atomic weight systems considered here and are omitted in Eq. (1). They can be included a posteriori by perturbative techniques. In what follows, electronic and nuclear spin appear only through the Pauli principle. We now define an electronic hamiltonian by

$$H^e(\underline{r}; \underline{R}) = T^e(\underline{r}) + V(\underline{r}, \underline{R}), \quad (2)$$

* Contribution No. 6301.

which differs from the total one of Eq. (1) only by the absence of the nuclear kinetic energy operator T^n . The electronically adiabatic Born-Oppenheimer wavefunctions $\phi_i^e(\underline{r}; \underline{R})$ are defined as the electronically bound eigenfunctions of H^e which satisfy the Pauli principle for the electrons:

$$H^e(\underline{r}; \underline{R}) \phi_i^e(\underline{r}; \underline{R}) = E_i^{ad}(\underline{R}) \phi_i^e(\underline{r}; \underline{R}) \quad (3)$$

The symbol i specifies the complete set of quantum numbers needed to define the electronic state of the system. The eigenvalues $E_i^{ad}(\underline{R})$ depend on that state and on the positions of the nuclei and constitute the electronically adiabatic potential energy (hyper) surfaces. The nature and properties of these surfaces and of their interactions determine the structural and dynamical properties of bound and unbound molecular systems and distinguish them from nuclear and elementary particle ones. The theoretical calculation of these surfaces is an important objective of the field of quantum chemistry,³⁾ but is outside the scope of this review.

We now expand the electronic-nuclear wavefunction $\psi(\underline{r}, \underline{R})$ in the Born-Oppenheimer states:

$$\psi(\underline{r}, \underline{R}) = \sum_i \psi_i^n(\underline{R}) \phi_i^e(\underline{r}; \underline{R}) \quad (4)$$

The $\psi_i^n(\underline{R})$ are nuclear wavefunctions that are independent of the electronic coordinates. Their determination can be achieved by replacement of this expansion into the Schrödinger equation, which leads to the coupled equations,

$$[T^n(\underline{R}) + E_i^{ad}(\underline{R})] \psi_i^n(\underline{R}) + \sum_{i'} [\langle \phi_i^e | T_n | \phi_{i'}^e \rangle + 2 \langle \phi_i^e | \underline{v}^n | \phi_{i'}^e \rangle \cdot \underline{p}_n] \psi_{i'}^n(\underline{R}) = E \psi_i^n(\underline{R}), \quad (5)$$

where \underline{v}^n and \underline{p}^n are the total nuclear velocity and momentum operators, respectively, and E the total system energy. In this expression, the sum over i' couples different electronically adiabatic states through the dependence of the Born-Oppenheimer electronic wavefunctions $\phi_i^e(\underline{r}; \underline{R})$ on the nuclear coordinates \underline{R} . The Born-Oppenheimer approximation is obtained by assuming that this sum can be neglected with respect to the other terms in Eq. (5):

$$H_i^n(\underline{R}) \psi_i^n(\underline{R}) = E \psi_i^n(\underline{R}), \quad (6)$$

where

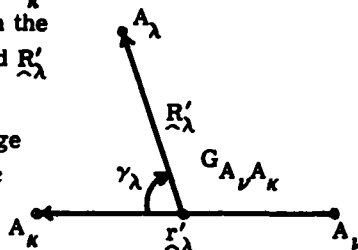
$$H_i^n(\underline{R}) = T^n(\underline{R}) + E_i^{ad}(\underline{R}) \quad (7)$$

is the effective nuclear hamiltonian and ψ_i^n is made to satisfy the Pauli principle for the exchange of identical nuclei. In this approximation, different electronic states do not couple with one another. It breaks down in regions of nuclear configuration space for which different potential energy surfaces approach one another or at high enough nuclear kinetic energies for the coupling terms to be non-negligible. Under these conditions, Eq. (5) rather than (6) must be used to solve the nuclear motion problem, with as many electronic states i' included as needed to appropriately describe the physical system under consideration.

The central goal in the scattering theory of molecular collisions is to obtain solutions to Eqs. (6) and (7) that satisfy the appropriate nuclear motion boundary conditions that characterize the physical process being considered. The rest of this paper is devoted to this topic.

3. The mapping of potential energy surfaces for triatomic systems

Consider a system of three nuclei A_λ , A_ν , A_κ and let $\underline{R}'_\lambda, \underline{r}'_\lambda$ be the position vectors indicated in the figure at the right. \underline{r}_λ is the A_ν to A_κ vector and \underline{R}'_λ that from the center of mass $G_{A_\nu A_\kappa}$ of those two particles to A_λ . γ_λ is the angle in the 0 to π range between those two vectors. Excluding the kinetic energy of the center of mass of the triatomic system, the nuclear motion hamiltonian of Eq. (7) is



$$H(\underline{R}'_\lambda, \underline{r}'_\lambda) = -\frac{\hbar^2}{2\mu_{\lambda, \nu\kappa}} \nabla_{\underline{R}'_\lambda}^2 - \frac{\hbar^2}{2\mu_{\nu\kappa}} \nabla_{\underline{r}'_\lambda}^2 + V(\underline{R}'_\lambda, \underline{r}'_\lambda, \gamma_\lambda) , \quad (8)$$

where $\mu_{\nu\kappa}$ and $\mu_{\lambda, \nu\kappa}$ are appropriate reduced masses and V is the electronically adiabatic potential energy surface E_i^{ad} . It is convenient to introduce the mass-scaled coordinates⁵⁾

$$\underline{R}_\lambda = a_\lambda \underline{R}'_\lambda \quad \underline{r}_\lambda = a_\lambda^{-1} \underline{r}'_\lambda \quad a_\lambda = (\mu_{\lambda, \nu\kappa} / \mu_{\nu\kappa})^{1/2} \quad (9)$$

in terms of which the nuclear hamiltonian becomes

$$H(\underline{R}_\lambda, \underline{r}_\lambda) = -\frac{\hbar^2}{2\mu} (\nabla_{\underline{R}_\lambda}^2 + \nabla_{\underline{r}_\lambda}^2) + V(\underline{R}_\lambda, \underline{r}_\lambda, \gamma_\lambda) , \quad (10)$$

and

$$\mu = [m_\lambda m_\nu m_\kappa / (m_\lambda + m_\nu + m_\kappa)]^{1/2} \quad (11)$$

is a mass that is unchanged if ν or κ coordinates are used instead of the λ ones. A $\lambda - \nu$ coordinate transformation is a rigid rotation in 6D configuration space.⁶⁾ In order to map the potential energy surface V , we define a 3D subspace of this configuration space by the spherical polar coordinates ρ , ω_λ , and γ_λ where ρ and ω_λ are defined by

$$\begin{aligned} \rho &= (R_\lambda^2 + r_\lambda^2)^{1/2} \\ \omega_\lambda &= 2 \tan^{-1}(r_\lambda / R_\lambda) \quad 0 \leq \omega_\lambda \leq \pi . \end{aligned} \quad (12)$$

The hyperspherical distance ρ is the same in ν and κ coordinates, and the factor 2 in the expression for the hyperangle ω_λ is chosen to establish a one-to-one correspondence between internal configurations of the triatomic system and points $P(\rho, \omega_\lambda, \gamma_\lambda)$ of the map.⁷⁾

A schematic map of a $V = \text{constant}$ surface in this 3D space is given in Fig. 1, for a system in which the three diatomics $A_\nu A_\kappa$, $A_\kappa A_\lambda$, and $A_\lambda A_\nu$ are stable. The three tubular regions along the axes labeled $Z_\lambda, Z_\nu, Z_\kappa$ represent those isolated diatoms. For a system for which only one of those diatoms exists, such as $\text{He} + \text{H}_2$ in its ground electronic state, only one such tube exists, as indicated schematically for the equipotential surface of Fig. 2. It is a useful property of the polar mapping described above that a $\rho, \omega_\lambda, \gamma_\lambda \rightarrow \rho, \omega_\nu, \gamma_\nu$ transformation is a rigid rotation in this 3D space around the Y_λ cartesian axis of this map.

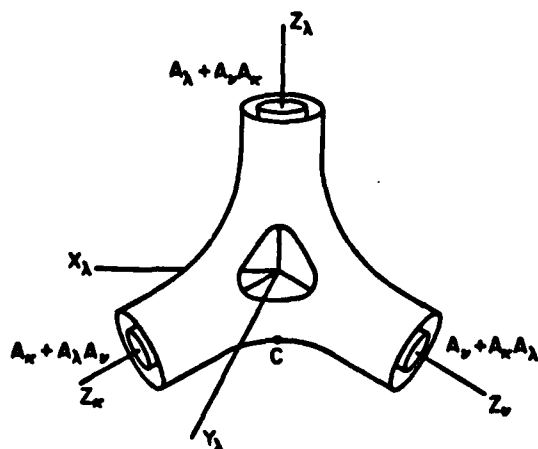


Fig. 1. Equipotential surface for an $A_\alpha A_\beta A_\gamma$ triatomic system for which molecules $A_\beta A_\gamma$, $A_\gamma A_\alpha$, and $A_\alpha A_\beta$ are stable.

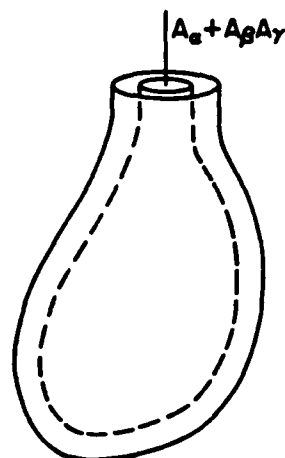


Fig. 2. Equipotential surface for an $A_\alpha A_\beta A_\gamma$ triatomic system for which $A_\beta A_\gamma$ is the only stable diatomic molecule.

The nature of the passageway between the separated atom-diatom channels in Fig. 1 or of the internal spacing between the two sheets of Fig. 2 guides the choice of coordinates, basis functions, and theoretical approaches to obtaining the scattering eigenfunctions of the hamiltonian of Eq. (10). A specific example of such a map of V is given in Fig. 3 for the ground state of the $H + H_2$ system.⁷⁾

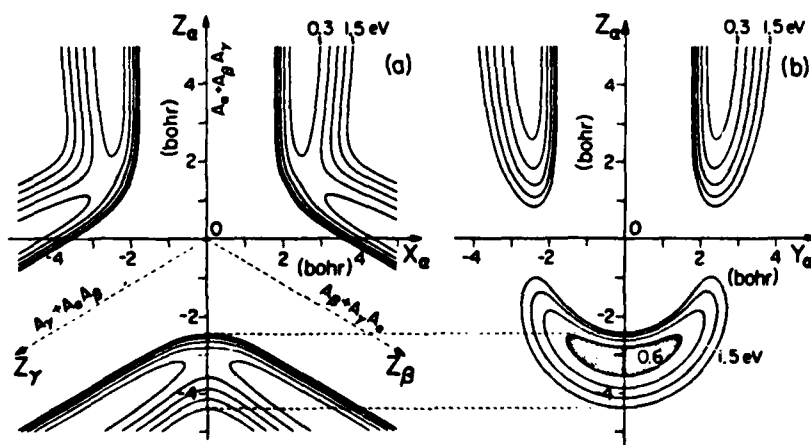


Fig. 3. Cuts of equipotential surfaces for H_3 . (a) Cut through $X_\alpha A_\alpha$ plane. (b) Cut through $Y_\alpha Z_\alpha$ plane.

The hatched enclosed area on the bottom of part (b) of that figure indicates the relatively narrow classically accessible passageway at a total energy of 0.6 eV (measured from the bottom of the isolated H_2 ground electronic state well) which connects the arrangement channels $A_\gamma + A_\alpha A_\beta$ and $A_\beta + A_\gamma A_\alpha$. An understanding of this internal topography is of primary importance for the development of practical accurate or approximate methods for solving the three-body quantum mechanical rearrangement scattering problem.

4. Scattering formalism in body-fixed coordinates

A convenient set of coordinates in which to describe the scattering problem is $R_\lambda, \theta_\lambda, \phi_\lambda, r_\lambda, \gamma_\lambda, \psi_\lambda$, where $R_\lambda, r_\lambda, \gamma_\lambda$ have been previously defined, $\theta_\lambda, \phi_\lambda$ are the Euler angles of R_λ in a laboratory-fixed frame, and ψ_λ is the angle between the R_λ, r_λ plane and the R_λ, z plane where z is a laboratory-fixed axis.

If the nuclear motion wavefunction is expanded in partial waves as

$$\psi(R_\lambda, r_\lambda) = \sum_{JM} C_{JM}^\lambda \psi_{JM}^\lambda \quad (13)$$

and the partial waves as

$$\psi_{JM}^\lambda(R_\lambda, r_\lambda, \gamma_\lambda, \theta_\lambda, \phi_\lambda, \psi_\lambda) = \sum_{\Omega_\lambda, j_\lambda} D_{M\Omega_\lambda}^J(\phi_\lambda, \theta_\lambda, 0) Y_{j_\lambda \Omega_\lambda}(\gamma_\lambda, \psi_\lambda) w_{j_\lambda \Omega_\lambda}^\lambda(R_\lambda, r_\lambda) \quad (14)$$

the distance-dependent functions w^λ can be shown to satisfy the coupled partial differential equations⁶⁾

$$\begin{aligned} t_{\Omega_\lambda, \Omega_\lambda-1}^{j_\lambda} w_{j_\lambda, \Omega_\lambda-1}^\lambda + t_{\Omega_\lambda, \Omega_\lambda}^{j_\lambda} w_{j_\lambda, \Omega_\lambda}^\lambda + t_{\Omega_\lambda, \Omega_\lambda+1}^{j_\lambda} w_{j_\lambda, \Omega_\lambda+1}^\lambda \\ + \sum_{j'_\lambda} V_{j_\lambda j'_\lambda}^{\lambda \Omega_\lambda} w_{j'_\lambda, \Omega_\lambda}^\lambda = E w_{j_\lambda, \Omega_\lambda}^\lambda, \end{aligned} \quad (15)$$

where

$$\begin{aligned} t_{\Omega_\lambda, \Omega_\lambda}^{j_\lambda}(R_\lambda, r_\lambda) = -\frac{\hbar^2}{2\mu} \left(\frac{1}{R_\lambda} \frac{\partial^2}{\partial R_\lambda^2} R_\lambda + \frac{1}{r_\lambda} \frac{\partial^2}{\partial r_\lambda^2} r_\lambda \right) + \frac{j_\lambda(j_\lambda+1)\hbar^2}{2\mu R_\lambda^2} \\ + \frac{\hbar^2}{2\mu R_\lambda^2} [J(J+1) - 2\Omega_\lambda^2 + j_\lambda(j_\lambda+1)] \end{aligned} \quad (16)$$

$$t_{\Omega_\lambda, \Omega_\lambda \pm 1}^{j_\lambda}(R_\lambda) = -\frac{\hbar^2}{2\mu R_\lambda^2} [J(J+1) - \Omega_\lambda(\Omega_\lambda+1)]^{\frac{1}{2}} [j_\lambda(j_\lambda+1) - \Omega_\lambda(\Omega_\lambda \pm 1)]^{\frac{1}{2}} \quad (17)$$

$$V_{j_\lambda j'_\lambda}^{\lambda \Omega_\lambda}(R_\lambda, r_\lambda) = \langle Y_{j_\lambda \Omega_\lambda}(\gamma_\lambda, \psi_\lambda) | V | Y_{j'_\lambda \Omega_\lambda}(\gamma_\lambda, \psi_\lambda) \rangle. \quad (18)$$

The only terms that couple Ω_λ , the quantum number of the component of total

angular momentum in the \hat{R}_λ direction, are those in the tumbling motion operators $t_{\Omega_\lambda, \Omega_\lambda \pm 1}^{J_\lambda}$ which, for many exchange reactions, are small. Their neglect

leads to the angular momentum decoupling approximations described in Sec. 5.

Equation (15) may be solved numerically by expansion in local vibrational eigenfunctions, with different coordinates used in different regions of R_λ, r_λ configuration space.⁹ Natural collision coordinates (NCC) can be used instead of $R_\lambda, r_\lambda, \gamma_\lambda$,^{9,10} as well as hindered rotor basis sets for that expansion.⁹

These NCC involve a translation coordinate, a vibration coordinate, and a bending angle between the \hat{r}_λ and \hat{r}_ν vectors. Integration of the coupled ordinary differential equations resulting from Eq. (15) or their analogs in different tubular regions of the 3D internal configuration space requires matching on appropriately chosen separation surfaces between those regions such as planes⁹ or more complicated surfaces.¹⁰ Once smoothly continuous solutions of the nuclear motion Schrödinger equation, valid everywhere in configuration space, are thereby determined, the scattering matrix is obtained and from it the desired cross sections.⁹⁻¹⁰ The Pauli principle for exchange of identical nuclei is imposed by post-antisymmetrization techniques.

The only accurate quantum mechanical 3D exchange reaction calculations performed so far are for the $H + H_2$ system. Two of these calculations agree quite well.^{9,10} The third one⁹ gives slightly different transition probabilities and integral cross sections, due in part to the use of a slightly different potential energy surface and in part to incomplete convergence. Only one of these calculations⁹ was performed for sufficient partial waves to a sufficient degree of convergence of both the magnitudes and the phases of the scattering matrix elements to yield accurate angular distributions.

5. Approximate methods

The methods described above will probably be able to generate accurate results for only a relatively small number of benchmark systems because of the extensive amount of computation involved. Approximate methods for solving the Schrödinger equation that do not introduce major distortions in the nature of the results will play a central role in the future of chemical dynamics. A few of these methods are discussed below.

5.1 ANGULAR MOMENTUM DECOUPLING APPROXIMATIONS

In these approximations, the $t_{\Omega_\lambda, \Omega_\lambda \pm 1}^{J_\lambda}$ terms in Eq. (15), or their counterparts in formulations using other systems of coordinates are neglected. This produces a high degree of decoupling of the equations, which greatly simplifies the calculations. Further approximations in the angular momentum part of $t_{\Omega_\lambda, \Omega_\lambda}^{J_\lambda}$ [see Eq. (16)] are usually also introduced.^{11,12}

Wyatt and co-workers decoupled the component of total angular momentum along a body-fixed axis which goes smoothly from reactants to products, for the $H + H_2$ ¹³ and $F + H_2$ ¹⁴ systems. Kuppermann and co-workers¹⁵ decoupled the component of total angular momentum on the relative approach vector in each of the three arrangement channel regions of the $H + H_2$ system and matched the solutions on separation planes. The state-to-state reactive scattering results are accurate to better than 10% for $H + H_2$. Kouri and co-workers¹⁶ use the infinite order-sudden approximation and a simple approach to transform from one arrangement channel to another. The state-to-state cross sections may be off by orders of magnitude, but average values are nevertheless quantitatively correct.

5.2 DISTORTED WAVE BORN APPROXIMATION

This approach was first introduced by Micha¹⁷⁾ and applied since in several versions by several workers.¹⁸⁻²¹⁾ If adiabatically distorted internal states are used, the method seems to work well at low collision energies.

5.3 SEMI-CLASSICAL AND CLASSICAL APPROXIMATIONS

The semi-classical methods were introduced by Miller²²⁾ and by Marcus²³⁾ in the early 1970's, and have been reviewed recently.^{1,24)} They work well for collinear collisions, but do not furnish long-lived resonances without major effort. To produce tunnelling effects, complex momentum or time is required. They are difficult to apply to 3D reactive systems and their use has been limited. The quasi-classical trajectory approximation,²⁵⁾ on the other hand, has been extensively used²⁾ and gives qualitatively correct results away from threshold.⁶⁾

5.4 COLLINEAR APPROXIMATION³⁾

By confining the three atoms to a space-fixed straight line, configuration space is reduced from six-dimensional to two-dimensional. For "collinearly dominated" potential energy surfaces (i.e., those that have a pronounced minimum for collinear configurations), this approach gives the correct qualitative dependence of reaction probabilities on reagent energy.⁶⁾ It also serves as a testing ground for approximate methods for solving two-dimensional problems, which can then be extended to six-dimensional ones.

6. Calculations for systems leading to changes in electronic state

In chemiluminescent reactions and, in many cases, ion-molecule reactions, the products can be on a different electronic potential energy surface than the reagents, implying a breakdown of the Born-Oppenheimer approximation. In order to perform calculations on such systems, at least two potential energy surfaces and their couplings must be used. This has been done for a few model collinear systems, among which are the $\text{Ba} + \text{N}_2\text{O} \rightarrow \text{BaO}^* + \text{N}_2$,²⁶⁾ $\text{H}^+ + \text{H}_2 \rightarrow \text{H}_2^+ + \text{H}$,²⁷⁾ and $\text{Ar}^+ + \text{H}_2 \rightarrow \text{ArH}^+ + \text{H}$ ²⁸⁾ reactions. The position of the seam between the surfaces greatly influences the probability of forming excited state products.²⁹⁾

This work was supported in part by a contract (No. F49620-79-C-0187) from the U. S. Air Force Office of Scientific Research.

REFERENCES

- 1) Dynamics of molecular collisions, ed. W. H. Miller (Plenum Press, New York, 1976)
- 2) Atom-molecule collision theory, ed. R. B. Bernstein (Plenum Press, New York, 1979)
- 3) J. N. L. Connor, Computer Phys. Comm. 17 (1979) 117
- 4) R. B. Walker and J. C. Light, Ann. Rev. Phys. Chem. (1981) in press
- 5) L. M. Delves, Nucl. Phys. 9 (1959) 391; 20 (1960) 275
- 6) A. Kuppermann, G. C. Schatz and M. Baer, J. Chem. Phys. 65 (1976) 4596
- 7) A. Kuppermann, Chem. Phys. Lett. 32 (1975) 374
- 8) G. C. Schatz and A. Kuppermann, J. Chem. Phys. 62 (1975) 2502; 65 (1976) 4642, 4668
- 9) A. B. Elkowitz and R. E. Wyatt, J. Chem. Phys. 62 (1975) 2504
- 10) R. B. Walker, E. B. Stechel and J. C. Light, J. Chem. Phys. 69 (1978) 2922
- 11) R. T Pack, J. Chem. Phys. 60 (1974) 633

- 12) P. McGuire and D. J. Kouri, J. Chem. Phys. 60 (1974) 2488
- 13) A. B. Elkowitz and R. E. Wyatt, Mol. Phys. 31 (1976) 189
- 14) M. J. Redmon and R. E. Wyatt, Chem. Phys. Lett. 63 (1979) 209
- 15) A. Kuppermann, G. C. Schatz and J. P. Dwyer, Chem. Phys. Lett. 45 (1977) 71
- 16) V. Khare, D. J. Kouri and M. Baer, J. Chem. Phys. 71 (1979) 1188; (1980) in press
- 17) D. A. Micha, Ark. Fys. 20 (1965) 425
- 18) M. Karplus and K. T. Tang, Discuss. Faraday Soc. 44 (1967) 56
- 19) B. H. Choi and K. T. Tang, J. Chem. Phys. 61 (1974) 5147; 65 (1976) 5161
- 20) Y. Y. Yung, B. H. Choi and K. T. Tang, J. Chem. Phys. 72 (1980) 621
- 21) D. C. Clary and J. N. L. Connor, Chem. Phys. Lett. 66 (1979) 493
- 22) W. H. Miller, J. Chem. Phys. 53 (1970) 3578
- 23) R. A. Marcus, J. Chem. Phys. 54 (1971) 3965
- 24) W. H. Miller, Adv. Chem. Phys. 30 (1975) 77
- 25) M. Karplus, R. N. Porter and R. D. Sharma, J. Chem. Phys. 43 (1965) 3259
- 26) J. M. Bowman, S. C. Leasure and A. Kuppermann, Chem. Phys. Lett. 43 (1976) 374
- 27) Z. H. Top and M. Baer, Chem. Phys. 25 (1977) 1
- 28) M. Baer and J. A. Beswick, Phys. Rev. A 19 (1979) 1559

END

FILMED

8-83

DTIC